

**Shielding Aspects of Accelerators, Targets  
and Irradiation Facilities – SATIF-8**

*Proceedings of the 8<sup>th</sup> Meeting*

22-24 May 2006  
Pohang Accelerator Laboratory (PAL)  
Nam-Gu Pohang, Gyongbuk  
Republic of Korea

© OECD 2010

**NUCLEAR ENERGY AGENCY**  
**Organisation for Economic Co-operation and Development**

## ORGANISATION FOR ECONOMIC CO-OPERATION AND DEVELOPMENT

The OECD is a unique forum where the governments of 30 democracies work together to address the economic, social and environmental challenges of globalisation. The OECD is also at the forefront of efforts to understand and to help governments respond to new developments and concerns, such as corporate governance, the information economy and the challenges of an ageing population. The Organisation provides a setting where governments can compare policy experiences, seek answers to common problems, identify good practice and work to co-ordinate domestic and international policies.

The OECD member countries are: Australia, Austria, Belgium, Canada, the Czech Republic, Denmark, Finland, France, Germany, Greece, Hungary, Iceland, Ireland, Italy, Japan, Korea, Luxembourg, Mexico, the Netherlands, New Zealand, Norway, Poland, Portugal, the Slovak Republic, Spain, Sweden, Switzerland, Turkey, the United Kingdom and the United States. The Commission of the European Communities takes part in the work of the OECD.

OECD Publishing disseminates widely the results of the Organisation's statistics gathering and research on economic, social and environmental issues, as well as the conventions, guidelines and standards agreed by its members.

*This work is published on the responsibility of the Secretary-General of the OECD. The opinions expressed and arguments employed herein do not necessarily reflect the official views of the Organisation or of the governments of its member countries.*

## NUCLEAR ENERGY AGENCY

The OECD Nuclear Energy Agency (NEA) was established on 1st February 1958 under the name of the OEEC European Nuclear Energy Agency. It received its present designation on 20th April 1972, when Japan became its first non-European full member. NEA membership today consists of 28 OECD member countries: Australia, Austria, Belgium, Canada, the Czech Republic, Denmark, Finland, France, Germany, Greece, Hungary, Iceland, Ireland, Italy, Japan, Luxembourg, Mexico, the Netherlands, Norway, Portugal, Republic of Korea, the Slovak Republic, Spain, Sweden, Switzerland, Turkey, the United Kingdom and the United States. The Commission of the European Communities also takes part in the work of the Agency.

The mission of the NEA is:

- to assist its member countries in maintaining and further developing, through international co-operation, the scientific, technological and legal bases required for a safe, environmentally friendly and economical use of nuclear energy for peaceful purposes, as well as
- to provide authoritative assessments and to forge common understandings on key issues, as input to government decisions on nuclear energy policy and to broader OECD policy analyses in areas such as energy and sustainable development.

Specific areas of competence of the NEA include safety and regulation of nuclear activities, radioactive waste management, radiological protection, nuclear science, economic and technical analyses of the nuclear fuel cycle, nuclear law and liability, and public information.

The NEA Data Bank provides nuclear data and computer program services for participating countries. In these and related tasks, the NEA works in close collaboration with the International Atomic Energy Agency in Vienna, with which it has a Co-operation Agreement, as well as with other international organisations in the nuclear field.

Corrigenda to OECD publications may be found on line at: [www.oecd.org/publishing/corrigenda](http://www.oecd.org/publishing/corrigenda).

© OECD 2010

You can copy, download or print OECD content for your own use, and you can include excerpts from OECD publications, databases and multimedia products in your own documents, presentations, blogs, websites and teaching materials, provided that suitable acknowledgment of OECD as source and copyright owner is given. All requests for public or commercial use and translation rights should be submitted to [rights@oecd.org](mailto:rights@oecd.org). Requests for permission to photocopy portions of this material for public or commercial use shall be addressed directly to the Copyright Clearance Center (CCC) at [info@copyright.com](mailto:info@copyright.com) or the Centre français d'exploitation du droit de copie (CFC) contact@[cfcopies.com](http://cfcopies.com).

## Foreword

Nuclear energy covers a field much wider than nuclear power. In fact, atomic and nuclear energy applications involve a large range of scientific and technological activities using a variety of machines and analysis techniques. Activities in this area have increased over the years and consequently the OECD/NEA Nuclear Science Committee is sponsoring more activities in this domain.

One of these activities concerns “Shielding Aspects of Accelerators, Targets and Irradiation Facilities” (SATIF). A series of workshops has been held during the last decade: SATIF-1 was held on 28-29 April 1994 in Arlington, Texas; SATIF-2 on 12-13 October 1995 at CERN in Geneva, Switzerland; SATIF-3 on 12-13 May 1997 at Tohoku University in Sendai, Japan; SATIF-4 on 17-18 September 1998 in Knoxville, Tennessee, United States; SATIF-5 on 17-21 July 2000 at OECD in Paris, France, SATIF-6 on 10-12 April 2002 at the Stanford Linear Accelerator Center (SLAC), Menlo Park, California, United States; SATIF-7 on 17-18 May 2004 at ITN, Sacavém, Portugal; and SATIF-8 was held on 22-24 May 2006 at the Pohang Accelerator Laboratory (PAL) POSTECH, Republic of Korea. SATIF-9 is scheduled for 2009 at the Spallation Neutron Source ORNL, Oak Ridge, TN, United States.

Each workshop is hosted by organisations having accelerator facilities and experts that enhance the interaction between local expertise and experts from the international community. SATIF-8 was held at the Pohang Accelerator Laboratory (PAL) POSTECH and the chairman of the workshop, H.S. Lee, arranged visits to their facilities.

This event was jointly organised by the:

- OECD Nuclear Energy Agency;
- Pohang Accelerator Laboratory (PAL);
- Radiation Safety Information Computational Center (RSICC);
- Shielding Working Group of the Reactor Physics Committee of Japan.

The current proceedings provide a summary of the discussions, decisions and conclusions together with the text of the presentations made at the eighth SATIF meeting.

This text is published on the responsibility of the Secretary-General of the OECD. The views expressed do not necessarily correspond to those of the national authorities concerned.

### ***Acknowledgements***

Acknowledgements are due to the members of the SATIF-8 Technical Programme Committee and in particular to H-S. Lee, chairman of the workshop, for their contribution in shaping the technical programme, and to all participants who contributed the valuable work and ideas described in these proceedings.



## Table of contents

Foreword.....		3
Executive summary .....		9
<b>Introduction</b> .....		<b>13</b>
<b>Chair: H.S. Lee</b>		
<i>T. Nakamura, L. Heilbronn</i>		
Introduction to “Handbook on Secondary Particle Production and Transport by High Energy Heavy Ions” .....		
		15
<i>Y. Sakamoto, O. Sato, H. Hirayama</i>		
Standard data of dose conversion coefficients in Japan.....		
		25
<i>A. Leuschner, A. Klett</i>		
A new method for pulsed neutron monitoring with the rem-counter LB 6411 and time-resolved readout.....		
		35
<b>Session I</b>	<b>Source term and related topics</b> .....	<b>43</b>
<b>Chair: S. Teichmann</b>		
<i>S. Teichmann</i>		
Shielding parameters of concrete and polyethylene for the PSI proton accelerator facilities .....		
		45
<i>B-H. Kim, H-K. Kim, S-W. Kwak, H-S. Lee</i>		
Calculation of the neutron spectra at the electron test linac of PAL and the MC50 proton accelerator of KIRAMS.....		
		55
<i>X.S. Mao, W.R. Nelson, A.A. Prinz</i>		
Comparison between the source terms used in SHIELD11 and the source terms calculated by FLUKA.....		
		65
<i>T. Sanami, M. Hagiwara, T. Oishi, S. Kamada, T. Okuji, M. Baba, M. Takada, N. Miyahara, H. Nakashima, Y. Iwamoto, S. Tanaka, T. Kaneko</i>		
Double differential cross-section of fragment production by tens of MeV protons and neutrons.....		
		67
<b>Session II</b>	<b>Shielding at high energy accelerators</b> .....	<b>77</b>
<b>Chair: T. Nakamura</b>		
<i>H. Nakashima, T. Shibata, Y. Nakane, F. Masukawa, N. Matsuda, Y. Iwamoto, M. Harada, S. Meigo, Y. Kasugai, F. Maekawa, H. Takada, C. Konno, M. Teshigawara, M. Ohi, T. Kai, H. Hirayama, T. Suzuki, T. Miura, M. Numajiri, N. Nakao</i>		
Radiation shielding design for the J-PARC project .....		
		79
<i>Y. Uwamino, N. Fukunishi, H. Sakamoto, S. Fujita</i>		
Safety design of the Radioactive Isotope Beam Factory (RIBF) at RIKEN .....		
		89
<i>A. Knapp, T. Radon, G. Moustafina, F. Gutermuth, G. Fehrenbacher</i>		
Monte Carlo simulations for the shielding of FLAIR .....		
		97
<i>M. Felcini, A. Herrera-Martínez, Y. Kadi, T. Otto, L. Tecchio</i>		
Design of the EURISOL multi-MW target assembly: Radiation and safety issues.....		
		105

	V. Vlachoudis, A. Ferrari, M. Magistris, M. Santana-Leitner Overview of the protection and shielding studies for the betatron cleaning insertion at LHC .....	115
<b>Session III</b>	<b>Induced radioactivity and activation data</b> .....	<b>123</b>
	<b>Chair: M. Silari</b>	
	M. Brugger, A. Ferrari, M. Magistris, S. Roesler, J. Vollaire Calculation of radioactive isotope production cross-sections with FLUKA and their application to radiological studies .....	125
	M.U. Khandaker, K. Kim, G. Kim, Y.S. Lee Experimental studies of proton-induced reaction cross-sections on natural molybdenum.....	145
	R. Qiu, H-S. Lee, S. Hong, J. Li Simulation and measurements of induced radioactivity in permanent magnet .....	153
	H. Matsumura, N. Nakao, K. Masumoto, K. Oishi, M. Kawai, T. Aze, A. Toyoda, M. Numajiri, K. Takahashi, M. Fujimura, Q. Wang, K. Bessho, T. Sanami Production yields of the radionuclides induced in various targets fixed in concrete shield at the 500-MeV neutron irradiation facility of KENS .....	161
	J-C. David, A. Boudard, S. Lemaire, S. Leray, S. Panebianco Megapie: Residue yields and radioactivity predictions with different models in MCNPX .....	171
	V. Hedberg, M. Magistris, M.N. Morev, M. Silari, Z. Zajacová Radioactive waste study of the ATLAS detector .....	181
<b>Session IV</b>	<b>Benchmarking – calculations and results</b> .....	<b>193</b>
	<b>Chairs: H. Hirayama, A. Leuschner</b>	
	Y. Iwamoto, S. Taniguchi, N. Nakao, T. Itoga, T. Nakamura, Y. Nakane, H. Nakashima, D. Satoh, H. Yashima, H. Yamakawa, K. Oishi, A. Tamii, K. Hatanaka Thick target neutron yield at 0 degree by 250 and 350 MeV protons.....	195
	M. Felcini, P. Vaz Proposal for multi-megawatt power target benchmarks .....	205
	N. Nakao, S. Taniguchi, S.H. Rokni, S. Roesler, M. Brugger, M. Hagiwara, H. Vincke, H. Khater, A.A. Prinz Measurement of neutron energy spectra behind shielding at 120 GeV/c beam facility, CERF .....	207
	N. Nakao, S.H. Rokni, M. Brugger, S. Roesler, H. Vincke, K. Kosako Calculation of high-energy neutron spectra with different Monte Carlo transport codes and comparison to experimental data obtained at the CERF facility .....	223
	H. Hirayama, Attenuation Length Sub-working Group of Japan Inter-comparison of medium-energy neutron attenuation in iron and concrete (6).....	237
	B. Rapp, J-C. David, V. Blideanu, D. Doré, D. Ridikas, N. Thiollière Benchmarking of the modelling tools within the EURISOL DS project .....	251
	J.E. Fernandez, V. Scot Benchmarking the MCSHAPE3D code with 1-D, 2-D and 3-D imaging experiments .....	261
	H-S. Lee, S. Ban, T. Sanami, K. Takahashi, T. Sato, R. Qiu Measurements and benchmark simulations of photo-neutron yields from targets irradiated by 2.0 and 2.5 GeV electrons.....	275
	C-W. Lee, Y-S. Cho, Y-O. Lee Analysis of the residual radiation field in the proton accelerator facility of the Proton Engineering Frontier Project (PEFP) in Korea .....	283

	G. Kim, A.K.M.M.H. Meaze, M.U. Khandaker, Y-D. Oh, H. Kang, M-H. Cho, I-S. Ko, W. Namkung, T-I. Ro, W-C. Chung, Y-A. Kim, K-J. Yoo, Y-O. Lee Measurement of neutron total cross-sections at the Pohang Neutron Facility .....	289
<b>Session V</b>	<b>Status of computer codes, cross-sections and shielding data libraries .....</b>	<b>295</b>
	<b>Chair: N.V. Mokhov</b>	
	I. Kodeli, E. Sartori, B.L. Kirk Status and future plans for the international radiations shielding and dosimetry experiments (SINBAD) database .....	297
	H. Henriksson, I. Kodeli, E. Sartori, B.L. Kirk Update on recent computer codes and data libraries of interest to SATIF – Status: May 2006 .....	303
	N.V. Mokhov Recent developments and applications of the MARS15 code .....	311
	K. Niita, H. Nakashima, T. Sato, N. Matsuda, Y. Iwamoto, Y. Sakamoto, H. Iwase, L. Sihver, D. Mancusi The present status of the PHITS code .....	313
	V. Vlachoudis, F. Ballarini, G. Battistoni, M. Campanella, M. Carboni, F. Cerutti, A. Empl, A. Fassò, A. Ferrari, E. Gadioli, M.V. Garzelli, A. Mairani, A. Mostacci, S. Muraro, A. Ottolenghi, M. Pelliccioni, L. Pinsky, J. Ranft, S. Roesler, P.R. Sala, D. Scannicchio, R. Villari FLUKA: New features and a general overview .....	321
	T. Koi, D.H. Wright Recent developments in Geant4 .....	329
<b>Session VI</b>	<b>Shielding in medical and industrial accelerator applications.....</b>	<b>339</b>
	<b>Chairs: N.E. Ipe, B.L. Kirk</b>	
	B.L. Kirk, A. Haghighat Computational Medical Physics Working Group .....	341
	W. Dittrich, T. Hansmann Radiation measurements at the RPTC in Munich for verification of shielding measures around the cyclotron area .....	345
	N.E. Ipe, A. Fassò Preliminary computational models for shielding design of particle therapy facilities .....	351
	H-J. Ryu, J-K. Lee, J-W. Kim, H-S. Kim, J-W. Kwon, J. Blaze Simulations and measurements of neutron equivalent doses for the proton therapy facility at the National Cancer Centre.....	361
	N.E. Ipe An overview of NCRP Report 151: Structural shielding design and evaluation report for megavoltage X- and gamma-ray radiotherapy facilities .....	367
	H-D. Kim, G-S. Cho, B-K. Cha, J-K. Ahn Estimation of radiation shielding for a cyclotron vault.....	373
	K. Oishi, K. Kazuaki, Y. Kobayashi, K. Kagawa, T. Nakamura Comparison between measured and calculated results of dose rate in 18 MeV X-ray radiotherapy room .....	381
	Annex 1: List of participants.....	391
	Annex 2: Technical programme .....	397

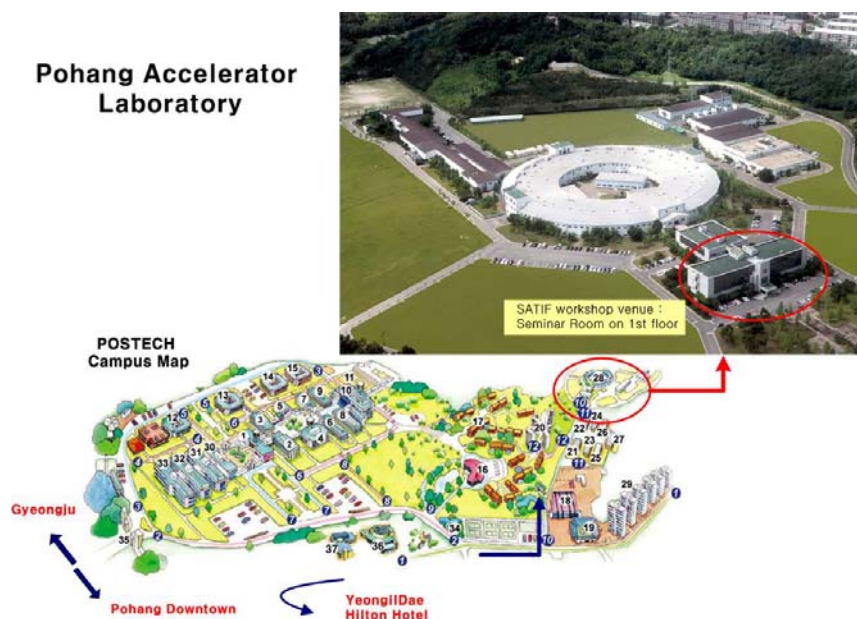


## Executive summary

The OECD/NEA Expert Group on Shielding Aspects of Accelerators, Targets and Irradiation Facilities (SATIF) meets every two years when it organises a Workshop in places where world-class facilities are operated, alternating between North America, Europe and the Far East. During these workshops progress and results form an agreed programme of work are presented and common actions and research initiatives promoted and started with the aim of achieving progress and enhancing international co-operation in this area of research.

The eighth SATIF workshop took place from 22-24 May 2006 and was hosted by the Pohang Accelerator Laboratory (PAL) POSTECH, Republic of Korea (see figure). The local organiser and Chair of the workshop was Dr. Hee-Seock Lee, from the Radiation Safety Division of PAL. It was attended by 48 specialists in radiation protection, radiation shielding and radiation dosimetry from 9 countries representing 27 different organisations active in this field (see Annex 1: List of participants).

**Figure 1: SATIF-8 workshop venue and facility visited**



The main topics discussed at SATIF-8 were:

- source term and related topics;
- dosimetry and related issues;
- shielding at high energy accelerator;
- induced radioactivity and activation data;
- benchmarking – calculations and results;
- status of computer codes, cross-sections and shielding data libraries;
- shielding in medical and industrial accelerator application.

The detailed programme is provided in Annex 2.

The SATIF technical and scientific activities are organised around the major categories of accelerator shielding/facilities/proton and ion accelerators, electron accelerators, photon and neutron sources. Shielding aspects related to accelerator facilities are of multidisciplinary nature and address cross-cutting issues. They imply the utilisation of state-of-the-art computer codes and modelling techniques.

Forty papers were submitted for presentation including results from benchmark studies and status of relevant computer codes, results from measurements such as thick target yields, intercomparison of the medium energy neutron attenuation in iron and concrete, measurement of high energy neutron spectra behind shields in facilities, measurements and benchmark simulations of photoneutron yields from targets, nuclear data relevant to the radiological safety for 100 MeV proton linac. The *Handbook on Secondary Particle Production and Transport by High-energy Heavy Ions* was also presented.

Further benchmarks are proposed.

One of the strong components of the specialists' group activities is benchmarking, in most cases with experimental data in support of computations. Such benchmarks and the results obtained were instrumental for the identification of the needs in modelling methodologies in non-conventional energy domains, such as the intermediate energy range (few hundreds of MeV), typical of emerging and innovative technological applications such as accelerator driven systems (ADS), spallation neutron sources and other high power target applications attracting the attention of different scientific communities.

Over the last decade, the activities and results obtained by the SATIF group have paved the way to major developments in computer codes and to the assessment of nuclear data needs. This is documented in the proceedings of the various SATIF meetings, as the present one.

Dosimetry- and shielding-related activities deserve special mention: ultimately for the benefit of radiation protection, such activities are associated with the utilisation of particle accelerators and radiation sources in different domains, from basic research up to medical applications and are another major domain of the SATIF activities. In this respect, the discussions held during SATIF-8 led to following statement by the specialists' group:

- Dosimetry-related activities are of cornerstone importance for the operation of existing facilities, as well as for the design of new and innovative facilities currently in project phase, associated with the operation of high intensity particle accelerators, high power targets.
- Developments and findings resulting from these activities are of course applicable to any other type of non-accelerator facilities (nuclear power plants, space applications, aircrew dosimetry, industrial applications of radiations, intrusive detection techniques, etc.).
- The SATIF group should strengthen its involvement in ongoing dosimetry-related activities of other groups at the international level (e.g. EURADOS – European Radiation Dosimetry Group, ANS/CMPWG – Computational Medical Physics Working Group, etc.), in order to contribute to fostering major achievements and developments, to exchange scientific results and to jointly promote initiatives (conferences, workshops, education and training, technical documents and reports, etc.). Such involvement should be endorsed by the Nuclear Science Committee.

A series of benchmarks were proposed to be started over the next two years:

- 1) Production yields of the radionuclides induced from various targets in concrete shield at the 500-MeV neutron irradiation facility of KENS by H. Matsumura (KEK), N. Nakao (KEK), K. Masumoto (KEK), K. Oishi (Shimizu Co.), M. Kawai (KEK), T. Aze (U. Tokyo), A. Toyoda(KEK), M. Numajiri (KEK), K. Takahashi (KEK), M. Fujimura (Nihon U.), Q. Wang (IHEP), K. Bessho (KEK), T. Sanami (KEK).
- 2) Thick target yield (TTY) at 0° by 250 and 350 MeV protons at the Research Center of Nuclear Physics (RCNP) cyclotron by Y. Iwamoto (JAEA).
- 3) AGS spallation target experiment by H. Nakashima and ASTE collaboration team.
- 4) Benchmarks on photoneutron spectrum, differential yields and angular distribution from targets irradiated by 2 GeV electrons based on measurements carried out at PAL by H.S. Lee.

- 5) Heavy ion benchmark based on data from HIMAC by K. Niita.
- 6) Proposal for a ADS and high power accelerator facilities benchmark by P. Vaz (ITN).
- 7) Revisiting the *Inter-comparison of the Neutron Attenuation in Iron and Concrete* (7) report results from improved modelling – experimental data for resolving discrepancy, by Hideo Hirayama (KEK). N. Mokhov will suggest a list of published lambda measurements and an experiment with 120 GeV p into a beam dump
- 8) Computational medical physics benchmark(s), by B.L. Kirk (RSICC); benchmarks are being set up; this will be reported on at SATIF-9.
- 9) SHARE benchmark exercise (for modellers and code developers) by S. Leray (CEA): to be defined; this will be reported on at SATIF-9.

Benchmarks are open to model/code developers and code users. Code users are recommended to show their results to code authors, in particular in case of large discrepancies compared with experimental results, to ensure that the code is used with competence, and the appropriate model features or parameters are used.

The first five benchmarks were recommended for inclusion into the Shielding and Dosimetry Experiments Database (SINBAD).

The main objectives of the SATIF workshops were revisited and approved as follows:

- promote the exchange of information among experts in the field of accelerator shielding and related topics,
- identify areas where international co-operation can be fruitful;
- carry on a programme of work in order to achieve progress in specific priority areas.

The deliverables:

- assessment of needs in experimental data for the validation of models and codes;
- organisation of shielding experiments;
- collection and compilation of experimental data sets;
- assessment of models, computer codes, parametrisations and techniques available for accelerator shielding design purposes;
- validation of computer codes and models available to perform particle transport simulation and organisation of international benchmark and intercomparison exercises;
- organisation of workshops and co-organisation of conferences relevant in the area of its scope and computing radiation dosimetry;
- publication of workshop proceedings; and editing of an “Accelerator Shielding Handbook”.

It was agreed to hold the ninth workshop in connection with the joint 11<sup>th</sup> International Conference of Radiation Shielding and Radiation Protection (ICRS11 & RPS-2008), to be held probably at the SNS Facility in Oak Ridge, TN, USA. Progress in benchmarks and results from experiments, code and database developments will be presented.

The new Executive/Scientific Committee for SATIF-9 was elected as follows: Ph. Ferguson (ORNL) (next Chair), H. Hirayama (KEK), B. Kirk (RSICC), H.S. Lee (PAL, current Chair), A. Leuschner (DESY), N. Mokhov (FNAL), T. Nakamura (U. Tohoku), S. Rokni (SLAC), E. Sartori (OECD/NEA), M. Silari (CERN), P. Vaz (ITN).

To summarise, SATIF activities have contributed for more than a decade to enhancing the role NEA is playing in promoting international co-operation in scientific areas related to nuclear energy (at large), radiation physics and the application of ionising radiations in different fields of science and technology. Such actions are in line with the NEA Programme of Work and the main lines of activity set out in the NEA Strategic Plan.



# Introduction

***Chair: H.S. Lee***



## Introduction to "Handbook on Secondary Particle Production and Transport by High Energy Heavy Ions"

**Takashi Nakamura,<sup>1</sup> Lawrence Heilbronn<sup>2</sup>**

<sup>1</sup>Tohoku University, Cyclotron and Radioisotope Centre, Japan

<sup>2</sup>Lawrence Berkeley National Laboratory, University of California, USA

### Abstract

*With increasing the multi-purpose use of high energy, heavy ion accelerators, the secondary particle production and transport by high energy heavy ions are therefore current interesting topics. In this handbook, we have compiled the experimental results on DDX (double differential neutron production cross-section data), TTY (thick target neutron production yield data), heavy-ion produced neutron transport data, and spallation products production cross-section data taken at HIMAC. In addition to the HIMAC results, we have included some experimental results taken at other heavy ion accelerators of energies above about 100 MeV/nucleon. Also, we have included the calculation models and codes for heavy ion reaction and transport. The numerical data recorded in the CD-ROM is attached in the handbook. We do hope that this handbook will be useful for various applications.*

## 1 Introduction

The high energy heavy ion accelerator facilitates the progress of accelerator science and research, such as the discovery of new super-heavy nuclei and unstable nuclei, clinical studies and treatments of the cancer therapy. The high energy heavy ion constituents of cosmic radiation must also be considered in space exploration. Heavy ion accelerator facilities are now operating or planned for construction in the world, and radioactive beam facilities using the spallation products from intense heavy ion beams are also under construction for these various purposes. In these high energy, heavy particle facilities many secondary particles are created from nucleus-nucleus interactions, and these particles, especially neutrons, can produce radioactivities induced in accelerator and structural materials, air, water, and soil, and can penetrate through the facility building into the surrounding environment. It is therefore quite necessary to evaluate the emission of secondary particles, especially neutrons and the creation of the residual nuclei in various materials, in order to estimate the source terms of accelerator shielding design, and also to calculate the dose delivered in the human body during the therapeutic irradiation.

When one of the editors, Takashi Nakamura, had performed the shielding design of the HIMAC facility (Heavy Ion Medical Accelerator in Chiba) at the National Institute of Radiological Sciences (NIRS), Japan more than 15 years before, there existed no available experimental data on neutron production from heavy ions and no available computer codes for the heavy-ion transport calculation at all. The HIMAC accelerator has been operated for heavy-ion therapy mainly using C ion beam and also opened for scientific research studies since 1994. A Japanese group (Tohoku University, High Energy Accelerator Research Organisation (KEK), Institute of Physical and Chemical Research (RIKEN), National Institute of Radiological Sciences (NIRS), headed by Takashi Nakamura) has done a series of systematic experiments on secondary particle production and transport by heavy ions over the past ten years from 1994. In 2000, an American group (Lawrence Berkeley National Laboratory (LBNL), Michigan State University, and Colorado University) co-ordinated by Lawrence H. Heilbronn, joined the HIMAC experiments.

We have compiled the experimental results on DDX (double differential neutron production cross-section data), TTY (thick target neutron production yield data), heavy-ion produced neutron transport data, and spallation products production cross-section data taken at HIMAC. In addition to the HIMAC results, we have included some experimental results taken at other heavy ion accelerators of energies above about 100 MeV/nucleon. Also, we have included the calculation models and codes for heavy ion reaction and transport. Our comprehensive experimental results are summarised in a handbook [1]. The handbook includes the following subjects: secondary neutron yields from thick targets, secondary neutron yields from thin targets, measurements of HZE neutrons behind shielding, production cross-sections of spallation products created in HZE reactions, moving source parameterisation of thick-target neutron yields and neutron production cross-sections, application of data to benchmark transport model calculations. The numerical data recorded in the CD-ROM is attached in the handbook. We do hope that this handbook will be useful for various applications, especially useful as benchmark data for Monte Carlo code analysis and evaluation.

## 2 Secondary neutron yields from thick targets

Table 1 lists the double differential (in energy and angle) thick-target (stopping length) neutron yield experiments summarised in a handbook [1]. The projectile and energy, target material and thickness, measured angle, and accelerator facility are shown. HIMAC is the Heavy Ion Medical Accelerator at the National Institute of Radiological Sciences in Chiba, Japan. NSCL is the National Superconducting Cyclotron Laboratory at Michigan State University in East Lansing, Michigan, USA. SREL is the now defunct Space Radiation Effects Laboratory that was located in Newport News, Virginia, USA. Bevelac is the now defunct high energy heavy ion accelerator that was at Lawrence Berkeley National Laboratory in Berkeley, CA, USA.

**Table 1: Summarised lists of thick target neutron yield experiments using heavy ions [1]**

Projectile (MeV/nucleon)	Targets (cm)	$\theta$ (deg)	Facility
He (100)	C (5.0) Al (4.0) Cu (1.5) Pb (1.5)	0 to 90	HIMAC
He (155)	Al (8.26)	10 to 160	NSCL
He (160)	Pb (3.9)	0 to 150	SREL
He (177.5)	C (14.7) H <sub>2</sub> O (22.9) Steel (4.4) Pb (3.9)	0 to 150	SREL
He (180)	C (16.0) Al (12.0) Cu (4.5) Pb (5.0)	0 to 90	HIMAC
C (100)	C (2.0) Al (1.0) Cu (0.5) Pb (0.5)	0 to 90	HIMAC
C (155)	Al (8.26)	10 to 160	NSCL
C (180)	C (6.0) Al (4.0) Cu (1.5) Pb (1.5)	0 to 90	HIMAC
C (400)	C (20.0) Al (15.0) Cu (5.0) Pb (5.0)	0 to 90	HIMAC
Ne (100)	C (1.0) Al (1.0) Cu (0.5) Pb (0.5)	0 to 90	HIMAC
Ne (180)	C (4.0) Al (3.0) Cu (1.0) Pb (1.0)	0 to 90	HIMAC
Ne (400)	C (11.0) Al (9.0) Cu (3.0) Pb (3.0)	0 to 90	HIMAC
Si (800)	C (23.0) Cu (6.5)	0 to 90	HIMAC
Ar (400)	C (7.0) Al (5.5) Cu (2.0) Pb (2.0)	0 to 90	HIMAC
Fe (400)	C (6.0) Al (4.0) Cu (1.5) Pb (1.5)	0 to 90	HIMAC
Nb (272)	Nb (1.0) Al (1.27)	3 to 80	Bevalac
Nb (435)	Nb (0.51)	3 to 80	Bevalac
Xe (400)	C (3.0) Al (2.0) Cu (1.0) Pb (1.0)	0 to 90	HIMAC

As one example of these experimental results, Figure 1 gives the neutron energy spectra at angles of 0 to 90 degrees produced from thick C, Al, Cu and Pb targets bombarded by 400 MeV/nucleon C ions at HIMAC [2]. The neutron spectra were obtained by the TOF method using the NE213 scintillator. The measured spectra are compared with the PHITS (Particle and Heavy Ion Transport System) Monte Carlo code [3]. Three components can be clearly seen in the spectra. In general, the spectra in the forward direction have a broad peak at the high energy end. The peak energy usually occurs at about 60 to 70% of the beam energy per nucleon. As the target mass becomes lighter and the projectile mass increases, the high energy peak becomes more prominent. Most of the neutrons in this high energy, forward region come from the break-up of the projectile and direct knock-on processes. Neutrons with energies up to 2.5 times the incoming beam energy per nucleon can be produced by these processes. At energies below 20 MeV, the spectra are dominated by the breakup of the target. Because the target remnant is moving slowly in the lab frame, that source of neutrons is essentially isotropic. As such, target-like neutrons can be seen at all angles. As target mass increases, the relative contribution to the overall spectra from target breakup increases. At intermediate energies and intermediate angles, the spectra are dominated by the decay of the overlap region, where a sizeable number of projectile nucleons and target nucleons mix and can undergo several nucleon-nucleon collisions. The PHITS calculation gives good agreement with the measured spectra excluding the high energy region at 0 degree.

### 3 Secondary neutron yields from thin targets

Table 2 lists the double differential (in energy and angle) thin-target neutron yield (neutron production inclusive cross-section) experiments summarised in a handbook [1]. The projectile and energy, target material and thickness, measured angle and accelerator facility are shown in Table 2. RIKEN is the Institute of Physical and Chemical Research in Wako, Saitama, Japan.

**Table 2: Summarised lists of thin target neutron yield experiments using heavy ions [1]**

Projectile (MeV/nucleon)	Targets (g/cm <sup>2</sup> )	$\Theta$ (deg)	Facility
He (135)	C(0.216), Al(0.162), Cu(0.268), Pb(0.340)	0 to 110	RIKEN
He (230)	Al(5.40), Cu(5.38)	5 to 80	HIMAC
C (135)	C(0.216), Al(0.162), Cu(0.268), Pb(0.340)	0 to 110	RIKEN
C (290)	C(1.80), Cu(4.47), Pb(2.27), marsbar(5.0)	5 to 80	HIMAC
C (400)	C(9.0), Cu(13.4), Pb(9.08)	5 to 80	HIMAC
N (400)	C(1.78), Cu(2.69)	5 to 80	HIMAC
Ne (135)	C(0.216), Al(0.162), Cu(0.268), Pb(0.340)	0 to 110	RIKEN
Ne (337)	C(3.06), Al(3.38), Cu(3.81), U(5.60)	30 to 90	Bevalac
Ne (400)	C(1.80), Cu(4.47), Pb(2.27), ISS wall(2.97)	5 to 80	HIMAC
Ne (600)	Li(2.97), C(3.60), CH <sub>2</sub> (2.40), Al(3.98), Cu(4.47), Pb(4.54), marsbar(5.0)	5 to 80	HIMAC
Ar (95)	C(0.216), Al(0.162), Cu(0.268), Pb(0.340)	0 to 110	RIKEN
Ar (400)	C(0.72), Cu(1.34), Pb(1.70)	5 to 80	HIMAC
Ar (560)	C(1.08), Cu(1.79), Pb(2.27), marsbar(5.0)	5 to 80	HIMAC
Fe (500)	Li(0.903), CH <sub>2</sub> (0.957), Al(1.285)	5 to 80	HIMAC
Kr (400)	Li(0.47), C(0.55), CH <sub>2</sub> (0.46), Al(0.54), Cu(0.90), Pb(1.02)	5 to 80	HIMAC
Xe (400)	Li(0.48), C(0.27), CH <sub>2</sub> 0.2, 0.3), Al(0.26), Cu(0.45), Pb(0.57)	5 to 80	HIMAC

As one example of these experimental results, Figure 2 gives the neutron energy spectra at angles of 5 to 80 degrees produced from thick C, Cu and Pb targets bombarded by 290 MeV/nucleon C ions [4]. The neutron spectra were obtained by the TOF method using the NE213 scintillator. The measured spectra are compared with the moving source model [1], the QMD (Quantum Molecular Dynamics) code [5] and the HIC (Heavy Ion Collision) code [6]. At forward angles (0° for the RIKEN experiments, 5° for the HIMAC experiments), there is a prominent peak centred near the beam energy per nucleon. As the angle increases, the prominence of the peak decreases to a point at about 20° where the peak is insignificant. The high energy neutrons in the region of this forward peak come mainly from the breakup of the projectile, along with direct knock-out neutrons from the target. Neutrons are detected at energies 2 to 3 times the beam energy per nucleon, which is a phenomenon attributable to the collective Fermi motion inside the nucleus adding a momentum kick during the collision. At energies below 10-20 MeV, the spectra are dominated at all angles by the decay of the target remnant. The exponential behaviour of the cross-section with energy in this region suggests the target remnant decays by an equilibrium process. At intermediate energies (above 10 to 20 MeV, below the beam energy per nucleon), there is a component that becomes less pronounced as the angle increases. This component is dominated by the pre-equilibrium decay of the overlap region between the projectile and the target.

The moving source model consisting of three components above-described gives the best fit to the measured spectra, and the QMD code gives much better agreement with the measured ones than the HIC code based on the classical model of intranuclear-cascade reaction.

#### 4 Measurements of HZE neutrons behind shielding

Recently, measurements have been made of neutrons behind shielding materials at heavy-ion accelerator facilities. Table 3 gives an overview of those experiments, showing the beams and targets used to produce the neutrons, the shielding material and thickness used, and the type of detection system used [1]. The experiments done with the 400 MeV/nucleon C beams were performed at HIMAC, and the 155 MeV/nucleon experiments were done at the NSCL. Another shielding experiment at HIMAC which is not included in Table 3 has been recently published [7].

**Table 3: Summarised lists of neutron shielding experiments using heavy ion beams [1]**

Projectile (AMeV)	Target used to produce neutrons	Shielding material	Range of shielding thicknesses	Detection system(s) used
C (400)	Cu	Concrete	0-250 cm	Self-TOF, NE-213, Activation foils
C (400)	Cu	Iron	0-100 cm	Self-TOF, NE-213
C (400)	Cu	Concrete Iron	0-400 cm 0-100 cm	TEPC
He, C, and O (155)	Hevimet	Concrete Iron	0-440 cm	Bonner Spheres

In HIMAC experimental arrangements, neutrons were produced by stopping 400 MeV/nucleon  $^{12}\text{C}$  ions in a 5-cm thick Cu (10x10 cm square) target. The concrete and iron shields were 50- and 10-cm thick slabs, respectively, both of  $100 \times 100$  cm square, and they were placed centered and normal to the beam axis. Figure 3 shows the neutron fluxes (# per steradian per MeV per ion) behind 0, 50, 100, 150, 200 cm of concrete, and 0, 20, 40, 60, 80, 100 cm of iron, using the self-TOF detector and the NE213 detector, together with the source neutron spectrum [8]. The self-TOF detector gives the neutron spectra above the low-energy threshold of 100 MeV because low energy recoils range out in the radiator, and below 600 MeV due to a lack of statistically-significant events. The spectra have a broad peak around 200 to 300 MeV, and little softening of the spectra can be seen with increasing shield thickness. The NE213 detector gives the neutron spectra from 20 to 800 MeV. Both spectra given by self-TOF and NE213 are generally in good agreement each other, although the broad peaks are not seen in the NE213 spectra. The dashed lines show MCNPX calculations of the spectra. The calculations, in general, give a harder spectrum than do the measurements. Below 100 MeV, the calculations overestimate the data as the shielding thickness increases. Between 100 and 400 MeV, the agreement between experiment and calculation is good. The agreement between calculation and experiment is quite good over the entire energy range (20-800 MeV) at 20 cm iron shield, and 50, 100, 150 cm concrete shields.

## 5 Production cross-sections of spallation products created in HZE reactions

An important component in the design of heavy-ion accelerator facilities is an accurate estimation of the radioactivities induced by spallation products in accelerator components and in shielding materials. To this end, the production cross-sections for various spallation products have been measured from heavy-ion reactions by several groups. Table 4 shows the various beams, targets and facilities used in the experiments [1]. PPA is the Princeton Particle Accelerator (now defunct) in USA and TWA-ITEP is the U10 synchrotron Terawatt Accumulator of the Moscow Institute for Theoretical and Experimental Physics in Russia.

The HIMAC series of experiments [9] used a target stack comprised of two to seven 5-mm thick Cu plates of 10 cm by 10 cm squares. In between each plate, samples of C (0.2-mm thick,  $5 \times 5$  cm square), Al (0.1-mm thick,  $9 \times 10$  cm<sup>2</sup>), and Cu (0.1-mm thick,  $9 \times 10$  cm<sup>2</sup>) were placed in order to measure the spatial distributions of spallation products, and to determine the energy dependence on the cross-section. Foils of the same thickness were placed at the front of the stack to measure the reaction cross-sections and mass-yield distributions.

The data can be summed over the same mass numbers to produce mass-yield distributions. As one example, Figure 4 shows the mass-yield distributions (in mb) of 35 nuclides from  $^7\text{Be}$  to  $^{65}\text{Zn}$  for the 400-MeV/nucleon C and Ne ions interacting in a Cu target compared with the PHITS calculations. The PHITS calculations give good agreement with the experimental results, excluding an underestimation for some nuclides.

**Table 4: Listing of the beams, energies (MeV/nucleon), targets and facilities used to measure spallation product cross-sections [1]**

Beam	Energy	Target	Facility
<sup>14</sup> N	278 AMeV	natCu	PPA
<sup>12</sup> C	2083 AMeV	natCu	Bevalac
<sup>40</sup> Ar	2000 AMeV	natCu	Bevalac
<sup>12</sup> C	2100 AMeV	natCu	Bevalac
<sup>20</sup> Ne	211 AMeV	natCu	Bevalac
<sup>20</sup> Ne	377 AMeV	natCu	Bevalac
<sup>12</sup> C	135 AMeV	natCu	RIKEN
<sup>4</sup> He	100 AMeV	C, Al, Cr, Fe, Ni, Cu, Pb	HIMAC
<sup>12</sup> C	100 AMeV	C, Al, Cr, Fe, Ni, Cu, Pb	HIMAC
<sup>20</sup> Ne	100 AMeV	C, Al, Cr, Fe, Ni, Cu, Pb	HIMAC
<sup>4</sup> He	230 AMeV	C, Al, Cr, Fe, Ni, Cu, Pb	HIMAC
<sup>12</sup> C	230 AMeV	Al, Cr, Fe, Ni, Cu, Pb	HIMAC
<sup>20</sup> Ne	230 AMeV	C, Al, Cr, Fe, Ni, Cu, Pb	HIMAC
<sup>40</sup> Ar	230 AMeV	C, Al, Cr, Fe, Ni, Cu, Pb	HIMAC
<sup>12</sup> C	400 AMeV	C, Al, Cr, Fe, Ni, Cu, Pb	HIMAC
<sup>20</sup> Ne	400 AMeV	C, Al, Cr, Fe, Ni, Cu, Pb	HIMAC
<sup>40</sup> Ar	400 AMeV	C, Al, Cr, Fe, Ni, Cu, Pb	HIMAC
<sup>28</sup> Si	800 AMeV	C, Al, Cr, Fe, Ni, Cu, Pb	HIMAC
<sup>12</sup> C	200 AMeV	<sup>63</sup> Cu, <sup>65</sup> Cu, Al, Co	TWA-ITEP

## 6 Conclusion

The work and data described here is from the efforts of scientists from Japan, the US, and Europe during the past 25 years. We have focused on research that is applicable to the general field of high energy (>100 MeV/nucleon), heavy ion transport. More specific applications in that field include accelerator design and shielding, medical physics and heavy-ion radiotherapy, and space-radiation transport and shielding design. It was our pleasure to survey the field to collect the most comprehensive data set we could find in four main areas: thick-target neutron yield measurements, neutron production cross-sections, measurements of neutrons behind shielding, and spallation products production cross-sections.

### Acknowledgements

We, the editors, very gratefully acknowledge the following persons for giving us the numerical data together with the tables and graphs in their experimental and computational work:

For DDX (double differential neutron production cross-section data), Mr. Hisaki Sato, Tohoku University (Present address: Toshiba Co. Ltd.) and Dr. Yoshiyuki Iwata (NIRS). For TTY (thick target neutron production yield data), Dr. Tadahiro Kurosawa, Tohoku University (Present address: Advanced Institute of Science and Technology). For neutron transport data, Dr. Michiya Sasaki, Tohoku University (Present address: Central Research Institute of Electric Power Industries), Dr. Tomoya Nunomiya, Tohoku University (Present address: Fuji Electric Systems Co. Ltd.) and Dr. Reginald Ronnigen (Michigan State University). For spallation products production cross-section data, Dr. Hiroshi Yashima, Tohoku University (Present address: Research Reactor Institute, Kyoto University) and Dr. Yuri Titarenko (Institute for Theoretical and Experimental Physics, Russia). For moving source model, Dr. Takashi Kato, Tohoku University (Present address: Nikken Sekkei Co. Ltd.). For giving many references and supporting comments with the PHITS code, Dr. Hiroshi Iwase, Tohoku University (Present address: GSI (Gesellschaft fuer Schwerionenforschung), Germany).

## References

- [1] T. Nakamura, L. Heilbronn, *Handbook on Secondary Particle Production and Transport by High-energy Heavy Ions*, published by World Scientific in January 2006.
- [2] T. Kurosawa, N. Nakao, T. Nakamura, H. Iwase, H. Sato, Y. Uwamino, A. Fukumura, *Phys. Rev.*, C 62 (2000) 044615.
- [3] H. Iwase, K. Niita, T. Nakamura, *J. Nucl. Sci. Technol.* 39 (2002) 1142.
- [4] Y. Iwata, T. Murakami, H. Sato, H. Iwase, T. Nakamura, T. Kurosawa, L. Heilbronn, R.M. Ronningen, K. Ieki, Y. Tozawa, K. Niita, *Phys. Rev.*, C 64 (2001) 054609.
- [5] J. Aichelin, *Phys. Rep.*, 202 (1991) 233; K. Niita, S. Chiba, T. Maruyama, H. Takada, T. Fukahori, Y. Nakahara, A. Iwamoto, *Phys. Rev.*, C52 (1995) 2620.
- [6] H.W. Bertini, T.A. Gabriel, R.T. Santoro, O.W. Hermann, N.M. Larson, J.M. Hunt, ORNL-TM-4134, Oak Ridge National Laboratory (1974).
- [7] Y. Kumamoto, Y. Noda, Y. Sato, T. Kanai, T. Murakami, *Health Phys.*, 88 (2005) 469.
- [8] M. Sasaki, E. Kim, T. Nunomiya, T. Nakamura, N. Nakao, T. Shibata, Y. Uwamino, S. Ito, A. Fukumura, *Nucl. Sci. Eng.*, 141 (2003) 140.
- [9] H. Yashima, Y. Uwamino, H. Iwase, H. Sugita, T. Nakamura, S. Ito, A. Fukumura, *Radio Chimica Acta*, 91 (2003) 689; *ibid. Nucl. Instrum. Meth.*, B 226 (2004) 243.

**Figure 1: Comparison of the measured neutron spectra with the PHITS calculations for 400 MeV/nucleon C ion on thick (stopping-length) C and Cu targets**

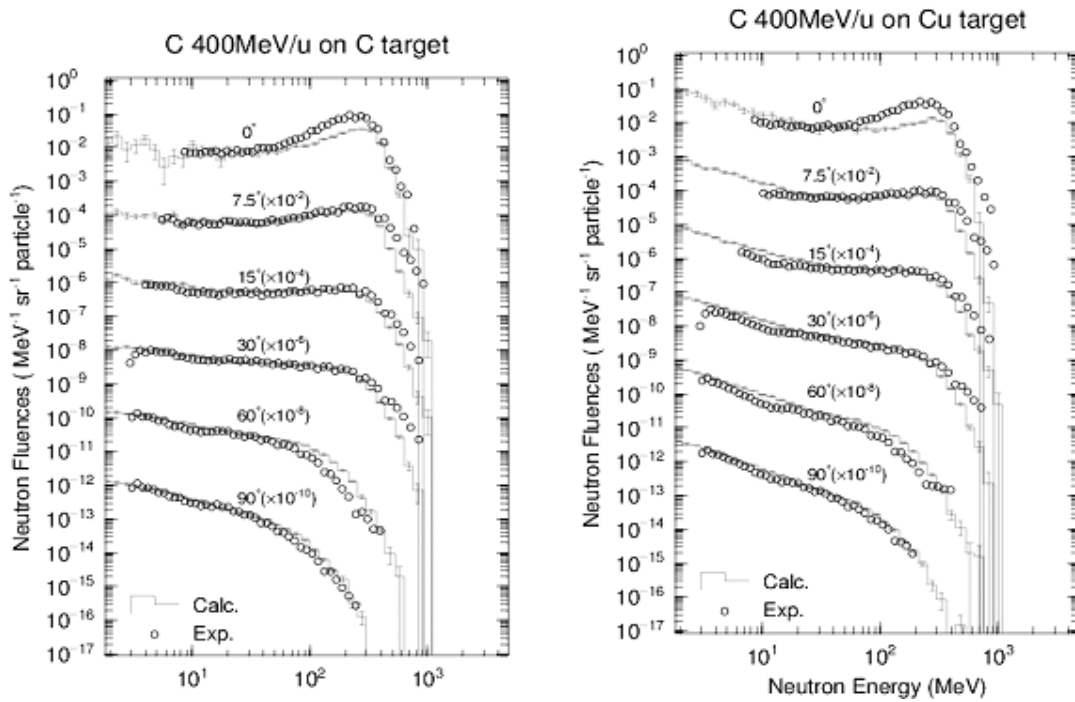


**Figure 2: Double-differential neutron production cross-sections for 290 MeV/nucleon C ions**

The targets are (a) C, (b) Cu and (c) Pb. The solid curves are the calculated results by the moving source model. The dashed and dot-dashed curves are the results of the QMD and HIC calculations, respectively.

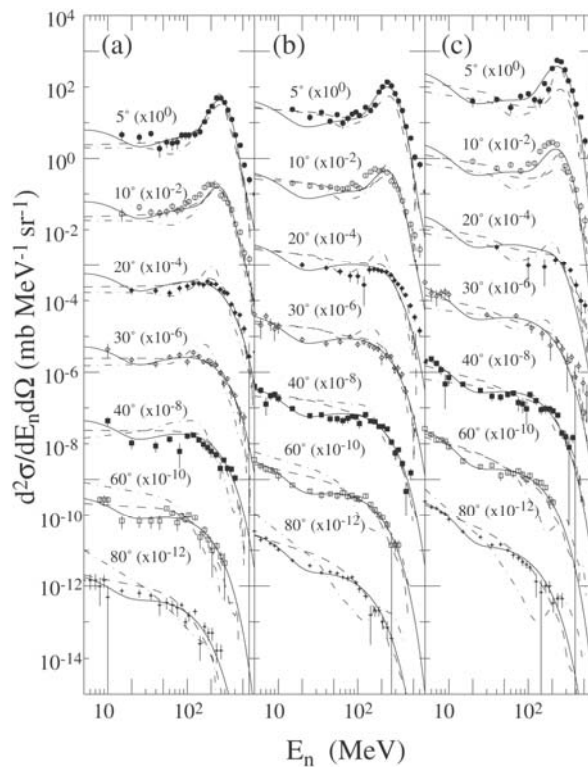


**Figure 3: Comparison of measured and calculated neutron energy spectra penetrating through (a) concrete and (b) iron shields**

Solid lines are the measured results of the self-TOF detector, dot-dash lines are of the NE213 detector. Dotted lines are the MCNPX calculations and broken line is the source neutron spectrum [2] generated from the Cu target bombarded by 400 MeV/nucleon C ions.

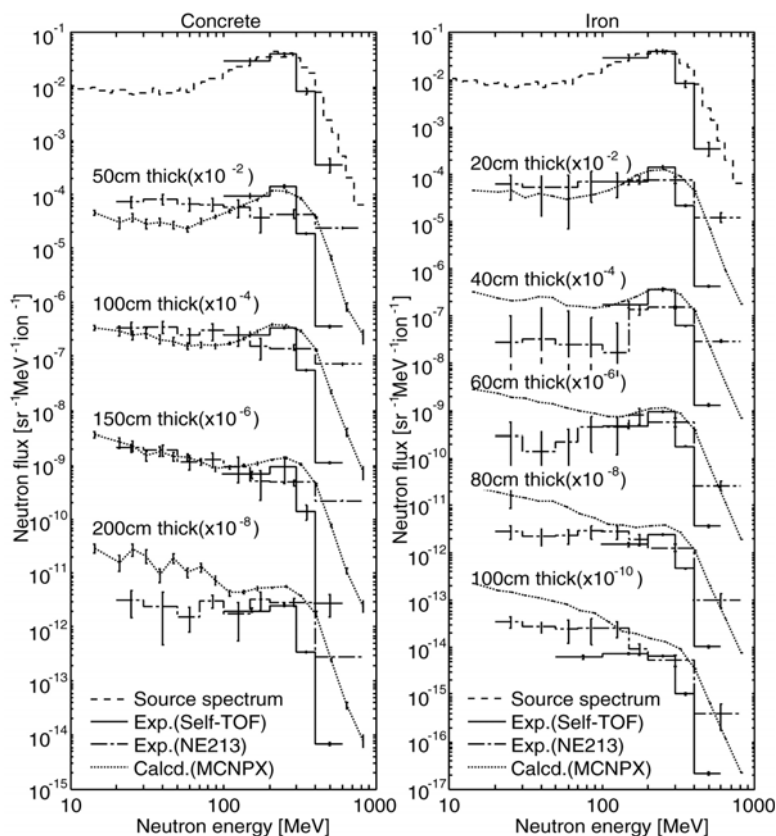
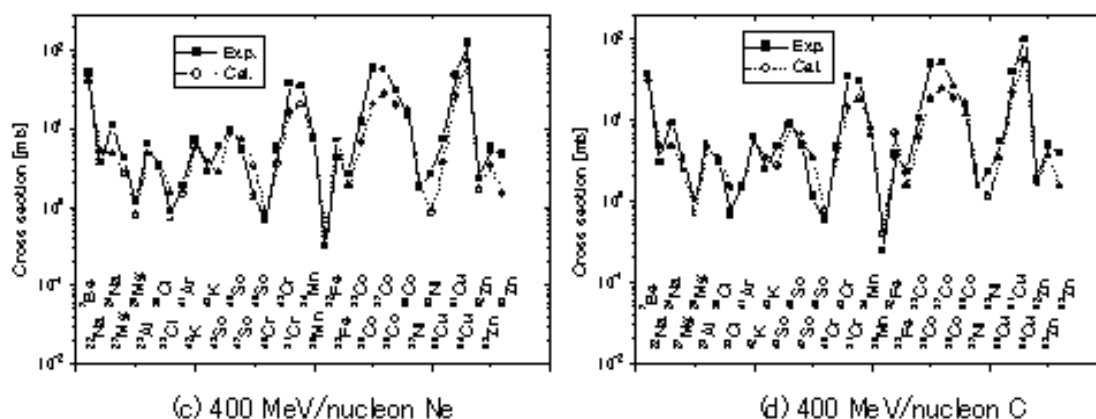


**Figure 4: Comparison of measured and calculated reaction cross-sections of spallation products in Cu for 400 MeV/nucleon C and Ne projectiles with the PHITS calculations**





## Standard data of dose conversion coefficients in Japan

**Yukio Sakamoto**

Japan Atomic Energy Agency, Japan

**Osamu Sato**

Mitsubishi Research Institute, Inc., Japan

**Hideo Hirayama**

High Energy Accelerator Research Organisation, Japan

### Abstract

*“Radiation dose conversion coefficients for radiation shielding calculations: 2004” has been published by the Standards Committee in the Atomic Energy Society of Japan. This standard gives effective dose conversion coefficients based largely on the ICRP recommendations in 1990, and the conversion coefficients evaluated in Japan to obtain effective dose for photons having energies up to 10 GeV and for neutrons having energies up to 5 GeV. This standard also gives group-wise dose conversion coefficients in the energy group structures of multi-group cross-section libraries frequently used in shielding calculations.*

## Introduction

The Standards Committee of Atomic Energy Society of Japan is set to prepare Nuclear Standards, which are developed on the basis of latest knowledge and experiences through the process realising fairness, impartially and transparency [1]. The Subcommittee on Radiation Shielding, the Research Reactor Technical Committee and the Standards Committee deals with standardisation of methods and data used in shielding calculations, which are dose conversion coefficients, gamma-ray build-up factors and typical composition of shielding materials.

Fluence-to-dose conversion coefficients are necessary to estimate dose rate in radiation shielding calculations by the discrete ordinates method, the Monte Carlo method, etc. New values of radiation dose conversion coefficients were provided by the International Commission on Radiological Protection (hereafter, ICRP) when ICRP published new recommendations in 1977 [2] and 1990 [3], and general concepts with respect to radiation dose were modified accordingly. As a result, values of radiation dose conversion coefficients attached in the Japanese domestic law, the Radioactive Defect Protection Law, etc., have also been changed.

“Radiation dose conversion coefficients for radiation shielding calculations: 2004” [4] provides dose conversion coefficients from fluence rate to effective dose rate of photons and neutrons for use in radiation shielding calculations. This standard is based largely on the ICRP recommendations in 1990. However, original values based on research conducted in Japan have been retained primarily with respect to the following two items:

- 1) conversion coefficients to obtain effective dose of photons and neutrons in the high energy region;
- 2) group-wise conversion coefficients to obtain effective dose.

## Status of effective dose conversion coefficients data

Table 1 shows the energy range and irradiation geometries of the effective dose conversion coefficient data set, ICRP Publication 74 [5], domestic law in Japan, and high energy data sets [6-8]. The values of the effective dose conversion coefficients attached in the domestic law in Japan, the Radioactive Protection Law, were adopted only for AP irradiation geometry in which the effective dose is greater than those in other irradiation geometries for lower energy radiation. In this standard, the values of effective dose conversion coefficients were adopted for photons with energy from 0.01 MeV to 10 GeV, and for neutrons with energy from 1 MeV to 5 GeV, which exceed the energy range in ICRP Publication 74 and domestic law in Japan.

**Table 1: Energy range and irradiation geometries of the effective dose conversion coefficient data set**

Dataset	Photons	Neutrons
ICRP Publication 74	0.01 MeV – 10 MeV 6 geometries (AP, PA, RLAT, LLAT, ROT, ISO)	1 MeV – 180 MeV 6 geometries (AP, PA, RLAT, LLAT, ROT, ISO)
Domestic law in Japan	0.01 MeV – 10 MeV AP geometry	1 MeV – 20 MeV AP geometry
High energy data	EGS4: 1 MeV – 10 GeV FLUKA: 0.05 MeV – 100 GeV	HETC-3STEP: 20 MeV – 10 GeV FLUKA: 1 meV – 100 GeV
Scope in this standard	0.01 MeV – 10 GeV AP geometry	1 MeV – 5 GeV AP geometry

## Contents of standard

The object radiation in this standard was photons with energy from 0.01 MeV to 10 GeV and neutrons with energy from 1 MeV to 5 GeV. The values of effective dose per unit fluence and effective dose rate per unit fluence rate were listed in the form of energy point data and energy group averaged data. The fitting formula in the polynomial expression was also shown.

## Source data of standard

Table 2 shows the source data of standard. The values for lower photons and neutrons were based in the data from ICRP Publication 74 for AP irradiation geometry, which were corresponding to those attached in the domestic law in Japan. The values for photons with energy above 5 MeV were based in the data from EGS4 results [8,9] which were obtained for the vacuum condition around phantom and included the effect of secondary electron transport, because the secondary electrons produced by high energy photons have large range. The values for neutrons with energy above 20 MeV were based in the data from HETC-3STEP results [8] which were calculated by using the radiation weighting factor for high energy neutrons, 5.

**Table 2: Source data of standard**

Radiation	Energy range	Source	Geometry	Comments
Photons	0.01 MeV - 5 MeV	ICRP Publication 74	AP	Kerma approximation
	5 MeV - 10 GeV	EGS4 results	AP	Secondary electron transport Vacuum around phantom
Neutrons	< 20 MeV	ICRP Publication 74	AP	
	20 MeV - 5 GeV	HETC-3STEP results	AP	Radiation weighting factor, 5

## Characteristic of standard data for photons

In ICRP Publication 74, the effective dose conversion coefficients for photons were obtained from effective dose per air Kerma multiplied by air Kerma conversion coefficients. As air Kerma conversion coefficients for high energy photons above 10 MeV were not listed in the ICRP report and effective dose conversion coefficients for high energy photons were listed in the form from unit fluence to effective dose, the values for the all energy region were also listed in the form from unit fluence to effective dose.

As energy of secondary electrons produced by low energy photons is small and its range is also small, the Kerma approximation holds good that the energy of secondary electrons is deposited around the collision point between photons and medium atoms. Figure 1 shows the effect of secondary electron transport in effective dose conversion coefficients for AP irradiation by photons. Effective dose conversion coefficients by using Kerma approximation were two decade greater than those with secondary electron transport at 10 GeV photons. The values cited in the standard were data obtained by using secondary electron transport.

Figure 2 shows effective dose conversion coefficients for photons in various irradiation geometries. Effective dose conversion coefficients in AP irradiation of low energy photons were greater than those in other irradiation geometries, and from that reason those for AP irradiation were adopted as attached values in domestic law. On the other hand, the maximum values of effective dose conversion coefficients in the irradiation geometries were varied with photon energy from AP geometry to ISO geometry. An adoption of maximum effective dose conversion coefficients caused excessive margin. For the consistency to low energy photons, effective dose conversion coefficients for high energy photons in AP irradiation were also adopted.

The evaluated data of effective dose conversion coefficients for photons in ICRP Publication 74 have no presentation of error bar. The statistical errors contained in EGS4 results were eliminated by the smoothing procedure for 1 MeV span data of EGS4 results [9] from 5 MeV to 20 MeV.

Figure 1: Effect of secondary electron transport in effective dose conversion coefficients for photons

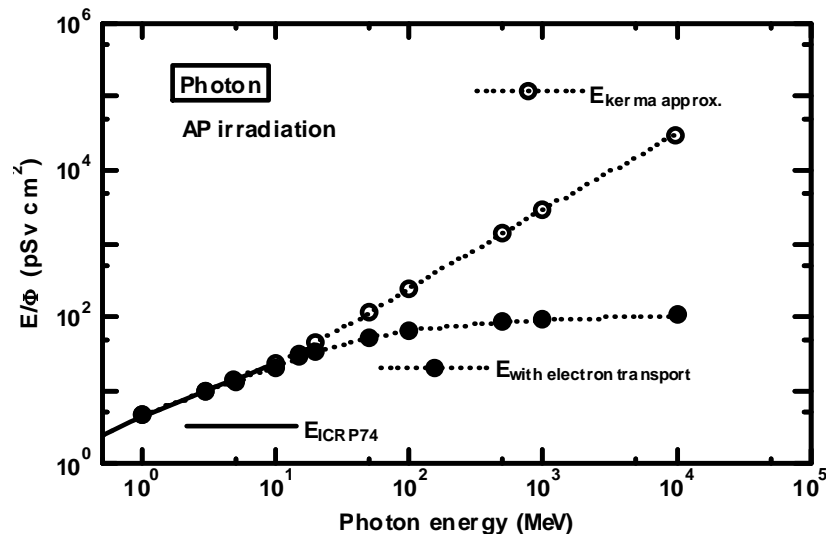
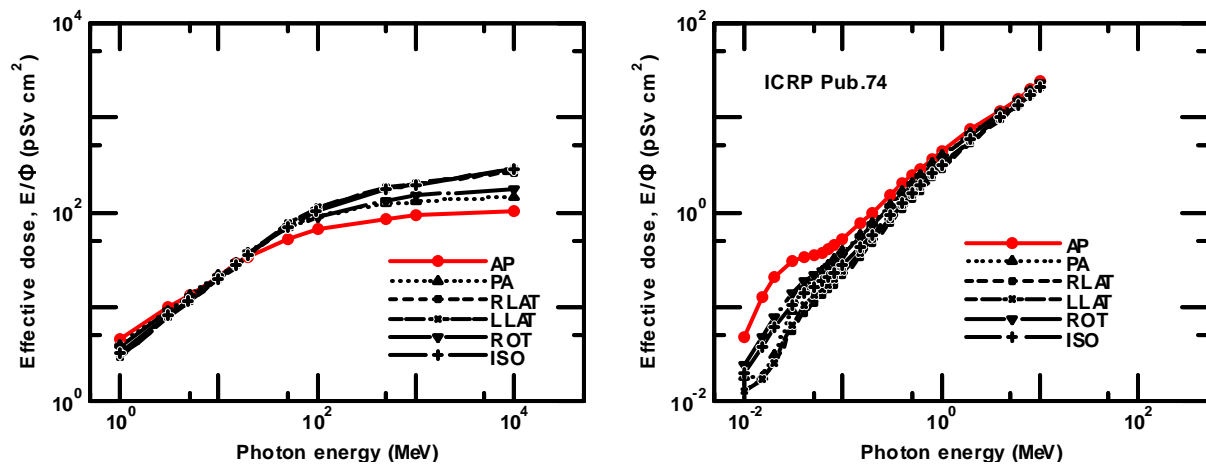


Figure 2: Effective dose conversion coefficients for photons in various irradiation geometries



### Characteristic of standard data for neutron

Effective dose conversion coefficients were evaluated by using of radiation weighting factor ( $w_R$ ). Figure 3 shows the radiation weighting factor and body averaged quality factor for neutrons. Radiation weighting factors for high energy neutrons is 5 and its value is greater than the body averaged quality factors which are evaluated from the effective dose equivalent divided by the effective absorbed dose. In this standard, effective dose conversion coefficients for high energy neutrons were corresponding to those evaluated by using  $w_R = 5$ .

Figure 4 shows effective dose conversion coefficients for neutron in various irradiation geometries. Effective dose conversion coefficients in AP irradiation of low energy neutrons were greater than those in other irradiation geometries same as photon case, and from that reason those for AP irradiation were also adopted as attached values in domestic law. From the same reason, effective dose conversion coefficients for high energy neutrons in AP irradiation were adopted in this standard.

Figure 3: Radiation weighting factors and body averaged quality factors for neutrons

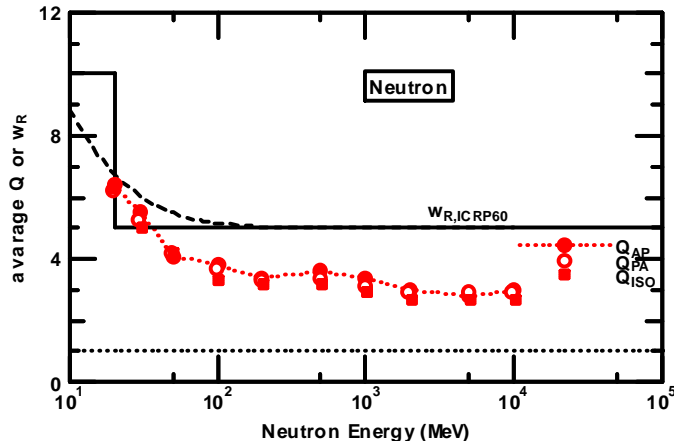


Figure 4: Effective dose conversion coefficients for neutron in various irradiation geometries

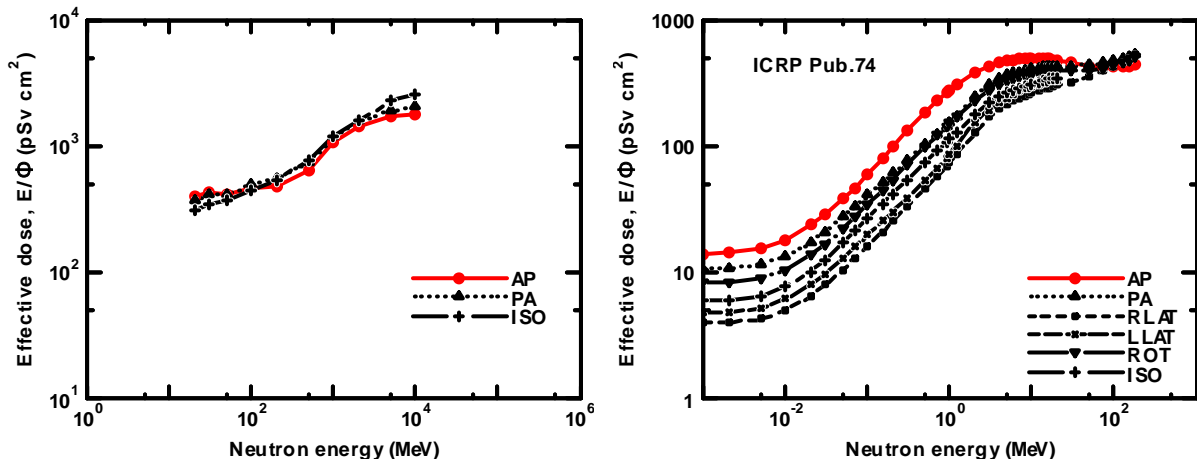
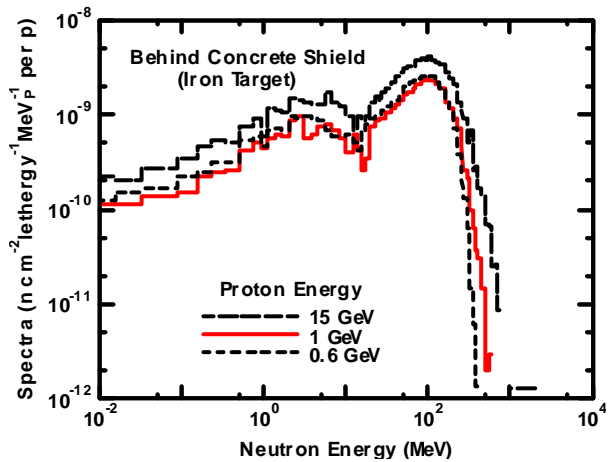
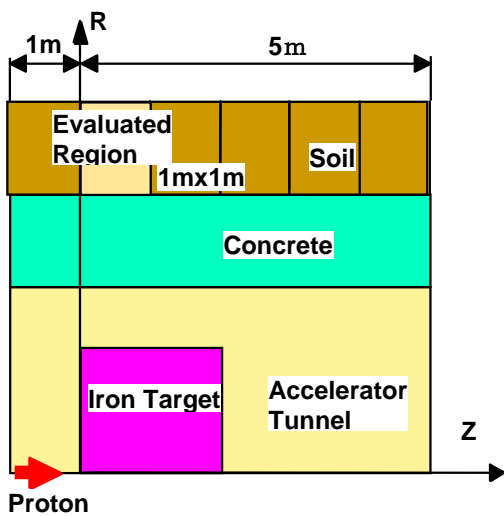
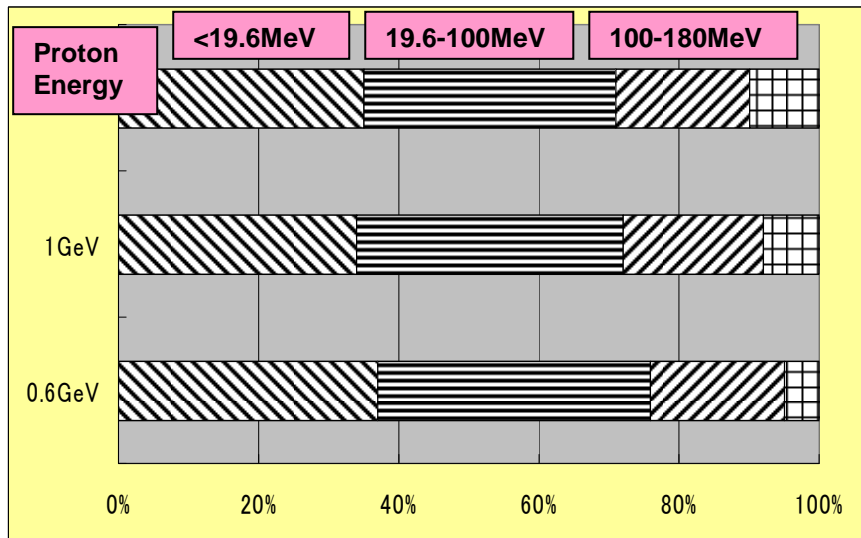


Figure 5: Concrete transmitted neutron spectra and calculation model



The contribution of each energy region neutrons to total dose was evaluated by using the typical concrete transmitted neutron spectra [10]. Figure 5 shows calculation model and concrete transmitted neutron spectra. Proton energy is 0.6 GeV, 1 GeV and 1.5 GeV, respectively, and concrete transmitted neutron spectra were calculated NMTC/JAM code [11,12]. Figure 6 shows dose contribution of each energy neutrons, below 19.6 MeV, 19.6-100 MeV, 100-180 MeV, and above 180 MeV. There is some discrepancy in effective dose conversion coefficients between irradiation geometries and evaluation code, but the contribution due to neutron above 180 MeV is smaller than about 10%. So the difference of dose conversion coefficients between irradiation geometries and evaluated codes was eliminated in view of total dose.

Figure 6: Dose contribution of each energy neutrons



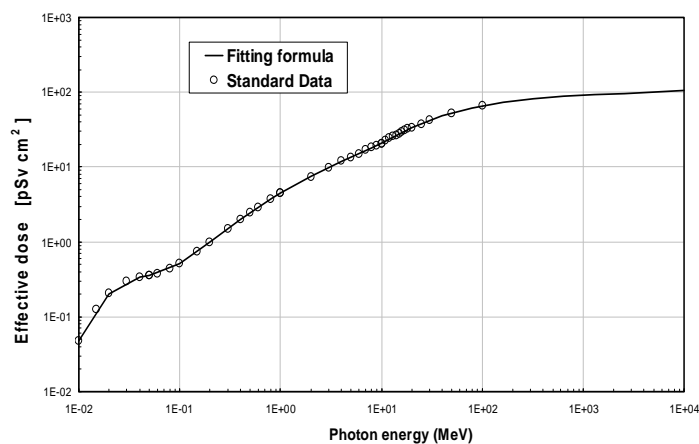
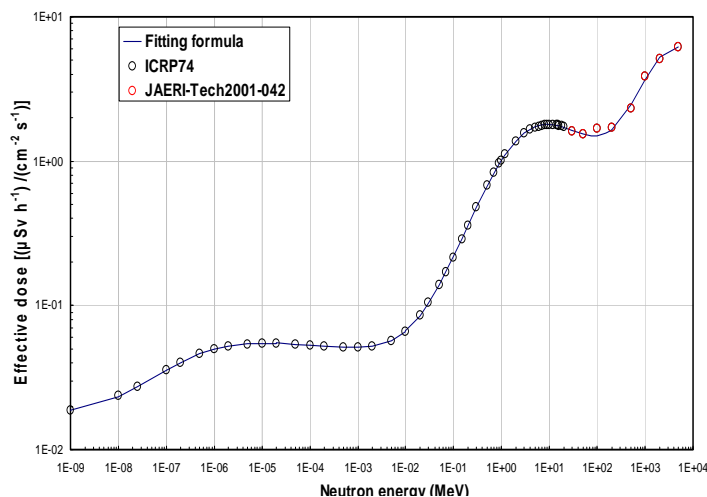
### Fitting formula for effective dose conversion coefficients expressed by polynomial

The dose conversion coefficients for desired energy, not fixed energy, are often needed in shielding calculations. In the standard, fitting formula of effective dose conversion coefficients ( $E/\Phi$ ) expressed by Equations (1) and (2) are prepared for photons and neutrons, respectively.  $E_\gamma$  and  $E_n$  are energy for photons and neutrons,  $M_\gamma^m$  and  $M_n^m$  are fitting parameters for photons and neutrons, respectively. Fitting parameters with five-digit number were obtained for four regions of photon and neutron energy region.

$$[E/\Phi]_{\text{photon}} = \exp \left\{ \sum_{m=0}^4 M_\gamma^m \times (\ln E_\gamma)^m \right\} \quad (1)$$

$$[E/\Phi]_{\text{neutron}} = \exp \left\{ \sum_{m=0}^5 M_n^m \times (\ln E_n)^m \right\} \quad (2)$$

Figures 7 and 8 show the fitting of effective dose conversion coefficients for photons and neutrons, respectively. The fitting error for photons was less than 3%. The fitting error for low energy neutrons below 20 MeV was less than 2%, and that for high energy neutrons above 20 MeV was less than 6% except for 100 MeV data, which was not smoothed data and its fitting error was about 10%. Attached EXCEL file can calculate the effective dose conversion coefficients for desired energy of photons and neutrons.

**Figure 7: Fitting of effective dose conversion coefficients for photons****Figure 8: Fitting of effective dose conversion coefficients for neutrons**

### Group averaged dose conversion coefficients for typical shielding group constants

In shielding calculations, the discrete ordinate codes such as ANISN and DOT are used with group averaged cross-section libraries. Group averaged dose conversion coefficients were also prepared for four typical shielding group constants shown in Table 3. Ambient dose equivalent conversion coefficients are needed for the shielding calculations of transport casks.

### Summaries

In the standard of dose conversion coefficients in Atomic Energy Society of Japan, effective dose conversion coefficients for photons and neutrons were published beyond the energy range in ICRP Publication 74 and domestic law in Japan. It provides the fitting formula for effective dose and group averaged data for typical shielding group constants, also. EXCEL data file is furnished with standard book, which contains the various tables and the tool to calculate the effective dose conversion coefficients in desired energy by fitting formula.

**Table 3: Group averaged data**

Energy group structure (n/γ)	Effective dose (E)	Ambient dose equivalent (H*(10))
DLC23/CASK [13] (22n/18γ)	○	○
JSD-J2 [14] (100n/20γ)	○	○
VITAMIN-B6 [15] (199n/42γ)	○	○
High energy (extended HILO86R [16] up to 3 GeV) (78n/22γ)	○	—

## References

- [1] Atomic Energy Society of Japan (AESJ), [www.soc.nii.ac.jp/aesj/index-e.html](http://www.soc.nii.ac.jp/aesj/index-e.html).
- [2] International Commission on Radiological Protection (ICRP), *Recommendations of the International Commission on Radiological Protection*, ICRP Publication 26, Oxford, Pergamon Press (1977), reprinted (with additions) in 1987.
- [3] ICRP, *Recommendations of the International Commission on Radiological Protection*, ICRP Publication 60, *Annals of ICRP*, 21 (1-3), Oxford, Pergamon Press (1990).
- [4] AESJ, "Radiation Dose Conversion Coefficients for Radiation Shielding Calculations: 2004", *Standards of Atomic Energy Society of Japan*, AESJ-SC-R002:2004, Atomic Energy Society of Japan (2004).
- [5] ICRP, *Conversion Coefficients for Use in Radiological Protection Against External Radiation*, ICRP Publication 74, *Annals of ICRP*, 26 (3/4), Oxford: Elsevier Science (1996).
- [6] M. Pelliccioni, "Overview of Fluence-to-effective Dose and Fluence-to-ambient Dose Equivalent Conversion Coefficients for High Energy Radiation Calculated Using the FLUKA Code", *Radiation Protection Dosimetry*, Vol. 88, No. 4, pp. 279-297 (2000).
- [7] A. Ferrari, M. Pelliccioni, "On the Conversion Coefficients for Cosmic Ray Dosimetry", *Radiation Protection Dosimetry*, Vol. 104, No. 3, pp. 211-220 (2003).
- [8] Y. Sakamoto, O. Sato, S. Tsuda, N. Yoshizawa, S. Iwai, S. Tanaka, Y. Yamaguchi, *Dose Conversion Coefficients for High-energy Photons, Electrons, Neutrons and Protons*, JAERI 1345 (January 2003) (in Japanese).
- [9] O. Sato, private communication.
- [10] Y. Sakamoto, Y. Yamaguchi, *Dose Conversion Coefficients in the Shielding Design Calculation for High Energy Proton Accelerator Facilities*, JAERI-Tech 2001-042 (2001) (in Japanese).
- [11] K. Niita, Y. Nara, H. Takada, H. Nakashima, S. Chiba, Y. Ikeda, *Analysis of the Proton-induced Reactions at 150 MeV – 24 GeV by High Energy Nuclear Reaction Code*, JAERI-Tech 99-065 (1995).
- [12] K. Niita, "High Energy Nuclear Reaction Code JAM", *Proceedings of the 1999 Symposium on Nuclear Data*, JAERI-Conf 2000-005, 98 (2000).
- [13] "CASK – 40 Group Coupled Neutrons and Gamma-Ray Cross-section Data", *RSIC Data Library Collection*, DLC-23 (1973).

- 
- [14] Mitsubishi Atomic Power Industry Co., *Preparation of Shielding Nuclear Constant*, No. 3, PNC TJ 206 84-01 (1984) (in Japanese).
- [15] J.E. White, R.Q. Wright, D.T. Ingersoll, R.W. Roussin, N.M. Greene, R.E. MacFarlane, "VITAMIN-B6: A Fine-group Cross-section Library Based on ENDF/B-VI for Radiation Transport Application", *Proceedings of the International Conference on Nuclear Data for Science and Technology*, Gatlinburg, Tennessee, pp. 733-736 (1994).
- [16] H. Kotegawa, Y. Nakane, A. Hasegawa, S. Tanaka, *Neutron-photon Multigroup Cross-sections for Neutron Energies Up to 400 MeV: HILO86R – Revision of HILO86 Library*, JAERI-M 93-020 (1993).



## **A new method for pulsed neutron monitoring with the rem-counter LB 6411 and time-resolved readout**

**Albrecht Leuschner**

Deutsches Elektronen-Synchrotron, DESY, Germany

**Alfred Klett**

Berthold Technologies, Germany

### **Abstract**

*High-energy accelerators can produce strongly time-structured radiation fields. Such dose shots are generated at linear machines with low duty cycles as well as at circular machines when complete fills are instantaneously lost. The main dose component is due to high-energy neutrons occurring at that time structure. Usually, moderated rem-meters based on proportional chambers fail here as they extremely suffer from dead time effects. Therefore a new method for pulsed neutron dose monitoring was developed and investigated. It's based on an unstable intermediate state with a short half life. In this case, high-energy neutrons produce the  ${}^9\text{Li}$  nuclide by spallation of the carbon in the moderator of the rem-counter LB 6411 from BERTHOLD Technologies. Its daughter nuclide is a neutron emitter. So, delayed neutrons are registered with a half life of 170 ms in time-resolved readout with 1 ms resolution. The response was measured along with passive dose meters in the radiation field behind the lateral concrete shielding of a 7.5 GeV proton transfer line.*

## Introduction

Almost all modern accelerators make use of radio-frequency structures for acceleration of charged particles. The primary beam is bunched and any beam interaction causes a pulsed field of secondary radiation. Behind thick shielding of high-energy accelerators the radiation intensity is attenuated by several orders of magnitude and mainly high-energy neutrons ( $E_n > 20$  MeV) (Dinter, 1996a, 2000) contribute to the total dose. The time structure of the radiation fields is in many cases quasi-continuous and active dose meters work properly. But there are also strongly time dependent radiation fields. In principle there are two different time structures: transient processes and repetitive processes. As the instantaneous dose rate levels might be extremely high active dose meter may suffer from unpredictable dead time effects.

The character of a transient process might be illustrated with an example from DESY. The circular electron-proton collider HERA was upgraded to increase its luminosity. A failure in the magnet system caused a complete loss of the stored proton beam within a few milliseconds. This event occurred near an experimental hall and caused severe damages in the vacuum system. In addition there was also a considerable amount of residual radioactivity detected. Measurements with passive dose meters (TLD600-TLD700 in a polyethylene cylinder, thorium radiator on Macrofol foil) resulted with doses of approximately 1 mSv for this pulse, while active Andersson-Braun (AB) counters under responded severely by several orders of magnitude.

In general, transient events are rare. But they may generate not only severe hardware damages but also relatively large dose increments up to several mSv. Considering such events in terms of "dose rate" concepts might be completely misleading. In a short period time scale dose rate might not be measurable and would be a more or less meaningless quantity. In terms of long periods the event might not even occur again. Only integrated dose increments of the entire event can be registered by passive dose meters and by very few active instruments.

According to the specific time structure of an accelerator the radiation fields may be repetitive. This is for instance true at the new linear electron accelerators of the free-electron lasers FLASH and XFEL. It holds also for synchrotron radiation sources like SPring8, ESRF, APS; BESSY-II and PETRA-III because of the top-up operation mode. The repetitions rates are up to 10 Hz with duty cycles of less than 0.01. Regardless of transient events that could occur also at these accelerators the radiation field is a sequence of dose shots which have to be measured. The dose increment per shot is expected to be much smaller as for the transient case but may well reach a few  $\mu$ Sv. For example, if the accelerator is in a bad condition a repetition rate of 1 Hz and a dose of 1  $\mu$ Sv per shot would lead to an average dose rate of 3.6 mSv/h behind shielding. This exposure has to be measured properly and machine operation has to be interrupted as early as reasonably possible.

## The principle of the new detection method

In 2005 a collaboration between Berthold Technologies and DESY was formed in order to develop a new system for the measurement of pulsed neutron radiation based on existing LB 6411 neutron dose rate monitors. With the new method, the LB 6411s are read-out time resolved with 1 ms resolution and delayed neutrons from the following reaction chain are detected. High-energy neutrons with energies above 40 MeV produce the  ${}^9\text{Li}$  nuclide in the polyethylene moderator via the spallation reaction  ${}^{12}\text{C}(n,X){}^9\text{Li}$  with a cross-section in the range between 0.1...1 mbarn [9]. It is unstable and decays with a half life of 178 ms:  ${}^9\text{Li} \rightarrow {}^9\text{Be}^* + \beta^- + \nu$ . The  ${}^9\text{Be}^*$  nuclide instantaneously disintegrates by emitting a fast neutron:  ${}^9\text{Be}^* \rightarrow 2\alpha + n$ . Thus, the detected neutrons are having a time spectrum according to the decay with 178 ms half life. The prompt radiation pulse with time zero can be detected utilising the prompt detector counts.

## Description of the detector system

The new detection concept utilises rem counters as neutron detectors and their moderators as  ${}^{12}\text{C}$  target to produce  ${}^9\text{Li}$  nuclei. We used the Berthold probes LB 6411 and LB 6411-Pb as rem-counters. For data acquisition with time resolved readout a new small data-logging unit, the Berthold LB 5360 was newly developed.

### **Neutron dose rate probes LB 6411 and LB 6411-Pb**

The neutron dose rate meter Berthold LB 6411 measures ambient dose equivalent  $H^*(10)$  for neutrons. It was developed as a consequence of the recommendations of the Internal Commission on Radiological Protection published in ICRP 60 (ICRP, 1991). The probe utilises for neutron detection a cylindrical  $^3\text{He}$  proportional counter tube centred in a polyethylene moderating sphere with diameter 25 cm. The probe's weight is about 10 kg. The response to neutron dose rate is 2.83 counts/nSv for bare  $^{252}\text{Cf}$ . The neutron energy range covers thermal energies up to 20 MeV. The energy dependent neutron response is tuned with internal neutron absorbing layers and it is  $\pm 30\%$  between 50 KeV and 10 MeV. A detailed description of the detector together with calibration data from the PTB and results of MCNP calculations was published elsewhere (Klett, 1997).

As it is well known that conventional rem-counters suffer from severe under responses at higher neutron energies, a special version LB 6411-Pb for neutron energies up to 1 GeV was recently developed. It is the LB 6411 with an additional external spherical layer of lead with a thickness of 10 mm. High energy neutrons are generating in the lead spallation neutrons and increase thus the response at higher energies. The overall weight is approximately 35 kg. The detector was calibrated in the CERF reference field at CERN/Geneva (Mitaroff, 2002) and showed an excellent dose response to high energy neutrons (Klett, 2004). The measured response at CERF relative to the required response was 98.8%, while it was for a conventional LB 6411 only 68.9%.

### **Time resolved readout**

The counting rates of the neutron detectors were acquired with time resolved readout with the newly developed small data acquisition system Berthold LB 5360. The unit is based on a Motorola 68340 CPU (max. 24.117 MHz). On board it has a real time clock, 128 KByte RAM, 1 MByte flash, a serial RS232 port and two counting channels for maximum rates up to 7.48 MHz. We used for this experiment readout time slices of exactly 1 ms, which were controlled by the real time clock. The minimum time slice would be 122  $\mu\text{s}$ . The system auto-synchronises to the accelerator's beam pulses using a trigger threshold condition. During a beam pulse the prompt counting rate is relatively high and exceeding this threshold the burst is identified. The system records for subsequent events the time difference relative to the beam pulse and accumulates and stores the counts as time-difference histograms. The data logger LB 5360 is analysing these histograms and if required is also transferring them periodically to a host or network.

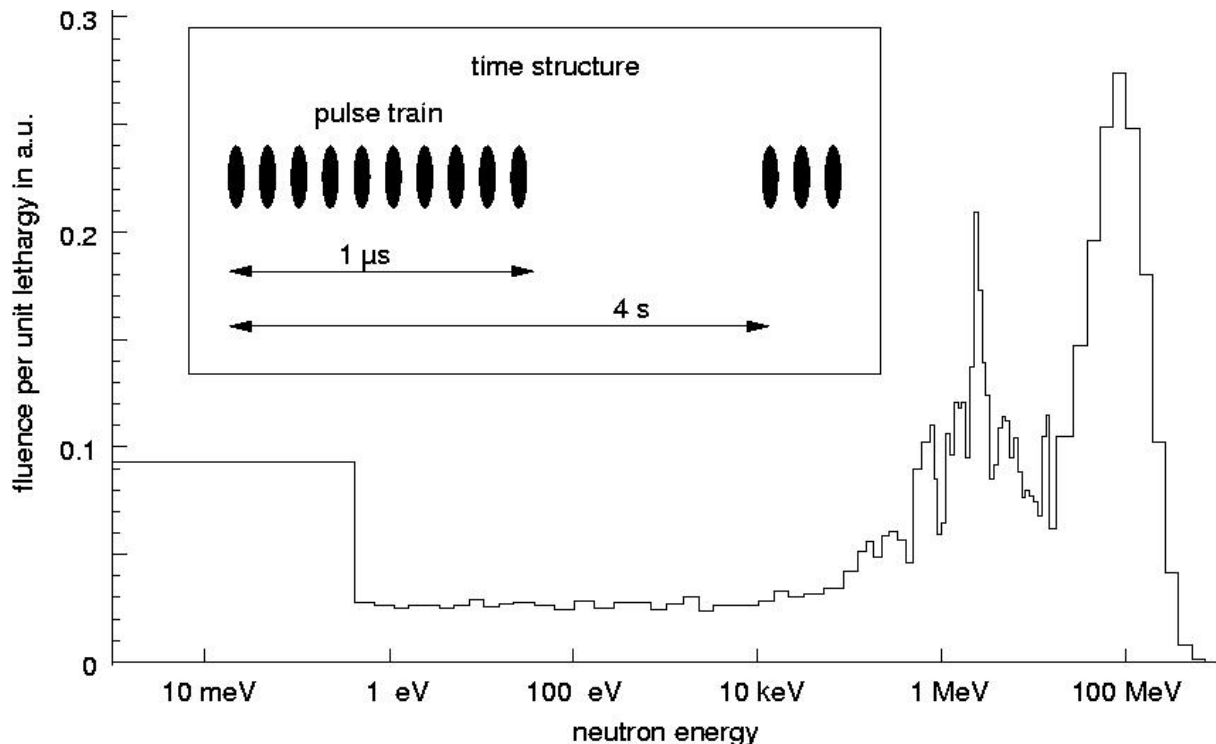
### **Measurements with pulsed neutron radiation**

These instruments were for the first time successfully tested with pulsed neutron fields on 9-10 March 2006 at DESY. The reference doses were determined with passive dose meters.

### **Beam and irradiation conditions**

The pulsed radiation field was generated by a 7.5 GeV proton beam in the transfer tunnel from the DESY III synchrotron to the PETRA storage ring. For this experiment a bending magnet in the injection line was switched off, in order to generate a complete beam loss in the shielding. It consisted of the concrete walls of the tunnel and the hall and soil in between and it had about 2.5 m of total thickness. Behind the shielding was the irradiation platform inside the PETRA experimental hall. It was located in lateral direction to the beam at a distance of about 3.2 m. The neutron ambient dose equivalent per primary proton was estimated by a "point source, line of sight" model to be  $4 \times 10^{-17}$  Sv (Dinter, 1996a). On the irradiation platform the neutron energy spectrum is expected to be in equilibrium for standard concrete as it is shown in Figure 1. The time structure of the proton beam is given by bunch trains with a spacing of 4 s. A single train consists of 10 bunches spaced by 96 ns. It is almost 1  $\mu\text{s}$  long and has a total charge of  $1 \times 10^{12}$  protons. A single bunch train generates a dose quantum of 40  $\mu\text{Sv}$  on the irradiation platform.

**Figure 1: Energy spectrum of the neutron fluence in lethargy representation on the irradiation platform. The inserted box displays the time structure of the proton beam.**



## Experimental results

The LB 6411 Pb and the LB 6411 together with passive neutron dose meters were simultaneously irradiated with 101 shots. Several passive dose meters were used to measure accumulated doses not affected by dead time effects. Reference dose increments for a single shot were extracted for comparison.

### Reference dose

The bubble detectors BD-PND from Bubble Technology Industries with a sensitivity of  $13 \mu\text{Sv}/\text{bubble}$  (Am-Be source) measured a dose of  $27 \mu\text{Sv}$ . It is due to low-energy neutrons only as bubble detectors are not sensitive to high-energy neutrons.

At DESY sets of two different passive dose meters are commonly used. Both, the pair of TLD600/700 in a Polyethylene cylinder and the Thorium radiator on Macrofol foil are calibrated for the entire high-energy neutron spectrum behind thick lateral concrete shielding. Their doses of  $50 \mu\text{Sv}$  and  $54 \mu\text{Sv}$  were measured, respectively. This agreement validates the assumption of a standard concrete equilibrium energy spectrum. The reading of the TLD700 leads to a  $\gamma$ -dose of  $7 \mu\text{Sv}$ .

The reference neutron doses for a single shot were chosen to be  $27 \mu\text{Sv}$  for the low-energy part and  $50 \mu\text{Sv}$  for the whole neutron spectrum.

### LB 6411 data processing

The counts of the LB 6411 were coherently accumulated shot by shot. The prompt counts were used as a trigger for auto-synchronisation. The raw data time spectrum is shown in Figure 2. On the very left the prompt peak can be seen.

For further analysis the following steps were applied: Normalising for a single shot, setting time zero right after the prompt peak and rebinning the time in logarithmically equidistant bins. The result is drawn in Figure 3, left. In order to have a closer look onto the time spectrum a lethargy representation is displayed in Figure 3, right. The normalisation is chosen such that the peak maximum corresponds to the integral number of counts of the decay pattern. The solid line is a two-exponentials fit. The high peak with a life time of 1.5 ms is the time-of-flight signal due to thermal neutrons from the source region. With a speed of 2.2 m/ms one gets a distance of 3.3 m representing the real geometry very well. The smaller peak with a life time of 245 ms is caused by the delayed neutrons from the  ${}^9\text{Li}$  decay.

**Figure 2: Accumulated raw data of the LB 6411 Pb from 101 shots are shown in a semi-log plot with equidistant (1 ms) time binning**

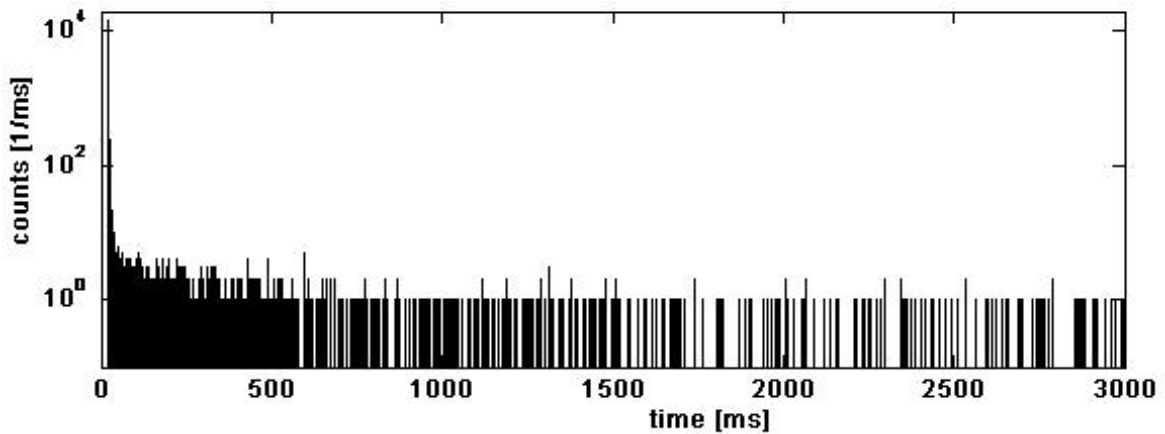
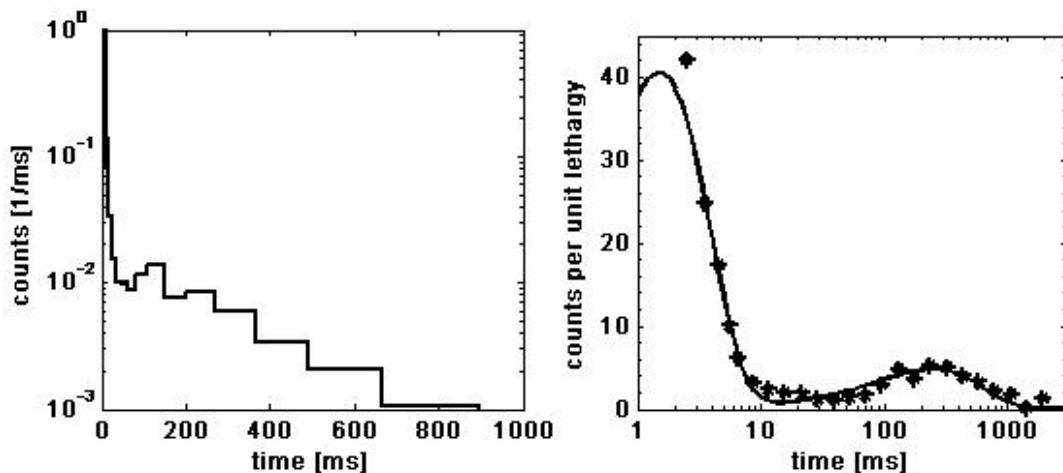


**Figure 3: Single shot response of the LB 6411 Pb in logarithmic time binning**

Time zero is right after the prompt peak. On the left, there is the semilog plot of the measured time spectrum with the time axis adapted to the  ${}^9\text{Li}$  decay. The plot on the right shows the same data (\*) in lethargy representation. The solid line is a two-exponential fit to the data. The normalisation is chosen such that the peak maximum corresponds to the integral number of counts of the decay pattern, that are 40 and 5 counts for the thermal neutron peak and the  ${}^9\text{Li}$  neutron peak respectively.



**Comparison to reference**

The results are summarised in Table 1. The upper part belongs to the LB 6411 and the lower part to the LB 6411 Pb. Any data correspond to a single shot.

The total number of counts for both rem-counters leads to doses that underestimate the reference value by several orders of magnitude. This is the case with the normal operation mode of the rem-counters.

In the time-resolved operation mode there is a clear response due to the delayed neutrons of the  ${}^9\text{Li}$  decay. With the reference dose of the high-energy part of the neutron spectrum the sensitivities of the LB 6411 and the LB 6411 Pb are calculated to be 0.26 and 0.21 counts/ $\mu\text{Sv}$  respectively.

**Table 1: Data of the single shot response of the LB 6411 Pb and LB 6411**

Device name	Quantity	Time constant	Number of counts	Sensitivity [counts/ $\mu\text{Sv}$ ]	Dose readout [ $\mu\text{Sv}$ ]	Reference dose [ $\mu\text{Sv}$ ]
LB 6411	Total	$\Delta = 3000$ ms	250	2830	0.09	27
	Thermal neutrons	$\tau = 1.5$ ms	87.3			
	${}^9\text{Li}$ neutrons	$\tau = 245$ ms	6.0	0.26		23
LB 6411 Pb	Total	$\Delta = 3000$ ms	155	2830	0.05	50
	Thermal neutrons	$\tau = 1.5$ ms	40.5			
	${}^9\text{Li}$ neutrons	$\tau = 245$ ms	4.8	0.21		23

The response due to thermal neutrons cannot be compared to a reference dose as it contains only those thermal neutrons coming from the source region far away. But both versions of the LB 6411 differ considerably. The Lead shell of the LB 6411-Pb might reduce the response due to thermal neutrons more than expected so far.

## Conclusion

There are functional prototypes of the time-resolved readout LB 5360 for the rem-counters LB 6411 and LB 6411-Pb from Berthold Technologies, Germany. Their responses due to pulsed high-energy neutrons were measured. The sensitivities are 0.26 and 0.21 counts/ $\mu\text{Sv}$  respectively. This method can be applied in pulsed high-energy neutron fields with repetition rates up to 5 Hz.

## Acknowledgements

The authors would like to thank M. Salmani, W. Clement and B. Mukherjee for handling and reading the passive dose meters and the DESY machine crews for delivering the proton beam at the right time to the right position.

## References

- Dinter, H., K. Tesch (1976), "Moderated Rem Meters in Pulsed Neutron Fields", *NIM*, 136, 389-392.
- Dinter, H., B. Racky, K. Tesch (1996), "Neutron Dosimetry at High-energy Accelerators", *NIM*, A 376, 104-114.
- Dinter, H., K. Tesch, D. Dworak (1996a), "Studies on the Neutron Field Behind Shielding of Proton Accelerators. Part I: Concrete Shielding", *NIM*, A 368, 265-272.
- Dinter, H., et al. (2000), "Calculation of Hadron Yields Around Thick Targets and Doses Behind Concrete Shielding of High-energy Electron Accelerators", *NIM*, A 455, 460-469.

International Commission on Radiological Protection (ICRP) (1991), *1990 Recommendations of the International Commission on Radiological Protection*, ICRP Publication 60, *Annals of the ICRP*, Vol. 21, No. 1-3.

Kellogg, D.A. (1953), "Cross Sections for Products of 90 MeV Neutrons on Carbon", *Physical Review*, Vol. 90, No. 2, 224-232.

Klett, A., B. Burgkhardt (1997), "The New Remcounter LB6411: Measurement of Neutron Ambient Dose Equivalent  $H^*(10)$  According to ICRP60 with High Sensitivity", *IEEE Transactions on Nuclear Science*, Vol. 44, No. 3, pp. 757-759, June.

Klett, A., et al. (2004), "A Neutron Dose Rate Monitor for High Energies", *Proceedings of the 3<sup>rd</sup> International Workshop on Radiation Safety of Synchrotron Radiation Sources (RadSynch'04/Spring-8)*, Yoshihiro Asano (Ed.), Mikazuki, Hyogo, Japan, 17-19 November.

Mitaroff, A., M. Silari (2002), "The CERN-EU High Energy Reference Field (CERF) Facility for Dosimetry at Commercial Flight Altitudes and in Space", *Rad. Prot. and Dos.*, Vol. 102, No. 1, pp. 7-22.



## **Session I**

### **Source term and related topics**

***Chair: S. Teichmann***



## Shielding parameters of concrete and polyethylene for the PSI proton accelerator facilities

**Sabine Teichmann**

Paul Scherrer Institut, Switzerland

### Abstract

*The Paul Scherrer Institut (PSI) operates 72-MeV, 250-MeV and 590-MeV proton accelerator facilities. To provide a simple, systematic approach to arising shielding questions within new projects, MCNPX has been used to calculate angle-dependent shielding parameters of concrete, i.e. dose-rate source terms and attenuation lengths, for protons with these three energies striking a stopping-length iron target. Two calculational models (tallies at various levels within a shielding sphere and tallies on the outside of a shielding sphere of varying thickness) and two cross-section sets (ENDF/B-VI and LA150) have been examined. Polyethylene has also been considered as shielding material for 72-MeV protons. The contributions of photons and neutrons to the total dose rate were analysed. The results are compared to available measurements.*

## Introduction

The Paul Scherrer Institut (PSI) has been operating 72-MeV and 590-MeV proton accelerator facilities since 1974. An upgrade of the 590-MeV facility from 2 to 3 mA DC proton currents is in progress. In addition to the existing target stations for isotope and meson production and the spallation neutron source SINQ, an ultra-cold neutron source (UCN) is currently under construction, which will be fed by the 590-MeV ring cyclotron. In 2005, commissioning tests began on the new medical cyclotron at PSI. It produces 250-MeV protons, which can be degraded down to 70 MeV, to feed the existing proton therapy area, two new treatment rooms and one experimental area.

To provide a simple, systematic approach to shielding problems arising within new projects, the Monte Carlo particle transport code MCNPX version 2.5.f [1] has been used to calculate angle-dependent shielding parameters, *i.e.* dose-rate source terms and attenuation lengths that can be used for the dose rate  $H$  behind a shield:

$$H(E_p, \theta, d(\theta)) = \frac{1}{r^2} \left( H_{0,1}(E_p, \theta) e^{-\frac{d(\theta)}{\lambda_1(E_p, \theta)}} + H_{0,2}(E_p, \theta) e^{-\frac{d(\theta)}{\lambda_2(E_p, \theta)}} \right) \quad (1)$$

where  $E_p$  is the proton beam energy,  $r$  is the distance from the target to the point of interest,  $d(\theta)$  is the effective shielding thickness under angle  $\theta$  (*i.e.* the length of shielding material that is being traversed),  $H_{0,i}(E_p, \theta)$  and  $\lambda_i(E_p, \theta)$  are parameters for the angle-dependent source terms and attenuation lengths for small and large shielding depths.

Calculations were made for the following cases (proton energy, shielding material):

- 1) 72 MeV, normal concrete;
- 2) 72 MeV, polyethylene (PE);
- 3) 250 MeV, normal concrete;
- 4) 590 MeV, normal concrete.

An angular range from 0 to 90 degrees in steps of 10 degrees was considered.

## Calculational models

The principle of the method is described in [2]. A cylindrical block of iron, with dimensions shown in Table 1, is used as the target for the proton beam. It is located at the centre of a spherical shielding shell, 3 to 5 m thick and with a large inner radius of at least 90 m, so that effects related to the curvature and to neutron scattering can be neglected. The compositions of the used shielding materials are given in Table 2. Geometry splitting and Russian roulette are used as variance reduction techniques. The shielding is subdivided into shells of 15 to 20 cm thickness. With increasing radius, the shells are assigned increasing importance values. The ratio of the importance values between adjacent shells never exceeds a factor 2. Surface flux tallies (F2-tallies), segmented into angular bins of 10 degree widths between 0° and 90° are used to score outgoing energy-dependent neutron and photon fluxes. They are folded with energy-dependent conversion factors for the ambient dose equivalent, listed in Tables 3 and 4.

Final results were obtained by using the fluxes and dose rates at the surface crossing boundaries every 15-20 cm (Model 1). By employing cosine-binning, only the outward-directed particle fluxes were selected. The effect of reflection off the outer shells on the results was thus minimised. However, multiple reflected particles going outwards are still being scored. To investigate this effect, a more realistic model was used for a few reference cases. In this model, surface fluxes were scored at the outermost boundary of a shielding shell with three different thicknesses (Model 2): 0.9 m, 1.35 m and 1.95 m for 72 MeV; 1 m, 2 m and 3 m for 250 MeV; 1.4 m, 2.4 m and 3.4 m for 590-MeV protons.

Furthermore, two different sets of neutron cross-section libraries have been used with Model 1: LA150 (Model 1a) and ENDF/B-VI (Model 1b).

Unless otherwise noted, results and discussions refer to Model 1a.

**Table 1: Parameters of the iron target used in the simulations;  $\rho = 7.8 \text{ g/cm}^3$** 

$E_p$ [MeV]	Thickness [mm]	Radius [mm]	Proton range [mm]
72	10	7	7.6
250	75	58	68
590	284	220	274

**Table 2: Chemical compositions used in the simulations for normal concrete ( $\rho = 2.31 \text{ g/cm}^3$ ) and polyethylene ( $\rho = 0.95 \text{ g/cm}^3$ ) in atomic fractions**

	H	C	O	Mg	Al	Si	Ca	Fe
Concrete	0.1064	0.2530	0.4446	0.0233	0.0075	0.0213	0.1415	0.0024
PE	0.6667	0.3333						

**Table 3: Used flux-to-dose conversion factors for neutrons,  $CF_n$** 

The factors for energies up to 100 MeV are taken from [3], above that from [4]

$E_n$ [MeV]	$2.5 \cdot 10^{-8}$	0.024	0.144	0.25	0.57	1.2	2.5	2.8	3.2	5.0	14.8
$CF_n$ [pSv cm <sup>2</sup> ]	11.4	20.2	134	215	355	433	437	433	429	420	561
$E_n$ [MeV]	19	30	50	75	100	150	200	300	400	500	600
$CF_n$ [pSv cm <sup>2</sup> ]	600	515	400	330	300	285	285	306	349	420	487

**Table 4: Used flux-to-dose conversion factors for photons,  $CF_p$** 

The factors are taken from [5]

$E_\gamma$ [MeV]	0.01	0.015	0.02	0.03	0.04	0.05	0.06	0.08	0.10	0.15	0.20
$CF_p$ [pSv cm <sup>2</sup> ]	0.082	0.84	1.04	0.81	0.61	0.51	0.51	0.56	0.62	0.87	1.23
$E_\gamma$ [MeV]	0.3	0.4	0.5	0.6	0.8	1.0	1.5	2.0	3.0	4.0	5.0
$CF_p$ [pSv cm <sup>2</sup> ]	1.81	2.36	2.78	3.46	4.29	5.18	6.92	8.25	10.40	10.70	10.40
$E_\gamma$ [MeV]	6.0	8.0	10.0								
$CF_p$ [pSv cm <sup>2</sup> ]	9.57	9.10	8.80								

## MCNPX results

As an example, Figure 1 shows calculated spectra of outgoing neutrons between 0 and 10 degrees for different concrete shielding thicknesses. The source spectrum is included as well.

For each angular bin, the relative contributions to the total dose rate of neutrons above and below 19 MeV and of photons up to 10 MeV have been extracted as a function of depth within the shielding material. Since the neutron dose rate measurement instruments routinely used at PSI for survey purposes have a very low efficiency for neutrons above about 20 MeV, this information is needed to estimate the total neutron dose rate from the measured dose rate. Results for the forward and lateral angular range are shown in Figures 2-5. It can be seen that for small depths within the shielding, the contribution of the low-energy neutrons dominates strongly in all cases. With increasing depth, the contribution of the high-energy neutrons rises and then levels off at around 40-50% for concrete shielding. Due to this change in the neutron spectrum, the double exponential function of Equation (1) is needed to accurately describe the dose attenuation over the whole shielding range. The effect is less pronounced in the case of 590-MeV protons at forward angles. In the case of polyethylene shielding, the neutron dose is dominated by the high-energy neutrons after a short distance into the shielding, whereas for concrete shielding, the high-energy neutron dose is lower or comparable to the low-energy neutron dose.

**Figure 1: Calculated neutron spectra in the forward direction at three depths within concrete shielding for 72-MeV, 250-MeV and 590-MeV protons. The spectra labelled “0 cm” correspond to the source spectrum.**

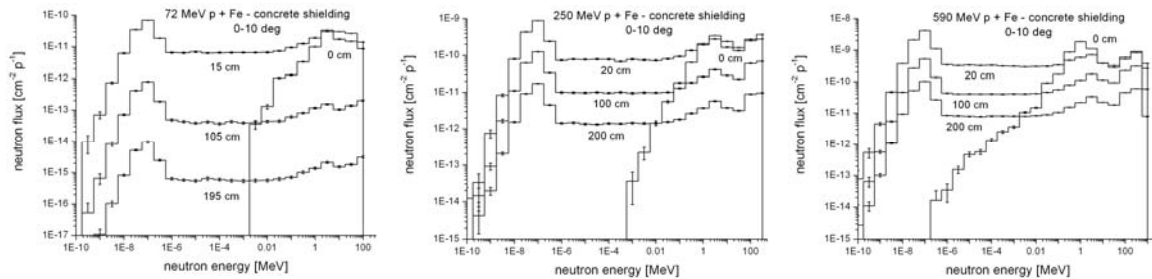


**Figure 2: Relative contributions to the total dose rate for 72-MeV protons and concrete shielding at forward and lateral angles**

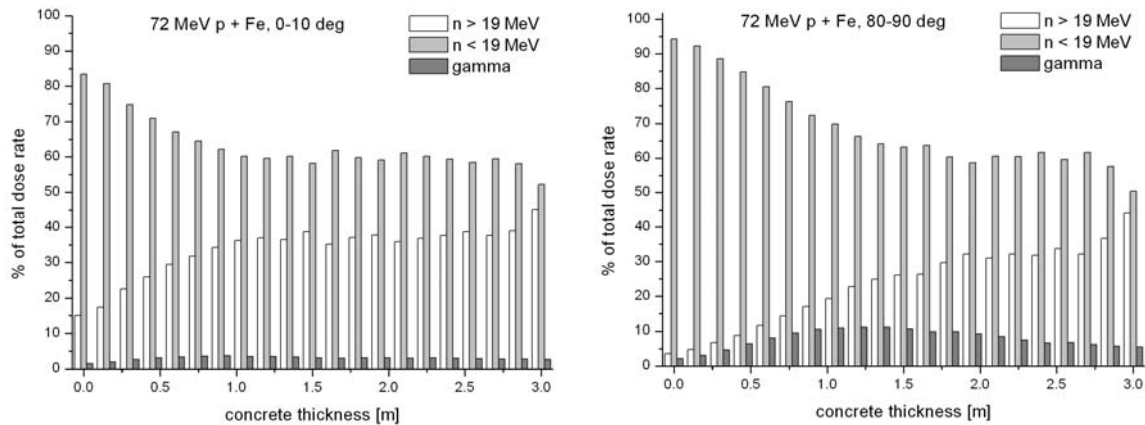
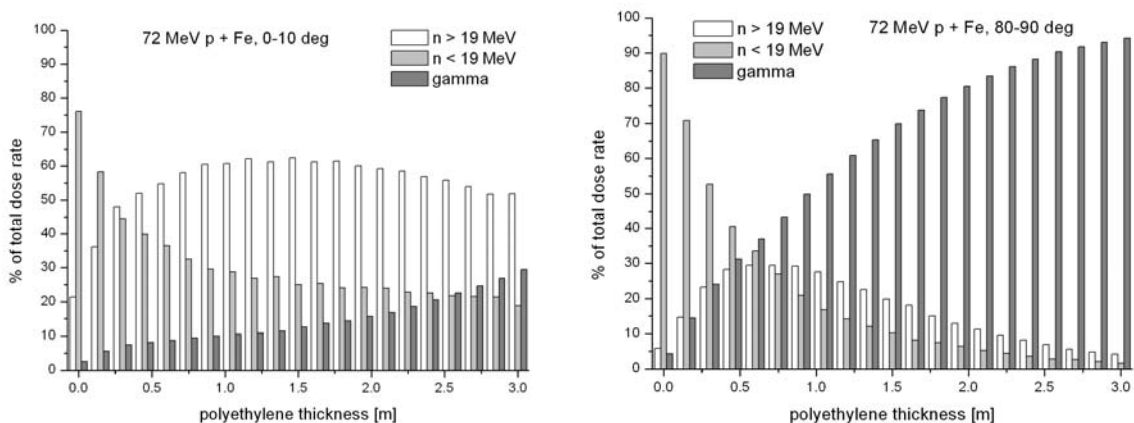


**Figure 3: Relative contributions to the total dose rate for 72-MeV protons and polyethylene shielding at forward and lateral angles**



The calculated contribution of photons is of the order of a few per cent in the case of concrete shielding but plays a prominent role in the case of polyethylene shielding, especially at more lateral angles and larger depths within the shielding. The high hydrogen content in polyethylene leads to a high production of neutron-capture photons with an energy of 2.2 MeV. The large contribution of photons to the total dose rate is thus expected in this case.

In all cases with concrete shielding, it can be seen that the relative contributions of high-energy neutrons increase for the last bin (which corresponds to the outermost surface) with respect to the previous bins. This effect is due to the use of Model 1 instead of Model 2. In Model 1, all scoring surfaces, except the last one, are followed by material which can backscatter neutrons. Due to multiple scattering, some of these backscattered neutrons are scored more than once. The probability for scattering is higher for the low-energy neutrons and their contribution to the dose rate is therefore raised. The neutron flux crossing the last surface will have much less contributions from multiple scattering and should more accurately reflect the more realistic conditions of Model 2. This was confirmed with the results from calculations using Model 2. Comparing the dose rate contributions for Model 1 and Model 2 at a specific shielding thickness shows that the low-energy neutron dose contribution is overestimated in the shell model (Model 1) by about 10%.

**Figure 4: Relative contributions to the total dose rate for 250-MeV protons and concrete shielding at forward and lateral angles**

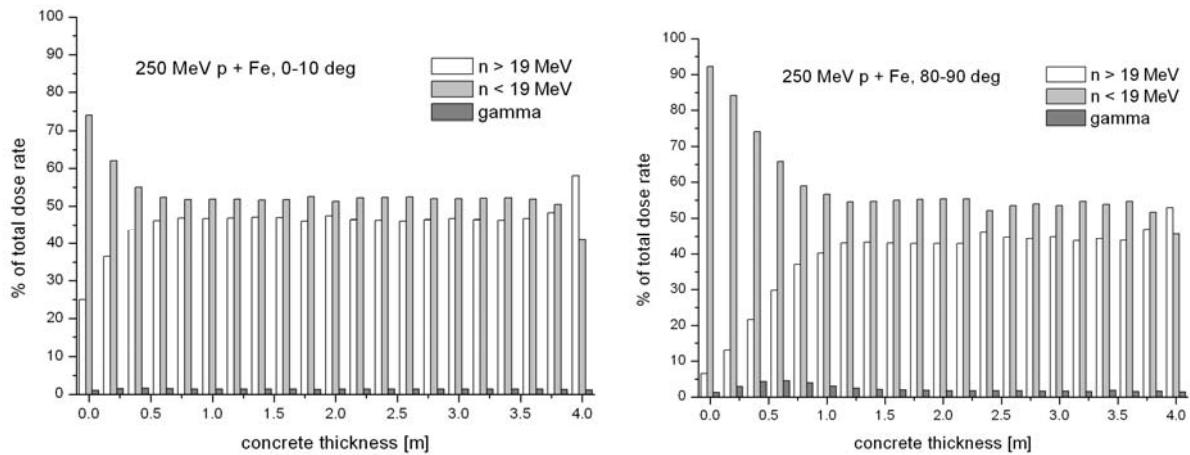
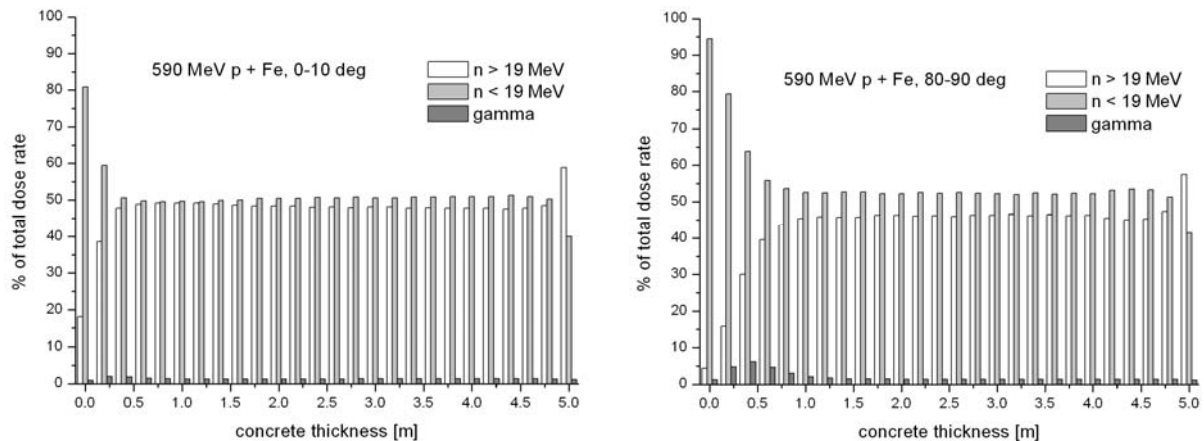


**Figure 5: Relative contributions to the total dose rate for 590-MeV protons and concrete shielding at forward and lateral angles**



## Data analysis

By plotting the calculated total dose rate  $H$ , multiplied with the square of the distance  $r$  from the target, against the shielding thickness [see Equation (1)], an exponential fit can be used to obtain attenuation lengths and source terms (dose rate extrapolated to zero shielding thickness).

## Model comparisons

For the comparison between the different employed models, a single exponential fit at larger shielding depths, where the neutron spectrum has reached an equilibrated state, was used. The different models were compared only for the cases with concrete shielding.

The attenuation lengths extracted from Model 2 (shielding shells with different thicknesses) do not differ significantly from those of Model 1 (shell model); the differences lie within  $\pm 1-3\%$ . The source terms are higher by about 2-20% for Model 1. A similar observation has been reported in [2].

The use of different cross-section libraries (Models 1a, 1b) did not lead to statistically significant variations in the attenuation lengths and source terms, although there seemed to be a tendency towards slightly smaller values for the attenuation lengths when using the ENDF/B-VI library instead of the LA150 library.

Analysing resulting dose rates for a specific shielding case showed that the attenuation lengths and source terms from Model 1a (shell model with LA150 libraries) seem to give the most conservative results, i.e. slightly higher dose rates for the same shielding thickness. It was therefore selected for the final calculations and data analysis.

**Figure 6: Total dose rate attenuation curves in concrete and polyethylene for 72-MeV protons (lines are eye guides only)**

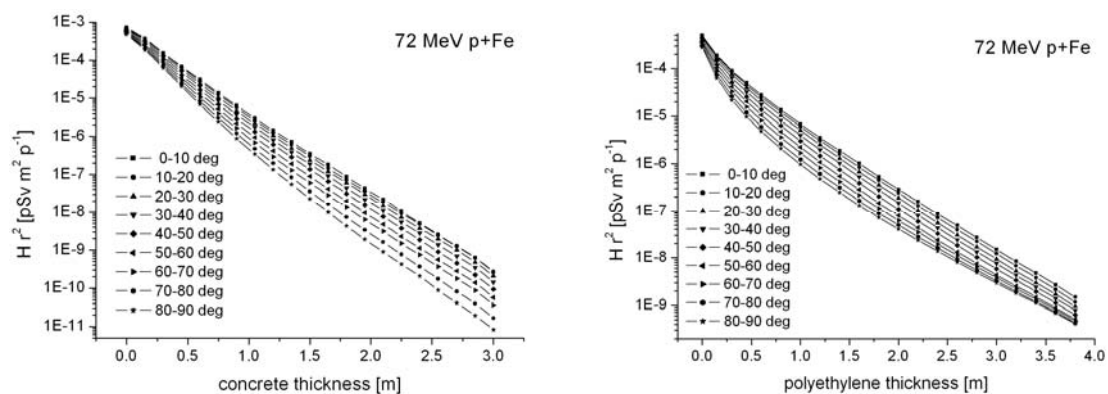
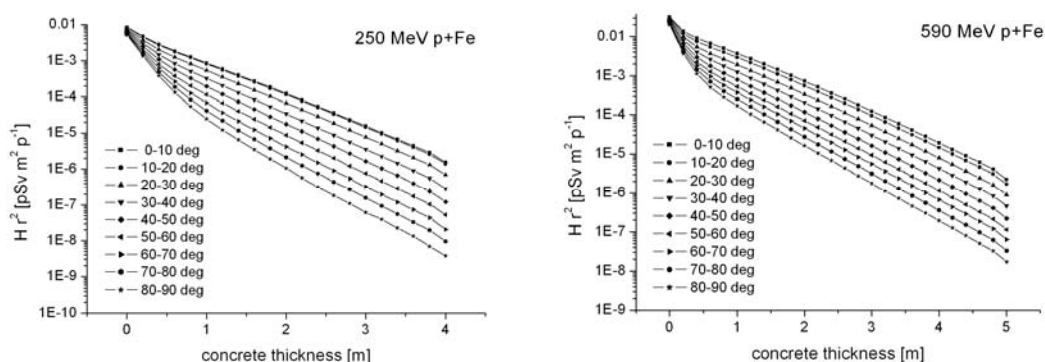


**Figure 7: Total dose rate attenuation curves in concrete for 250-MeV and 590-MeV protons (lines are eye guides only)**



### Shielding parameters

Figures 6 and 7 show the calculated total dose rate attenuation curves from Model 1a for all angular ranges. The data were fitted with a non-linear least-square method for each angular bin, using the graphing and analysing program Origin 6.1 [6]. Dose rates scored at the innermost and outermost boundaries were not used. In general, use of the double exponential fit according to Equation (1) gives the best fitting results. The parameter pairs  $(H_{0,1}, \lambda_1)$  and  $(H_{0,2}, \lambda_2)$  correspond to the small-depth and large-depth exponential functions, respectively. As discussed earlier, the change in the neutron spectrum at small depths is less pronounced for 590 MeV at forward angles, so that a fit with one exponential gives good results here. In all cases, the correlation coefficient R was larger than 0.995, indicating a very good fit. The results for the shielding parameters and their statistical errors are listed in Tables 5-8.

**Table 5: Source terms and attenuation lengths in concrete for 72-MeV protons on Fe**

Angular bin	$H_{0,1}$ [ $10^{-16}$ Sv m <sup>2</sup> p <sup>-1</sup> ]	$\lambda_1$ [g/cm <sup>2</sup> ]	$H_{0,2}$ [ $10^{-16}$ Sv m <sup>2</sup> p <sup>-1</sup> ]	$\lambda_2$ [g/cm <sup>2</sup> ]
0-10°	5.50 ± 0.30	32.94 ± 1.44	3.60 ± 0.40	49.73 ± 0.52
10-20°	6.70 ± 0.20	35.84 ± 0.62	2.00 ± 0.20	51.84 ± 0.54
20-30°	6.60 ± 0.10	34.68 ± 0.45	1.80 ± 0.10	51.41 ± 0.41
30-40°	6.30 ± 0.09	33.91 ± 0.37	1.50 ± 0.10	50.74 ± 0.37
40-50°	6.00 ± 0.07	32.60 ± 0.33	1.30 ± 0.09	49.51 ± 0.34
50-60°	6.00 ± 0.05	32.14 ± 0.26	0.90 ± 0.07	49.24 ± 0.37
60-70°	5.80 ± 0.04	31.46 ± 0.23	0.60 ± 0.05	48.96 ± 0.43
70-80°	5.60 ± 0.04	30.39 ± 0.22	0.50 ± 0.05	46.68 ± 0.46
80-90°	5.50 ± 0.04	29.95 ± 0.21	0.40 ± 0.05	45.66 ± 0.63

**Table 6: Source terms and attenuation lengths in polyethylene for 72-MeV protons on Fe**

Angular bin	$H_{0,1}$ [ $10^{-16}$ Sv m <sup>2</sup> p <sup>-1</sup> ]	$\lambda_1$ [g/cm <sup>2</sup> ]	$H_{0,2}$ [ $10^{-16}$ Sv m <sup>2</sup> p <sup>-1</sup> ]	$\lambda_2$ [g/cm <sup>2</sup> ]
0-10°	2.80 ± 0.09	15.62 ± 0.53	1.20 ± 0.06	31.65 ± 0.22
10-20°	2.80 ± 0.05	15.61 ± 0.29	1.10 ± 0.03	31.35 ± 0.13
20-30°	2.60 ± 0.03	15.87 ± 0.22	0.90 ± 0.02	31.15 ± 0.12
30-40°	2.40 ± 0.03	15.79 ± 0.18	0.70 ± 0.02	31.40 ± 0.11
40-50°	2.20 ± 0.02	15.44 ± 0.15	0.50 ± 0.01	31.65 ± 0.11
50-60°	2.00 ± 0.02	15.22 ± 0.13	0.300 ± 0.008	31.98 ± 0.11
60-70°	1.80 ± 0.02	14.80 ± 0.12	0.200 ± 0.005	32.86 ± 0.11
70-80°	1.70 ± 0.02	14.17 ± 0.10	0.100 ± 0.003	33.88 ± 0.10
80-90°	1.40 ± 0.02	14.26 ± 0.09	0.099 ± 0.002	35.13 ± 0.11

**Table 7: Source terms and attenuation lengths in concrete for 250-MeV protons on Fe**

Angular bin	$H_{0,1}$ [ $10^{-15}$ Sv m <sup>2</sup> p <sup>-1</sup> ]	$\lambda_1$ [g/cm <sup>2</sup> ]	$H_{0,2}$ [ $10^{-15}$ Sv m <sup>2</sup> p <sup>-1</sup> ]	$\lambda_2$ [g/cm <sup>2</sup> ]
0-10°	2.11 ± 0.08	26.10 ± 2.26	6.40 ± 0.07	115.40 ± 0.30
10-20°	2.16 ± 0.05	26.01 ± 1.26	6.18 ± 0.04	114.53 ± 0.17
20-30°	3.30 ± 0.04	31.97 ± 0.61	4.44 ± 0.03	109.23 ± 0.17
30-40°	5.42 ± 0.27	28.48 ± 0.97	3.10 ± 0.03	102.32 ± 0.19
40-50°	5.12 ± 0.14	32.31 ± 0.67	2.05 ± 0.02	97.35 ± 0.23
50-60°	5.03 ± 0.09	33.80 ± 0.52	1.31 ± 0.02	92.85 ± 0.29
60-70°	4.92 ± 0.07	34.79 ± 0.42	0.81 ± 0.02	88.44 ± 0.38
70-80°	4.86 ± 0.06	33.92 ± 0.36	0.53 ± 0.02	84.87 ± 0.47
80-90°	4.85 ± 0.06	32.19 ± 0.33	0.38 ± 0.02	79.08 ± 0.60

**Table 8: Source terms and attenuation lengths in concrete for 590-MeV protons on Fe**

Angular bin	$H_{0,1}$ [ $10^{-15}$ Sv m <sup>2</sup> p <sup>-1</sup> ]	$\lambda_1$ [g/cm <sup>2</sup> ]	$H_{0,2}$ [ $10^{-15}$ Sv m <sup>2</sup> p <sup>-1</sup> ]	$\lambda_2$ [g/cm <sup>2</sup> ]
0-10°	–	–	20.34 ± 0.07	133.78 ± 0.11
10-20°	–	–	16.88 ± 0.03	131.81 ± 0.07
20-30°	–	–	12.62 ± 0.02	125.27 ± 0.06
30-40°	–	–	9.60 ± 0.02	119.13 ± 0.06
40-50°	23.80 ± 1.10	21.26 ± 0.45	5.83 ± 0.02	117.20 ± 0.09
50-60°	18.69 ± 0.48	24.47 ± 0.34	4.16 ± 0.02	113.04 ± 0.11
60-70°	16.08 ± 0.30	26.52 ± 0.29	3.05 ± 0.02	109.53 ± 0.12
70-80°	14.55 ± 0.21	27.88 ± 0.25	2.20 ± 0.01	105.70 ± 0.14
80-90°	13.43 ± 0.17	28.46 ± 0.22	1.55 ± 0.01	102.37 ± 0.18

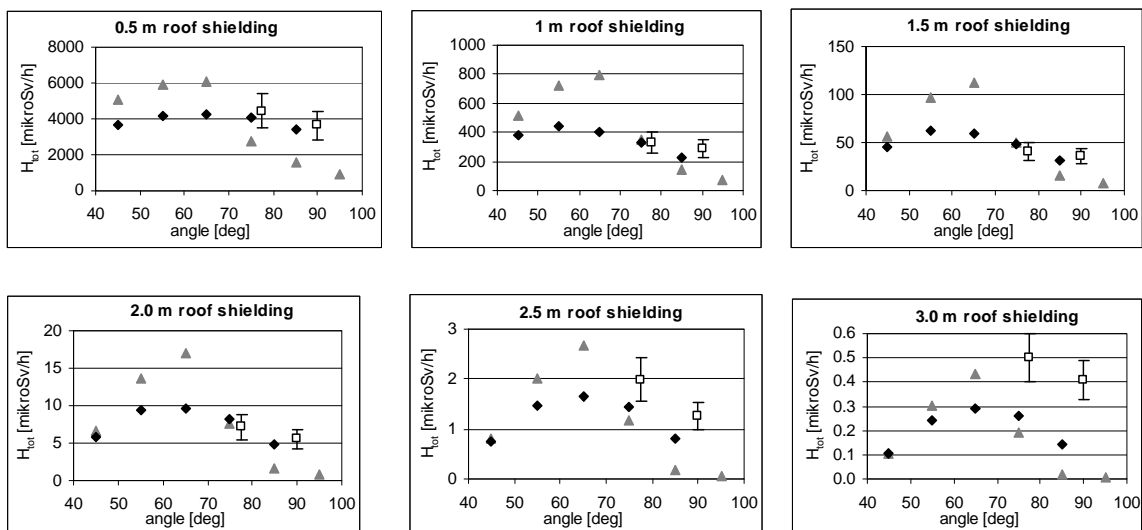
### Comparison with available measurements

Many of the existing shielding installations at PSI consist of combinations of iron with concrete and the calculated parameters are not applicable for those cases. Also, it is generally difficult to find good measurement locations with well defined conditions. Measured data for comparison purposes are therefore scarce and are restricted at the moment to a proton energy of 250 MeV.

Results of measurements for the new medical cyclotron facility PROSCAN at PSI were reported in Ref. [7]. 250-MeV protons were stopped in a cylindrical copper block of 100 mm diameter and 70 mm length and dose rates were measured on the roof made of varying thicknesses of concrete. In Figure 8, the results of [7] are shown together with calculated total dose rates using the shielding parameters from Table 7. Calculated values using the parameters from [8] (only available for a single exponential), which were used for the comparison in [7], are also shown. A density of 2.4 g/cm<sup>3</sup> was used for concrete (specification for shielding blocks at PSI).

**Figure 8: Comparison of measured and calculated total dose rates for 250-MeV protons**

Experimental data (open squares) are taken from [7]. The calculated values (black diamonds) represent angular bins of ±5°. Calculated values using the parameters from [8] are also shown for comparison (grey triangles). The angular uncertainty of the measured data is about ±2°.



The agreement is very good except for the cases with 2.5 and 3 m shielding. At these thicknesses, the value of the concrete density becomes increasingly important. Using 2.3 g/cm<sup>3</sup> leads to 30-40% larger calculated dose rates and better agreement. Also, the measurements at 3 m shielding are close to the detection limit of 0.1 μSv/h and may be affected by background which was not properly

considered. The calculated total dose rates with the parameters from Table 7 have a smoother dependence on angle than the calculated dose rates using the parameters from [8], with generally higher values at lateral angles and a less pronounced peak around 60°. For 0.5 m shielding and around 90°, they give a better agreement.

Preliminary dose rate surveys at the PROSCAN facility also seem to be in good agreement with calculations presented here.

The measured relative contribution of photons to the total dose rate varies with the shielding thickness, but is approximately 10% ([7] and confirmed during the preliminary dose rate surveys at the PROSCAN facility). This is higher than the 2-4% calculated here (see Figure 4). General experience at the PSI facilities indicates that the calculated dose rate contributions of photons in concrete shielding are underestimated, although precise measurements are difficult because of high background levels. However, photons still play a minor role for the total dose rate behind concrete shielding.

## Conclusions

The calculations of shielding parameters of concrete and polyethylene are part of an effort to provide a simple, systematic approach to shielding questions arising at the PSI proton accelerator facilities. In general, a double exponential gives a better fit over the whole shielding range between 15 cm and 5 m. The resulting two pairs of source-term and attenuation-length parameters correspond to an exponential function for small and large shielding depths, respectively. This is also reflected in the change of the relative contributions to the total dose rate of neutrons above or below 19 MeV as a function of shielding depth. In the case of polyethylene shielding, photons play an important role. For concrete shielding, the dose rate is dominated by neutrons, with a high-energy neutron component of about 40-50% at larger shielding depths.

Use of the shell-model approximation leads to an overestimation of the source terms by 2-20%, while the attenuation lengths are not significantly affected; the dose-rate contribution of neutrons below 19 MeV is overestimated within the shielding by about 10%. In view of other uncertainties, this is considered to be a good approximation. The two choices of cross-section libraries did not lead to significantly different results.

Comparisons with measurements for 250-MeV areas at PSI show good agreement for the total dose rate. The contribution of photons seems to be underestimated for concrete shielding, but this is of little importance to the total dose rate. The used flux-to-dose conversion factors for higher-energy photons could be part of the reason for this discrepancy.

Since many shielding installations at PSI consist of a combination of iron and concrete, additional calculations are planned to incorporate that option. It is also foreseen to include other target materials, e.g. carbon and lead. More measurements under well-defined conditions are needed to validate the calculational methods.

## References

- [1] J.S. Hendricks, *et al.*, MCNPX, Version 2.5.f, Los Alamos National Laboratory, Los Alamos, NM, USA, LA-UR-05-0891 (2005).
- [2] S. Agosteo, *et al.*, "Attenuation Curves in Concrete of Neutrons from 100-400 MeV per Nucleon He, C, and Ne Ions", *Proc. of the 6<sup>th</sup> Specialists Meeting on Shielding Aspects of Accelerators, Targets and Irradiation Facilities (SATIF-6)*, 10-12 April 2002, Stanford, CA, USA, OECD/NEA, Paris, pp 65-75 (2004).

- [3] *Verordnung über die Personendosimetrie*, Swiss Federal Publication, SR 814.501.43 (2000).
- [4] A.V. Sannikow, E.N. Savitskaya, *Ambient Dose Equivalent Conversion Factors for High Energy Neutrons Based on the New ICRP Recommendations*, Institute for High Energy Physics report, Russia, pp. 95-98 (1995).
- [5] A. Ferrari, M. Pelliccioni, "On the Conversion Coefficients from Fluence to Ambient Dose Equivalent", *Radiation Protection Dosimetry*, Vol. 51, No. 4, pp. 251-255 (1994).
- [6] OriginLab Corporation, One Roundhouse Plaza, Northampton, MA 01060, USA, [www.originlab.com](http://www.originlab.com).
- [7] S. Teichmann, et al., "Dose Rate Measurements Behind Different Shielding for 250 MeV Protons on a Thick Copper Target", *Proc. of the 6<sup>th</sup> Specialists Meeting on Shielding Aspects of Accelerators, Targets and Irradiation Facilities (SATIF-6)*, 10-12 April 2002, Stanford, CA, USA, OECD/NEA, Paris, pp. 37-45 (2004).
- [8] S. Agosteo, et al., "Double Differential Distributions and Attenuation in Concrete for Neutrons Produced by 100-400 MeV Protons on Iron and Tissue Targets", *Nucl. Instr. and Meth.*, B 114, pp. 70-80 (1996).

## Calculation of the neutron spectra at the electron test linac of PAL and the MC50 proton accelerator of KIRAMS

**Bong-Hwan Kim,<sup>1</sup> Hyun-Ki Kim,<sup>2</sup> Seong-Woo Kwak,<sup>3</sup> Hee-Seock Lee<sup>4</sup>**

<sup>1</sup>Korea Atomic Energy Research Institute

<sup>2</sup>Korea Institute of Radiological and Medical Science

<sup>3</sup>National Nuclear Management and Control Agency, Korea

<sup>4</sup>Pohang Accelerator Laboratory, POSTECH, Korea

### Abstract

*The MCNPX was used to calculate the neutron fluence spectra generated by using the lead and beryllium targets bombarded with electron and proton, respectively, at the electron test linac of PAL and the MC50 proton accelerator of KIRAMS in a series of works for a quantification of the neutron fields. Neutrons were assumed to be produced from a target struck by electrons with an energy of 65 MeV and from two Be targets of different thickness, 1.0 and 10.5 mm, bombarded by 35 and 45 MeV protons respectively. Major geometrical configurations such as a beam stopper and the gantry to collimate the neutron at the MC50 facility were simulated to describe the neutron fields as realistically as possible while a simple geometry was considered in the case of the linac of PAL. Additional calculation of the neutron spectrum at the facility of National Accelerator Centre (NAC) in South Africa was performed for the purpose of a comparison.*

## Introduction

From the seventies, intense neutron sources have been developed by using an accelerator which can accelerate the charged particle from 10 to 70 MeV and used for applications in the field of radiobiology, radiotherapy and materials research [1-4]. Especially the neutron therapy facilities have favoured the use of a thick Be target and protons as the projectiles to produce the fast neutrons because a given cyclotron can accelerate protons to twice the energy to which it can accelerate deuterons and thus produce intense neutron fields per unit current applied. On the other hand, photon and neutron sources produced from the targets of a high atomic number by high energetic electrons have been used for a radiation shielding analysis and a nuclear reaction cross-section measurement.

Accurate information of neutron sources such as the energy and fluence is important and needs to be supplied to beam users for an analysis of their work done. Unfortunately these do not seem to be enough so that the neutron fluence spectra at the measurement place are known clearly. There are only a few measurements for quantifying the neutron fields at accelerator facilities and some results are different from each other due to difficulties in the measurement technique, the operational condition and a complication of the instrumentations implemented [1-4].

This study is a series of works for a quantification of the neutron field produced at the neutron therapy room of KIRAMS and at the electron test linac of PAL through the determination of the spectral information and thus the calculation results can be used for unfolding the measured data of the neutron spectrometer like a Bonner Sphere.

## Description of the MC50, NAC and linac facilities

KIRAMS has operated the MC50 cyclotron (MC50) for neutron therapy and radioisotope production since 1986 [5] while it is being used only for RI production and irradiation test for a material research. The MC50 accelerates protons with an energy of 45 MeV and it has several beam ports for a proton or neutron irradiation. Beam current is controlled from a few nA to ten mA. NAC of South Africa accelerates protons to 66 MeV and it has a 19.6 mm thick Be target while the MC50 has a 10.5 mm thick Be target.

The electron linac of PAL accelerated electrons with an energy of 65 MeV in this measurement. The test linac consists of an electron linac, a water-cooled Ta target and an 11-metre long time-of-flight (TOF) measurement path. A 5.5 cm thick lead block as a target to produce the neutron fields was placed in front of the Ta target holder and the overall length of the linac was about 15 m.

Major configurations of the MC50, NAC and linac facilities were extracted from useful literatures and summarised in Table 1.

Schematic diagram of the neutron beam guide of the MC50 cyclotron (inside the gantry) is shown in Figure 1. The major geometry surrounding the target of the NAC facility is similar to that of the MC50 unit except for the total length of the collimator and the thickness of the Be target and the primary iron filter. Key parameters such as the proton energy, the thickness of the target and the primary filter were changed to fit the geometry of the NAC but the beam collimator was the gantry of the MC50 unit.

Geometry of the thin Be target and its surroundings is simple because it has no collimator and no filter. Neutrons from the thin target were emitted omni-directionally and had an angular distribution. A 6 mm thick aluminium was added to stop 35 MeV protons and it also contributed to producing neutron through the (p,n) reaction like in other targets because a proton of 35 MeV cannot be fully stopped in a thin Be target.

The thick lead target was placed between an electron beam tube and the water cooled Ta target in this calculation and therefore the beam direction of the neutrons from the target of the electron linac was approximately  $4\pi$ .

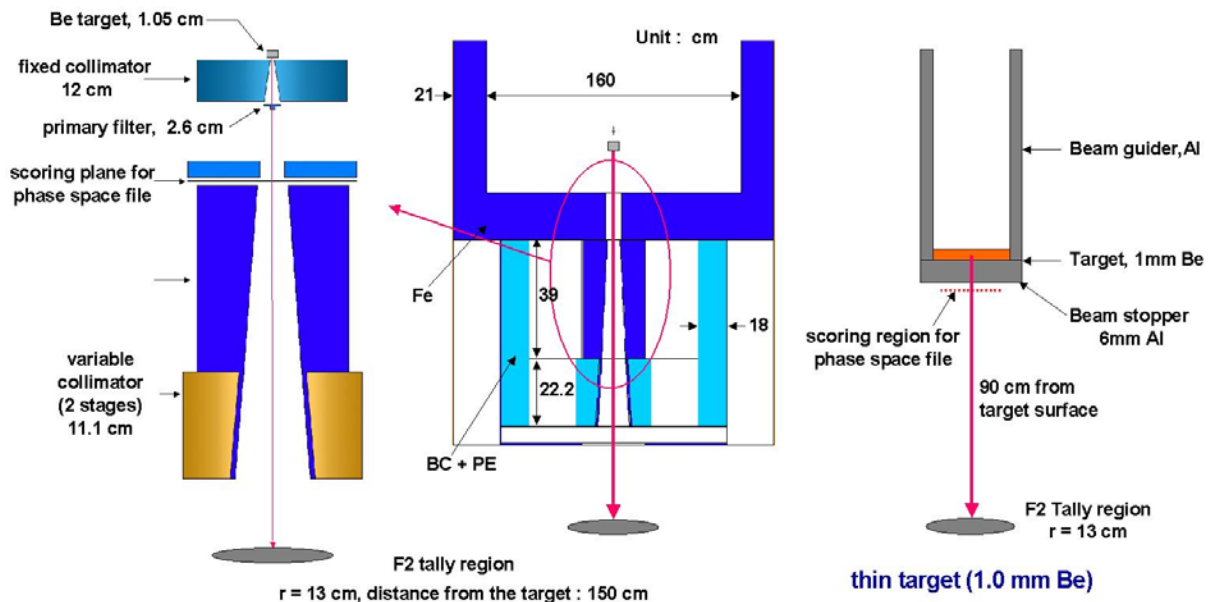
Schematic drawings of the MC50 and linac facilities are shown in Figure 1 and Figure 2.

**Table 1: Configuration of the MC50, NAC and linac facilities**

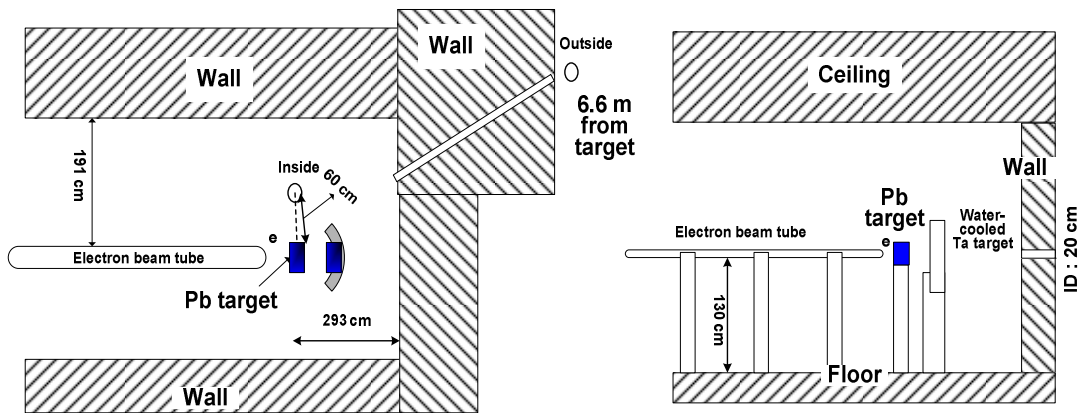
	MC50 [1,5]		NAC [6,7]	Linac
	Thick target	Thin target	Thick target	Thick target
Target (thickness, mm)	Be (10.5)	Be (1.0)	Be (19.6)	Pb (50)
Energy (particle, max. : MeV)	(p, 45)	(p, 35)	(p, 66)	(e, 65)
Stopping material	Cu + water	Al (0.6 cm)	Cu + water	–
Flattening filter (Primary filter, cm)	Fe (2.6)	–	Fe (0.8)	–
Hardening filter (thickness, cm)	Lucite (5.0)	–	PE (2.0)	–
Beam direction	Isocentric	$4\pi$	Isocentric	$4\pi$
Distance from target (cm)	150/300	90/175	150	60/660
Beam size (cm)	Diameter (13)	Diameter (13)	$10 \times 10$	–
Collimator type	Variable jaw	–	Variable jaw	Hole
Collimator material	Fe + PE	–	Fe + PE	Concrete

### Calculation of the neutron fluence spectra

The MCNPX code (Ver. 2.4) [8] was used to calculate the neutron fluence spectra of two kinds of neutron sources at the reference position of the neutron therapy room of KIRAMS. Nuclear physics mode for a neutron production using the  $p + \text{Be}$  reaction was the Bertini model which is one of the models prepared in the MCNPX code for high energy particle physics because it is still not appropriate to use the nuclear data library of Be except for H, C, N, O, Al, Si, P, Ca, Cr, Fe, Ni, Cu, Nb, W, Hg, Pb and Bi. Proton energy was 35 and 45 MeV for MC50 and 66 MeV for NAC respectively. Both the neutron transport and the photonuclear reaction in the Be target and its surrounding materials such as a water blanket or an aluminium cover including a housing for stopping a proton were considered when an energetic proton interacted with them.

**Figure 1: Schematic drawing of the beam collimator in the gantry of the MC50 unit and the geometry of a thin Be target**


**Figure 2: Schematic drawing of a plane (left) and a side (right) view of the target room and calculation points (marked with o)**



Calculation was performed in two stages. First the neutron fluence near the target housing or the entrance of the bulk collimator of the gantry was scored and then transported to the reference position of the geometry, 90 and 150 cm, from the target. The surface crossing tally, F2, and a phase space tally were used for this kind of work. Cut-off energies of the proton, neutron and photon for a phase space tally were 1 MeV, 1 keV and 5 MeV respectively and each of them was determined by considering the neutron yield and a threshold energy in the case of a photonuclear reaction of the key materials near the target.

Neutron fluence spectra at the reference position were calculated from 1 MeV to the maximum energies of 35 and 45 or 66 MeV in log-equidistant intervals of 20 points per decade. For the neutron fluence spectra of the NAC facility used for benchmarking the calculation result the energy interval was set to 2 MeV from 0 to 66 MeV. The effects of the materials surrounding the Be target were investigated especially for the thin target because a 35 MeV proton can penetrate a 1.0 mm thick Be target when considering the CSDA range of a 35 MeV proton in beryllium is about 1.423 g/cm<sup>2</sup> and it produces neutron through the (p,n) reaction with the materials in the target housing or beam stopper.

Two kinds of photoneutron spectra, at inside and outside the target room, produced from the thick lead target bombarded by the electron beams of 65 MeV at the PAL were simulated by using a similar method to the case of MC50 of KIRAMS. The energy cut-off for the transport of electron and photon was 6.73 MeV corresponding to the threshold energy of the photonuclear reaction of the natural lead [9]. The F2 and a phase space tally were used to obtain the spectral distribution of the neutron at the distance of 0.6 and 6.6 m from the target and at the spherical surface enclosing a cubic lead target which has a side of the 10 radiation lengths (r.l.), dimensions of 5.5 × 5.5 × 5.5 cm<sup>3</sup>, respectively. The target thickness of 10 radiation lengths in the case of a lead is known for a neutron production to be saturated and therefore it can be used for the optimum condition of creating neutrons [9].

Neutron fluence spectra at the reference position were calculated from 1 MeV to the maximum energy of the neutrons produced by 65 MeV electrons in log-equidistant intervals of 10 points per decade. The electron was considered as a pencil beam and the photo-neutron sources were sampled at the surface of an angle of 90 and 30 degrees off-axis to the incident electron beam for the position of 0.6 and 6.6 m, inside and outside the target room, respectively. The data for the neutron transport and the photonuclear reaction were the LA150 and ENDF60 library, while the data for the electron and photon were the EL03 and MCPLIB2 respectively.

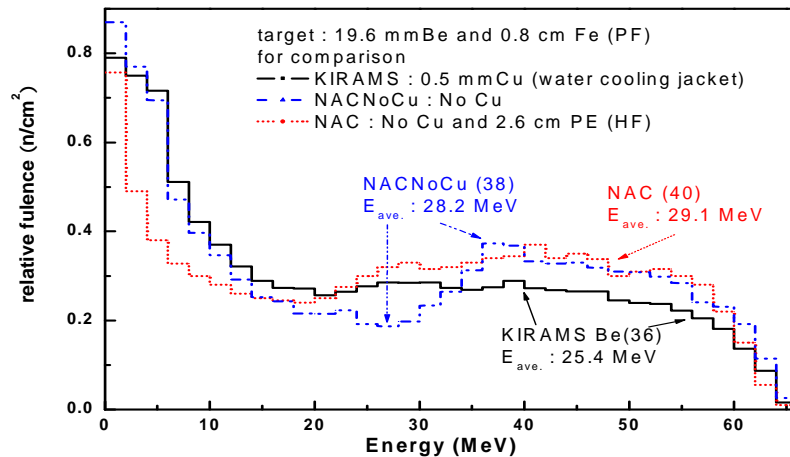
## Results and discussion

In the benchmark calculation using the main parameters of the operation condition of the NAC facility as shown in Figure 3 there was a little difference in the shape of the neutron spectra of the energy region from 25 to 35 MeV. Even though the target cooling jacket of the water and copper at the NAC facility was excluded [6] in the simulation of the neutron beam a small edge in the neutron

spectra was found while a valley was found in the case of using the geometry of KIRAMS (NACNoCu of legend in Figure 3). This needs to be investigated further because it is likely to be the effect of the presence of the surrounding materials for cooling the target and housing. Other major variables causing the differences in the spectral shape between the two facilities are the beam size and kinds of hardening filtrations and these can also be other factors that change the shape of the neutron spectra. General shape of the whole spectra between the two facilities was not different and the calculation of the neutron fluence spectra by using the MCNPX code was found to be reasonable for this kind of work.

**Figure 3: Comparison of the calculated neutron fluence spectra according to the operation condition of the NAC facility**

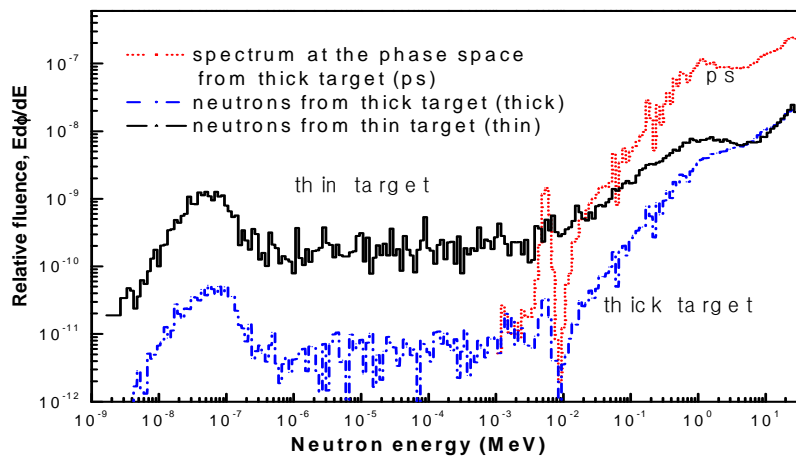
Numbers in a parentheses mean a neutron peak energy of the spectra in the high energy region over 20 MeV (PF : primary filter, HF: hardening filter)



Several measurements indicated that the neutron spectra produced from the thick Be target struck by protons were a relatively intense low energy component attributed to the evaporation neutrons followed by a region of an approximately constant fluence from about 10 MeV to near the kinetic limit and then a steep decrease to the maximum energy [10-12]. But it was the measurement under the condition without a beam hardening filtration and the neutron spectrum produced by using a 66 MeV proton and a thick Be target showed a broad peak at neutron energies between 20 and 40 MeV as well as a similar low energy part [3]. These shapes were also found in this calculation.

**Figure 4: Neutron fluence spectra produced from the thick (10.5 mm Be) and thin (1.0 mm Be) target and phase space spectra at 45 cm from the thick target inside gantry**

The hill side below a high energy peak is from another neutron source of the (p,n) reaction with materials near the Be target



Neutron fluence spectra produced from the thin and thick Be target of the MC50 cyclotron at KIRAMS are shown in Figure 4 and Figure 5. Resonance peak of the iron was shown in a phase space spectrum and it appeared to be only a small peak at the reference position of 150 cm from the target. There was a big change in the spectrum between at the phase space and at the reference position due to the beam collimation and filtration inside the gantry. A typical shape of the thermal neutron peak was found because the amounts of scattered neutrons were considerable in the therapy room. Among six neutron spectra shown in Figure 5 a neutron spectrum marked with (6) in the figure had a different shape due to its different position which was about 60 degree off the proton beam direction to the target.

**Figure 5: Calculated neutron fluence spectra of KIRAMS**

Presented in lethargy format,  $Ed\phi/dE$ , after normalising the group fluence

G: Gantry, 35/45: proton energies accelerated, H: Horizontal beam, and other numbers: the distance in cm from the target

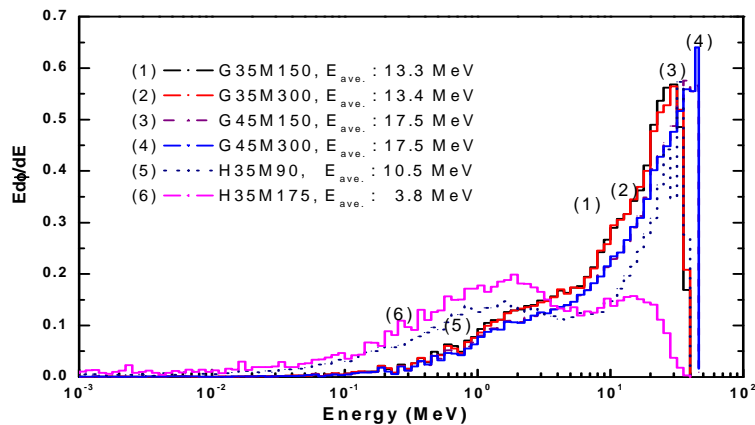
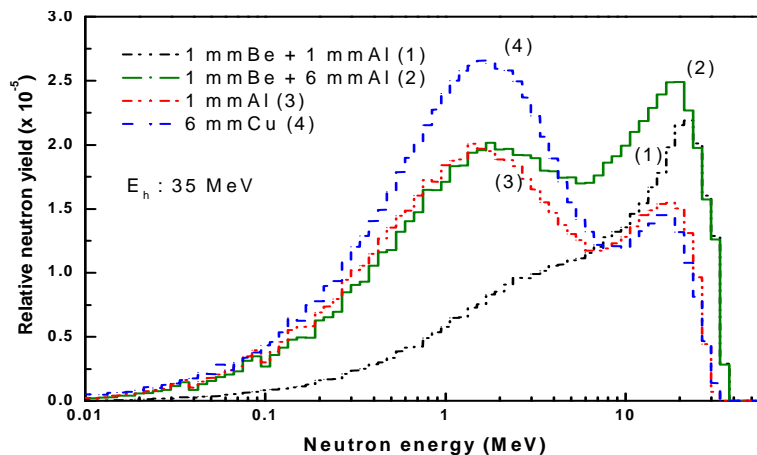


**Figure 6: Difference in neutron production with the target and its surrounding material in the case of 35 MeV proton bombarding the 1.0 mm Be target**

(3) and (4) are the case of no Be target with an aluminium and a copper cover is directly struck by energetic protons



Two spectra were similar except for the hill side of the neutron spectrum for the case of a thin target below a high energy peak of about 20 MeV. It was verified by investigating the effects of the beam stopping material backside of the thin target, 1 mm Al in the target housing and 5 mm Al as an additional proton beam stopper. Differences in the neutron production spectra with the target and its surrounding material for a 35 MeV proton bombarding the 1.0 mm thick Be target are shown in Figure 6. According to this figure, the neutron yields increase with the thickness of the aluminium and it means that aluminium itself would be a target which produced neutrons with a peak near 1 MeV.

Table 2 shows a summary of the calculated neutron spectra in this work. Neutron yields of the (p,n) and photonuclear reaction are summarised in Table 3. According to Table 3 the neutron yields are increasing with the incident energy of the proton and the thickness of the target. The spectrum weighted average energy of neutron field produced from the thick target was larger than that from the thin target struck by a 35 MeV proton in this calculation but it could not be directly related due to differences of the beam direction and the geometry for collimation. The effect of a beam hardening in the gantry appeared as the average energy of the neutron field at the reference position increased compared with that of a phase space inside the gantry.

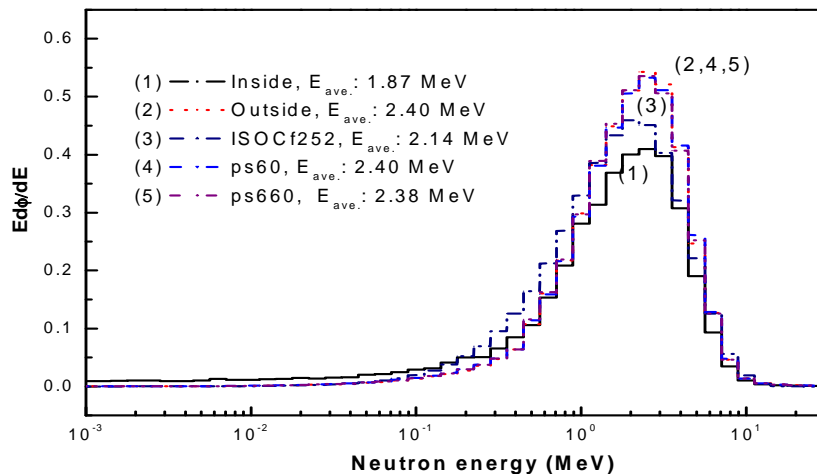
**Table 2: Summary of the calculated neutron fields of the MC50 and the test linac**

Proton or electron energy accelerated (MeV)	MC50 (KIRAMS)						Linac (PAL)	
	45		35		35		65	
Target or beam geometry	Gantry		Gantry		Horizontal, open		Open (90°)	Collimated (30°)
Average energy of neutron field at phase space, SSW (MeV)	14.1		10.7		8.16		2.4	2.38
Fluence to dose equivalent conversion factor of SSW (pSv.cm <sup>2</sup> )	452		524		419		390	391
Distance from target (cm)	150	300	150	300	90	175*	60	660
Average energy of neutron field (MeV)	17.5	17.5	13.3	13.4	10.5	3.8	1.87	2.4
Fluence to dose equivalent conversion factor (pSv.cm <sup>2</sup> )	469	466	472	469	395	300	324	391

\* This is the same position as the case of distance of 300 cm from the target of gantry. The neutron beam direction of the horizontal geometry was orthogonal to that of the neutrons from gantry.

**Figure 7: Calculated neutron fluence spectra inside and outside the target room of the linac of PAL and the reference spectrum recommended by ISO-8529**

Presented in lethargy format,  $E d\phi/dE$ , after normalising the group fluences



According to the photoneutron production cross-section the dominant neutron production phenomena all over the whole energy is expressed as the giant dipole resonance due to the huge amount of low energy photon and the large absorption cross-section at low energy. The photoneutron spectra from this giant resonance process have a similar shape of the fission spectrum which is described by a Maxwellian distribution with a temperature  $T$  in the range of  $0.5 \text{ MeV} \leq T \leq 1.5 \text{ MeV}$  such as  $N(E) = a \cdot E^{1/2} \cdot \exp(-E/T)$ , where  $a$  is a constant. But at energies higher than about 10 MeV the photoneutron spectrum has been known for having the shape of a simple exponential function,  $N(E) \sim E^{-\alpha}$ , where  $\alpha$  is in the range of 1.7 to 3.0 with neutron energy [13,14].

As shown in Figure 7 the calculated spectra inside and outside the target room of the 65 MeV electron linac was similar to the fission spectrum which is described as the Maxwellian distribution with a temperature of 1.4 MeV and as the ISO reference spectrum of a  $^{252}\text{Cf}$  source. The spectrum weighted average energy of the neutron field of inside the target room was lower than that of a phase space and outside the target room because there was a contribution of scattered neutrons from the wall and floor of the target room.

**Table 3: Comparison of the neutron yields with the thickness of target and the particle energy**

Particle accelerated	Energy (MeV)	Target (mm)	Yield (%)
Proton	66	Be (19.6)	10.1
	45	Be (10.5)	4.77
	35	Be (10.5)	3.05
	35	Be (1.0)	1.31
Electron	65	Pb (50)	1.86

As discussed so far, the neutron beam qualities produced from a Be target struck by energetic protons are very dependent on the energy of incident particle, the target thickness, the presence of a target cooling jacket, and the primary and hardening filtration even though the accelerators have a similar geometrical configuration.

These calculation results were used to quantify the neutron fields at KIRAMS and at the PAL as an initial estimation of the neutron spectrum, which is priori information for the final spectrum to be determined by measurement and is crucial for unfolding the measured data of a Bonner Sphere, the few channel unfolding [15].

### Acknowledgements

This study was the partial product of the national long-term projects for expansion of research foundation supported by the Ministry of Science and Technology.

### References

- [1] ICRU, *Nuclear Data for Neutron and Proton Therapy and for Radiation Protection*, ICRU Report 63, 10-14 (2000).
- [2] N.M. Crout, et al., "In Situ Neutron Spectrometry to 60 MeV in a Water Phantom Exposed to a Cancer Therapy Beam", *Phys. Med. Biol.*, 36, 507 (1991).
- [3] D.T.L. Jones, et al., "Neutron Fluence and Kerma Spectra of a p(66)/Be(40) Clinical Source", *Med. Phys.*, 19, 1285-1291 (1992).
- [4] M.A. Lone, et al., "Characteristics of Neutrons From Be Targets Bombarded with Protons, Deterons and Alpha Particles", *Nucl. Instr. Meth.*, 189, 515-523 (1981).
- [5] S.Y. Yoo, et al., "Dosimetric Characteristics of the KCCH Neutron Therapy Facility", *J. Korean. Soc. Ther. Radiol.*, 6, pp. 85-90 (1988).
- [6] M.A. Ross, et al., "Calculated Fluence Spectra at Neutron Therapy Facilities", *Radiat. Prot. Dosim.*, Vol. 70 (1-4), pp. 481-484 (1997).
- [7] T.D. Bohm, et al., "Monte Carlo Calculations to Characterizate the Source for Neutron Therapy Facilities", *Med. Phys.*, 26, 783-792 (1999).

- [8] LANL, *MCNPXTM User's Manual, Version 2.4.0*, (RSIC-CCC-715), LA-CP-02-408 (2002).
- [9] W.P. Swanson, "Improved Calculation of Photoneutron Yields Released by Incident Electron", *Health Phys.*, Vol. 37, pp. 347-358 (1979).
- [10] R.G. Graves, et al., "Neutron Energy Spectra of d(49)-Be and p(41)-Be Neutron Radiotherapy Sources", *Med. Phys.*, 6, pp. 123-128 (1979).
- [11] J.L. Ullmann, et al., "Improved Measurement of Neutron Spectrum from 35 MeV Protons on Thick Beryllium", *Med. Phys.*, pp. 396-397 (1981).
- [12] F.M. Waterman, et al., "Neutron Spectra from 35 and 46 MeV protons, 16 and 28 MeV Deuterons, and 44 MeV <sup>3</sup>He Ions on Thick Beryllium", *Med. Phys.*, 6, pp. 432-435 (1979).
- [13] K. Tesch, "Data for Simple Estimates of Shielding Against Neutrons at Electron Accelerators", *Particle Accelerators*, Vol. 9, pp. 201-206 (1979).
- [14] NCRP, *Radiation Protection for Particle Accelerator facilities*, NCRP Report No. 144, pp. 59-61 (2003).
- [15] A.V. Alevra, T.J. Thomas, "Neutron Spectrometry in Mixed Fields: Multisphere Spectrometers", *Radiat. Prot. Dosim.*, 107, No. 1-3, pp. 37-72 (2003).



## Comparison between the source terms used in SHIELD11 and the source terms calculated by FLUKA<sup>1</sup>

**X.S. Mao, W.R. Nelson,\* A.A. Prinz**  
Stanford Linear Accelerator Center, USA

\*Department Associate in the Radiation Physics Group

### Abstract

SHIELD11 is an analytical code for performing shielding calculations used at SLAC. It uses simple analytic expressions for the production and attenuation of photons and neutrons resulting from electron beams striking thick targets. SHIELD11 code is based on five-component model: Direct Gamma, Indirect Gamma, Giant-Resonance Neutron (GRN), Mid-Energy Neutron (20 MeV-100 MeV), High-Energy Neutron (>100 MeV). FLUKA Monte Carlo code was used to study direct gamma and three neutron components used in SHIELD11.

Photon absorbed dose rate from a thick iron target was measured by D.A.G. Neet at SLAC in 1965. In Neet's experiment, a 990-MeV and 10-Watt beam hit an iron target with radius of 3" and length of 15". The dose was measured using an air ionisation chamber with thin aluminium walls (ZEUS). We simulated the energy deposition on the air ionisation chamber using FLUKA. The energy deposition was converted to absorbed dose. The measurements and FLUKA calculations agree within  $\pm 30\%$ . The measurements and SHIELD11 calculations agree within  $\pm 50\%$ , except in the 0-degree direction. SHIELD11 underestimates the dose rate in the 0-degree direction by 60%.

FLUKA was used to score the neutron yields using a 10-GeV electron beam to hit thick targets (Al, Fe, Sb, Pb). Total neutron yields produced from the targets were divided into two energy ranges: from 20 MeV to 100 MeV and greater than 100 MeV. SHIELD11 overestimated the GRN, mid and high neutron yield by a factor of three, six and two respectively. The neutron yields per steradian produced from the iron target as a function of the angle were presented. The high-energy neutron yield per steradian in lateral direction agreed within  $\pm 10\%$  between the SHIELD11 and FLUKA calculations.

This work was supported by Department of Energy contract DE-AC02-76SF00515.

---

1. The full paper was not available at the time of the printing of the proceedings. Interested readers can obtain a copy of the PowerPoint presentation in PDF format upon request (cpsreq@nea.fr).



## Double differential cross-section of fragment production by tens of MeV protons and neutrons

**T. Sanami, M. Hagiwara**

High Energy Accelerator Research Organisation (KEK)

**T. Oishi, S. Kamada, T. Okuji, M. Baba**

Cyclotron Radioisotope Centre, Tohoku University

**M. Takada, N. Miyahara**

National Institute of Radiological Science

**H. Nakashima, Y. Iwamoto, S. Tanaka,\* T. Kaneko**

Japan Atomic Energy Agency

### Abstract

Double differential cross-sections (DDX) of fragment production from neutron-induced and proton-induced reactions have been measured in the intermediate-energy region to confirm the applicability of theoretical models. A Bragg curve counter with an enhanced energy dynamic range and detection efficiency was developed to measure the DDXs. DDXs of Li, Be, B and C production were obtained for 70 MeV proton-induced reactions on C, Al and Si. DDXs of Li, Be and B were obtained for 65 MeV neutron-induced reactions on C. These results were compared with theoretical calculations with different intra nuclear cascade models.

---

\* Present organisation: Nippon Advanced Technology Co., Ltd.

## Introduction

The energy deposition of a fragment produced by a nuclear reaction has considerable effects in a material irradiated by an intermediate-energy (tens of MeV) neutron because the fragment has a high linear energy transfer (LET). To estimate the effect, a data set of the energy and angular distribution (double differential cross-section – DDX) of a fragment is indispensable. DDX is also helpful to investigate the mechanism of fragment production. For this requirement, there has been much effort to construct DDX data [1,2]. Theoretical models to calculate fragment production and transport have been developed to evaluate this effect [3]. To confirm their validity, experimental data are highly desired.

Direct measurements of fragments from neutron-induced reactions are difficult because there is no mono-energetic neutron source with high intensity in the tens of MeV energy range. In addition, a high-efficiency detector with the capability of particle identification is important to measure fragments because the production rate is quite low compared with other light particles. To meet this requirement, we have developed a Bragg curve counter (BCC) for neutron-induced fragment measurements. Using the BCC, DDX at 0-deg. of fragments from carbon were successfully obtained using a quasi mono-energetic neutron source. In addition, the BCC has been applied to measure the DDX of fragments from proton-induced reactions on C, Al and Si.

In this paper, we describe DDXs for fragment production by protons and neutrons in the intermediate energy region. The data were obtained by a specially designed BCC. The experimental method is also summarised briefly. These results are compared with theoretical calculations with different intra nuclear cascade models to confirm their applicability.

## Bragg curve counter

A Bragg curve counter (BCC) is an ionisation chamber with a Frish grid [4]. A schematic illustration of the BCC is shown in Figure 1. A fragment that enters the counter produces ionisation electrons along its trajectory. These electrons drift to the anode plate through a grid while keeping their distribution, which represents the energy-loss distribution, i.e. the Bragg curve. The first part and whole integral of the anode signal correspond to the Bragg peak height and the energy of the fragment, respectively. The Z-number is determined from the Bragg peak height.

Figure 1: Schematic illustration of Bragg curve counter

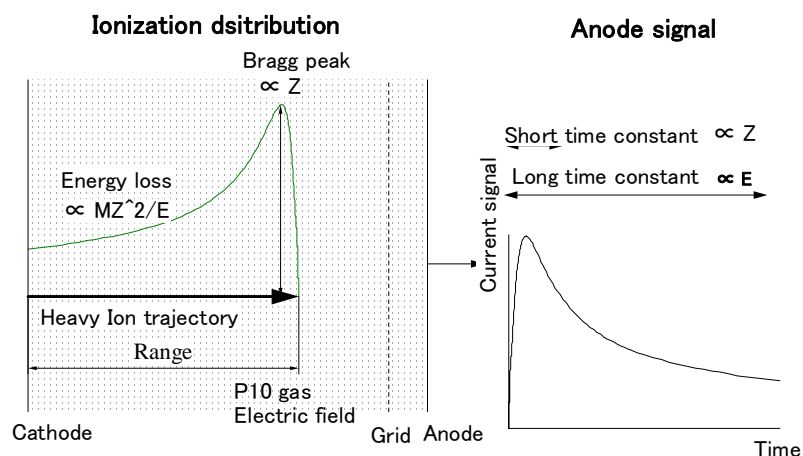
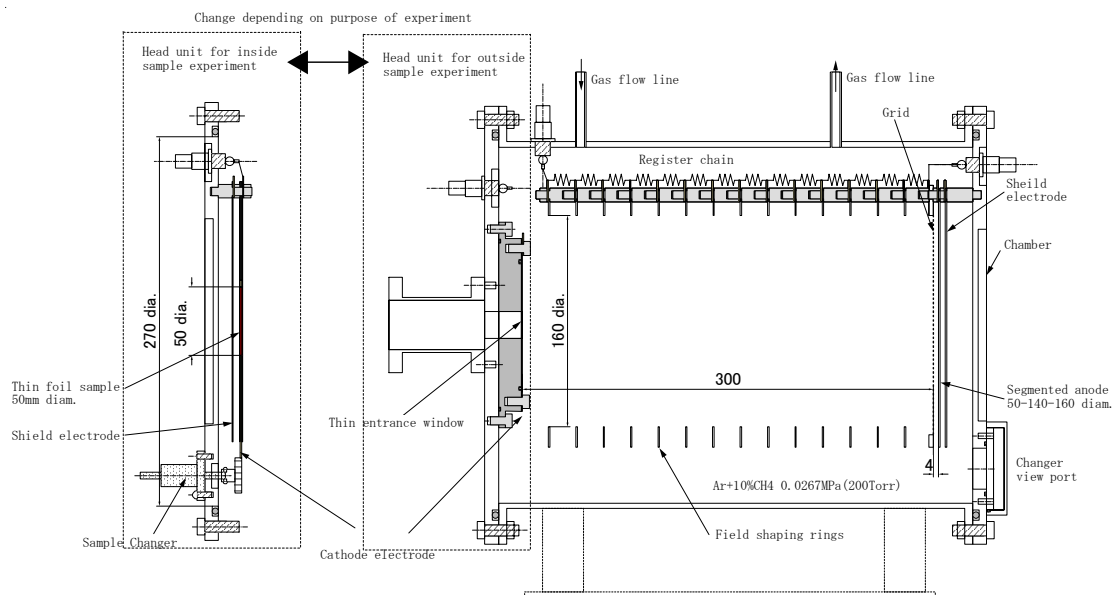


Figure 2 shows a schematic drawing of our BCC. Details of the chamber are presented in other papers [5,6]. The chamber has two different head units, which are exchanged for experimental purposes. One head has a thin entrance window of 2.5  $\mu\text{m}$  thick aluminised Mylar to permit fragment to enter the chamber from outside. The head unit is designed to measure proton-induced reactions. The other head unit, which is designed to measure neutron-induced reactions, can mount the sample foil on the cathode in the chamber. The configuration of the head unit can achieve a large detection efficiency of fragments.

**Figure 2: Schematic drawing of the Bragg curve counter**

The effective diameter of the electrode is 160 mm. The distances between the cathode and the grid, and the grid and the anode are 300 mm and 5 mm, respectively. Field-shaping rings are inserted with 20 mm steps to maintain a homogeneous electric field. The grid consists of gold-plated tungsten wires (0.1 mm in diam.) spaced by 1.0 mm. The shielding inefficiency was calculated to be 3.1% [6]. A counting gas of 0.0267 MPa Ar+10%CH<sub>4</sub> is used in a gas flow mode to maintain its qualities. High voltages of -960 V, 0 V and +60 V through RC-filters are applied to the cathode, the grid and the anode, respectively. In this condition, the strength of the electric field reaches 0.18 V/cm/Torr, which makes the electron drift time from the cathode to the grid less than 6  $\mu$ s. For these parameters, the saturation curve and the energy linearity were confirmed using an  $\alpha$  source and ion beams of C, O and Ne at the AVF cyclotron at Cyclotron Radioisotope Centre, Tohoku University (CYRIC).

## Experiment

Details of the experimental setup are already described in references [5-7]. Only an outline is presented in the following sections for the proton and neutron incident cases separately.

### Proton-induced reaction

The proton-induced fragmentation experiment has been performed using the AVF cyclotron at the National Institute of Radiological Science (NIRS). Figure 3 shows the experimental setup. Samples of 4  $\mu$ m thick polypropylene, 2  $\mu$ m thick aluminium and 310  $\mu$ g/cm<sup>2</sup> Si on Ta were mounted on a sample changer located at the centre of a scattering chamber. Protons with an energy of 70 MeV bombard the sample, and then entered a Faraday cup made of graphite. The fragments from the sample are measured with BCC at 30, 60, 90, 135 degrees. In this set-up, the ambiguity of the angle is less than 2 degrees. Owing to the large solid angle of the BCC, only 1 hour is sufficient for each sample with a beam current of  $\sim$ 30 nA. Figure 4 shows the two-dimensional spectrum on the energy vs. Bragg peak for a silicon sample. Excellent separation of each fragment and the signal-to-noise ratio were confirmed up to Z = 8 (oxygen) in the energy region where particles are separated by the difference of the Bragg peak-value. In the case of the Si sample, fragments from Ta backing were subtracted using Ta data (less than 10% from the Si sample). In the data analysis, the data of time difference between cathode and anode signals were used to improve particle identification at the low-energy side [7]. The energy spectrum was extended to high-energy fragments, which punch through the BCC, using the correction method with the relationship between a deposit energy and an incident energy calculated by the SRIM code [7].

Figure 3: Experimental set-up for the proton-induced fragment measurement

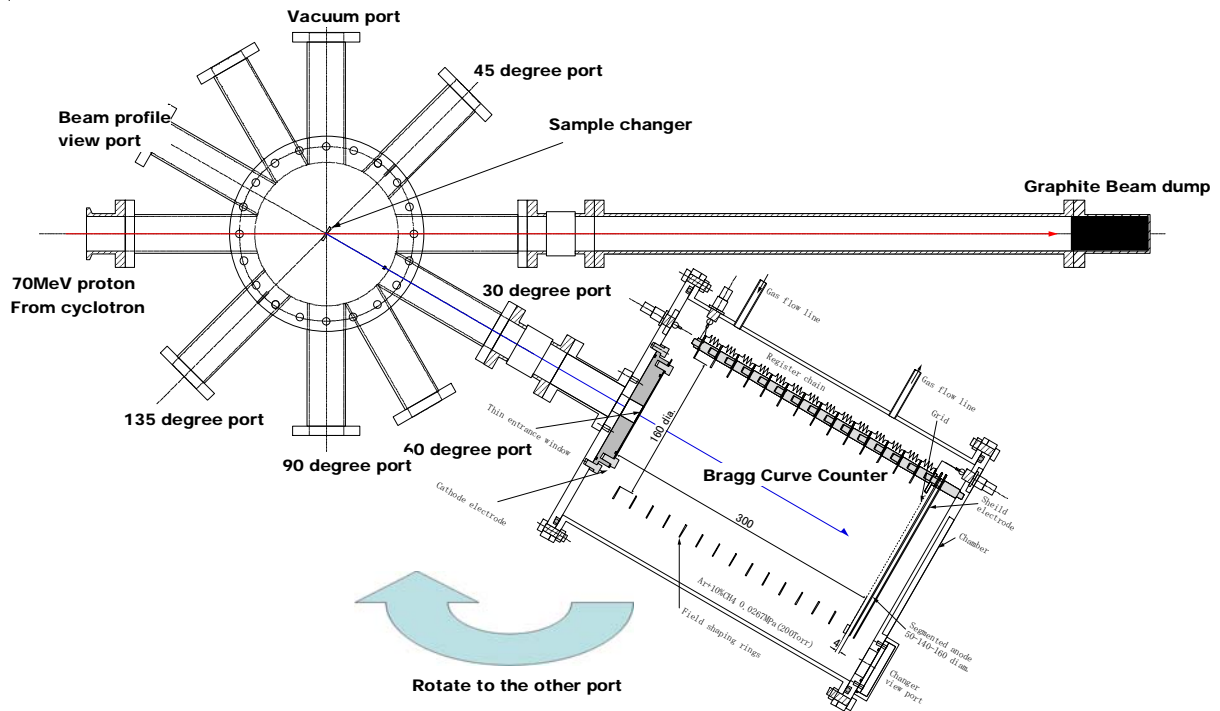
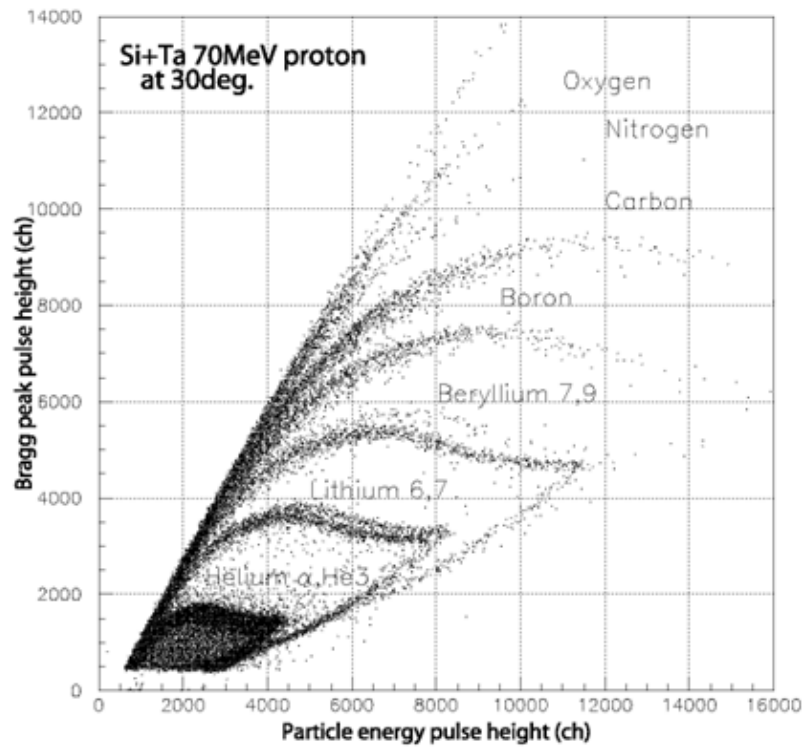


Figure 4: Two-dimensional spectrum on the energy vs. Bragg peak for a silicon sample



### Neutron-induced reaction

The neutron experiment has been performed using a new intense neutron beam facility at Cyclotron Radioisotope Centre, Tohoku University (CYRIC). Figure 5 shows the experimental arrangement. Neutrons with an energy of 65 MeV are produced via the  ${}^7\text{Li}(p,n)$  reaction with a 70 MeV proton beam and metallic lithium target, thickness of which is equivalent to 2 MeV energy-loss for the beam. The average proton beam current is about 1–1.5  $\mu\text{A}$ . The energy spectrum of neutrons is quasi-monoenergetic. The intensity of monoenergetic peak neutrons is  $4.7 \times 10^9$  [n/sr/ $\mu\text{C}$ ] at  $0^\circ$  [8].

**Figure 5: Experimental set-up for the neutron-induced fragment measurement**

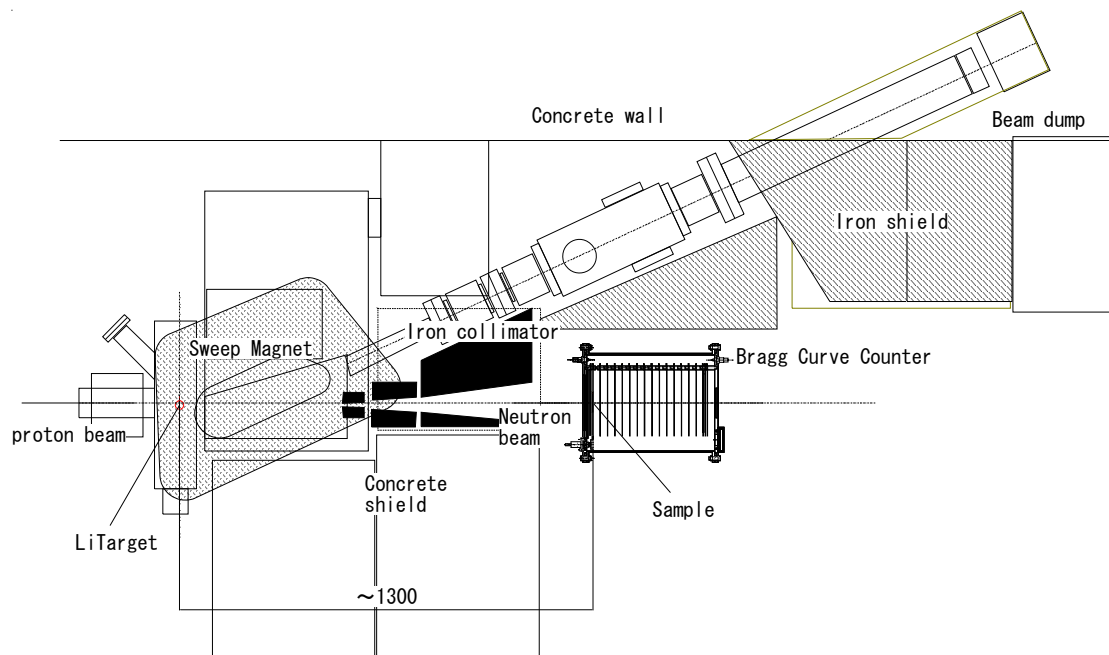
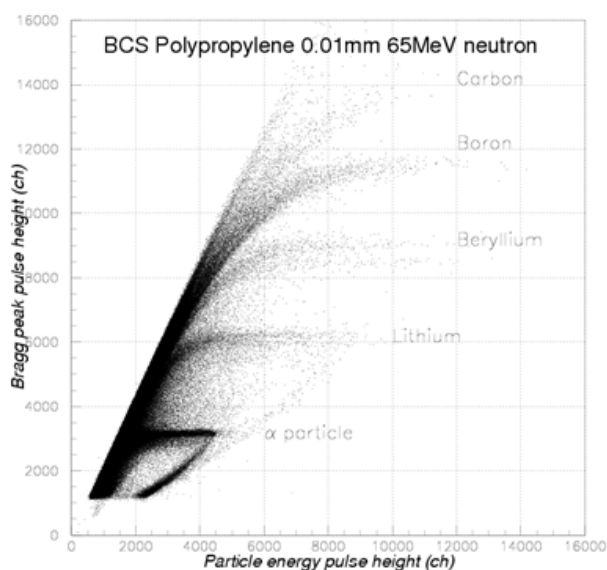


**Figure 6: Two-dimensional spectrum on the energy vs. Bragg peak for a polypropylene sample [Poly. (10  $\mu\text{m}$ ) + Au (100  $\mu\text{m}$ )]**

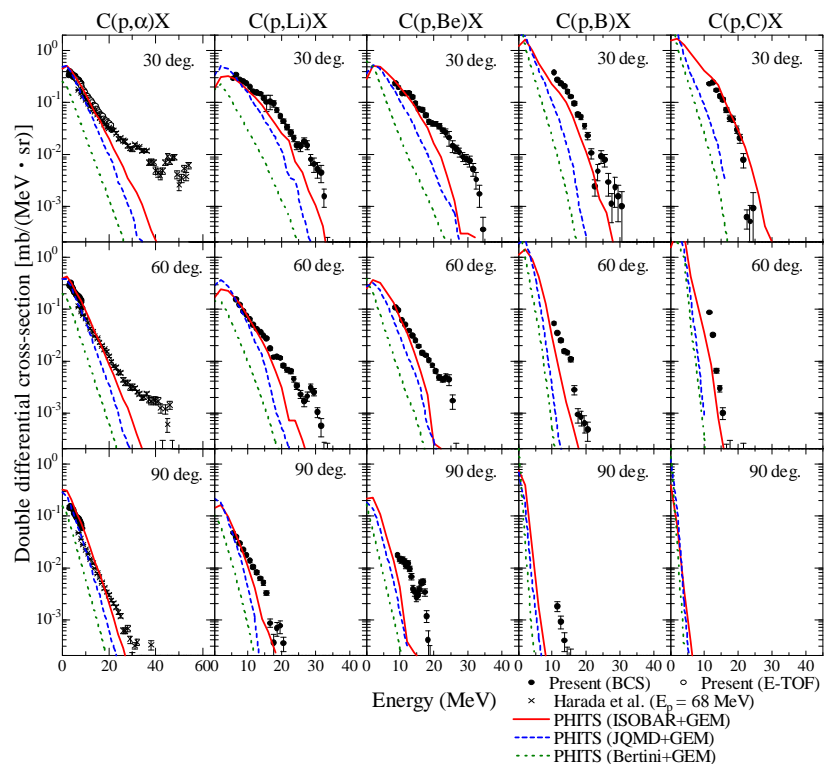


The BCC with the head unit for an internal sample was placed at 1.3 m from the Li target. The arrangement provided  $\sim 10^6$  [n/(cm·s)] neutron flux at the sample position. Samples were 10  $\mu\text{m}$  thick polypropylene with 100  $\mu\text{m}$  Au baking and 100  $\mu\text{m}$  Au baking mounted on a sample changer, which also acted as a cathode electrode. Almost all fragments emitted in forward angle from the sample were measured using this apparatus. To determine detection efficiency precisely, the anode plate was divided to 3 parts. The centre part was a 50 mm diameter circle to measure fragments emitted in a forward angle with respect to the chamber axis. The others were a concentric ring shape to reject any large-angled fragments. By using this rejection, an efficiency curve as a function of fragment energy for each Z number was determined based on the range data, and examined experimentally. Figure 6 shows the two-dimensional spectrum on the energy vs. Bragg peak for a polypropylene sample with this rejection. Owing to rejection of large-angled events, excellent separation of each fragment and the signal-to-noise ratio were confirmed up to  $Z = 5$  (Boron) in the energy region where particles were separated by the difference in the Bragg-peak value. Background events that originated from the chamber body and the counting gas were eliminated using the data of the Au (100  $\mu\text{m}$ ) sample.

### Double differential cross-section

After identifying fragments using the two-dimensional spectra on the energy vs. Bragg peak, energy spectra were obtained using energy calibration data, which were determined by the punch-through edge and peak of  $\alpha$  particles from an  $^{241}\text{Am}$  source. The results are given in the following sections for the proton and neutron-incident case separately.

**Figure 7: He, Li, Be, B, C production double-differential cross-sections of carbon for a 70 MeV proton at 30, 60, 90 degrees**



### Proton-induced reaction

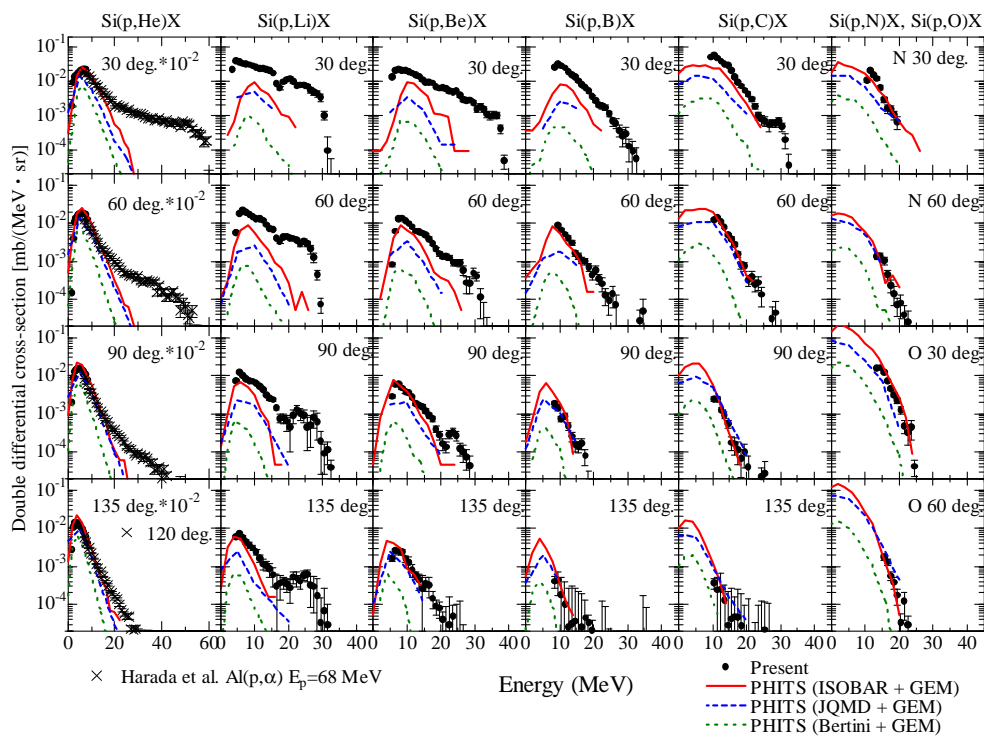
Figure 7 shows the DDXs of the Li, Be, B, C production of carbon for 70 MeV protons at 30, 60, 90, 135 degrees along with the calculations of PHITS [3] and data by Harada, *et al.* [9]. The calculations were carried out using three different intra-nuclear cascade models (Bertini, JQMD, ISOBAR) combined

with one evaporation model (GEM). Considerable amounts of fragments whose energy reached to 20 MeV were observed as a result of the 70 MeV proton-induced reaction. The magnitude of this result is similar to the other experimental data [10].

Figure 8 shows a comparison of the silicon data. Aluminium data, which were almost the same as the silicon one, were also obtained. The discrepancies between experiment and calculation on high-energy part of light fragments are larger than in the carbon case. In contrast, the calculation represents the experimental data well for relatively heavy fragments. The threshold energies of the experimental data were determined from the thicknesses of the sample and the entrance window of the BCC. These thicknesses could be reduced by an experimental setup focusing at low-energy fragments.

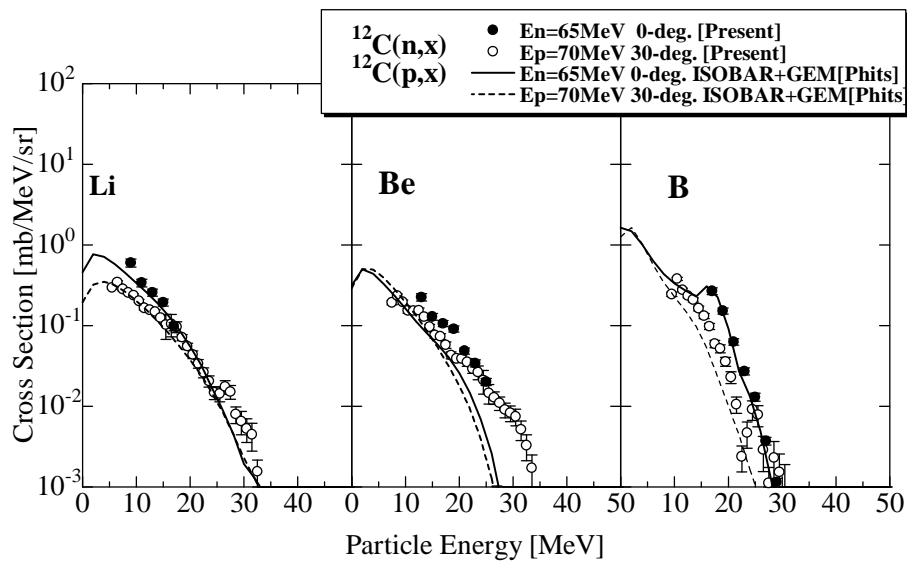
For both results, the ISOBAR model generally reproduces the experimental data except for the data of light fragments. Calculations with the Bertini model remarkably underestimate all of the results. This means that we should pay much attention to what model is embedded in the calculation code to estimate the deposition energy correctly in this energy range. At the forward angle of lithium and beryllium DDXs, the experimental data show a different shape from the other data. An underestimate of lighter fragment production was also observed by another experiment [12]. This fact indicates that a new reaction mechanism is indispensable to reproduce these components. These results indicate that we have to choose an adequate model to calculate the effects influenced by fragment production, such as energy deposition in the  $\mu\text{m}$ -order area.

**Figure 8: He, Li, Be, B, C production double-differential cross-sections of silicon for a 70 MeV proton at 30, 60, 90, 135 degrees**



### Neutron-induced reaction

Figure 9 shows the DDXs of lithium, beryllium and boron from a 65 MeV neutron-induced reaction on carbon. For a comparison between the results, the DDXs of these fragments by proton induced reactions at 30-degree and PHITS calculations are also plotted. The effects by low-energy continuum neutrons of a quasi-mono energetic source were considered using the ratio of the fragment spectra by monoenergetic neutrons to quasi-mono energetic neutrons calculated by the PHITS code. The relatively small energy dynamic range of the neutron results is due to a no-correction of the punch through fragments. The lithium and boron results are in good agreement with the results of PHITS using the ISOBAR option. For beryllium, the calculation results markedly underestimate the experimental one.

**Figure 9: Experimental results for carbon compared with the proton beam result and PHITS calculation**

## Conclusion

We measured the double differential cross-section (DDX) of light fragments from proton and neutron-induced reactions in the tens of MeV energy region. To measure the DDX, we developed a Bragg curve counter (BCC), a particle identification method using a cathode signal, a correction method for a punch-through fragment and a method to determine the efficiency of fragment detection for an internal sample. The DDXs of fragments from proton-induced reactions could be measured efficiently by using this system. This means that the system can provide systematic results of fragment DDX as a function of the incident energy and target nucleus. By combining the DDXs of hydrogen and helium isotope emission, the DDXs of every particle are available in this energy range. The data set must be effective not only to evaluate the theoretical model and parameters, but also to precisely estimate the irradiation effect. In addition, the DDX data of neutrons, which are only one type of data obtained by direct measurements in this energy range, provide important information about the difference from that of protons. The neutron data should be helpful to check the availability of the theoretical model and the parameters that are determined using the proton DDX data.

## References

- [1] M.B. Chadwick, et al., *IBM J. Res. Develop.*, 40, No. 1 (1996).
- [2] Y. Watanabe, et al., "Nuclear Data Evaluation for JENDL High Energy File", *Proc. Int. Conf. on Nuclear Data for Science and Technology*, Santa Fe, NM, USA, 26-30 September 2004, 326.
- [3] H. Iwase, et al., *J. Nucl. Sci. Technol.*, 36 (2002), 1142.
- [4] G.R. Gruhn, et al., *Nucl. Instrm. Meth.*, 196 (1982), 33.
- [5] M. Hagiwara, et al., *Proc. Int. Conf. on Nuclear Data for Science and Technology*, Santa Fe, NM, USA, 26-30 September 2004, 1031.

- [6] T. Sanami, *et al.*, *J. Nucl. Sci. and Tech. Suppl.*, 4 (2004), 502.
- [7] M. Hagiwara, *et al.*, *Proc. 2005 Symposium on Nuclear Data*, JAEA Tokai, Japan, February 2006, forthcoming.
- [8] M. Baba, *et al.*, *Nucl. Instrm. Meth.*, A428 (1999), 454.
- [9] M. Harada, *et al.*, *J. Nucl. Sci. and Technol.*, Suppl. 2, pp. 393-396 (2002).
- [10] C.T. Roche, *et al.*, *Phys. Rev.*, C14 (1976), 410.
- [11] K. Kwiatkowski, *et al.*, *Phys. Rev. Lett.*, 50 (1983), 1648.



## **Session II**

### **Shielding at high energy accelerators**

***Chair: T. Nakamura***



## Radiation shielding design for the J-PARC project

**Hiroshi Nakashima, Tokushi Shibata, Yoshihiro Nakane, Fumihiro Masukawa,  
Norihiro Matsuda, Yosuke Iwamoto, Masahide Harada, Shinichiro Meigo, Yoshimi Kasugai,  
Fujio Maekawa, Hiroshi Takada, Chikara Konno, Makoto Teshigawara, Motoki Ohi, Testuya Kai**  
Japan Atomic Energy Agency, Japan

**Hideo Hirayama, Takenori Suzuki, Taichi Miura, Masaharu Numajiri, Noriaki Nakao**  
High Energy Accelerator Research Organisation, Japan

### Abstract

*The J-PARC (Japan Proton Accelerator Research Complex) project is in progress, aiming at studies on the latest basic science and the advancing nuclear technology. In the project, the high-energy proton accelerator complex of the world highest intensity is under construction. Because of its very high beam power and its energy as well as the large-scale accelerator complex, we have encountered some difficult radiation problems in the radiation safety design. In order to overcome the problems on the shielding design for J-PARC, a calculation system with both simplified and detailed methods is used for the shielding design of J-PARC. This paper reviews the current status of the radiation shielding design for J-PARC by using the calculation system.*

## Introduction

Aiming at studies on basic sciences and the advancing nuclear technologies, the J-PARC (Japan Proton Accelerator Research Complex) project is being conducted under collaboration between High Energy Accelerator Research Organisation (KEK) and Japan Atomic Energy Agency (JAEA). J-PARC is composed of three accelerator facilities: a 600-MeV linac (LINAC), and 3 GeV rapid cycle synchrotron (3GeVRCs) and 50 GeV synchrotron (50GeVMR), and four experimental facilities: Material and Life Science Facility (MLF), Nuclear and Particle Physics Facility (NP), Nuclear Transmutation Experiment Facility and Neutrino Facility ( $\nu$ ), as shown in Figure 1. The high-energy proton accelerator complex with the world's highest intensity, 3 GeV beam of 1 MW maximum power, is under construction [1-3].

From the viewpoint of radiation shielding, the large-scale accelerator complex with high beam intensity and energy causes many difficult radiation problems in shielding design. Characteristics of J-PARC are: i) high beam power (up to 1 MW); ii) high beam energy (up to 50 GeV); iii) large-scale accelerator complex (3.6 km in length). Radiation problems come from: i) widely distributed radiation source; ii) thick shield; iii) many ducts and so on. On the other hand, shielding methods with high accuracy were strongly required for a detailed design study. In order to overcome the radiation problems, a calculation system with both simplified and detailed methods are applied for shielding design and safety analyses with estimating the accuracy of the methods by using experimental benchmark analyses [4-6]. This paper describes the current status of the radiation shielding design for J-PARC by using the combination method.

## Shielding design criteria

In Japan, "Laws concerning Prevention of Radiation Hazards due to Radioisotopes, etc." is main law for accelerator facilities. In the law, exposure limit for workers is 50 mSv/y and 100 mSv/5y based on ICRP 1990 recommendation. Under the limitation dose limits for each area are regulated as tabulated in Table 1. As the design criteria of shielding design for the J-PARC facility, half of the regulation for inside the site and one twentieth for site boundary were adopted by considering the safety factor of two and following the customs of other large accelerator facilities in Japan. For gaseous and liquid wastes, regulations on concentration and total amount by government and local government were adopted as the criteria. These wastes are managed by using confinement systems so as to keep the regulations. Activated air generated in rooms of the facilities will be controlled by a confinement system in rooms with negative pressure and a buffer region having monitoring system during operation, and released after waiting decay-out of nuclei with short life after operation and removing  $^7\text{Be}$  with HEPA filter in ventilation equipment. (Figure 2) As for activation in cooling system, the coolant is used in closed cycle during operation and released after monitoring the activity, mainly tritium, in disposal tanks.

## Shielding design conditions

It is difficult to exactly estimate primary beam-loss conditions in accelerator devices except for beam dumps and targets. In the shielding design of J-PARC, it is assumed that the average beam loss is less than 1 W/m at almost all part of the beam line of the accelerators so as to permit the hands-on maintenance, based on the experience and estimation at various high energy accelerator facilities [7-9].

Proposed beam operation times are 5 500 hours for LINAC and 3GeVRCs, 5 000 hours for 50 GeV MR and MLF, and 4 000 hours for NP and  $\nu$ . About 10 campaigns of three-week continuous operation and one-week maintenance are expected with two-month long maintenance in a year.

## Shielding methods

Because the beam loss assumption has a large uncertainty, exact calculations for the shielding design with detailed methods make little sense. Considering the large uncertainty in source term estimation, we basically employ semi-empirical formulas and/or simplified methods for almost of the design. However, it is difficult to apply the simplified methods for the design calculations at the target, the beam dump and the injection and extraction points of the accelerator, because the geometries are

complicated and the large beam losses are expected. Although usually very time consuming, some detailed methods must be applied for the design calculations there. Thus, a calculation system with both simplified and detailed methods is used for the shielding design of J-PARC [6].

As for the simplified methods, for bulk-shielding calculations by specifying the beam-loss rates and the beam energy for the calculations at almost all parts of the accelerator, the Tesch's formula [10] for a proton energy of below 1 GeV and the Moyer model [11] above 1 GeV are used. For labyrinths of access ways and ducts in facilities, simple empirical formulas of Nakamura and Uwamino [12] and a simplified duct streaming code, DUCT-III [13,14] are applied. In order to estimate the dose due to radiation at the site boundary, Stapleton's formula [15] is applied for all skyshine sources. A PC-based calculation system composed of simplified formulae for bulk shield and the empirical formula for neutron skyshine, named SSCAT [16], is used for comprehensive radiation safety estimation of whole facilities in J-PARC.

In detailed methods, a calculation system combined with various codes is used, as shown in Figure 3 [5]. In this system, several Monte-Carlo codes PHITS [17], MARS14 [18] and MCNPX [19], are used for high-energy particle transport calculation, making full use of the characteristics of each code. The PHITS code is a multi-purpose particle and heavy ion transport Monte Carlo code based on the NMTC/JAM code [20]. The combined system of the PHITS and DCHAIN-SP 2001 [21] codes is used to design a spallation neutron target system in J-PARC, because the code system can easily estimate the evolution of induced radioactivity and nuclear heating in the spallation target and radiation damage of the target structure. The MCNPX code is famous and widely used for the designs, because the code has various kinds of estimators and variance reduction techniques. The MARS code can calculate the radiation flux and dose in a rather short time, compared with other Monte-Carlo codes. The MARS code can easily connect with the STRUCT code [22] calculating proton beam tracing in accelerators and the ANSYS code for calculating heat transfer. The MCNP-4 code [23] with a nuclear data set, JENDL-3.3 [24], is applied for low-energy neutrons up to 20 MeV and photons. The DCHAIN-SP 2001 code with mainly the FENDL-Dosimetry file [25] is used for induced radioactivity and dose estimations due to residual nuclei in the machine components and the wall of the accelerator room.

## Benchmarking

In order to study the accuracy of the methods and make clear the differences among the results by the methods, some benchmark analyses on thick target neutron yield, beam dump, bulk shielding, streaming and skyshine were carried out. As an example of benchmarking, comparisons of the calculated dose-equivalent due to skyshine radiation among the Stapleton's formula, the SHINE-III [25] and NMTC/JAM codes are presented in Figure 4. It has been shown that the calculations are in very good agreement with each other from the point of very near to the source region up to a distance of 2 000 m for neutrons generated by 600 MeV and 3 GeV proton beams [5].

## Shielding designs

In shielding design for J-PARC, numerous calculations have been done for estimation of shielding thickness on bulk shields, effective dose rate due to radiation streaming on ducts and access paths, effective dose rate due to skyshine at site boundary and activities in air, water and structural materials such as wall, target and accelerator devices. Calculated results on nuclear heating and radiation damage are applied for mechanical and thermo-hydraulic design of a mercury target and estimation of life time of target vessel. In this chapter, some typical examples are presented from some facilities in J-PARC.

Figure 5 shows the dose distribution due to beam loss at the 30-degree beam dump in linac tunnel. In the calculation proton beam of 190 MeV and 100 W irradiates the beam dump embedded in the concrete wall of LINAC tunnel. By using the calculated results, the size of the beam dump itself and thickness of the concrete wall around the beam dump were designed. The calculated neutron flux was used for estimation of effective dose rate at the ground surface. The neutron and proton fluxes were used for estimation of activities in air of the accelerator room and in water of coolant used for accelerator devices, and the estimated activities applied to design the ventilation system and cooling system.

Effective dose rate distribution along a duct at 3GeV RCS is shown in Figure 6, which is the calculated result by the PHITS code due to the average beam loss of 1 W/m at quadrupole magnets of 3GeV RCS. It is presented in the figure that the generated radiation attenuates of about 5, order of magnitude in the two-bend duct, but a thin concrete shield was required to be below the design criteria.

Dose distribution due to beam loss at air in a duct in front of a fast beam dump of 7 kW for 50GeV MR was calculated by the MARS code. In the calculation an effect of air in the beam duct was examined and it was presented that the high power beam of 7 kW required an additional shield in case that the duct was filled by air as shown in Figure 7.

Many items were calculated in design of MLF [13]. For the mercury target design, neutron yield from the target was calculated and moderator performance was estimated. For shielding, effective dose around the target and residual activities in the target were estimated. Nuclear heat distribution was calculated for structural design on cooling system. Radiation damage of the target vessel irradiated by the proton beam was estimated and the maintenance scenario was planned. Figure 8 shows the distribution of nuclear heat on horizontal plane around a mercury target calculated by the PHITS code as an example of estimations. In the calculation the target for a neutron spallation source is irradiated by proton beams of 3 GeV and 1 MW. Nuclear heat above about 0.1 W/cc/MW is generated at the proton beam window and the mercury target, and a few amount of nuclear heat in the shields around the target is observed. The distribution of the nuclear heat was used as the design parameter of the cooling system of the beam window, target and shields.

## Summary

J-PARC is a large-scale experimental facility consisting mainly of a high-intensity, high-energy proton accelerator of top world class. Thus, shielding design for J-PARC must be prudent, concerning radiation safety aspect more than for the existing accelerator facilities. In order to secure safety, attaining economical rationality, the shielding design and safety evaluations are performed by a combined method of the simplified and sophisticated methods with reliable data. Safety factor of two was applied for the shielding design based on experimental benchmarking. As the first step of a safety review, we obtained an approval for use of linac. Safety review will be done for approval in use of other facilities: 3GeV RCS, 50GeV MR, MLF, NP and  $\nu$ , in the near future.

## References

- [1] S. Nagamiya, "JAERI-KEK Joint Project on High Intensity Proton Accelerators", *J. Nucl. Sci. and Technol.*, Suppl. 1, pp. 40-48 (2000).
- [2] S. Tanaka, "High Intensity Proton Accelerator Project in JAPAN (J-PARC)", *Radiation Protection Dosimetry*, 115, pp. 33-43 (2005).
- [3] S. Nagamiya, "Construction Status of the J-PARC Project", *J. of Nucl. Materials*, 343, pp. 1-6 (2005).
- [4] N. Sasamoto, et al., "Status on Shielding Design Study for the High-intensity Proton Accelerator Facility", *J. Nucl. Sci. Technol.*, Suppl. 2, 1264 (2002).
- [5] H. Nakashima, et al., "Radiation Safety Design for the J-PARC Project", *Radiation Protection Dosimetry*, 115, pp. 564-568 (2005).
- [6] H. Nakashima, et al., "Radiation Shielding Study for the J-PARC Project", to be submitted to *Proc. on Topical Meeting of Radiation Protection and Dosimetry* (2006).
- [7] I. Yamane, *Radiation Protection Measures for the Maintenance Service of JHF 3-GeV Ring*, KEK internal report, 98-7 (1998).

- [8] J. Alonso, "Beam Loss Working Group Report", *Proc. of the 7<sup>th</sup> ICFA Mini-workshop on High Intensity High Brightness Hadron Beams*, 51 (1999).
- [9] H. Nakashima, et al., "Estimation of Activity and Dose Distributions Around a Proton LINAC Induced by Beam Spill", *J. Nucl. Sci. Technol., Suppl.* 1, 870-874 (2000).
- [10] K.A. Tesch, "Simple Estimation of the Lateral Shielding for Proton Accelerators in the Energy Range 50 to 1 000 MeV", *Radiation Protection Dosimetry*, 11, 165 (1985).
- [11] B.J. Moyer, "Method of Calculation of the Shielding Enclosure for the Berkeley Bevatron", *Proc. 1<sup>st</sup> Int. Conf. Shielding Around High Energy Accelerators*, 65 (1962).
- [12] Y. Uwamino, et al., "Measurement and Calculation of Neutron Leakage from a Medical Electron Accelerator", *Med. Phys.*, 13 (3), 374 (1986).
- [13] R. Tayama, et al., *DUCT-III, A Simple Design Code for Duct-Streaming Radiations*, KEK internal report 2001-8, KEK (2001).
- [14] F. Masukawa, et al., *Verification of the DUCT-III for Calculation of High Energy Neutron Streaming*, JAERI-Tech 2003-018, Japan Atomic Energy Research Institute (2003).
- [15] G.B. Stapleton, et al., "Accelerator Skyshine: Tyger, Tyger, Burning Bright", *Particle Accel.*, 44 (1), 1 (1994).
- [16] T. Masumura, et al., *Simplified Shielding Calculation Table (SSCAT) system*, JAERI-Data/Code 2000-026 (2000) (in Japanese).
- [17] H. Iwase, et al., "Development of General-purpose Particle and Heavy Ion Transport Monte Carlo Code", *J. Nucl. Sci. Technol.*, 39, 1142 (2002).
- [18] N.V. Mokhov, *The MARS Code System User's Guide*, Fermilab-FN-628 (1995); N.V. Mokhov and O.E. Krivosheev, *MARS Code Status*, Fermilab-Conf-00/181 (2000), [www-ap.fnal.gov/MARS](http://www-ap.fnal.gov/MARS).
- [19] L.S. Waters (Ed.), *MCNPX Users Manual – Version 2.1.5*, TPO-E83-G-UG-X-00001, LANL (1999).
- [20] K. Niita, et al., *High Energy Particle Transport Code NMTC/JAM*, JAERI-Data/Code 2001-007, Japan Atomic Energy Research Institute (2001).
- [21] T. Kai, et al., *DCHAIN-SP 2001: High Energy Particle Induced Radioactivity Calculation Code*, JAERI-Data/Code 2001-016, JAERI (2001) (in Japanese).
- [22] I. Baishev, A. Drozhdin, N.V. Mokhov, *STRUCT Program User's Reference Manual*, SSCL-MAN-0034 (1994).
- [23] J.F. Briesmeister (Ed.), *MCNP – A General Monte Carlo N-particle Transport Code*, Version 4A, LA-12625, LANL (1993).
- [24] K. Shibata, et al., "Japanese Evaluated Nuclear Data Library Version 3 Revision-3: JENDL-3.3", *J. Nucl. Sci. Technol.*, 39, 1125 (2002).
- [25] A.B. Pashchenko, *IAEA Consultants' Meeting on Selection of Evaluations for the FENDL/A-2 Activation Cross Section Library – Summary Report*, INDC (NDS)-341, IAEA (1996).
- [26] T. Tsukiyama, et al., "SHINE-III: Simple Code for Skyshine Dose Calculation up to 3 GeV Neutrons", *J. Nucl. Sci. Technol., Supplement* 1, 640 (2000).
- [27] Material and Life Science Experimental Facility Construction Team, *High Intensity Proton Accelerator Project (J-PARC) Technical Design Report Material & Life Science Experimental Facility*, JAERI-Tech 2004-001 (2004) (in Japanese).

**Table 1: Radiation dose limit in the Japan regulation**

Area	Radiation dose limits
Controlled area	1 mSv/1week
Boundary of controlled area	1.3 mSv/3months
Site boundary	250 $\mu$ Sv/3months

**Figure 1: Bird's eye view of planned J-PARC facilities**

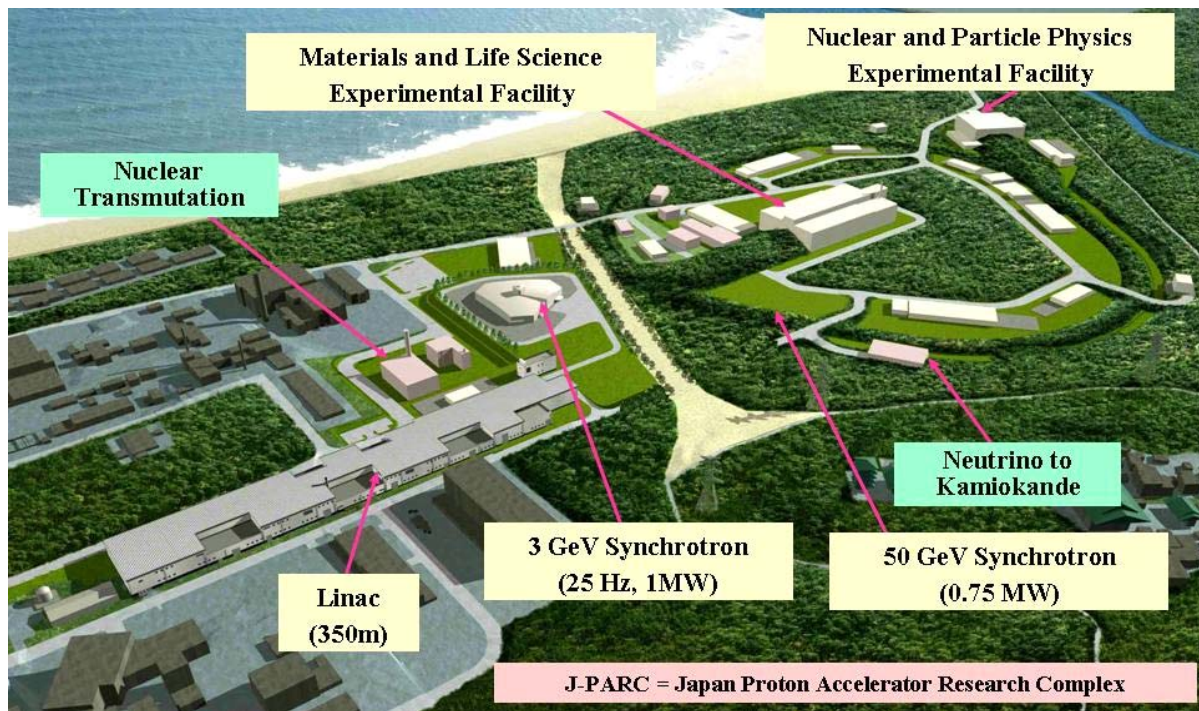


**Figure 2: Conceptual view of air confinement system for J-PARC**

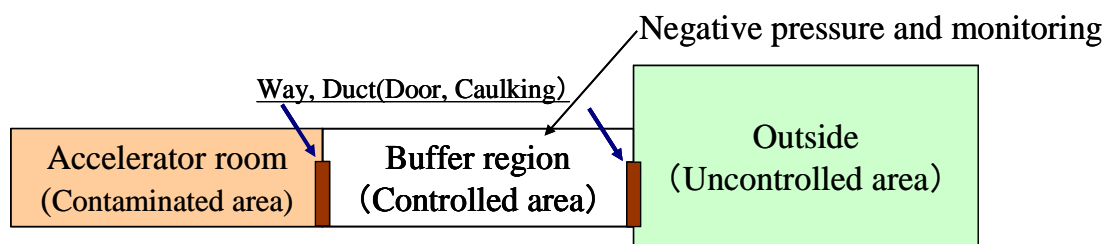


Figure 3: Calculation flow of radiation and activity for J-PARC [5]

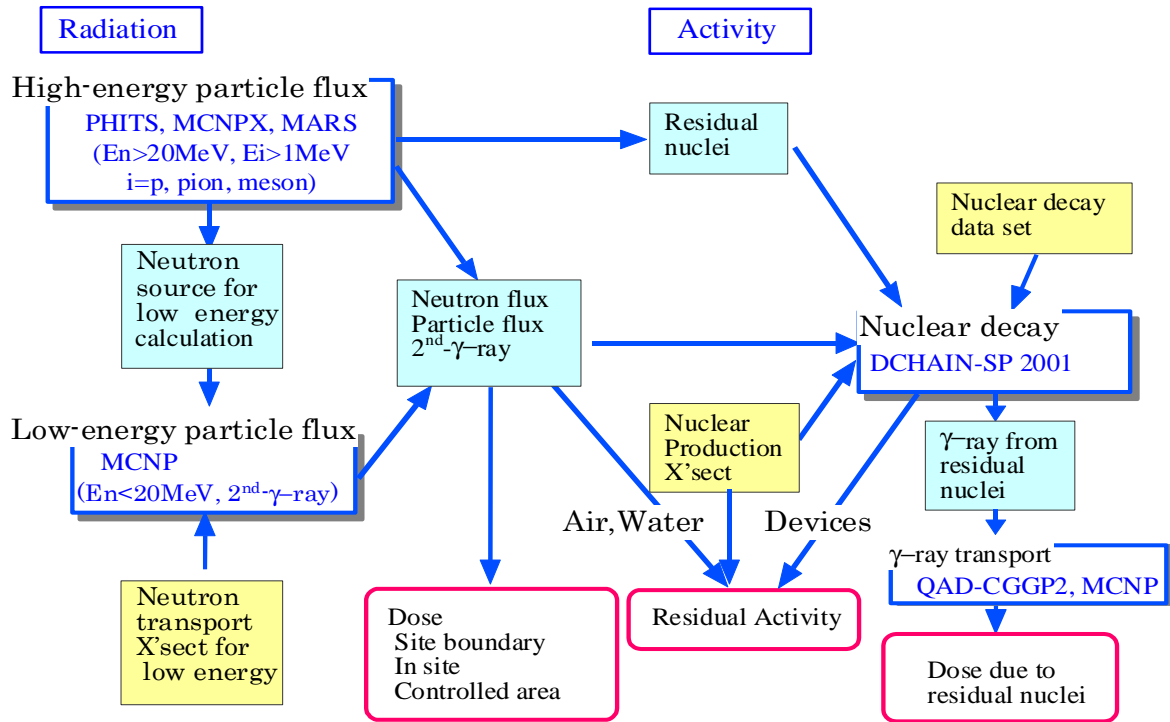
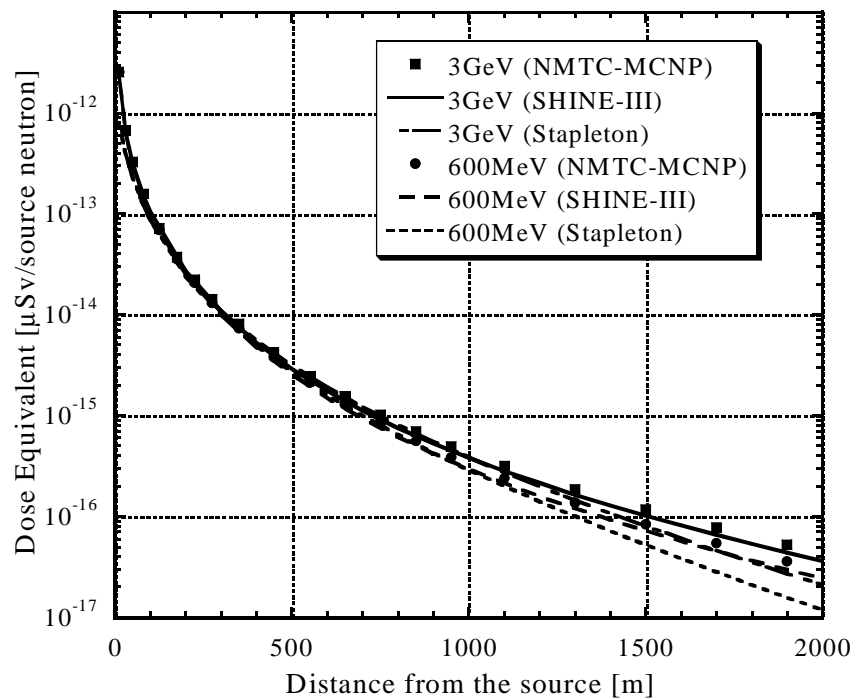
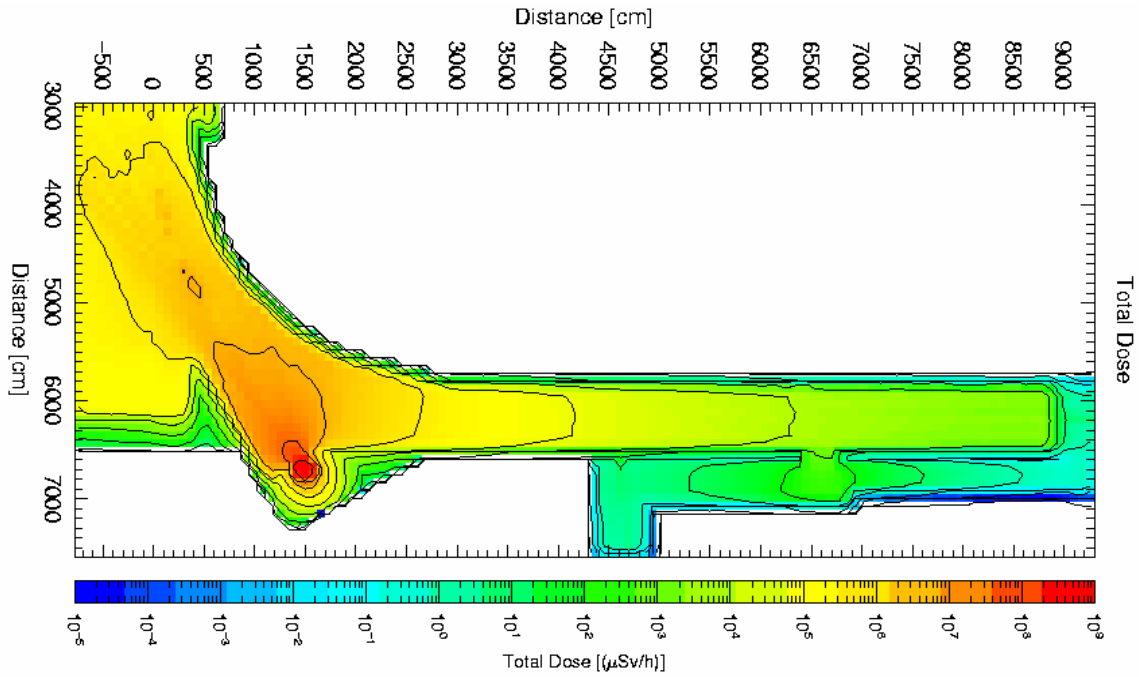


Figure 4: Comparison of the skyshine dose as a function of the distance from the source among Stapleton's equation, the SHINE-III code and the NMTC-MCNP code [5]



**Figure 5: Dose distribution due to beam loss at 30-degree beam dump in LINAC tunnel**



**Figure 6: Effective dose rate distribution in a duct due to the average beam loss of 1W/m at quadrupole magnets at 3GeV RCS**

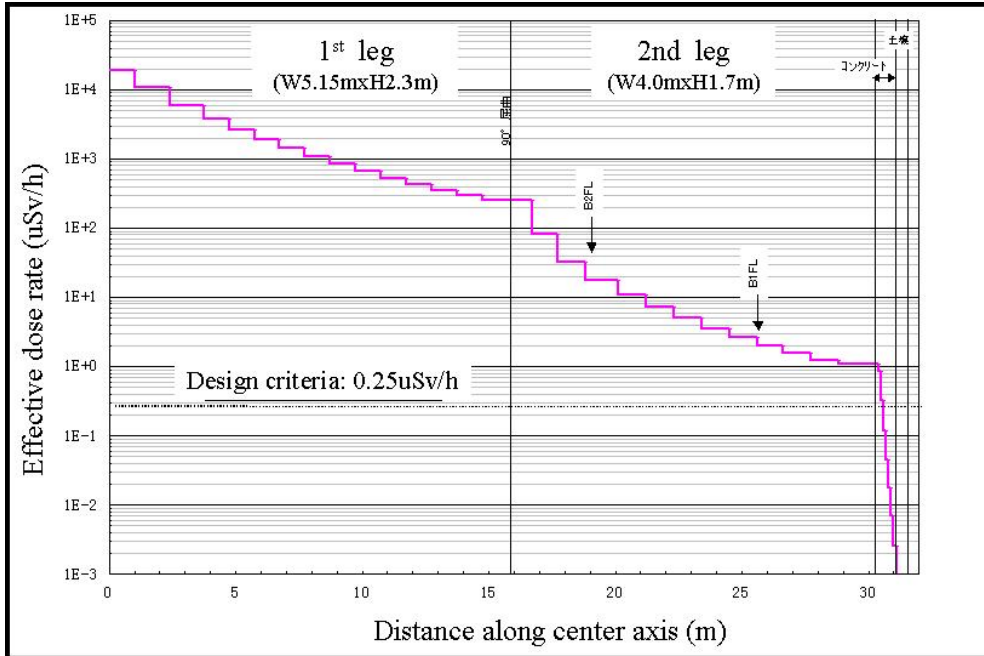


**Figure 7: Dose distribution due to beam loss at air in a duct in front of a fast beam dump of 7 kW for 50GeVMR calculated by the MARS code**

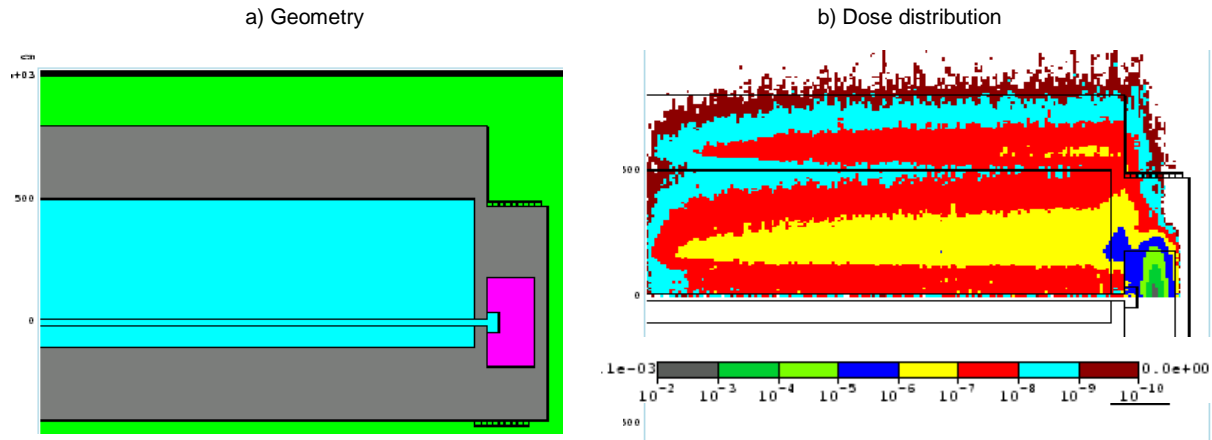
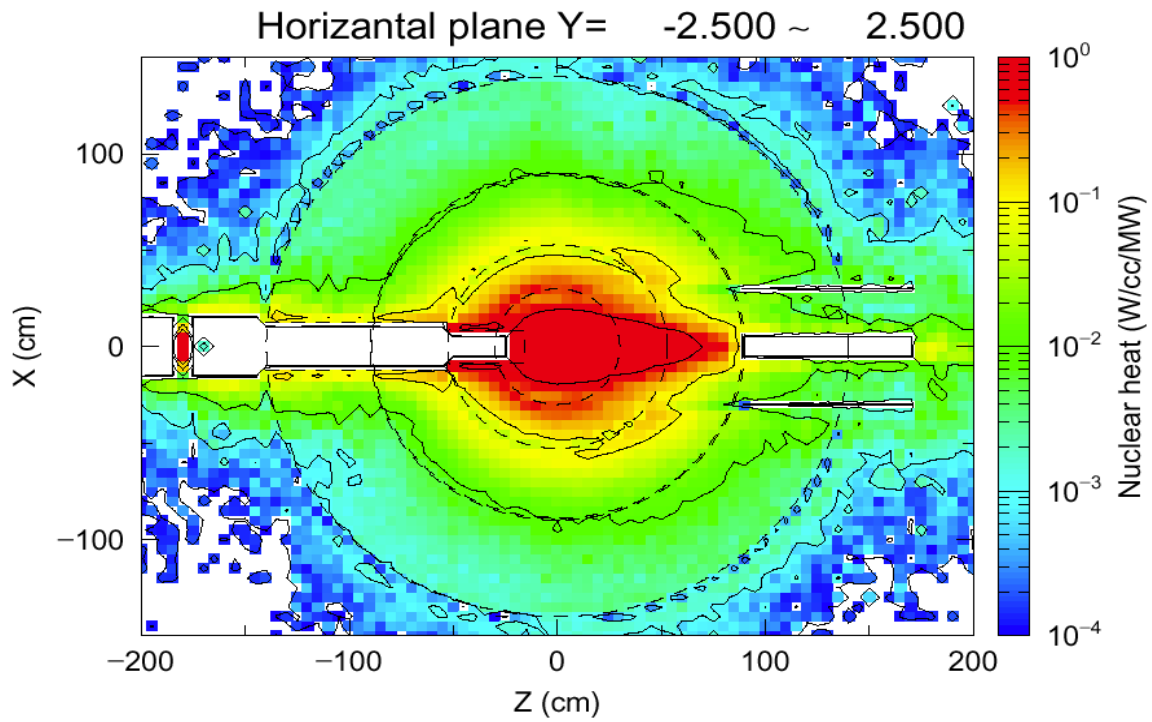


**Figure 8: Distribution of nuclear heat on horizontal plane around a mercury target calculated by the PHITS code**





## Safety design of the Radioactive Isotope Beam Factory (RIBF) at RIKEN

**Yoshitomo Uwamino, Nobuhisa Fukunishi, Hisao Sakamoto, Shin Fujita**  
RIKEN, Japan

### Abstract

*The RIBF is a facility-expanding project. It consists of three ring cyclotrons, a projectile-fragment separator, and the experimental facilities. The final stage cyclotron is superconducting and its maximum energy is 400 MeV/u for ions lighter than Fe and 350 MeV/u for up to uranium. The beam intensity is 1  $\mu\text{A}$  ( $6 \times 10^{12}$  particle/s) for any element at the final goal. The secondary neutron production measured at HIMAC was used for the source term of the shielding calculations. The deep penetration of high-energy neutrons was calculated by using the ANISN code with the DLC-119/HILO86R group constants. Three types of radiation monitors are installed and their threshold levels for the beam stop are sent to the radiation safety interlock system.*

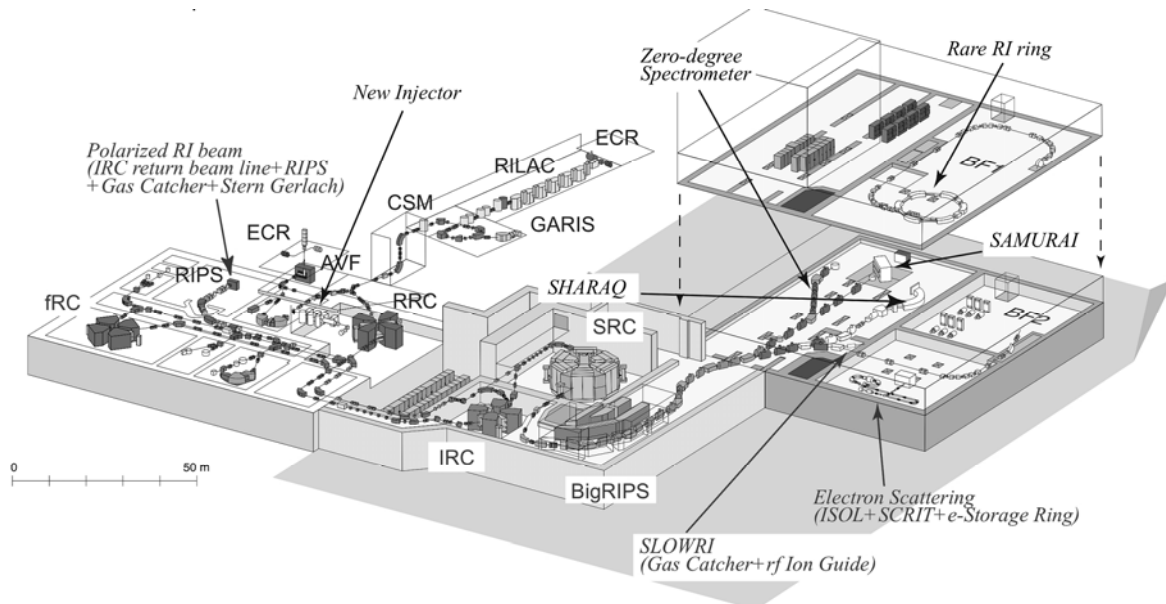
## Introduction

The RIKEN Radioactive Isotope Beam Factory (RIBF) is a facility-expanding project. Three ring cyclotrons and a projectile-fragment separator are now under construction. Studies with unstable nuclide beams will be performed on wide spread fields of pure and applied sciences.

RIBF is a high-energy high-intensity heavy ion accelerator facility, and its shield mostly made of ordinary concrete is very thick at a position where a significant beam loss is expected. Shielding design, therefore, must be made rationally. Heavy ion beams of several hundred MeV energy region are available at HIMAC of NIRS in Chiba, Japan, and neutron productions of thick target bombardment were measured by Kurosawa, *et al.* [1]. These data are used for the shielding calculation of RIBF.

The shield is designed on the basis of an estimated beam loss, and the beam loss monitoring and the on-line radiation monitoring are very important at a large accelerator facility. In this report the outline of RIBF, shielding design and the radiation monitoring system are described.

**Figure1: Bird's eye view of the RIKEN Accelerator Research Facility after the RIBF construction is finished**



## Outline of the RIKEN RI beam factory

RIBF is now under construction next to the present RIKEN Accelerator Research Facility (RARF) as shown in Figure 1. The present RARF on the white background in the left consists of an AVF cyclotron, RIKEN Ring Cyclotron (RRC), and a variable-frequency heavy-ion RIKEN Linear Accelerator (RILAC). The K-number of RRC is 540 MeV.

As the RIBF project which is mostly shown on the gray background in Figure 1, a fixed frequency Ring Cyclotron (fRC) is placed in the present facility, and the Intermediate stage Ring Cyclotron (IRC) and the Superconducting Ring Cyclotron (SRC) are under construction in the RIBF accelerator building. The K-number of the final stage cyclotron, SRC, is 2 500 MeV.

Big-RIPS which stands for Big RIKEN Projectile-fragment Separator is constructed in the accelerator building and provides unstable RI beam to the experimental devices which are installed in the experimental building.

Figure 2 is the schematic of the beam delivering. The RILAC beam is sent to RRC and also can be used for the low energy experiment such as the synthesis of the super heavy element. The AVF cyclotron at the Nishina building can be used independently when RILAC beam is injected to RRC. The

ions extracted from RRC heavier than Kr are pre-accelerated by fRC before they injected to IRC. At the RIBF accelerator building two cyclotrons of IRC and SRC are used sequentially.

All the buildings except for RILAC are underground, and the top of the shielding roof is at the ground level. The beam line is 14 m below the ground level.

The beam energies and intensities are listed in Table 1. The intensities at the beginning and at the final goal are shown. Ions of carbon to uranium will be accelerated. Maximum energies are 400 MeV/u for ions from C to Fe, and 350 MeV/u for ions Co to U. The final goal of the intensity is 1  $\mu$ A for any beam. The operation of RIBF will be started by the end of March 2006 with relatively low intensities.

**Figure 2: Schematic of the beam delivering at RIKEN Accelerator Research Facility. The hatched part is the constructing RIBF.**

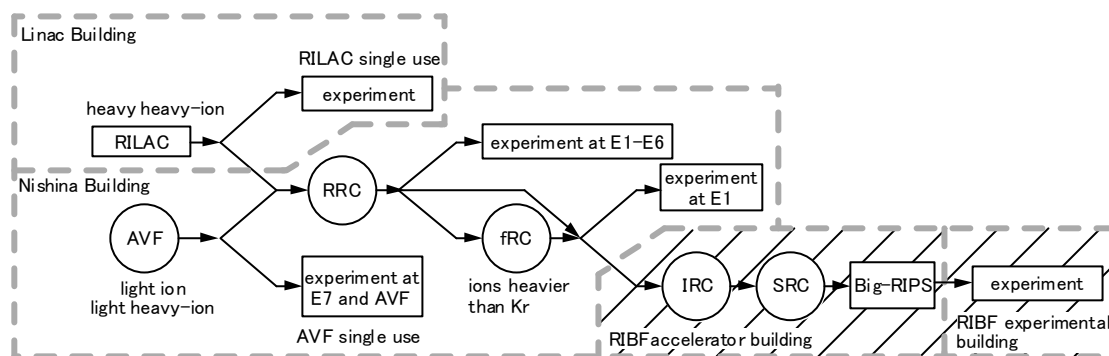


**Table 1: Beam characteristics of the final stage cyclotron, SRC**

Ion	Energy	Intensity at beginning	Intensity of final goal
${}^6\text{C}$ to ${}_{26}\text{Fe}$	400 MeV/u	30 pA	1 000 pA
${}_{27}\text{Co}$ to ${}_{36}\text{Kr}$	350	30	1 000
${}_{37}\text{Rb}$ to ${}_{83}\text{Bi}$ , ${}_{92}\text{U}$	350	10	1 000

## Shielding design

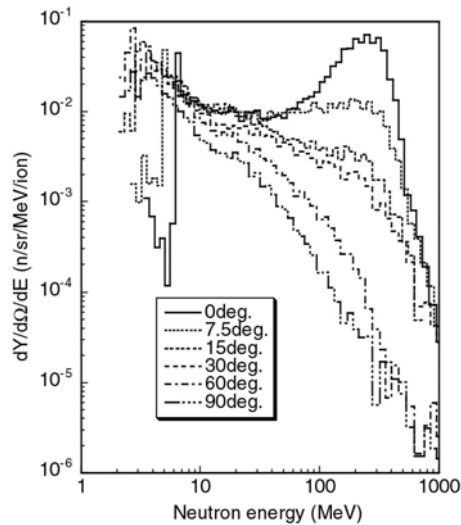
The design criteria in effective dose rate are shown in Table 2. The values in the radiation controlled area and at the boundary of radiation controlled area are the requirements of the law. The value for the office in the institute comes from the ICRP recommendation, and the value at the site boundary is the promise to Wako city. The limit at the outer surface of the underground wall is to control the induced radioactivity production in the soil, and to keep the exposure on a person who may drink the underground water of the site boundary below 10  $\mu$ Sv/year.

**Table 2: Design criteria of effective dose rate**

Place	Dose rate limit
Radiation controlled area	25 $\mu$ Sv/h (1 mSv/week)
Boundary of radiation controlled area	2.6 $\mu$ Sv/h (1.3 mSv/3 month)
Office in site	0.5 $\mu$ Sv/h (250 $\mu$ Sv/3 month)
Site boundary	50 $\mu$ Sv/year
Outer surface of the underground wall	1.3 mSv/hour

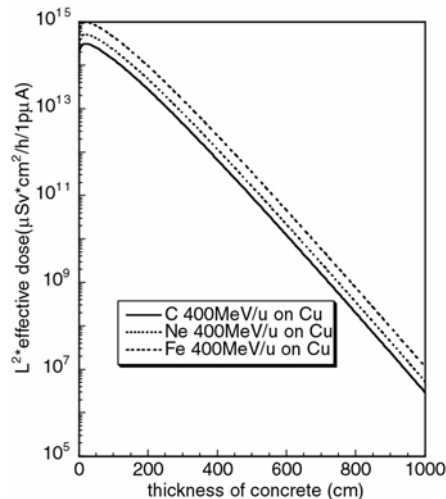
The beam losses assumed in the shielding design are 10 pA at the injection and the extraction points of IRC and SRC. 10 pA corresponds to 1% loss of the 1  $\mu$ A beam which is the final goal. These relatively low loss rates will be kept by the radiation monitoring.

**Figure 3: Double differential neutron production of a thick Cu target bombarded by a 400 MeV/u Ne beam**

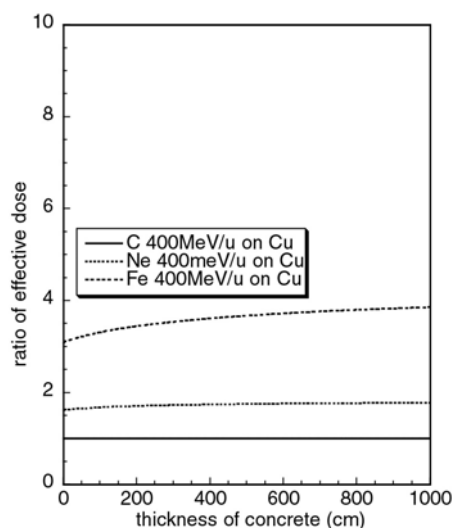


High energy heavy-ion beams are available at HIMAC of NIRS, and neutron productions at thick targets bombarded by 100 to 400 MeV/u beams were measured by Kurosawa, *et al.* [1]. The results of 400 MeV/u Ne beam bombardment on a Cu target are shown in Figure 3. The spectra have strong fluctuations at low energies. Low energy neutrons, however, hardly affect the neutron dose behind a thick shield, and these fluctuations can be ignored.

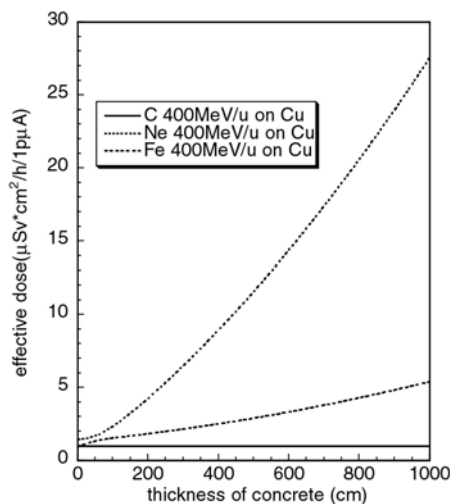
**Figure 4: Effective dose distributions of 0-degree neutrons in a concrete shield for the cases of 400 MeV/u C, Ne and Fe beam bombardment on Cu target**



These measured production data were used as a source term of the ANISN calculation, and the DLC-119/HILO86R [2] group cross-sections were used. Since the highest energy of the HILO86R constants is 400 MeV, the neutrons of energy higher than 400 MeV are treated as of 400 MeV and the number of them is multiplied by  $E_n/400$ , where  $E_n$  is the neutron energy in MeV. The total energy is conserved with this procedure.

**Figure 5: Ratios of the effective dose distributions of 0 degree neutrons shown in Figure 4**

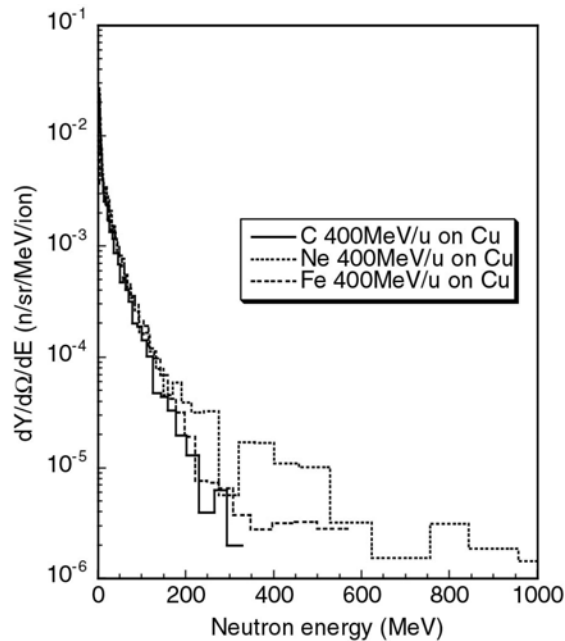
The ANISN calculation was performed with many source neutrons of Kurosawa's measurements to estimate the projectile mass dependence. Figure 4 shows the effective dose attenuations of neutrons produced in 0 degrees at a thick Cu target bombarded by 400 MeV/u C, Ne and Fe beams. The shield is 10 m thick ordinary concrete. Ratios of the effective doses to that of C beam are shown in Figure 5. The mass ratios of Ne and Fe to C are 1.7 and 4.7, respectively. It can be conservatively said from Figure 5 that the effective dose behind a thick shield is proportional to the projectile mass when the extrapolation is made to heavier projectile.

**Figure 6: Ratios of the effective dose distributions of 90-degree neutrons**

While similar results are obtained in the cases of 7.5 degrees to 60 degrees emission neutrons, a curious result of 90-degree neutrons is seen and shown in Figure 6. This comes from the existence of high energy neutrons for Ne and Fe beams as shown in Figure 7. It can hardly be thought from the kinematics that neutrons of energy above 400 MeV are produced in 90-degree. If the neutrons of energy higher than 400 MeV are omitted, the effective dose distribution becomes reasonable.

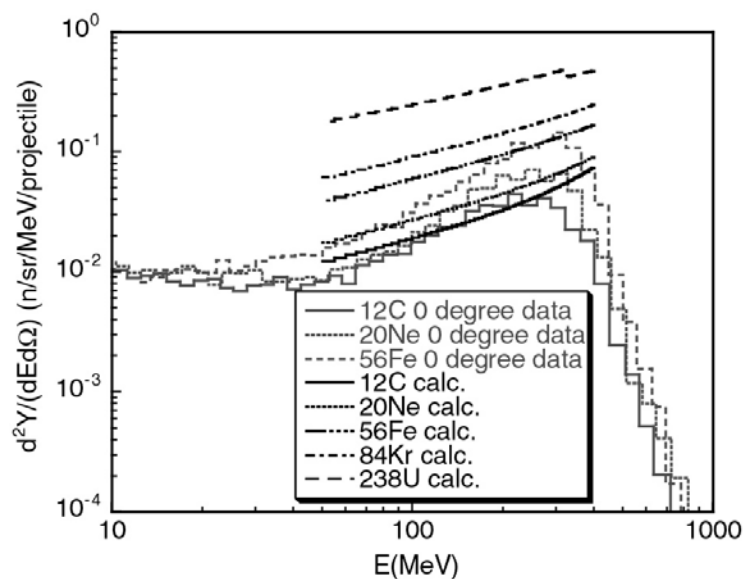
The calculated results are compared with the shielding experiment by Kumamoto performed at HIMAC with the 400 MeV/u C and Ne beams [3]. The ANISN results are 7.5 times larger than the measured value at 0 degree, and 1.4 to 2.1 times larger in the cases of 13 degrees to 55 degrees.

**Figure 7: Double differential neutron production at 90 degrees of 400 MeV/u C, Ne and Fe beam bombardment on Cu target**



Neutron production by U beam was considered separately since the range is very short, U fissions and U is much heavier than the target nuclide. The reaction cross-section was taken from the Kox's empirical formula [4], and 25% neutrons run away in the forward direction between 0 degrees and 7.5 degrees with the same velocity of the projectile nucleus. With this assumption the forward neutron productions of C, Ne, Fe, Kr and U were calculated, and the results are compared with the measurements [1] in Figure 8. The above assumption seems reasonable from these comparisons. The neutron production by U beam is estimated to be 2.2 times larger than the Kr beam in the forward direction. In the lateral direction, on the other hand, the neutron yield of U becomes smaller than that of Ne because of its large velocity of the centre of mass.

**Figure 8: The calculated neutron production spectra in the forward direction between 0 to 7.5 degrees are compared with the measured data of  $^{12}\text{C}$ ,  $^{20}\text{Ne}$ ,  $^{56}\text{Fe}$  bombardment**



For the determination of the shield thickness, the dose distributions for the Kr beam were considered as the base, and the values were multiplied by 2.2 for the forward direction between 0 degrees to 30 degrees.

The calculated and modified results of ANISN were fitted with the following simple exponential formula:

$$E = E_0 \exp(-t/\lambda)/r^2 \quad (1)$$

where  $E_0 = 2.9 \times 10^{16} \mu\text{Sv cm}^2/\text{h}/1\text{-}\mu\text{A}$  (at 0-deg),  $6.4 \times 10^{15}$  (7.5-deg),  $1.4 \times 10^{15}$  (15-deg),  $9.8 \times 10^{14}$  (30-deg),  $2.6 \times 10^{13}$  (60-deg),  $6.2 \times 10^{12}$  (90-deg):

$\lambda = 49$  cm (for concrete) and 19.6 cm (for iron);

$t =$  shield thickness;

$r =$  distance from the beam-loss point.

This formula was used in the decision of the shield thicknesses which are briefly shown in Table 3.

**Table 3: Shield thicknesses at RIBF. Unit is meter and material is ordinary concrete if not specified.**

Room	North wall	West wall	South wall	East wall	Roof	Floor
BT* to IRC	2	2	2**	2	2	2
IRC	2	2	2**	2/0.5+0.5Fe	3	3**
SRC	3.5/2.5	3	2	2	3	3**
BT to Big-RIPS	1.5+1.7Fe	0.5+0.5Fe	2+1.4Fe	–	4.8	4/5.5**
Big-RIPS	2	2	2**	2.5**	2	4/5.5**
Experimental	1.5**	1.5**	1.5	2	1.5	1.5

\* Beam transport room.

\*\* Outside is soil.

## Radiation monitors and interlock system

Three types of radiation monitors are installed in RIBF, and the interlock signals from these monitors are sent to the radiation safety interlock system.

### Beam loss monitor

A simple plastic scintillator of 2.5-cm diameter and 2.5-cm length is used as a beam loss monitor, because it is sensitive to high-energy neutrons which are the dominant source component for thick shield. The pulse count rate of the discriminator and the anode current are read for low-level and high-level radiation fields, respectively.

### Neutron dose equivalent monitor

Neutrons are the dominant component of the radiation around the facility, and a conventional hand-held neutron dose equivalent monitor, a so-called rem counter, can be used as a simple and relatively cheap radiation monitor. The NSN21001 dose equivalent monitor of Fuji Electric Co. Ltd. has high sensitivity, and the MAR-566 dose equivalent monitor of Aloka Co. Ltd. is water resistant. About 20 monitors are installed in the radiation controlled area. These monitors have logarithmic voltage output of five decades. The voltage signal is converted into current signal, and sent to the analogue input of the radiation safety interlock system.

### Area monitor

Neutron and gamma-ray radiation area monitors are commercially available. The centre console of them records and displays the data, and their performance is very high. They are expensive, however, and 12 pairs of neutron and gamma-ray monitors are distributed at the outside of the accelerator rooms, at the boundary of the radiation controlled area and at the site boundary.

### **Radiation safety interlock system**

A radiation safety interlock system, HIS (Houshasen [which means “radiation” in Japanese] Interlock System), is installed. This system controls all the devices connected to it, that is, radiation shutters, beam stoppers, radiation monitors, shielding doors, beam status indicator, alarm siren, and so on.

HIS consists of five I/O stations and two personal computers. Each station has a programmable logic controller (PLC) and an I/O board. The signals join the I/O boards through multi connectors which facilitate connection and disconnection of the station at the site when we repair or test the system.

The most important devices for safety, that is, the shielding doors and the radiation shutters, are double-monitored by the two systems independently, one is HIS and the other is the Beam Interlock System (BIS) of which purpose is to protect the accelerator and the beam-line components. This concept is succeeded from the design of the existing facility.

### **Summary**

A high-energy high-intensity heavy ion accelerator facility, RIBF, is under construction, and operation will be started by March 2007. Shielding calculations were performed by using the ANISN code with the source neutron spectra measured at HIMAC. The calculation gave conservative results compared with the shielding experiment. Three types of radiation monitoring systems are installed for the beam loss control.

### **References**

- [1] T. Kurosawa, et al., *J. Nucl. Sci. Technol.*, 36, 1 (1999).
- [2] H. Kotegawa, et al., *Neutron-photon Multigroup Cross-sections for Neutron Energies up to 400 MeV: HILO86R – Revision of HILO86 library*, JAERI-M 93-020, Japan Atomic Energy Research Institute (1993).
- [3] Y. Kumamoto, Y. Noda, Y. Sato, T. Kanai, T. Murakami, *Health Phys.*, 88 (2005) 469.
- [4] Kox, et al., *Phys. Rev.*, C35 (1987) 1678.

## Monte Carlo simulations for the shielding of FLAIR

**A. Knapp, T. Radon, G. Moustafina, F. Gutermuth, G. Fehrenbacher**  
Gesellschaft für Schwerionenforschung mbH, Darmstadt, Germany

### Abstract

*The Gesellschaft für Schwerionenforschung (GSI) is a heavy ion research facility, which performs basic and applied research in physics and related natural science disciplines. The GSI currently comprises the heavy ion synchrotron SIS18 which is fed by the linear accelerator UNILAC. With this combination several experimental areas including the fragment separator FRS and the storage ring ESR can be served.*

*In the next years the GSI will contribute to a new international accelerator facility called FAIR (Facility for Antiproton and Ion Research). The present SIS18 will be used as an injector for a 100/300 Tm double heavy ion synchrotron SIS100/300. This synchrotron will provide intensities of up to  $10^{12}$  particles per second for uranium beams with energies of 2 GeV per nucleon. Furthermore with this facility it will be possible to produce antiprotons in a wide energy range. The Facility for Low-energy Antiproton and Ion Research (FLAIR) makes use of the beams of antiprotons and highly-charged ions. It comprises mainly two storage rings (LSR and USR), the universal trap facility HITRAP and five experimental caves.*

*The shielding of the FLAIR facility of FAIR will be presented on the basis of several Monte Carlo simulations for radiation transport with the latest version of the FLUKA code (FLUKA 2005.6). The production of secondary particles and their migration through the shielding walls made of concrete is calculated to optimise the shape and the thickness of the shielding in order to preserve the limits of the German Radiation Protection Ordinance.*

## Introduction

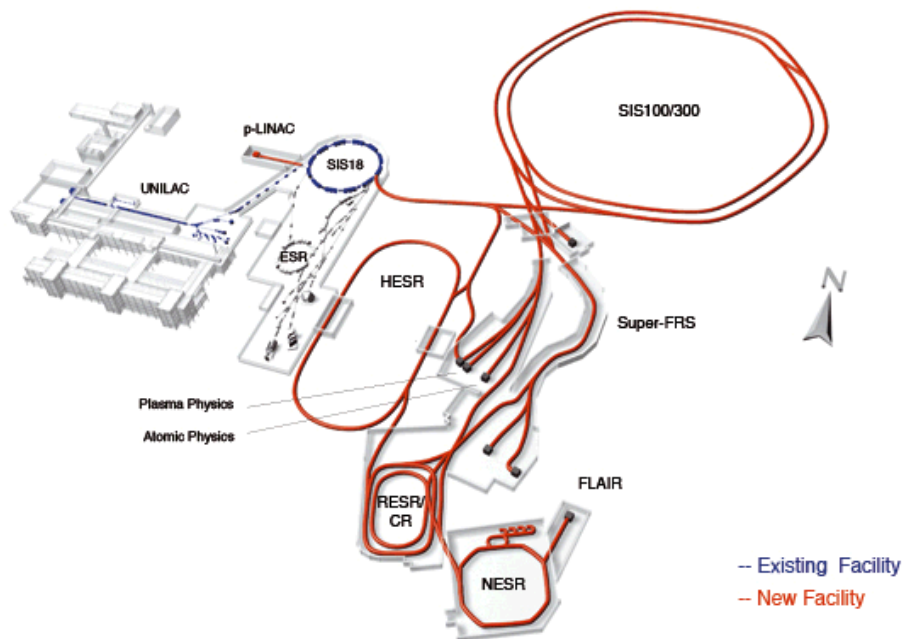
The GSI accelerator facility<sup>1</sup> consists of the UNiversal Linear ACcelerator UNILAC, the heavy ion synchrotron SIS18 and several experimental areas including a fragment separator and a storage ring. Using SIS18 all elements of the periodic system (from hydrogen to uranium) can be accelerated to about 90% of the speed of light.

The new facility FAIR (Facility for Antiproton and Ion Research) will be an international accelerator facility<sup>2</sup> of the next generation. It consists of a double ring synchrotron SIS100/300 (circumference ~1200 m) with 100 and 300 Tm maximum magnet bending power. Several facilities such as the High Energy Storage Ring HESR, the Collector Ring CR, the Recycled Experimental Storage Ring RESR, the new Experimental Storage Ring NESR and the Super FRagment Separator SFRS are connected to this double ring. Figure 1 shows a sketch of the planned FAIR facility.

The present SIS18 will be used as an injector for the SIS100/300. It will provide intensities of  $10^{12}$  particles per second for uranium beams with energies of 2 GeV per nucleon. Furthermore with this facility it will be possible to produce antiprotons with intensities around  $10^7$  per second in a wide energy range (from 14 GeV down to several eV).

**Figure 1: Sketch of the existing GSI facility (left) and the planned future project FAIR (right)**

The meaning of the abbreviations can be found in the text [2]



It is foreseen to produce the antiprotons by an intense 29 GeV proton beam (delivered by the SIS100) shot on a special production target. Up to  $10^{13}$  protons per cycle will thus produce  $10^8$  antiprotons every five seconds. The antiprotons are then pre-cooled at 3 GeV in the CR by a stochastic cooling system. Afterwards, the antiprotons are transferred to the decelerator ring RESR, where the accumulation of up to  $7 \cdot 10^{10}$  antiprotons is foreseen. The antiprotons are accelerated for experiments with high energy antiprotons in the HESR or directly transferred to the NESR, which is used to decelerate the beam to 30 MeV that is then transferred to the Facility for Low-energy Antiproton and Ion Research (FLAIR) [1]. The location of the FLAIR hall in relation to the other facilities of FAIR can be seen in Figure 1.

1. More information on the GSI can be found at [www.gsi.de](http://www.gsi.de).

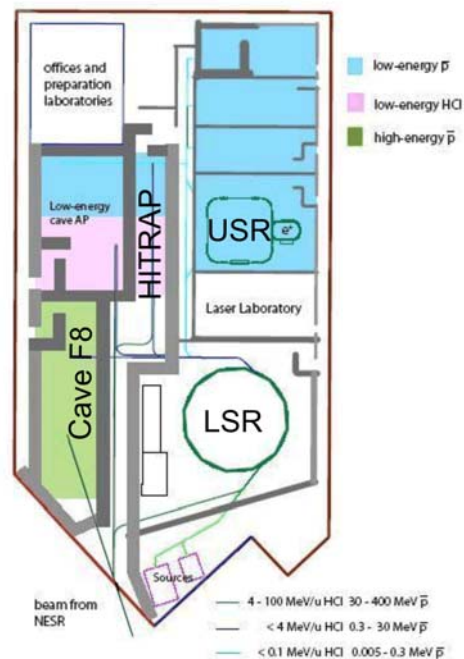
2. [www.gsi.de/fair/index.html](http://www.gsi.de/fair/index.html) displays more information about this facility, its features and the planned experiments.

## FLAIR

Within the FLAIR hall two storage rings and a universal trap facility will provide antiprotons in an energy range between 300 MeV and several eV, which make low energetic antiproton experiments possible like: precision measurements of properties of the antiproton as well as precision spectroscopy of anti-hydrogen. This is most relevant for tests of the CPT theorem and other fundamental symmetries and interactions.

In the following the devices of FLAIR will be described in detail: The facility consists of two storage rings – the low-energy storage ring (LSR) and the ultra-low energy storage ring (USR) – and a universal trap facility (HITRAP = Heavy Ion TRAP). Antiprotons coming from the NESR have an energy of 30 MeV. The LSR will be mainly used to decelerate the antiprotons down to 300 keV. However, with the LSR it is also possible to accelerate the antiprotons up to 90 MeV. After the extraction at the LSR the 300 keV antiprotons will further be decelerated in the USR down to an energy up to 20 keV. The ion trap facility HITRAP decelerates heavy highly-charged ions (coming from the NESR) and antiprotons (coming from the LSR) from 4 MeV/u down to cryogenic temperatures. Figure 2 shows a sketch of the planned FLAIR building.

Figure 2: Sketch of the FLAIR facility [3]



## German radiation protection ordinance

During beam time always a small fraction (~10%) of antiprotons hit beam components such as magnets, tubes or chambers. For antiproton experiments a total beam loss of 100% has to be assumed. These beam losses cause annihilation of the antiprotons and the production of high energetic particles like neutrons, gammas, etc.; thus beam losses cause ionising radiation.

In the German radiation protection ordinance dose limits are set which will affect the design of the FLAIR facility. One of the rules is that the dose to the public inside the premises must not exceed 1 mSv per year. If you want the area outside the experimental areas or accelerators freely accessible to the staff and assume 2 000 working hours, one gets to a dose rate of 0.5  $\mu$ Sv per hour. The GSI determines this dose rate as limit for the areas outside the experimental areas: Therefore the main task is to calculate the minimum required thickness of the concrete shielding to ensure a dose rate of less than 0.5  $\mu$ Sv per hour for all areas outside the shielding walls.

## Calculations

All simulations were performed using the Monte Carlo code FLUKA [4,5].<sup>3</sup> Importance weighting was applied for variance reduction. In the following the calculation for the LSR, USR, HITRAP and Cave F8 will be presented.

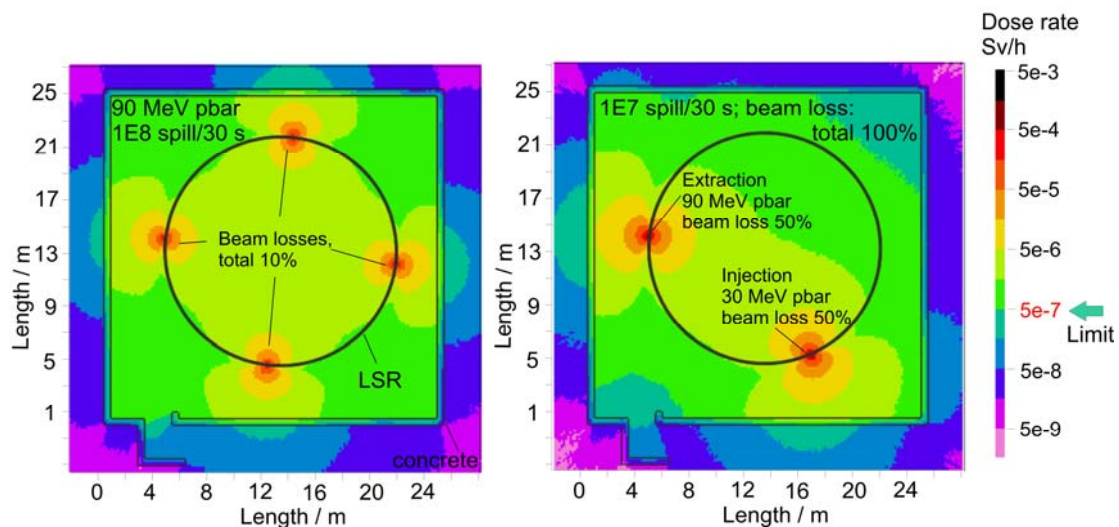
### LSR

To calculate the required thickness of the concrete shielding two calculations are performed according to two different scenarios: During normal operation only a small fraction (approximately 10%) of the beam will be lost homogeneously in the ring. However, for the setup and conditioning of the LSR a total loss of 100% of the beam must be assumed. The standard beam pipes in the LSR will be made from 2 mm thick steel. Taking into account the mass of all magnets (approximately 100 tonnes) an average thickness of 10 mm steel of the beam tube demonstrates the total amount of steel.

Figure 3 shows the two calculations according to a 10% beam loss, which is represented by four discrete positions, at a beam intensity of  $10^8$  particles per 30 seconds (Figure 3 left) and a 100% beam loss for a reduced beam intensity by a factor of 10. The calculation shows that a 50 cm thick concrete wall is needed to assure a dose rate below  $0.5 \mu\text{Sv/h}$  behind the shielding walls.

**Figure 3: Two Monte Carlo calculations of the LSR**

Left:  $10^8$  antiprotons per 30 seconds at 90 MeV. The total loss of 10% is represented by four positions. Right: The antiprotons have an energy of 30 MeV at the injection and 90 MeV at the extraction. The total beam loss is 100%. To keep the thickness of the concrete walls unchanged, the intensity has to be decreased by a factor of 10.



### USR

The USR shall provide antiprotons in the energy range between 20 keV and 300 keV for both in-ring experiments and effective injection into traps. To calculate the required thickness again one has to take into account the beam intensity, the beam energy and the thickness of the beam tube. Figure 4 shows the calculation according to 100% beam loss (worst case scenario). The thickness of the beam tube is assumed to 5 mm. The intensity is  $10^6$  per 20 seconds, which is on average  $5 \cdot 10^5$  antiprotons per second.

3. The latest FLUKA version is FLUKA 2005.6 (July '05). More information about this Monte Carlo program can be found under [www.fluka.org](http://www.fluka.org).

The thickness of the concrete walls has to be between 50 and 100 cm. The shielding walls for this cave are thicker than the one for the LSR cave. This is mainly due to the lower distance between the beam line of the storage ring to the shielding walls.

**Figure 4: Dose rate plot of the USR**

The antiprotons have an energy of 300 keV; the beam intensity is  $5 \times 10^5$  per second. The beam loss is 100%, which is represented by eight discrete positions.

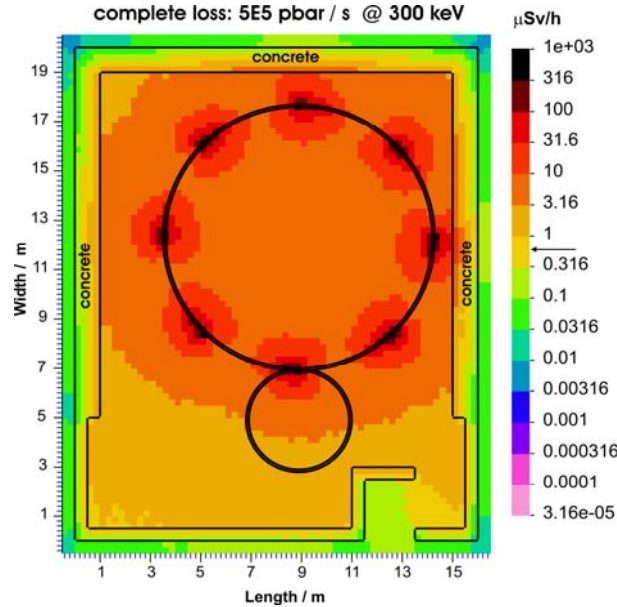
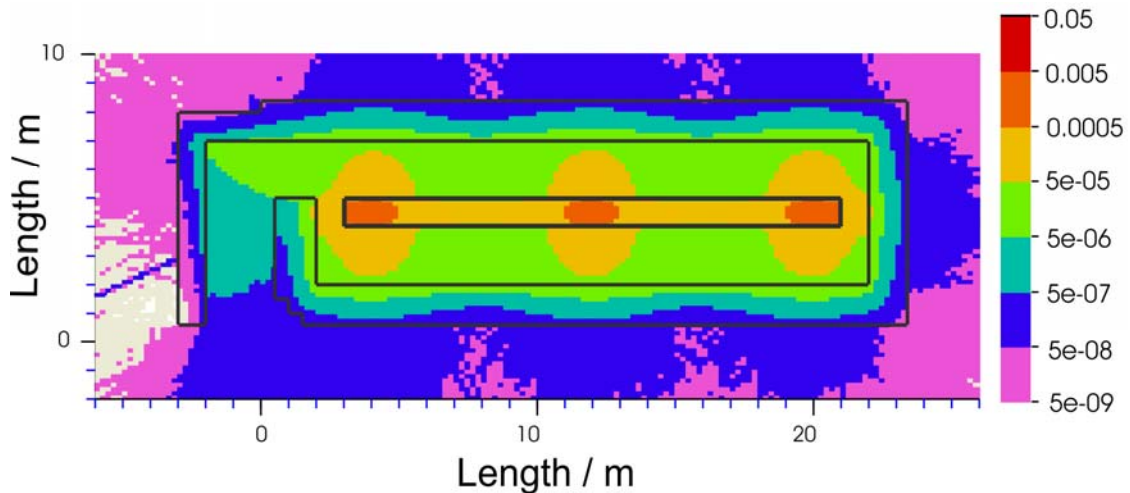


**Figure 5: Dose rate plot of HITRAP**

There is a 100% beam loss, which is represented by three discrete positions, at an intensity of  $10^8$  antiprotons per 50 seconds. The antiprotons have an energy of 4 MeV. The unit of the dose rate is Sv per hour.



**HITRAP**

The ion trap facility HITRAP will decelerate heavy highly-charged ions and antiprotons from 4 MeV/u down to cryogenic temperatures. The antiprotons coming from the LSR have a maximum energy of 4 MeV/u. The intensity of the beam is  $10^8$  per 50 seconds. Figure 5 shows a worst case scenario. The

beam loss of 100% is represented by three discrete positions. The calculation shows that a minimum thickness of 140 cm for the concrete shielding around the HITRAP facility is needed. For the maze entrance the concrete walls need a thickness of 100 cm.

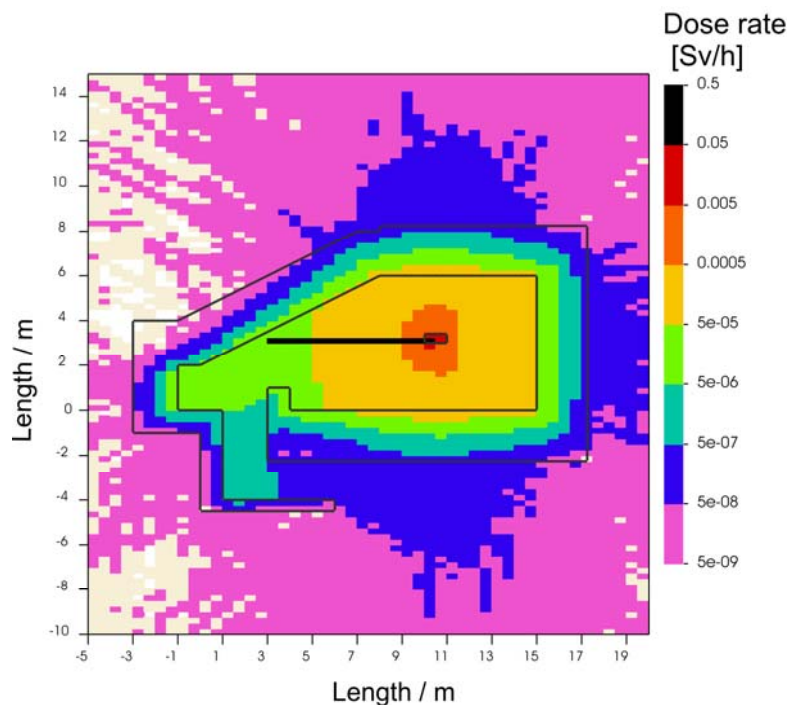
### Cave F8

Cave F8 is an experimental cave for further development of the tumour therapy operated with antiproton beams from the NESR. Scientists expect a better tumour therapy by using antiprotons, because antiprotons annihilate when stopped in material. The annihilation produces residual nuclear fragments of high charge and low energy, which deposit a large biological dose in the direct surrounding of the antiproton stopping distribution. Since the cooled low-emittance antiproton beams can be stopped in a well-defined region, the presumably large energy deposited locally makes them a suitable tool for tumour therapy. If this effect is confirmed, the method can be extended at FLAIR where the high energy antiproton beams (50-300 MeV) needed to penetrate deep enough into human tissue are available directly from the NESR [6].

Figure 6 shows a dose map of Cave F8 operated with antiprotons having an energy of 300 MeV with an intensity of  $10^7$ . For the calculation a phantom with the outside dimensions  $40 \times 40 \times 100 \text{ cm}^3$  is used. The beam loss is 100%. To maintain a large experimental area the maze is taken to the outside. Figure 6 shows that a thick concrete wall of 225 cm around the phantom is needed to maintain a dose rate of below  $0.5 \mu\text{Sv}$  per hour. However, the shielding walls of the maze entrance can be even thinner.

**Figure 6: Dose rate plot of Cave F8**

The antiprotons hit the target with an intensity of  $10^7$  per second with an energy of 300 MeV. There is a 100% beam loss in the target, which is a cuboid made of water with the dimensions of  $40 \times 40 \times 100 \text{ cm}^3$  acting as phantom.



### Conclusion

The Gesellschaft für Schwerionenforschung and the international co-operation partners plan the new accelerator facility of the next generation which is able to produce antiprotons with high intensities in a wide energy range. Connected to this Facility for Low-energy Antiproton and Ion Research (FLAIR) will deal with low energetic antiprotons.

The Monte Carlo code FLUKA was used to calculate the shielding design of the FLAIR building. Emphasis is put on the two storage rings LSR and USR, the universal trap facility HITRAP and the anti-proton tumour therapy Cave F8. Depending on the energies and the intensities of the antiproton beam different thickness (from 50 cm up to 225 cm) of the concrete shielding is needed for the different caves.

## References

- [1] C.P. Welsch, "FLAIR Project at GSI", *International Workshop on Beam Cooling and Related Topics*, COOL05, Galena, IL, USA (2005).
- [2] [www.gsi.de/fair/overview/accelerator/index.html](http://www.gsi.de/fair/overview/accelerator/index.html).
- [3] [www.oeaw.ac.at/smi/flair/](http://www.oeaw.ac.at/smi/flair/).
- [4] A. Fassò, A. Ferrari, J. Ranft, P.R. Sala, *FLUKA: A Multi-particle Transport Code*, CERN Yellow Report, INFN/TC\_05/11, SLAC-R-773 (2005) (in press).
- [5] A. Fassò, A. Ferrari, S. Roesler, P.R. Sala, G. Battistoni, F. Cerutti, E. Gadioli, M.V. Garzelli, F. Ballarini, A. Ottolenghi, A. Empl, J. Ranft, "The Physics Models of FLUKA: Status and Recent Developments", *Computing in High Energy and Nuclear Physics 2003 Conference (CHEP2003)*, La Jolla, CA, USA, 24-28 March, 2003, (paper MOMT005), eConf C0303241 (2003), arXiv:hep-ph/0306267.
- [6] E. Widmann, "FLAIR, a Facility for Low-energy Antiproton and Ion Research", *XLII Nuclear Physics Meeting*, Bormio (January 2004).



## Design of the EURISOL multi-MW target assembly: Radiation and safety issues

**Marta Felcini,<sup>1,4</sup> Adonai Herrera-Martínez,<sup>1</sup> Yacine Kadi,<sup>1</sup> Thomas Otto,<sup>2</sup> Luigi Tecchio<sup>3</sup>**

<sup>1</sup>CERN Accelerators and Beams Department, Geneva, Switzerland

<sup>2</sup>CERN Safety Commission, Geneva, Switzerland

<sup>3</sup>INFN Laboratori Nazionali di Legnaro, Legnaro Italy

<sup>4</sup>University of California Los Angeles, Physics Department, Los Angeles USA

### Abstract

The multi-MW target proposed for the EURISOL facility will be based on fission of uranium (or thorium) compounds to produce rare isotopes far from stability. A two-step process is used for the isotope production. First, neutrons are generated in a liquid mercury target, irradiated by the 1 GeV proton or deuteron beam, provided by the EURISOL linac driver. Then, the neutrons induce fission in a surrounding assembly of uranium carbide. R&D projects on several aspects of the target assembly are ongoing. Key criteria for the target design are a maximum beam power capability of 4 MW, a remote handling system with minimum downtime and maximum reliability, as well as radiation safety, minimisation of hazards and the classification of the facility. In the framework of the ongoing radiation characterisation and safety studies, radiation transport simulations have been performed to calculate the prompt radiation dose in the target and surrounding materials, as well as to determine shielding material and angle-dependent parameters. In this paper, we report the results of these studies and the proposed radiation shield design for the multi-MW target area. Furthermore, accurate estimates have been performed of the amount of fissile elements being produced in the uranium target assembly, for typical running conditions, in order to understand the implications for the classification of the facility. The results are reported and briefly discussed.

Project supported by EC under EURISOL DS Contract no. 515768 RIDS, [www.eurisol.org](http://www.eurisol.org).

## Introduction

The proposed European Isotope Separation On-Line (EURISOL) facility [1] is an ISOL-type next-generation Radioactive Ion Beam (RIB) facility which will provide RIB intensities two to three orders of magnitudes higher than in existing RIB facilities. The EURISOL physics programme will address fundamental questions related to nuclear structure and many-body interactions between hadrons, as well as the precision study of nuclear interactions, which determine element formation in stars and have important implications in the understanding of stellar and galaxy evolution. Furthermore, the availability of such a high-intensity radioactive ion source will open up new opportunities to test fundamental symmetries of the Standard Model at low energy, which are complementary to those performed with high-energy experiments. The possibility of producing a pure beam of electron neutrinos (or their antiparticles) through the beta-decay (beta beam) of radioactive ions circulating in a high-energy storage ring, for neutrino precision experiments, is also under study.

In the ISOL method, isotopes are produced by spallation or fission reactions in thick targets. This method is complementary to in-flight isotope production, used for instance in the FAIR project at GSI (Darmstadt, Germany). In the EURISOL Design Study (DS) [2], two baseline designs for isotope production targets are considered: a direct target and a fission target.

The direct target is the extension to higher beam power of existing ISOL targets at ISOLDE (CERN, Switzerland), ISAC (TRIUMF, Canada) or SPIRAL (GANIL, France). A proton beam deposits a power of up to 100 kW in the EURISOL direct target. There is a physical limitation to the maximum power rating of such a target, which is given by the capability to shed excess heat and to maintain a temperature in the target below the target limit for thermal disintegration.

A fission target coupled to a spallation neutron source is a way to overcome this power limit of the direct targets. This is the option considered for the multi-MW target assembly of the EURISOL facility. A multi-MW 1 GeV proton beam generates spallation neutrons in a liquid mercury target [3]. The neutrons in turn induce fission reactions in an actinide target assembly surrounding the spallation neutron source. The liquid mercury target can withstand and evacuate much higher beam power than a solid direct target. The isotope production efficiency (expressed as isotopes per unit beam power) of the fission target depends largely on the geometry of the spallation neutron source, the actinide target and the neutron-moderating or reflecting materials. Similar efficiencies as for direct targets can be achieved. The target material for the fission target is a low-density actinide-carbide, for example  $UC_x$  or  $ThC_x$ , where  $x$  lies between 3 and 4.

**Table 1: Dimensions and  $UC_x$  filling of the two ring-shaped fission targets placed around the spallation neutron source in a MMW fission following proposals by Tecchio, *et al.* [4]**

	Small target	Large target	Total
Length	20 cm		
Thickness	2.8 cm		
Inner radius	12.1 cm	19.1 cm	
Volume	4 750 cm <sup>3</sup>	7 213 cm <sup>3</sup>	11 963 cm <sup>3</sup>
$UC_x$ density, filling factor	3.0 gcm <sup>-3</sup> , 85%		
$UC_x$ mass	12.1 kg	18.4 kg	30.5 kg

In contrast to the direct actinide target, where the dominating reactions are spallation and fast fission with protons, isotope production in a fission target is dominated by neutron reactions: fission of  $^{238}U$  with fast neutrons, and of  $^{235}U$  with epithermal and thermal neutrons. A third neutron-induced reaction, neutron capture on  $^{238}U$ , leads to the breeding of fissile elements in the target, the most important being  $^{239}Pu$ . The multi-MW target assembly is described in Section 2.

R&D projects on several aspect of the target assembly are ongoing. Key criteria for the target design are a maximum beam power capability of 4 MW, remote handling system with minimum downtime and maximum reliability, as well as radiation safety, minimisation of hazards and the classification of the facility.

In the framework of the ongoing radiation characterisation and safety studies, detailed radiation transport simulations have been performed to calculate the prompt radiation dose in the target and surrounding materials, as well as determine shielding material selection and angle-dependent

parameters. We report in Section 3 the results of these studies and the proposed radiation shield design for the multi-MW target area. Furthermore, estimates have been performed of the amount of fissile elements being produced in the uranium target assembly for typical running conditions in order to understand the implications for the classification of the facility. These results are reported in Section 4 and briefly discussed.

**Figure 1: Isometric view of the fission target assembly**

A mercury target, serving as spallation neutron source (green), is surrounded by two ring-shaped target containers filled with uranium carbide, as fissile material (grey). Isotopes created in the fission targets move by diffusion through evacuated tubes (blue) the ion source(s). A graphite moderator (grey) is enclosing the spallation source plus fission target assembly. The whole target is mounted in a stainless steel vacuum vessel (light grey).

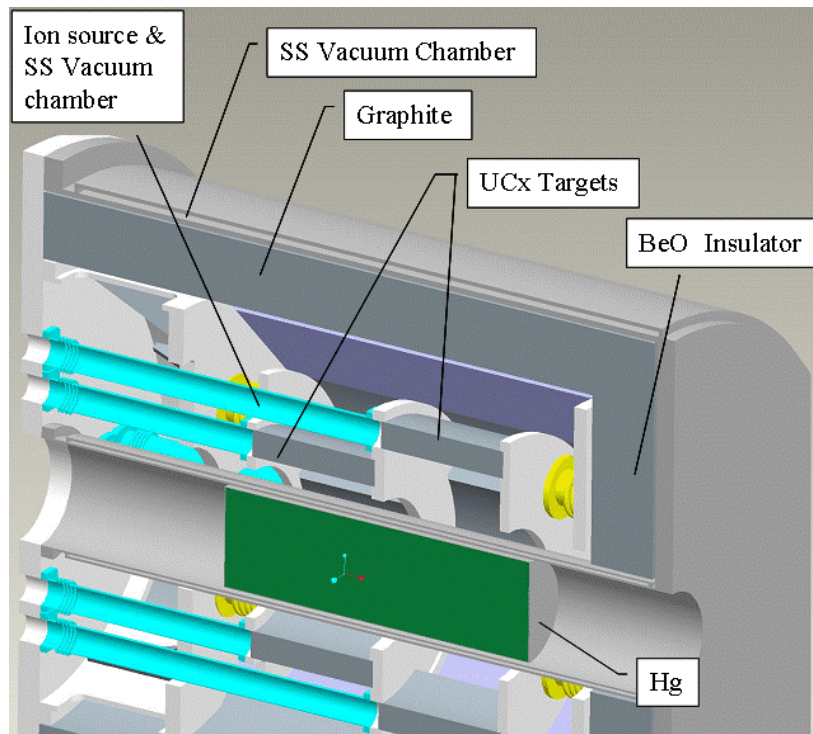
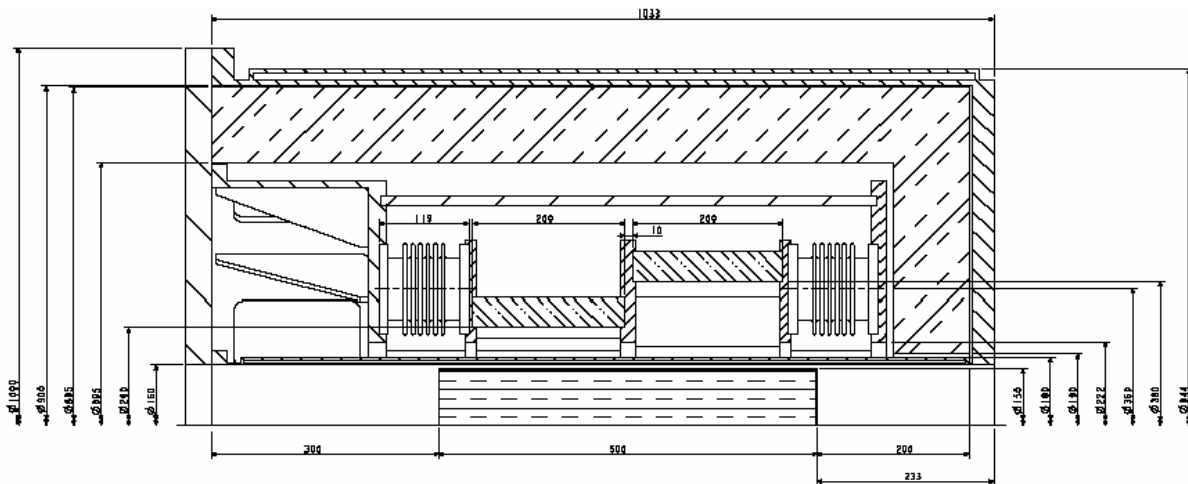


**Figure 2: Assembly drawing of the fission target assembly as proposed in [4]. Length and diameter of the assembly are approximately 100 cm each.**



## The multi-MW target assembly

### Geometry

The multi-MW target assembly consists of a spallation neutron source, converting the proton beam from the accelerator into neutrons, and a target in which a fissile isotope undergoes reactions with fast or with thermal neutrons, producing radioactive isotopes as fission products.

The present target design [3,4] is preliminary. However it is detailed enough to make meaningful radiation characterisation and safety studies and predictions on the production rates of (radioactive) isotopes within the target, including actinides.

The spallation neutron source is a 50 cm long, 16 cm diameter cylindrical steel vessel filled with mercury (Hg) [3]. Two ring-shaped tantalum containers with tungsten heat screens are placed around the cylindrical neutron source. The targets are filled with pellets made from uranium carbide (stoichiometric notation:  $UC_x$ , with  $x \approx 3$ ) with a density of  $3 \text{ g cm}^{-3}$ , occupying 85% of the volume [4]. Table 1 shows the dimensions and mass of the  $UC_x$  targets. Figure 1 is an isometric view of the target and Figure 2 an assembly drawing. The  $UC_x$  target containers are held in place with supports made from beryllium oxide (BeO). A 10 cm thick graphite moderator encloses the spallation source/fission target azimuthally and downstream, perpendicularly to the beam axis.

### Target material

The actinide target material to be used in the multi-MW fission target has not been decided yet. In current direct isotope production targets, depleted uranium is the most frequently used actinide. This material accounts for 50% of all targets used at ISOLDE (CERN). Depleted uranium is a by-product of nuclear fuel production. It contains 99.7%  $^{238}\text{U}$ , 0.3%  $^{235}\text{U}$  and a smaller amount of  $^{234}\text{U}$ . It is well suited for the production of direct targets where the fission reactions are caused mainly by fast protons and secondary particles (neutrons, pions). For the multi-MW fission target assembly, the choice of natural uranium (0.7% of  $^{235}\text{U}$ ) as target actinide would have advantages, because it would better exploit the epithermal and thermal neutrons emerging from the spallation source and from the moderator.

In a realistic setting, the fission target assembly will be embedded in massive radiation shielding. The shielding must be considered when estimating isotope production and fissile isotope breeding rates because it moderates and reflects neutrons from the spallation source, increasing the efficiency of isotope production per primary beam proton. In this paper, a cylindrical steel shielding has been assumed, as described in the next Section. Upstream of the target, the shielding is closed by an end cap, leaving only a narrow penetration for the proton beam line. Downstream of the target, a mobile shielding end cap has to be arranged, allowing retrieving the target assembly to a (shielded and confined) maintenance position.

### Simulation

The Monte Carlo (MC) radiation transport program FLUKA [5] is used to perform simulations of the dose rate fields in the multi-MW fission target assembly and the surrounding materials, as well as the calculation of isotope production. The main components of the fission target assembly and the shielding are described with the combinatorial geometry package of FLUKA. The isotope production rates are determined by the fluence spectra of secondary particles (neutrons, pions, protons) from the spallation source in the fission target material.

In the MC simulation, a Gaussian-profiled proton beam with  $\text{FWHM} = 3.54 \text{ cm}$  impinges on the centreline of the mercury target. The production of isotopes ("residual nuclei") is scored with the RESNUCLE card, employing models for interactions of nuclei with hadrons and tabulated cross-sections for interactions with neutrons with  $E_{\text{kin}} < 19.6 \text{ MeV}$ .

## Dose rates and shielding design for the multi-MW target station

One of the technological challenges of this multi-MW facility is the very intense radiation field created by the secondary particles produced in the target and the surrounding materials. This imposes stringent constraints on the construction, as well as on the operation and maintenance of the target and its

associated equipment. To ensure safe operation, the target station must be encapsulated in a thick shield to attenuate the radiation dose outside the shield to acceptable values. The shield around the target must be designed to satisfy a number of requirements. The shield must be sufficiently thick, but at the same time the amount of material used for the shield must be minimised, to reduce construction and disposal costs. The volume inside the shield around the target must also be minimised to facilitate evacuation of the target area and avoid air activation. At the same time, the small distance between the target and the shielding material implies that: i) the radiation level at the target area is increased by the back-scattered particles; ii) high power density is deposited in the inner shield layer, requiring shield cooling; iii) the inner shield layer will be highly activated. With these constraints in mind, the shielding materials, thickness and shape must be optimally chosen.

We propose to use a two-component shield, made of an inner layer from steel and an outer layer from concrete.

The purpose of the prompt radiation shield is to reduce the radiation dose outside the shield to values below the operational dose rate limits defined by the legislation. They are different in different countries. Since we do not know in which country the EURISOL facility will be sited, we have chosen the limit of 1  $\mu\text{Sv/h}$ , as a typically permissible dose rate in supervised radiation areas. Thus, our objective is to design a prompt radiation shield for the multi-MW fission target, in the configuration as described in the previous Section, exposed to 1 GeV 4 MW proton beam, such that the dose rate at the outer surface of the shield is inferior to 1  $\mu\text{Sv/h}$ .

For the purpose of shield design, given the beam power and energy, the prompt radiation dose rate  $H$  can be approximated by the point source, line-of-sight attenuation formula:

$$H(\theta, d, R) = H_0(\theta) \exp\{-\sum_i d_i / \lambda_i(\theta)\} / R^2 \quad (1)$$

where  $\theta$  and  $R$  are the co-ordinates (azimuthal angle and distance) of the point where the dose rate is measured and  $d = \sum_i d_i$  is the total distance traversed by the radiation in different successive shielding materials.  $H_0(\theta)$  is the source term, depending upon the azimuthal angle  $\theta$ . It gives the dose rate at a unit distance from the source before any shielding material and it depends on the source intensity and geometry. Once the source term and the attenuation lengths  $\lambda_i$  in the different shielding materials are known, it is possible to determine, as a function of  $\theta$ , the shield thickness  $d_i$  of the different materials, needed to attenuate the radiation dose by the desired factor. It is useful to remind that the attenuation length in a given material depends upon the composition in terms of particle types (protons, neutrons, pions, etc.) of the radiation field.

Our strategy [6] to design the radiation shield for the multi-MW target is the following. We use the FLUKA MC code to simulate the particle transport through the target and shielding materials and calculate the dose rate spatial distribution  $H(\theta, R)$ , in a reference shield geometry. Then we fit the parameters  $H_0(\theta)$  and  $\lambda_i(\theta)$  for subsequent determination of the angular-dependent extension  $t_i(\theta)$  of the shielding shells, making use of Eq. (1).

The shield reference configuration is a two-component layered steel and concrete cylindrical monolith, completely encapsulating the target. It is composed of an inner steel cylinder of 2 m constant thickness, of 60 cm inner radius, closed at the two ends by 2 m thick end-caps, sited at about 20 cm distance from the target ends. The steel layer is followed by a 2 m thick concrete layer, also cylindrical in shape, closed by 2 m thick end-caps. The chosen thickness values are sufficiently large to allow establishing particle equilibrium, after which the radiation field composition, in terms of particle types, stays unchanged with the penetrated material depth. Consequently, a reliable determination of the source term and attenuation length values can be performed.

The isodose contours, as a function of the longitudinal co-ordinate  $z$  and the radial co-ordinate  $r$  (cylindrical symmetry is assumed in the simulation) are shown in the upper panel of Figure 3. The target and shield geometry as used in the simulation are superimposed to the dose contours. The subdivision of the steel shield in 20 layers and of the concrete shield in 10 layers indicates the regions where suitable MC biasing factors have been applied, to achieve adequate particle statistics at all depths in the shielding materials. After conversion from cylindrical  $(r, z)$  to spherical co-ordinates [ $R = (r^2 + z^2)^{1/2}$ ,  $\theta = \arccos(z/R)$ ] dose rates as a function of  $R$  for two different values of  $\theta$ , in the beam direction ( $\theta = 0^\circ$ ) and perpendicular to the beam direction ( $\theta = 90^\circ$ ) are shown in the lower panels of Figure 3. In the two cases, the contributions to the dose rate from the different particle types are also shown.

The dose rate values are then plotted as a function of the radiation depth  $d$  in the shielding material ( $d(\theta) = R - g(\theta)$ ,  $g(\theta)$  being the distance of the shield inner edge from the co-ordinate origin), in different  $\theta$  bins of 4 degree widths, going from 0 (beam direction) to 180° (beam opposite direction). Then, these curves are fitted using an exponential function  $\exp(a + bd)$  and the values of the source term and attenuation length derived from the fitted values [ $H_0 = \exp(a)$ ,  $\lambda = -1/b$ ]. As an example the attenuation curves in steel for  $\theta$  values between 0° and 90° are shown in the upper panel of Figure 4. The fitted values of  $H_0$  and  $\lambda$  in steel as a function of  $\theta$  are given in the lower panel of Figure 4. The larger values of the source term  $H_0$  in the backward direction ( $\theta > 90^\circ$ ) may seem unnatural, as one would expect lower dose values in the backward direction. This is indeed the case, as lower  $\lambda$  values in the backward direction compensate the higher  $H_0$  values. In the fit, we have chosen deliberately to minimise the uncertainties on the  $\lambda$  parameters, while allowing relatively bigger uncertainties on the  $H_0$  parameters [6]. In this way, as  $\lambda$  enters exponentially, while  $H_0$  enters linearly in Eq. (1), we minimise the uncertainty on the calculated  $H(\theta, d, R)$  values induced by the uncertainties on the  $H_0$  and  $\lambda$  fitted values.

The  $\lambda$  values have also been determined in the concrete shield and used, together with the fitted  $H_0$  and  $\lambda$  parameter values in steel, to evaluate the thickness of steel and concrete, as a function of  $\theta$ , such that the dose rate at the outer surface of the shield is inferior to 1  $\mu\text{Sv/h}$ . The result is shown in Figure 5. The needed concrete thickness  $t_{\text{conc}}$  is given as a function of  $\theta$  for different values of the steel thickness  $t_{\text{steel}}$ . Here  $t_{\text{steel}}$  is defined as the thickness of the steel cylinder, along the axis and of the end caps, encapsulating the target. The inner dimensions of the steel cylinder are the same as described above, for the reference shield geometry.

Given the cost of steel, about a factor of 25 more expensive than concrete, we propose to use 1 m thick steel cylinder followed by a concrete shield of variable thickness as a function of  $\theta$ , as indicated in Figure 5 for  $t_{\text{steel}} = 1$  m. For  $\theta = 0, 90$  and  $180^\circ$  a concrete thickness values of about 900, 850 and 650 cm, respectively, are needed after 1 m thick steel shield cylinder, to reduce the dose rate to 1  $\mu\text{Sv/h}$ .

### Breeding of fissile material in the multi-MW target

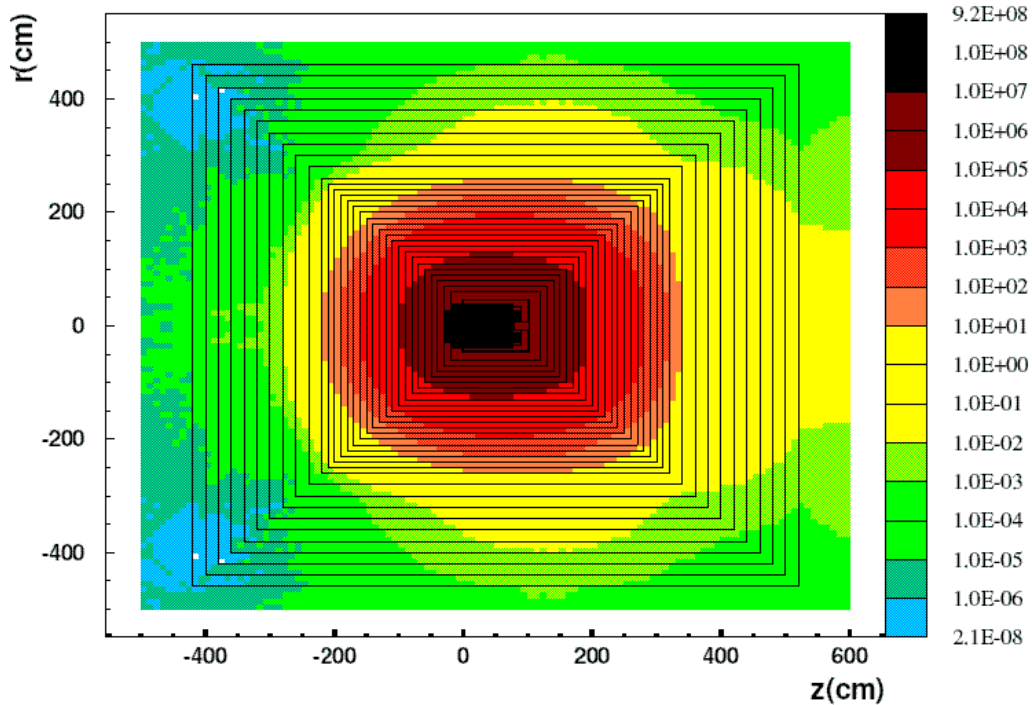
Fissile isotope breeding in five different fission target designs has been studied [7]. Their characteristics are described in the second column of Table 2. The standard ISOLDE UCx target has been added as an example for direct targets. The designs U0 and Th0, in absence of shielding, although unrealistic, allow drawing conclusions on the relative merits of different actinide materials for isotope production and breeding of fissile elements. Comparison between the designs U0 and U1 will reveal the influence of the shielding. The designs U1, U2 and U3 can be considered as realistic, keeping in mind that the different  $^{235}\text{U}$  content will have effects on isotope production (as shown in the fifth column of Table 2).

The method used for the calculation is described in detail in [7]. The results in terms of estimates of fissile isotope production are reported in the last two columns of Table 2.

The studied fission target assemblies show approximately the same efficiency (see column 5 of Table 2) as a standard ISOLDE UCx target in the production per incident proton of spallation and fission elements lighter than the target material. Reducing the size of the fission target would reduce this efficiency. As it can be seen in Table 2, one isotope alone,  $^{239}\text{U}$ , is produced more copiously than all others taken together, in the case of a UC<sub>x</sub> target. Essentially all of it will decay into  $^{239}\text{Pu}$ . In direct targets (e.g. the ISOLDE target), breeding of heavier isotopes is practically absent because only few low-energy neutrons are available for its production. The presence of the shielding, in the configuration described in the previous sections, increases the production of  $^{239}\text{U}$  (and thus  $^{239}\text{Pu}$ ) by 70%. This figure may vary depending on the exact arrangement of shielding. The higher  $^{235}\text{U}$  content enhances the production of fission products due to a better exploitation of epithermal and thermal neutrons; however it does not influence the neutron spectrum and capture rate and thus breeding of  $^{239}\text{U}/^{239}\text{Pu}$ .

In the Th-based fission target, slightly more fissile isotopes are bred than in the U-based target, for slightly less fission products.  $^{233}\text{U}$  presents the similar risks for radiation protection and the same issues for nuclear security as  $^{239}\text{Pu}$ . In this respect there is no advantage in considering Th as base material for fission targets. The comparison with a standard ISOLDE target, as an example for a direct target, also shows that the production of fissile elements, as compared to that of lighter isotopes, is highly reduced in the direct target with respect to the fission target assembly.

Figure 3: (Top) Isodose rate curves as function of r and z (cylindrical co-ordinates used for the simulation). Dose rate values, in Sv/h, are given here and in the following figures for 4 MW 1 GeV proton beam impinging on the target.



(Bottom) Dose rate as a function of  $R = (r^2 + z^2)^{1/2}$  for two different values of  $\theta$ , in the beam direction ( $\theta = 0$  degrees) and perpendicular to the beam direction ( $\theta = 90$  degrees). In the two cases, the contributions to the dose rate from the different particle types are also shown.

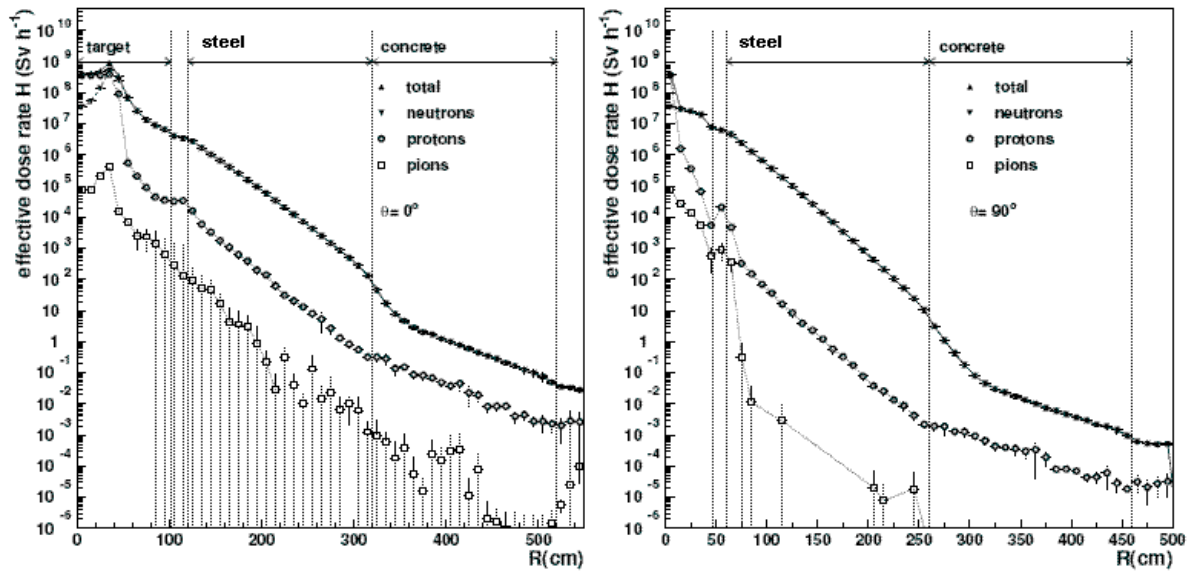


**Figure 4: (Left) Effective dose attenuation curves in steel, as a function of steel depth, for different  $\theta$  values. (Right) The values of  $H_0$  and  $\lambda$ , obtained from the fit of the attenuation curves, are shown as a function of  $\theta$ .**

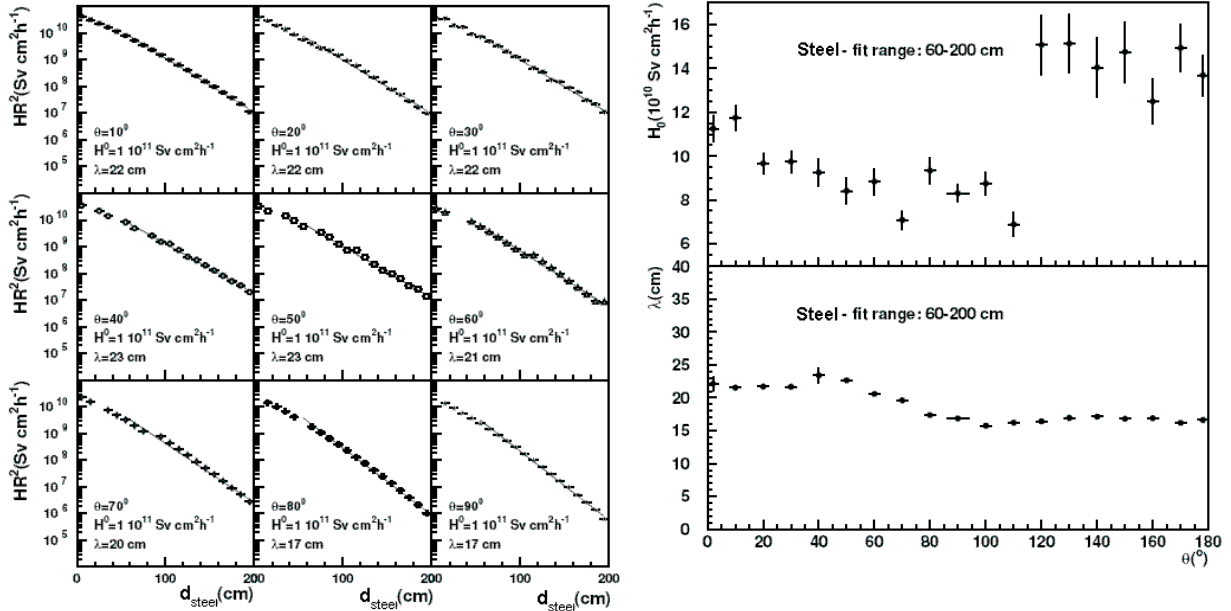


**Figure 5: Concrete shield thickness, as a function of the azimuthal angle  $\theta$ , needed to attenuate the effective dose rate to  $10^{-6}$  Sv/h at the outer shield surface**

The curves are given for six different values of the inner steel cylinder thickness  $t_{steel}$  (see text). The upper curve is for  $t_{steel} = 100$  cm while the lower curve is for  $t_{steel} = 300$  cm, with the intermediate curves given for intermediate  $t_{steel}$  values in the order shown in the subtitle. The points are the result of the dose rate calculation, Eq. (1), using the source term and attenuation length values, obtained from the fit of the simulation data as explained in the text. The curves are the results of a polynomial fit to the points and their uncertainties.

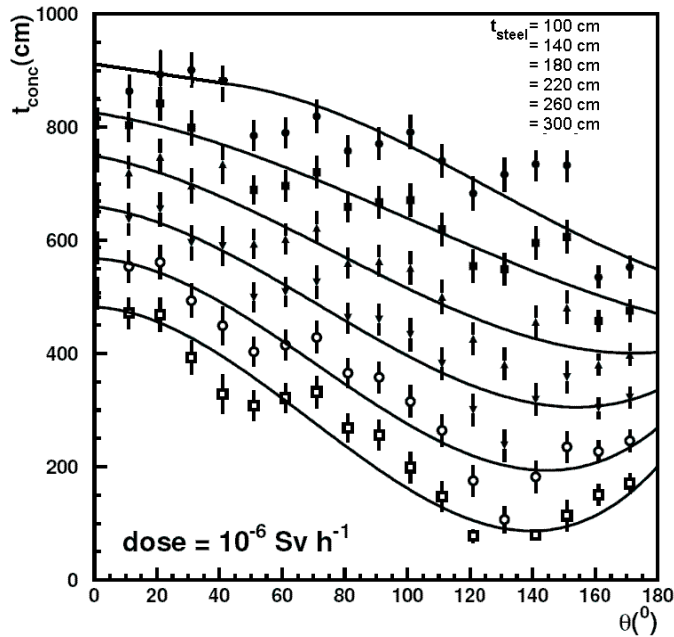


**Table 2: Estimate of fissile isotope production in a UC<sub>3</sub> (ThC<sub>3</sub>) target, for five different configurations [7]**

Columns 2, 3 and 4 show the characteristics and shielding conditions used for the calculation (see text). Column 5 gives the production per proton of isotopes lighter than <sup>239</sup>U. Columns 6 and 7 give the production of <sup>239</sup>U (<sup>233</sup>Th for Type Th0) per proton and the implied production of <sup>239</sup>Pu (<sup>233</sup>U for Type Th0) during 3 000 hours with a 4 MW proton beam. Isotope production in an ISOLDE-UC<sub>x</sub> target is added for comparison.

Target type	Common characteristics	Actinide used for target	Steel shielding	Light (A< <sup>239</sup> ) isotopes per proton	<sup>239</sup> U* per proton	<sup>239</sup> Pu* for 4 MW power 3 000 h running time	
				Atoms	Atoms	Atoms	Mass(g)
U0	Target material UC <sub>3</sub> (ThC <sub>3</sub> ), Target mass 30.5 kg, 10 cm C moderator	<sup>238</sup> U	No	0.31	0.407	1.09 10 <sup>23</sup>	43.4
Th0		<sup>232</sup> Th	No	0.21	0.427	1.15 10 <sup>23</sup>	45.6
U1		<sup>238</sup> U	Yes	0.32	0.68	1.83 10 <sup>23</sup>	72.5
U2		<sup>nat</sup> U (0.7% <sup>235</sup> U)	Yes	0.47			
U3		<sup>dep</sup> U (0.3% <sup>235</sup> U)	Yes	0.44			
ISOLDE	Target material UC <sub>3</sub> , dir. irradiation by E = 1.4 GeV proton beam	<sup>dep</sup> U (0.3% <sup>235</sup> U)	No	0.33	9.6 10 <sup>-4</sup>	–	–

\* <sup>233</sup>Th/<sup>233</sup>U for Type Th0.

In multi-MW target assemblies for isotope production based on uranium carbide, the isotope <sup>239</sup>U is produced by neutron capture on <sup>238</sup>U more abundantly than all other isotopes taken together. Practically all of the <sup>239</sup>U will decay into <sup>239</sup>Pu, the burn-up of this isotope in the target being very low. Similar conclusions apply to targets based on thorium carbide for the production of the fissile isotope <sup>233</sup>U. In a realistic target design, including the effects of radiation shielding on the neutron fluence, more than 70 g of <sup>239</sup>Pu would be produced per year, irrespective of the presence of <sup>235</sup>U in the target material. Rules for safeguarding fissile materials under the international nuclear Non-proliferation Treaty (NPT) will have to be applied to the EURISOL multi-MW targets.

## Summary

The EURISOL facility will provide RIBs with intensities two to three orders of magnitudes higher than in present facilities, opening up unprecedented opportunities for investigations and discoveries in nuclear physics, astrophysics and particle physics.

This paper focuses on the EURISOL multi-MW target, designed for the production of rare isotopes far from stability. The proposed design makes use of a liquid mercury target, directly irradiated by a multi-MW proton beam, for the production of an intense neutron flux. The neutrons in turn irradiate a surrounding assembly of uranium carbide targets in which isotopes are produced by neutron-induced fission reactions. A detailed layout of the multi-MW target assembly has been proposed and its key features are being studied.

Prompt radiation dose calculations in the target and the surrounding materials have been performed, the radiation attenuation through materials has been analysed and its angular dependence parameterised. It has been shown that with a 1 m thick steel monolith encapsulating the target, followed by 7 m (up-stream of the target) to 9 m (down-stream of the target) thick concrete shield, the radiation dose outside the shield can be kept below the limit of 1 µSv/h, as permissible dose rate in supervised radiation areas.

In terms of nuclear safety, the quantities of hazardous isotopes were calculated, showing no particular advantage in using Th as fissile material rather than U, due to the breeding of <sup>233</sup>U, as problematic for proliferation as <sup>239</sup>Pu. Moreover, Th targets present lower RIB production rates than U targets, for the same beam power and energy. These results are an essential input in the finalisation of the target design and in the process leading to the classification of the facility.

## References

- [1] The EURISOL Collaboration, *The EURISOL Report – A Feasibility Study for a European Isotope Separation On-line Radioactive Ion Beam Facility*, European Commission Contract No. HPRI-CT-1999-50001, December 2003, [www.ganil.fr/eurisol/Final\\_Report.html](http://www.ganil.fr/eurisol/Final_Report.html).
- [2] EURISOL Design Study, [www.eurisol.org/site01/index.php](http://www.eurisol.org/site01/index.php).
- [3] A. Herrera-Martinez, Y. Kadi, *EURISOL-DS Multi-MW Target Preliminary Study of the Liquid Metal Proton-to-neutron Converter*, CERN-AB-Note-2006-013 (2006); *Neutronic Calculations for the Baseline Configuration of the Multi-MW Mercury Target*, EURISOL DS/TASK2/TN-05-03 (2005).
- [4] L. Tecchio, *et al.*, EURISOL DS WP4, forthcoming.
- [5] A. Fassò, A. Ferrari, J. Ranft, P.R. Sala, *FLUKA: A Multi-particle Transport Code*, CERN-2005-10 (2005), INFN/TC\_05/11, SLAC-R-773 FLUKA (and references therein).
- [6] M. Felcini, *Optimised Radiation Shield Design for the EURISOL Multi-MW Target Station*, CERN-AB-Note-2006-015 (2006).
- [7] Th. Otto, *Breeding of Fissile Isotopes in EURISOL Multi-megawatt Targets*, Report CERN-SC-2006-020-RP-IR (2006).

## Overview of the protection and shielding studies for the betatron cleaning insertion at LHC

**V. Vlachoudis, A. Ferrari, M. Magistris, M. Santana-Leitner**  
CERN, European Organisation for Nuclear Research, Switzerland

### Abstract

*The 350 MJ of stored beam energy at LHC and the small spot size at 7 TeV/c poses strict requirements for the collimation system. Two insertions (IR3, IR7) are dedicated to beam cleaning with the design goals of absorbing part of the primary beam halo and of the secondary radiation. The tertiary halo which escapes the betatron cleaning insertion in IR7 may heat the cold magnets at unacceptable levels, if no additional absorber is used. Moreover, the transverse energy and intensity carried by the beam lays three orders of magnitude above the values of current facilities thereby requiring careful calculations of the heat deposition in the collimators and in other fragile units. The present paper provides an overview of the intensive study by means of FLUKA simulation to shield and protect all sensitive equipment against overheating and radiation damage in the harsh environment of IR7 during normal collimation and for various accident scenarios*

## Introduction

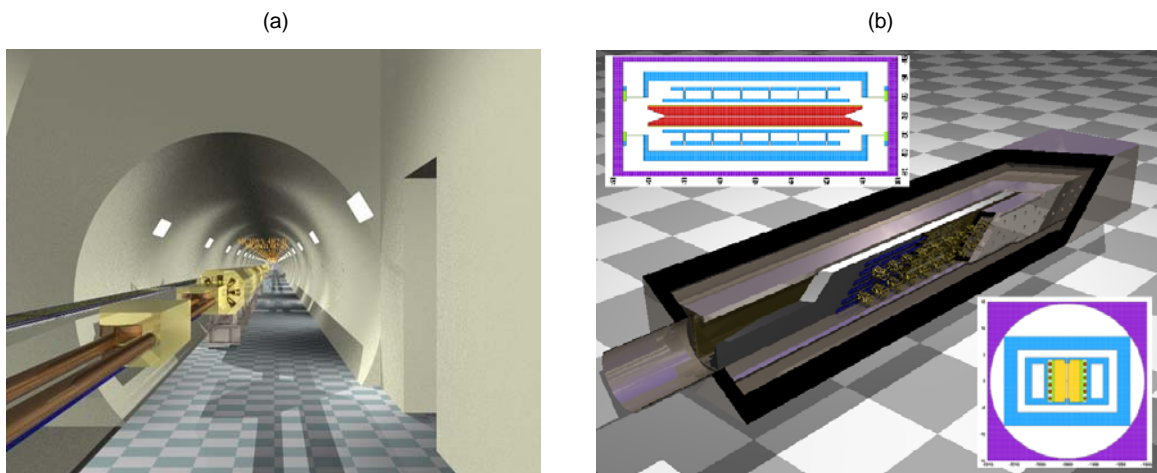
For nominal performance at LHC, each of the two rings will store 2808 bunches of  $1.1 \times 10^{11}$  protons at 7 TeV each, the total stored energy in both beams amounts to 350 MJ. This high beam power must be handled in a super-conducting environment, severely constraining the fraction of the beam that can be lost in a cold magnet. Even a tiny fraction  $\sim 5 \text{ mW/cm}^3$ , equivalent to  $1/10^9$  of the total beam power, is sufficient to quench a magnet if it is deposited in its cold parts [1]. Given that beam losses cannot be completely avoided, the high loss rates of protons associated to the intense LHC beams require a powerful collimation system, designed to restrict the mechanical aperture in the machine and to clean the primary halo and the secondary radiation. A set of active and passive absorbers is used to reduce down to acceptable levels the tertiary halo which escapes the collimation systems, so that quenches of magnets are avoided. The present paper gives an overview of the challenging and broad simulation work, performed in the last years to protect and shield those sensitive equipments. The intranuclear cascade code FLUKA [2,3] was used for the simulation, with the help of many of user written routines, and processing scripts.

## Simulation set-up description

The survey required to model a long section of the LHC tunnel, 1.5 km in total including the straight section and part of the two arcs upstream and downstream of the straight section [Figure 1(a)] [4,5]. There are over 250 beam objects, namely: primary and secondary collimators, passive and active absorbers, warm and cold dipoles, bending magnets, quadrupoles, sextupoles, orbit correctors and various beam instrumentation. The position, orientation, material assignment and magnetic field strength characterising of each object is determined by the optics of the beam. Due to the complexity involved in modelling such geometry, it was decided to follow a modular approach by means of user-written programs.

**Figure 1: Photo realistic views created with the PovRay ray-tracing program as modelled in FLUKA**

(a) Inner view of part of the IR7 insertion, where part of the straight section is visible together with the corrector dipoles (MCBC) and warm quadrupoles (MQW). (b) Section of a secondary collimator (TCS). Light effects and colours have been added with PovRay.



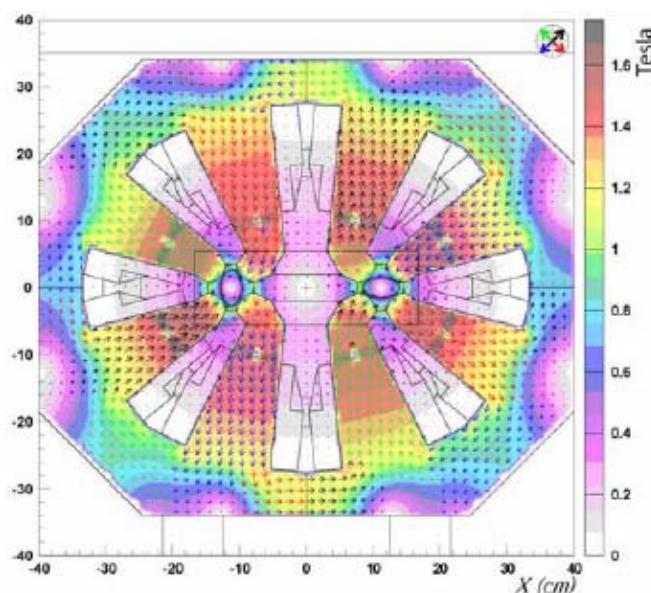
A prototype of each object listed above was modelled with full details and stored in a “parking” area next to the tunnel for later mapping via the LATTICE card of FLUKA. The transformation of each object was performed by allocating a bounding body in the input file for the replicated item in the geometry, and then an automatically generated lattic.f Fortran routine has made the conversion of the lattice co-ordinates to the prototype reference system, located in the parking area.

There are two kinds of collimators, primary (TCP) and secondary (TCS). The primary collimators (TCP) have 100 cm long graphite jaws where the central 60 cm stick out slightly to intercept the beam halo at 6 sigma (the value of  $\sigma$  depends on the beta function of the beam), plus an additional tapering

of 10 cm at both sides. The secondary collimators (TCS) [Figure 1(b)] have 100 cm long graphite jaws entirely sitting at 7 sigma, plus the 10 cm of tapering on both sides. The choice of materials for the collimators of the LHC was limited to low Z-materials, like graphite or beryllium [4,6,7]. This choice is not motivated by the normal operational scenarios but rather by accidental rapid impacts of beams, either at injection or, more severely, during a coast at 7 TeV. For accidents at 7 TeV neither beryllium nor graphite will melt locally, but cracks and permanent deformations of the collimator side face are to be expected.

The tilt of the jaws follows the beam divergence at the location of the collimator. Several ideas have been studied to address the problem of the variable location of the collimator jaws, position and tilt. Finally it was decided to change at runtime the position and orientation of the collimator jaws planes. This was performed inside the `lattice.f` routine for every single step when a particle entered a new collimator lattice. The beam lines including the surrounding tunnel for the dispersion suppressors and all the elements were automatically generated, by the `Rexx` [8] script, using the latest beam optics [9].

**Figure 2: Cross-section of geometry and magnetic field map of a warm quadrupole (MQW)**



Each LHC magnet has its own magnetic field mapping that is defined in various ways, *i.e.* analytic form and 2-D interpolation grid including possible symmetries (Figure 2). Therefore, a special file format was created to allow a common and more flexible description of all cases. The format describes a field through 2-D linear interpolation, or else by using the analytic form of the field (for constant fields and perfect quadrupoles), or both, including symmetries and co-ordinate transformation. For example the field of the quadrupoles was described inside the vacuum pipes using the analytic form, while outside it was linearly interpolated from a 2-D grid. The intensity or the gradient of each magnetic field as well the rotation and positioning in the ARC were dynamically assigned by the generating `Rexx` script for each element to ensure the correct optics and beta functions of the beam.

For such a cumbersome setup there is no unique biasing scheme. The applied technique was to adjust the importance of the regions, and to enable Russian roulette splitting of secondary particles produced in a collision, inversely proportional to their average distance from each of the two beam lines. However, for every simulation run, a dedicated biasing scheme was additionally introduced for the regions of interest.

The map of the primary inelastic collisions, *i.e.* the position where the particles are lost on the collimators, was calculated using a multi-turn cleaning process simulated initially by the `COLLTRACK V5.4` [10] code and recently by the `SixTrack` [11] program. The tracking program has recorded into a file all inelastic and diffractive scattering interactions parameters, position and direction of the lost proton. The individual cascade starts by forcing the `FLUKA` code to create an inelastic nuclear interaction of a

proton inside the collimators jaws at the position given by the tracking program reading randomly the co-ordinate and the direction of the lost protons. Several scenarios have been used for different machine operating conditions, the most critical ones being:

1. For nominal running, a transient period of up to 10 s is accepted with a peak loss rate of  $4 \times 10^{11}$  p/beam/s lost for the 0.2 h beam life time scenario [12], corresponding to 450 kW of power vanished in the cleaning insertions.
2. A total yearly average loss rate, estimated to be  $4.1 \times 10^{16}$  p/yr during the operation of the LHC.
3. Due to a spontaneous rise of one of the extraction kicker modules during the coast, part of the 7 TeV/c beam (six bunches of  $1.1 \times 10^{11}$  p) is spread across the front of a collimator jaw.
4. Faulty kick by the injection kicker, where a full batch of protons hit the front of a collimator jaw at 450 GeV/c.

Since the betatron cleaning (IR7) is far away from the high luminosity interaction points, no other source of particle losses were taken into account.

### Protection of the super-conducting elements

The betatron cleaning insertion is the “hottest” region in the LHC ring, where almost all of the beam cleaning will take place there. Therefore the radiation levels expected in IR7 during operation are very high. Some of the cold magnets will not survive unless adequately protected from radiation generated on the primary and secondary collimators located 300 m upstream. Special equipments (the so-called active absorbers) are thus needed to prevent secondary particles from reaching the superconducting coils. The absorbers are very similar to the secondary collimators (TCS) having copper jaws with an inset of tungsten [13] with an aperture at  $10 \sigma$ . Due to the lower radiation environment in the arc a higher Z material could be used. copper and tungsten were chosen because of their high density and good thermal properties. Like with the collimators, absorbers can have any orientation in space and jaw tilt. The possible locations where absorbers could be installed were limited by the space availability and by cleaning constraints. On the one hand, the longer is the distance from the magnet to be shielded the lower is the influence of the absorber on the magnet. On the other hand, if the absorber is too close to the magnet, the cascade generated in the absorber may reach and quench the magnet. A large set of simulations were needed in order to optimise the use of absorbers.

The initially large number of possible combinations (three loss scenarios, two absorber orientations, two beams, four locations and different length of the primary collimators) was reduced by general considerations after a first set of simulations. Despite all the assumed simplifications, a very large number of simulations were needed to obtain good accuracy. The reason is that the probability of having a particle interacting in a coil 300 m downstream of the collimators is utterly small, because the presence of absorbers reduces the initial radiation levels in the cold aperture by 2 orders of magnitude. Biasing techniques and high energy thresholds in elements in the warm section allowed reducing the CPU time per history from 120 seconds to 2-3 seconds.

The first quadrupole (MQTL) is the most sensitive element because of its location, relatively close to the collimators. After a long and detailed investigation of the various scenarios, the conclusion was that three absorbers per beam can safely keep the energy deposition in the first MQTL below the quenching limit of 5 mW/cm<sup>3</sup>. Figure 3 shows the reduction of the radiation level in the dispersion suppressor downstream of the last absorber, for various absorber set-ups. Configurations with only two absorbers cannot grant sufficient protection.

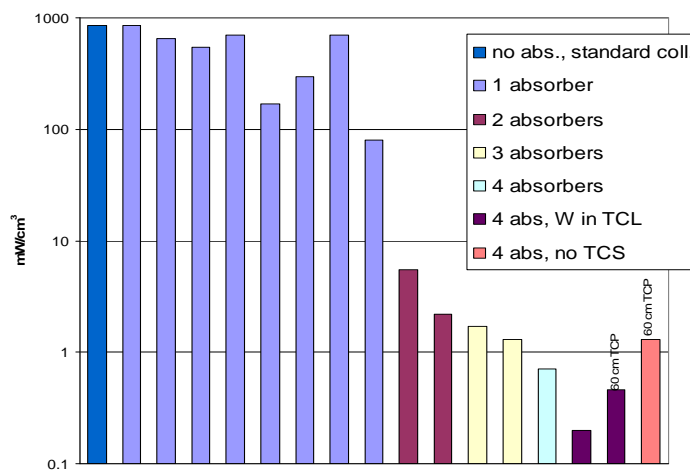
### Protection of the warm elements

Another critical part of the work was focused on the shielding of the warm objects close to the primary collimators. Although these units they do not operate in a superconducting regime nor do they contain delicate electronic equipment, they still cannot stand whatever level of radiation. Among them there is the epoxy used in the insulator blocks or in the coils of the magnets, the pipes whose wrapping film must ensure the heating during out-gassing, the flanges, where asymmetric irradiations can cause pressure in-leaks, or the collimators, whose jaws must remain flat to function properly. The addition

of passive absorbers and the use of appropriate materials shall guarantee a correct operation of all items. Passive absorbers (TCLPA) are shielding devices that are mounted around the vacuum pipe, with a fix aperture in contrast with the active absorbers that have movable jaws.

**Figure 3: Maximum power density in the superconducting coils of the MQTL, for various active absorbers scenarios**

It is visible that to reduce the power density below the quench limit of  $5 \text{ mW/cm}^3$  at least three absorbers are needed



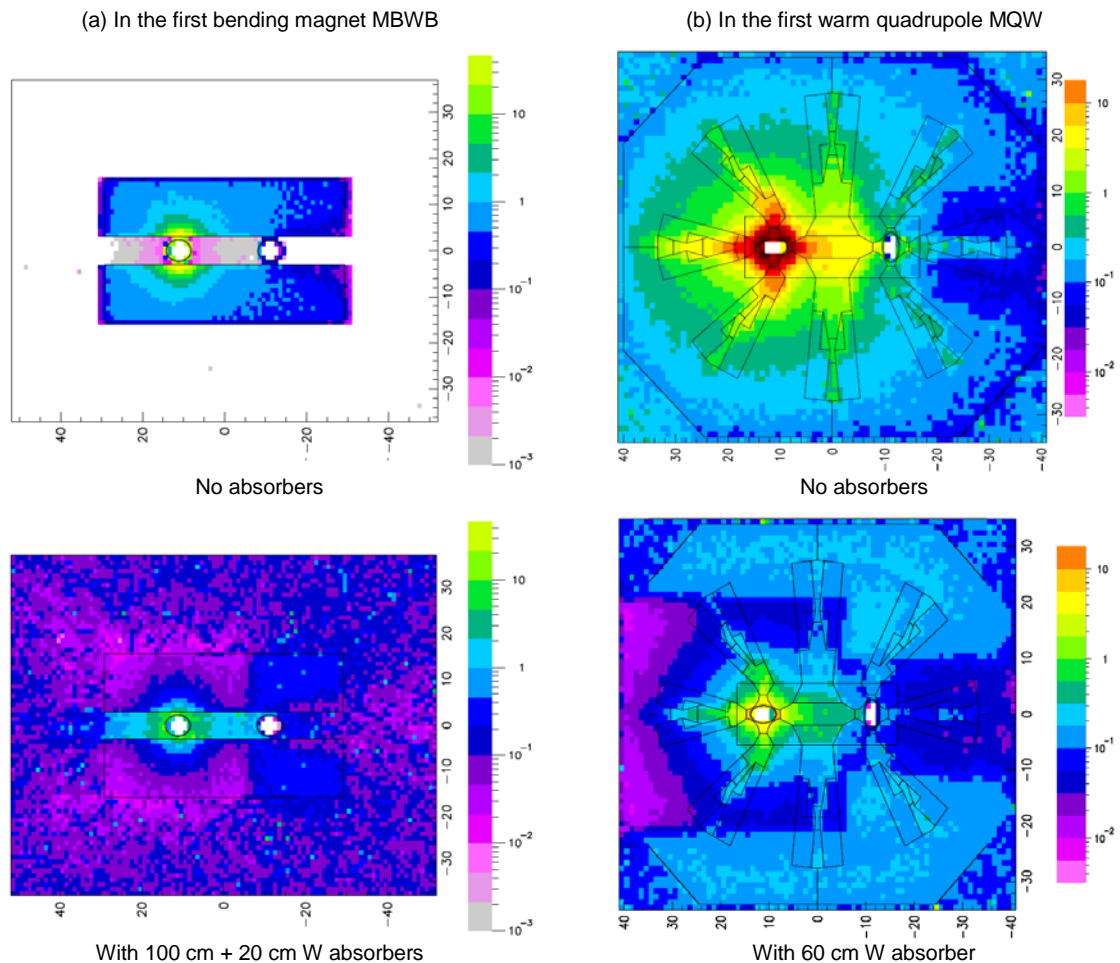
Several solutions have been investigated in detail, starting the simulations with an ideal absorber made of black body,<sup>1</sup> steel or tungsten. The ideal black hole absorber was used to tune the aperture and the lateral dimensions of the passive absorber. This step provided valuable information about the lower limit that we can expect and the dimensions of the absorber to be used. Furthermore, it made obvious that there is a need to use an ellipsoid aperture of 29.5 mm horizontal and 22 mm vertical (smaller than the beam pipe), to filter a great number of halo particles. The external lateral dimension is of the order of  $45 \times 45 \text{ cm}^2$ , to be able to decrease the dose to the coils from 85 MGy/y down to 1.5 MGy/y, below the goal limit of 3 MGy/y [14]. The length was defined as a function of the space availability and of course of the material choice. It is evident that the higher Z material used will have a better cleaning efficiency; therefore the final choice was to use tungsten for both its good thermal properties and high density (Table 1). The simulation showed that a further reduction of the dose on both bending magnets (MBWB and MBWA) could be done either in expense of constraining more the aperture (which would limit the functionality of the machine especially during injection) or by installing a second, shorter (20 cm) passive absorber in the spacing between the two magnets.

**Table 1: Dose peaks in the coils of the two MBW magnets for various passive absorber configurations**

Absorber	MBWB (MGy/y)	MBWA (MGy/y)
None	85	25
Black hole	0.5	1.4
100 cm Fe	4.8	3.9
100 cm W	2	3.9
100 cm W + 20 cm W	2	2.4

A similar approach has been followed for the shielding of the warm quadrupole MQW after the first secondary collimator. The initial dose on the coils was reaching levels of 13 MGy/y. With the use of a an equivalent tungsten passive absorber of length 60 cm in front of the MQW the dose in the coils drops down to 1.8 MGy/y.

1. A fictitious FLUKA material used to terminate particle trajectories. Any particle reaching a black hole boundary is discarded.

**Figure 4: Dose maps (MGy/y) before and after the introduction of the passive absorbers**


### Simulation accuracy

The systematic error involved in simulating the cascade of 7 TeV beams is a combination of several factors, which are in most cases difficult, or even impossible, to predict. The main sources of error are:

- Errors due to the physics modelling: i) in the uncertainty in the inelastic p-A extrapolation cross-section at 7 TeV lab; ii) uncertainty in the modelling used from the simulation code. One would expect a factor of 1.3 on the integral quantities scored like energy deposition (peak included), while for multi differential quantities the uncertainty can be much worse.
- Errors due to the assumptions used in the description of the geometry and of the materials under study. Usually it is difficult to quantify this uncertainty; experience has shows that a factor of 2 can be taken as a safe limit [15].
- Errors when having beams grazing at small angles the surfaces of the collimators, where the surface roughness is not taken into account. A factor of 2 can be taken as a safe choice.

### Conclusions

The LHC betatron cleaning insertion has been extensively studied by means of FLUKA simulation, on a 64 CPU Linux cluster. A modular approach in the geometry definition was chosen, and all the relevant elements, magnets and collimators were implemented with high precision. During normal operation

the betatron cleaning should be able to remove safely 450 kW of beam power for period up to 10 s. At the same time we have to guarantee that the power density on the coils of the superconducting magnets 300 m downstream of the collimation system will never rise above the quench limit of 5 mW/cm<sup>3</sup>. Analysis of the results showed that to prevent superconducting magnets from quench, at least three absorbers are needed made of a high Z material like tungsten. As for the case of the warm objects, passive absorbers made of tungsten are needed in order to ensure that the yearly dose to the epoxy of the coils is below the limit of 3 Gy/y to guarantee a life span of 10 years.

## References

- [1] J.B. Jeanneret, D. Leroy, L. Oberli, T. Trenkler, *LHC Project Report 44* (1996).
- [2] A. Fassò, A. Ferrari, P.R. Sala, "Electron-photon Transport in FLUKA: Status", *Proceedings of the MonteCarlo 2000 Conference*, Lisbon, 23-26 October 2000, A. Kling, F. Barao, M. Nakagawa, L. Tavora, P. Vaz (Eds.), Springer-Verlag Berlin, pp. 159-164 (2001).
- [3] A. Fassò, A. Ferrari, J. Ranft, P.R. Sala, "FLUKA: Status and Prospective for Hadronic Applications", *Proceedings of the MonteCarlo 2000 Conference*, Lisbon, 23-26 October 2000, A. Kling, F. Barao, M. Nakagawa, L. Tavora, P. Vaz (Eds.), Springer-Verlag Berlin, pp. 955-960 (2001).
- [4] V. Vlachoudis, et al, "Consequences of Regular and Irregular Beam Impact on the LHC Collimators", *Proceedings of MC2005*, 7 December 2004.
- [5] M. Santana-Leitner, et al., *IR7 FLUKA Simulations*, CERN-AB Internal Report 2006, forthcoming.
- [6] R. Assmann, et al., "Requirements for the LHC Collimation System", *Proceedings of the 8<sup>th</sup> European Particle Accelerator Conference (EPAC02)*, Paris, France, 3-7 June 2002, E.P.S., Geneva (2002), p. 197, LHC Project Report 599.
- [7] R. Assmann, C. Fischer, J.B. Jeanneret, R. Schmidt, *Summary of the CERN Meeting on Absorbers and Collimators for the LHC*, LHC Project Note 282.
- [8] V. Vlachoudis, "BRexx Overview", *Rexx Symposium 2001*, Research Triangle Park, NC, May 2001.
- [9] O. Brüning, et al., *LHC Design Report. Volume I: The LHC Main Ring*, 4 June 2004, CERN-2004-003.
- [10] R. Assmann, et al., *Tools for Predicting Cleaning Efficiency in the LHC*, CERN-LHC-PROJECT-REPORT-639, *Proceedings of Particle Accelerator Conference (PAC 03)*, Portland, Oregon, 12-16 May 2003.
- [11] G. Robert-Demolaize, et al., "A New Version of Sixtrack with Collimation and Aperture Interface", *In Particle Accelerator Conference 05*, Editor, PAC05 proceedings.
- [12] R. Assmann, B. Goddard, G. Vossenberg, E. Weisse, *The Consequences of Abnormal Beam Dump Actions on the LHC Collimation System*, LHC Project Note 293.
- [13] M. Magistris, et al. "Study for Magnets and Electronics Protection in the LHC Betatron Cleaning Insertion", *Nucl. Inst. and Methods in Phys. Research A*, in press, submitted in September 2005.
- [14] S. Ramberger, *Review of Radiation Limits of the IR3/IR7 Warm Magnets*, <http://lhc-collimation.web.cern.ch/lhc-collimation/library/talks.htm>.
- [15] M. Huhtinen, N.V. Mokhov, *A Cross-comparison of MARS and FLUKA Simulation Codes*, FERMILAB-FN-697, 27 July 2000.



## **Session III**

### **Induced radioactivity and activation data**

***Chair: M. Silari***



## Calculation of radioactive isotope production cross-sections with FLUKA and their application to radiological studies

M. Brugger, A. Ferrari, M. Magistris, S. Roesler, J. Vollaire  
CERN, Geneva, Switzerland

### Abstract

*During the lifetime of a high-energy accelerator estimations of induced radioactivity are important in all its phases, such as design, operation and decommissioning. FLUKA's capability of making predictions for isotope production in hadronic showers has been subject to extensive benchmark experiments carried out in the last years. The accuracy of these predictions steadily improved with the advancements of models implemented into FLUKA, in particular after the introduction of a new evaporation/ fragmentation model and the improvements and extensions of the PEANUT model.*

*Whereas former activation studies focused on samples of selected materials and representative source spectra typical for high-energy accelerators, this paper gives a more general analysis of calculated isotope production cross-sections and their application to future radiation protection needs. In this paper a general approach is presented how to quantify calculation uncertainties and use pre-calculated cross-sections in order to fold them with expected energy spectra as encountered around accelerators, thus leading to fast and accurate results. The application of this approach is understood to be an indispensable ingredient, for example in order to efficiently calculate radionuclide inventories needed for disposal of radioactive waste towards the final repositories.*

*Based on a list of materials and radioactive isotopes, possible reaction channels can be derived for a certain application and energy-dependent isotope production cross-sections are calculated and compared to experimental data. Depending on the amount and accuracy of the available experimental data sets, as well as the production mechanisms of the radioisotopes, respective uncertainty factors can be derived. These factors mainly depend on the production mechanism and the energy range of interest, thus allow quantifying uncertainties in isotope production as calculated with FLUKA in a more global way. Pre-calculated isotope production cross-sections can then be used to estimate radionuclide inventories by folding the cross-sections with expected particle energy spectra. Typical spectra as encountered in high-loss regions of the LHC accelerator are shown and compared to those used in previous benchmark experiments.*

## Introduction

All stages in the life-cycle of a high energy accelerator require calculations of induced radioactivity. During the construction phase their results enter the design of components and the choice of materials, during operation they provide dose estimates for work on activated components and also the de-commissioning of an accelerator is based on studies of the nuclide inventory. For accelerators reaching TeV energies, a Monte Carlo code used for such calculations must be able to reliably predict nuclide production in interactions of all stable hadrons on arbitrary target elements and at energies ranging from that of thermal neutrons to several TeV. For this reason, most studies for the Large Hadron Collider (LHC) employ FLUKA [1,2] as it was found to be the most appropriate Monte Carlo code for estimations of induced radioactivity at this accelerator [3].

In principle, induced radioactivity can be calculated directly in the simulation of the particle cascade in the respective components. Radionuclides follow from the last step of an inelastic interaction and different options exist in FLUKA to score them at any location in the geometry. Moreover, the calculation of radioactive built-up and decay has been added recently such that accurate predictions for nuclide production and induced radioactivity can now be obtained from a single FLUKA simulation without further need to post-process the results.

Although being very convenient the latter one-step simulation is not always the most efficient way to achieve results. Examples for such situations include materials of low density, such as air, for which obtaining results with low statistical uncertainty may imply significant CPU-time if nuclides are calculated directly. Similarly, it is not always efficient to re-run the entire simulation if details in the geometry, such as the definition of trace elements in a material composition, or certain aspects in the nuclide production models have changed.

In these situations it is often more appropriate to follow a two-step approach, by calculating particle fluence spectra in the regions of interest and by folding them off-line with pre-computed, energy-dependent nuclide production cross-sections. These cross-sections can be obtained directly from FLUKA by simulating single collisions but can also include experimental information, if available, in the form of evaluated cross-sections. This two-step approach allows more flexibility and efficiency to explore different design options, for example, in studies of air activation, as well as for applications in which precise predictions are not necessarily required, such as for the radiological characterisation of radioactive waste.

The present study aims at building such a data-base of energy-dependent cross-sections. It is based on FLUKA predictions but also includes experimental data to verify calculated values. The most complete compilation of experimental information for our purposes can be found in Ref. [4]. In addition, dedicated benchmark experiments for activation of materials typically used in the construction of the LHC were performed over the past few years and serve as basis for a verification [3,5].

Cross-sections are calculated according to their relevance for radiological studies for the LHC and therefore cover so far reactions of protons, neutrons and charged pions on nuclei with masses up to zinc. Despite this present limitation the number of calculated cross-section data sets is enormous and a detailed comparison to experimental data can only be performed for selected reactions. For all other channels a more automated approach is attempted in which energy-averaged ratios of measured and calculated cross-sections are computed. These ratios are not meant to allow unambiguous conclusions but should give at least an indication on the performance of FLUKA for single reaction channels.

The prediction of the nuclide vector for radioactive waste considerations has been chosen as a first area of application of the new database. In particular, one of the most radioactive parts of the LHC, the collimation region, was selected. Based on an existing, detailed FLUKA geometry [6] of that area particle fluence spectra were calculated for a large number of different locations and were folded off-line with the pre-computed cross-sections for reactions leading to waste-relevant nuclides. As it is shown below, this approach allows an investigation of the sensitivity of the nuclide predictions on the shape of the fluence spectra and a reduction of all computed spectra to a sub-set of so-called characteristic spectra.

## Activation benchmark measurements at CERF

In the past years an extensive collection of samples of different materials such as aluminium, copper, stainless steel, iron, titanium, concrete, marble, boron nitride, carbon composite, and demineralised water were irradiated at the CERN-EU High-Energy Reference Field (CERF) facility [7], using the secondary mixed hadron beam from the Super Proton Synchrotron (SPS) accelerator. The facility is installed in one of the secondary beam lines (H6) from the Super Proton Synchrotron (SPS) at CERN. At this facility a cylindrical copper target (7 cm in diameter, 50 cm in length) is intercepting a positively charged hadron beam with a momentum of 120 GeV/c consisting of protons (34.8%), pions (60.7%) and kaons (4.5%).

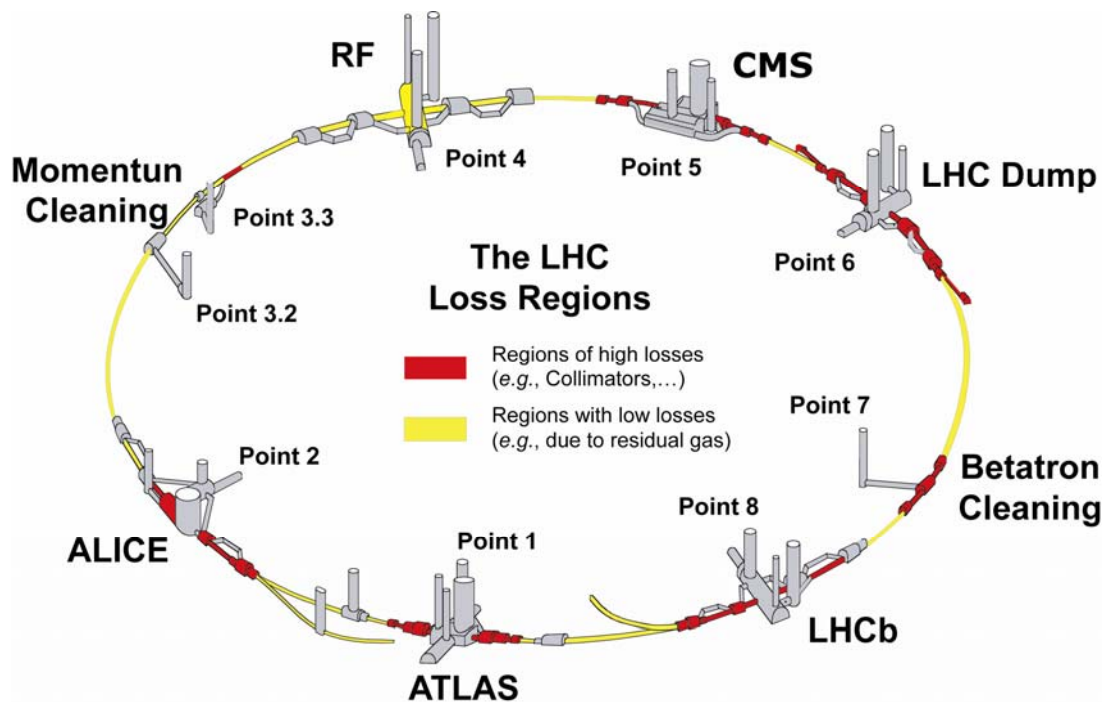
The copper target is surrounded by a concrete enclosure of 80 cm thickness. The CERF facility serves mainly for detector test and calibration purposes and thus provides instrumentation for accurately recording the beam properties (intensity and profile). As the latter is essential for benchmark experiments, the facility is well suited for studies of induced radioactivity. An air-filled Precision Ionisation Chamber (PIC) at atmospheric pressure, placed in the beam upstream of the copper target, monitors the intensity of the beam.

In the series of benchmark experiments emphasis was put on reducing uncertainties in both measurements and simulations in order to allow for an accurate benchmark of the FLUKA code. This included low-level gamma spectrometry measurements, appropriate treatment of the decay chains of isotopes in the gamma spectrometry and in the simulations, efficiency correction in the spectrometry, as well as detailed simulations of residual nuclei production with low statistical uncertainties. For each sample spectrometry, analyses were performed for several cooling times, which allowed identifying both short- and long-lived isotopes.

Further details concerning the experimental set-up, the beam conditions and the benchmark results can be found in [5,8,9].

**Figure 1: Distribution of high [red (dark grey)] and low [yellow (light grey)] loss regions around the LHC**

The two beam cleaning insertions (Points 3 and 7), the dump caverns and the inner triplets will be especially regions of elevated activation



## The collimation regions of the LHC

The LHC is a synchrotron-collider which accelerates and stores two intense beams of particles circulating in opposite directions. Its size and structure was given by the former LEP ring which consisted of eight so-called arcs with a bending radius close to 3.5 km linked together by eight 528 m long straight sections. The two beams of the LHC will be accelerated in two separate vacuum chambers side by side in the horizontal plane through the arcs and will cross over at dedicated interaction points (IP) in the centre of those straight sections dedicated to experiments. The high stored total energy and total beam current make the LHC not only a challenging project with respect to its construction, but also to the operation and protection of the accelerator itself.

High energy particle cascades induced by beam particle losses lead to the activation of material in the respective zone of the accelerator. At the LHC one can distinguish machine zones of high and low losses as shown in Figure 1.

The LHC requires numerous different elements in order to assure its stable operation, one of them being the beam cleaning or collimation system. During the high-energy collisions in the physics experiments, particles scattered elastically are emitted in the primary beam direction with the same momentum and a slight increase in transverse angle. The same effect occurs along the whole machine due to elastic interactions between the protons and the residual gas nuclei in the vacuum chamber. Furthermore, beam instabilities (non-linear beam dynamics) also contribute to an amplitude increase of the transverse and longitudinal beam distribution. All these effects will progressively push particles outside of the stable region, creating a so-called beam halo.

One of the challenging tasks in the design of the LHC is the need to ensure this halo to be intercepted at dedicated elements before it hits other parts of the accelerator, *e.g.* the cold inner part of a super-conducting magnet. Already a few per mille of the scattered particle flux interacting with a superconducting magnet would cause it to quench. Therefore, an efficient collimation system is required in order to ensure stable operation of the machine. For this purpose, the LHC includes two cleaning insertions, defined as those parts of the accelerator ring where particle losses are concentrated. One of which is dedicated to clean off-momentum particles, whereas the other captures particles outside a defined transverse boundary, requested to be smaller than the aperture of the remaining accelerator components.

The betatron cleaning insertions at IP7, which is showing the highest losses and where a complicated betatron cleaning system will undergo major upgrades within a phased approach of its installation, is in the following chosen as a test case to verify the presented approach of calculating secondary particle spectra and fold them with pre-calculated (or measured) isotope production cross-sections.

## The Monte Carlo code FLUKA

In an inelastic reaction of a high-energy hadron with a nucleus, hadrons will be produced, as well as many individual nucleons and some clusters of nucleons will be ejected from the struck nucleus during the various phases of the interaction. Depending on the mass of the remaining fragment(s) with respect to the mass of the original target nucleus the interactions are classified as spallation, deep spallation/fission or multi fragmentation. The residual nucleus will be left in a highly excited state and will most probably be unstable against radioactive decay. It will attempt to reach a stable configuration by a succession of decays of gradually increasing lifetime (possible exceptions might be metastable states). Low-energy neutrons, protons and pions interact with nuclei via resonance interactions, but these processes generally result in the removal of only a few nucleons from the struck nucleus which is left in a near-stable configuration.

The production of radionuclides in FLUKA [1,2] results directly from the description of hadronic interactions. It can therefore be modelled for any incoming hadron, target nucleus and energy. Interactions of low-energy neutrons ( $E < 19.6$  MeV) form the only exception, for which pre-tabulated cross-sections are used. If such cross-sections are not available for a certain target element, radionuclides are not generated in interactions on that element by default. For all other reactions, radionuclides follow directly from the last step of the interaction and results are thus influenced by all previous stages.

Hadronic collisions at energies above several GeV are described within the Dual Parton Model (DPM) which includes multiple interactions of the incoming hadron on target nucleons (so-called Gribov-Glauber theory). These high-energy hadron-nucleon interactions are followed by a sophisticated Generalised Intranuclear Cascade (GINC) model. At energies below a few GeV the description of the interaction starts immediately from the GINC model. The GINC terminates as soon as all produced hadrons (except nucleons) are either emitted, absorbed or decayed and all secondaries have reached energies below a few tens of MeV. The pre-fragment then enters the pre-equilibrium stage immediately followed by a detailed description of evaporation and fragmentation [3,10].

The evaporation module in FLUKA includes approximately 600 possible emitted particles and states with mass numbers below  $A = 25$ . The fragmentation of light nuclei ( $A < 18$ ) follows a Fermi break-up model considering about 50000 different combinations with up to six ejectiles. In addition, coalescence processes are treated in detail. The evaporation model has been improved recently, including the introduction of new level-densities and refined Coulomb barriers.

The implementation in FLUKA of nuclear interactions is called PEANUT. At the time of this study, the DPM was not part of PEANUT limiting the energy range for PEANUT to 5 GeV. An independent implementation of the DPM was responsible for the description of interactions at higher energies which, for historical reasons, included also an independent intra-nuclear cascade model, less-sophisticated than that of PEANUT. The boundary between the two implementations at 5 GeV was typically visible as discontinuity in energy-dependent quantities, such as nuclide production cross-sections, but was of no importance for many applications. Very recently, the DPM has been added to PEANUT allowing a coherent description of interactions at all energies. Moreover, quasi-elastic processes are now consistently modelled, such that the discontinuity should disappear in future releases of FLUKA.

As the character of this study is of more general nature these latest improvements in FLUKA have no direct implication on the conclusions and can be easily incorporated by replacing the nuclide production cross-sections.

Precise predictions about radioisotope production are by far the most demanding tasks for nuclear models. More recently, a vast experimental programme aimed at validating code predictions for radionuclide production have been carried out at CERF in view of the challenges posed by the LHC. The comparisons with the calculated results, both for radionuclide production [3] and for residual dose rates [9], have firmly established the reliability of the code and of its associated inventory evolution algorithms. Of course, since the accuracy of particle energy and spatial fluence predictions is always better than of radionuclide production, every time reliable experimental production cross-sections for a given isotope are available for all particles energies of interest, folding the computed fluences with evaluated experimental cross-sections is the most accurate approach.

## Calculations of cross-sections and comparison to experimental data

All radionuclide production cross-sections discussed in the following paragraphs were calculated with a non-standard FLUKA routine. It calls directly the inelastic interaction models for a given combination of projectile, target nucleus and energy and allows scoring of individual residual nuclei. It returns the inelastic cross-section as well as individual radionuclide production cross-sections as shown below.

For the application to waste studies at the CERN LHC accelerator, FLUKA cross-sections were calculated according to their relevance for radiological studies for the LHC and cover therefore so far reactions of protons, neutrons and charged pions on nuclei with masses up to zinc. In total 103 isotopes were studied ( $^3\text{H}$  up to  $^{72}\text{Zn}$ ) produced on 138 different target materials (heavier materials than Zn were considered as target material because of their importance as trace elements). All calculations were performed separately for the type of the projectile (p, n,  $\pi^+$  and  $\pi^-$ ) as well as for an energy range from 1 MeV to 10 TeV (except for neutrons where the lower limit was set to 19.6 MeV in order to coincide with the boundary below which tabulated values are used).

To verify the contribution of decay chains in case of isotopes up to zinc, in a first step cumulative (including the production term coming from possible decay reactions of mother isotopes) and non-cumulative cross-sections were compared as shown in Table 1. Cumulative yields contain all contributions from mother isotopes decaying via positive or negative beta decay and having a half-life smaller than the one of the respective isotope of concern.

In the example of isotopes being produced by protons on natural copper it can be seen that for the presented study in a first approximation contributions coming from radioactive decay chains are small (5.7% [ $^{51}\text{Cr}$ ] and 8.3% [ $^{49}\text{V}$ ]). Other projectiles and targets result in comparable contributions, thus for the presented study it was decided to use cumulative cross-sections only. For cases where the experimental data are given as non-cumulative only, calculated cumulative and non-cumulative cross-sections were compared to each other and didn't show a difference significant for the presented calculations.

**Table 1: Isotopes produced by protons on natural copper showing differences in their calculated values for cumulative and non-cumulative cross-sections**

Values are given as average difference (in per cent) of the respective energy-dependent cross-section for the two cases

Isotope	Cummulative Contribution [%]	Isotope	Cummulative Contribution [%]	Isotope	Cummulative Contribution [%]
<i>Al26</i>	0.027	<i>Cr55</i>	1.211323927	<i>Na24</i>	2.222
<i>Al29</i>	0.268	<i>Cu60</i>	0.266004106	<i>Ne24</i>	0.593
<i>Ar37</i>	0.110	<i>Cu61</i>	0.452601945	<i>Ni57</i>	0.013
<i>Ar39</i>	3.076	<i>F18</i>	0.122197941	<i>Ni59</i>	0.828
<i>Ar41</i>	1.089	<i>Fe53</i>	0.020957495	<i>Ni63</i>	2.634
<i>Ar42</i>	0.329	<i>Fe55</i>	1.833566652	<i>P33</i>	0.458
<i>Ar43</i>	0.572	<i>Fe59</i>	0.554082518	<i>S35</i>	2.091
<i>C14</i>	0.480	<i>Fe60</i>	0.089785773	<i>S37</i>	0.630
<i>Ca41</i>	0.040	<i>K43</i>	0.518175331	<i>Sc43</i>	0.106
<i>Ca45</i>	1.917	<i>K44</i>	0.647122696	<i>Sc49</i>	0.085
<i>Ca47</i>	1.318	<i>K45</i>	0.140056222	<i>Si31</i>	0.685
<i>Cl34</i>	0.010	<i>Mg27</i>	0.707324503	<i>Si32</i>	0.182
<i>Cl39</i>	0.227	<i>Mg28</i>	0.132847233	<i>Ti45</i>	0.017
<i>Cl40</i>	0.082	<i>Mn51</i>	0.022365327	<i>Ti51</i>	0.408
<i>Co55</i>	0.140	<i>Mn52</i>	1.546496611	<i>V47</i>	0.024
<i>Co56</i>	0.805	<i>Mn53</i>	3.840444367	<i>V48</i>	1.159
<i>Co57</i>	2.256	<i>Mn56</i>	0.683478807	<i>V49</i>	8.325
<i>Co61</i>	0.552	<i>Mn57</i>	0.363748906	<i>V52</i>	1.137
<i>Cr49</i>	0.028	<i>N13</i>	0.666154655	<i>V53</i>	0.416
<i>Cr51</i>	5.770	<i>Na22</i>	0.014799518	<i>Zn63</i>	0.003

Despite the present restrictions in isotopes and target materials typical for LHC applications, the number of calculated cross-section data sets is still enormous; a detailed comparison to experimental data can only be performed for selected reactions. The latter were chosen to be representative cases depending on the mass difference of the remaining fragment with respect to the mass of the original target nucleus, thus classified as spallation, deep spallation or multi-fragmentation and low-energy neutron reactions, their reaction mechanisms, as well as for their importance for studies concerning the radioactive waste at CERN. This allows testing the quality of FLUKA to predict such isotopes in different energy ranges.

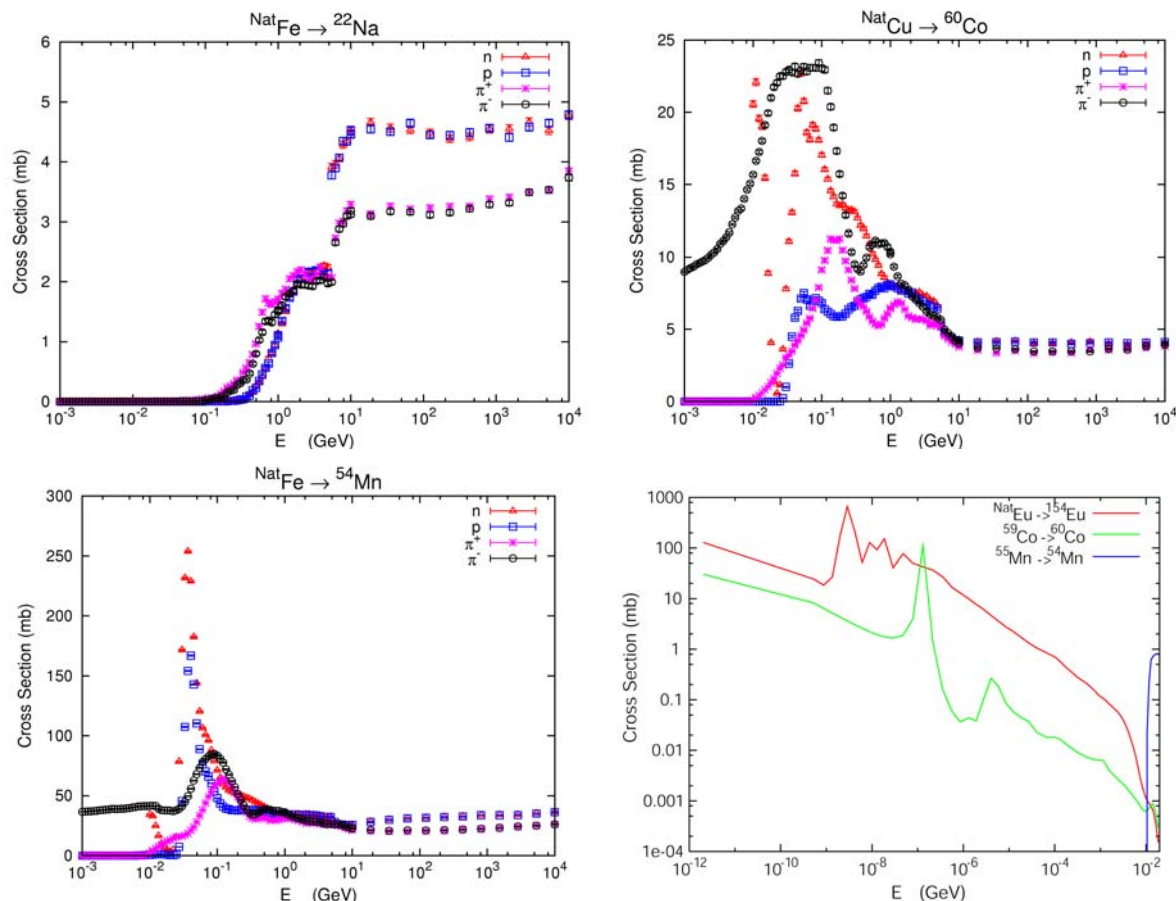
The selected cross-sections used for this study are:

- $^{22}\text{Na}$  produced on natural iron;
- $^{60}\text{Co}$  produced on natural copper;
- $^{54}\text{Mn}$  produced on natural iron;
- $^{54}\text{Mn}$  produced on natural manganese;
- $^{154}\text{Eu}$  produced on natural europium;
- $^{54}\text{Mn}$  produced on  $^{55}\text{Mn}$ ;
- $^{60}\text{Co}$  produced on  $^{59}\text{Co}$ .

The respective energy dependent isotope production cross-sections as calculated with FLUKA are shown in Figure 2.

**Figure 2: Energy-dependent isotope production cross-sections of the selected representative isotopes**

Please note that in the case of  $^{60}\text{Co}$  and  $^{54}\text{Mn}$  the shown neutron cross-sections are only valid for energies above 19.6 MeV. For energies below tabulated values have to be used as shown for  $^{154}\text{Eu}$  (produced on natural europium),  $^{60}\text{Co}$  ( $^{59}\text{Co}$ ) or  $^{54}\text{Mn}$  ( $^{55}\text{Mn}$ ).

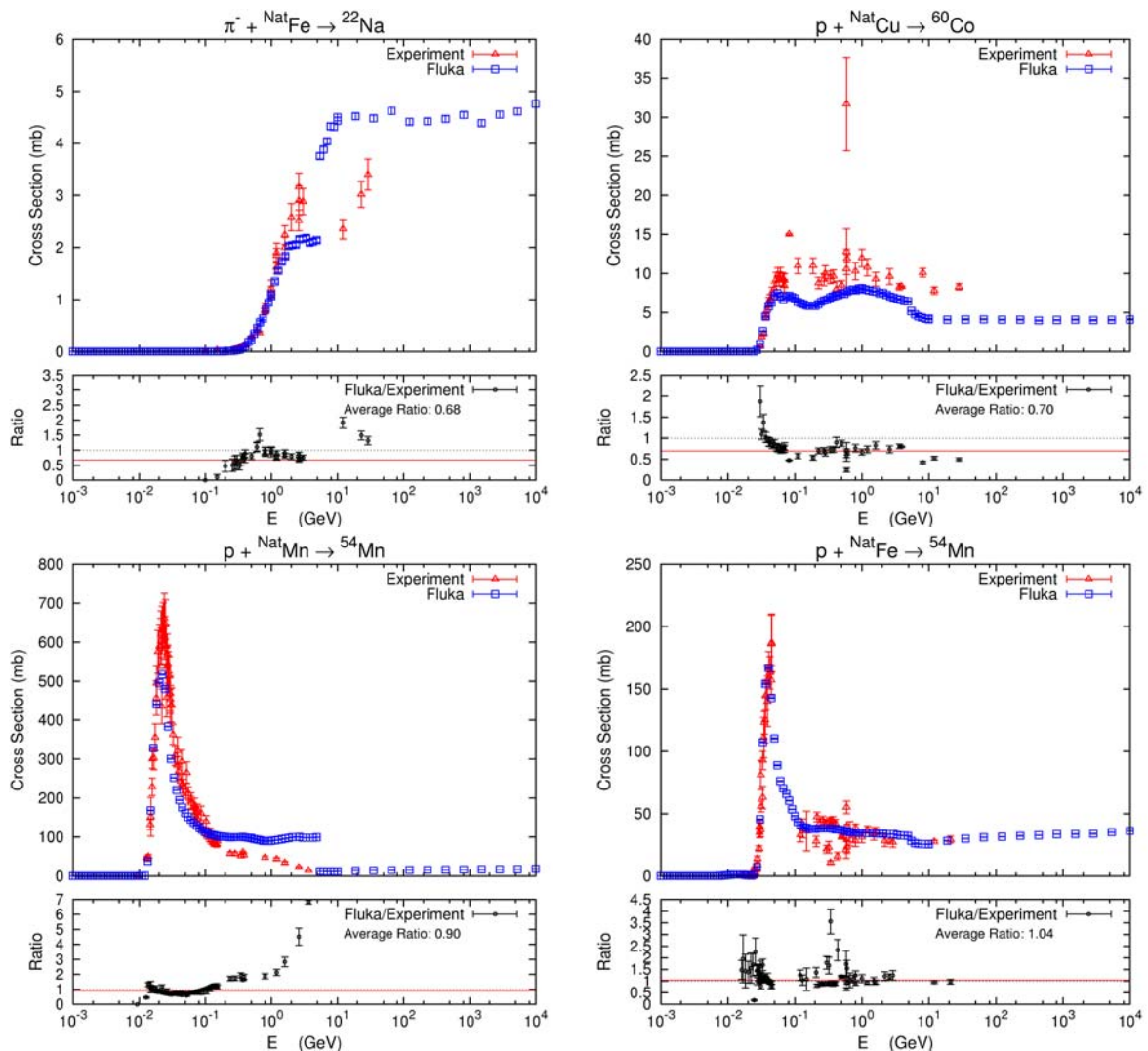


In a first analysis these isotope production cross-sections were compared with published values measured in numerous experiments and collected in the Landolt-Börnstein compendium [4]. It shall be noted that depending on the isotope some of the available experimental data tend to fluctuate significantly as a function of energy, thus for the representative isotopes cases were selected where a sufficiently high number of experimental data points are available. In general, the available experimental data is more numerous for proton induced reactions and scarce in case of pions.

Figure 3 furthermore shows the calculated FLUKA cross-sections together with the experimental data and gives the ratio of the two as a function of energy. Average values can be extracted assuming a uniform contribution of the cross-section in energy and are shown in the graph as “Average Ratio”. However, for a final conclusion for any application the respective shape of the energy dependent spectra has to be taken into account when applying these ratios.

In order to judge the agreement between measured and calculated values of residual activation in case of a mixed energy spectra, those average values have to be newly calculated based on the actual particle energy spectra, thus can be significantly different than the presented results. It shall thus be noted that the current comparison focuses rather on the general method without giving a detailed analysis for all isotopes, e.g. those relevant for a waste characterisation at hadron accelerators (e.g. the LHC). For the latter detailed studies will be necessary taking into account the respective irradiation history in order to judge the influence of build-up and decay; the irradiation conditions in order to deduce the final shape of particle spectra; the detailed chemical composition of studied materials in order to define important trace elements.

**Figure 3: Comparison of experimental and calculated energy-dependent production cross-sections for the selected representative isotopes of this study**



For all other channels a more automated approach is attempted in which energy-averaged ratios of measured and calculated cross-sections are computed as shown in Figure 3. As mentioned before, these ratios are not meant to allow unambiguous conclusions but should give at least an indication on the performance of FLUKA for single reaction channels.

Table 2 (for proton-induced reactions) and Table 3 (for pion-induced reactions) show a comparison for all isotopes and target materials where experimental cross-sections are available, including the respective average ratio between FLUKA cross-sections and experimental ones, together with further information on the available experimental data, thus their number and energy range. Please note that isotopes showing an error which exceeds 40% were not taken into account.

It can be seen that such a comparison can only give a first quantitative picture with the further need to make a deeper analysis for the isotopes important for the relevant study. This is supported by the fact of the observed good agreements between measurements and simulations as performed at CERF. The results presented in Tables 2 and 3 can further be used to compare the calculated FLUKA production cross-sections and the available experimental data collection with the experimental data obtained at the CERF facility at CERN [3,5,8,9]. Together with the information on production channels, the respective half-life of the isotope this results in a comparison as shown for copper as example in Table 4.

The latter table shows gives for selected target materials, all produced isotopes, their half-lives, and the respective projectile, the following information:

- the isotope ratios assumed in the natural composition of the simulation;
- the respective production reaction channels;
  - “s” ... spallation;
  - “H” ... tritium;
  - “n” ... neutron;
  - “α” ... alpha;
  - “p” ... proton;
- “Land” ... average ratios between FLUKA and Landolt Börnstein data [4];
- “#ofDp” ... number of available data in the Landolt Börnstein compendium;
- “CERF” ... ratios observed during the CERF experiments [3,5,8,9].

This preliminary study shows the clear need to further compare on a detailed basis the available experimental data, the results as obtained at CERF and the currently available data for isotope production cross-sections as calculated with FLUKA. With respect to the application for the radioactive waste this has to be done for all isotopes of interest and will finally lead to a quantification of the underlying uncertainties in both, simulations and experiment.

### Typical particle spectra for the LHC

Due to the complexity and heterogeneity of the LHC machine, finding one representative radiation field which can be used for the assessment of any radiological quantity is not possible. However, for one area and its associated beam loss mechanisms, it is possible to calculate with FLUKA any particle spectra which can be used for the calculation of such quantities. In the case of the presented application to the radioactive waste, it is sufficient to limit the spectra calculation to protons, neutrons and pions for which the production cross-sections were computed as explained before.

A detailed description of the beam cleaning insertion where an important fraction of the protons from the beam are lost was thus used to investigate the sensitivity of radioactive nuclei production to specific characteristics of the radiation field such as the distance and shielding between the loss points and the object of interest. The FLUKA geometry includes the beam line components such as the collimators, dipole and quadrupole magnets as well as the tunnel structure. Figure 6 shows the distribution of collimators and magnets along the beam pipe on a longitudinal cut of the FLUKA geometry.

The spectra were scored at the different locations of the collimators or magnets leading to the calculation of 400 different spectra. The collimators are represented by two carbon jaws surrounded by a water layer and a copper cooling plate both enclosed in a steel tank. Particle spectra were scored in the jaws in which the 7 TeV beam particles interact as well as in the water. The magnets are represented using a simplified layout including the steel yoke, one copper and one water ring representing the coils and the water cooling system. The spectra were scored in the yoke as well as in the water. A cut of collimators and magnets as they are implemented in the FLUKA geometry and the locations where the spectra are scored is shown in Figure 7.

For the tunnel structure, a realistic configuration is implemented in the FLUKA geometry. Spectra were scored in the floor of the tunnel, in the walls and in the air; the latter two were divided into three different sections for scoring purposes. Furthermore, spectra were also calculated in the different water pipes which go through the beam cleaning insertions. A cut of the tunnel perpendicular to the beam axis is represented in Figure 8.

It has to be noted that the spectra calculation is performed with FLUKA using a track length estimator, thus the scored quantity corresponds to the average over an extended object and do not reflect the possible heterogeneity of the field insight the object. For example, in the case of the floor or of the water pipes, the spectra can locally be very different close to a loss point from the spectra which are averaged over the entire length of the beam cleaning insertion.

**Table 2: Overall comparison (FLUKA/experiment) of proton-induced experimental [4] and with FLUKA calculated energy-dependent production cross-sections for all isotopes where experimental data were available (statistical error below 40%)**

In addition to the average ratio and its error also the number of available data points as well as their energy range is shown

Target	Isotope	Average Ratio	Error [%]	Number of Data Points	minimum Energy [GeV]	maximum Energy [GeV]	Average Energy [GeV]	Target	Isotope	Average Ratio	Error [%]	Number of Data Points	minimum Energy [GeV]	maximum Energy [GeV]	Average Energy [GeV]
Al	H3	0.413	26.673	23	0.016	25.000	2.017	Fe	Sc48	0.611	15.538	6	0.500	12.000	3.150
Al	Be7	2.863	15.860	143	0.028	300.000	2.890	Fe	V48	0.933	12.893	46	0.039	21.000	1.251
Al	Be10	3.370	13.381	34	0.057	1.200	0.323	Fe	Cr48	1.545	21.541	6	0.150	12.000	2.485
Al	C11	1.301	6.304	11	0.400	300.000	31.356	Fe	Cr51	0.318	19.201	40	0.013	21.000	0.651
Al	Na22	1.127	13.055	312	0.022	300.000	1.337	Fe	Mn52	3.174	18.173	4	0.024	12.000	3.281
Al	Na24	0.346	13.996	216	0.010	300.000	2.122	Fe	Mn54	1.035	15.705	69	0.016	21.000	0.856
Ca	Na22	0.719	10.296	13	0.168	24.000	2.836	Fe	Mn56	0.585	39.707	5	0.150	12.000	2.862
Ca	Na24	0.371	15.606	11	0.100	2.600	1.073	Fe	Fe52	0.972	18.787	11	0.019	12.000	1.076
Ca	Mg28	0.337	27.814	5	1.200	2.600	1.840	Fe	Fe53	0.331	36.762	2	0.150	0.660	0.405
Ca	Cl36	0.887	13.641	8	0.150	24.000	3.591	Fe	Co55	1.098	15.262	66	0.013	12.000	0.311
Ca	K42	0.974	18.017	5	1.200	2.600	1.840	Fe	Co56	0.613	14.532	255	0.005	21.000	0.235
Ca	K43	1.606	12.864	7	0.800	2.600	1.543	Mg	Be7	1.188	15.800	52	0.042	23.000	1.047
C	H3	1.388	14.422	14	0.150	6.200	1.533	Mg	Be10	1.606	14.365	22	0.062	23.000	1.901
C	Be7	0.949	11.240	174	0.025	300.000	2.820	Mg	Na22	1.094	10.906	119	0.006	24.000	0.940
C	Be10	0.987	12.400	17	0.031	1.600	0.207	Mg	Na24	0.603	13.499	98	0.018	2.900	0.244
C	C11	0.631	4.607	189	0.018	300.000	2.517	Mn	Be7	1.164	16.215	11	0.282	2.600	1.129
C	Co7	1.293	16.240	17	0.277	12.000	2.316	Mn	Be10	1.432	26.475	15	0.059	2.600	0.714
Co	Be10	1.121	22.354	4	0.233	0.380	0.308	Mn	Na22	0.670	22.350	19	0.100	2.600	1.050
Co	Na22	0.410	35.066	25	0.100	12.000	1.349	Mn	Na24	0.442	36.966	6	0.100	3.650	1.592
Co	Na24	0.466	20.727	13	0.100	12.000	2.616	Mn	Mg28	0.490	24.040	4	1.200	3.650	2.283
Co	Mg28	0.339	21.313	6	1.000	12.000	5.325	Mn	Cl36	0.664	9.774	4	0.239	0.384	0.313
Co	P32	0.911	22.024	4	1.760	2.750	2.253	Mn	K43	0.401	14.251	9	0.239	3.650	1.234
Co	Cl36	0.789	16.563	4	0.233	0.380	0.308	Mn	Sc46	0.513	9.303	10	0.239	3.650	1.170
Co	K42	0.865	16.126	12	0.150	18.300	4.128	Mn	Sc47	0.858	17.182	21	0.076	3.650	0.314
Co	K43	0.540	17.362	17	0.150	18.300	3.456	Mn	Sc48	0.921	30.955	21	0.076	3.650	0.407
Co	Sc44	1.818	9.951	4	0.500	12.000	4.298	Mn	V48	0.824	11.505	37	0.047	3.650	0.407
Co	Sc46	0.499	10.642	24	0.170	12.000	1.712	Mn	Cr48	2.162	34.667	25	0.061	3.650	0.292
Co	Sc48	1.017	16.054	9	0.500	12.000	3.759	Mn	Cr51	0.687	9.665	62	0.016	3.650	0.252
Co	Cr48	1.428	20.827	21	0.069	12.000	1.752	Mn	Mn52	1.806	12.256	45	0.027	3.650	0.328
Co	Cr51	0.866	9.735	58	0.049	12.000	0.435	Mn	Mn54	0.899	9.977	75	0.009	3.650	0.195
Co	Mn52	1.214	13.155	51	0.049	12.000	0.435	Mn	Fe52	1.457	16.118	83	0.038	3.650	0.130
Co	Fe52	1.167	19.073	32	0.062	3.650	0.234	Na	Be7	2.668	17.412	17	0.031	5.700	0.434
Co	Co55	1.149	17.288	50	0.042	12.000	0.735	Na	Na22	1.187	10.595	38	0.015	5.700	0.252
Co	Co56	1.275	11.928	98	0.027	12.000	0.468	Ni	Be7	1.459	17.022	29	0.065	23.000	2.274
Co	Co57	0.366	10.967	136	0.012	12.000	0.329	Ni	Be10	1.200	34.260	23	0.053	2.600	0.545
Co	Co58	1.329	9.359	64	0.012	12.000	0.646	Ni	Na22	0.611	25.276	21	0.100	23.000	2.610
Co	Ni56	1.919	26.240	25	0.038	1.600	0.140	Ni	Na24	0.410	26.475	17	0.100	12.000	2.800
Co	Ni57	2.706	12.529	93	0.019	12.000	0.283	Ni	Mg28	0.297	29.588	3	3.650	12.000	8.217
Cr	Cr51	4.348	6.919	17	0.014	0.600	0.051	Ni	P32	0.970	33.458	9	0.130	2.900	1.009
Cr	Mn52	4.634	15.615	17	0.006	0.600	0.032	Ni	Cl36	0.611	13.640	6	0.230	1.200	0.537
Cr	H3	1.305	33.185	4	0.660	25.000	15.665	Ni	K42	0.411	14.642	7	0.500	12.000	4.364
Cu	Be7	1.331	14.867	30	0.065	30.000	4.868	Ni	K43	0.368	17.651	7	0.500	12.000	4.364
Cu	Na22	0.463	23.821	22	0.100	30.000	8.092	Ni	Sc43	1.040	13.095	4	0.500	2.000	3.788
Cu	Na24	0.476	21.312	45	0.050	800.000	40.155	Ni	Sc44	1.894	11.896	4	0.500	12.000	6.288
Cu	Mg28	0.546	20.605	7	1.000	400.000	63.550	Ni	Sc46	0.491	11.113	19	0.211	12.000	1.923
Cu	P32	2.562	30.069	5	0.120	24.000	4.303	Ni	Sc47	0.322	20.317	9	0.500	12.000	3.550
Cu	Ar39	0.422	12.328	12	0.540	29.000	14.141	Ni	Sc48	0.348	27.585	3	9.000	12.000	8.217
Cu	Ar42	0.737	26.288	9	0.600	29.000	13.239	Ni	V48	1.644	23.605	9	0.130	2.900	0.992
Cu	K42	0.637	15.167	23	0.150	400.000	26.735	Ni	Cr48	2.744	23.633	4	0.500	12.000	6.288
Cu	K43	0.583	19.582	26	0.150	30.000	8.496	Ni	Cr51	0.673	15.764	17	0.036	9.000	1.656
Cu	Ca47	1.030	38.768	3	1.600	24.000	12.533	Ni	Mn52	0.435	13.431	36	0.036	12.000	1.473
Cu	Sc43	0.656	21.272	5	0.500	24.000	8.230	Ni	Mn54	0.748	12.045	33	0.041	12.000	1.334
Cu	Sc44	1.513	9.139	9	0.500	28.000	9.082	Ni	Mn56	0.228	23.558	4	0.500	12.000	6.288
Cu	Sc46	0.555	9.526	26	0.200	28.000	3.699	Ni	Fe52	0.706	14.600	49	0.045	12.000	0.608
Cu	Sc48	0.160	17.965	26	0.200	28.000	3.646	Ni	Fe59	0.591	25.872	13	0.211	12.000	1.601
Cu	V48	0.640	10.553	27	0.090	400.000	18.331	Ni	Co55	0.504	13.044	132	0.005	12.000	0.311
Cu	Cr49	1.133	20.510	7	0.184	24.000	3.729	Ni	Co56	1.246	14.083	71	0.016	9.000	0.373
Cu	Cr51	0.557	9.077	26	0.110	28.000	3.634	Ni	Co57	3.104	11.858	138	0.005	12.000	0.311
Cu	Mn52	1.112	9.755	35	0.065	400.000	14.154	Ni	Co58	0.988	12.219	15	0.024	12.000	1.423
Cu	Mn54	0.812	8.885	39	0.046	28.000	2.486	Ni	Co60	1.088	15.937	13	0.211	2.600	0.724
Cu	Mn56	0.632	12.778	14	0.090	28.000	5.913	Ni	Ni56	0.542	19.239	49	0.018	12.000	0.847
Cu	Fe52	1.130	25.478	22	0.090	30.000	6.377	O	Be7	0.610	15.303	119	0.030	19.000	0.709
Cu	Fe53	0.546	16.856	45	0.049	30.000	3.307	Si	H3	0.056	21.429	7	0.021	3.000	0.538
Cu	Co55	1.171	13.843	52	0.070	30.000	2.817	Si	Be7	1.383	17.456	109	0.031	24.000	0.766
Cu	Co56	1.150	12.226	84	0.044	30.000	1.794	Si	Be10	2.336	22.255	33	0.050	23.000	1.258
Cu	Co57	0.883	11.540	93	0.026	30.000	1.591	Si	Na22	0.895	16.465	165	0.018	24.000	0.693
Cu	Co58	0.814	10.267	92	0.026	30.000	1.632	Si	Na24	0.453	16.664	89	0.026	2.900	0.308
Cu	Co60	0.699	11.159	41	0.031	28.000	1.679	Si	Al28	0.520	20.469	20	0.018	0.103	0.056
Cu	Co61	0.900	16.107	11	0.090	30.000	10.211	Si	Sc44	1.037	13.870	24	0.013	12.000	0.547
Cu	Ni56	0.808	34.693	54	0.058	28.000	1.046	Ti	Sc47	1.005	15.081	33	0.011	0.584	0.067
Cu	Ni57	1.901	11.498	102	0.041	28.000	1.389	Zn	Be7	1.380	20.555	2	0.500	12.000	6.250
Cu	Cu60	0.944	15.453	57	0.036	30.000	1.611	Zn	K42	0.663	20.393	2	0.500	12.000	6.250
Cu	Cu61	0.779	17.061	51	0.020	30.000	2.522	Zn	K43	1.045	22.364	2	0.500	12.000	6.250
Cu	Cu64	0.950	11.154	38	0.016	28.000	1.018	Zn	Sc44	2.699	14.773	2	0.500	12.000	6.250
Cu	Zn61	0.473	29.751	6	0.030	0.047	0.038	Zn	Sc46	0.815	15.314	2	0.500	12.000	6.250
Cu	Zn62	0.938	13.524	73	0.011	28.000	1.004	Zn	Sc47	0.809	36.730	2	0.500	12.000	6.250
Cu	Zn63	0.782	15.003	83	0.005	28.000	0.419	Zn	V48	1.092	13.164	2	0.500	12.000	6.250
Fe	H3	1.686	31.897	4	0.130	25.000	12.645	Zn	Cr48	2.063	24.336	2	0.500	12.000	6.250
Fe	Be7	1.408	17.892	39	0.085	24.000	2.882	Zn	Cr51	0.668	12.628	2	0.500	12.000	6.250
Fe	Be10	1.329	26.897	26	0.058	2.600	0.674	Zn	Mn52	1.593	12.963	2	0.500	12.000	6.250
Fe	Na22	0.663	19												

**Table 3: Overall comparison of pion-induced experimental [4] and with FLUKA calculated energy-dependent production cross-sections for all isotopes where experimental data were available (statistical error below 40%)**

In addition to the average ratio and its error also the number of available data points as well as their energy range is shown

Projectile: Positive Pions								Projectile: Negative pions							
Target	Isotope	Average Ratio	Error [%]	Number of Data Points	minimum Energy [GeV]	maximum Energy [GeV]	Average Energy [GeV]	Target	Isotope	Average Ratio	Error [%]	Number of Data Points	minimum Energy [GeV]	maximum Energy [GeV]	Average Energy [GeV]
AlNat	Na24	0.438	6.752	18	0.050	0.389	0.186	AlNat	C11	1.002	18.487	6	0.450	1.760	1.107
CNat	C11	0.915	7.099	68	0.030	0.550	0.196	AlNat	Na22	0.929	16.577	7	0.069	0.285	0.176
CuNat	V48	0.683	18.187	4	0.050	0.350	0.173	AlNat	Na24	0.450	6.267	24	0.050	0.500	0.204
CuNat	Cr49	0.891	39.969	4	0.050	0.350	0.173	CuNat	C11	1.432	7.145	130	0.030	2.360	0.657
CuNat	Cr51	0.502	23.002	4	0.050	0.350	0.173	CuNat	Sc46	0.557	35.848	3	0.100	0.350	0.213
CuNat	Mn52	1.026	16.424	5	0.050	0.350	0.151	CuNat	V48	0.824	24.889	4	0.050	0.350	0.173
CuNat	Mn54	0.622	17.898	4	0.050	0.350	0.173	CuNat	Cr49	1.000	34.267	4	0.050	0.350	0.173
CuNat	Mn56	0.536	18.510	5	0.050	0.350	0.151	CuNat	Cr51	0.615	19.335	4	0.050	0.350	0.173
CuNat	Fe52	0.791	30.550	5	0.050	0.350	0.151	CuNat	Mn52	1.100	21.592	5	0.050	0.350	0.151
CuNat	Co55	0.982	19.878	4	0.050	0.350	0.173	CuNat	Mn54	0.590	16.412	4	0.050	0.350	0.173
CuNat	Co56	0.880	26.479	4	0.050	0.350	0.173	CuNat	Mn56	0.547	19.484	5	0.050	0.350	0.151
CuNat	Co57	0.771	15.086	4	0.050	0.350	0.173	CuNat	Fe59	0.670	28.886	5	0.050	0.350	0.151
CuNat	Co58	0.760	13.365	4	0.050	0.350	0.173	CuNat	Co55	1.023	21.373	4	0.050	0.350	0.173
CuNat	Co61	0.991	29.983	4	0.050	0.350	0.173	CuNat	Co56	0.837	27.433	4	0.050	0.350	0.173
CuNat	Ni57	1.480	20.580	5	0.050	0.350	0.151	CuNat	Co57	0.839	17.850	4	0.050	0.350	0.173
CuNat	Cu61	1.113	13.646	4	0.050	0.350	0.173	CuNat	Co58	0.809	14.338	4	0.050	0.350	0.173
CuNat	Zn62	1.431	25.742	5	0.050	0.350	0.151	CuNat	Co61	0.926	22.295	4	0.050	0.350	0.173
								CuNat	Ni57	1.713	28.735	5	0.050	0.350	0.151
								CuNat	Cu61	1.089	16.858	4	0.050	0.350	0.173
								FeNat	Sc46	0.621	13.081	5	0.060	0.278	0.140
								FeNat	Mn54	0.677	11.549	5	0.060	0.278	0.140
								SiNat	Na24	0.354	7.148	22	0.050	0.500	0.220

**Table 4: Comparison of all available cross-section data for natural copper as target material**

The table shows (columns from left to right) the produced isotope, its half life, the respective projectile (p...proton, pi+...positively charged pion, pi-...negatively charged pion), the isotope ratios of the natural composition (including the respective ratio in per cent) and its reaction channels (s...spallation, t...tritium, n...neutron, a...alpha, p...proton) as well as ratios observed as average values for the data compendium [4] and the experiments performed at CERF [3,5,8,9].

Isotope	Half Life	P	29	Cu	L	#	C	Isotope	Half Life	P	29	Cu	L	#	C	Isotope	Half Life	P	29	Cu	L	#	C
		o	63	65	a	of	E			o	63	65	a	of	R			o	63	65	a	of	R
		j	69	31	d.	P.	F			j	69	31	d.	P.	F			j	69	31	d.	P.	F
Be7	53.29d	p	s	s	1.33	30																	
Na22	2.603a	p	s	s	0.46	22	0.72	V48	15.97d	pi+	s	s	0.64	27	1.16	Co56	77.26d	pi+	s	s	1.15	84	1.04
Na24	14.96h	p	s	s	0.47	45	0.42			pi-	s	s	0.83	4				pi-	s	s	0.84	4	
Mg28	20.9h	p	s	s	0.55	7	0.25	Cr48	21.6h	pi+	s	s	0.86	4	0.92			pi+	s	s	0.88	93	0.85
Al28	2.246m	n	s	s	0.25					p	s	s	1.13	7	1	Co57	271.79d	pi+	s	s	0.77	4	
P32	14.26d	p	s	s	2.56	5		Cr49	42m	pi+	s	s	0.89	4				pi-	s	s	0.84	4	
S38	2.83h	p	s	s	1.02	2				pi-	s	s	1	4		Co58	70.86d	pi+	s	s	0.81	92	0.91
Cl39	56m	p	s	s	0.47	2				p	s	s	0.56	26	1.06			pi+	s	s	0.76	4	
Cl39	56m	p	s	s	0.42	12		Cr51	27.7d	pi+	s	s	0.5	4				pi-	a	s	0.81	4	
Ar41	1.83h	p	s	s	0.45	2	0.39			pi-	s	s	0.62	4		Co60	5.272a	p	pap	s	0.7	41	0.9
Ar42	33a	pi+	s	s	0.27	2				p	s	s	1.11	35	0.68			p	s	pap	0.9	11	0.68
K42	12.36h	p	s	s	0.74	9		Mn52	5.6d	pi+	s	s	1.03	5		Co61	1.65h	pi+	s	a	0.99	4	
		pi-	s	s	0.64	23	0.66			pi-	s	s	1.1	5				pi-	a	a	0.93	4	
		p	s	s	0.49	2		Mn54	312.2d	p	s	s	0.81	39	1.13	Ni56	6.075d	p	s	s	0.81	54	
		pi+	s	s	0.58	26	0.81			pi+	s	s	0.62	4				p	s	s	1.9	102	0.76
		pi-	s	s	0.63	2				pi-	s	s	0.59	4		Ni57	36.0h	pi+	s	s	1.48	5	
		pi-	s	s	0.65	3		Mn56	2.58h	p	s	s	0.64	14	0.81			pi-	s	s	1.71	5	
Ca47	4.54d	p	s	s	1.03	3	0.59			pi+	s	s	0.54	5		Ni65	2.52h	n	/	np	1.46		
Sc43	3.89h	p	s	s	0.66	5	0.4			pi-	s	s	0.55	5		Cu60	23m	p	ptn	s	0.94	57	0.78
Sc44	3.92h	p	s	s	1.51	9	0.89											p	pt	s	0.78	51	0.87
Sc46	83.82d	pi+	s	s	0.67	3		Fe52	8.27h	pi+	s	s	0.79	5				pi+	a	s	1.11	4	
		pi-	s	s	0.56	3				p	s	s	0.55	45	0.82	Cu61	3.4h	pi-	-2n	s	1.09	4	
		pi+	s	s	0.58	4	1.09	Fe59	44.5d	pi+	s	s	0.51	4				p	/	pd	0.95	38	0.63
		p	s	s	0.16	26	1.39			pi-	a	s	0.67	5		Cu64	12.7h	p	p2n	s	0.94	73	1.05
Sc47	3.35d	pi+	s	s	0.67	3				p	s	s	1.17	52	0.66			pi+	+2n	s	1.43	5	
Sc48	43.67h	pi+	s	s	0.67	3		Co55	17.54h	pi+	s	s	0.98	4		Zn62	9.13h	pi+	+2n	s	1.43	5	
		pi-	s	s	0.69	4				pi-	s	s	1.02	4		Zn65	244.3d	n	/	/	0.97		

**Figure 6: Cross-section of the FLUKA geometry used to simulate the hadronic cascade development induced by proton losses in the collimators**

Stars indicate the locations where particle spectra were scored

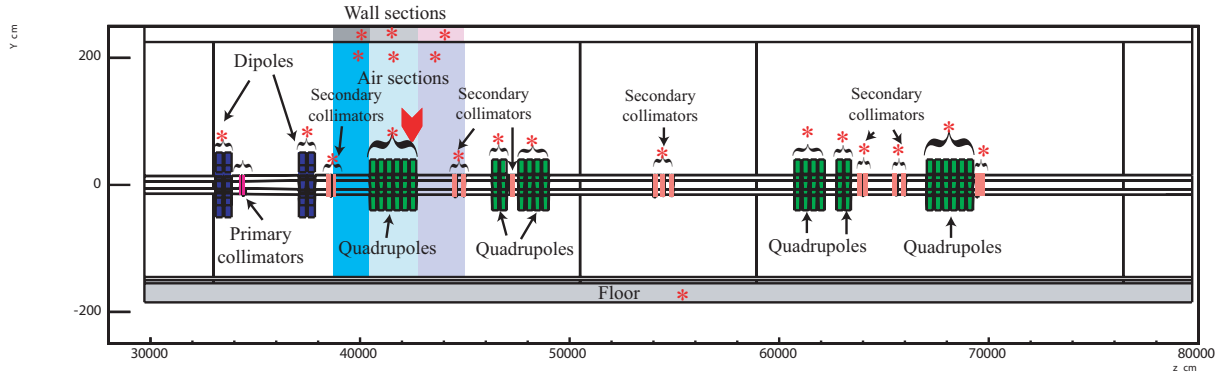


**Figure 7: Cross-sectional view of a quadrapole (left) and a collimator (right)**

The locations where the spectra are scored are indicated with red stars

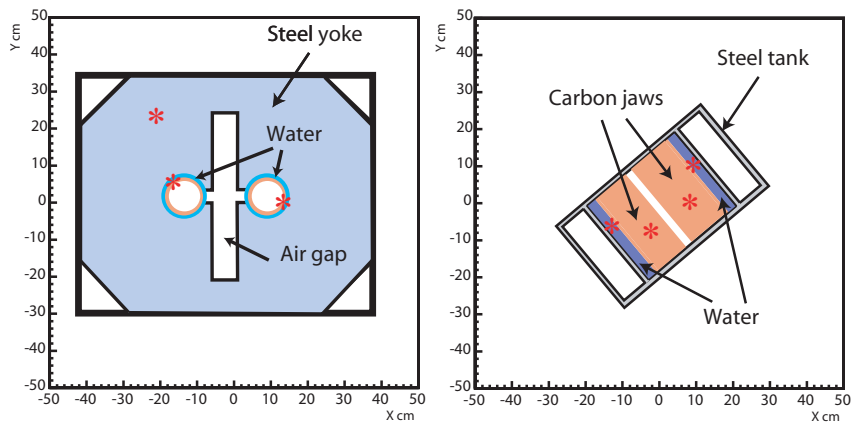
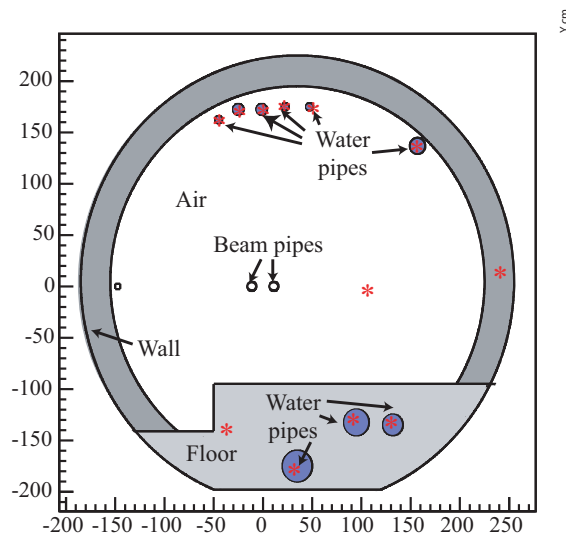


**Figure 8: Cross-section of the tunnel geometry perpendicular to the beam axis**

The locations where spectra are scored are indicated with stars



Several criteria can be defined to compare a set of spectra (in our case for four particle types) to another one at a different location. The strategy which is chosen here is to limit the study to changes in shape without taking into account the intensity which strongly depends on the distance between the region of interest and the loss points (collimators). Consequently, in a first step the spectra set is normalised to unity. The four energy spectra are integrated and the sum allows the determination of the normalisation factor.

It has to be noted that the neutron spectrum is treated in a specific way since in FLUKA the transport of neutrons below 19.6 MeV is performed using a multi-group transport algorithm and (if available) evaluated isotope production cross-sections. In this study, for the calculation of radioactive nuclei production, these low-energy neutron cross-sections were extracted from the code and folded separately with the neutron respective spectra below 19.6 MeV.

Once the sum of the fluences of protons, neutrons (above 19.6 MeV), positive pions and negative pions is normalised to unity, instead of comparing the shapes of different spectra sets for all energies, they are first multiplied with production cross-sections to limit the comparison to the part of the spectra where cross-sections are significant.

**Table 5: Radioactive nuclei production calculated for the five different reactions (ranging from “low” to “high” energies reaction channels) and different locations selected out of the numerous studied spectra sets considered**

The production calculated in the CERF samples is also indicated, the one in the lateral sample was used for the final normalisation of the results. Please note that for the water cooling the case for the first primary collimator is special in the sense that the cascade does not yet reach a maximum in the collimator, thus leads to particle spectra shifted to lower energies.

	Mn54 Mn	Mn54 Fe	Co60 Cu	Na22 Fe	Be7 Cu
Wall 1St Section	1.08E+00	1.14E+00	1.09E+00	4.78E-01	4.41E-01
Wall 3rd Section	1.15E+00	1.16E+00	1.09E+00	4.93E-01	4.41E-01
Pipe in the Floor	1.23E+00	1.34E+00	1.27E+00	1.13E-01	1.12E-01
1St Quad. Yoke	1.15E+00	1.19E+00	1.09E+00	4.93E-01	4.41E-01
Last Quad. Yoke	1.23E+00	1.25E+00	1.18E+00	3.48E-01	3.24E-01
Pipe in the air	1.00E+00	1.03E+00	1.00E+00	7.25E-01	6.76E-01
1St Quad. Water	1.00E+00	1.03E+00	1.00E+00	8.55E-01	7.65E-01
Last Quad. Water	1.00E+00	9.69E-01	1.00E+00	9.57E-01	8.82E-01
2nd Air section	9.23E-01	9.06E-01	9.00E-01	1.41E+00	1.26E+00
Beam pipe 2nd section	9.23E-01	8.59E-01	8.82E-01	1.33E+00	1.21E+00
1St Prim. Coll. Water	9.23E-01	9.38E-01	1.00E+00	6.38E-01	5.29E-01
2nd Prim. Coll. Water	7.46E-01	7.50E-01	8.09E-01	1.74E+00	1.41E+00
3rd Prim. Coll. Water	7.46E-01	7.50E-01	8.00E-01	1.74E+00	1.44E+00
2nd Second. Coll. Water	7.46E-01	7.34E-01	7.91E-01	1.74E+00	1.56E+00
3rd Second. Coll. Water	7.46E-01	7.19E-01	7.82E-01	1.74E+00	1.59E+00
Last Second. Coll. Water	7.69E-01	7.50E-01	8.18E-01	1.59E+00	1.44E+00
Beam pipe 1st section	5.31E-01	5.63E-01	6.18E-01	2.75E+00	2.41E+00
2nd Primary jaws	4.92E-01	5.47E-01	6.09E-01	2.90E+00	2.38E+00
1St Secondary jaws	6.00E-01	6.09E-01	6.82E-01	2.46E+00	2.15E+00
Last Secondary jaws	5.85E-01	5.94E-01	6.64E-01	2.46E+00	2.21E+00
CERF Downstream	5.69E-01	6.09E-01	6.64E-01	2.75E+00	2.44E+00
CERF Lateral	1.00E+00	1.00E+00	1.00E+00	1.00E+00	1.00E+00

Five different reactions are considered to take into account different reaction channels. Cross-sections were selected based on the physics mechanism involved or on the contribution of the produced isotope to the activity in the waste after significant cooling times. Those cross-sections are, ranging from the ones which can be qualified as being important at low energies to the ones dominating at higher energies, Mn54 produced respectively on Mn and Fe, Co60 produced on Cu, Na22 produced on Fe and Be7 produced on Cu.

For each reaction, the four response spectra are then integrated and the sum corresponds to the number of radioactive nuclei produced per cm of hadron track length and by units of volume. In order to validate, the general method presented here for waste calculations and particularly the relevance of the experimental verification of the FLUKA predictions, the spectra were also compared to the representative spectra in the samples which were irradiated in the CERF facility. The same procedure

described for the spectra calculated in the beam cleaning insertion is applied to two spectra sets corresponding to samples located respectively laterally and downstream the target. A part of the results obtained for the numerous studied locations is presented in Table 5 for the four reactions which were considered. The production is normalised to the one calculated in the CERF sample located laterally from the target in order to facilitate the comparison between the different locations and the CERF results.

Since the calculation of radioactive nuclei production for waste characterisation does not require a very high accuracy the spectra sets calculated in the beam cleaning insertion can be subdivided into four main groups by using the values as calculated for the five reactions (see Table 5). For each group one representative spectra set is selected and can then be used for the calculation of radioactive nuclei production at any location.

The four representative spectra sets can be characterised by the relative contribution of neutrons, protons and pions to the radionuclide production. The relative contribution is also strongly correlated to possible energy peaks of the respective spectra, *e.g.* of the positive and negative pions in the intermediate energy range or the neutron and proton spectra showing a maximum around 100 MeV and 200 MeV respectively in all cases.

- a) The first representative spectra set is the one scored in the yoke of the first quadrupole magnet module situated after the first secondary collimators. The hadronic radiation field is dominated by neutrons. Charged hadrons account only for approximately 20% of the isotope production. In terms of radioactive nuclei production, this spectrum is found representative of the situation inside the walls and floor or of pipes buried in the floor.
- b) The second representative spectra set is the one scored in the water ring surrounding the copper beam pipe. The hadronic field is rather similar than in the previous case except that the charged hadrons contribution is relatively more important and peaked at a higher energy.
- c) The third representative spectra set is scored in the water layer representing the cooling system of the first secondary collimator jaw. The contribution of the four hadron types considered is more or less equivalent in this case.
- d) The last spectrum set represents the extreme case of an object which would be located very close to the beam. In this case, positive and negative pion contributions are dominant and peaked at an even higher energy than in the previous case. This spectrum is representative of radioactive nuclei production very close or inside to the beam and consequently to the loss points.

The two first representative spectra appear to be similar in their shape to the CERF spectra located laterally to the beam target while the two other spectra sets correspond to an intermediate situation between the spectra calculated laterally and downstream of the CERF target. The locations corresponding to the same groups appear with the same colour in Table 5. The particle spectra for the different groups are represented in Figure 9.

In order to evaluate the accuracy of the method, the error which is made on the radioactive nuclei production when the representative spectra is used instead of the real one is presented in Table 6 for several extreme cases.

As an additional cross check, the same approach was studied for the part of the neutron spectra below 19.6 MeV. Several reactions like  $^{108}\text{Ag}$  production on natural Ag,  $^{57}\text{Co}$  on Ni,  $^{60}\text{Co}$  production on  $^{59}\text{Co}$ , Cu and Ni were considered. It appears that in the case of the low energy part of the neutron spectrum, finding representative spectra is less obvious than for the high energy components of the hadron field. This is due to the fact that the production of radioactive nuclei is very sensitive to possible resonances in the cross-sections. However, the same representative locations used for high energy reactions were used as a first approximation. For more accurate results a further study of additional production cross-sections should be performed. Figure 10 shows the four neutron spectra after normalisation at the four representative locations.

Table 6 shows that the disagreement reaches its maximum for reactions occurring at high energies and especially in the case of particle spectra of the first group (being sensible for source spectra at lower energies). However, in this case, radioactive nuclei induced by high energy particles will not dominate the radioactive waste considerations, thus is a good confirmation of the accuracy of the method for the selected application.

**Figure 9: Particle spectra at the different representative locations, expressed in units of lethargy and after normalisation to 1 cm of hadron track length**

(a) magnet yoke, (b) magnet water, (c) collimator water, (d) collimator jaw

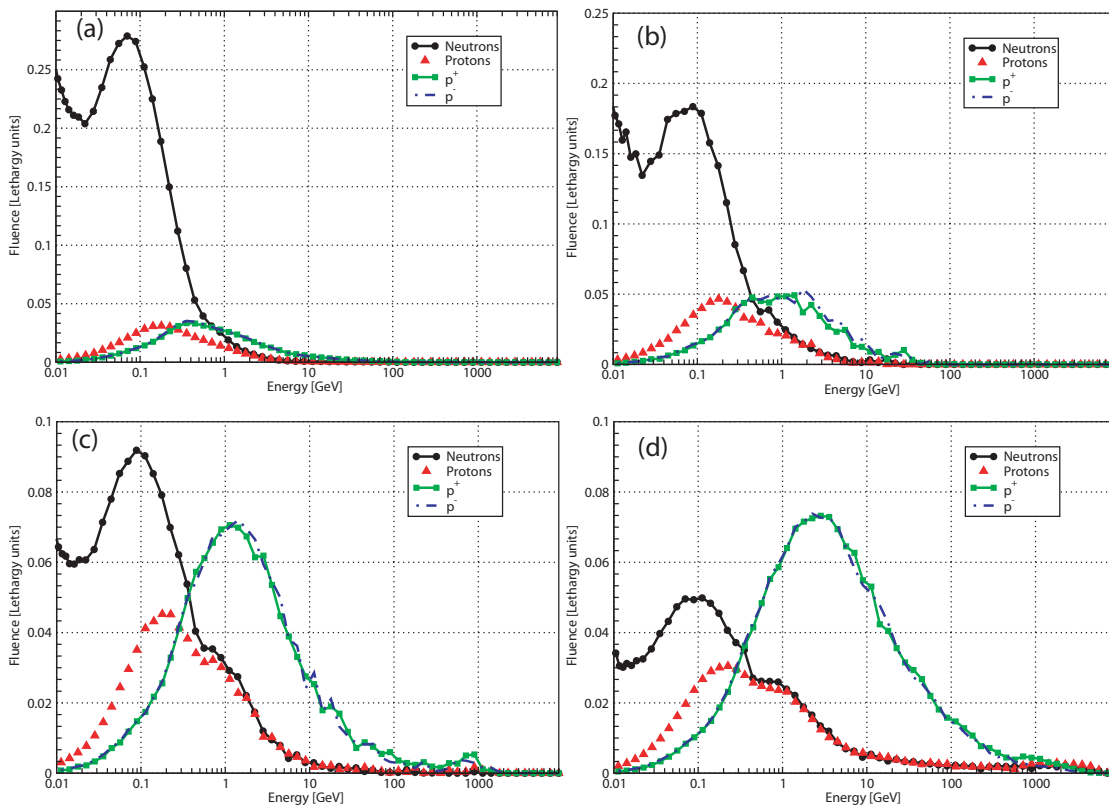


**Figure 10: Neutrons spectra below 19.6 MeV at the four representative locations**

Please note that due to the normalisation to the total track length spectra shown in Figure 9 cannot be directly joined

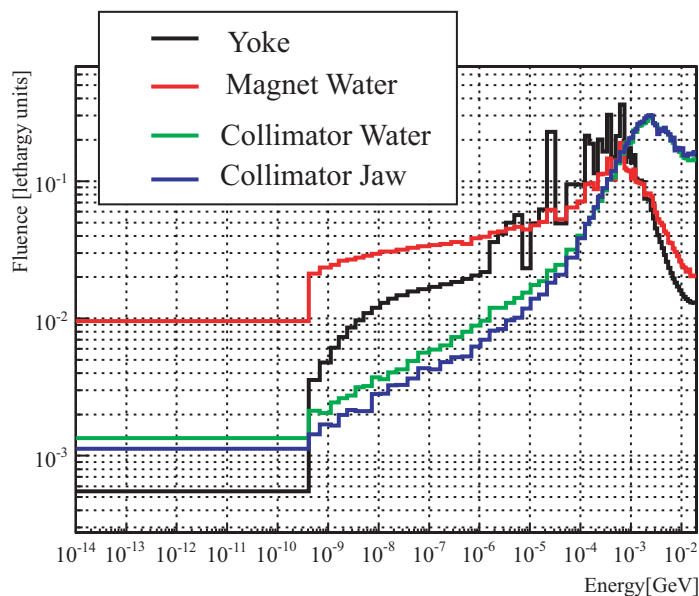


**Table 6: Relative difference in per cent when comparing the isotope production as either calculated with the representative spectra or instead with the respective actual spectrum**

	Mn54 Mn	Mn54 Fe	Co60 Cu	Na22 Fe	Be7 Cu
Wall 1St Section	1.08E+00	1.14E+00	1.09E+00	4.78E-01	4.41E-01
Wall 3rd Section	1.15E+00	1.16E+00	1.09E+00	4.93E-01	4.41E-01
Pipe in the Floor	1.23E+00	1.34E+00	1.27E+00	1.13E-01	1.12E-01
1St Quad. Yoke	1.15E+00	1.19E+00	1.09E+00	4.93E-01	4.41E-01
Last Quad. Yoke	1.23E+00	1.25E+00	1.18E+00	3.48E-01	3.24E-01
Pipe in the air	1.00E+00	1.03E+00	1.00E+00	7.25E-01	6.76E-01
1St Quad. Water	1.00E+00	1.03E+00	1.00E+00	8.55E-01	7.65E-01
Last Quad. Water	1.00E+00	9.69E-01	1.00E+00	9.57E-01	8.82E-01
Third Quad. Water	1.00E+00	9.69E-01	1.00E+00	9.28E-01	8.53E-01
2nd Air section	9.23E-01	9.06E-01	9.00E-01	1.41E+00	1.26E+00
Beam pipe 2nd section	9.23E-01	8.59E-01	8.82E-01	1.33E+00	1.21E+00
1St Prim. Coll. Water	9.23E-01	9.38E-01	1.00E+00	6.38E-01	5.29E-01
2nd Prim. Coll. Water	7.46E-01	7.50E-01	8.09E-01	1.74E+00	1.41E+00
3rd Prim. Coll. Water	7.46E-01	7.50E-01	8.00E-01	1.74E+00	1.44E+00
2nd Second. Coll. Water	7.46E-01	7.34E-01	7.91E-01	1.74E+00	1.56E+00
3rd Second. Coll. Water	7.46E-01	7.19E-01	7.82E-01	1.74E+00	1.59E+00
Last Second. Coll. Water	7.69E-01	7.50E-01	8.18E-01	1.59E+00	1.44E+00
1st Second. Water	7.69E-01	7.50E-01	8.09E-01	1.59E+00	1.44E+00
Beam pipe 1st section	5.31E-01	5.63E-01	6.18E-01	2.75E+00	2.41E+00
2nd Primary jaws	4.92E-01	5.47E-01	6.09E-01	2.90E+00	2.38E+00
1St Secondary jaws	6.00E-01	6.09E-01	6.82E-01	2.46E+00	2.15E+00
Last Secondary jaws	5.85E-01	5.94E-01	6.64E-01	2.46E+00	2.21E+00
CERF Downstream	5.69E-01	6.09E-01	6.64E-01	2.75E+00	2.44E+00
CERF Lateral	1.00E+00	1.00E+00	1.00E+00	1.00E+00	1.00E+00

### Application to the characterisation of radioactive waste

A collection of selected cross-sections and the knowledge of how well they are reproduced by FLUKA should form the basis for the establishment of a library for the determination of the nuclide inventory of radioactive waste at CERN. The motivation for the creation of a nuclide inventory is the search for a practicable method for the classification and characterisation of radioactive waste stemmed from the CERN accelerators. Accelerator operation results in material with specific activation too high to allow it to be recycled or to be unconditionally disposed. Irrespective of the method to be used for its disposal, a detailed knowledge of the nuclide inventory in the material is essential. High accuracy is not necessarily required, but the knowledge of the tolerance in many aspects (*e.g.* chemical composition, isotope production cross-sections, etc.) is of utmost importance.

Detection of radioactivity is relatively easy but the identification and quantification of the actual nuclides in the inventory is, at best, experimentally challenging and time consuming. The selection and analysis of samples is the regular technique for linking an inventory to a waste item. However, this technique is impracticable; it is time consuming and involves too much handling of the activated material contradicting the ALARA principle. Also, as measurement techniques are specific to the class of nuclides being assayed, theoretical inventory predictions are necessary for the design of the analysis programme.

In order to characterise the radioactive waste which has been produced at CERN in the last decades, gamma-spectroscopy measurements must be accompanied by predictions of induced radioactivity. This last step is particularly important for estimating the activity of nuclides which are difficult to detect, *e.g.*  $^{36}\text{Cl}$  and  $^{55}\text{Fe}$ . The nuclide inventory, which depends on the material composition and irradiation history, can then be normalised to the surface dose-rate which is measured on the actual waste before packaging and/or specific isotopes being characteristic for the respective material ("fingerprints"). In this way one can complete the predictions based on our information about the waste (chemical composition and location in the accelerator) with a measurement which reflects the actual number of particles responsible for the activation. This method is usually referred to as "fingerprint method".

Decoupling the estimate of isotope production cross-sections and particle spectra is an essential simplification by allowing each to be made with calculation methods specific to their individual needs. Folding the cross-sections with the appropriate spectra results in production rates serving as basis for the calculation of total isotope produced in the respective radioactive waste.

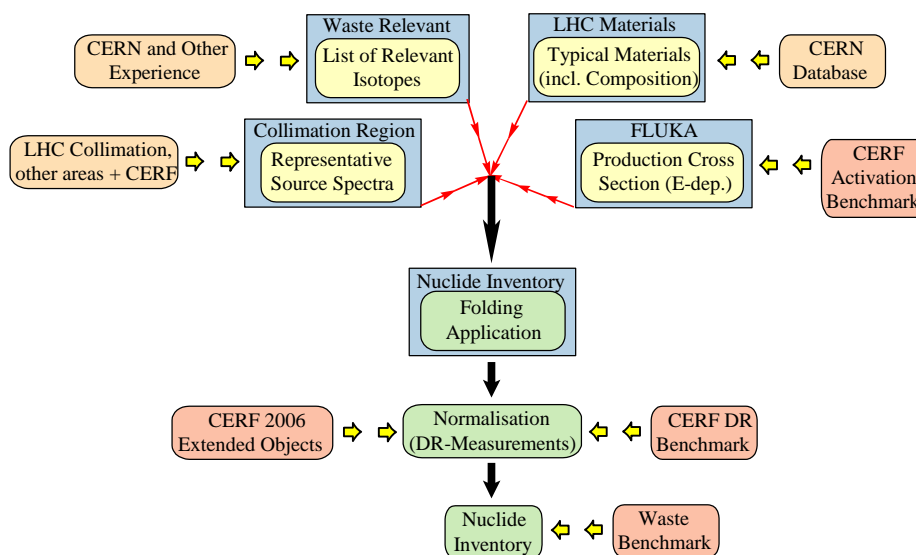
As it regards the FLUKA predictions, the exactness of the nuclide inventory relies on the cross-sections which are predicted or used by the code, on its capability of simulating the hadronic shower and on the calculation of build-up and decay of the produced nuclides. The validation of FLUKA with the past CERF experiments was an important achievement for the future waste characterisation. A good agreement between experimental values and predictions finally allow applying the fingerprints method to a large collection of objects which have been activated during real operation of the accelerator.

However, for a given specific activity, the contact dose-rate strongly depends on the geometry of the object. In particular, both the phenomenon of self-absorption and the non-uniform distribution of radioactive nuclides in the item of waste have an impact on the dose measurement. Depending on the prediction of the distribution and on the choice of the points to be measured, different conclusions can be drawn on the same radioactive item. It is therefore essential to test the accuracy of respective gamma spectroscopy and dose rate measurements with FLUKA predictions in a case where all these factors (shape, irradiation, material composition...) are well known.

All these ingredients finally lead to a scheme of necessary steps in order to quantify uncertainties and prove the needed accuracy of the nuclide vector approach in order to characterise the nuclear waste being produced at the CERN accelerators, especially the new LHC. As shown in Figure 11, this starts by developing a list of waste relevant materials and their detailed chemical composition based on an internal database. In addition, the list of relevant radioactive isotopes can be deduced from experience at CERN as well as taken from the experimental campaign carried out at CERF during the past years.

**Figure 11: Schematic approach for the characterisation of radioactive waste in order to study the applicability of the nuclide vector approach to waste characterisation at high energy accelerators**

This includes the basic requirements, the benchmark experiments as well as detailed studies of isotope production cross-sections



One furthermore needs a set of representative spectra being deduced by comparing spectra at all regions expected to produce radioactive waste. By folding with isotope production cross-sections and comparing the production yields for all source spectra it is possible to quantify the introduced uncertainties. Either model based (Monte Carlo, FLUKA) or evaluated experimental cross-sections can be used. The underlying uncertainties can then again be quantified by related benchmark measurements as carried out at the CERF facility or by comparing the calculated results to those available in evaluated databases.

This leads then to the definition of a possible nuclide inventory with underlying quantified uncertainties. In a next step one has to define the final normalisation of the results by either using dose rate measurements or the specific activity of representative isotopes. In order to quantify this final step leading to the definition of the nuclide inventory two additional benchmark measurements are needed. One regarding the accuracy of residual dose rates predicted with FLUKA (as successfully carried out during several benchmark experiments at CERF) and an experimental study of the influence on the agreement between measurement and simulation of residual activation when activating extended objects. The latter study includes the accuracy of mobile gamma spectrometers for so-called “fingerprint” measurements in order to determine the specific activity of representative isotopes (the latter currently being carried out at CERF).

A final step concerns the eventual application of the approach to *e.g.* the LHC in order to determine its nuclide inventory. During early operation of the LHC an accompanying experiment is needed in order to proof the above considered and quantified findings leading to the needed accuracy when predicting radioactive waste at high-energy accelerators like the CERN LHC.

## Summary

All stages in the life-cycle of a high energy accelerator require calculations of induced radioactivity. For accelerators reaching TeV energies, a Monte Carlo code used for such calculations must be able to reliably predict nuclide production in interactions of all stable hadrons on arbitrary target elements and at energies ranging from that of thermal neutrons to several TeV. Most studies for the Large Hadron Collider (LHC) employ the Monte Carlo code FLUKA which was found to be the most appropriate Monte Carlo code for estimations of induced radioactivity at this accelerator as demonstrated in numerous benchmark experiments.

A general analysis of calculated isotope production cross-sections and their application to future radiation protection needs was presented. The approach showed how to quantify calculation uncertainties and use pre-calculated cross-sections in order to fold them with expected energy spectra as encountered around accelerators, thus leading to fast and accurate results.

Based on a list of materials and the produced radioactive isotopes, possible reaction channels were derived and energy-dependent isotope production cross-sections were calculated and compared to experimental data. Depending on the amount and accuracy of the available experimental data sets, as well as the production mechanisms of the radioisotopes, respective uncertainty factors were derived and quantified in a first approximation. These factors mainly depend on the production mechanism and the energy range of interest, thus allow quantifying uncertainties in isotope production as calculated with FLUKA in a more global way. It shall be noted that the latter needs a more careful analysis of the available data.

The prediction of the nuclide vector for radioactive waste considerations has been chosen as a first area of application. In particular, one of the most radioactive parts of the LHC, the collimation region, was selected. Based on an existing, detailed FLUKA geometry of that area particle fluence spectra were calculated for a large number of different locations and were folded off-line with the pre-computed cross-sections for reactions leading to waste-relevant nuclides. This approach allowed an investigation of the sensitivity of the nuclide predictions on the shape of the fluence spectra and a reduction of all computed spectra to a sub-set of so-called characteristic spectra.

The application of this approach is understood to be an indispensable ingredient, for example in order to efficiently calculate radionuclide inventories needed for disposal of radioactive waste towards the final repositories.

## Acknowledgements

The authors are grateful to Alberto Fassò, Doris Forkel-Wirth and Luisa Ulrici for many stimulating discussions.

## References

- [1] A. Fassò, A. Ferrari, J. Ranft, P.R. Sala, *FLUKA: a Multi-Particle Transport Code*, CERN-2005-10 (2005), INFN/TC\_05/11, SLAC-R-773.
- [2] A. Fassò, A. Ferrari, S. Roesler, P.R. Sala, G. Battistoni, F. Cerutti, E. Gadioli, M.V. Garzelli, F. Ballarini, A. Ottolenghi, A. Empl, J. Ranft, "The Physics Models of FLUKA: Status and Recent Developments", *Computing in High Energy and Nuclear Physics 2003 Conference (CHEP2003)*, La Jolla, CA, USA, 24-28 March 2003, (paper MOMT005), eConf C0303241 (2003), arXiv:hep-ph/0306267.
- [3] M. Brugger, A. Ferrari, S. Roesler, L. Ulrici, "Validation of the FLUKA Monte Carlo for Predicting Induced Radioactivity at High-energy Accelerators", *Proceedings of the International Conference of the 7<sup>th</sup> International Conference on Accelerator Applications*, Venice, Italy, 2005, *Nuclear Instruments and Methods in Physics Research Section A*, Volume 562, Issue 2, pp. 814-818.
- [4] Landolt-Börnstein, *Zahlenwerte und Funktionen aus Naturwissenschaften und Technik, Radionuklidproduktion bei mittleren Energien*, Bd. 13, Springer Verlag, 1991.
- [5] M. Brugger, S. Roesler, L. Ulrici, "Benchmark Study of Radionuclide Production with FLUKA", *Proceedings of the Monte Carlo 2005 Conference*, Chattanooga, TN, USA, 17-21 April 2005.
- [6] M. Brugger, S. Roesler, "Remanent Dose Rates Around the Collimators of the LHC Beam Cleaning Insertion", *Proceedings of the 10<sup>th</sup> International Conference on Radiation Shielding, ICRS-10*, Funchal (Madeira), Portugal, 9-14 May 2004, *Radiat. Prot. Dosim.* (2005), Vol. 115, No. 1-4, pp. 470-474.
- [7] A. Mitaroff, M. Silari, "The CERN-EU High-energy Reference Field (GERF) Facility for Dosimetry at Commercial Flight Altitudes and in Space", *Radiat. Prot. Dosim.*, 102, pp. 7-22 (2002).
- [8] M. Brugger, H. Khater, S. Mayer, A. Prinz, S. Roesler, L. Ulrici, H. Vincke, "Benchmark Studies of Induced Radioactivity Produced in LHC Materials, Part I: Specific Activities", *Radiation Protection Dosimetry*, 116, pp. 6-11 (2005).
- [9] M. Brugger, H. Khater, S. Mayer, A. Prinz, S. Roesler, L. Ulrici, H. Vincke, "Benchmark Studies of Induced Radioactivity Produced in LHC Materials, Part II: Remanent Dose Rates", *Radiation Protection Dosimetry*, 116, pp. 12-15 (2005).
- [10] A. Ferrari, *et al.*, "Nuclear Models in FLUKA: Present Capabilities, Open Problems and Future Improvements", invited talk in *Proceedings of the International Conference on Nuclear Data for Science and Technology*, Santa Fe, NM, 26 September-1 October 2004, R.C. Haight, M.B. Chadwick, T. Kawano, P. Talou (Eds.), *AIP Conference Proceedings* 769, 1197-1202 (2005).



## Experimental studies of proton-induced reaction cross-sections on natural molybdenum

**Mayeen Uddin Khandaker, Kwangsoo Kim, Guinyun Kim**  
Department of Physics, Kyungpook National University, Daegu

**Young Seok Lee**  
Pohang Accelerator Laboratory, Pohang University of Science and Technology, Pohang

### Abstract

*The proton-induced reaction cross-sections for the reactions of  $^{nat}\text{Mo}(p, xn)^{99m, 96(m+g), 95g, 95m, 94g}\text{Tc}$  were measured by using a stacked-foil technique in the energy range of 10-30 MeV at the MC50 cyclotron of the Korea Institute of Radiological and Medical Sciences. The radioactivity of the activation products was determined by the high-resolution  $\gamma$ -ray spectrometry. Excitation functions for the production of  $^{99m}\text{Tc}$ ,  $^{96(m+g)}\text{Tc}$ ,  $^{95m}\text{Tc}$ ,  $^{95g}\text{Tc}$ , and  $^{94g}\text{Tc}$  radioisotopes were measured, and compared with the earlier reported experimental data. The present measurements are in generally good agreement with all other reported data and the theoretical data from MENDL-2P in the investigated energy region.*

## Introduction

Beside the general interest of basic nuclear physics, the activation data in the intermediate energy regions are of increasing importance for a wide variety of applications: medical radioisotope production, and radiation therapy, spallation neutron sources, radiation and shielding effects in space, accelerator-based nuclear waste transmutation and energy production. The activation cross-sections on different structural and instrumentation materials induced by proton reactions have primary importance. Natural molybdenum (Mo) is an important structural material. The cross-section data on molybdenum are of interest for wide area; the thin layer activation technique (TLA) to determine the ratio of wear, corrosion and erosion processes of molybdenum, radiation safety, and estimation of radioactive wastes. Molybdenum is used as target material for the production of medical radioisotopes like as  $^{99m}\text{Tc}/^{99}\text{Mo}$ ,  $^{96}\text{Tc}$ , etc.  $^{99}\text{Mo}$  is the parent nuclide of the daughter  $^{99m}\text{Tc}$ , which is widely used in diagnostic nuclear medicine.

We used a natural molybdenum as the target material for the production of medically important radioisotopes; such as production of  $^{99m}\text{Tc}$ ,  $^{96(m+g)}\text{Tc}$ ,  $^{95m}\text{Tc}$ ,  $^{95g}\text{Tc}$ , and  $^{94g}\text{Tc}$ . This isotope production via proton induced reaction on natural molybdenum is very advantageous because of its metallic form, favourable physiochemical characteristics (good thermal and electrical conductivity, and its very high melting point: 2 896 K) and of its low buying cost [1]. These isotopes can be produced commercially by nuclear reactors. But the facility is not available around the world and is also expensive. These radioisotopes can also be produced by accelerator, though currently no supply of accelerator-produced isotopes of these kinds are available anywhere in the world. But, it is possible to produce the medically important radioisotopes such as  $^{99m}\text{Tc}$  and  $^{99}\text{Mo}$  by proton bombardment on natural molybdenum via one proton-one neutron and two neutron emission reactions, respectively. Several authors [2-4] have reported a variety sets of data for proton induced activation cross-sections on molybdenum in the medium energy range. But large discrepancies are found among these sets of data. Therefore, the available data are not sufficient and reliable for the application in production of isotopes from molybdenum target in the medium energy range.

This work was performed to measure the production cross-sections of  $^{99m}\text{Tc}$ ,  $^{96(m+g)}\text{Tc}$ ,  $^{95m}\text{Tc}$ ,  $^{95g}\text{Tc}$ , and  $^{94g}\text{Tc}$  radioisotopes in proton induced reactions on natural molybdenum in the energy range 10-30 MeV using a stacked-foil activation technique and the azimuthally varying field-type (AVF) MC-50 cyclotron at Korea Institute of Radiological and Medical Sciences (KIRAMS).

## Experimental technique

In the present work, the excitation functions of  $^{nat}\text{Mo}(p,xn)^{99m,96(m+g),95g,95m,94g}\text{Tc}$  reactions were measured by using a stacked-foil activation technique combined with high resolution gamma-ray spectrometry. Special care was taken in preparation of uniform targets with known thickness, determination of the proton energy degradation and the intensity of the proton beam along the stacked target, and also in determination of the activities of the samples.

High purity (>99.99%) molybdenum foil (100  $\mu\text{m}$  thick) with a natural isotopic composition ( $^{92}\text{Mo}$  14.84%,  $^{94}\text{Mo}$  9.25%,  $^{95}\text{Mo}$  15.92%,  $^{96}\text{Mo}$  16.68%,  $^{97}\text{Mo}$  9.55%,  $^{98}\text{Mo}$  24.13% and  $^{100}\text{Mo}$  9.63%) was used as the target for the irradiation. Monitor foils of copper (100- $\mu\text{m}$  thick) and aluminium (100- $\mu\text{m}$ -1.2mm thick) with known cross-sections were also included in the stack.

These three types of foils were stacked together as Al-Cu-Mo, and five groups were set together in an aluminium holder for the irradiation. The aluminium and the copper foils were used to monitor the beam intensity and to degrade the beam energy, respectively. These stacked samples were then irradiated for 30 minutes at a proton energy of 35 MeV, a diameter of 1 mm, and a beam current of 45-50 nA in the external beam line of the MC-50 cyclotron. The beam intensity was kept constant during irradiation. It was necessary to ensure that equal areas of the monitor and the target foils intercepted the beam. The irradiation geometry was kept in a position so that the foils received the maximum beam intensity.

## Data analysis

The activities of the radioisotopes produced from the target and the monitor foils were measured continuously using high purity germanium detector (HPGe) for the gamma-ray measurements. The source-to-detector distances was kept long enough (10–80 cm) to assure low dead time and a point-like geometry. The HPGe-detector was coupled with a 4096 multi-channel analyser (MCA) with the associated electronics to determine the photo-peak area of the gamma-ray spectrum. The spectrum analysis was done using the program Gamma Vision 5.0 (EG&G ORTEC). In consideration of the cases of long-lived radionuclide, the activity measurements were done after a sufficient cooling time. This was done to ensure complete decay of most of the undesired short-lived nuclide so that we could identify and separate the complex gamma lines easily. The detection efficiency as a function of the gamma energy for the HPGe-detector was determined experimentally by using standard gamma-ray sources with known strengths,  $^{133}\text{Ba}$ ,  $^{57}\text{Co}$ ,  $^{60}\text{Co}$ ,  $^{137}\text{Cs}$ ,  $^{54}\text{Mn}$ , and  $^{109}\text{Cd}$  at 10 to 80 cm from the endcap of the detector.

The proton beam intensity was determined via the monitor reactions,  $^{\text{nat}}\text{Cu}(p,x)^{62,65}\text{Zn}$ . The beam energy degradation along the stack was determined using the computer program SRIM-2003 [5] by assuming the incident energy of 35 MeV. The activities of the Cu monitor foils and of the Al energy-degrader foils were measured in the same geometry as the molybdenum targets and with the same HPGe detector calibrated by using the above-mentioned standard gamma-ray sources. The use of multiple monitor foils decreases the probability of introducing unknown systematic errors in the activity determination.

The cross-sections of the investigated reactions in the proton energy range 10–30 MeV were determined by using the well-known activation formula:

$$\sigma = \frac{\text{CPS} \times \exp^{\lambda t_d}}{\varepsilon \times N \times \phi \times I_\gamma (1 - \exp^{-\lambda t_{\text{irr}}})} \quad (1)$$

where CPS is a net counts per second under a photo peak,  $\lambda$  is the disintegration constant,  $I_\gamma$  is gamma ray intensity,  $\varepsilon$  is the efficiency of the detector,  $t_{\text{irr}}$  is the irradiation time,  $\phi$  is the proton flux,  $t_d$  is the decay time, and  $N$  is the total number of target nuclide. The nuclear data for the monitors and molybdenum used in this calculation were taken from the table of radioactive isotopes [6], and the threshold energies were calculated using the Qtool in the Los Alamos National Laboratory T-2 Nuclear Information Service [7]. The standard cross-section data for the monitors was taken from the data base for medical radioisotope production [8].

The total uncertainty of the measured experimental cross-section data mainly depends on the quality of the monitor data used, the uncertainty in the number of target nuclei (uniformity and thickness of the used target foils), the counting statistics and peak area determination, the separation of complex peaks, the nuclear data and gamma-ray abundance, and the detector efficiencies that are used in the data evaluation. The total uncertainties of the measured cross-sections were calculated by considering the statistical uncertainties and other uncertainties. The total uncertainties were derived as follows; the statistical error (1–13%), the error in the monitor flux (2–4%), the error due to the beam flux energy (2–4%), the error due to the detector efficiency (0.5–2%), and the error due to the gamma-ray intensity (1–2%). The overall uncertainty of the cross-section measurements was around 10%.

**Table 1: Measured production cross-sections of  $^{99\text{m}},^{96(\text{m}+\text{g})},^{95\text{m}},^{95\text{g}},^{94\text{g}}\text{Tc}$  radioisotopes**

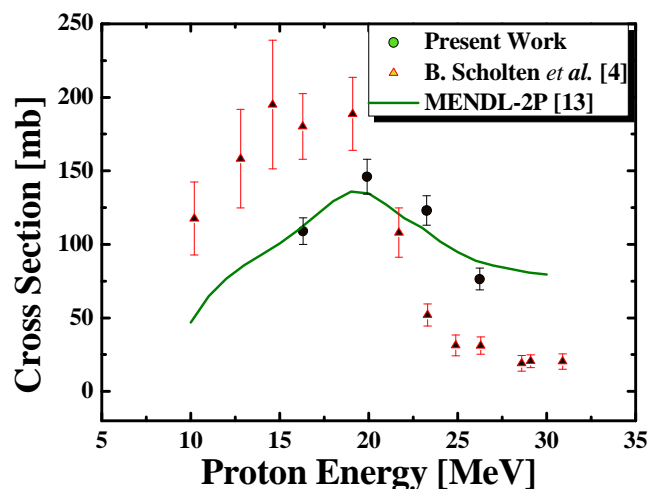
Produced nuclide	Cross-sections (mb) at energies				
	26.235 MeV	23.252 MeV	19.931 MeV	16.311 MeV	11.755 MeV
$^{99\text{m}}\text{Tc}$	$76.38 \pm 7.30$	$123.0 \pm 10.03$	$146.0 \pm 11.96$	$109.0 \pm 9.04$	–
$^{96(\text{m}+\text{g})}\text{Tc}$	$161.00 \pm 13.29$	$134.06 \pm 12.29$	$115.08 \pm 11.25$	$133.60 \pm 12.48$	$127.80 \pm 14.07$
$^{95\text{m}}\text{Tc}$	$43.75 \pm 5.22$	$51.10 \pm 8.17$	$50.47 \pm 6.46$	$50.53 \pm 6.65$	$44.22 \pm 7.64$
$^{95\text{g}}\text{Tc}$	$148.30 \pm 11.92$	$155.60 \pm 12.68$	$138.60 \pm 11.45$	$119.40 \pm 10.34$	$70.00 \pm 7.74$
$^{94\text{g}}\text{Tc}$	$73.72 \pm 6.69$	$74.12 \pm 6.99$	$62.48 \pm 6.24$	$51.63 \pm 5.12$	$29.60 \pm 3.84$

## Results and discussions

The measured production cross-sections of the  $^{99m}\text{Tc}$ ,  $^{96(m+g)}\text{Tc}$ ,  $^{95g}\text{Tc}$ ,  $^{95m}\text{Tc}$ ,  $^{94g}\text{Tc}$  radioisotopes for the proton-induced reactions on molybdenum are presented in Table 1 and compared with other existing data in Figures 1-5 respectively. The production cross-section of  $^{99m}\text{Tc}$  is calculated by analysing the 140.51-keV gamma-ray peak. Basically, this radionuclide can be produced in two processes. One is direct process through the reaction  $^{100}\text{Mo}(p,2n)^{99m}\text{Tc}$  and the other is indirect process via  $^{100}\text{Mo}(p,pn)^{99}\text{Mo} \rightarrow ^{99m}\text{Tc}$  reaction. Also, theoretically, the reaction  $^{98}\text{Mo}(p,\gamma)^{99m}\text{Tc}$  can contribute to the production cross-section of  $^{99m}\text{Tc}$ , but in the present calculation, we did not consider this process because the cross-section of the  $^{98}\text{Mo}(p,\gamma)^{99m}\text{Tc}$  reaction is negligible [4], so we only considered the formation of a radionuclide in an isomeric state.

The present result for  $^{99m}\text{Tc}$  radionuclide formation is shown in Figure 1. We found a good agreement with the evaluated data MENDL-2P [13]. The data reported by Scholten, *et al.* [4] is much higher than our data in the proton energy less than 20 MeV and much lower than our data in other proton energy region. In their experiment, they worked with the 97.4% and 99.5% enriched  $^{100}\text{Mo}$  and  $^{98}\text{Mo}$  sample, respectively but we used natural molybdenum. Moreover, it should be emphasised that the  $^{100}\text{Mo}(p,2n)^{99m}\text{Tc}$  reaction cannot be compared to a normal (p,2n) reaction because the product activity is from an isomeric state. Actually, the systematic is generally valid for total (p,xn) cross-sections but not for the formation of higher spin isomers. Even detailed statistical model calculations incorporating a pre-compound model and nuclear structural effects are often incapable of reproducing the isomeric cross-section [9]. An accurate experimental data base is, thus, crucial to consider the feasibility of this reaction for a possible production of  $^{99m}\text{Tc}$  at a cyclotron. A limiting factor in this regard would be the level of co-produced long-lived  $^{99g}\text{Tc}$  impurity. Experimentally, this is very hard to determine and was outside the scope of the present work.

Figure 1: Production cross-section of  $^{nat}\text{Mo}(p,xn)^{99m}\text{Tc}$



The radioisotope  $^{96m}\text{Tc}$  decays into  $^{96g}\text{Tc}$  through the internal conversion process (98%) and contributes to a very weak gamma line and are not suitable for quantitative assessment.  $^{96m}\text{Tc}$  also decays into  $^{96}\text{Mo}$  by electron capture and positron emission, but the gamma lines emitted during the decay are also very weak and not independent. Moreover, as the half-life of  $^{96m}\text{Tc}$  is only 51 minutes, it decays completely during greater than few hours of cooling time. However,  $^{96}\text{Nb}$  also have very small (because the production cross-section of the  $^{96}\text{Nb}$  nuclide is on the order of 1-2 mb) contribution in 778.224-keV gamma line. As  $^{96m}\text{Tc}$  emits very weak gamma line that is not suitable for analysis, and the production cross-section of  $^{96}\text{Nb}$  is small; that is why an improper cooling time or an incomplete separation of its contribution will cause only a minor error in the resulting cross-section of the  $^{96g}\text{Tc}$  production. As in the present experiment, we considered a short cooling time, that is why by analysing the 778.224-keV gamma-ray peak, we were able to get the production cross-section of  $^{96(m+g)}\text{Tc}$  radionuclide through the (p,xn) reaction.

Basically, to obtain the reliable results, we measured the production cross-section of  $^{96(m+g)}\text{Tc}$  radionuclide but not the  $^{96g}\text{Tc}$  radionuclide, because we know that for a short cooling time both ( $^{96m}\text{Tc}$  and  $^{96g}\text{Tc}$ ) radionuclides contribute to the 778.224-keV gamma-ray peak. We confirmed consistency between the results at 812.5 keV and at 778.2 keV. We found that the result obtained by analysing the 812.5-keV peak had a slightly smaller cross-section than the 778.224-keV peak; this is optimistic because 812.5 keV is the intensity independent gamma peak for the  $^{96g}\text{Tc}$  radionuclide. However, the measured excitation function of  $^{96(m+g)}\text{Tc}$  production is shown in Figure 2. It is a sum of three processes:  $^{96}\text{Mo}(p,n)^{96}\text{Tc}$  ( $Q = -3.79$  MeV),  $^{97}\text{Mo}(p,2n)^{96}\text{Tc}$  ( $Q = -10.69$  MeV), and  $^{98}\text{Mo}(p,3n)^{96}\text{Tc}$  ( $Q = -19.42$  MeV). Our results showed very good agreement with the recent data reported by Takacs, et al. [10], and Uddin, et al. [11] and evaluated data in MENDL-2P [13], and this fact confirms the reliability of the measured cross-section values of  $^{96(m+g)}\text{Tc}$  production.

Figure 2: Production cross-section of  $^{nat}\text{Mo}(p,xn)^{96(m+g)}\text{Tc}$

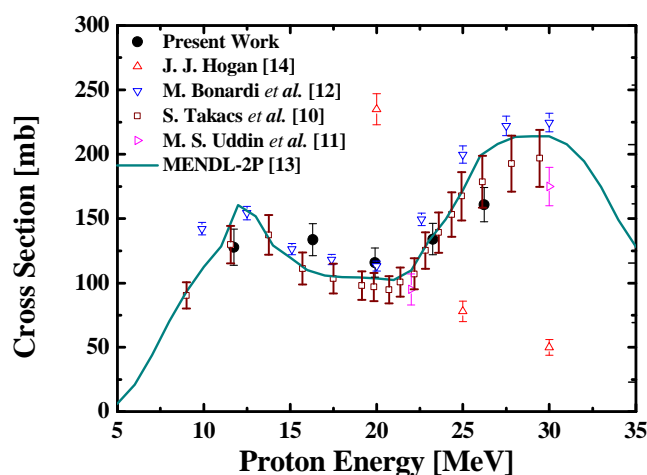
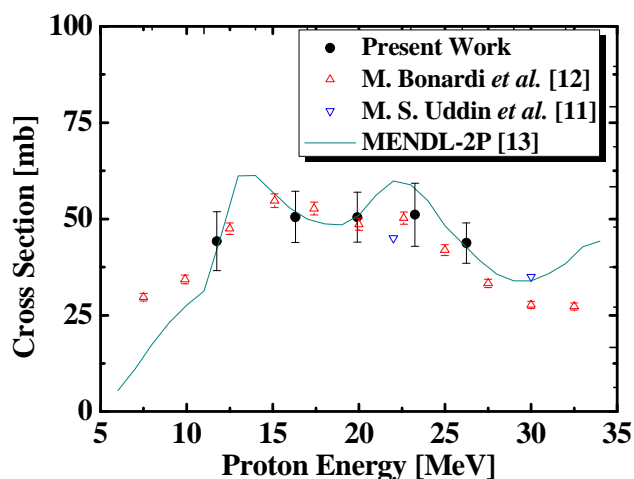


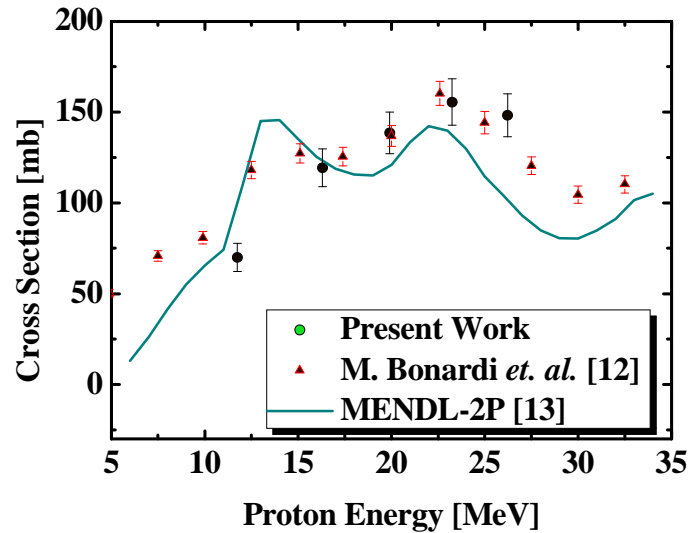
Figure 3: Production cross-section of  $^{nat}\text{Mo}(p,xn)^{95m}\text{Tc}$



The production cross-section of  $^{95m}\text{Tc}$  is calculated by analysing the 835.149-keV ( $I_\gamma = 26.63\%$ ) gamma peak and the 204.117 keV ( $I_\gamma = 63.25\%$ ) gamma peak which includes some contributions from the  $^{95m}\text{Nb}$  reaction. The present analysis used only the 835.149-keV gamma peak, which is independent of other processes. The present result for  $^{95m}\text{Tc}$  radionuclide formation is shown in Figure 3. The availability of the reported cross-sections for this ( $^{95m}\text{Tc}$ ) radionuclide formation is not sufficient. However, we compared our data with the recent published values published by Bonardi, et al. [12], Uddin, et al. [11], and contained in MENDL-2P [13], and we got good agreement.

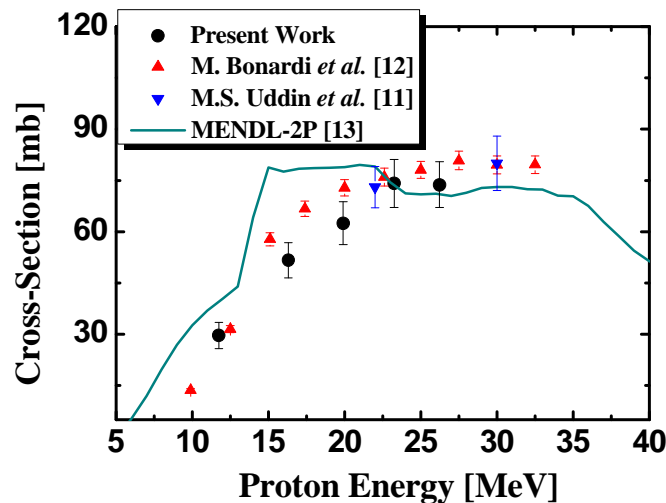
In order to calculate the production cross-section of  $^{95g}\text{Tc}$  radionuclide, we considered the 765.789-keV gamma line and confirmed the result with the 1073.713-keV gamma line. The present result for  $^{95g}\text{Tc}$  radionuclide formation is shown in Figure 4. This is the sum of the  $^{95}\text{Mo}(p,n)^{95}\text{Tc}$  ( $Q = -2.47$  MeV),  $^{96}\text{Mo}(p,2n)^{95}\text{Tc}$  ( $Q = -11.74$  MeV),  $^{97}\text{Mo}(p,3n)^{95}\text{Tc}$  ( $Q = -18.44$  MeV), and  $^{98}\text{Mo}(p,4n)^{95}\text{Tc}$  ( $Q = -27.09$  MeV) processes. In this case, our results showed good agreement with the latest data reported by Bonardi, *et al.* [12] and with the value estimated by MENDL-2P [13].

Figure 4: Production cross-section of  $^{nat}\text{Mo}(p,xn)^{95g}\text{Tc}$



In order to identify the  $^{94g}\text{Tc}$ , it was necessary to follow the decay of the gamma-emission at 702.630-keV, since the gamma ray at 871.097-keV is shared with the metastable state. The present result of  $^{94g}\text{Tc}$  radionuclide formation is shown in Figure 5. Our results showed good agreement with the data reported by Bonardi, *et al.* [12] and Uddin, *et al.* [11] and with the value estimated by MENDL-2P [13]. Due to the short half-life and the existence of numerous reaction channels, this radionuclide was produced abundantly in the investigated energy region studied in the present work.

Figure 5: Production cross-section of  $^{nat}\text{Mo}(p,xn)^{94g}\text{Tc}$



## Conclusions

We measured the excitation functions for the production of  $^{99m}\text{Tc}$ ,  $^{96(m+g)}\text{Tc}$ ,  $^{95m}\text{Tc}$ ,  $^{95g}\text{Tc}$ , and  $^{94g}\text{Tc}$  radioisotopes with an overall uncertainty in the range of 10% for proton-induced reactions on natural molybdenum in the energy range of 10-30 MeV by using a stacked-foil activation technique at the MC-50 cyclotron of KIRAMS. The present measurements are in good agreement with other experimental data reported by Takacs, *et al.* [10] Uddin, *et al.* [11], and Bonardi, *et al.* [12], and with the evaluated data in MENDL-2P [13].

## Acknowledgements

The author would like to express their sincere thanks to the staffs of the MC-50 Cyclotron Laboratories for their cordial help in performing the irradiations of the samples. This work is partly supported through the Project number M2-0409-0001 of the Ministry of Science and Technology (MOST) and through the Science Research Centre (SRC) programme of the Centre for High Energy Physics, Kyungpook National University.

## References

- [1] R.B. Firestone, C.M. Baglin, F.S.Y. Chu, *Table of Isotopes*, 8<sup>th</sup> Edition, Update on CD-ROM, Wiley, New York (1998).
- [2] S.M. Kormali, D.L. Swindle, E.A. Schweikert, *J. Radiat. Chem.*, 31, 437 (1976).
- [3] P.M. Grant, B.R. Erdal, H.A. O'Brien, *Appl. Radiat. Isot.*, 34, 1631 (1983).
- [4] B. Scholten, R.M. Lambrecht, H. Vera Ruiz, S.M. Qaim, *Appl. Radiat. Isot.*, 51, 69 (1999).
- [5] J.F. Ziegler, J.P. Biersack, U. Littmark, *SRIM 2003 code, Version 96.xx, The Stopping and Range of Ions in Solids*, Pergamon, New York (2003).
- [6] E. Browne, R.B. Firestone, *Table of Radioactive Isotopes*, V.S. Shirley (Ed.), Wiley, New York (1986).
- [7] *Reaction Q-values and Thresholds*, Los Alamos National Laboratory, T-2 Nuclear Information Service, <http://t2.lanl.gov/data/qtool.html>.
- [8] *Monitor Cross-section Data*, [www-nds.iaea.org/medical/cup62zn.html](http://www-nds.iaea.org/medical/cup62zn.html).
- [9] S.M. Qaim, in *Proceedings of International Conference on Nuclear Data for Science and Technology*, J.K. Dickens (Ed.), Gatlinburg, TN, May (1994), p. 186.
- [10] S. Takacs, F. Tarkanyi, M. Sonck, A. Hermanne, *Nucl. Instr. Meth.*, B 198, 183 (2002).
- [11] M.S. Uddin, M. Hagiwara, F. Tarkanyi, F. Ditroi, M. Baba, *Appl. Radiat. Isot.*, 60, 911 (2004).
- [12] M. Bonardi, C. Birattari, F. Groppi, E. Sabbioni, *Appl. Radiat. Isot.*, 57, 617 (2002).
- [13] *Medium Energy Activation Cross-sections Data: MENDL-2P*, [www-nds.iaea.org/nucmed.html](http://www-nds.iaea.org/nucmed.html).
- [14] J.J. Hogan, *Phys. Rev.*, C6, 810 (1972).



## Simulation and measurements of induced radioactivity in permanent magnet

Rui Qiu,<sup>1,2</sup> Hee-Seock Lee,<sup>1</sup> Sukmo Hong,<sup>1</sup> Junli Li<sup>2</sup>

<sup>1</sup>Pohang Accelerator Laboratory, POSTECH, Pohang, South Korea

<sup>2</sup>Tsinghua University, Beijing, China

### Abstract

To avoid unjustified exposure of personnel and environment, the induced radioactivity in permanent magnet used in synchrotron light source, has been studied. At the same time, the investigation on the activation of permanent magnet is a new approach to analyse the mechanism of radiation induced demagnetisation, which is an important issue on the insertion device of synchrotron light sources.

The activation of the permanent magnet is estimated with Monte Carlo simulation and validated with experiment. The yields of remnant nuclides in permanent magnet due to 2.5 GeV incident electrons and secondary particles are estimated with Monte Carlo code, FLUKA (2005 version). The saturated activity of each radioactive isotope is derived and compared with the exempt level. The remnant dose rate at 1m from the magnet due to these radioactive nuclides is calculated. Cooling time dependence of the dose rate is also derived according to the half life of the radioactive nuclides. The spatial distribution of induced radioactivity inside the magnet is also investigated. Different targets (Cu, Ta) and different magnets ( $\text{Nd}_2\text{Fe}_{14}\text{B}$ ,  $\text{Sm}_2\text{Co}_{17}$ ) are used and the results are compared.

In the experiment, the magnet samples are irradiated by 2.5 GeV electron beam from an injection linac of Pohang Light Source. The gamma spectrometry is done with an HPGe detector. Monte Carlo simulation with MCNP5 is used to get the accurate efficiency of the detector. The calculation and measurement results for  $\text{Nd}_2\text{Fe}_{14}\text{B}$  in Cu target case are compared and they agree within a factor of 2 for most of the isotopes.

## Introduction

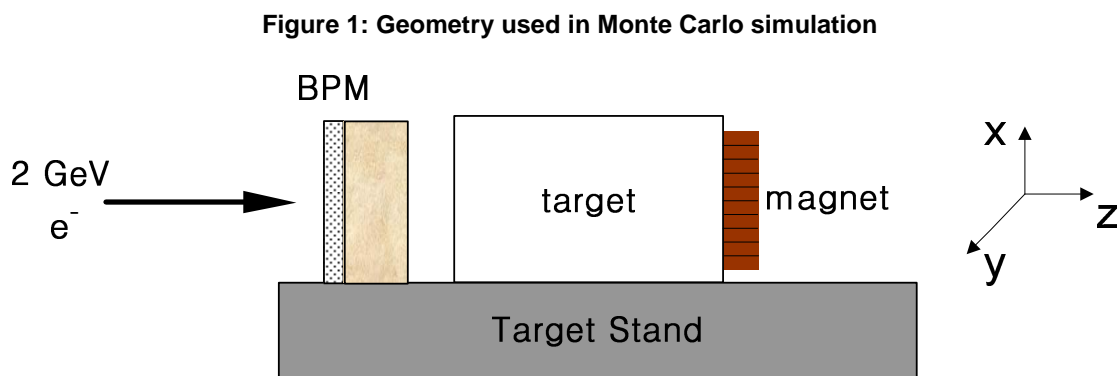
One of the main radiation safety issues at high energy electron accelerators is the activation in beam line components and equipments. This is the case not only during the operation and maintenance of the machine but also in decommissioning and final disposal of the activated materials. In all cases, accurate calculations of the radionuclide inventory are required in order to avoid unjustified exposure of personnel and environment.

Many permanent magnets are used at insertion devices and other components in accelerators. Usually, the material of the magnets is  $\text{Nd}_2\text{Fe}_{14}\text{B}$  or  $\text{Sm}_2\text{Co}_{17}$ . During operation these magnets endure the radiation from primary electrons and the secondary particles such as neutrons, protons, pions and muons. The accurate estimation of the induced activity in the permanent magnets is necessary for the radiation protection of the maintenance radiation worker. In this work Monte Carlo simulation and measurement are carried out to estimate the radionuclide production in the permanent magnets at the electron linac of Pohang Light Source.

At the same time, the demagnetisation of permanent magnets due to radiation damage is one of the most important issues of future light sources [1-4]. However, the mechanism of the demagnetisation caused by radiation is still not clear. Some experiments have been carried out at the electron linac of Pohang Light Source [5,6]. This work will also give some useful information on the effects of the radiation to permanent magnets.

## Calculation model and method

The beam energy is 2.5 GeV and the beam has a 5 mm × 10 mm cross-sectional dimension. The schematic geometry in this Monte Carlo simulation is shown in Figure 1. The simulation was performed with a target or without a target (no target case). When there was a target, the beam was injected into a 40 mm-thick target block after passing through a 1 mm-thick beam profile monitor and a 10 mm-thick backing Bakelite. The magnet was put behind the target. The electromagnetic gamma shower was developed and neutrons were generated due to the high energy electrons and photons. When there was no target, the beam was incident on the magnet directly.



The magnet material was  $\text{Nd}_2\text{Fe}_{14}\text{B}$  or  $\text{Sm}_2\text{Co}_{17}$ . The magnet sample was of the same size as the magnet for the standard in-vacuum undulator [4]. They were 46 mm × 12 mm × 8 mm blocks. In order to find out the spatial distribution of induced radioactivity inside the magnet, the magnet was divided into 23 pieces, each of which had a dimension of 2 mm × 12 mm × 8 mm. The target material was Cu or Ta. The physical properties of the targets are shown in Table 1.

**Table 1: Physical properties of the targets**

Target	Z	A	$X_0$ (cm)	Thickness (cm)
Copper (Cu)	29	63.5	1.43	4.2 (2.94 $X_0$ )
Tantalum (Ta)	73	180.9	0.41	4.0 (9.75 $X_0$ )

Monte Carlo code FLUKA [7] was used to simulate the particle interaction and transport in these materials. Neutrons were transported down to thermal energies; the cut-off thresholds for electrons and photons were:  $ecut = 1$  MeV,  $pcut = 100$  keV. The amount of residual nuclei generated in the magnets was recorded and analysed.

## Calculation results

### Saturation activity and remnant dose rates

The saturated activity was deduced from the amount of residual nuclei considering the normal beam intensity of the electron accelerator ( $1.45E+10$  electrons/s). The saturated specific activities of the radioactive isotopes in different targets cases were compared with their exempt activity concentrations [8] as shown in Table 2.

**Table 2: Saturated specific activity of radioactive nuclides generated in  $Nd_2Fe_{14}B$  (46 mm × 12 mm × 8 mm)**

Nuclide	$t_{1/2}$ (day)	Saturated specific activity			Exempt activity concentration (Bq g <sup>-1</sup> )
		Cu target (Bq g <sup>-1</sup> )±(%)	Ta target (Bq g <sup>-1</sup> )±(%)	Without target (Bq g <sup>-1</sup> )±(%)	
<sup>7</sup> Be	5.30E+01	4.32E+02 ± 6.40	1.51E+02 ± 4.80	1.08E+02 ± 7.70	1.00E+03
<sup>41</sup> Ar	7.63E-02	3.63E+01 ± 20.00	– –	3.10E+01 ± 42.90	1.00E+02
<sup>42</sup> K	5.17E-01	7.77E+02 ± 3.70	2.16E+01 ± 27.60	4.84E+02 ± 1.50	1.00E+02
<sup>43</sup> K	9.25E-01	2.66E+02 ± 13.70	1.44E+01 ± 10.60	1.66E+02 ± 21.70	1.00E+01
<sup>46</sup> Sc	8.38E+01	3.65E+03 ± 6.40	2.26E+02 ± 9.80	1.53E+03 ± 7.60	1.00E+01
<sup>47</sup> Sc	3.40E+00	1.79E+03 ± 15.70	8.61E+01 ± 26.90	7.80E+02 ± 1.90	1.00E+02
<sup>48</sup> Sc	1.80E+00	4.96E+02 ± 4.30	2.16E+01 ± 33.30	2.81E+02 ± 2.60	1.00E+01
<sup>48</sup> V	1.60E+01	1.85E+04 ± 0.90	1.42E+03 ± 3.40	6.82E+03 ± 5.50	1.00E+01
<sup>51</sup> Cr	2.77E+01	7.19E+04 ± 0.70	1.33E+04 ± 2.00	1.55E+04 ± 0.20	1.00E+03
<sup>52</sup> Mn	5.59E+00	4.52E+04 ± 1.90	8.90E+03 ± 1.40	8.38E+03 ± 5.20	1.00E+01
<sup>54</sup> Mn	3.12E+02	2.47E+05 ± 0.10	7.71E+04 ± 0.40	2.96E+04 ± 0.70	1.00E+01
<sup>56</sup> Mn	1.08E-01	8.56E+03 ± 1.10	2.69E+03 ± 3.10	1.86E+03 ± 3.80	1.00E+01
<sup>52</sup> Fe	3.42E-01	1.63E+03 ± 10.10	2.10E+02 ± 11.40	3.74E+02 ± 11.50	1.00E+01
<sup>59</sup> Fe	4.45E+01	5.13E+00 ± 13.20	1.09E+01 ± 10.20	2.90E-01 ± 34.70	1.00E+01
<sup>56</sup> Co	7.72E+01	2.47E+03 ± 4.70	1.33E+02 ± 8.70	8.73E+02 ± 7.40	1.00E+01
<sup>57</sup> Co	2.72E+02	8.67E+01 ± 12.80	– –	4.32E+01 ± 8.90	1.00E+02
<sup>123</sup> I	5.50E-01	5.05E+01 ± 14.30	– –	1.15E+02 ± 12.50	1.00E+02
<sup>131</sup> Cs	9.69E+00	3.63E+01 ± 20.00	– –	1.36E+02 ± 6.20	1.00E+03
<sup>141</sup> Ce	3.25E+01	4.47E+02 ± 9.50	3.05E+01 ± 36.10	1.36E+02 ± 42.90	1.00E+02
<sup>147</sup> Nd	1.10E+01	7.54E+04 ± 0.10	4.67E+04 ± 0.90	4.73E+03 ± 2.80	1.00E+02

It shows that the saturated activity is higher in Cu target case than in Ta target case for most of the nuclides. The main reason is probably due to different physical thickness of the two targets. As Ta has higher Z and shorter  $X_0$  compared to Cu, the physical thickness of the Ta target ( $9.75X_0$ ) is much longer than the Cu target ( $2.94X_0$ ). Therefore the radiation field near the magnet is much different in the two target cases. The electromagnetic shower developed more thoroughly in the Ta target so there are more high energy photons (higher than 10 MeV) near the magnet in Cu target case [9]. And more radioactive nuclides are generated from photonuclear reactions in Cu target case.

With the saturated activity and gamma dose rate constant,  $\Gamma$  of each radioactive isotope [10,11], the remnant dose rates at 1m from the magnet and the contribution of each isotope in different target cases were calculated, as shown in Table 3. It could be found that the remnant dose rate is also highest in Cu target case. Among these radioactive nuclides <sup>54</sup>Mn acts as the biggest contributor to the total remnant dose rate. This isotope is mainly produced by bremsstrahlung photons via <sup>56</sup>Fe( $\gamma, np$ )<sup>54</sup>Mn as <sup>56</sup>Fe has a natural abundance of 91.72%. The fractions of the main isotopes are different for different target conditions.

**Table 3: Remnant dose rates at 1 m from the Nd<sub>2</sub>Fe<sub>14</sub>B magnet and the contribution of each isotope**

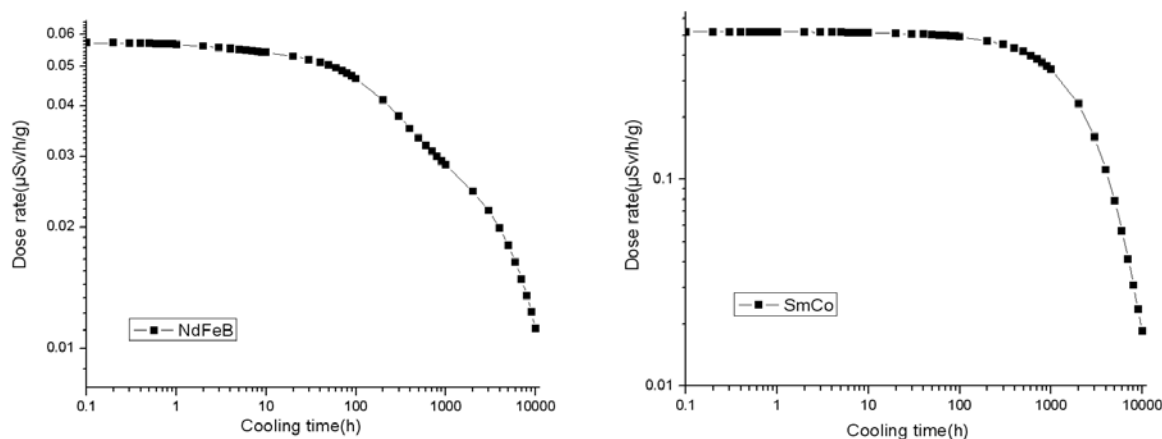
Nuclide	t <sub>1/2</sub> (day)	Γ (fSv h <sup>-1</sup> ·Bq <sup>-1</sup> )	Cu target		Ta target		Without target	
			D	Fraction	D	Fraction	D	Fraction
			(fSv·h <sup>-1</sup> g <sup>-1</sup> )	(%)	(fSv·h <sup>-1</sup> g <sup>-1</sup> )	(%)	(fSv·h <sup>-1</sup> g <sup>-1</sup> )	(%)
<sup>7</sup> Be	5.30E+01	7.8	3.36E+03	0.01	1.18E+03	0.01	8.44E+02	0.01
<sup>41</sup> Ar	7.63E-02	180	6.50E+03	0.01	–	–	5.60E+03	0.05
<sup>42</sup> K	5.17E-01	36.36	2.82E+04	0.05	7.86E+02	0.01	1.76E+04	0.17
<sup>43</sup> K	9.25E-01	160.2	4.26E+04	0.07	2.31E+03	0.02	2.66E+04	0.25
<sup>46</sup> Sc	8.38E+01	283	1.03E+06	1.80	6.38E+04	0.44	4.32E+05	4.12
<sup>47</sup> Sc	3.40E+00	18.45	3.31E+04	0.06	1.59E+03	0.01	1.44E+04	0.14
<sup>48</sup> Sc	1.80E+00	455	2.25E+05	0.39	9.83E+03	0.07	1.28E+05	1.22
<sup>48</sup> V	1.60E+01	397	7.34E+06	12.78	5.63E+05	3.88	2.71E+06	25.80
<sup>51</sup> Cr	2.77E+01	4.3	3.10E+05	0.54	5.71E+04	0.39	6.64E+04	0.63
<sup>52</sup> Mn	5.59E+00	326	1.48E+07	25.72	2.90E+06	20.00	2.73E+06	26.04
<sup>54</sup> Mn	3.12E+02	114	2.81E+07	48.96	8.82E+06	60.80	3.36E+06	32.04
<sup>56</sup> Mn	1.08E-01	250	2.14E+06	3.73	6.73E+05	4.64	4.64E+05	4.42
<sup>52</sup> Fe	3.42E-01	122.4	2.00E+05	0.35	2.57E+04	0.18	4.58E+04	0.44
<sup>59</sup> Fe	4.45E+01	147	7.57E+02	0.00	1.61E+03	0.01	4.47E+01	0.00
<sup>56</sup> Co	7.72E+01	350	8.64E+05	1.51	4.64E+04	0.32	3.05E+05	2.90
<sup>57</sup> Co	2.72E+02	17.5	1.52E+03	0.00	–	–	7.57E+02	0.01
<sup>123</sup> I	5.50E-01	46.44	2.34E+03	0.00	–	–	5.37E+03	0.05
<sup>131</sup> Cs	9.69E+00	16.56	5.97E+02	0.00	–	–	2.25E+03	0.02
<sup>141</sup> Ce	3.25E+01	15.4	6.84E+03	0.01	7.40E+02	0.01	2.10E+03	0.02
<sup>147</sup> Nd	1.10E+01	29.1	2.20E+06	3.83	1.36E+06	9.36	1.38E+05	1.31
Total			5.74E+07	–	1.45E+07	–	1.05E+07	–

**Table 4: Remnant dose rates at 1 m from the Sm<sub>2</sub>Co<sub>17</sub> magnet and the contribution of each isotope**

Nuclide	t <sub>1/2</sub> (day)	Γ (fSv h <sup>-1</sup> Bq <sup>-1</sup> )	As (Bq g <sup>-1</sup> )±(%)	Exempt activity concentration (Bq g <sup>-1</sup> )	D (fSv h <sup>-1</sup> g <sup>-1</sup> )	Fraction (%)
<sup>43</sup> K	9.25E-01	1.60E+02	1.52E+02 ± 14.3	1.00E+01	2.43E+04	0.00
<sup>46</sup> Sc	8.38E+01	2.83E+02	2.20E+03 ± 2.7	1.00E+01	6.24E+05	0.13
<sup>47</sup> Sc	3.40E+00	1.85E+01	1.51E+03 ± 3.4	1.00E+02	2.78E+04	0.01
<sup>48</sup> Sc	1.80E+00	4.55E+02	4.61E+02 ± 9.6	1.00E+01	2.10E+05	0.04
<sup>48</sup> V	1.60E+01	3.97E+02	7.89E+03 ± 0.1	1.00E+01	3.13E+06	0.63
<sup>51</sup> Cr	2.77E+01	4.30E+00	2.41E+04 ± 3.3	1.00E+03	1.04E+05	0.02
<sup>52</sup> Mn	5.59E+00	3.26E+02	1.15E+04 ± 2.6	1.00E+01	3.77E+06	0.76
<sup>54</sup> Mn	3.12E+02	1.14E+02	9.28E+04 ± 2.6	1.00E+01	1.06E+07	2.14
<sup>56</sup> Mn	1.08E-01	2.50E+02	1.17E+04 ± 3.5	1.00E+01	2.93E+06	0.59
<sup>52</sup> Fe	3.42E-01	1.22E+02	2.52E+02 ± 14.3	1.00E+01	3.07E+04	0.01
<sup>59</sup> Fe	4.45E+01	1.47E+02	4.06E+03 ± 0.6	1.00E+01	5.95E+05	0.12
<sup>56</sup> Co	7.72E+01	3.50E+02	3.16E+02 ± 2.7	1.00E+01	1.11E+05	1.69
<sup>57</sup> Co	2.72E+02	1.75E+01	2.39E+04 ± 0.3	1.00E+02	4.18E+05	2.72
<sup>58</sup> Co	7.09E+01	1.31E+02	7.71E+05 ± 0.1	1.00E+01	1.01E+08	93.92
<sup>60</sup> Co	1.93E+03	3.05E+02	3.57E+06 ± 0.8	1.00E+01	1.08E+09	0.30
<sup>147</sup> Pm	9.49E+02	6.08E-04	5.10E+03 ± 1.1	1.00E+04	3.10E+00	0.00
<sup>147</sup> Nd	1.10E+01	2.91E+01	3.16E+02 ± 0.2	1.00E+02	9.22E+03	0.00
<sup>152</sup> Eu	4.93E+03	1.78E+02	4.03E+02 ± 3.7	1.00E+01	7.19E+04	0.01
<sup>153</sup> Sm	1.95E+00	1.67E+01	3.74E+05 ± 0.6	1.00E+02	6.24E+06	1.26
Total					4.19E+10	

The saturated activity of radioactive nuclides in  $\text{Sm}_2\text{Co}_{17}$  magnet and the remnant dose rates was calculated and listed in Table 4. In this calculation Cu target was used. The kinds of the radioactive nuclides are different with the ones in  $\text{Nd}_2\text{Fe}_{14}\text{B}$  magnet.  $^{58}\text{Co}$  is very important as 93.9% of the total remnant dose rate is contributed by it. It is mainly generated by photonuclear reaction  $^{59}\text{Co}(\gamma, n)^{58}\text{Co}$ .

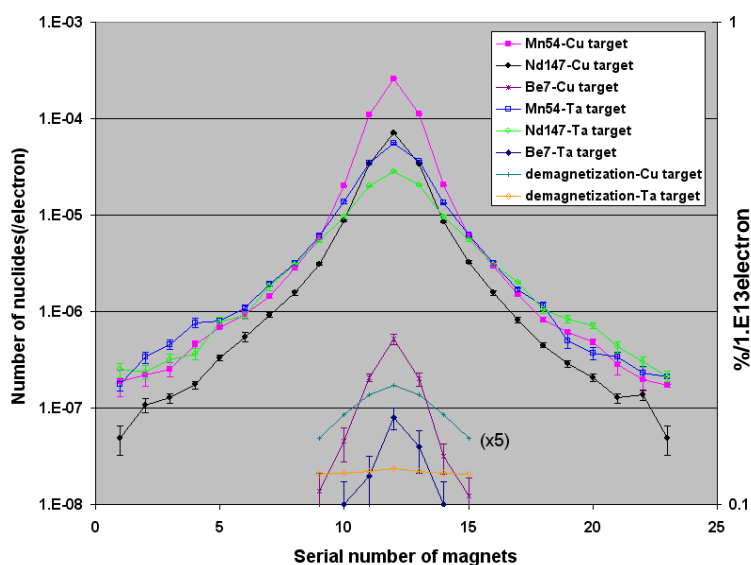
Figure 2: Time dependence of the remnant dose rates for two kinds of magnets



As the kinds of the radioactive nuclides and their half lives are different for  $\text{Sm}_2\text{Co}_{17}$  and  $\text{Nd}_2\text{Fe}_{14}\text{B}$  magnet, the remnant dose rate also shows different time dependence. Figure 2 shows respectively the remnant dose rates at 1m as a function of cooling time for the two kinds of magnets.

Generally the remnant dose rates decrease slowly for the two kinds of magnets. It is because most of the big contributors belong to long half life radioisotopes. The remnant dose rate in  $\text{Sm}_2\text{Co}_{17}$  magnet is about 1 order higher than  $\text{Nd}_2\text{Fe}_{14}\text{B}$  at first, but after 10 000 hours (416 days) the difference is much smaller. For  $\text{Nd}_2\text{Fe}_{14}\text{B}$ , up to 30 hours cooling time,  $^{56}\text{Mn}$  is the dominant isotope;  $^{52}\text{M}$  and  $^{48}\text{V}$  dominate in the following 1 month and finally  $^{54}\text{Mn}$  is dominant at longer cooling time. As for  $\text{Sm}_2\text{Co}_{17}$ , the fraction of short half life time isotopes is very small, so the remnant dose rate decrease follows the decay of  $^{58}\text{Co}$ .

Figure 3: Spatial distribution of the calculated production rates of three different radioactive nuclides



### Spatial distribution of the induced activity

As has mentioned before, the spatial distribution of the induced activity was investigated by dividing the magnet sample into 23 pieces along x axis. In this simulation, Cu target and Nd<sub>2</sub>Fe<sub>14</sub>B magnet were used. These 23 pieces were numbered from top to bottom and the amounts of the residual nuclei were recorded respectively in different pieces. Figure 3 shows the spatial distributions of the production rates of three different radioactive nuclides in Cu target and Ta target cases.

<sup>54</sup>Mn and <sup>147</sup>Nd are highly produced isotopes. <sup>7</sup>Be is investigated because it is generated from B, which is supposed to be very important in the demagnetisation of Nd<sub>2</sub>Fe<sub>14</sub>B magnet [12]. The second axis shows the magnetic field decrease of Nd<sub>2</sub>Fe<sub>14</sub>B magnet. The distribution of demagnetisation is flatter in Ta target case, the distribution of produced isotope in Ta target is also not as sharp as in Cu target case.

### Experiments

The experiment setup accorded with the geometry used in the simulation as shown in Figure 1. Cu target and Nd<sub>2</sub>Fe<sub>14</sub>B magnet was used. The magnet sample was divided into 23 pieces as was mentioned earlier. These samples were irradiated at the 2.5 GeV electron linac of Pohang Light Source for 236 minutes. During irradiation the total number of electrons was 2.109E+14. After irradiation the specific activities of the samples were measured at different cooling times.

### Gamma spectrometry

The gamma spectrometry measurements were performed with a coaxial P-type High-purity Germanium (HPGe) detector by Canberra (relative efficiency 20%). The activities of the irradiated samples were measured at different cooling times. As the shape of the magnet sample is not standard, the efficiencies at different distances were calculated with Monte Carlo codes MCNP5. This calculation was validated by comparison with measurement for the efficiencies of some point sources. The difference between the calculation and measurement result is below 30%.

### Results and comparison

Table 5 gives the activities of several isotopes when the irradiation was finished in the magnet sample which number is 12. It is the one at the beam centre position. The results are compared between measurement and calculation. In calculation the produced rate was evaluated with FLUKA and the activity was calculated considering the decay during irradiation. The errors represent statistical uncertainties only.

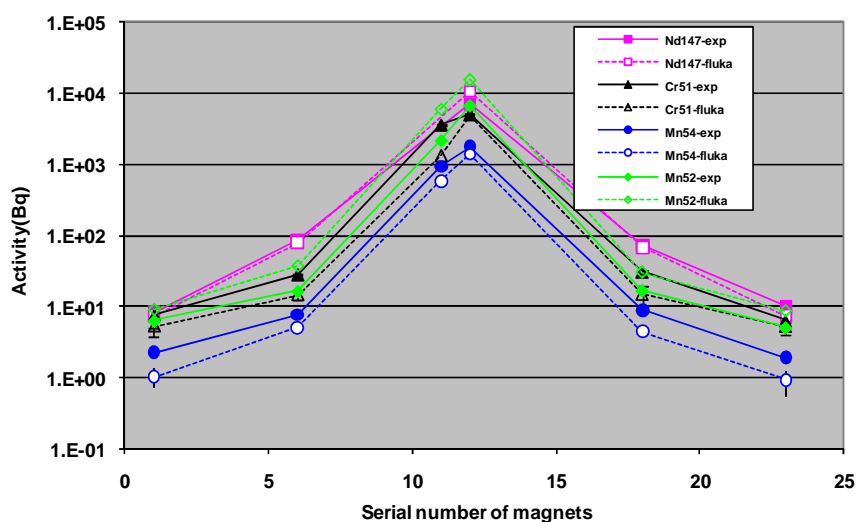
**Table 5: Induced activities in Nd<sub>2</sub>Fe<sub>14</sub>B sample (number 12 at beam centre position)**

Nuclide	t <sub>1/2</sub>	A-exp	Error	A-fluka	Error	Exp/fluka
	(day)	(Bq)	(%)	(Bq)	(%)	
<sup>7</sup> Be	5.30E+01	5.88E+01	7.35	1.96E+01	4.00	3.00
<sup>43</sup> K	9.25E-01	4.86E+02	1.83	6.87E+02	5.90	0.71
<sup>46</sup> Sc	8.38E+01	1.39E+02	2.44	1.19E+02	2.30	1.14
<sup>47</sup> Sc	3.40E+00	2.00E+03	1.41	1.53E+03	4.30	1.31
<sup>48</sup> Sc	1.80E+00	5.39E+02	8.49	6.92E+02	9.30	0.78
<sup>48</sup> V	1.60E+01	2.02E+03	0.83	3.04E+03	2.00	0.66
<sup>51</sup> Cr	2.77E+01	6.01E+03	0.75	6.07E+03	0.80	0.99
<sup>52</sup> Mn	5.59E+00	5.64E+03	0.83	1.87E+04	0.70	0.32
<sup>54</sup> Mn	3.12E+02	1.78E+03	0.58	1.67E+03	0.30	1.07
<sup>56</sup> Mn	1.08E-01	1.45E+05	4.00	9.26E+04	0.50	1.57
<sup>52</sup> Fe	3.42E-01	1.20E+04	1.31	9.31E+03	4.80	1.28
<sup>56</sup> Co	7.72E+01	3.80E+01	8.42	8.70E+01	3.40	0.44
<sup>141</sup> Ce	3.25E+01	5.00E+01	5.21	2.86E+01	2.90	1.75
<sup>147</sup> Nd	1.10E+01	6.76E+03	0.41	1.32E+04	0.30	0.51

The calculated and measured activities agree with each other with a factor of 2 for most of the isotopes. The light nuclide  $^7\text{Be}$  was underestimated by FLUKA most probably due to the fact that multi-fragmentation processes are not implemented in the code [13].

The spatial distribution of the induced activities of three different radioactive isotopes when the irradiation was finished was shown in Figure 4. The calculation results also agree with the experiment results in the other magnet samples.

**Figure 4: Spatial distribution of the induced activities of three different radioactive isotopes**



## Conclusions

The induced radioactivity in permanent magnet used for insertion device of synchrotron radiation light source was investigated with both Monte Carlo simulation and experiment. The saturated specific activities of the radioactive isotopes in different targets cases were calculated FLUKA code and compared with their exempt activity concentrations. The saturated activity is higher in Cu target case for most of the nuclides probably because high energy (higher than 10 MeV) photon fluence is higher.

The remnant dose rates at 1 m from the magnets were also calculated and compared under different target conditions. In Cu target case the remnant dose rate is relatively high. The time dependence of the remnant dose rates was also derived and compared for two different kinds of magnet ( $\text{Nd}_2\text{Fe}_{14}\text{B}$ ,  $\text{Sm}_2\text{Co}_{17}$ ). The remnant dose rates decrease slowly due to the big contribution of the long half life isotopes such as  $^{54}\text{Mn}$  in  $\text{Nd}_2\text{Fe}_{14}\text{B}$  and  $^{58}\text{Co}$  in  $\text{Sm}_2\text{Co}_{17}$ .

In experiment the irradiation was performed with  $\text{Nd}_2\text{Fe}_{14}\text{B}$  magnet and Cu target. The gamma spectrometry measurements were carried out with a coaxial P-type High-Purity Germanium (HPGe) detector. The induced activities of sample number 12 at beam centre position agreed with calculated values in a factor of 2 except  $^7\text{Be}$ .

In the comparison of the spatial distribution of induced activities between measurement and calculation, good agreement was found. It followed the property of spatial distribution of the demagnetisation. This result would give us some information about demagnetisation phenomenon. More work is needed to find out the relationship between induced activity and demagnetisation.

## Acknowledgements

The authors are grateful to James C. Liu for many discussions and his good suggestions on this study.

## References

- [1] E.W. Blackmore, *IEEE Trans. Nucl. Sci.*, NS-32, pp. 3669-3671 (1985).
- [2] S. Okuda, K. Ohashi, N. Kobayashi, *Nucl. Instr. and Meth.*, B 94, p. 227 (1994).
- [3] J.R. Cost, R.D. Brown, A.L. Girgi, J.T. Stanley, *IEEE Trans. Magn.*, MAG-24, pp. 2016 (1988).
- [4] Y. Ito, K. Yasuda, R. Ishigami, S. Hatori, O. Okada, K. Ohashi, S. Tanaka, *Nucl. Instr. and Meth.*, B183, pp. 323-328 (2001).
- [5] T. Bizen, T. Tanaka, Y. Asano, *et.al.*, *Nucl. Instr. and Meth.*, A 467-468, pp. 185-189 (2001).
- [6] T. Bizen, Y. Asano, T. Hara, X. Marechal, T. Seike, T. Tanaka, H.S. Lee, D.E. Kim, C.W. Chung, T. Kitamura, *Nucl. Instr. and Meth.*, A515, pp. 850-852 (2003).
- [7] A. Ferrari, P.R. Sala, A. Fassò, *et al.*, *FLUKA Manual (Program Version 2002)*, [R] INFN (2002).
- [8] "International Basic Standards for Protection Against Ionizing Radiation and for the Safety of Radiation Sources", *IAEA Series No.115-1*, Vienna (1994).
- [9] R. Qiu, H-S. Lee, T-Y. Koo, J. Li, "Monte Carlo Study in Radiation Damage Experiments of Permanent Magnets by High Energy Electrons", *The 9<sup>th</sup> International Conference on Synchrotron Radiation Instrumentation* (2006).
- [10] M. Barbier, *Induced Radioactivity*, Appendix A, Amsterdam, North Holland (1969).
- [11] D. Delacroix, J.P. Guerre, P. Leblanc, C. Hickman, "Radionuclide and Radiation Protection Data Handbook 2002", *Radiation Protection Dosimetry*, Vol. 98, No. 1 (2002).
- [12] X-M. Maréchal, T. Shintake, "Radiation Damages on Permanent Magnets: Challenges for the Future Light Sources", *AIP Conf. Proc.* 705, 282 (2004).
- [13] M. Brugger, H. Khater, S. Mayer, *et al.*, *Radiation Protection Dosimetry*, Vol. 116, No. 1-4, pp. 6-11 (2005).

## **Production yields of the radionuclides induced in various targets fixed in concrete shield at the 500-MeV neutron irradiation facility of KENS**

**H. Matsumura,<sup>1</sup> N. Nakao,<sup>1</sup> K. Masumoto,<sup>1</sup> K. Oishi,<sup>2</sup> M. Kawai,<sup>1</sup> T. Aze,<sup>3</sup> A. Toyoda,<sup>1</sup>  
M. Numajiri,<sup>1</sup> K. Takahashi,<sup>1</sup> M. Fujimura,<sup>4</sup> Q. Wang,<sup>5</sup> K. Bessho,<sup>1</sup> T. Sanami<sup>1</sup>**

<sup>1</sup>High Energy Accelerator Research Organisation (KEK), Tsukuba, Japan

<sup>2</sup>Institute of Technology, Shimizu Corporation, Tokyo, Japan

<sup>3</sup>Graduate School of Science, The University of Tokyo, Tokyo, Japan

<sup>4</sup>Graduate School of Integrated Basic Sciences, Nihon University, Tokyo, Japan

<sup>5</sup>The Institute of High Energy Physics (IHEP), Beijing, China

### **Abstract**

*We performed a shielding experiment with high-energy neutrons produced from a tungsten target bombarded with 500-MeV protons and penetrated through a concrete shield in the 0 degree direction. Using an activation method, we observed many radioactive products induced by neutrons with energies ranging from thermal to 500 MeV and obtained their production yields from various target elements at depths of 0 to 4 m from the surface of the concrete shield.*

## Introduction

In high-energy proton accelerator facilities, high-energy neutrons are secondarily produced upon bombardment with a proton beam. Such neutrons have high penetrability, and induce activation of the surrounding materials. The spectra of the neutrons and activation of the materials are generally estimated using Monte-Carlo simulation codes. It is very important to confirm experimentally their confidence from the benchmark.

However, only few experiments for the benchmark have been performed so far. In particular, there are no experimental data pertaining to the conditions of “high energy neutron”, “0 degree direction”, and “thick concrete shield.” We therefore constructed a high-energy neutron-beam course at KEK Neutron Science Laboratory (KENS) at the High Energy Accelerator Research Organisation (KEK) [1,2]. The course has seven irradiation slots inside a 4-m thick concrete shield. High-energy neutrons were guided to the shield through a collimator of 2.19-m length from a tungsten-target assembly which completely stopped 500-MeV primary protons.

Using this course, we have been accumulating experimental data for following: i) the spectrum and attenuation characteristics of the neutrons in the concrete shield; ii) the activation products induced by high-energy neutron irradiation in the well-known system at KENS. With regard to the first point, an activation method is most suitable for detecting neutrons in the limited spaces in the concrete. Therefore, we have measured the yields of the radioactive products from various targets and observed the attenuation profiles of the neutrons. The yields obtained from the various nuclear reactions with different Q-values can indirectly provide information on the energy spectra of the neutrons and their intensities. With regard to the second point, we measured many yields of the spallation products from various targets induced by high-energy neutrons. Following this, charge distributions and mass yield curves were elucidated from the yields. In this paper, we introduce a part of our experimental data [1-7], including the preliminary data, obtained using the high-energy neutron-beam course at KENS.

## Experimental procedure

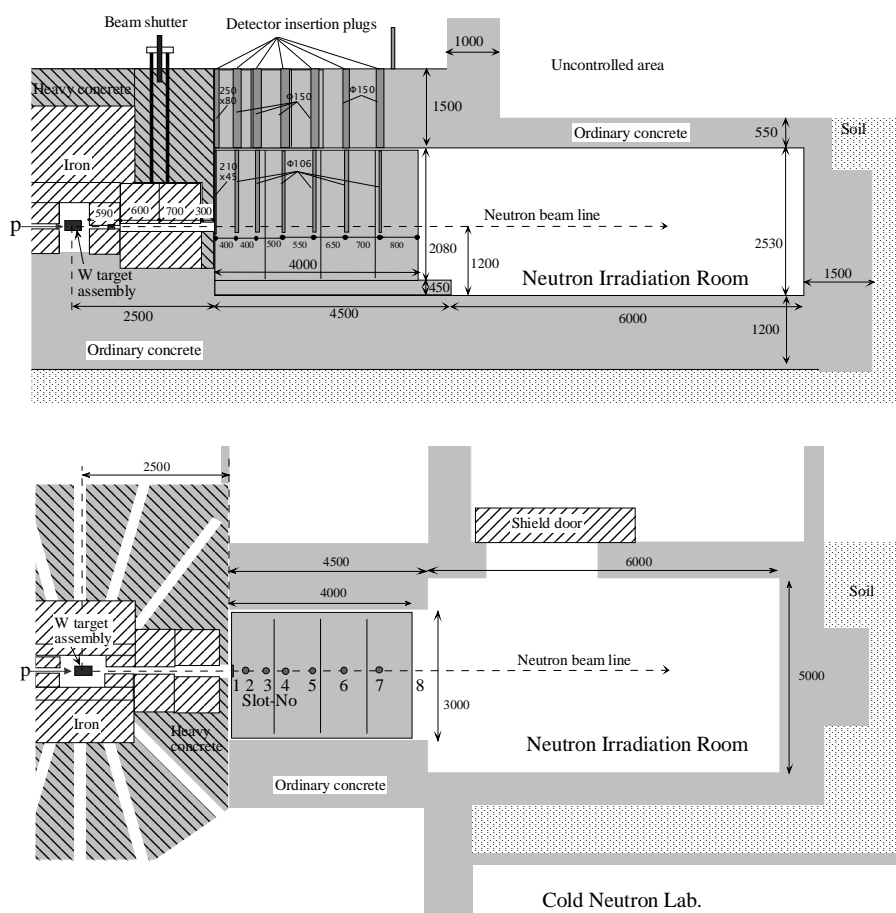
### *The 500-MeV neutron irradiation facility of KENS*

The high-energy neutron-beam course of KENS was designed for this shielding experiment. Figure 1 shows the cross-sectional views of the KENS high-energy neutron-beam course and the arrangement of the shielding experiment. Secondary neutrons were produced by bombarding with 500-MeV protons on four tungsten blocks placed in the tungsten-target assembly. Since the total thickness of the tungsten blocks was 11.68 cm, the primary protons were completely stopped in the tungsten blocks. The produced secondary neutrons were passed through a 10-cm stainless-steel block placed downstream in the target assembly, and collimated with an iron beam guide to lead in zero-degree direction. The collimated beam finally reached to a beam exit of 20 cm width  $\times$  15 cm height located in a distance of 250 cm from the target assembly and irradiated on an ordinary concrete of 4 m thickness which borders on the beam exit. The concrete has eight irradiation positions referred to as “slot 1” to “slot 8”. They are positioned along the neutron beam direction in the concrete shield. The slots 1, 2, 3, 4, 5, 6, 7, and 8 were located on 0, 40, 80, 130, 185, 250, 320, and 400 cm depth from the surface of the concrete shield, respectively. The more details of this course were described in [1,2].

### *Irradiation*

The targets of  $\text{Na}_2\text{CO}_3$ ,  $\text{MgO}$ ,  $\text{Al}$ ,  $\text{Si}$ ,  $\text{KCl}$ ,  $\text{K}_2\text{CO}_3$ ,  $\text{CaCO}_3$ ,  $\text{Sc}$ ,  $\text{Ti}$ ,  $\text{V}$ ,  $\text{Cr}$ ,  $\text{Mn}$ ,  $\text{Fe}$ ,  $\text{Co}$ ,  $\text{Ni}$ ,  $\text{Cu}$ ,  $\text{Zn}$ ,  $\text{In}$ ,  $\text{Au}$ ,  $\text{Au}$  covered with  $\text{Cd}$ , and  $\text{Bi}$  were irradiated at slots 1, 2, 3, 4, 5, 6, 7, and/or 8. The targets were individually sealed in polyethylene bags. Plastic capsules containing the targets were fixed at the bottom of the shield plugs and inserted into the 8 slots, and set on the beam axis. Nine irradiations were carried out. The irradiation duration was typically one week. The average current of the primary protons was typically 6-7  $\mu\text{A}$ . The fluctuation of the primary proton current was monitored during the irradiation. The beam fluctuation was corrected for radioactive decays if necessary.

**Figure 1: Cross-sectional views of the KENS high-energy neutron beam course and the arrangement of the shielding experiment**



## Measurements of the radioactive products

### Spallation products from $^{197}\text{Au}$

After irradiation,  $\gamma$ -ray spectrometry was performed with HP Ge detector systems. The radioactivities of  $^{196}\text{Au}$ ,  $^{194}\text{Au}$ ,  $^{192}\text{Au}$ ,  $^{188}\text{Pt}$ ,  $^{189}\text{Ir}$ ,  $^{185}\text{Os}$ ,  $^{183}\text{Re}$ ,  $^{181}\text{Re}$ , and  $^{175}\text{Hf}$  were determined non-destructively. On the other hand,  $^{173}\text{Lu}$ ,  $^{171}\text{Lu}$ ,  $^{169}\text{Yb}$ , and  $^{167}\text{Tm}$  could not be detected directly because of their low activity and high activity of  $^{198}\text{Au}$  and neighbour spallation products. Therefore, they were measured after radiochemical group-separation of rare-earth elements. The radioactivity measurements of target set in the backward from slot 5 were more difficult than that set at front side due to their attenuation. For the targets of slots 5 to 7, low background  $\gamma$ -ray counting was performed with an anti-Compton and/or X- $\gamma$  coincidence system which HP Ge detector coupled with 3 NaI scintillation counters. All of the yields were cumulative for the respective  $\beta^+$ -decay and/or electron-capture chains. The details of the samples for the targets of slots 1 to 5 and the chemical procedure were described in [5]. Since the details of the samples and data analysis for the targets of slots 5 to 7 are preliminary, they have not published yet.

### Chlorine-36

After irradiation, chlorine was chemically separated from each irradiated target and finally precipitated as AgCl. The amount of the  $^{36}\text{Cl}$  was determined by accelerator mass spectrometry (AMS) in the Micro Analysis Laboratory, Tandem Accelerator (MALT) at the Research Centre for Nuclear Science and Technology, the University of Tokyo. The details were described in [6].

### Other products

After irradiation,  $\gamma$ -ray spectrometry was non-destructively performed with HP-Ge detectors to determine the radioactivities of the products from the various targets. The yields of  $^{22,24}\text{Na}$  from Cl were obtained by subtracting the yields in  $\text{K}_2\text{CO}_3$  from those in KCl. In order to detect  $^{198}\text{Au}$  from Au and Au covered with Cd, the irradiated gold foils were also simultaneously exposed to an imaging plate (IP). The exposed IP was scanned with a bio-imaging analyser. The details of the activity determination with the IP were described in [3]. The yields induced by epithermal neutrons were measured from the Au targets covered with Cd. We could obtain the yields induced by thermal neutrons by subtracting the yields in the Cd-covered Au from those in the non-covered Au.

## Results and discussion

Many yields were collected in this work. The unit of the yield is  $\text{atom}^{-1}\mu\text{C}^{-1}$ , which indicates the production probability per target atom and per  $\mu\text{C}$  of the primary protons. We explain the measured yields in following two separate sections.

### Attenuation profiles of the neutrons obtained by the activation method

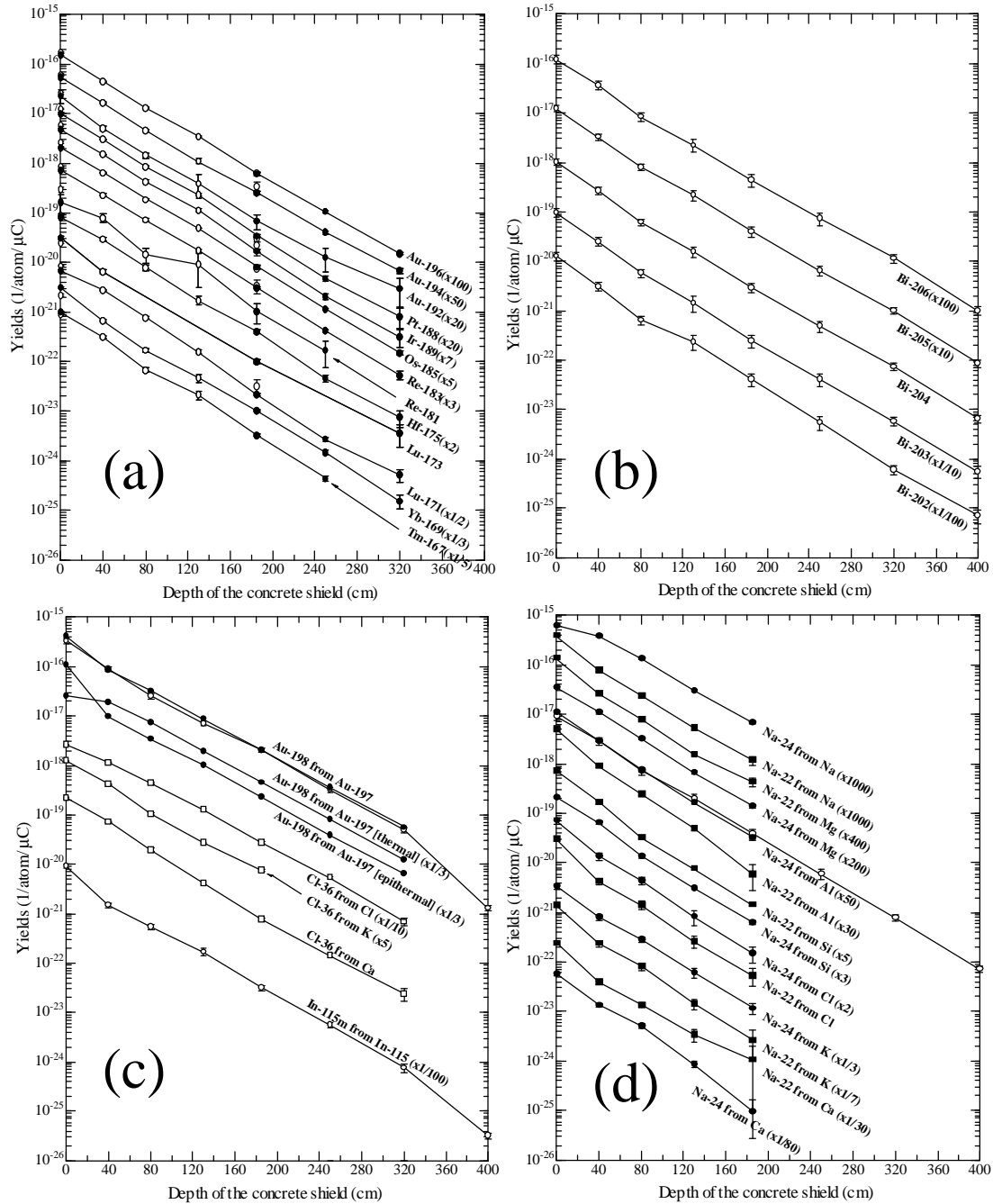
In the activation method, the detectable energy of the neutrons depends on the reaction threshold energy. Using the energy dependence, we can indirectly derive information on the spectrum profile, intensity, and attenuation of the neutrons from the product yields in the various reactions. Accordingly, at the slots 1-8, we measured the yields of the following products:

- (1) 13 spallation products ( $^{196}\text{Au}$ ,  $^{194}\text{Au}$ ,  $^{192}\text{Au}$ ,  $^{188}\text{Pt}$ ,  $^{189}\text{Ir}$ ,  $^{185}\text{Os}$ ,  $^{183}\text{Re}$ ,  $^{181}\text{Re}$ ,  $^{175}\text{Hf}$ ,  $^{173}\text{Lu}$ ,  $^{171}\text{Lu}$ ,  $^{169}\text{Yb}$ , and  $^{167}\text{Tm}$ ) from a  $^{197}\text{Au}$  target;
- (2)  $^{202-206}\text{Bi}$  in  $^{209}\text{Bi}(n, xn)$  reactions;
- (3)  $^{198}\text{Au}$  from a  $^{197}\text{Au}$  target and a  $^{197}\text{Au}$  target covered with Cd;
- (4)  $^{115\text{m}}\text{In}$  from  $^{115}\text{In}$ ;
- (5)  $^{36}\text{Cl}$  from  $^{\text{nat}}\text{Cl}$ ,  $^{\text{nat}}\text{K}$ , and  $^{\text{nat}}\text{Ca}$  targets;
- (6)  $^{24}\text{Na}$  and  $^{22}\text{Na}$  from  $^{23}\text{Na}$ ,  $^{\text{nat}}\text{Mg}$ ,  $^{27}\text{Al}$ ,  $^{\text{nat}}\text{Si}$ ,  $^{\text{nat}}\text{Cl}$ ,  $^{\text{nat}}\text{K}$ , and  $^{\text{nat}}\text{Ca}$  targets.

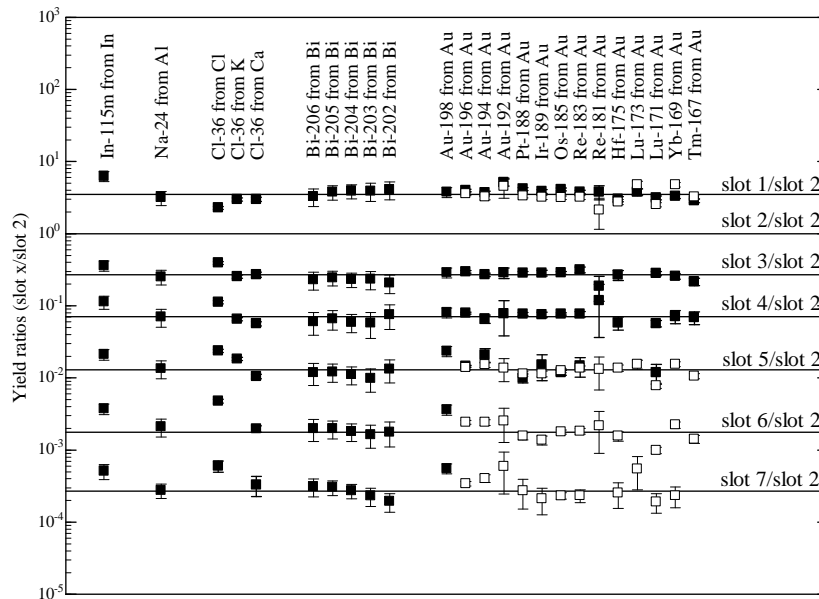
The effective energies of the yields are estimated at to be 8-500 MeV for (1), 10-100 MeV for (2), thermal and epithermal reactions for (3), and 1-10 MeV for (4), and thermal to several 100 MeV for (5) and (6). In particular, the threshold energy in the Au spallation products covers the widest energy range among the measured targets in this work. The threshold energy of  $^{197}\text{Au}(n,2n)^{196}\text{Au}$  is 8.1 MeV, which is the lowest among the (1) products. The effective neutron energy for this reaction is estimated at around 10 MeV. On the other hand, the threshold energy of  $^{197}\text{Au}(n,10p21n)^{167}\text{Tm}$  is 202.9 MeV, which is the highest among the measured reactions. The effective neutron energy for this reaction is estimated to be in the range of 350 to 500 MeV [5]. As the results, the effective energies of the 13 Au spallation products are in the range of 10 to 500 MeV. Furthermore, whole neutron energies were completely covered using all the productions of (1) to (6).

In Figure 2, the measured yields of (a) the spallation products from  $^{197}\text{Au}$ , (b) the products of the  $^{209}\text{Bi}(n,xn)$  reactions, (c)  $^{198}\text{Au}$  from  $^{197}\text{Au}$ ,  $^{36}\text{Cl}$  from Cl, K, and Ca, and  $^{115\text{m}}\text{In}$  from  $^{115}\text{In}$ , and (d)  $^{24}\text{Na}$  and  $^{22}\text{Na}$  were plotted as a function of the depth from the surface of the concrete shield. The open and the closed symbols joined by solid lines represent the reported [1,5,6] and preliminary experimental yields, respectively. All the yields are exponentially attenuated in the concrete shield and their slopes appear similar regardless of the reactions.

**Figure 2: Measured attenuation profiles of the various yields of (a) the spallation products from  $^{197}\text{Au}$ , (b) products of  $^{209}\text{Bi}(n, xn)$  reactions, (c)  $^{198}\text{Au}$  from  $^{197}\text{Au}$ , and  $^{36}\text{Cl}$  from Cl, K, and Ca, and (d)  $^{24}\text{Na}$  and  $^{22}\text{Na}$  from various targets**



In order to compare the details of the relative yield variations, the ratios of the yields at each slot to those at slot 2 are plotted in Figure 3. The open symbols denote the experimental values published in [1,5,6], while the closed symbols denote the preliminary values. The solid lines indicate the average for the Au spallation products. This figure shows the relative change in the energy spectra of the neutrons passing through the concrete shield. The ratios are almost constant except in the low-energy reactions such as  $^{35}\text{Cl}(n,\gamma)^{36}\text{Cl}$ ,  $^{197}\text{Au}(n,\gamma)^{198}\text{Au}$ ,  $^{197}\text{Au}(n,2n)^{196}\text{Au}$ , and  $^{115}\text{In}(n,n')^{115\text{m}}\text{In}$  where the threshold energy is lower than approximately 10 MeV. The ratios of the yields of the low-energy reactions are

**Figure 3: Ratios of the yields at slots 1, 3, 4, 5, 6, and 7 to those at slot 2**


slightly higher than the others at slots deeper than slot 3. Therefore, without changing the profile of the neutron spectrum in the range of 10 to 500 MeV, the intensity is exponentially attenuated with an increase in the depth of the concrete, although there was a small build-up of low-energy neutrons at depths below 40 cm.

### Production yields of radioisotopes from various targets

The yields obtained from the Au target are also available for the benchmark of the residual products from heavy targets. All the yields are cumulative for the respective  $\beta^+$ -decay and/or electron-capture chains. Since the measured nuclides are closed to stable isotopes, the yields can be approximately regarded as mass yields according to the spallation characteristics. In Figure 4, the yields from Au target are plotted as a function of the product mass number. The open symbols denote the experimental values published in [5], while the closed symbols denote the preliminary experimental values. The solid lines drawn through the points are provided as a visual guide. On the semi-log graph, it is evident that each mass yield curve decreases steeply in an arc with a decrease in the product mass number.

For the benchmark of the residual products from medium targets, we measured the yields of the spallation products from the  $^{45}\text{Sc}$ ,  $^{\text{nat}}\text{Ti}$ ,  $^{\text{nat}}\text{V}$ ,  $^{\text{nat}}\text{Cr}$ ,  $^{55}\text{Mn}$ ,  $^{\text{nat}}\text{Fe}$ ,  $^{59}\text{Co}$ ,  $^{\text{nat}}\text{Ni}$ ,  $^{\text{nat}}\text{Cu}$ , and  $^{\text{nat}}\text{Zn}$  targets at slot 2. Although the charge distribution characteristics were unclear for the neutron-induced spallation, we attempted to fit the spallation yields to an empirical five-parameter formula derived by Rudstam [9] that was successfully applied to photospallation reactions [8]. Rudstam's formula (CDMD formula) for charge distribution (CD) and mass yield distribution (MD) is:

$$Y(Z, A) = \frac{\sigma P R^{2/3} \exp[PA - R | Z - SA + TA^2 |^{3/2}]}{1.79[\exp(PA) - 1]}$$

where  $Y(Z, A)$  indicates the independent yield of a nuclide ( $Z, A$ ) obtained from the target ( $Z_t, A_t$ ) and  $P, \sigma, R, S,$  and  $T$  are free parameters. The parameter  $P$  defines the slope of the MD;  $\sigma$ , the total inelastic cross-section;  $R$ , the width of the CD; and  $S$  and  $T$ , the location of the CD through the most probable charge  $Z_p = SA - TA^2$ . Figure 5 shows the CD of the spallation products from the  $^{45}\text{Sc}$ ,  $^{\text{nat}}\text{Ti}$ ,  $^{\text{nat}}\text{V}$ ,  $^{\text{nat}}\text{Cr}$ ,  $^{55}\text{Mn}$ ,  $^{\text{nat}}\text{Fe}$ ,  $^{59}\text{Co}$ ,  $^{\text{nat}}\text{Ni}$ ,  $^{\text{nat}}\text{Cu}$ , and  $^{\text{nat}}\text{Zn}$  targets. The open squares indicate independent yields (I); reverse triangles, cumulative ones for  $\beta^+$  and/or electron-capture decay (C+); and triangles, cumulative ones for  $\beta^-$  decay (C-). The solid lines indicate the CD obtained by the fitting, and the dashed and dotted lines represent the cumulative yields for C+ and C- estimated using the CDMD formula,

Figure 4: Mass yields of the spallation products from  $^{197}\text{Au}$

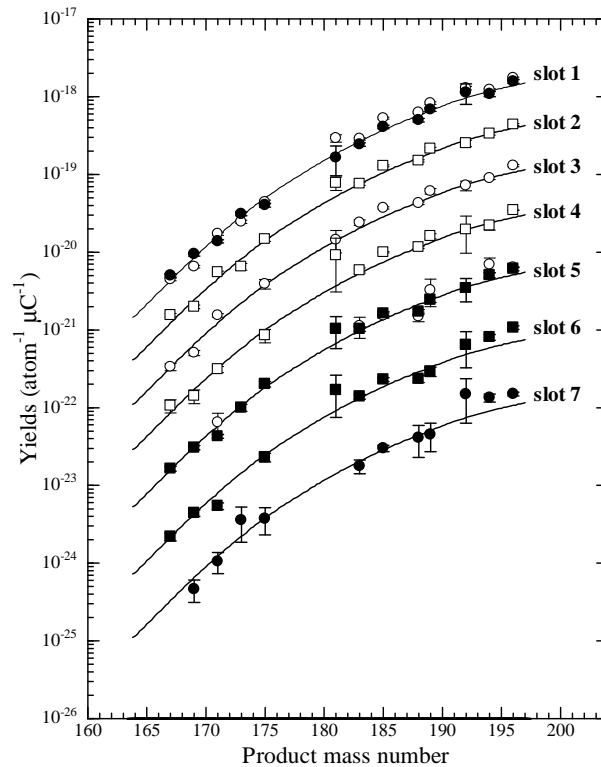
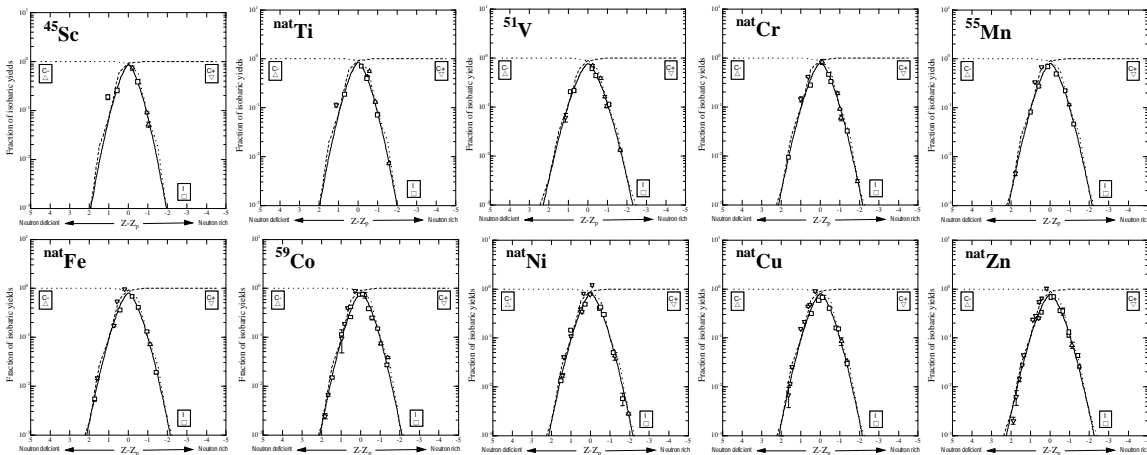
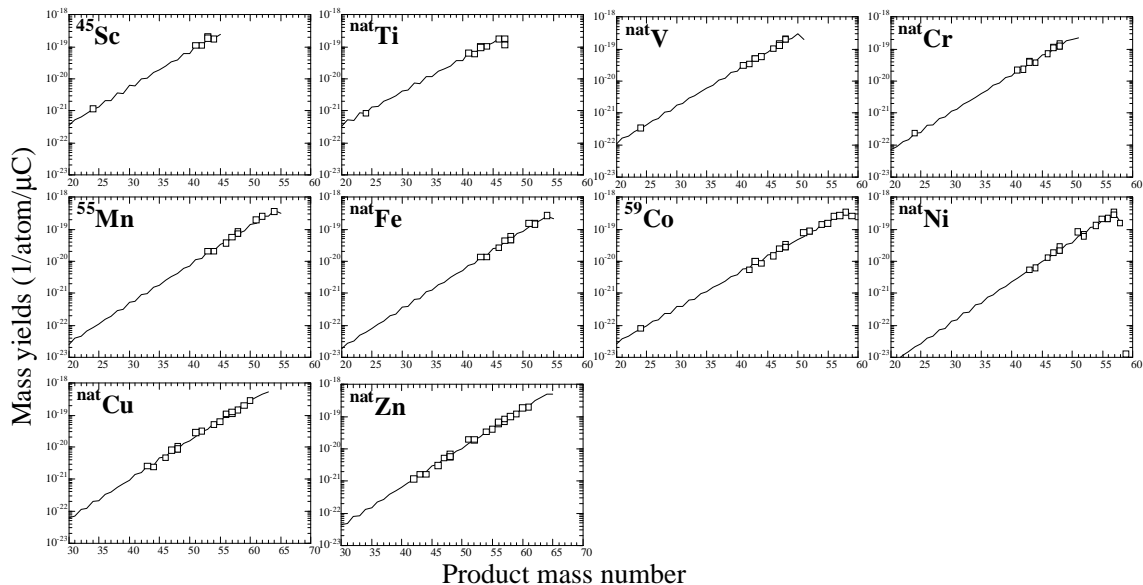


Figure 5: Charge distributions of the spallation products from the  $^{45}\text{Sc}$ ,  $\text{natTi}$ ,  $\text{natV}$ ,  $\text{natCr}$ ,  $^{55}\text{Mn}$ ,  $\text{natFe}$ ,  $^{59}\text{Co}$ ,  $\text{natNi}$ ,  $\text{natCu}$ , and  $\text{natZn}$  targets



respectively. As shown in the figure, the results of these fittings are very good for all the products and targets. Therefore, it was confirmed that the CDMD formula was useful for the yields of the neutron spallation residues obtained at KENS.

Mass yield curves were calculated using the CDMD parameters. Figure 6 shows the MD for the  $^{45}\text{Sc}$ ,  $\text{natTi}$ ,  $\text{natV}$ ,  $\text{natCr}$ ,  $^{55}\text{Mn}$ ,  $\text{natFe}$ ,  $^{59}\text{Co}$ ,  $\text{natNi}$ ,  $\text{natCu}$ , and  $\text{natZn}$  targets. The solid lines represent the calculated mass yields. The squares indicate the experimental mass yields compensated with estimated yields of unmeasured products. We were able to obtain the MD for a wide range of product mass number.

**Figure 6: Mass yields from  $^{45}\text{Sc}$ ,  $\text{natTi}$ ,  $\text{natV}$ ,  $\text{natCr}$ ,  $^{55}\text{Mn}$ ,  $\text{natFe}$ ,  $^{59}\text{Co}$ ,  $\text{natNi}$ ,  $\text{natCu}$ , and  $\text{natZn}$  targets**

Furthermore, we have been measuring the yields of the spallation products from other targets such as  $^{89}\text{Y}$ . Systematic measurements of fixed products, such as  $^7\text{Be}$ ,  $^{10}\text{Be}$ ,  $^{24}\text{Na}$ , and  $^{22}\text{Na}$ , from various targets are also useful for benchmark. The yields will be reported in the near future, some of them have already been published in [7].

## Conclusion

Applying an activation method, we successfully investigated the spectrum profile, intensity, and attenuation of the neutrons in the concrete shield at KENS. The profile of the neutron spectrum ranging from 10 to 500 MeV was kept and the intensity was exponentially attenuated with an increase in the depth of the concrete, although there was a small build-up of low-energy neutrons at depths below 40 cm. Furthermore, the CDMD formula was demonstrated to be suitable for the neutron spallation at KENS. Using this formula, the charge distributions of the yields and mass yield curves of medium targets were obtained. Furthermore, mass yield curves in an Au spallation are available to benchmark the residual products of heavy targets. In addition to the data, we will provide the further data in the near future.

## Acknowledgements

The authors thank the NML beam line staff of KEK for their valuable assistance in conducting the experiments. We appreciate the experimental assistance of Mr. K. Eda and Mr. K. Iijima of the Radiation Science Centre of KEK in placing and extracting the irradiation samples in the KENS experiments. We would also like to express our thanks to the staff at the Research Centre for Nuclear Science and Technology of the University of Tokyo for their helpful co-operation in the AMS measurements.

## References

- [1] N. Nakao, et al., "Arrangement of High Energy Neutron Irradiation Field and Shielding Experiment Using 4m Concrete at KENS", *Radiat. Prot. Dosim.*, 116, 553-557 (2005).
- [2] N. Nakao, et al., "KENS Shielding Experiment (1): Measurement of Neutron Attenuation Through 4 m Concrete Shield Using a High Energy Neutron Irradiation Room", *Proc. 2<sup>nd</sup> iTRS International Symposium on Radiation Safety and Detection Technology (ISORD-2)*, 24-25 July 2003, Tohoku University, Sendai, Japan, *J. Nucl. Sci. Technol.*, Suppl. 4, 26 (2004).
- [3] Q. Wang, et al., "KENS Shielding Experiment (2): Measurement of the Neutron Spatial Distribution Inside and Outside of a Concrete Shield Using an Activation Foil and an Imaging Plate Technique", *Proc. 2<sup>nd</sup> iTRS International Symposium on Radiation Safety and Detection Technology (ISORD-2)*, Tohoku University, Sendai, Japan, 24-25 July 2003.
- [4] K. Oishi, et al., "Measurement and Analysis of Induced Activities in Concrete Irradiated by High Energy Neutrons at KENS Neutron Spallation Source Facility", *Radiat. Prot. Dosim.*, 115, 623-629 (2005).
- [5] H. Matsumura, et al., "Characteristics of High-energy Neutrons Estimated Using the Radioactive Spallation Products of Au at the 500-MeV Neutron Irradiation Facility of KENS", *Radiat. Prot. Dosim.*, 116, 1-5 (2005).
- [6] T. Aze, et al., *Measurement of the <sup>36</sup>Cl production Rates from Cl, K, and Ca in Concrete at the 500-MeV Neutron Irradiation Facility at KENS*, KEK Preprint 2005-99.
- [7] H. Matsumura, et al., "Target Dependence of Beryllium Fragment Production in Neutron- and Alpha-induced Nuclear Reactions at Intermediate Energies", *Radiochim. Acta*, 93, 497-501 (2005).
- [8] S.R. Sarkar, et al., "Photospallation of Complex Nuclei at Intermediate Energies. II", *Radiochim. Acta*, 55, 139-154 (1991).
- [9] G. Rudstam, et al., "Systematics of Spallation Yields", *Naturforschg.*, 21a, 1027-1041 (1966).



## **Megapie: Residue yields and radioactivity predictions with different models in MCNPX**

**J-C. David, A. Boudard, S. Lemaire, S. Leray, S. Panebianco**  
CEA Saclay, DSM/DAPNIA, France

### **Abstract**

*During the last years, numerous experiments dedicated to spallation reactions have been performed and coupled to the development of codes. Among these studies, a lot of efforts have been devoted to the validation of the intra-nuclear cascade (INC) model, INCL4 [1], developed in a collaboration between Saclay and the University of Liège, combined with the evaporation-fission model, Abla [2] from GSI. These models have been implemented into the transport code MCNPX2.5.0 [3], so that we can easily compare them to the other models already included (Bertini [4] and Isabel [5] for INC part, Dresner [6] for the de-excitation step, and also the CEM2k [7] stand alone combination). In this paper, we will study the residue production in a real spallation target, the Megapie target [8] that will be irradiated next July at PSI. The differences between the models predictions for masses and activity rates will be shown and discussed.*

## Introduction

Spallation reactions, and their by-products, appear as a useful tool for basic research, technological applications and even mankind purposes. Some of the nuclei produced in these reactions are exotic, neutron rich for example. Thus numerous facilities, referred as Radioactive Ion Beam (RIB), already built (Spiral - GANIL), planned (Spiral2-GANIL, Fair-GSI) or studied (Eurisol, RIA) are based on these reactions. Another important feature is the large amount of emitted neutrons during the process (20-25 neutrons per proton for the reaction  $p(1\text{ GeV})+\text{Pb}$ , for instance). These neutrons can be used to drive subcritical reactors, so called Accelerator Driven System (ADS), which could be helpful for nuclear waste transmutation. Some projects already exist such as Myrrha or SAD. These neutrons can also directly irradiate materials as it is done in material testing reactors, but with a larger spectrum. The American Spallation Neutron Source (SNS) which started this year is one of the existing examples.

Spallation reactions consist of an energetic light particle impinging a nucleus. Particle can be a nucleon or a light ion ( $d$ ,  $t$ ,  $^3\text{He}$ ,  $\alpha$ ) with a kinetic energy ranging from 100-200 MeV.A to about 2.5 GeV.A. Some models are able to give unexpected rather good results even below 100 MeV [9]. Due to the large range of energy considered we cannot rely on data as it is done for low energy neutrons (below 20 or 150 MeV), and models are needed. Those models consider a reaction often divided into two steps: a first and fast one, the IntraNuclear Cascade (INC), followed by the second slower, the de-excitation (evaporation and/or fission). A third one is sometimes proposed in between, the pre-equilibrium stage.

We can find numerous models for the INC (Bertini, Isabel, INCL4, CEM, FLUKA (peanut) [10]...) and for the de-excitation as well (Dresner (with RAL [11] or ORNL [12] for fission), GEM [13], Abl, FLUKA ...). In the past years several of these models have been improved thanks to the new data obtained for light particle production (mainly neutrons, but also light charged particles) and for residue production (through inverse kinematics (GSI) or  $\gamma$ -spectrometry). Data mentioned here are devoted to thin targets, where models can be easily tested. Existing data on thick targets are scarce and principally focused on neutron production. To reproduce them we first have to develop models that produce the correct level and nature of emitted particles, with their spectra. They must also describe the reaction for incident particle in a wide energy range, because of secondary particle emission, with lower energies than the primary projectile and inducing also spallation reactions.

At CEA-Saclay, our spallation group is involved, on the experimental side, with measurements at Saturne [14] (particle) and GSI (residue within FRS [15] and now Spaladin [16]), but also, on the modelling side, with INCL4, and finally in the implementation of INCL4 and Abl in the transport codes LAHET3.16 [17] and MCNPX2.5.0. Comparisons of models to data have been done within different frameworks (Hindas [18], Eurisol [19]...). We are now interested in doing some predictions for real spallation targets and especially Megapie. We will present in the following comparisons of different codes or code combinations available in MCNPX to experimental data (thin and thick targets). Then we will explain how we can obtain, with the use of CINDER'90 combined with MCNPX, the masses of the residues and activities associated for a given irradiation time and at several steps after shutdown. Finally, we will show the results obtained with different models in MCNPX for the Megapie target.

## Models/data comparisons

The use of tools can only be efficient if one knows how good they are for a given purpose.

Comparison of models to data for thin target (test of the physics of the model for given projectile, energy and target) and for thick targets (real targets, test of all possible incident particles with a wide energy range) is a tremendous task. So we will show, in the following, few results obtained with the different models included in MCNPX and will compare them to experimental data.

### Thin targets

Data shown or discussed below are taken from [20] for neutrons, [21] for the light charged particles and [15], [22] for the residues.

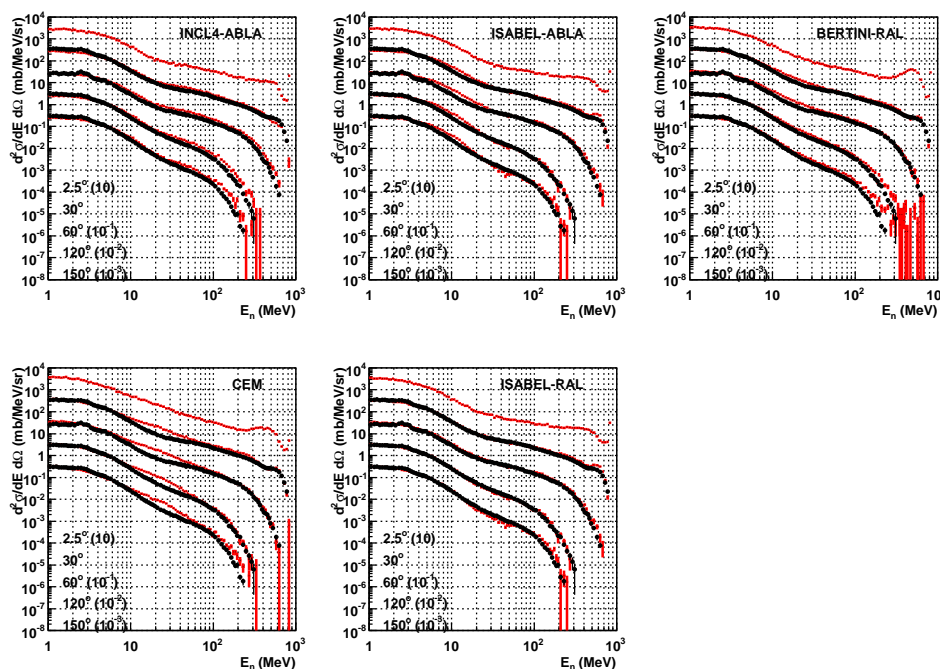
## Neutron

It should be mentioned that Bertini is always used with the pre-equilibrium process, as recommended by the authors of LAHET3.16.

Neutron energy spectrum is easily reproduced by the different models. Their agreement with experimental data is quite good (Figure 1), even if some improvements remain to be done.

**Figure 1: Neutron spectra for the reaction p(800 MeV)+Pb – five model combinations available in MCNPX2.5.0**

Here “RAL” means Dresner combined with RAL fission model



## Light charged particle

Figures discussed below can be seen in the B. Rapp, et al. report “Benchmarking of the modelling tools within the EURISOL DS project”, task 4 of this SATIF-8 meeting.

Proton spectra are not so well reproduced as for neutrons, but results are still good.

The situation is different for  $\alpha$  spectra. Whatever the model used the result is in strong disagreement with experimental data. If we focussed our attention on INCL4-Abla, the shortcomings are due to the fact INCL4 does not emit  $\alpha$  (or any other lcp with  $A > 1$ ), so it misses the high energy part of the energy spectrum. In addition Abla, for the evaporation stage, do not consider the emission of d, t or  $^3\text{He}$  and parameters or ingredients, used to model the evaporation process, are sometimes too simple (coulomb barriers and capture cross-sections, for instance). New improved versions of INCL4 and Abla solving these problems are studied and available, but not yet implemented in transport codes.

## Residue

INCL4-Abla (or Isabel-Abla) reproduces well the mass and charge distributions, except for the residues produced after a long evaporation process. Bertini-Dresner reaches the same level of agreement except for the fission part (Figure 2) which is in bad agreement with experimental data.

INCL4-Abla is able to reproduce quite well excitation functions (Figure 3), which is not always the case for Bertini-Dresner.

Figure 2: Mass distribution for p+Pb at 1 GeV.A

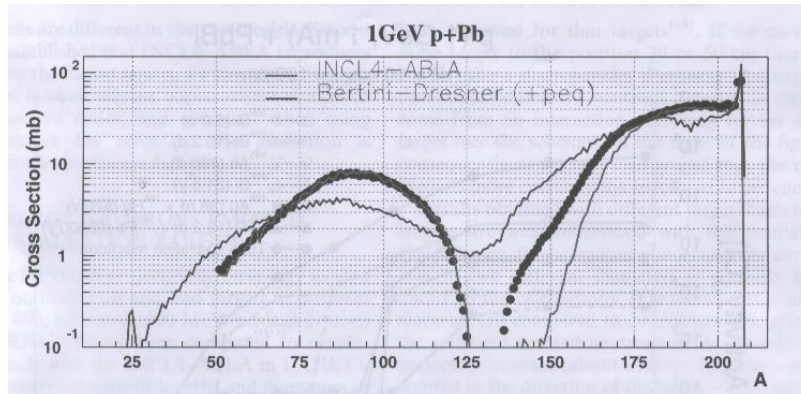


Figure 3: Excitation functions for the reaction p(70 MeV→2.6 GeV)+Pb, INCL4\_Abla is red and Bertini\_Dresner blue

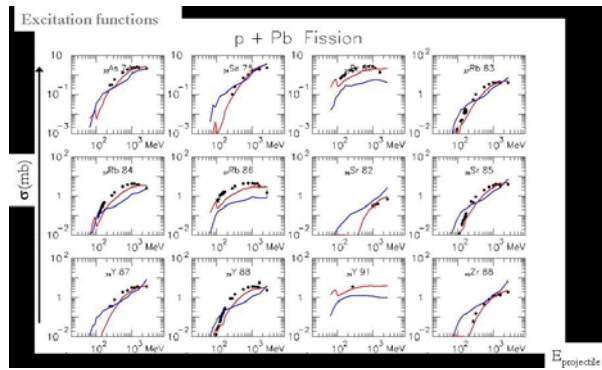
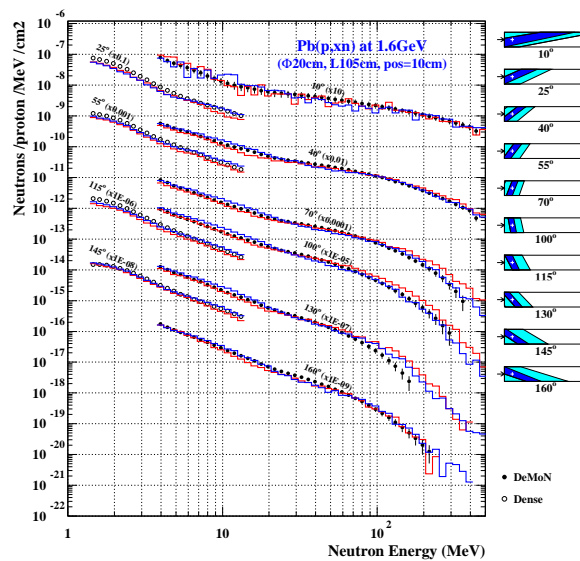


Figure 4: Comparisons of neutron spectra between SATURNE data (black points), INCL4\_Abla model (red line) and Bertini\_Dresner model (blue line) for p(1.6 GeV)+Pb



### Thick targets

Data are scarce compared to thin targets and mainly dedicated to neutron spectra.

References used below are [23] for the neutrons and [24] for the residues.

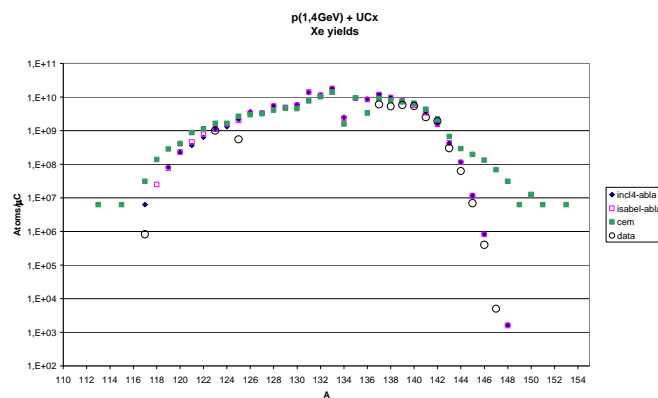
#### Neutron

As for thin targets, the neutron spectra are equally well reproduced by the models. As a result the choice of the model is not crucial for such observables.

#### Residue

Very few data exist for residue production in thick target. Here we show Xe isotopic distributions obtained at CERN with an UCx target. Discrepancies appear between the models predictions. INCL4-Abla and Isabel-Abla give rather good results.

**Figure 5: Production yields of Xe isotopes from ISOLDE UC\_x targets. Three models are compared to the data.**



### MCNPX-CINDER'90

For each spallation targets, there are two different steps: irradiation and cooling time. In order to calculate nuclei production one needs to produce the nuclei and let them decay, since most of them are radioactive. The production is due to the spallation reaction, but also to neutron reactions at low energies. Then, to get the nuclei produced at a given time (during irradiation and after) we use for spallation residue production the multi-particle transport code MCNPX2.5.0 combined with the material evolution programme CINDER'90 [25]. It will compute the nuclei produced by low energy neutrons (spectrum given by MCNPX) and take into account the radioactive decays.

### Megapie

The Megapie project, at PSI (Switzerland) within the SINQ facility, aims at demonstrating the feasibility of a liquid Lead-Bismuth spallation target [8]. The beam will be a 575 MeV and 1.4 mA proton beam (~0.8 MW). A detailed view is shown below (Figure 6).

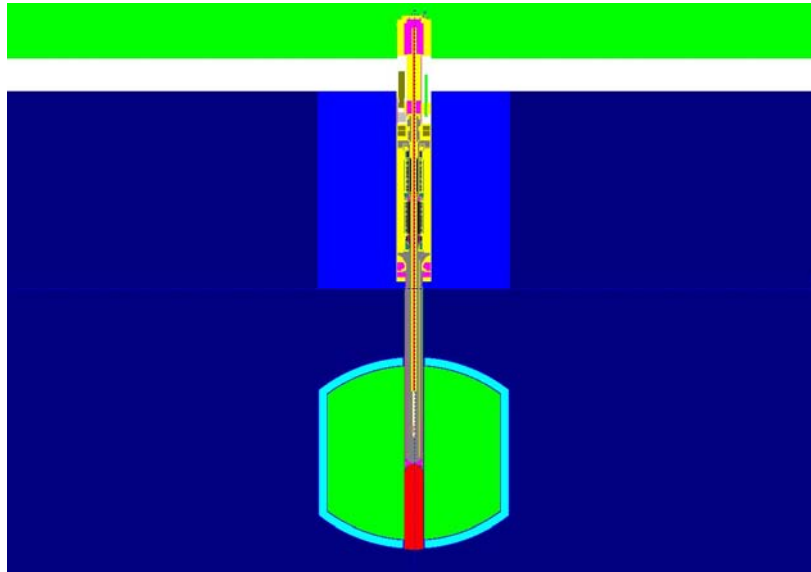
A comprehensive work has already been performed within the X9 group for the R&D of Megapie [26]. Proton and neutron fluxes, power deposition, radiation damage and isotope production have been calculated with several code systems. For all of these observables no significant differences are found, except for isotope production. Since for this benchmark MCNPX was only used with the default option for the high energy part, that is Bertini for the INC stage and Dresner for the de-excitation stage, we decided to compare this default option to the other better and/or still improved combination models, which are INCL4-Abla, Isabel-Abla and CEM2k.

**Activities in four different places**

Activities obtained by the different codes are compared in four different places made of four different materials. These materials are 316L (Stainless steel), T91 (mainly Iron), AlMg3 and Pb-Bi target. 316L is in the central rod (yellow in Figure 6). T91 is around the Pb-Bi target from the bottom to the top. AlMg3 is between the heavy water (green) and the light water (blue).

**Figure 6: Megapie geometry used for MCNPX**

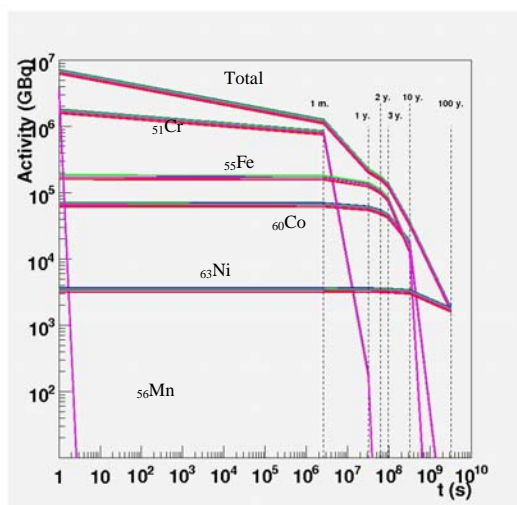
Proton beam comes from the bottom. The liquid Pb-Bi target (grey) is surrounded by heavy water (green). The upper part is dedicated to the cooling.



316L

The models give the same results within around 15%.

**Figure 7: On the left, activities are plotted for above-mentioned models. Total and main contributors are shown. On the right a table gives the ratio (%) to INCL4\_Abla for main contributors.**



INCL4-Abla  
Isabel-Abla  
CEM2k  
Bertini-Dresner

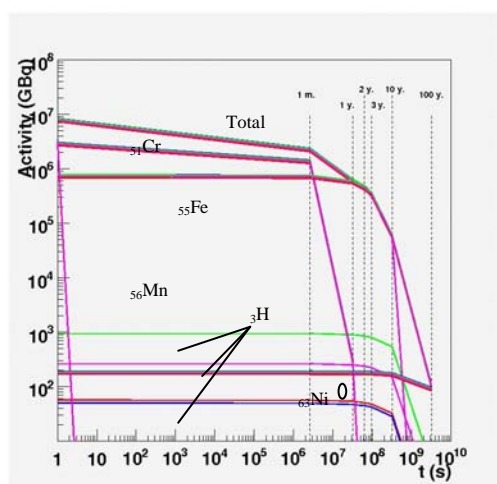
	1s	1m	1y	2y	3y	10y	100y
<b>Mn56</b>	15 6 12	15 6 12					
<b>Cr51</b>	15 6 12	15 6 12	15 6 12	15 6 12	15 6 12		
<b>Fe55</b>	15 7 16						
<b>Co60</b>	15 6 12						
<b>Ni63</b>	15 6 12						

Isabel\_Abla  
Bertini-Dresner  
CEM2k

T91

All results agree within 15%, except for the activity coming from  $^3\text{H}$  where Isabel and INCL4 give the same value, while Bertini and CEM2k are respectively 4 times and 16 times higher. This isotope comes from either the spallation reaction or from low energy neutron reaction. In fact this result is not surprising since neither INCL4, Isabel nor Abla emits tritium when Bertini-Dresner and CEM2k do it. Since we saw that these models produce approximately the same neutron flux (Figure 1), the low energy neutron interactions cannot explain the production of  $^3\text{H}$ . The implementation of tritium emission by INCL4 and Abla is in progress, and we know that the production of tritium by CEM2k is too high as it can be seen on the Figure 5 of the B. Rapp, et al. report, task 4 of this SATIF-8 meeting.

Figure 8: See Figure 7 for explanations



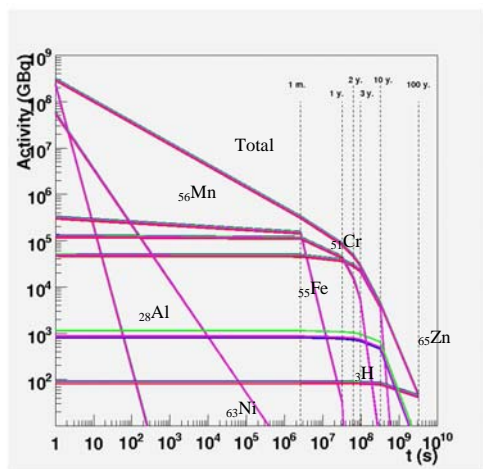
INCL4-Abla  
Isabel-Abla  
CEM2k  
Bertini-Dresner

	1s	1m	1y	2y	3y	10y	100y	
	-12	-12	-12	-12	-12	-12	-12	Isabel_Abla
H 3	366	366	366	366	366	366	366	Bertini-Dresner
	1578	1578	1578	1578	1578	1578	1578	CEM2k
Cr51	15	15	15	15	15			
	6	6	6	6	6			
	12	12	12	12	12			
Mn56	15	15						
	6	6						
	12	12						
Fe55	14	14	14	14	14	14	14	
	7	7	7	7	7	7	7	
	14	14	14	14	14	14	14	
Ni63	15	15	15	15	15	15	15	
	6	6	6	6	6	6	6	
	11	11	11	11	11	11	11	

AIMg3

The conclusions are similar to the previous ones for T91, except that here the material is far from the beam. As a consequence, only the low energy neutrons play a role for the tritium production. That explains the little difference observed (36%).

Figure 9: See Figure 7 for explanations



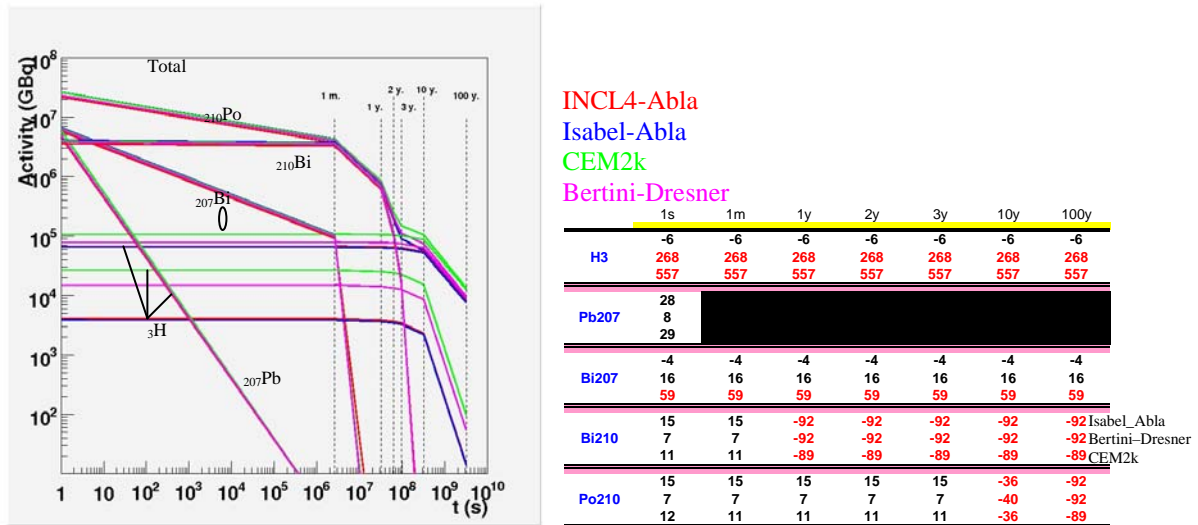
INCL4-Abla  
Isabel-Abla  
CEM2k  
Bertini-Dresner

	1s	1m	1y	3y	10y	100y	
	-5	-5	-5	-5	-5	-5	
H 3	4	4	4	4	4	4	
	36	36	36	36	36	36	
Al28	13	-11					
	6	5					
	11	32					
Cr51	13	13	13	13			
	6	6	6	6			
	11	11	11	11			
Mn56	13						
	6						
	11						
Fe55	13	13	13	13	13	13	
	6	6	6	6	6	6	
	11	11	11	11	11	11	
Ni63	14	14	14	14	14	14	
	6	6	6	6	6	6	
	11	11	11	11	11	11	
Zn65	13	13	13	13	13	13	
	6	6	6	6	6	6	
	11	11	11	11	11	11	

**Pb-Bi target**

The situation is a bit more complicated in the target. All models agree within 30% or even less, except for tritium, <sup>207</sup>Bi and <sup>210</sup>Pb. The <sup>3</sup>H case has been explained previously. For <sup>207</sup>Bi the difference is not so important since only CEM2k show a discrepancy around 60%. To explain it, one should first know from which channel this isotope is produced, <sup>206</sup>Pb is a candidate, and secondly, look at the behaviour of these models on experimental isotopic distributions for element close to the target. Concerning <sup>210</sup>Pb differences begin to appear only after 1 year. This isotope can be produced directly by spallation, but also by the radioactive decay of <sup>210</sup>Pb, and INCL4 produces more <sup>210</sup>Pb than all other models.

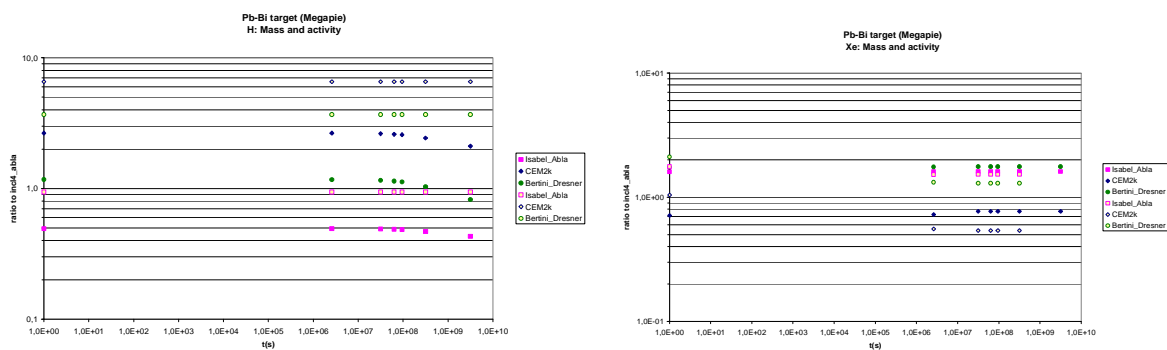
**Figure 10: See Figure 7 for explanations**



**Volatiles**

We plot below H and Xe masses and activities ratio to INCL4\_Abla for the three others models: Isabel\_Abla, CEM2k and Bertini\_Dresner.

**Figure 11: H (left) and Xe (right) activity and mass (bi-colour points) ratio to INCL4\_Abla for Isabel\_Abla, CEM2k and Bertini\_Dresner model**



For hydrogen, mass is mainly due to proton and activity to tritium, so we observe the same differences or similarities between the models as the ones seen before concerning tritium.

For xenon, coming from the fission process, the results are within a factor two. If mass and activity have different ratios, the reason has to be found in the isotopic distributions. Thus Zanini, et al. [27] showed the same behaviour for Bertini\_Dresner compared to INCL4\_Abla, since the former predicts

bigger mass than the latter. Nevertheless, one has to mention that in this paper results are obtained with a 1.4 GeV proton beam while the Megapie beam is a 0.575 GeV proton beam, so, if it gives us an explanation, energies and materials considered must be as close as possible and one has to use it carefully. For example, if we change the material, UCx instead of Pb-Bi, with a 1.4 GeV proton beam, the ratio of Isabel\_Abla obtained here (Figure 11) is not easy to explain when looking at Figure 5.

## Conclusion

This study aimed at comparing models available in the transport code MCNPX2.5.0: default option Bertini-Dresner and three other models, some still under development, INCL4-Abla, Isabel-Abla and CEM2k. Comparisons have been performed for the Megapie project that is a liquid lead-bismuth spallation target.

The results obtained on activities, with four different materials, but also on masses for volatile elements in the target, show some discrepancies. Different reasons may explain these results. Fission process modelling can explain the differences for volatile like Xe (Figure 11). For tritium production, some models have to improve the evaporation predictions. Finally, the INC models may give a different level of isotope production for nuclei close to the spallation target ( $^{210}\text{Bi}$ ).

## References

- [1] A. Boudard, et al., *Phys. Rev.*, C 66 (2002) 044615.
- [2] A.R. Junghans, et al., *Nucl. Phys.*, A 629 (1998) 655.
- [3] *The MCNPX Version 2.5.0 User's Manual*, LA-CP-05-0369, April 2005.
- [4] H.W. Bertini, *Phys. Rev.*, 131, (1963) 1801; H.W. Bertini, *Phys. Rev.*, 188, (1969) 1711.
- [5] Y. Yariv, Z. Fraenkel, *Phys. Rev.*, C 20 (1979) 2227; Y. Yariv, Z. Fraenkel, *Phys. Rev.*, C 24 (1981) 488.
- [6] L.W. Dresner, ORNL-TM-196 (1962).
- [7] S.G. Mashnik, A.J. Sierk, *Recent Developments of the Cascade-Exciton Model of Nuclear Reactions*, Los Alamos National Laboratory Report LA-UR-01-5390, Los Alamos (2001).
- [8] Megapie, <http://megapie.web.psi.ch/>.
- [9] J. Cugnon, P. Henrotte, *Eur. Phys. J.*, A16 (2003) 393-407.
- [10] A. Ferrari, P.R. Sala, A. Fassò, J. Ranft, *FLUKA: A Multiparticle Transport Code*, CERN2005-10 (2005), INFN/TC-05/11, SLAC-R-773; <http://pcfluka.mi.infn.it/> (March 2006).
- [11] F. Atchison, "Spallation and Fission in Heavy Metal Nuclei Under Medium Energy Proton Bombardment", *Proc. Meeting on Targets for Neutron Beam Spallation Source*, Jülich, 11-12 June 1979, pp. 17-46, G.S. Bauer (Ed.), Jul-Conf-34, Kernforschungsanlage Jülich GmbH, Germany (1980).
- [12] J. Barish, T.A. Gabriel, F.S. Alsmiller, R.G. Alsmiller, Jr., "Hetfis": *High-Energy Nucleon-Meson Transport Code with Fission*, ORNL/TM-7882 (Jul 1981), 26 p.
- [13] S. Furihata, *Nucl. Inst. and Meth.*, B171 (2000) 251.
- [14] S. Leray, *Phys. Rev.*, C 65, 044621 (2002).

- [15] W. Wlazlo, et al., *Phys. Rev. Lett.*, 84 (2000) 5736 / arXiv nucl-ex/0002011; J. Benlliure, et al. *Nucl. Phys.*, A 683 (2001) 513-539; F. Rejmund, et al., *Nucl. Phys.*, A 683 (2001) 540-565; T. Enqvist, et al., *Nucl. Phys.*, A 686 (2001) 481-524; M. Bernas, et al., *Nucl. Phys.*, A 725 (2003) 213-253 / arXiv nucl-ex/0304003; J. Taieb, et al., *Nucl. Phys.*, A 724 (2003) 413-430 / arXiv nucl-ex/0302026.
- [16] S. Pietri, *AIP Conference Proceedings*, 26 April 2006, Volume 831, Issue 1, pp. 535-537.
- [17] LAHET Version 3.16, LA-UR-01-1655, 18 June 2001.
- [18] HINDAS, EC Contract No. fikw-ct-2000-00031, final report (2004).
- [19] EURISOL Design Study web page, [www.eurisol.org](http://www.eurisol.org) (March 2006).
- [20] W.B. Amian, et al., *Nucl. Sci. Eng.*, Vol. 112, 1992, p. 78.
- [21] B. Rapp, et al., CEA Saclay, Mar. 2006, <http://eurisol.wp5.free.fr/>, TN-06-04.
- [22] J-C. David, et al., *XVI International Workshop on Physics of Nuclear Fission IPPE*, Obninsk, Russia, 7-10 October 2003 (and references therein), <http://nucleus.ru/fission2003/schedule.htm>.
- [23] J-C. David, et al., *Proceedings of the International Workshop on Nuclear Data for the Transmutation of Nuclear Waste*, GSI-Darmstadt, Germany, 1-5 September 2003, ISBN 3-00-012276-1 (and references therein).
- [24] U.C. Bergmann, et al., *Production Yields of Noble-gas Isotopes from ISOLDE UC\_x/graphite Targets*, CERN-EP/2002-048.
- [25] W.B. Wilson, et al., "Status of CINDER'90 Codes and Data", *Proc. 4<sup>th</sup> Workshop on Simulating Accelerator Radiation Environments*, 13-16 September 1998, Knoxville, Tennessee, USA, pp. 69-79, Los Alamos National Laboratory Report, LA-UR-98-361 (1998).
- [26] L. Zanini, *Summary Report for MEGAPIE R&D Task Group X9: Neutronic and Nuclear Assessment*, PSI Bericht, Nr. 05, 12 December 2005, ISSN 1019-0643.
- [27] L. Zanini, et al., "Volatile Elements Production Rates in a 1.4 GeV Proton-irradiated Molten Lead-bismuth Target", *Proceedings of the Int. Conference on Nuclear Data for Science and Technology*, Santa Fe, NM, USA, 26 September-1 October 2004.

## Radioactive waste study of the ATLAS detector

V. Hedberg,<sup>1,2</sup> M. Magistris,<sup>2</sup> M.N. Morev,<sup>3</sup> M. Silari,<sup>2</sup> Z. Zajacová<sup>2,4</sup>

<sup>1</sup>University of Lund, Sweden

<sup>2</sup>CERN, 1211 Geneva 23, Switzerland

<sup>3</sup>MEPhI, Moscow, Russian Federation

<sup>4</sup>Slovak University of Technology, Bratislava, Slovak Republic

### Abstract

Extensive simulations with the FLUKA Monte Carlo code were performed using a complex model of the ATLAS detector, consisting of more than 800 regions, to estimate the production of radioactive waste and the evolution of its radiological characteristics. The source of particles was created with an offline generator of  $p$ - $p$  collisions. Specific biasing techniques in the transport of low-energy neutrons and the latest heavy-fragment evaporation model were adopted. A virtual isotropic source of neutrons was also used to estimate the region volumes by scoring the neutron track-length inside each region. FLUKA allows scoring the nuclide production-rate per  $p$ - $p$  interaction. The activity of each nuclide after a predefined irradiation cycle was normalised online to reference values taken from the European or Swiss legislations, to obtain an absolute estimate of the radiological hazard. The impact of changing the waiting time on the zoning was investigated. The activation of the detector was also calculated with the general analytical activation formula from the fluxes of high-energy hadrons and low-energy neutrons obtained from simulations with the GCALOR code. The results compare well with the FLUKA predictions.

## Introduction

The installation of the CERN Large Hadron Collider (LHC) is under completion in a circular tunnel 27 km in circumference, previously housing the Large Electron Positron (LEP) collider. The tunnel, placed at a depth varying between 50 and 175 m, straddles the Swiss/French border on the outskirts of Geneva. LHC is designed to collide two counter rotating beams of protons or heavy ions. Proton-proton collisions are foreseen at an energy of 7 TeV per beam with a planned start-up in 2007. Each proton beam with full intensity consists of 2808 bunches, each bunch containing  $1.15 \times 10^{11}$  protons at the start of a nominal fill. The total energy stored in the nominal beam at top energy is 334 MJ. This enormous amount of energy will partly be deposited at the beam dumps at the end of each physics period, partly be dissipated in collimators and a certain fraction will convert into secondary particles following collisions at the centre of the experimental apparatus. Interaction of the primary and secondary particles with any material will generate induced radioactivity.

The LHC machine and the experiments are classified as Nuclear Basic Installation (*Installation Nucléaire de Base*, INB) in France. The French legislation requires that INB installations provide – among other things – a radioactive waste study before starting operation. A compulsory part of the study is the identification of areas where radioactive waste may be produced from areas where only the production of conventional waste is expected. In case of the LHC experiments this translates into the identification of a boundary dividing the experimental cavern into two zones – a radioactive waste zone and a conventional waste zone. This paper describes the calculations performed in order to determine the zoning of the ATLAS experiment.

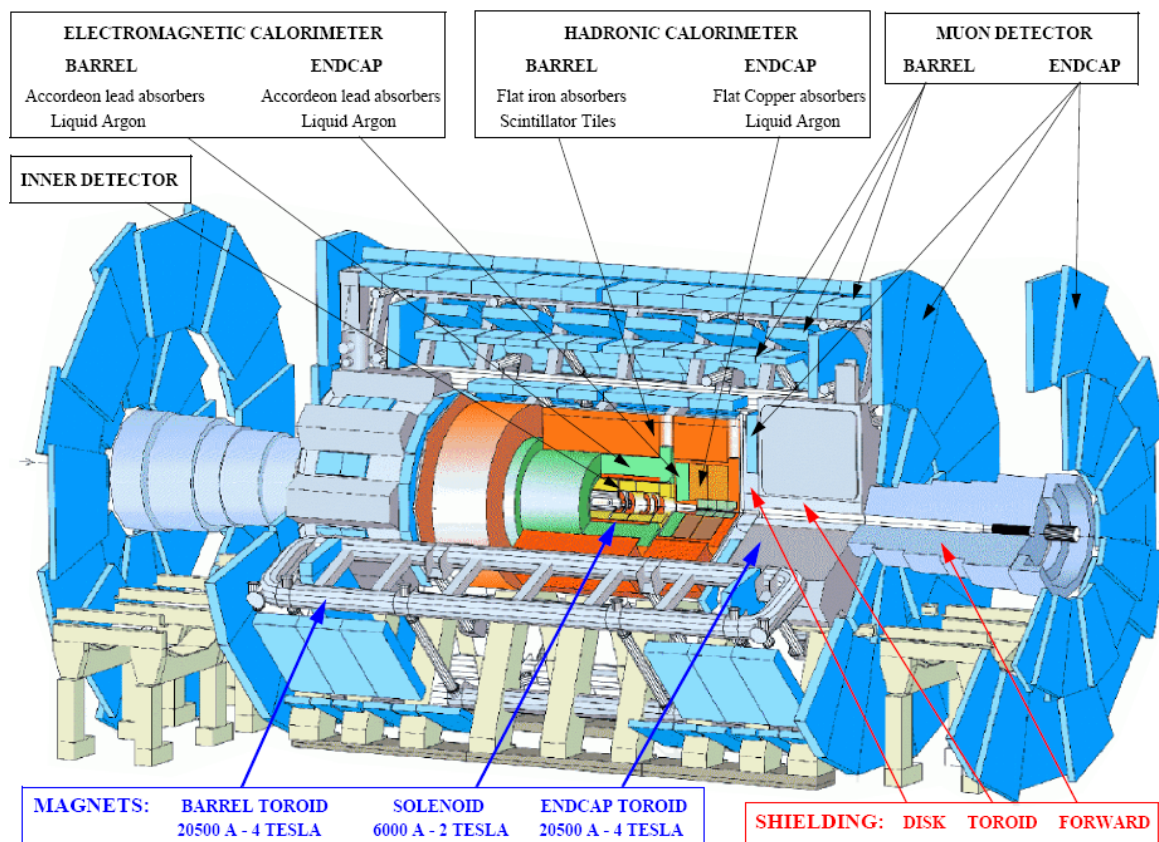
ATLAS (A Toroidal LHC Apparatus), the biggest of the LHC experiments, is installed in an underground cavern. ATLAS is 42 m long, 11 m in radius and weighs approximately 7 000 tonnes (Figure 1). It is one of the two high-luminosity, general-purpose LHC detectors (together with CMS). Beams of protons will collide at its centre with a centre of mass energy of 14 TeV and a design luminosity of  $10^{34} \text{ cm}^{-2} \text{ s}^{-1}$ . The collisions will create a harsh radiation environment that will cause activation of material, some (and eventually all) of which will become radioactive waste. The activation of the ATLAS detector was calculated with the aim to determine the boundary between the radioactive waste zone and the conventional waste zone. Three different calculation methods were employed. Two approaches relied on extensive simulations with the FLUKA Monte Carlo code, the third method was based on the analytical activation formula and prior knowledge of particle fluxes obtained from GCALOR simulations. This paper describes the three methods (referred to as FLUKA A, FLUKA B and GCALOR), their respective results and the degree of agreement between them.

## Zoning classification criteria

French legislation does not provide unconditional clearance levels (i.e. threshold values below which a material can be considered as non-radioactive) for specific activity (activity per unit mass) in materials to be released into the public domain. Release of material is only allowed after a detailed theoretical study supported by experimental measurements. The aim of such a study is to establish a “zoning” (*zonage*) of the facility (accelerator tunnel, experimental areas, etc.), i.e. a classification of areas where material may or may not have been activated. To demonstrate that a given component or material is “non-radioactive”, i.e. “conventional”, one has to prove that beam losses around the ring, or any other activation mechanism, can only produce “insignificant” amounts of radioactivity. For the *zonage* study of the LHC machine and experiments an operational limit was adopted for each radionuclide, equal to 1/10 of the exemption values as given by the European Directive (EU) of 13 May 1996 [1], following the same approach adopted for the decommissioning of LEP [2]. For most radionuclides found in accelerator components the EU exemption limit is 10 Bq/g (exceptions are, e.g. tritium and  $^7\text{Be}$ , for which the values are  $10^6$  Bq/g and  $10^3$  Bq/g, respectively). For radionuclides for which a value was not provided by the EU directive, the Swiss exemption limits (which essentially correspond to 1/10 of the EU values) [3] were adopted.

A major constraint imposed by the French legislation is that material or equipment classified as “radioactive” in the zoning study cannot be declassified as “conventional” after a measurement, no matter how accurate the latter is in showing no traces of induced radioactivity. Material can be “declassified” only by revising the zoning of its area of origin. If the zoning study is too pessimistic, one may end up with storing as radioactive a large amount of material, which is actually posing

Figure 1: Cut away view of the ATLAS detector



absolutely no radiological risk if released. On the other hand, one cannot be too optimistic either, since if too many anomalies (*écarts* in French) are detected (i.e. material classified as conventional in the zoning study but found to be radioactive by measurement) the French authorities can intervene and stop operation. The zoning study has therefore to be as realistic as possible.

### Calculation method FLUKA A

Methods A and B were both based on the use of the FLUKA Monte Carlo code [4,5]. Aspects common to the two methods were the geometry, the source and the physical settings of the simulations. A complex model of the ATLAS detector consisting of more than 800 regions was used. The source of particles was created with an offline generator of p-p collisions. The electromagnetic component of the radiation field was disregarded as its contribution to induced radioactivity is minor as compared to that generated by the hadronic component. Low energy neutrons were included in the calculations all the way down to thermal energy. A new evaporation model was used and heavy fragment evaporation was requested.

Method A consists of estimating the production rate of radioisotopes per region and per p-p collision with the RESNUCLEI option of FLUKA, followed by an offline treatment of the results for the build-up and the decay of radioactivity and the normalisation of the results to the radionuclide-specific exemption limits. In order to calculate the specific activity per region, the region volumes had to be calculated. A special Monte Carlo technique was developed for this purpose. All regions were assigned as vacuum and were enclosed in a virtual spherical isotropic source of neutrons. The track-length of these neutrons inside a region is proportional to its volume.

With this FLUKA method, the number of regions that can be investigated in one round of simulations is limited. The method was applied to 157 out of the 810 regions constituting the ATLAS geometry. The selection of the regions to be investigated was mainly governed by the need to gain rapidly a first insight into the level of activation of the different detector structures. Using this method, the results of the FLUKA simulations give the number of radioactive isotopes per region normalised to one p-p collision event. Scaling the results by the number of events corresponding to the length and intensity of the irradiation was used to account for the build-up of activity. The build-up of activity during irradiation and the decrease during the beam-off time was treated analytically by solving the Bateman equations to the third generation of decay products. This type of post-processing is less complete than the online treatment (method B, which treats the whole decay chain) but provides equivalent results for target elements lighter than lead. In addition, it has the advantage that the irradiation and cooling time conditions can be changed offline without repeating the FLUKA simulations.

Many of the regions of the ATLAS geometry are quite large and may correspond in reality to detector modules with finer structures. Scoring per region can only provide the average value of activity in the whole volume without any information on the distribution within the region. This has the unfavorable effect that hot spots in "cold" regions cannot be detected by this method. On the other hand, scoring in large regions offers the advantage of better statistics.

### Calculation method FLUKA B

From the physics point of view the greatest difference between methods A and B lies in the accuracy with which the build-up and decay of radioactivity are treated. An online treatment with the exact analytical solution of the Bateman equations was recently implemented in FLUKA [6]. This treatment provides a more accurate approach to the production and time evolution of residual nuclei because it considers all possible successive decays down to the last stable decay product (while method A stops at the third generation). In addition, it allows FLUKA to simulate complex irradiation conditions consisting of several periods of irradiation and intermittent cooling times. Furthermore, it records the exact position where every nuclide was produced and therefore provides the user with the induced radioactivity distribution. Method B exploited these new features of FLUKA.

Normalisation of the results with the exemption limits was also implemented in an online weighting routine. The results for individual radioisotopes (specific activity, mass and atomic number) are lost in the simulation process and the quantity provided by the FLUKA calculation reduces to:

$$\sum_i \frac{A_i}{LE_i}$$

where  $i$  is the produced radioisotope,  $A_i$  is its specific activity and  $LE_i$  is its exemption limit. For simplicity in the following we shall call this quantity  $\text{sum}_i(A_i/LE_i)$ . The analysis of these results is easier but the complementary information on the production of individual radioisotopes retained by method A is extremely valuable.

Scoring was requested on a region-independent RZ geometrical mesh encompassing the whole detector. The individual bins had 5 cm in Z, 5 cm in R and extended over the full azimuthal angle. The detector being almost symmetric around its axis, a precise spatial distribution of activity can be obtained and, at the same time, bins are large enough to provide good statistics.

### Calculation method GCALOR

The third method uses an entirely independent approach from the two described above. The specific activity was calculated with the general analytical activation formula:

$$A_i = n \int \sigma_i(E) \phi(E) dE \times \text{BuildUp}(T, t)$$

where  $i$  is the index of the produced radionuclide,  $A_i$  is its specific activity,  $n$  is the number of target nuclei per gram,  $\sigma_i$  is the production cross-section of radionuclide  $i$ ,  $\phi$  is the particle flux and  $\text{BuildUp}(T, t)$  is the function responsible for the activity build-up, which depends on irradiation time  $T$  and cooling

time  $t$ . In the simplest case when the decay chain includes only one nuclide, the function is calculated as  $\text{BuildUp}(T,t) = (1 - e^{-\lambda_i T})e^{-\lambda_i t}$ , where  $\lambda_i$  is the decay constant of radionuclide  $i$ . For longer decay chains the build-up function is calculated analytically by solving the Bateman equations to the third generation of decay products. All radionuclides with half-life exceeding one hour and having three or less radioactive progeny were explicitly treated. The contribution of all other short-lived activation products through decay chains was accounted for by appropriately increasing the production cross-sections for the explicitly treated nuclides (*i.e.* use was made of the cumulative cross-sections). This is a rather reasonable simplification taking into account that with a few exceptions most of the known radionuclides with half-life exceeding one hour have three or less radioactive progenies.

The fluxes of high-energy hadrons and low-energy neutrons on a fine spatial mesh were obtained from simulations with the GCALOR code in the GEANT geometry implementation of the ATLAS detector [7]. The cross-sections for proton induced activation were calculated with the Silberberg-Tsao [8,9] and the Rudstam formulas [10]. The proton cross-sections were also used for pions and neutrons with energy exceeding 20 MeV. Cross-sections for neutrons with energy below 20 MeV originated from various evaluated nuclear data libraries ENDFB-6.8, JEFF-2.2, etc.

The activation was calculated for an extensive list of materials, assuming each time a single material for all detector components. For each material, the maps of  $\sum_i (A_i/LE_i)$  were plotted over the detector volume, highlighting the  $10^{-1}$  isoline. Taking into account the material composition of the detector components and the  $10^{-1}$  isoline for each of the materials, it is possible to reconstruct which of the components will be activated to more than 1/10 of the exemption limit.

## Results

With method A it was possible to identify some regions that qualified as radioactive waste zone and others that would only contain conventional waste. Knowing the position of those regions and which part of the detector they represent it was possible to estimate roughly which detector components should fall inside or outside the radioactive waste zone. For example, the calculations showed that the large muon spectrometer systems, which form the outermost detector layer, will fall outside the zone while at least some of the calorimeter subcomponents will be inside. The calculations confirmed that regions such as the collimator and the shielding pieces close to the beam pipe were highly activated.

Based on the results of method A, the boundary defining the zoning was expected to lie within the calorimeter. The ATLAS calorimeter consists of the inner liquid argon calorimeter, which is enclosed in a cryostat, and the outer tile calorimeter. The two systems are distinct from the point of view of assembling and dismantling. While it was certain that most of the liquid argon calorimeter qualifies for the radioactive waste zone, it was not clear whether the tile calorimeter will also have to be included, or whether the boundary could lie between the two systems. Another point of interest was the End Cap Toroid as it was unclear whether it should be included in the radioactive waste zone or not.

More precise information on the position of the zoning boundary could be provided by method B, which offered the possibility of performing calculations on a geometrical mesh covering the whole detector, rather than to a limited and somewhat arbitrary selection of regions. Calculations were performed assuming 10 years of LHC operation and examining different cooling times (10 days, 100 days and 2 years). An ATLAS operational year consists of 120 days of continuous running at nominal luminosity of  $10^{34} \text{ cm}^{-2} \text{ s}^{-1}$  and 245 days with no running. Since comparatively short-lived radionuclides are not relevant for the present study, a continuous operation over the entire year at scaled down luminosity (*i.e.* about 1/3 of the nominal one) was assumed. All results are based on this assumption. Figure 2 shows the results after 100 days of cooling time. The plotted quantity is the  $\sum_i (A_i/LE_i)$ . Areas for which  $\sum_i (A_i/LE_i) < 0.1$  lie outside the radioactive waste zone. To the best possible approximation, the areas above 0.1 should be included inside this zone. Some exceptions to this rule can be made, provided that they are well understood and justified. To account for this, results were plotted to show also the layers where  $\sum_i (A_i/LE_i)$  is between 0.1-0.3 and 0.3-1.0.

The evolution of the  $\sum_i (A_i/LE_i)$  with cooling time is shown in Figures 3-5. The plots are zoomed on the central part of the detector (0-7 m in Z, 0-4 m in R), which includes the liquid argon and the tile calorimeters. Already after 10 days of cooling (Figure 3), most of the tile calorimeters would qualify for placement outside the radioactive waste zone. However, its inner layers should fall inside the zone,

**Figure 2: Residual radioactivity in ATLAS for 10 year operation followed by 100 days of cooling time**

Values are the weighted sum of the specific activity normalised to the radionuclide-specific exemption limits,  $\sum_i (A_i/LE_i)$

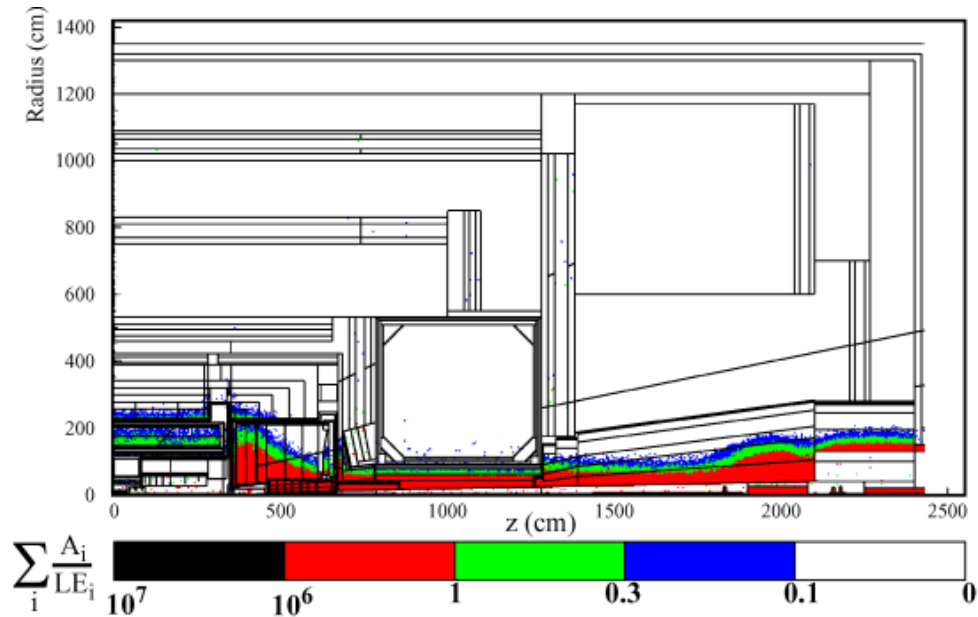


**Figure 3: Plot of  $\sum_i (A_i/LE_i)$  for the central part of the ATLAS detector (0-7 m in Z, 0-4 m in R), 10 year operation followed by 10 days of cooling time**

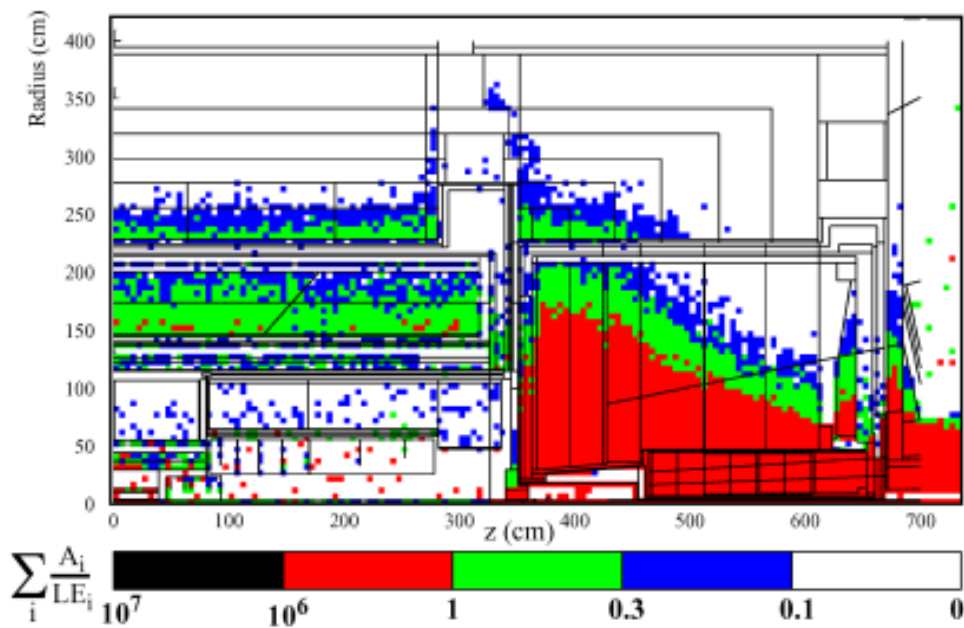


Figure 4: Plot of  $\sum_i (A_i/LE_i)$  for the central part of the ATLAS detector (0-7 m in Z, 0-4 m in R), 10 year operation followed by 100 days of cooling time

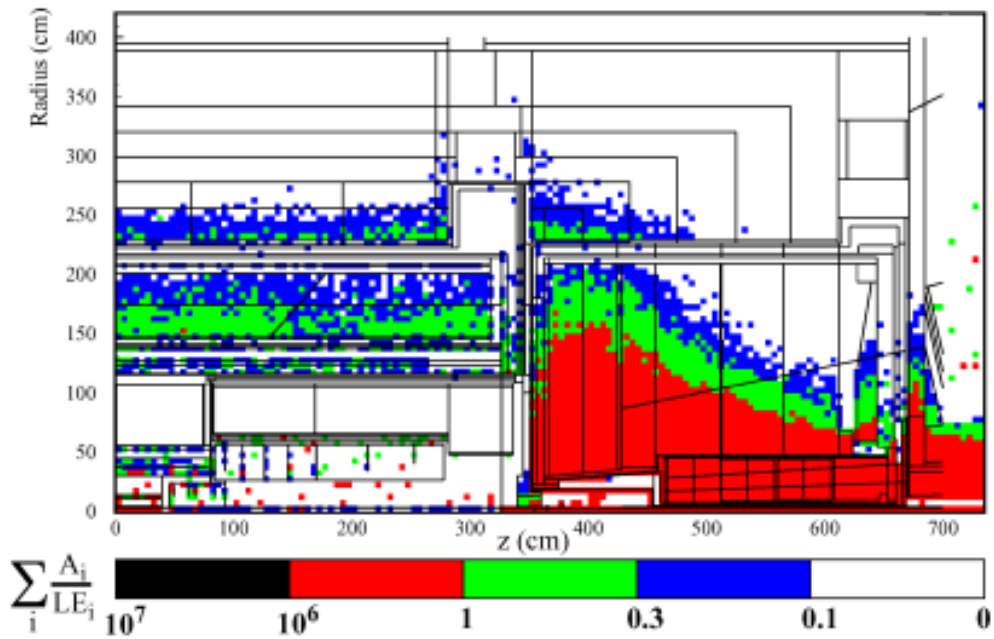
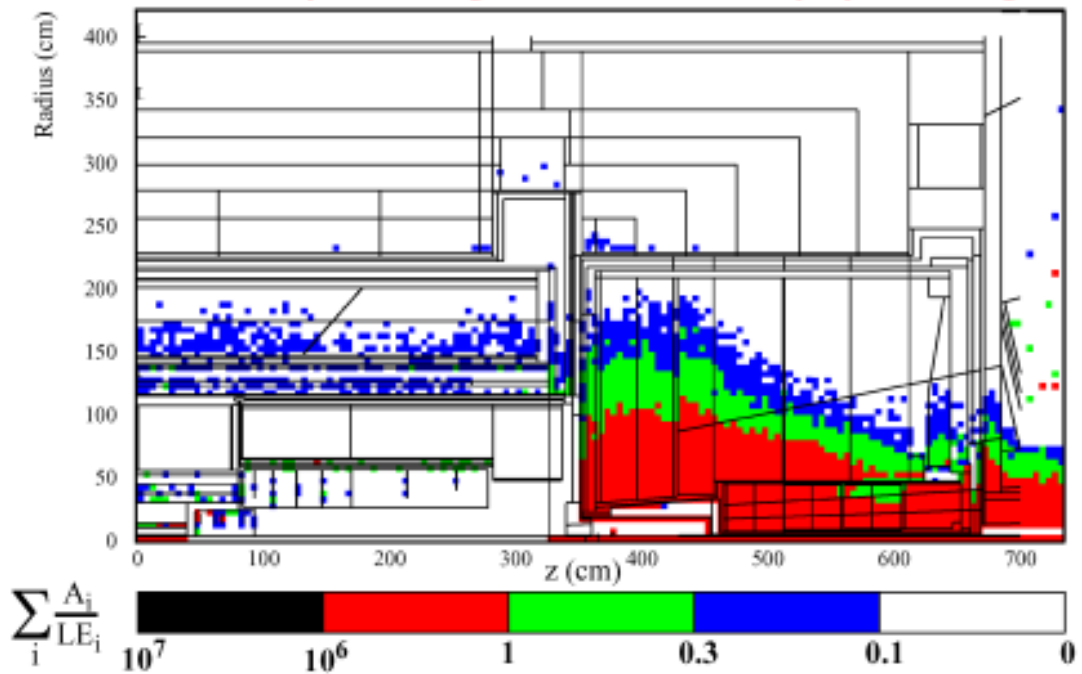


Figure 5: Plot of  $\sum_i (A_i/LE_i)$  for the central part of the ATLAS detector (0-7 m in Z, 0-4 m in R), 10 year operation followed by 2 years of cooling time



which might imply that the whole tile calorimeter (which consists of 64 wedges) would have to be included since it cannot easily be split along R. After 100 days of cooling (Figure 4) the situation remains the same from the zoning point of view, although it is visible that the specific activity in the tile calorimeter decreased and most of the areas with  $\sum_i(A_i/LE_i) \in [0.3, 1.0]$  after 10 days of cooling belong now to the layer where  $\sum_i(A_i/LE_i) \in [0.1, 0.3]$ . After 2 years of cooling (Figure 5) the activity in the tile calorimeter has decayed enough so that the entire structure would qualify for placement in the conventional waste zone.

Extensive calculations with the GCALOR method produced large amount of results. For each of the 21 materials studied, the high-energy hadron and low-energy neutron activations were calculated and the sum of the two were plotted in form of maps showing the  $\sum_i(A_i/LE_i)$ . This was repeated for several different assumptions of irradiation and cooling times, and for different cross-section sets. Four examples are shown in Figures 6-9, corresponding to calculations for Al, Ni, Co and stainless steel (69% Fe, 18% Cr, 11% Ni, 1.8% Mn and 0.2% Co), after 10 years of irradiation, followed by 100 days of cooling, based on cross-sections calculated with the Silberberg-Tsao formula for high-energy hadrons and library data for neutrons.

If the whole detector were made of aluminium, the  $10^{-1}$  isoline of  $\sum_i(A_i/LE_i)$ , marking the radioactive waste zone, would reach a maximum radius of less than 3 metres at a distance of 3-4 m from the interaction point (and about 1 m beyond 3-4 in Z). This location corresponds to the peak visible in the FLUKA calculations between the barrel and the extended barrel parts of the tile calorimeter. If the detector were made of nickel, the zone would be larger, extending 4 metres at the location of this peak and including another broad peak, almost 5 metres in radius stretching between 6 and 13 metres from the interaction point. The second peak cuts through the End Cap Toroid. If the detector were made of cobalt, practically the whole cavern would fall within the radioactive waste zone. This is due to the low-energy neutron activation, particularly the reaction  $^{59}\text{Co}(n, \gamma)^{60}\text{Co}$ . For most of the other materials (Fe, Cu, Pb, Au, Re, W, Sn, Nb, Mn, Cr, Ti, Si, C and Be) the zoning boundary lies below that of nickel. Only alloys with more than 0.1% cobalt, 1% antimony, 10% zinc and 1% silver have zoning boundaries larger than nickel.

After determining that no such alloys are used in ATLAS (the cobalt content in stainless steel was a particular concern), it was found that nickel represents the worst case for a cooling time of 100 days, and iron for a cooling time of 2 years (in fact, a large fraction of the detectors and the shielding is made of iron). The results for nickel at 100 days and iron at 2 years are in good agreement with the FLUKA simulations.

## Conclusions

The results of the present calculations served as a basis for the decision on the zoning of the ATLAS experiment. Other aspects influencing the decision were the expected irradiation conditions and cooling times that the detector will experience, the likelihood and time horizon in which a component might become waste, the physical boundaries of the components, and the need to prevent overestimation of the radioactive waste zone while ensuring that to the current best knowledge it includes all areas where radioactive waste may be produced.

Most ATLAS detector components will only become waste at the time of decommissioning of the LHC. For this reason, the FLUKA calculations were based on a simplified running scenario consisting of 10 years of homogeneous irradiation, which corresponds to 10 years of LHC operation at a luminosity  $10^{34} \text{ cm}^{-2} \text{ s}^{-1}$  for 120 days per year. Other operation scenarios were explored by the GCALOR method but it was found that the duration of the irradiation did not exert a strong influence on the zoning. The length of the cooling time, however, makes a large difference on the zoning. For example, the tile calorimeter would fall outside of the radioactive waste zone if the cooling time would be 2 years, but if the cooling time would be 100 days it would either have to be included inside the zone as one piece, or the zone will cut through it, which would imply cutting the component at the time of its dismantling, in order to separate the radioactive material from the conventional one. Two years of waiting is not unreasonable, especially for massive components, considering that the dismantling of the detectors will not start immediately after the LHC ends operation and that it will take a considerable amount of time.

**Figure 6: Isolines of  $\sum_i(A_i/LE_i)$  calculated with GCALOR and the Silberberg-Tsao cross-sections for aluminium, 10 year operation followed by 100 days of cooling time**

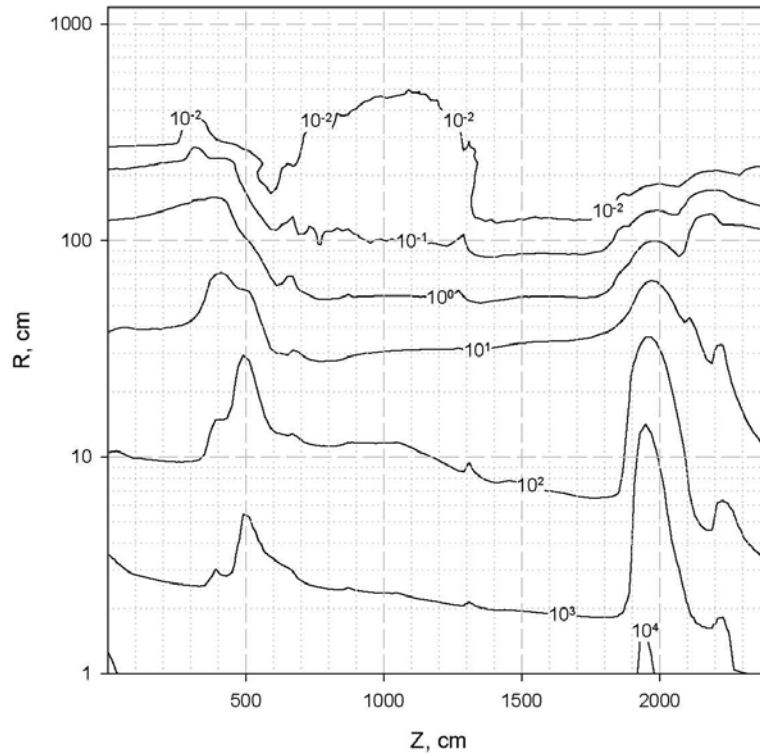


**Figure 7: Isolines of  $\sum_i(A_i/LE_i)$  calculated with GCALOR and the Silberberg-Tsao cross-sections for nickel, 10 year operation followed by 100 days of cooling time**

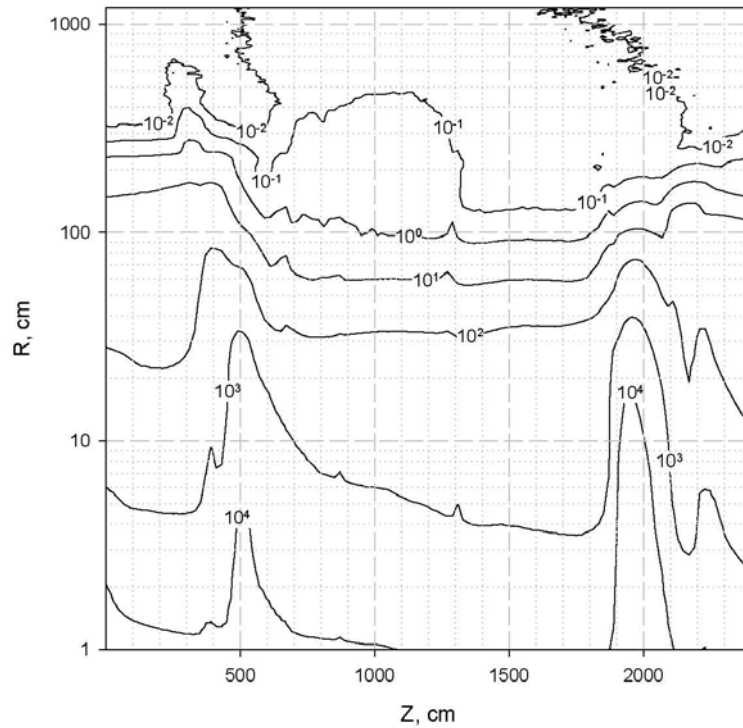


**Figure 8: Isolines of  $\sum_i(A_i/LE_i)$  calculated with GCALOR and the Silberberg-Tsao cross-sections for cobalt, 10 year operation followed by 100 days of cooling time**

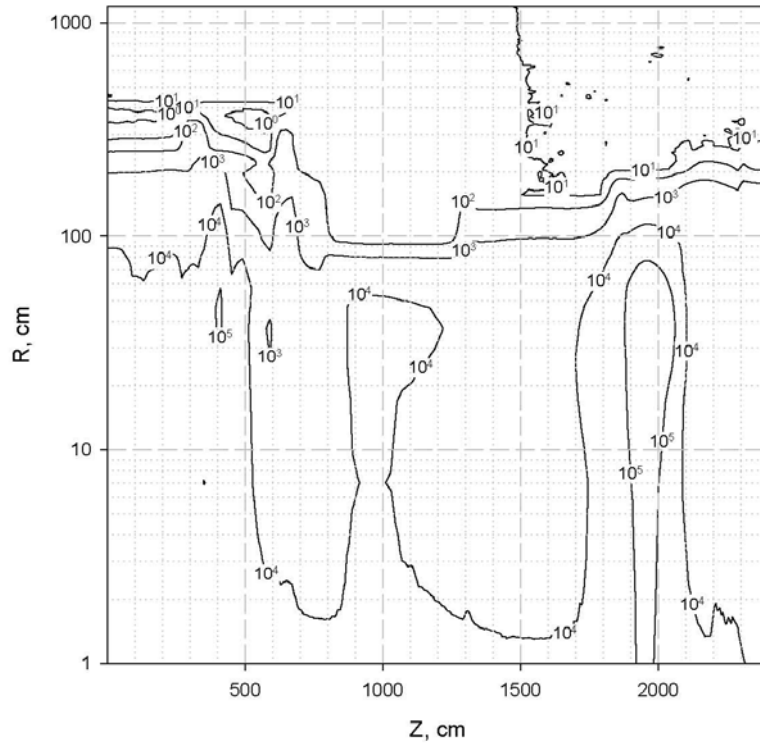
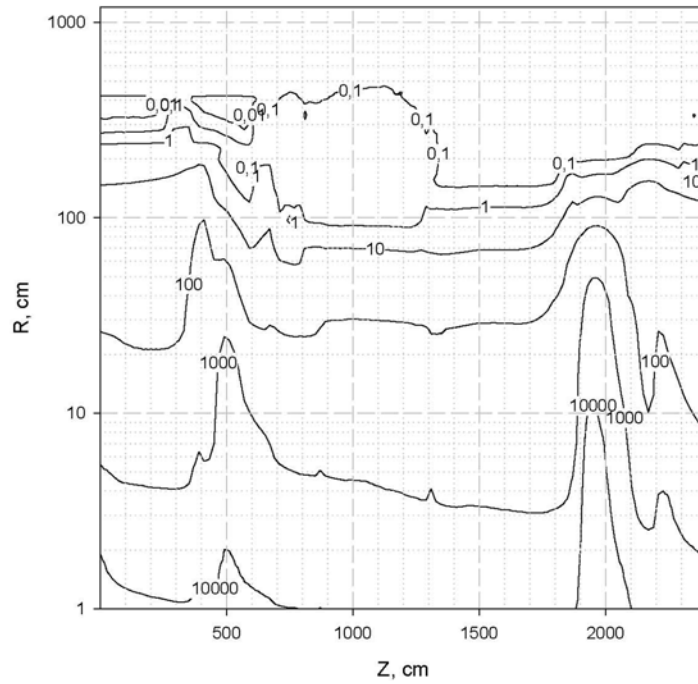


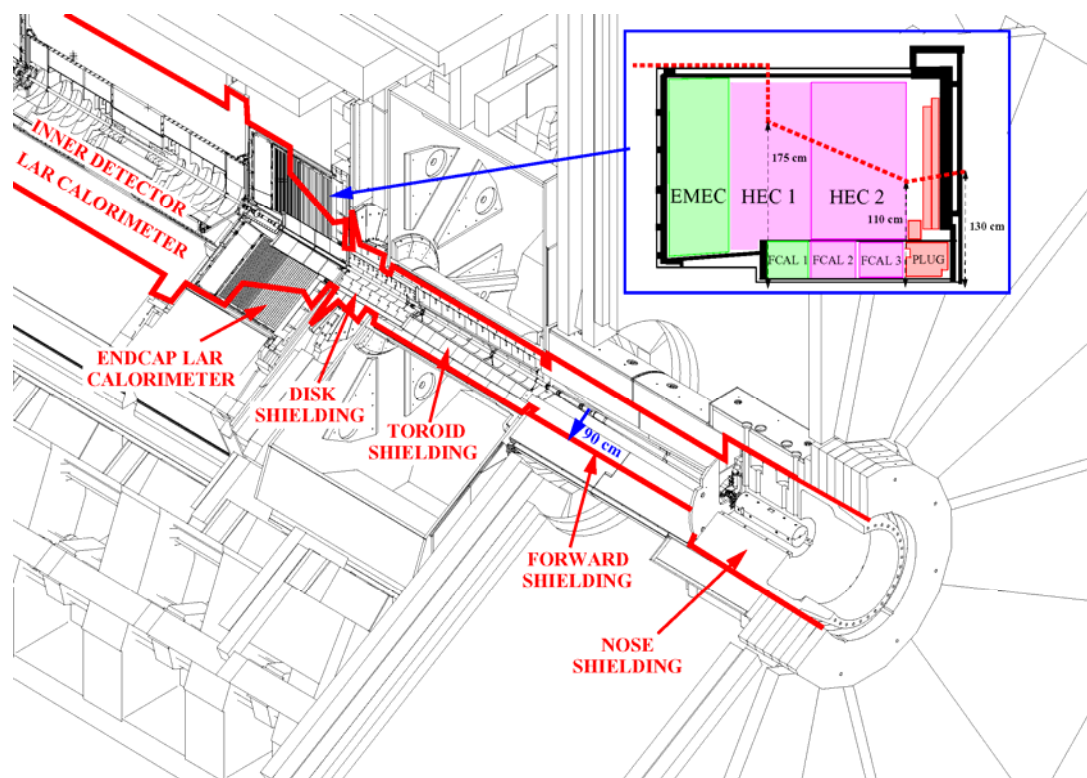
**Figure 9: Isolines of  $\sum_i(A_i/LE_i)$  calculated with GCALOR and the Silberberg-Tsao cross-sections for stainless steel, 10 year operation followed by 100 days of cooling time**



Malfunctioning and irreparable pieces that will be replaced during maintenance operations might become waste prior to the final decommissioning. Within the first 1 to 3 years of operation, LHC will most likely operate at luminosity lower than the nominal one and the calculations assuming 10 years of operation at nominal luminosity do present an overestimation for these cases. On the other hand, a faster handling of equipment can be expected during the active LHC lifetime than during its decommissioning. It is therefore reasonable to assume shorter cooling times. Based on the LEP experience, the cooling time of 100 days was selected.

For these reasons, the zoning of the ATLAS detector assumed 100 days of cooling in general but allowed for 2 years of cooling for large structures that will require heavy machinery (*e.g.* crane) for their removal. Initially, the zoning was based on the assumption that it should follow physical boundaries of the components. Later, another zoning was proposed, which cuts through the middle of some components, thus reducing the volume of radioactive waste by about 25%. The reasoning behind this effort is that it would allow deciding at the time of the decommissioning to either cut the component along the zoning boundary or dispose of the whole piece according to the rules that apply to waste originating from the radioactive waste zone, depending on what would be preferable at that time. Taking all of the above into considerations, the zoning of the ATLAS detector was drawn as shown in Figure 10. The proposed zoning will be submitted for evaluation to the French authorities.

**Figure 10: Radiological zoning of the ATLAS detector**



### **Acknowledgements**

The ATLAS geometry used in the FLUKA simulations was originally written by A. Ferrari (CERN) and later improved by I. Dawson (University of Sheffield). The particle spectra used in the GCALOR calculations were kindly provided by M. Shupe (University of Arizona).

## References

- [1] “Council Directive 96/29/Euratom of 13 May 1996 Laying Down Basic Safety Standards for the Protection of the Health of Workers and the General Public Against the Dangers Arising from Ionizing radiation”, *Official Journal of the European Communities* L 159 (29 June 1996).
- [2] M. Silari, L. Ulrici, “Investigation of Induced Radioactivity in the CERN Large Electron Positron Collider for its Decommissioning”, *Nuclear Instruments and Methods*, A526, 510-536 (2004).
- [3] Swiss “Ordonnance sur la radioprotection” (ORaP).
- [4] A. Fassò, A. Ferrari, J. Ranft, P.R. Sala, *FLUKA: a Multi-particle Transport Code*, CERN-2005-10 (2005), INFN/TC\_05/11, SLAC-R-773.
- [5] A. Fassò, A. Ferrari, S. Roesler, P.R. Sala, G. Battistoni, F. Cerutti, E. Gadioli, M.V. Garzelli, F. Ballarini, A. Ottolenghi, A. Empl, J. Ranft, “The Physics Models of FLUKA: Status and Recent Developments”, *Computing in High Energy and Nuclear Physics 2003 Conference (CHEP2003)*, La Jolla, CA, USA, 24-28 March 2003 (paper MOMT005), eConf C0303241 (2003), arXiv:hep-ph/0306267.
- [6] V. Vlachoudis and the FLUKA Collaboration (CERN, INFN), “FLUKA: New Features and a General Overview”, these proceedings.
- [7] S. Baranov, M. Bosman, I. Dawson, V. Hedberg, A. Nisati, M. Shupe, *Estimation of Radiation Background, Impact on Detectors, Activation and Shielding Optimization in ATLAS*, ATL-GEN-2005-001, pp. 62-72 (2005).
- [8] C.H. Tsao, R. Silberberg, “Partial Cross Sections in High-energy Nuclear Reactions and Astrophysical Applications. 1. Targets with  $Z \leq 28$ ”, *Astrophysical Journal Supplement*, Vol. 25, 315-333 (1973).
- [9] C.H. Tsao, R. Silberberg, “Partial Cross Sections in High-energy Nuclear Reactions and Astrophysical Applications. 2. Targets Heavier than Nickel”, *Astrophysical Journal Supplement*, Vol. 25, 335-367 (1973).
- [10] G. Rudstam, “Systematics of Spallation Yields”, *Zeitschrift für Naturforschung*, A21, 1027-1041 (1966).

## **Session IV**

### **Benchmarking – calculations and results**

***Chairs: H. Hirayama, A. Leuschner***



## Thick target neutron yield at 0 degree by 250 and 350 MeV protons

**Yosuke Iwamoto,<sup>1</sup> Shingo Taniguchi,<sup>2</sup> Noriaki Nakao,<sup>3</sup> Toshiro Itoga,<sup>4</sup>  
Takashi Nakamura,<sup>4</sup> Yoshihiro Nakane,<sup>1</sup> Hiroshi Nakashima,<sup>1</sup> Daiki Satoh,<sup>1</sup>  
Hiroshi Yashima,<sup>5</sup> Hiroshi Yamakawa,<sup>6</sup> Koji Oishi,<sup>6</sup> Atsushi Tamii,<sup>7</sup> Kichiji Hatanaka<sup>7</sup>**

<sup>1</sup>Japan Atomic Energy Agency, Japan

<sup>2</sup>Japan Synchrotron Radiation Research Institute, Japan

<sup>3</sup>Stanford Linear Accelerator Centre, USA

<sup>4</sup>Cyclotron and Radioisotope Centre, Tohoku University, Japan

<sup>5</sup>Research Reactor Institute, Kyoto University, Japan

<sup>6</sup>Shimizu Corporation, Japan

<sup>7</sup>Research Centre of Nuclear Physics, Osaka University, Japan

### Abstract

*Neutron energy spectra at 0 degree produced from stopping-length thick graphite, aluminium, iron and lead targets bombarded by 250 MeV and 350 MeV protons were measured at the neutron TOF course at RCNP of Osaka University. The neutron energy spectra were obtained by using the time-of-flight technique in the energy range from 10 MeV to incident proton energy. To compare the experimental results, Monte Carlo calculations by the PHITS and MCNPX codes using the JENDL-HE and the LA150 evaluated nuclear data files were performed. It was found that these calculated results at 0-degree generally underestimated the experimental results for all targets in the energy range above 20 MeV.*

## Introduction

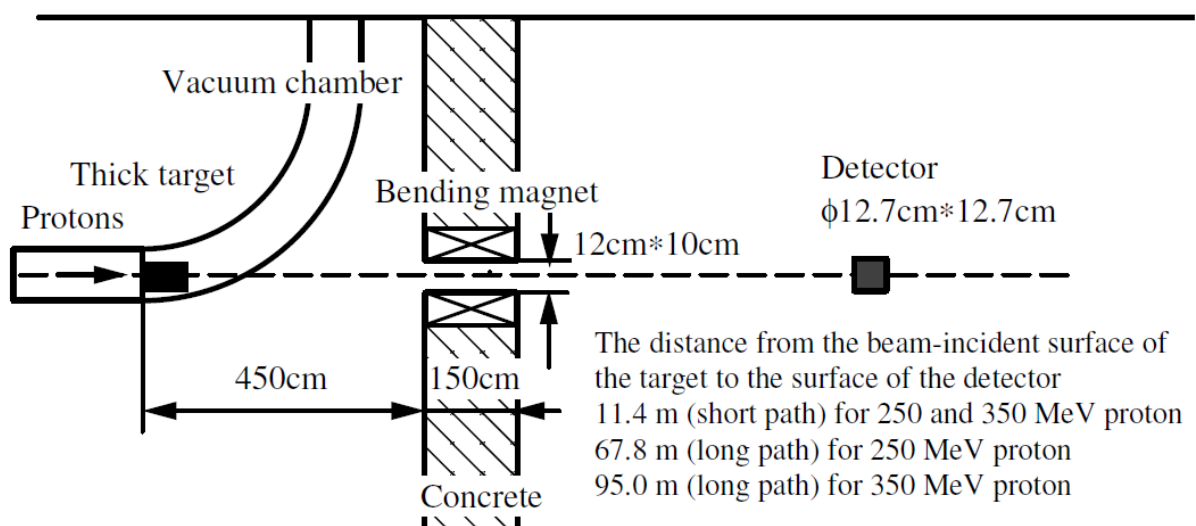
In the shielding design of high-energy (over 100 MeV) proton accelerator facilities, it is important to estimate the energy spectra of the secondary particles, especially neutrons, produced by beam losses in thick materials of beam line apparatus and the beam dump as source terms. Various Monte Carlo transport calculation codes (PHITS [1], MCNPX [2] and MARS [3]) have been widely employed for high-energy particle transport calculation. The PHITS code is a multiple-purpose particle and heavy ion transport Monte Carlo code system based on the NMTC/JAM code [4]. The MCNPX code is widely used for the design because the code has various kinds of estimators and variance reduction techniques. These calculations can use the high-energy evaluated nuclear data, such as the LA150 library [5] and the JENDL-HE file [6]. The accuracy of these calculated results has been verified by the benchmark experimental data.

For over 100 MeV proton incidence, these calculation codes tend to well reproduce thick target neutron yield (TTY) at large emission angles [7,8], while these fail to reproduce over 20 MeV neutron yields at 0 degree for 210 MeV proton incidence at RIKEN [7]. No other experimental TTY at 0 degree are available. The present codes have not been thoroughly checked on TTY at 0-degree. Therefore, we have measured TTY for over 10 MeV neutrons from thick graphite, aluminium, iron and lead targets at 0 degree bombarded by 250 and 350 MeV protons at the TOF course of the RCNP (Research Centre of Nuclear Physics) ring cyclotron of Osaka University. In this paper, the measurements and the calculated results of the PHITS and MCNPX codes using the LA150 library and the JENDL-HE file are reported.

## Experiment

The experiments were carried out at the neutron TOF course of the RCNP ring cyclotron of Osaka University. A schematic view of the experimental arrangement is illustrated in Figure 1. The repetition period of the incident proton beam from the cyclotron was extended to about 800 ns by using a beam chopper to avoid contamination from lower energy neutrons. The chopper trigger signal was used as the stop signal for the TOF measurement. The characteristics of the targets used in this work are summarised in Table 1. The thick target, which is held by an acrylic support for insulation in order to measure the proton beam current, was set in a vacuum chamber. The targets were covered with aluminium foil to absorb secondary electrons emitting from the targets.

Figure 1: Illustration of experimental set-up at RCNP

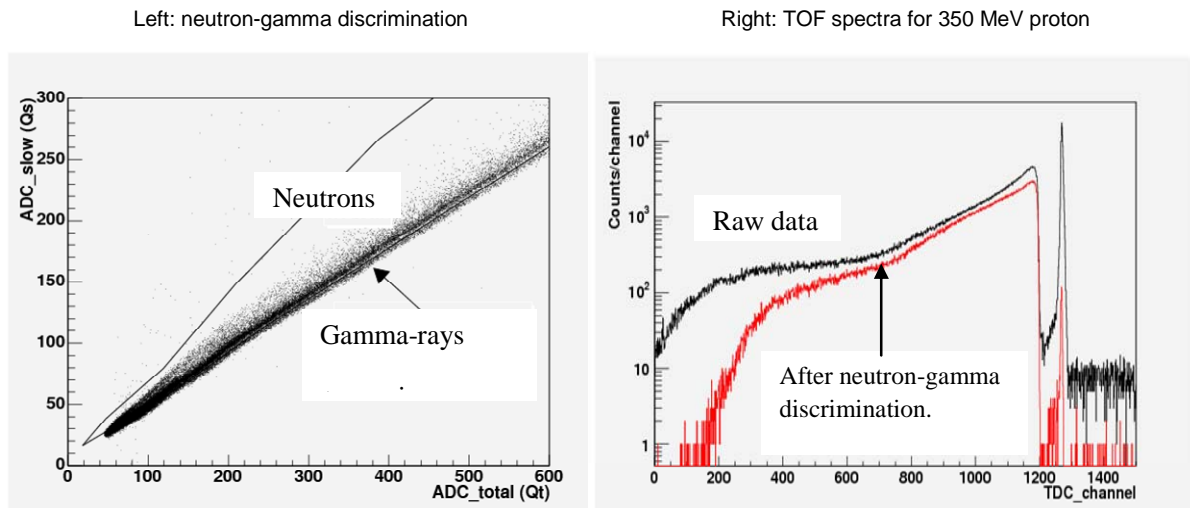


The neutrons produced at 0-degree direction were transported to the TOF course through the 150-cm thick iron collimator of a 12-cm high and 10-cm wide opening, while charged particles were rejected by a vertical bending magnet equipped in the collimator. The neutron TOF measurements were performed using an NE213 organic liquid scintillator (12.7-cm diameter by 12.7-cm long) coupled to a photomultiplier. The distances from the beam-incident surface of the target to the surface of the detector are summarised in Figure 1. The long path measurements were carried out to get good time resolution in higher energy region. The beam current were kept in 0.2 nA for the short path and 5 nA for the long path in the 250 MeV measurement and 0.5-0.6 nA and 17-20 nA in the 350 MeV measurement, respectively. The current of the proton beam was monitored with a current integrator coupled to the targets.

**Table 1: Target characteristics and stopping range in the target**

Material	Density (g/cm <sup>3</sup> )	Size at 250 MeV (cm)	Stopping range at 250 MeV (cm)	Size at 350 MeV (cm)	Stopping range at 350 MeV (cm)
Graphite	1.76	6.0 × 6.0 × 27.5	25.0	6.0 × 6.0 × 46.0	41.2
Al	2.72	φ6.0 × 20.0	18.0	φ6.0 × 34.5	31.3
Fe	9.12	φ6.5 × 7.5	6.93	φ6.5 × 13.5	12.0
Pb	11.3	6.0 × 6.0 × 7.5	6.76	6.0 × 6.0 × 12.5	11.6

**Figure 2: Measured raw data**



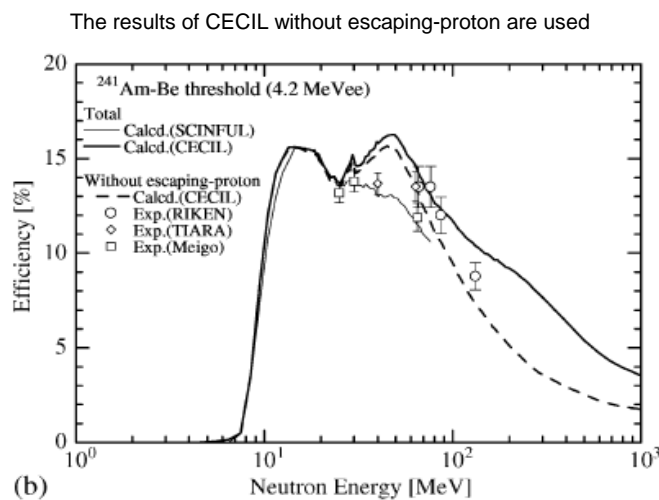
The detector is sensitive to neutrons and gamma rays. The neutron-gamma discrimination was performed by a pulse shape analysis as follows: the charge delivered by the photomultiplier is measured by ADC (Lecroy FERA 4300B) during two different time intervals, a total one (300 ns long) and a delayed one (300 ns long delayed by 60 ns) giving two charge values (Qt) and (Qs), respectively. A two-dimensional plot of Qt vs. Qs allows the separation of neutrons and gamma rays, which is shown in Figure 2 (left).

The neutron TOF spectrum was measured using TDC (Lecroy TFC 4303). The start signal of the TDC was delivered from the photomultiplier and the chopper trigger signal was used as the stop signal. Figure 2 (right) presents the TOF spectra for the iron target at the incident proton energy of 350 MeV. The flash gamma-rays emitted from target nuclei appear as a peak. The flash gamma-ray peak was taken as the reference of the time difference between the flash gamma-ray peak and individual neutron events. As shown in flash gamma-ray peak of Figure 2 (right) after neutron-gamma discrimination, gamma-ray rejection was not complete, and the uncertainties of the gamma-ray rejection were estimated as 5%.

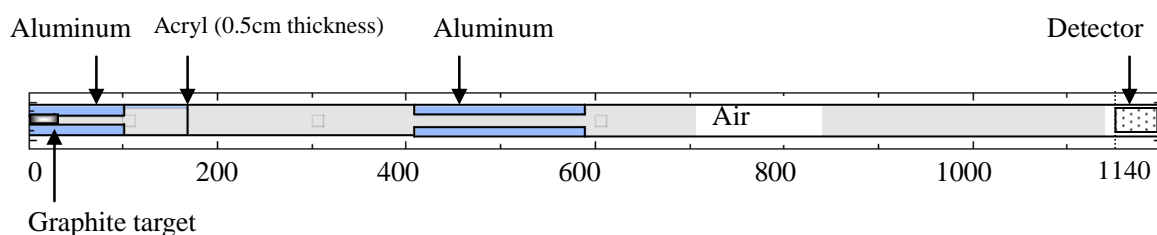
## Data analysis

The TOF spectra of neutrons were converted to the neutron energy spectra. In the TOF distribution analysis, neutron events above the  $^{241}\text{Am}$ -Be (4.2 MeVee) bias were summed up and neutron TOF distributions in wide energy range above 10 MeV were obtained. Neutron detection efficiencies were obtained from calculation results of the CECIL code [9]. In the neutron-gamma ray discrimination, the pulse shapes from high-energy neutron events in which recoil protons escape the detector are close to those from gamma-ray events, and these events were eliminated from the neutron events. Corresponding to the elimination of high energy neutrons, the recoil proton events escaped from the detector were also excluded in the CECIL calculation. The results of CECIL without escaping-proton are shown in Figure 3 [10]. The results without escaping-proton agree with the measurements within 15% in the energy region between 10 and 206.8 MeV for 4.2 MeVee bias. In this work, the CECIL results without escaping-proton were employed to calculate the efficiency of a NE213 neutron detector.

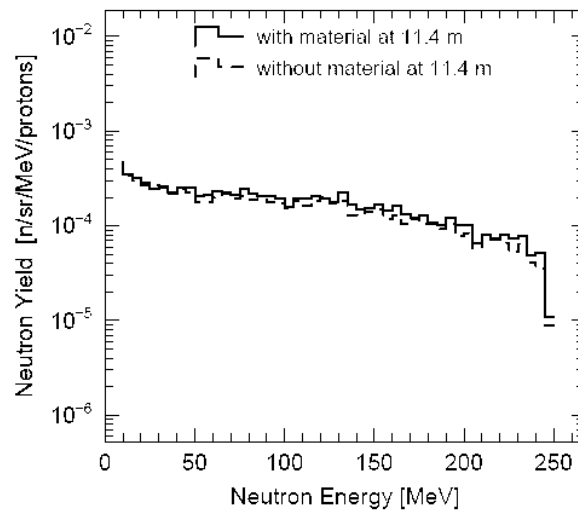
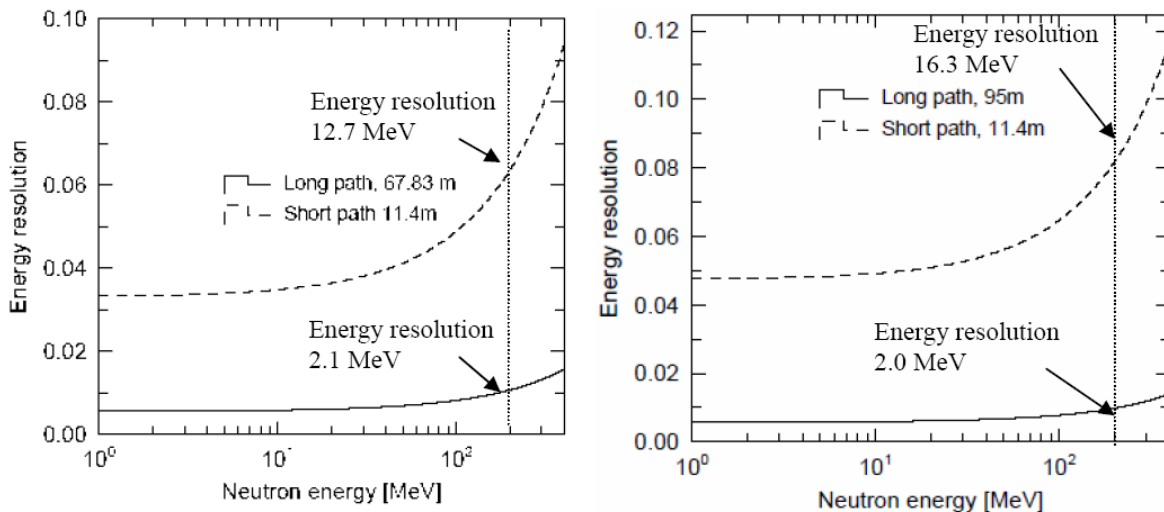
**Figure 3: Neutron detection efficiency of NE213 scintillator for Am-Be**



**Figure 4: Vertical cross-sectional view used in the PHITS calculation for investigating scattered neutrons by materials**



On the way of the flight path, the neutrons traverse the beam window and air. The effect of high-energy neutrons scattered by surrounding materials was investigated by using the Monte Carlo particle transport code, PHITS with the Intra-Nuclear Cascade (INC) model based on the Bertini model [11]. Vertical cross-sectional view in PHITS calculation is shown in Figure 4. Neutron yield for 250 MeV proton incidence on a thick graphite at 11.4 m was calculated. Calculated results with and without the material and air are shown in Figure 5. It clearly appears that neutrons crossing the detector are almost negligible in the neutron energy above 10 MeV. The uncertainty of scattered high-energy neutrons is set to be within 3%.

**Figure 5: Calculated results with and without materials and air at 11.4 m****Figure 6: Energy resolution of the graphite with 27.5 cm thickness for 250 MeV proton (left) and 46 cm thickness for 350 MeV proton (right)**

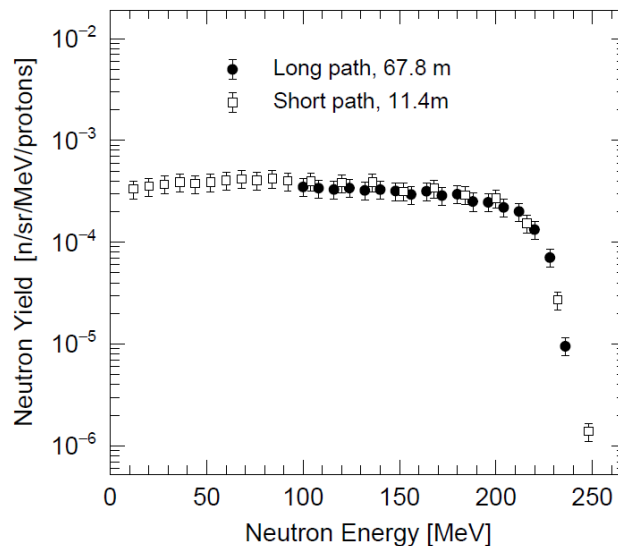
Uncertainties on the TTY determination are due to statistical and systematic errors. The statistical uncertainties at the neutron spectra determination varied from 0.5 to 5%. The systematic error comes mainly from gamma ray rejection, neutron detection efficiency and high-energy neutrons scattered by materials and air, which were determined to 3 and 15%, respectively. The neutron energy resolution depends on the time and the geometrical component and is given by:

$$\frac{\sigma_E}{E} = \gamma(\gamma + 1) \left[ \left( \frac{\sigma_l}{l} \right)^2 + \left( \frac{\sigma_t}{t} \right)^2 \right]^{1/2}$$

with  $\gamma$  the Lorentz factor,  $\sigma_t/t$  the time resolution,  $\sigma_l/l$  the geometrical component. The time component estimated from FWHM of the flash gamma-ray peak was 1.2 ns. The geometrical component comes from the target thickness and from the size of the sensitive area of the detector. The energy resolution for graphite target is plotted as a function of the neutron energy in Figure 6. The TOF method with long path allows neutron energy measurement with a good resolution better than 2%.

Figure 7 displays measured TTY obtained for a thick aluminium target at 250 MeV. Data obtained with the short path measurement (squares) and the long one (filled circles) are shown. It can be seen that in the overlap regions, i.e. between 100 and 250 MeV, both results show good agreement within the error bars. Although neutron energy spectra in the energy range from 10 MeV to maximum energy were obtained using short path results, better energy resolution results of the long path measurements were employed for the energy range above 100 MeV.

**Figure 7: Experimental results at short path and long path for iron at 250 MeV proton**



### Monte Carlo calculation

The neutron production process mainly consists of two mechanisms. First, the nucleus is excited by the projectile and emits particles with high-energies, and afterwards it de-excites via evaporation of light particles with low energies. The model combination of Bertini/GEM implemented in PHITS and Bertini+LA150 in MCNPX were employed for the comparison with the measured results. For the MCNPX calculation, LA150 were used for neutron and proton transport under 150 MeV. In JENDL-HE files developed recently, the cross-sections for neutron and proton induced reactions up to 3 GeV are included for 132 nuclides in total, except for lead. In this paper, PHITS calculations with only JENDL-HE files were also done in the energy range up to incident proton energy.

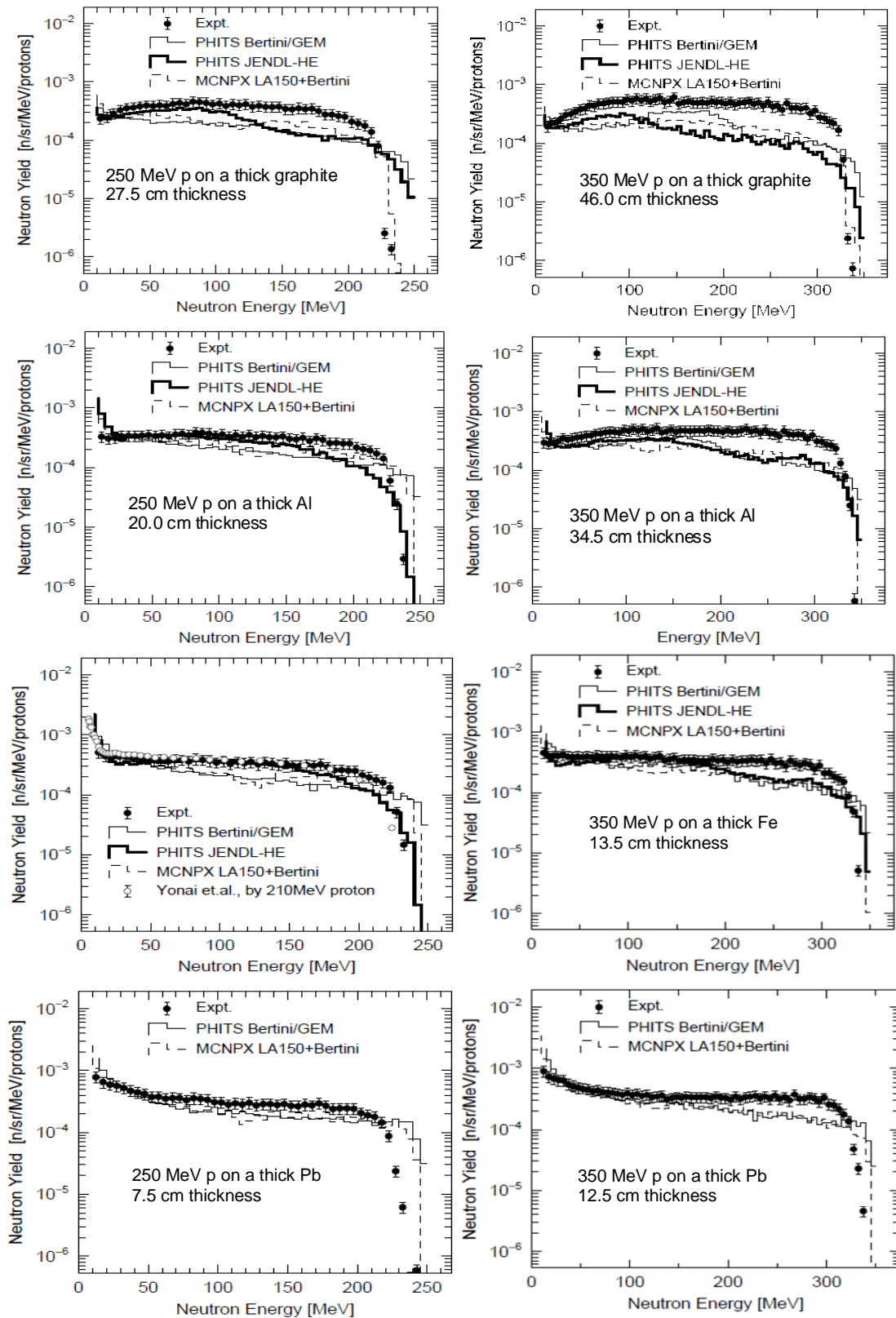
In order to minimise the computing time, only the target is taken into account in the calculation geometry. All calculated neutron fluxes were not changed in the solid angle of 1-degrees. Therefore, in all calculations, the neutron detector was set at 8 m from the surface of the target in void region, equal to solid angles of 0.46-degrees.

### Comparison with measured and calculated results

The measured and the calculated neutron energy spectra from thick targets for 250 and 350 MeV proton incidences are shown in Figure 8. The measured data for 210 MeV incidence on the full-stop length thick iron target at RIKEN [7] are also indicated in this figure. The main difference between the two experiments is caused the different energy resolution due to flight path. The energy resolution at 200 MeV is 12 MeV at RIKEN, while good energy resolution of 4 MeV at RCNP. These experimental results give good agreement each other for the energy below 200 MeV.

Calculated results of PHITS with Bertini/GEM and MCNPX with LA150+Bertini underestimate the experimental results in the neutron energy range from 30 MeV to incident energy. The underestimation of the calculations is also found in the experiment at RIKEN [7].

**Figure 8: Measured and calculated neutron energy spectra at 0-degree for 250 and 350 MeV proton incidence**



Those may result from the underestimation of neutron-production DDX (double differential cross-sections) at small angles and the strong self-shielding in target nucleus. On the other hand, the calculated result with JENDL-HE file gives good agreement with experimental results below 100 MeV on graphite and below 150 MeV on aluminium and iron.

Maximum neutron energies of calculated results for a graphite target are different each other in PHITS with Bertini/GEM and MCNPX with LA150+Bertini in spite of using same physics of Bertini. This is mainly due to the different parameters used in their Bertini code, i.e. mean free path, Fermi distribution, Pauli blocking and so on. The Calculated result of MCNPX gives good agreement with the measured result around incident energy, though, maximum neutron energy of PHITS calculation is larger than measured data. Validation is necessary for Bertini of PHITS.

The high energy close to the incident energy corresponds to quasielastic NN collisions in thick target is not appeared in all results. Actually, in thick targets, most of the protons interact near the surface and lead to the emission of high-energy, forward-peaked neutrons. The further multiple reactions of the forward peaked neutron through penetration consequently may decrease the peaked neutron flux.

**Figure 9: Neutron yields integrated above 20 MeV at 0-degree for 250 MeV (left) and 350 MeV (right) proton incidence as a function of the mass**

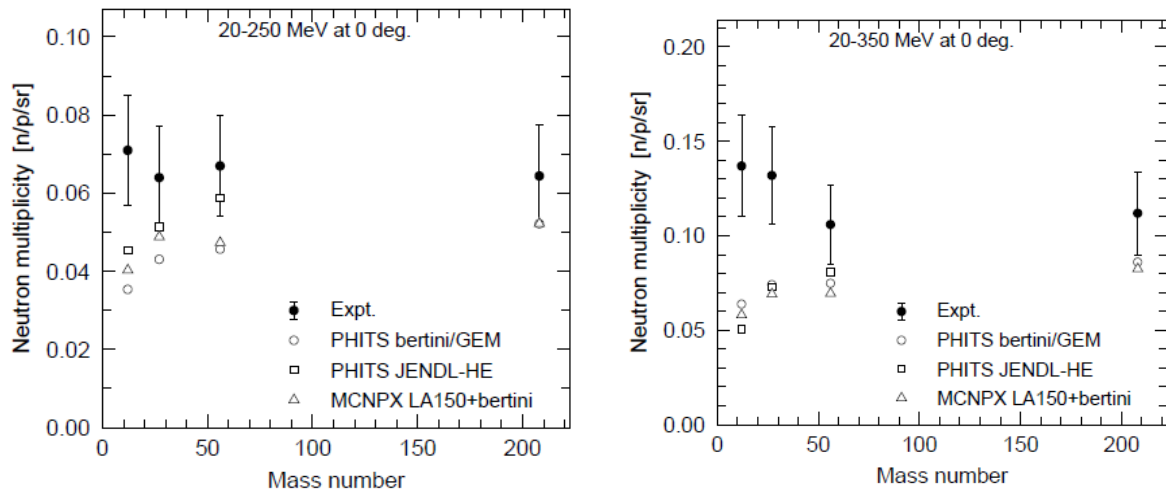


**Figure 10: Neutron yields integrated above 20 MeV at 0-degree for graphite (left) and iron (right) proton incidence as a function of incident proton energy**

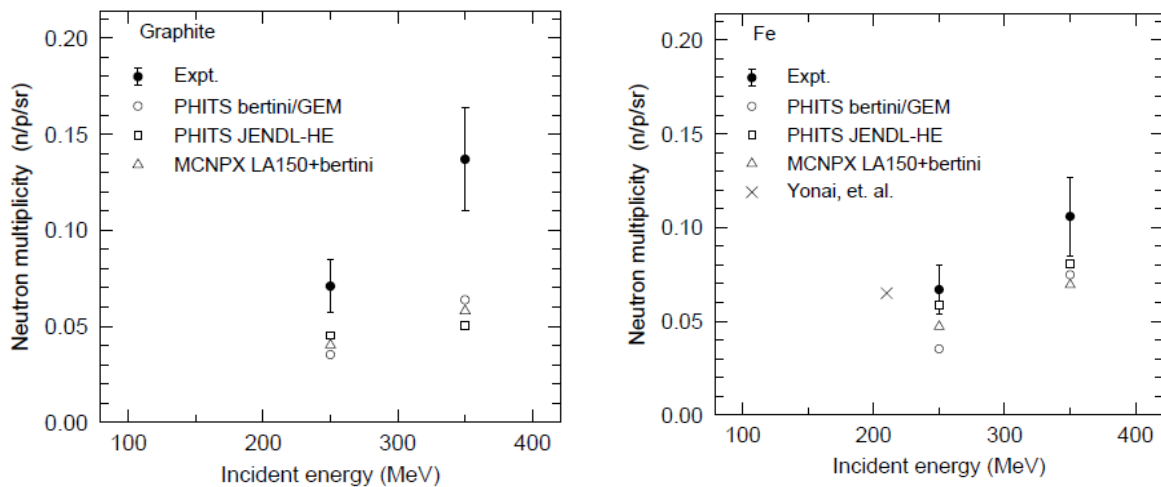


Figure 9 shows the neutron yields integrated at 0-degree above 20 MeV by 250 and 350 MeV protons as a function of the target mass, respectively. Neutron yields versus incident energy for the graphite and the iron targets are also shown in Figure 10. Neutrons above 20 MeV are corresponding roughly to cascade neutrons. All calculated results underestimate the experimental data, especially for graphite and aluminium at 350 MeV. While, for aluminium and iron at 250 MeV, calculated results with JENDL-HE file agree with measured results within the error bar.

The difficulty of the consideration with thick targets is that several effects are combined. For instance, the detected neutrons have been produced by different spallation reactions at different energies, and covered different distances through the target. Therefore, it is important to get the thin target neutron yields to understand the exact reason of the discrepancy.

## Summary

Neutron energy spectra produced in the forward direction from thick graphite, aluminium, iron and lead targets bombarded by 250 and 350 MeV protons were measured by the TOF method at RCNP of Osaka University. The experimental data were compared with the calculated results of the PHITS and MCNPX codes. All calculations give lower neutron energy spectra than the experimental ones for all targets above 20 MeV and must be improved for neutron production at 0-degree. These measured data will be useful as benchmark data for investigating the accuracy of the Monte Carlo simulation and for the shielding design of accelerator facilities.

## Acknowledgements

The authors express their gratitude to the accelerator staff of RCNP for generous support of this experiment and to Dr. Y. Sakamoto with JAEA, Dr. K. Niita with RIST and Dr. Y. Uwamino with RIKEN for their useful discussions.

## References

- [1] H. Iwase, K. Niita, T. Nakamura, *J. Nucl. Sci. Technol.*, 39 (2002) 1142.
- [2] L.S. Waters (Ed.), *MCNPX User's Manual Version 2.4.0*, LA-CP-02-408, Los Alamos National Laboratory, Los Alamos, New Mexico (2002).
- [3] N.V. Mokhov, Fermilab-FN-628, 1995; N.V. Mokhov, O.E. Krivosheev, C.C. James, Fermilab-Conf-04/053 (2004).
- [4] K. Niita, S. Meigo, H. Takada, *et al.*, *High Energy Particle Transport Code NMTC/JAM*, JAERI-Data/Code 2001-007, Japan Atomic Energy Research Institute (2002).
- [5] M.B. Chadwick, P.G. Young, S. Chiba, S.C. Frankle, G.M. Hale, H.G. Hughes, A.J. Koning, R.C. Little, R.E. MacFarlane, R.E. Prael, L.S. Waters, *Nucl. Sci. Eng.*, 131 (1999) 293.
- [6] Y. Watanabe, *et al.*, *AIP Conference Proceedings*, 769 (2005) 1646.
- [7] S. Yonai, T. Kurosawa, H. Iwase, *et al.*, *Nucl. Instr. and Meth.*, A 515 (2003) 733.
- [8] S. Meigo, H. Takada, S. Chiba, *et al.*, *Nucl. Instr. and Meth.*, A 431 (1999) 521.
- [9] R.A. Cecil, B.D. Anderson, R. Madey, *Nucl. Instr. And Meth.*, 161 (1979) 439.
- [10] N. Nakao, T. Kurosawa, T. Nakamura, Y. Uwamino, *Nucl. Instr. and Meth.*, A 463 (2001) 275.
- [11] H.W. Bertini, *Phys. Rev.*, 188 (1969) 1711.



## Proposal for multi-megawatt target benchmarks

**M. Felcini**  
CERN

**P. Vaz**  
ITN, Portugal

### Introduction

During the last years a number of innovative applications have emerged in several fields of science and technology, requiring the utilization of intense proton beams with energies ranging in the hundreds of MeV up to a few GeV impinging on targets of heavy materials (lead, bismuth, mercury, tungsten, etc.). These applications and related projects are related to the transmutation of nuclear waste using accelerator-driven systems (ADS), energy production (EA), production of radioactive ion beams (EURISOL), the operation of intense spallation neutron sources (SNS), among others.

Common to these applications is the need to perform calculations of the unprecedented high doses and fluxes of particles generated by spallation in the nuclear reactions induced by proton and neutrons in the target. The simulation of the cascade of particles generated inside the target and the propagation of particles through the surrounding structural and shielding materials is of relevance for different purposes, mainly for radiation protection and shielding, for nuclear safety, for radiation damage induced in the materials and for thermal-hydraulic computations.

Considering the energy range of interest (hundreds of MeV up to a few GeV) and the type of physics (hadronic), the Monte Carlo simulation of the particle transport inside the target and through the surrounding materials must be done using the experimental cross-section data available in the libraries available complemented by the predictions of theoretical models. Therefore, some variability of the results can be expected using different models and algorithms, if different computer programs are used.

The calculations and simulations of the energy deposition in the targets and particle fluxes and doses can be performed using the available tools representative of the state-of-the-art in computational radiation physics and radiation transport using Monte Carlo tools (FLUKA, MCNPX, MARS, Japanese codes) and must, whenever available, be compared with experimental data sets.

In the sequence, a two-component benchmark is proposed: one of the components is related to the operation of ADS systems, with a proton beam if energies in the 350-800 MeV impinging on a thick target, with different materials being considered, the other is related to the operation of multi-MW targets such as the one of EURISOL, with proton energies in the GeV range.

The purpose of the benchmarks hereafter proposed is to compare the predictions from different codes used to compute the reference problems and to assess the uncertainties associated to the utilisation of different codes.

## Specification of the multi-MW target benchmarks

### Proton energy

- 350 MeV, 5 mA (MYRRHA-ADS)
- 600 MeV, 2.5 mA (XT-ADS, currently considered under the FP6 EUROTRANS project)
- 800 MeV, 20 mA (EFIT, for the industrial transmuter to be deployed in the “long term”)
- 1 000 MeV (EURISOL-related studies and other applications)
- 2 000 MeV (EURISOL-related studies and other applications)

### Geometry

- Cylindrical

Energy (MeV)	R (cm)	Z (cm)	Target materials
350	5	15	Lead-bismuth
600	10	35	Lead-bismuth (liquid), lead, tungsten, mercury
800	15	60	Lead-bismuth (liquid), lead, tungsten, mercury
1 000 and 2 000	8	50 85	Mercury, lead-bismuth (liquid), lead, tungsten

### Beam profile (spatial distribution)

- Gaussian
- Elliptical (to be defined)

### Type of computations

- Energy deposition (Kw/mA/cm<sup>3</sup>) in the target
- Neutron and proton fluxes (mesh tally of the cylinder) versus energy
- Neutron and proton fluxes versus energy across the external cylindrical surface
- Neutron and proton fluxes versus energy across the top and bottom surface of the cylinder
- Neutron yield (n/p)
- dpa (displacement per atom per mA) vs. R in the target
- dpa (displacement per atom per mA) vs. Z in the target
- Hydrogen and helium production (appm per mA)
- Spallation product vector (mass distribution/yield of the spallation products)

### Computer codes used

- FLUKA
- MARS
- MCNPX
- Japanese Monte Carlo codes

## Measurement of neutron energy spectra behind shielding at 120 GeV/c hadron beam facility, CERF

**N. Nakao,<sup>1\*</sup> S. Taniguchi,<sup>2</sup> S.H. Rokni,<sup>1</sup> S. Roesler,<sup>3</sup> M. Brugger,<sup>3</sup>**

**M. Hagiwara,<sup>4</sup> H. Vincke,<sup>1,3</sup> H. Khater,<sup>1</sup> A.A. Prinz<sup>1</sup>**

<sup>1</sup>Stanford Linear Accelerator Centre (SLAC), USA

<sup>2</sup>Japan Synchrotron Radiation Research Institute (JASRI), Japan

<sup>3</sup>CERN, Switzerland

<sup>4</sup>Cyclotron Radioisotope Centre (CYRIC), Japan

### Abstract

Neutron energy spectra were measured behind the lateral shield of the CERF (CERN-EU High Energy Reference Field) facility at CERN with a 120 GeV/c positive hadron beam (a mixture of mainly protons and pions) on a cylindrical copper target (7-cm diameter by 50-cm long). NE213 organic liquid scintillator (12.7-cm diameter by 12.7-cm long) was located at various longitudinal positions behind shields of 80- and 160-cm thick concrete and 40-cm thick iron. Neutron energy spectra in the energy range between 32 MeV and 380 MeV were obtained by unfolding the measured pulse height spectra with the detector response functions which have been experimentally verified in the neutron energy range up to 380 MeV in separate experiments. Since the source term and experimental geometry in this experiment are well characterised and simple, and results are given in the form of energy spectra, these experimental results are very useful as benchmark data to check the accuracies of simulation codes.

---

\* Present address: Fermilab, MS220, P.O. Box 500, Batavia, IL 60510, USA.

## 1 Introduction

Estimates of high-energy neutron production and transmission through shielding are very important at high-energy electron and hadron accelerator facilities because high-energy neutrons have high penetrability through shielding and contribute significantly to external dose. Modern Monte Carlo codes provide reliable predictions of radiation fluences in accelerator facilities even for complicated facility structures. However, accuracies for the production and transmission of secondary neutrons generated by high energy beams, especially above 1 GeV, are not well known because of lack of experimental data.

This paper reports the shielding experiment at CERN carried out in August 2004. Several recent shielding experiments in accelerator facilities with high-energy neutrons are summarised in Table 1, and their characteristics are compared with those of this work. Distinctive features of this work are highest particle energy (120 GeV/c) and the variety of measured angles (13-133 degrees). Also, various thicknesses of typical shielding materials (concrete and iron) are used, and results are given as neutron-energy spectra outside the shield. The CERF facility has a simple structure of beam line and shielding, and the source term is clearly defined. The data constitute a useful benchmark to verify the accuracy of radiation transport codes.

## 2 CERF facility

This experiment was performed at the 120 GeV/c hadron beam line facility CERF at CERN, which was developed to provide a neutron calibration field outside the shield [10].

### 2.1 Shielding structure and material

This facility has a comparatively simple structure of beam line and shielding, and the source term is clearly defined. Figure 1 shows the beam line of the CERF facility with 80- or 160-cm thick concrete for side shields and 80-cm thick concrete and 40-cm thick iron for roof shield. Densities of shielding materials and composition of the concrete shield are given in Tables 2 and 3, respectively. The iron roof consists of two kinds of iron materials of 20-cm thickness as shown in Figure 1.

### 2.2 Beam line and target

The beam line is inclined horizontally at approximately 2.1 degrees as shown in Figure 1. A copper target (50-cm thick, 7-cm diameter) was placed at two different locations, A or B, as shown in Figure 1. An activation experiment was performed simultaneously: small irradiation samples were placed behind the target and water bottles were placed on both sides of the target. The effect on the shielding experiment of interactions in these irradiation samples is negligible.

### 2.3 Particle, profile, structure and intensity of beam

A positively charged hadron beam consisting of a mixture of protons (34.8%), pions (60.7%) and kaons (4.5%) with momentum of 120 GeV/c impacted on the target. This beam is secondarily generated in a thin target by an accelerated proton beam, and only positive particles of the above momentum are transported to the CERF beam line. The beam profile was measured with a wire chamber, and has an approximately Gaussian distribution ( $\sigma_v = 9.16$  mm,  $\sigma_h = 11.2$  mm) with tails removed by a rectangular collimator. An alignment of the target was confirmed by putting a Polaroid film on the front surface of the copper target whenever the target location was changed.

Beam intensity can be changed by changing the width of the collimator located upstream of the beam transport line. This does not generate background neutrons for the CERF experiment. The cycle length is 16.8 seconds with a spill length of 4.8 seconds, and beam particles come uniformly in the spill.

## 2.4 PIC beam monitor

The number of incident beam particles was measured by a PIC (precision ionisation chamber) beam monitor. The beam intensity per PIC-count was calibrated to be about  $2.3 \times 10^4$  beam particles. The uncertainty in the calibration factor is 0.4% [11]. The PIC monitor is located upstream of the target location B on the beam line.

## 3 Measurement of neutron energy spectra

### 3.1 Detector set-up

Neutron measurements were carried out using an NE213 organic liquid scintillator (12.7-cm diameter by 12.7-cm long) with an R4144 photomultiplier tube (Hamamatsu Photonics). Two NE102A plastic scintillators (veto counters) of rectangular shape and 5-mm thickness were used to reject charged particles from the beam line. A larger (30-cm by 30-cm) veto counter (L-Veto) was located upstream of the NE213 detector mainly to reject muon background, and a smaller (15-cm by 15-cm) veto counter (S-veto) was placed in front of the NE213 counter to reject charged particles (from the beam line) that penetrate the shielding wall or roof.

Figure 2 shows photos of the detectors set up for neutron energy spectra measurements behind the (a) iron shield roof and (b) concrete shield at 90 degrees from the copper target. The distances between the NE213 detector and shield surface were 3-cm and 7.5-cm for concrete and iron shield cases, respectively, as shown in Figure 1. Figure 3 shows a sketch of the detectors set up behind the concrete shield with the interactions of neutron and charged particles.

### 3.2 Electronic measurement circuit

The electronic measurement circuit is shown in Figure 4. Two high voltage power supplies (ORTEC 556) were used for three PMTs (photomultipliers). One of them was used for the NE213 and S-veto counter, supplying -1 650 V. The other one supplied -1 500 V to the L-veto counter.

The anode signal from the NE213 detector was divided in two by a signal divider and fed to CFD1 (Constant fraction discriminator #1) and an ADC (Analogue to Digital Converter) through delay and attenuator modules. CFD1 rejected pulses lower than the threshold for the NE213 detector. Charged particle events (especially muons) from upstream, detected by the large veto counter (L-veto), were rejected in a coincidence module (Coin1). The next coincidence module (Coin2) rejected the events that occurred during the computer busy supplied by a GG (gate and delay generator). The signals to ADCs from the NE213 were total or slow components which were generated by gating in the total or the slow (decay) region of the signal pulse as shown in Figure 5. The signals from the small veto counter (S-veto) were fed to the ADC to get the total pulse height of charged particle events from the shield.

The ADC gate opens when the NE213-detector events do not coincide with the L-veto counter event or computer busy. The ADC accepts the NE213 pulses (total and slow component) and the S-veto pulses. The ADC data were recorded to the computer in event-by-event mode using the Kakuken On-line Data Acquisition System (KODAQ) [12].

The numbers of events from CFD1, Coin1 and Coin2 were counted by 3 scalers as shown in Figure 4. Scaler-1 counted the number of events of the NE213 detector whose pulses were above the threshold in CFD1. Scaler-2 counted the number of events after rejecting the L-veto events, and Scaler-3 counted the events remaining after rejecting the L-veto events and those occurring during computer busy. The number of events taken and recorded in the computer is equivalent to that on Scaler-3.

Muon events detected by the L-Veto counter were not recorded because they occurred too frequently and increased computer busy. Therefore, the L-veto events were only recorded during the initial stage of this experiment (in order to determine appropriate threshold for muon elimination). After setting the L-Veto threshold in CFD2, measurements were carried out with the INHIBIT-1 signal from CFD2 connected to Coin1 to reject the L-veto events automatically, as shown in Figure 4.

### 3.3 Measurement location

One detector set was used for this experiment, and was located at different positions behind the shield (as shown in Figure 1) in order to measure neutron energy spectra behind different materials, thicknesses and angles from the target. The detector locations and their approximate angles with respect to the beam line (relative to the beam interaction points on the front surfaces of targets A and B) are given in Table 4. When the copper target was located at position B, measurements were carried out behind the 160-cm side concrete (B1-B3), 80-cm side concrete (B4, B5), and above the 40-cm iron roof (I1-I3). For target location A, measurements were carried out behind 80-cm thick concrete (A1-A3).

For the side concrete positions (A1-A3, B1-B5), the detector was located at the same height as the beam line, as shown in Figure 2(b). Above the iron roof (I1, I2, I3), the detector was located just above the beam line as shown in Figures 1 and 2(a). The detector location at I2' above the 40-cm thick iron roof was off-axis at a transverse distance of 100-cm from the I2 location as shown in the upper part of Figure 1.

### 3.4 Neutron background measurement

Charged-particle and photon events detected by the NE213 detector can be rejected in offline analysis as described in Sections 4.1 and 4.2. However, neutrons originating from beam losses in neighbouring beam lines, which might be included in the measured data, also need to be eliminated. The neutron background measurements at each detector position were carried out with no beam in H6 (our beam line), thus only accounting for contributions from neighbouring beam lines (H4 and H8). For normalisation purposes, the number of beam spills was counted both for normal and background measurements. The beam intensities at the targets in the neighbouring beam lines (H4 and H8) were observed to confirm the background stability during both the normal and background measurements.

## 4 Data analysis

Event-by-event data recorded in the measurement contains the following three values in each event:

- NE213 total pulse height (Total);
- NE213 slow component (Slow);
- S-veto total pulse height (S-veto).

These data were sorted to one or two-dimensional distributions for various types of analysis.

### 4.1 Charged particle discrimination

Event-by-event data were sorted to two-dimensional distributions (2-D plots) of S-veto or L-veto versus Total, and one-dimensional distributions for the two veto counters as shown in Figure 6.

Figure 6(a) shows events, recorded during the initial stage of the experiment for tune up the circuit, in which there is a coincidence between the L-veto counter and the NE213 detector. The muon component can be seen above roughly channel 180, and these events should be rejected. Using this information, the threshold of CFD2 in Figure 4 was determined during the experiment, and used to make the INHIBIT-1 signals for CFD1.

In Figure 6(b), events due to charged particles that penetrated the shielding can be seen above roughly channel 150 in the S-veto pulse height distribution. These charged-particle events were recorded in all the measurements, and they were rejected in the analysis.

### 4.2 N- $\gamma$ separation

Figure 7 shows a 2-D plot of the Total versus Slow components of the NE213 signals along with a magnified view of the low channel region. Since the slow component was obtained by integrating the decay part of the detector signal pulse as shown in Figure 5, electron events generated from  $\gamma$ -rays appear in lower channels and are clearly separated from protons, deuterons and alpha events generated by neutrons. Background muons coming from directions which were not covered by the two veto counters also contribute to the electron component and can be rejected in this process.

The neutron events were selected by eliminating the electron and muon events from the 2-D plot in Figure 7. In this process, escaping-protons (which go out through the detector wall) are also eliminated because the pulse shape of the signal of the escaping-protons is close to that of electrons and therefore the escaping-proton events overlap in the electron events [13], as shown in Figure 7. This does not affect final results because the escaping-proton component is not included in the response functions [14] used in this unfolding analysis, either.

### 4.3 Light output calibration

A light output calibration is generally performed to convert the ADC channel into a light unit in MeVee (MeV electron equivalent) using the reference light outputs. The  $^{60}\text{Co}$  light output corresponding to 1.15 MeVee is determined to be the channel having 0.303 times the counts of the Compton edge due to 1.17 and 1.33 MeV  $\gamma$ -ray from  $^{60}\text{Co}$ . The  $^{241}\text{Am-Be}$  light output corresponding to 4.2 MeVee is determined to be the channel having 0.664 times the counts of the Compton edge due to 4.43 MeV  $\gamma$ -ray from  $^{241}\text{Am-Be}$ . A 0-point (0 MeVee), which is independent of the supplied high voltage or gain, can be measured by putting a  $50\Omega$  terminator on the ADC. More details about calibration are described in Ref. [15].

### 4.4 Normalisation

Three scalers were placed in the measurement circuit as shown in Figure 4. The total number of events detected by the NE213 scintillator for each run was recorded by Scaler-1. The number of event triggers was recorded by Scaler-2, and does not include those events that are coincident with the L-Veto counter (mostly muon event). The number of events recorded in the computer was measured by Scaler-3. Not included are events that occurred during computer busy. Computer live ratio, that is the ratio of the number of recorded events to the number of triggered events, is used to correct for counting loss due to computer-busy. The number of incident beam particles was obtained using the calibration factor of  $2.3 \times 10^4$  beam particles per PIC beam monitor count. After scaling by the "Computer live ratio", the corrected number of incident beam particles for the corresponding recorded event data was obtained.

In the background runs, PIC beam monitor counts were not available (there was no beam on the target). In order to get normalisation factors for background runs, the "expected" number of the incident beam particles for the background run was estimated using a ratio of the number of beam particle to the number of spills during the normal and background measurements. This worked properly since stabilities could be confirmed for the beam intensities at the targets in the neighbouring beam lines (H4 and H8) from SPS log data during both for normal and background measurements in each location. The neutron-background subtraction process will be described in Section 4.7.

More details about normalisation process with numerical data tables for each run are described in Ref. [15].

### 4.5 Probability of pulse pile-up

This section describes the possibility of pulse pile-up in the NE213 scintillator during the measurements, which decreases detector efficiency. The following two possibilities are discussed here to clarify the pile-up issues:

- chance coincidence from high intensity, especially due to of muon background;
- coincidence due to multiple secondary-particle productions by the high energy beam.

More details about pulse pile up analysis process with numerical data tables for each run are described in Ref. [15].

#### 4.5.1 Coincidence from high beam intensity

From the trigger ratio (the ratio of the number of triggers to the total number of NE213 detector events), the fraction of muon events can be roughly estimated since the events that coincide with the L-Veto counter were vetoed in the trigger circuit. For example, 62% of detected events were rejected in the

circuit in I3 measurement, as reflected in the trigger ratio of 0.38. This run had the highest count rate (11 764 count/sec). The count rates are already corrected with the beam spill period of 4.8 seconds during the 16.8 sec cycle as described in Section 2.3. Muons come from upstream uniformly during the beam spill.

From Ref. [16], the probability of escaping from pile-up  $P(0)$  is expressed as follows when the interactions occur uniformly in time:

$$P(0) = \exp(-n\tau) \quad (1)$$

where  $n$  is the interaction rate in the detector and  $\tau$  is the resolution time (100 nsec).

The resolution time is  $\sim 100$  nsec, which is the ADC gate width for the total pulse-height of the NE213 as shown in Figure 5. Using Equation (1), the count rate is described as:

$$m = n \exp(-n\tau) \quad (2)$$

where  $m$  is the count rate in the detector (11 764 count).

When  $m = 11\,764$ ,  $n = 11\,778$  is given from Equation (2). Therefore,  $P(0) = 0.9988$  from Equation (1). That means the pile up probability is 0.12%. We conclude that this chance coincidence is negligible.

#### 4.5.2 Multiple secondary-particle production

Even one interaction of a high energy beam particle on the target produces hundreds of secondary particles from the target simultaneously. This multiplicity is independent of the beam intensity. The pile-up possibility is very high inside the tunnel, especially in the forward direction. Here, the pile-up possibility outside the shield in the lateral direction is verified for the case of this experiment.

There are two possible cases that reduce detection efficiency due to pile-up:

- 1) If a neutron is detected with a proton simultaneously as shown in the sketch of Figure 3, one piled-up pulse is recorded, but this event would be rejected in the analysis due to the proton's interaction with the S-veto counter.

*Interaction: 1 neutron, 1 proton  $\rightarrow$  recorded event: 1  $\rightarrow$  analysed event: 0*

- 2) If two neutrons are detected, one piled-up pulse is recorded.

*Interaction: 2 neutrons  $\rightarrow$  recorded event: 1  $\rightarrow$  analysed event: 1*

Both (1) and (2) can be clarified using 2-D plots of the total vs. the slow component of the NE213 detector, as shown in Figure 8. This distribution shows all the recorded event data, including charged particles which would be eliminated later by the S-veto threshold (see Section 4.1).

In this experiment, pulse pile up occurs if more than two pulses come during the gate opening as shown in Figure 9, even if pulses are not piled up physically such as (b) in Figure 9. In this case, although both total and slow components increase their integrations, the slow component increases a lot more because the peak part of the following pulse is also involved. As shown in Figure 8, therefore, pile-up events appear in the higher channel region of the slow-component in the 2-D plot [8]. Figure 10 shows a total pulse-height distribution of pile-up events for the location B5 (Run26), which is the most forward (smallest angle) position from the target, compared with raw data. It can be seen that the pile-up event component is negligible, and all other measurements have less amount of the component than that of location B5.

## 4.6 Response function matrix

The numerical data of the response matrix which was made from the response functions of the NE213 scintillator which have been measured in the neutron energy range up to 390 MeV at the RCNP cyclotron facility at Osaka University [14]. The matrix contains 19 light output groups for 18 neutron energy groups from 12 to 380 MeV. The uncertainty of the response function is 15%.

However, in the shielding experiment, since some of neutrons come from the side direction especially for location B4 and B5, detector response in the shielding experiment might be slightly different from the measured response functions by parallel neutron beam from front surface.

#### 4.7 Neutron background subtraction

The normalisations for normal and background measurements were already described in Section 4.4. The light-output distributions bunched in light energy group of the response matrix after background subtractions were used in the unfolding. Actually, the background subtractions and group bunching process mentioned above were carried out at the same time during the unfolding process described in the next section. Figures of the light-output distributions for normal and background of each run are described in Ref. [15].

The neutron background originated from the beam line adjacent to ours (outside our beam line's shielding), and it depended on the neighbouring beam intensity and on our detector location. More background contribution at location A (where the concrete side shielding is thinner) and at location I above the roof than was observed at locations B1-B3. Although no background measurements were performed at B1 and B3, the background at these locations, like that at B2, is considered to be negligible due to the thick shielding.

#### 4.8 Unfolding

Neutron energy spectra were obtained by the unfolding method using the FORIST code [17]. A window function makes the unfolded neutron spectra smoother without the fluctuations which are caused by uncertainties in the light calibration, response function and the measured pulse-height distribution. In this work, in order to avoid fluctuation, and also in order not to lose the original spectral shape, a 30% window was given for most of the neutron energy groups.

#### 4.9 Uncertainty

The statistics of the measured light output distribution (normal and background) and the uncertainty due to the unfolding process are already taken into account in the errors of the flux of each energy bin of the neutron energy spectra obtained by the FORIST code. In addition, an error in the absolute value of the response function (15%) was added in vector for all fluxes in each energy bin.

Neutron attenuation due to any interactions in the veto counter was assumed to be negligible in the analysis, but further investigation by simulation should be needed to prove it.

### 5 Results and discussions

The measured neutron energy spectra obtained by the unfolding method are shown in Figure 11 for 40-cm thick iron, 80- and 160-cm thick concrete. Although the unfolded neutron spectra were obtained from 12-380 MeV, the spectra below 30 MeV have a large uncertainty since the maximum light outputs of the response functions below 30 MeV are too close to their threshold. Therefore, only the unfolded neutron energy spectra above 32 MeV were employed as final results. Also, since the maximum neutron energy of the response matrix is 380 MeV, the experimental data above this energy could not be obtained. Bumps in the fluxes around the maximum energy can be seen in the spectra at forward angles below 50 degrees since neutrons with energy higher than 380 MeV are not negligible and contribute to the results of the maximum energy group in the unfolding process. For the results in the other lateral locations, neutron fluxes above 380 MeV are negligible, and no significant bump can be seen. Improved neutron spectra are expected to be obtained when extended response functions with wider neutron energy range are available in the future.

In terms of the absolute neutron flux, further investigation of detector response simulation is needed, especially above 100-MeV neutron energy, since the resulted neutron flux strongly depends on the measured response functions which were normalised by simulation results. Moreover, detector response might slightly change due to side injection and it should be also investigated in the future experiment and simulation.

### 6 Summary

High energy neutron measurements were performed at various locations behind lateral shields of concrete and iron using a 120 GeV/c hadron beam at the CERF facility at CERN, and energy spectra in the energy range from 32 to 380 MeV were obtained by an unfolding method.

The CERF facility has a simple structure of beam line and shielding, and the source term is clearly defined. This experiment explored different angles, shielding materials and thicknesses. The radiation field at CERF has been measured over many years with different instruments and this experiment provides a valuable extension towards spectral measurements of high energy neutrons.

The used spectrometer, the NE213, is an instrument which has been widely used for numerous measurements, it is well-tested and understood. However, in such a high energy beam facility, there were many difficulties of the measurements such as significant muon background and the pile-up of events within the same particles shower, and also difficulties of unfolding analysis with measured response functions which is hardly available above 20 MeV.

This experiment provides valuable data in order to benchmark Monte Carlo transport codes and evaluate their accuracy in this aspect. A first benchmark study is discussed in Ref [18].

### Acknowledgements

This work was supported by Department of Energy contract DE-AC02-76SF00515. We would like to thank the members of the Radiation Protection group at CERN for their great help in this experiment.

### References

- [1] N. Nakao, H. Nakashima, T. Nakamura, Sh. Tanaka, Su. Tanaka, K. Shin, M. Baba, Y. Sakamoto, Y. Nakane, "Transmission Through Shields of Quasi-monoenergetic Neutrons Generated by 43- and 68-MeV Protons: Part I – Concrete Shielding Experiment and Calculation for Practical Application", *Nucl. Sci. Eng.*, 124 (1996) pp. 228-242.
- [2] H. Nakashima, N. Nakao, Sh. Tanaka, T. Nakamura, K. Shin, Su. Tanaka, H. Takada, S. Meigo, Y. Sakamoto, Y. Nakane, M. Baba, "Transmission Through Shields of Quasi-monoenergetic Neutrons Generated by 43- and 68-MeV Protons: Part II – Iron Shielding Experiment and Analysis for Investigating Calculation Methods and Cross Section Data", *Nucl. Sci. Eng.*, 124 (1996), pp. 243-257.
- [3] N. Nakao, M. Nakao, H. Nakashima, Su. Tanaka, Y. Sakamoto, Y. Nakane, Sh. Tanaka, T. Nakamura, "Measurements and Calculations of Neutron Energy Spectra Behind Polyethylene Shields Bombarded by 40- and 65-MeV Quasi-monoenergetic Neutron Sources", *J. Nucl. Sci. Technol.*, 34 (4) (1997) pp. 348-359.
- [4] T. Nunomiya, N. Nakao, P. Wright, T. Nakamura, E. Kim, T. Kurosawa, S. Taniguchi, M. Sasaki, H. Iwase, Y. Uwamino, T. Shibata, S. Ito, D.R. Perry, "Measurement of Deep Penetration of Neutrons Produced by 800-MeV Proton Beam Through Concrete and Iron at ISIS", *Nucl. Instr. Meth.*, B 179 (2001) pp. 89-102.
- [5] T. Nunomiya, N. Nakao, P. Wright, T. Nakamura, E. Kim, T. Kurosawa, S. Taniguchi, M. Sasaki, H. Iwase, T. Shibata, Y. Uwamino, S. Ito, D.R. Perry, *Experimental Data of Deep-penetration Neutrons Through Concrete and Iron Shield at ISIS Spallation Neutron Source Facility Using an 800-MeV Proton Beam*, KEK Report 2001-24 (Feb. 2002).
- [6] M. Sasaki, N. Nakao, T. Nunomiya, T. Nakamura, A. Fukumura, M. Takada, "Measurements of High-energy Neutrons Penetrated Through Iron Shields Using Self-TOF Detector and an NE213 Organic Liquid Scintillator", *Nucl. Instr. Meth.*, B 196 (2002) pp. 113-124.

- [7] H. Nakashima, *et al.*, “Current Status of the AGS Spallation Target Experiment”, *Proc. of OECD/NEA Workshop on Shielding Aspects on Accelerator, Targets and Irradiation Facilities (SATIF-6)*, SLAC, Stanford, CA, USA, 10-12 April 2002, pp. 27-36, OECD/NEA, Paris (2003).
- [8] S. Taniguchi, T. Nakamura, T. Nunomiya, H. Iwase, S. Yonai, M. Sasaki, S.H. Rokni, J.C. Liu, K.R. Kase, S. Roesler, “Neutron Energy and Time-of-flight Spectra Behind the Lateral Shield of a High Energy Electron Accelerator Beam Dump”, *Nucl. Instr. Meth.*, A 503 (2003) pp. 595-605.
- [9] N. Nakao, *et al.*, “Arrangement of High-energy Neutron Irradiation Field and Shielding Experiment Using 4 m Concrete at KENS”, *Proc. 10<sup>th</sup> International Conference on Radiation Shielding (ICRS10)*, Madeira, Portugal, 9-14 May 2004; *Radiat. Prot. Dosim.*, Vol. 116, No. 1-4, pp. 553-557 (2005).
- [10] A. Mitaroff, M. Silari, “The CERN-EU High Energy Reference Field (CERF) Facility for Dosimetry at Commercial Flight Altitudes and in Space”, *Radiat. Prot. Dosim.*, 102, No. 1, 7-22 (2002).
- [11] Helmut Vincke, *et al.*, *Accurate PIC Calibration by the Use of a Coincidence of Two Scintillators*, CERN-SC-2004-090-RP-TN, CERN (2004).
- [12] K. Omata, *et al.*, *A Data Acquisition System Based on Personal Computer*, INS-REP-884, Institute for Nuclear Study, University of Tokyo (1991).
- [13] N. Nakao, T. Kurosawa, T. Nakamura, Y. Uwamino, “Absolute Measurements of the Response Function of an NE213 Organic Liquid Scintillator for the Neutron Energy Range up to 206 MeV”, *Nucl. Instr. and Meth.*, A 463 (2001) pp. 275-278.
- [14] S. Taniguchi, N. Nakao, H. Yamakawa, K. Oishi, T. Nakamura, A. Tamii, K. Hatanaka, T. Saito, “Measurement of Response Functions of Organic Liquid Scintillator for Neutron Energy Range up to 390 MeV”, *Proceedings of AccApp05*, Venice, Italy, 29 August-1 September 2005.
- [15] N. Nakao, S. Taniguchi, S.H. Rokni, S. Roesler, M. Brugger, M. Hagiwara, H. Vincke, H. Khater, A.A. Prinz, “Measurement of Neutron Energy Spectra Behind Shielding at 120 GeV/c Hadron Beam Facility, CERF”, *Slac Radiation Physics Note*, RP-06-06 (2006).
- [16] Glenn F. Knoll, *Radiation Detection and Measurement*, 3<sup>rd</sup> edition, John Wiley and Sons Inc. (2000).
- [17] R.H. Johnson, *FORIST, Neutron Spectrum Unfolding Code (FERDOR with Optimized Resolution Using an Iterative Smoothing Technique)*, PSR-92, RSIC/ORNL (1976).
- [18] N. Nakao, S.H. Rokni, M. Brugger, S. Roesler, H. Vincke, K. Kosako, “Calculation of High-energy Neutron Spectra with Different Monte Carlo Transport Codes and Comparison to Experimental Data Obtained at the CERF Facility”, these proceedings.

**Table 1: Recent shielding experiments at high energy accelerator facilities**

Facility Institution Country Year of experiment Reference	TIARA JAERI Japan 1992-1996 [1,2,3]	ISIS RAL UK 1998 [4,5]	HIMAC NIRS Japan 1998-2000 [6]	AGS BNL USA 2001 [7]	FFTB SLAC USA 2001-2002 [8]	KENS KEK Japan 2003 [9]	CERF CERN Switzerland 2004 This work
Accelerator	Proton Cyclotron	Synchrotron (spallation source)	Heavy ion Synchrotron	Alternating Gradient synchrotron	Electron Linac	Synchrotron (spallation source)	Super Proton Synchrotron (SPS)
Particle	p <sup>+</sup>	p <sup>+</sup>	<sup>12</sup> C <sup>6+</sup>	p <sup>+</sup>	e <sup>-</sup>	p <sup>+</sup>	p <sup>+</sup> , π <sup>+</sup>
Energy	45, 68 MeV	800 MeV	400 MeV/n	2.83, 24 GeV	28.7 GeV	500 MeV	120 GeV/c
Target	Thin Thick						
	<sup>7</sup> Li	Ta	Graphite	Ag	Al	W	Cu
Beam angle to the shield	0°	90°	0°	90°	90°	0°	13-133°
Shield (cm)	Concrete	25-200	20-120	50-250	50-500	274-396	40-400
	Iron	10-130	10-60	10-130	25-330		40
	Polyethylene	30-183					
Detector	NE213	5"φ x 5"		5"φ x 5"		5"φ x 5"	5"φ x 5"
	Bonner sphere	He-3 counter	Indium activation			<sup>6</sup> Li glass counter	
	Self-TOF			Self-TOF			
	Activation foil		Bi, C, Al	Bi	Bi, Co, Au Al, In		Bi, Al, In, Au
Energy spectra (MeV)	NE213	5-68		20-800		6-800	32-380
	Bonner sphere	(thermal)- 70	(thermal)- 400			(thermal)- 400	
	Self-TOF			100-600			
	Bi-activation			20-1000			
Activation reaction rate		Yes		Yes		Yes	

JAERI: Japan Atomic Energy Research Institute, Japan, RAL: Rutherford Appleton Laboratory, UK, NIRS: National Institute of Radiological Sciences, Japan, BNL: Brookhaven National Laboratory, USA, SLAC: Stanford Linear Accelerator Center, USA, KEK: Kou Enerugi Kasokuki Kenkyu Kikou (High Energy Accelerator Research Organisation), Japan, CERN: European Organisation for Nuclear Research, Switzerland.

**Table 2: Densities of materials**

Material	Density [g/cm <sup>3</sup> ]
Copper target	8.96
Iron roof (upper)	7.65
Iron roof (lower)	7.20
Concrete shield (see Table 2)	2.40

**Table 3: Typical composition of the concrete shielding at CERN (2.40 g/cm<sup>3</sup>)**

	[wt.%]	[atom/cm <sup>3</sup> ]		[wt.%]	[atom/cm <sup>3</sup> ]
H	0.561	8.04E+23	Si	16.175	8.32E+23
C	4.377	5.27E+23	S	0.414	1.87E+22
O	48.204	4.35E+24	K	0.833	3.08E+22
Na	0.446	2.80E+22	Ca	23.929	8.63E+23
Mg	1.512	8.99E+22	Ti	0.173	5.22E+21
Al	2.113	1.13E+23	Fe	1.263	3.27E+22

**Table 4: Detector locations and angles with respect to the beam line and target front surface in the respective target positions**

		Side concrete					Iron roof				
		80-cm thick		160-cm thick			40-cm thick				
Target A	Location	A3	A2	A1							
	Angle	40°	90°	133°							
Target B	Location	B5		B4	B3	B2	B1	I3	I2	I2'	I1
	Angle	13°		26°	50°	90°	110°	35°	90°	90°	130°

**Figure 1: Geometry of the CERF facility and detector locations. Beam comes from Q to P in the beam line in the figure.**

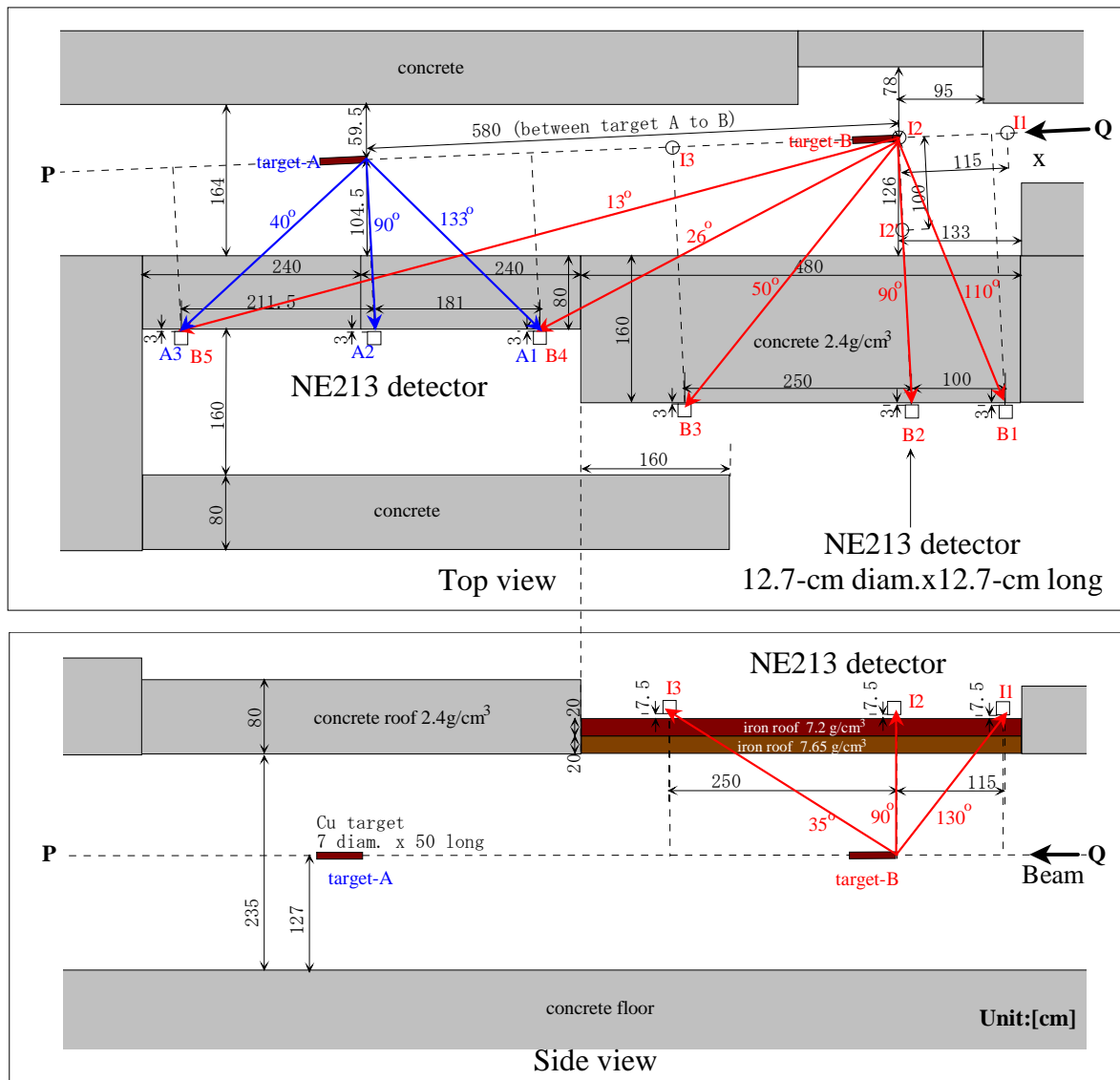


**Figure 2: Detectors set up (a) above the iron roof and (b) at the side concrete**

The stainless steel plate below the NE213 detector in figure (a) has a hole (15-cm diameter) in the centre, and no neutron attenuation occurs

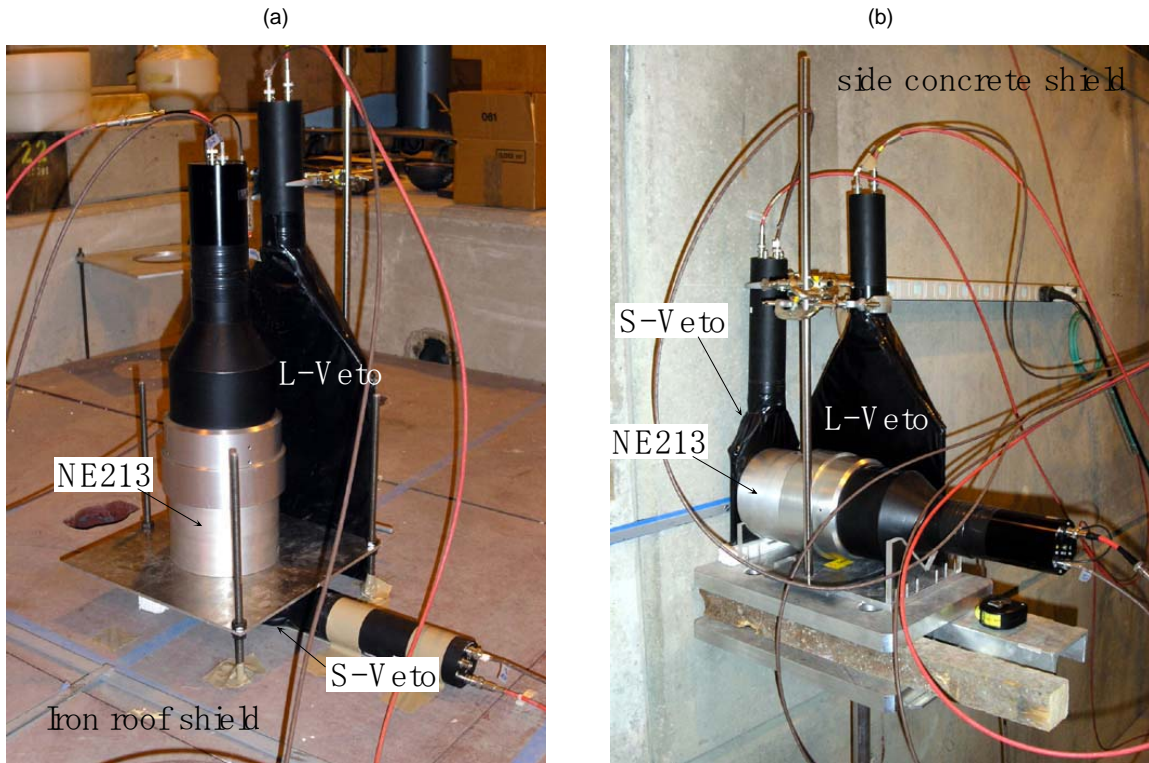


**Figure 3: Sketch of the detectors set-up with the interactions of neutron and charged particles**

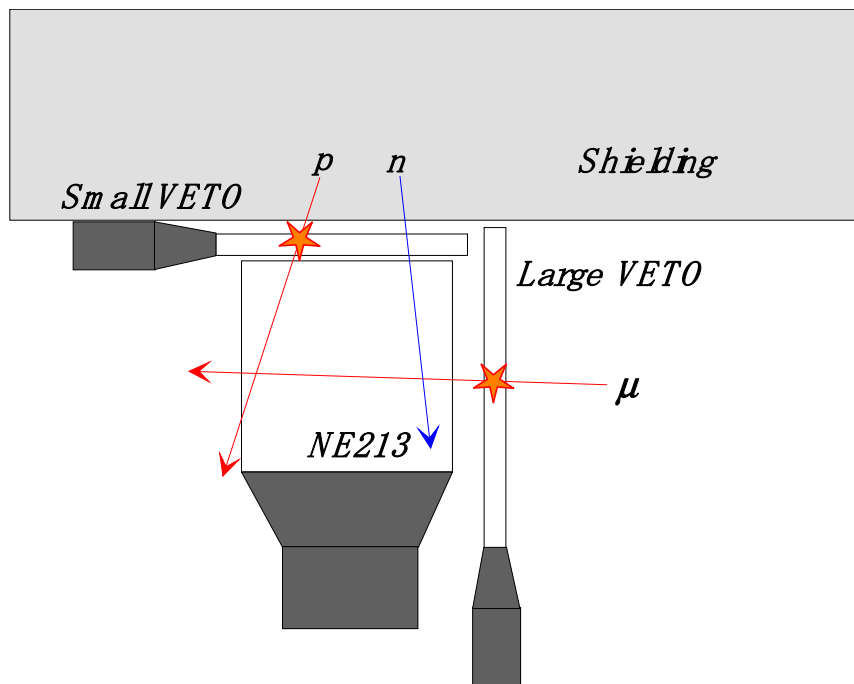


**Figure 4: Electronic measurement circuit**

PMT: photo multiplier, HV: High voltage power supply, CFD: constant fraction discriminator (ORTEC935), COIN: coincidence, GG: gate and delay generator, DIV: signal divider, INV: inverter, DLY: delay, ATT: attenuator, ADC: analogue to digital converter (LeCroy2249W). In the beginning of the experiment, L-veto event was recorded with ADC connection without INHIBIT-1 connection.

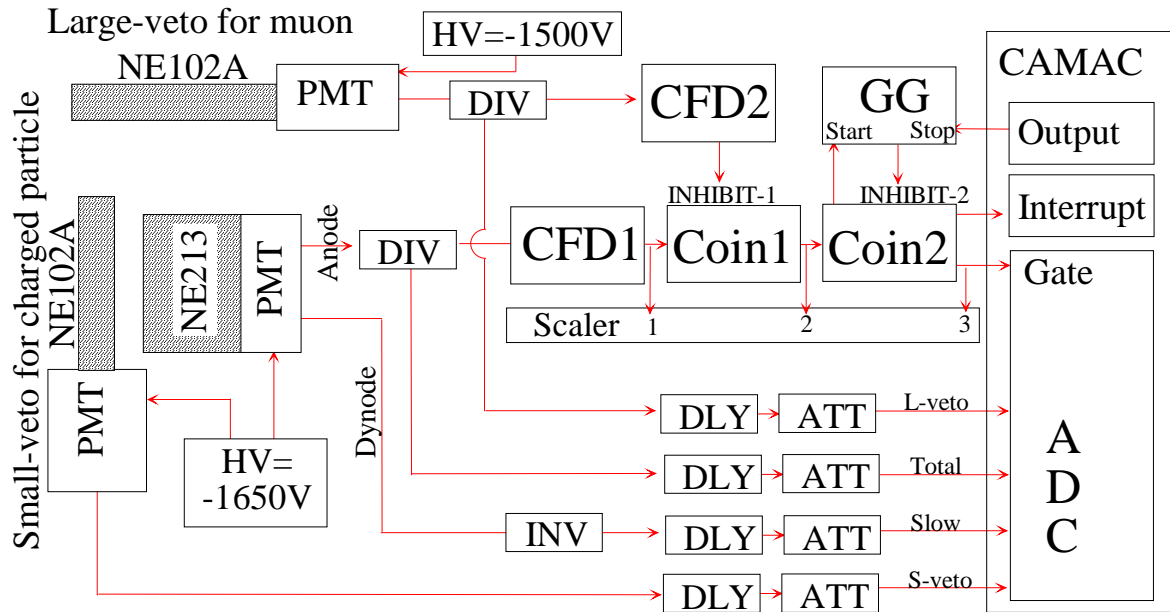


**Figure 5: The signals from the NE213 to ADC which were gated in the total pulse height and the slow (decay) component regions**

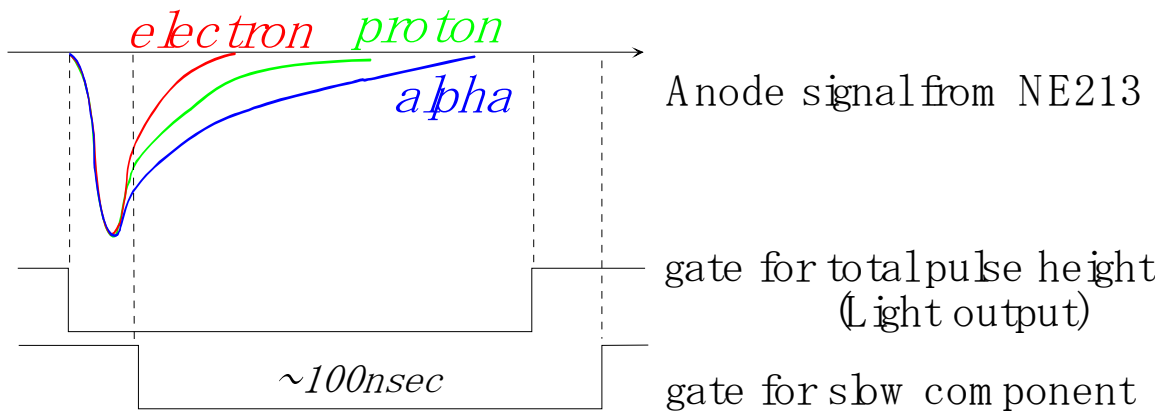


**Figure 6: Two-dimensional distributions of veto-counters versus NE213 total pulse height (light output) and one-dimensional distributions of veto-counters for (a) L-veto and (b) S-veto**

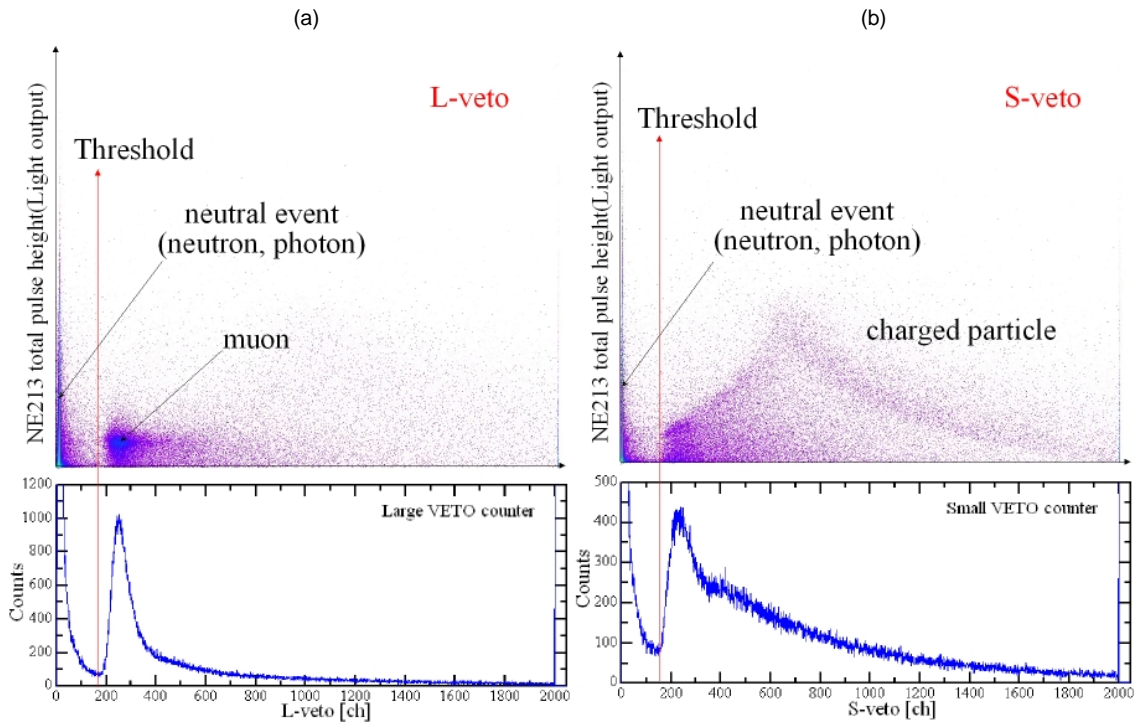


**Figure 7: Two dimensional distributions of slow component versus total pulse height of NE213 detector signal for (a) whole region and (b) magnified low channel region**

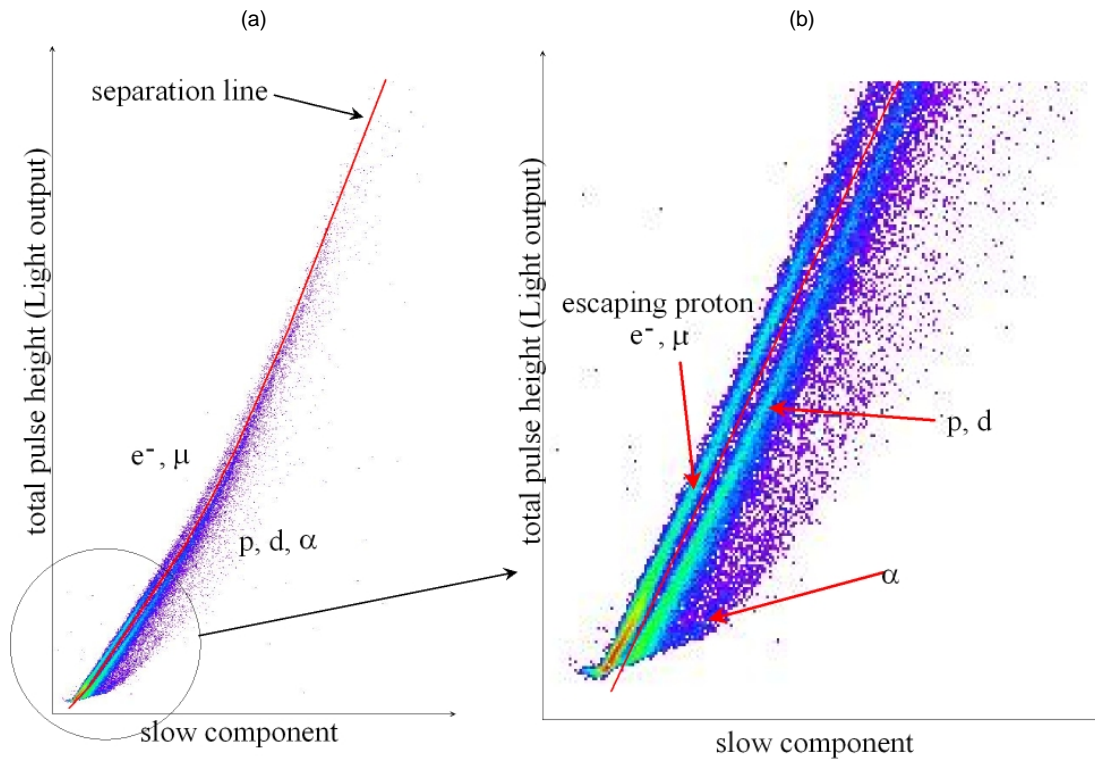


**Figure 8: Pile-up event selection from the two-dimensional distributions of slow component versus total pulse height of NE213 detector signal**

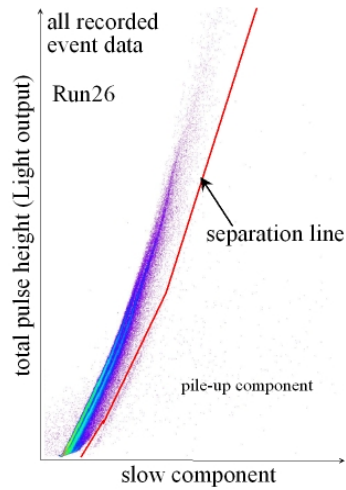


**Figure 9: Sketch of pile-up pulses during the ADC gates**

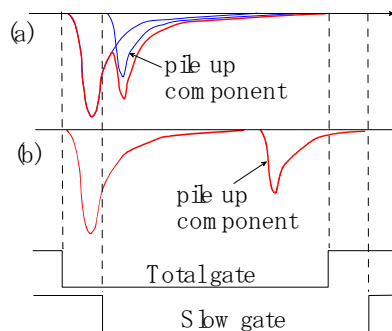


**Figure 10: Total pulse-height distributions for the raw data and pile-up events selected from two-dimensional distribution shown in Figure 8**

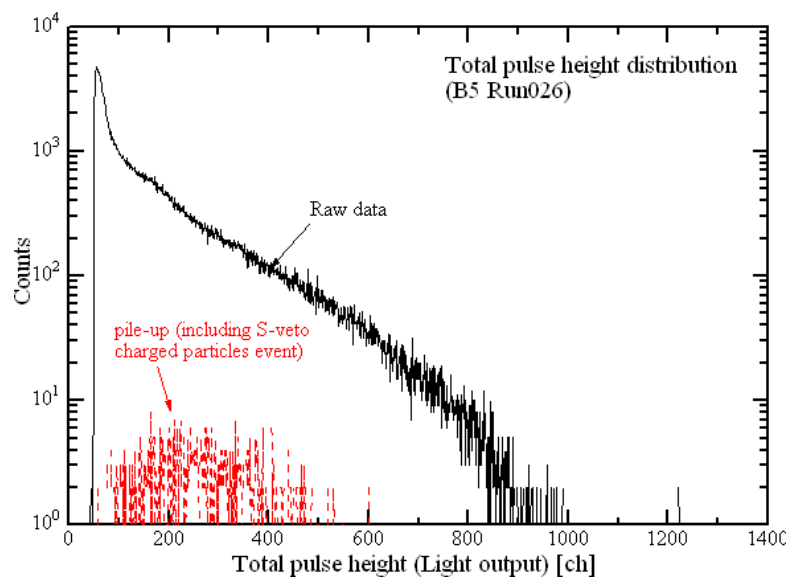
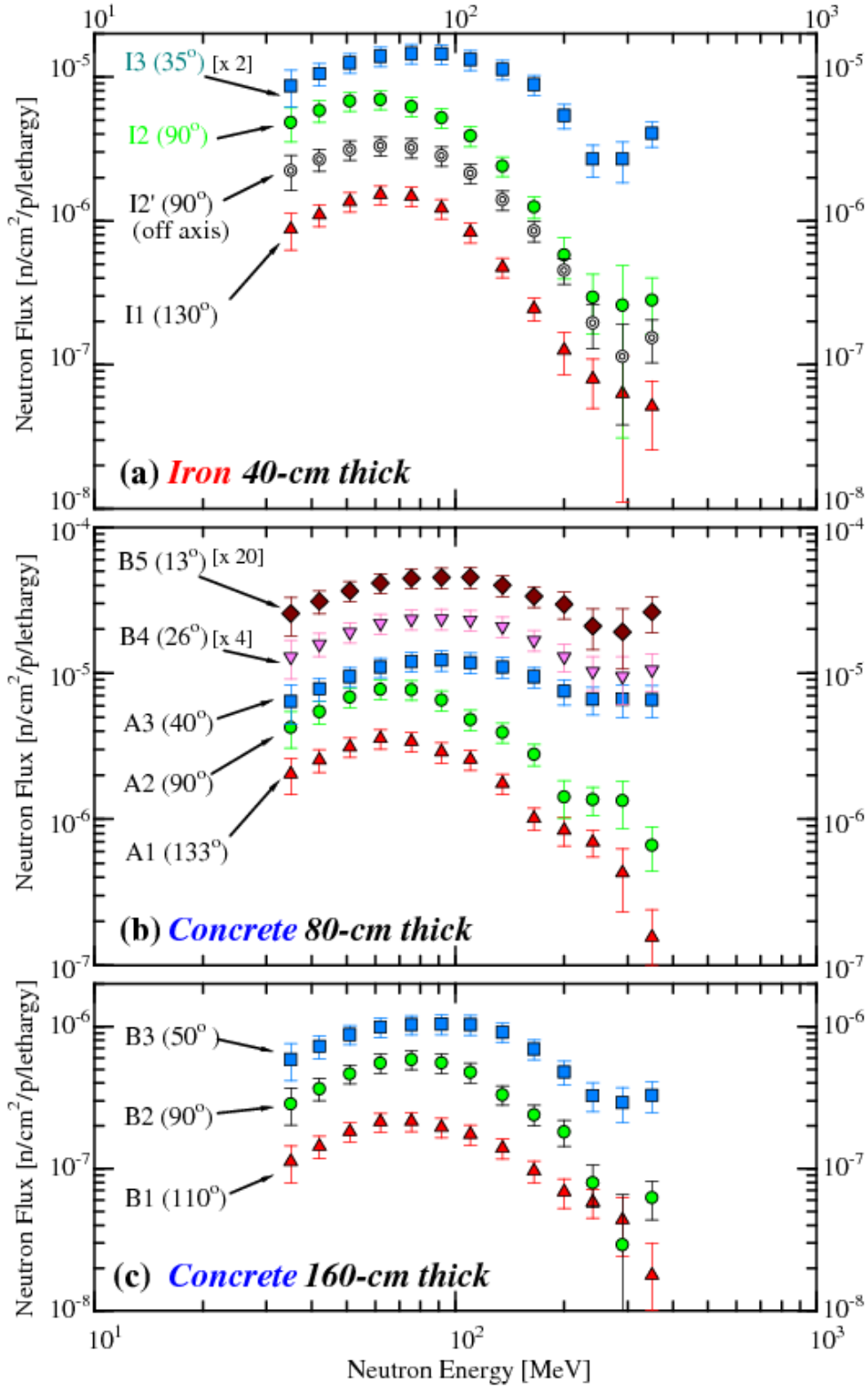


**Figure 11: Experimental neutron energy spectra behind (a) 40-cm thick iron, (b) 80-cm thick concrete and (c) 160-cm thick concrete**



## Calculation of high-energy neutron spectra with different Monte Carlo transport codes and comparison to experimental data obtained at the CERF facility

**N. Nakao, S.H. Rokni**

Stanford Linear Accelerator Centre, Stanford, USA

**M. Brugger, S. Roesler, H. Vincke**

CERN, Geneva, Switzerland

**K. Kosako**

Shimizu Corporation, Tokyo, Japan

### Abstract

Energy spectra of neutrons behind shielding of the CERN-EU High Energy Reference Field (CERF) facility were calculated with the FLUKA, MARS and PHITS codes for different measurement locations. At CERF a 120 GeV/c mixed hadron beam interacts with a copper target creating a stray radiation field which is then attenuated by a lateral shield of either 80 cm or 160 cm thick concrete or 40 cm thick iron. The measurement locations cover an angular range with respect to the beam axis between 13 and 110 degrees. Results for the energy range between several tens to several hundreds of MeV are compared to each other and to measurements performed with a NE213 liquid scintillator detector. For many locations the measured neutron fluence is within the results obtained with the different codes, with the experimental uncertainties covering all three calculated neutron spectra. Comparing the predictions of the three codes to each other it is observed that FLUKA and PHITS predict similar fluences, while the energy spectra calculated with MARS are slightly lower. In order to investigate differences, simulations were also performed for a simplified cylindrical geometry. Results demonstrate that they can be partially explained by differences in the high-energy hadron production in the copper target.

## Introduction

The radiation environment outside lateral, thick shielding at high-energy hadron accelerators is characterised by a large variety of particle types and energies. This so-called mixed radiation field typically consists of neutrons, protons, charged pions and photons with energies ranging from those of thermal neutrons to several tens of GeV. Often, neutrons dominate and determine the shower development through the shield. Moreover, they cause most of the dose to personnel behind the shield, with neutrons of high energies ( $E > 20$  MeV) contributing a significant fraction.

Modern particle interaction and transport codes are capable of calculating mixed radiation fields for arbitrary configurations. Uncertainties in predictions of neutron energy spectra typically increase with energy and have to be assessed based on results of benchmark measurements. Unfortunately, also the complexity of neutron measurements and their inherent uncertainties increase with energy explaining the lack of experimental data for neutron energy spectra above several tens of MeV.

The CERN-EU High Energy Reference Field (CERF) facility [1] has been used for many years to investigate the performance of radiation detectors to mixed fields. It is well-characterised and suitable for benchmark studies of high-energy neutron spectra outside hadron accelerator shielding. This fact motivated measurements with a NE213 liquid scintillator detector during the operation of CERF in the year 2004. [2] The NE213 detector is especially suited to detect high-energy neutrons and has been previously used in similar studies at electron accelerators or hadron accelerators of lower energy than accessible with CERF.

While the measurements are discussed elsewhere [2] this paper focuses on the simulations of the experiment with the FLUKA [3,4], MARS [5,6] and PHITS codes [7] and on the comparison of the calculated and measured high-energy neutron spectra. The aim of the study is to evaluate code predictions for energies above 20 MeV with a direct spectral measurement. Preliminary results obtained with the MARS code were published in Ref. [8] and are superseded by slightly higher fluence spectra presented in this work.

## The benchmark measurements

At the CERF facility a beam of positively charged hadrons (60.7%  $\pi^+$ , 34.8% p, 4.5%  $K^+$ ) with a momentum of 120 GeV/c is intercepted by a cylindrical copper target, 7 cm in diameter and 50 cm in length [1]. In the lateral direction, the target is surrounded by concrete (80 cm and 160 cm thicknesses) and by iron shielding (40 cm thickness). Beam intensities are monitored and well-known to within less than one per cent [9]. The facility allows for measurements both inside and outside of the shielding. The total length of the lateral shield of almost 10 m gives access to a wide range of angles with regard to the target and beam direction, between 130 degrees (upstream of the front face of the target) and 13 degrees (downstream of the target).

The neutron measurements were carried out with a NE213 organic liquid scintillator of a cylindrical shape (12.7 cm diameter and 12.7 cm length) [2]. Two 5 mm thick NE102A plastic scintillators of rectangular shape were used to reject background signal from charged particles. One of them was placed between the shield surface and the NE213 scintillator to detect charged particles accompanying the neutron cascade in the shield and a second one was placed upstream of the NE213 detector to detect muons originating from pion decays upstream in the beamline. A sophisticated data-reduction and analysis procedure comprising the “unfolding” of the pulse-height spectra with previously measured detector response functions then yielded neutron energy spectra between 32 MeV and 380 MeV.

Data were taken at a total of 12 different measurement locations, five of them behind 80 cm thick concrete shielding, three behind 160 cm thick concrete and four behind 40 cm thick iron shielding. Table 1 summarises locations, respective shielding thicknesses and angles with regard to the target front face and beam direction. Further details of the measurements are discussed in Ref. [2]. Figure 1 shows a sketch of the facility indicating the two target positions as well as the measurement locations.

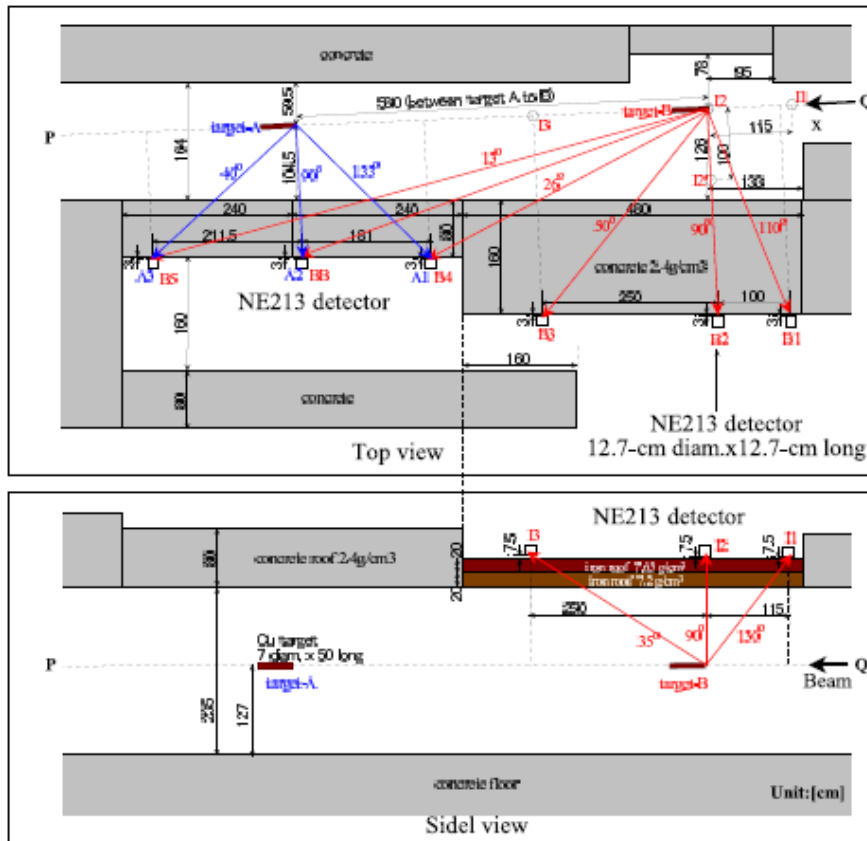
**Table 1: Summary of the measurement locations**

The table lists shielding materials, thicknesses as well as indices and angles of the locations. Angles refer to the beam direction with the origin of the co-ordinate frame at the target front face. Measurement location I2' denotes a location at 90° to the beam direction but laterally displaced by 1 m from the beam axis.

Material	Concrete		Iron			
	80 cm	160 cm	40 cm			
Location and angle	A1	133°	B1	110°	I1	130°
	A2	90°	B2	90°	I2	90°
	A3	40°	B3	50°	I2'	90°
	B4	26°	–	–	I3	35°
	B5	13°	–	–	–	–

**Figure 1: Layout of the CERF facility and measurement locations**

The upper figure represents a horizontal section indicating the detector positions behind the 80 cm and 160 cm thick concrete shields; the lower figure is a vertical section displaying the detector positions on top of the 40 cm thick iron shield.



**Details of the Monte Carlo calculations**

The experimental set-up was simulated with the latest versions of FLUKA [3,4] (Version 2005), MARS [5,6] (Version 15, update February 2006) and PHITS [7] (Version 1.97). All calculations use identical geometries, including dimensions of shielding items, their relative position, material compositions and beam characteristics.

The geometry of the CERF facility is rather simple; it consists of the above mentioned copper target placed inside a shielding enclosure. The lateral shielding consists of concrete of 80 cm and

160 cm thicknesses, beyond which the “concrete-measurement positions” are located. Part of the roof shield is made of iron-bars with a total thickness of 40 cm and allows for measurements behind iron shielding. Thus, the “iron-measurement positions” were in fact situated on top of the beamline shield with the NE213 detector facing downward. It should be noted that the beam axis, and therefore the axis of the copper target, is not parallel to the side walls of the shielding enclosure but points towards the latter under an angle of about 2.2 degrees (see Figure 1). Furthermore, the different angles of the measurement locations in case of the 80 cm concrete shield (see Table 1) were partially achieved by moving the target to a different position inside the shielding rather than by moving the position of the NE213 detector. All mentioned details were taken into account in the simulations.

Tables 2 and 3 summarise densities used for the different components as well as the elemental composition of the concrete shielding. The iron shield and the copper target were assumed to be pure materials as trace elements are not known and are anyway of minor importance for this study.

**Table 2: Densities of copper target and shielding materials used in the simulations**

Component	Density (g/cm <sup>3</sup> )
Copper target	8.96
Iron roof shield (lower 20 cm)	7.65
Iron roof shield (upper 20 cm)	7.20
Concrete shield	2.40

The simulations considered the actual beam composition (as given above) and the measured, Gaussian shape of the beam. The exact beam shape, however, was found to have negligible influence on the energy spectra outside the shielding (proven by simulations assuming pencil-beam).

Neutron energy spectra were calculated by scoring track-length of all neutrons reaching the detector volumes and normalising them to one beam particle. The detector volumes were simulated as air volumes (without detector enclosure) having the same size as the one of the NE213 scintillator (12.7 cm diameter and 12.7 cm length). So far, only preliminary simulations were performed to calculate the charged particle background subtraction with the NE102A scintillators which could induce a bias in the measurements and which is difficult to remove from the data without simulations (see below).

**Table 3: Elemental composition of concrete assumed in the simulations (given in per cent by weight)**

Element	Weight fraction (%)	Element	Weight fraction (%)
H	0.561	Si	16.175
C	4.377	S	0.414
O	48.204	K	0.833
Na	0.446	Ca	23.929
Mg	1.512	Ti	0.173
Al	2.113	Fe	1.263

Similarly, all neutrons entering the detector volumes were scored with the same relative weight, irrespective of their direction of incidence, which might cause an uncertainty due variations in the angular response of the NE213 detector. Further code-specific details are given below.

## FLUKA

All produced hadron types were considered in the particle cascade and transport. Since photons, electrons, positrons and muons were not of interest in this study the electromagnetic shower was disabled in the simulations. In order to accelerate the convergence of the fluence results in the detector positions, the hadron transport through the shielding was biased by subdividing the concrete shielding into layers of 20 cm thickness (7 cm in case of iron) and by applying particle splitting at the layer-boundaries according to the inverse of the particle attenuation. Neutrons were transported down to thermal energies, while other hadrons were followed until captured or ranged out. Beam particles of different types (see CERF beam composition given above) were sampled during the calculation in a user-written source routine. Results constitute averages over a total number of 56 Mio beam particles.

## MARS

The incident beam was assumed to consist of protons (34.8%) and positively charged pions only (65.2%). Kaons were considered to be equivalent to pions in this calculation. Secondary neutrons, protons, pions and muons were taken into account in the simulations with a lower energy cut-off of 1 MeV. Neutrons with energies below 14.5 MeV were transported using the MCNP-option in the MARS15 code. No variance reduction techniques were used.

## PHITS

As in case of MARS, the calculation considered the production and transport of neutrons, protons, pions, kaons and muons down to a cut-off energy of 1 MeV. In general, high-energy interactions were simulated using the JAM-model option above 3.5 GeV for nucleons and 2.5 GeV for mesons, respectively, and with the Bertini model at lower energies. Neutrons and protons with energies below 150 MeV were transported using the LA150 cross-section data library. Evaporation processes were described with the GEM model.

Results are averages over the cascades of 1.2 Mio. beam particles, 34.8% protons and 65.2% positively charged pions, respectively. In order to accelerate the convergence of the results, cell importance biasing was applied for the transport through the shield.

## Comparison of calculated and measured neutron energy spectra

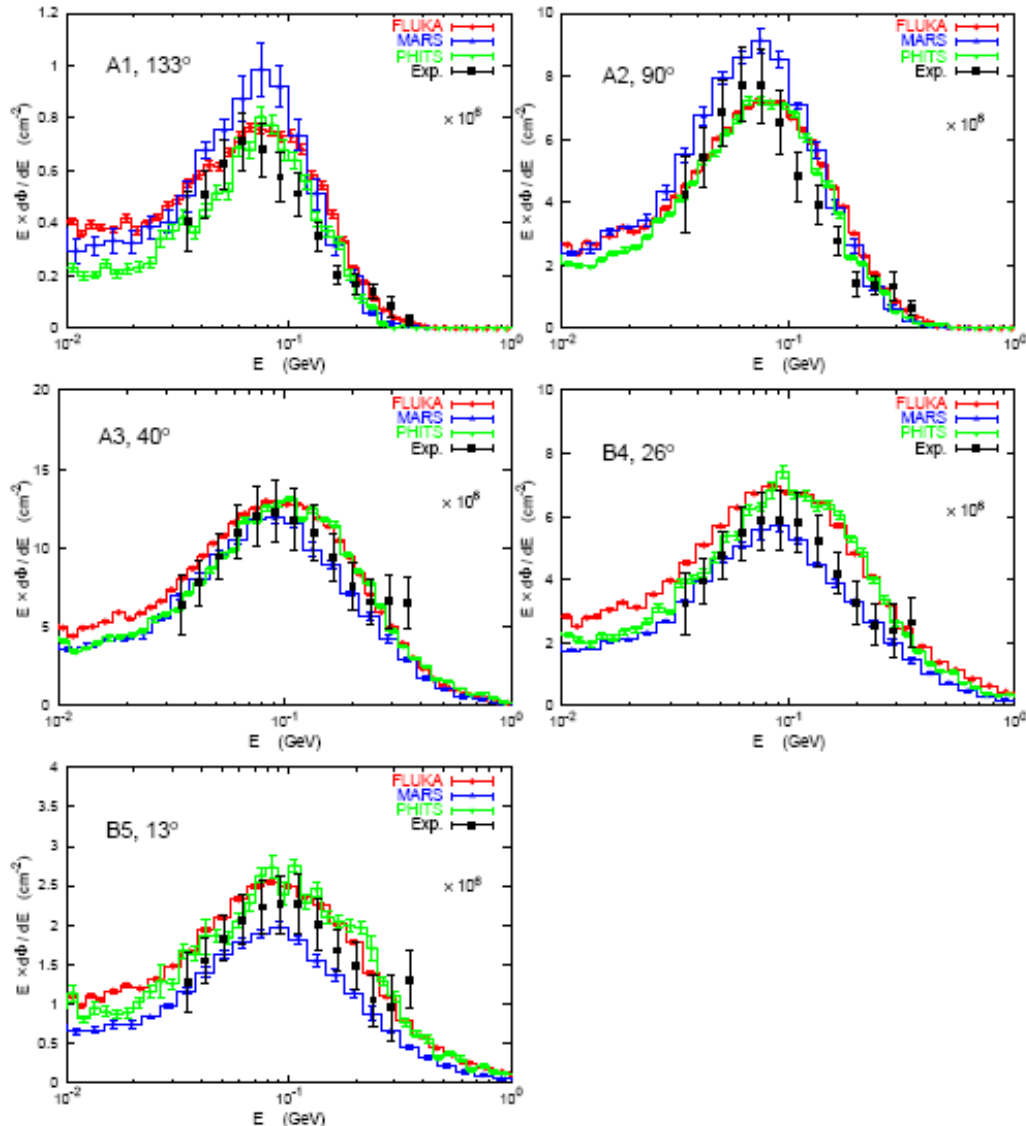
Neutron energy spectra calculated with the three different codes are compared to the measured spectra in Figures 2-4. Note that differential fluence spectra  $d\phi = dE$  were multiplied by the energy  $E$  in order to conserve that, in a logarithmic energy scale, areas under the histograms correspond to number of neutrons (so-called “lethargy”-representation). Displayed error bars indicate systematic and statistical uncertainties in case of experimental data and statistical uncertainties in case of calculations. Calculated spectra are given as histograms overlaid by data points with error bars at the corresponding geometrical bin averages. All spectra are normalised to one beam particle and multiplied by a factor of 106 to allow displaying them in a convenient scale.

By comparing the results of the different transport codes to each other it can be observed that all codes predict similar energy spectra (often within less than 20%) in backward direction and at 90 degrees, while at forward angles (detector positions A3, B4 and B5 for the 80 cm and B3 for 160 cm the concrete shield) the spectra calculated with MARS are generally lower, although less than a factor of two. The reason for the different fluence results obtained with MARS and FLUKA can be traced back to differences in the description of the particle shower in the copper target (see following section). In order to quantify the differences in the predictions of the codes the neutron fluence spectra were integrated with two different lower-energy cut-offs of 19.6 MeV and 100 MeV, respectively. The ratios between the values obtained for FLUKA and PHITS as well as for FLUKA and MARS are given in Table 4. As can be seen FLUKA and PHITS agree within 20% for all locations behind the concrete shield, except at backward angle (A1 and B1) where the ratio reaches 1.3 at high energy. The ratios for FLUKA and MARS increase with decreasing angle up to a value of 1.6 for location B5 and high energies.

The code predictions reproduce the measured spectra within their uncertainties up to about 100 MeV and tend in general to be higher above that energy. The flattening of the measured fluence observed for the 2-3 highest energy bins is an artefact of the unfolding due to the upper limit of 380 MeV of the detector response matrix and a non-negligible contribution of neutrons of higher energy. Generally, the agreement is better for the 80 cm (*e.g.* positions A2 and A3) than for the 160 cm thick concrete shield (*e.g.* positions B2 and B3). A systematic dependence of the agreement on the angle cannot be observed (see Figure 2). The experimental data for the iron shield carry larger uncertainties. This can be attributed to a significant muon background originating upstream in the beamline and a neutron background from the neighbour beamline with a magnitude completely uncorrelated with this benchmark experiment. Both had to be subtracted from the total signal introducing a non-negligible error. Despite this fact, calculated and measured spectra still agree below 100 MeV within the experimental error. In addition, differences in code predictions are larger behind the iron shield with a maximum ratio of the integral fluences of FLUKA and PHITS of 1.5 at high energy and location I1 (see Table 4).

**Figure 2: High-energy neutron spectra at the detector positions behind the 80 cm thick concrete shield (see also Figure 1 and Table 1)**

Measured energy spectra (labelled "Exp") are compared to results obtained with the different Monte Carlo codes. All spectra are normalised to one beam particle and multiplied by 106 to allow for a convenient scale.



The reasons for the overestimation of the measured fluence at high energy (>100 MeV) by the different codes is still under investigation. Both, a deficiency in the models and a bias in the experimental data cannot be excluded at this point. Two candidates for the latter were identified, the first being differences in the irradiation geometries of the detector response measurements and of this experiment. In particular, the energy response matrix based on vertical homogeneous incidence of neutrons on the detector front face might not be fully representative for the rather inhomogeneous irradiation conditions at CERF comprising a wide range of directions of incidence, including those on the side-surface of the detector. This effect has been studied with a simplified, cylindrical geometry from which it was concluded (see following section) that it should be negligible at 90° angle. As the degree of overestimation at high energy is rather independent on the angle it is unlikely to be due to the actual angular distribution of neutrons. It could have been unambiguously addressed with measurements performed at larger distance from the shield which would have selected only those neutrons emitted perpendicular to the shield.

A second bias might be present in the data at high energy due to the rejection of neutrons accompanied by charged particles or of neutrons causing themselves a veto signal when passing through the NE102A scintillators. In order to rule out this bias a simulation is required which includes the NE213 detector as well as the NE102A scintillators and an event-by-event analysis of the simulated data based on the applied threshold of the scintillator. This analysis has not been performed so far; thus, final conclusions concerning the overestimation by the models at high energy cannot be drawn at this point.

**Figure 3: As in Figure 2, here for the detector positions behind the 160 cm thick concrete shield**

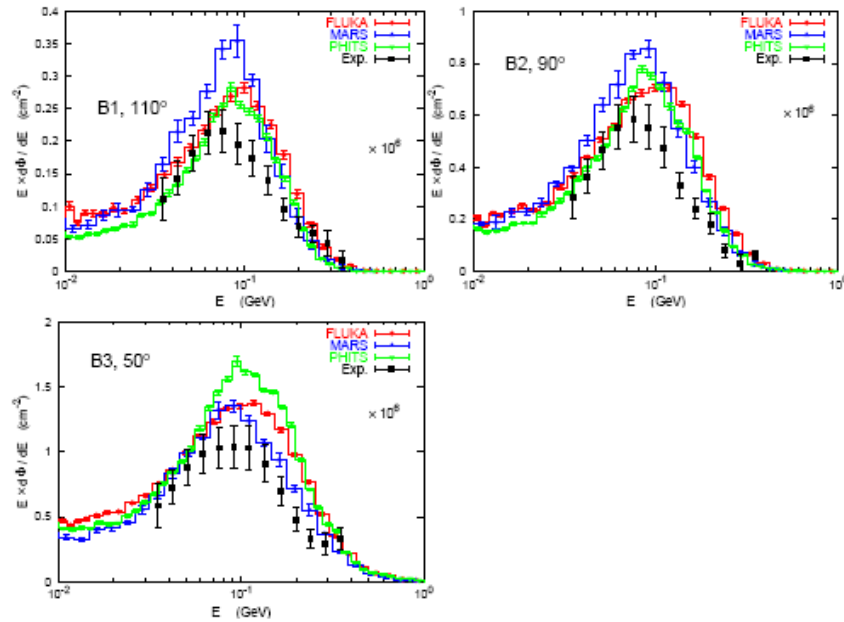


**Figure 4: As in Figure 2, here for the detector positions behind the 40 cm thick iron shield. Note that position I2' is at 90 with regard to the beam direction but displaced laterally by 1 m.**

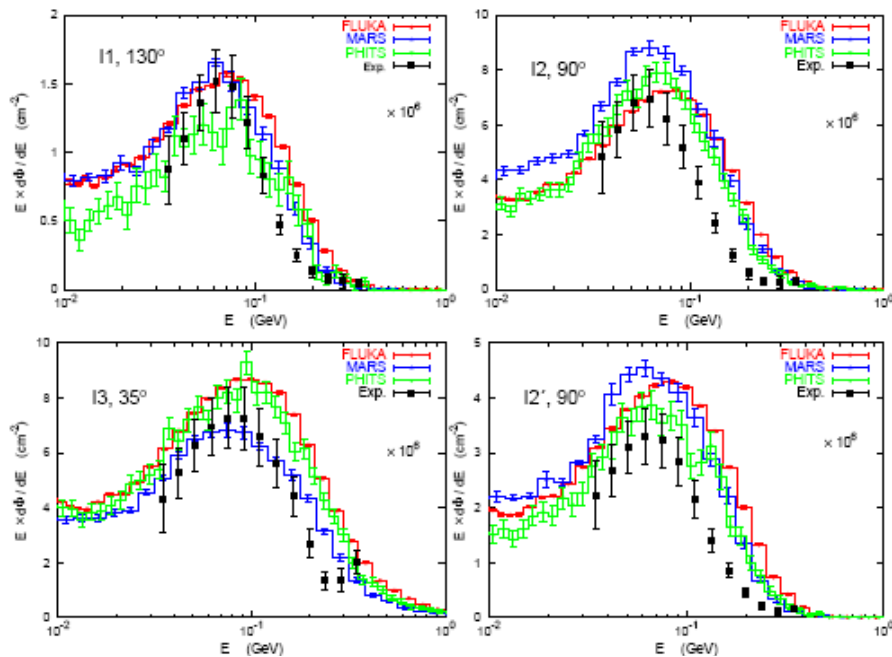


**Table 4: Ratios of integrated neutron fluence spectra obtained with FLUKA and PHITS and with FLUKA and MARS at the different measurement locations**

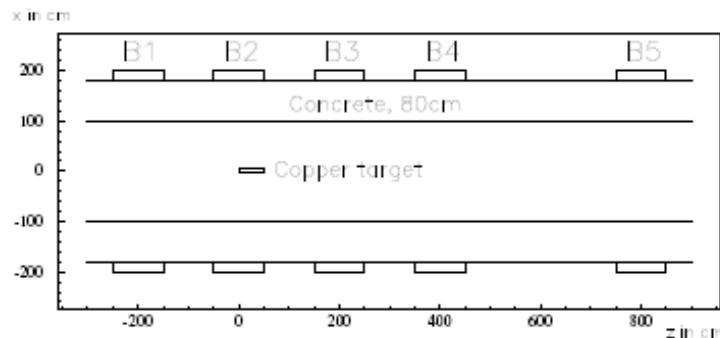
The values are given for two different lower cut-offs in energy of 19.6 MeV and 100 MeV, respectively

Location	FLUKA/PHITS		FLUKA/MARS	
	E > 19.6 MeV	E > 100 MeV	E > 19.6 MeV	E > 100 MeV
A1	1.21	1.29	0.96	1.14
A2	1.06	1.11	0.89	1.06
A3	1.05	0.98	1.17	1.23
B4	1.07	1.02	1.37	1.49
B5	1.00	0.94	1.43	1.53
B1	1.18	1.24	0.93	1.16
B2	1.09	1.19	0.97	1.23
B3	0.93	0.90	1.14	1.25
I1	1.33	1.46	1.07	1.33
I2	1.03	1.29	0.89	1.14
I3	1.07	1.14	1.33	1.52
I2'	1.21	1.42	1.03	1.32

### Additional calculations with a cylindrical geometry

The differences between the results obtained with MARS and FLUKA were subject to additional calculations. For this purpose the problem was simplified by a cylindrical geometry consisting of the copper target surrounded by an 80 cm thick concrete shield. The inner surface of the shield was defined at a radius of 1 m which corresponds roughly to the distance between the beam axis and lateral shield wall at the CERF facility. A schematic view of the FLUKA geometry is shown in Figure 5.

**Figure 5: Schematic view of the simplified, cylindrical geometry. The beam is hitting the copper target from the left side.**



Using this set-up, cascades induced by a 120 GeV/c beam of either protons or positively charged pions were simulated and neutron energy spectra scored at five different detector locations, labelled in the following with B1-B5, the index decreasing with angle. These positions were chosen to correspond approximately to the detector locations A1-A3, B4 and B5 in the CERF set-up. According to the cylindrical symmetry, the detector volumes were defined as concentric rings of 1 m length and 20 cm thickness. Apart from the geometry, all parameters of the simulations were kept identical to those for the CERF set-up. In addition, simulations were performed in which the concrete shield was replaced by vacuum. This modification allowed the calculation of the energy spectra as emitted from the copper target.

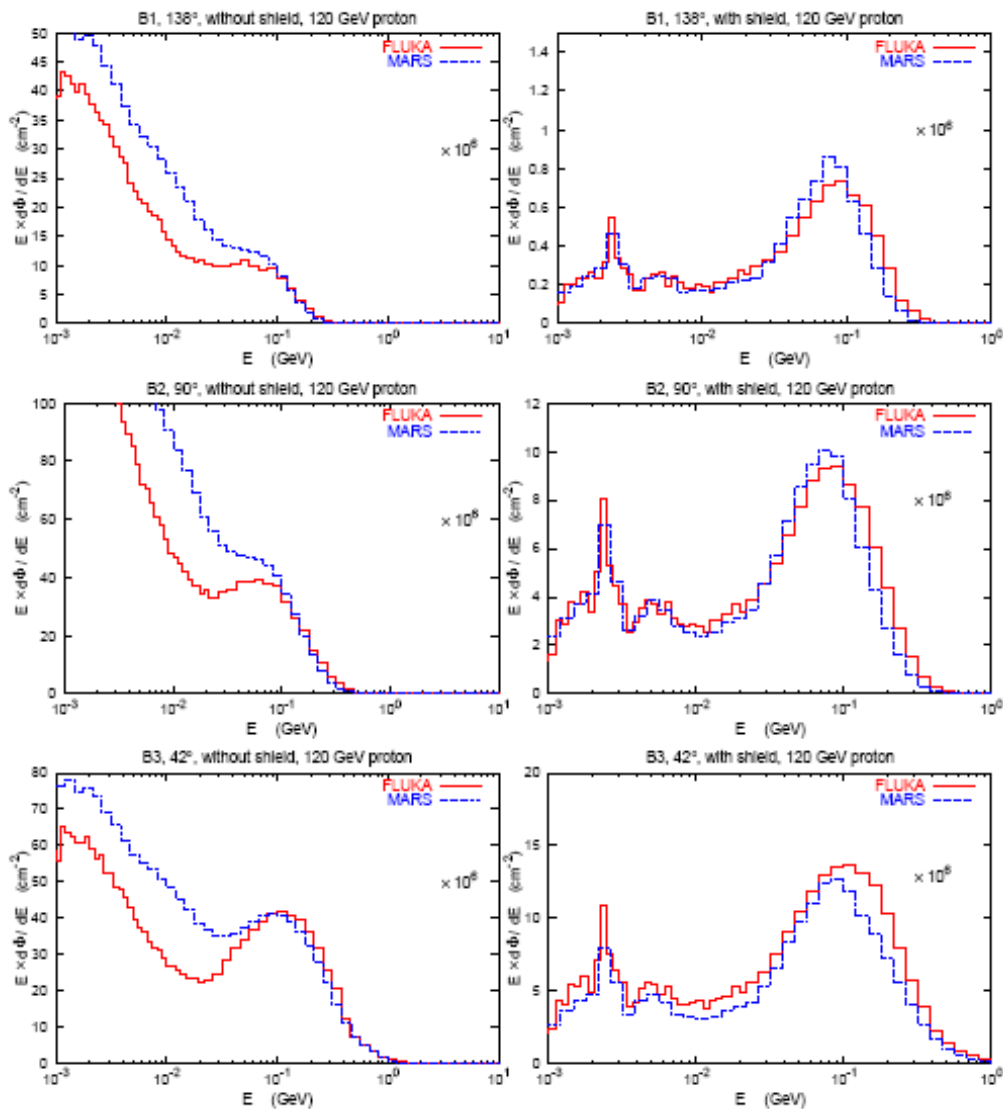
Results for the cylindrical geometry and proton beam are presented in Figures 6 and 7. As already mentioned, separate calculations were also performed for pion beam but found to lead to equivalent conclusions. The figures show, next to each other, the neutron energy spectra as emitted from the copper target (left graphs) and the spectra after attenuation through the concrete shield (right graphs).

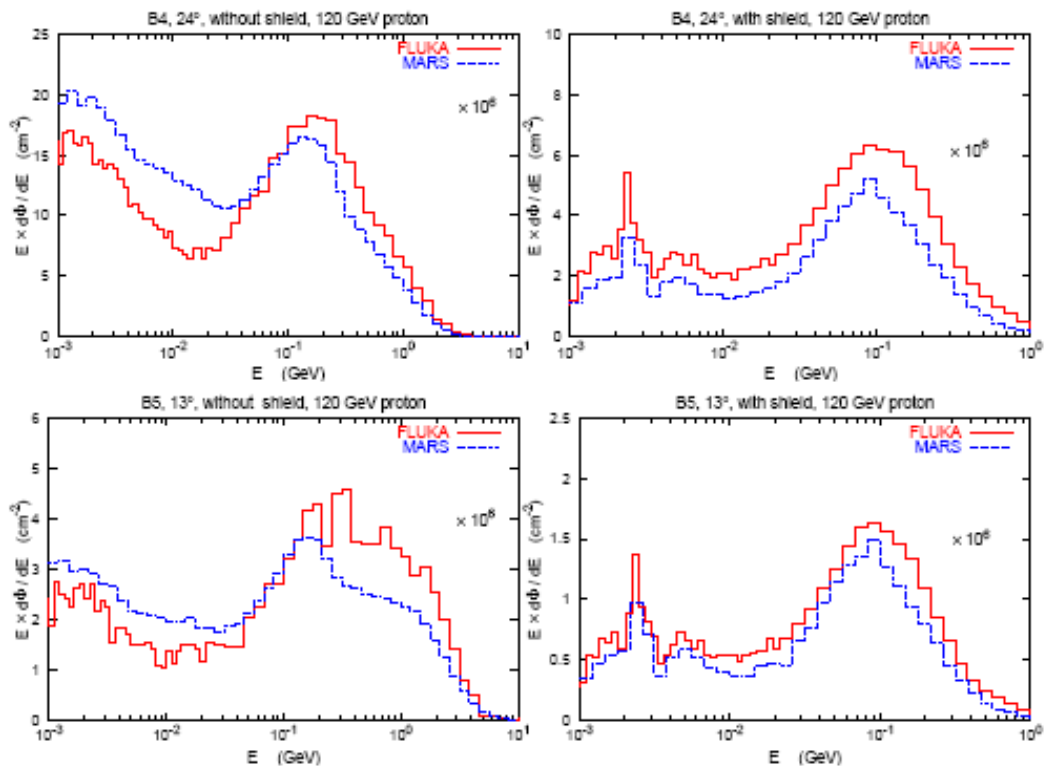
As before, spectra are normalised per one beam particle and scaled with a factor of 106 for a more convenient representation. In addition, Table 5 gives ratios of integrated fluence spectra as obtained with FLUKA and MARS for three different lower energy cut-offs of 1 MeV, 19.6 MeV and 100 MeV, respectively. Here, values are also given for pion beam.

Regarding the source spectra the following observations can be made: Below an energy of about 50 MeV the fluence predicted by MARS is higher by almost a factor of two than the one obtained with FLUKA. This is also reflected by the ratios of integrated fluence, especially those for the lowest energy cut-off of 1 MeV, although partially compensated by the opposite behaviour at high energies. Here, the situation reverses; MARS predicts the spectra to drop faster with energy (and thus the fluence to be lower) than FLUKA. This observation holds for all energies which would be visible on a logarithmic fluence scale (not shown here). It is most pronounced in forward direction (B5) where FLUKA-spectra are up to a factor of 1.4 higher than those calculated with MARS. Both features cause the peak in the spectra at about 100 MeV to be less pronounced in the MARS than in the FLUKA results.

**Figure 6: Neutron energy spectra at scoring positions B1-B3 in the cylindrical geometry**

Results of MARS and FLUKA are compared to each other. The left panels show the spectra emitted from the copper target, *i.e.* without shield, the right panels the spectra behind the shielding at the corresponding positions. Note the different energy scales used for both types of graphs.



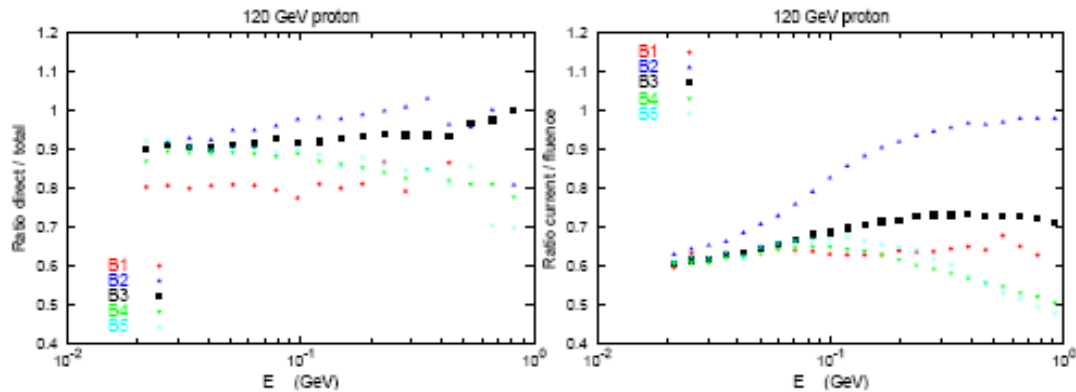
**Figure 7: As in Figure 6, here for the most forward scoring positions B4 and B5**

**Table 5: Ratios of integrated neutron fluence spectra obtained with FLUKA and MARS for scoring locations B1-B5 in the simplified geometry**

The values are given for three different lower cut-offs in energy of 1 MeV, 19.6 MeV and 100 MeV, respectively, as well as for the scenario without and with shield and both types of beam particles.

	Without shield		With shield	
	Proton	Pion+	Proton	Pion+
<b>E &gt; 1 MeV</b>				
<b>B1</b>	0.73	0.71	1.02	0.98
<b>B2</b>	0.74	0.72	1.06	1.04
<b>B3</b>	0.80	0.79	1.21	1.23
<b>B4</b>	0.91	0.90	1.46	1.53
<b>B5</b>	1.04	1.03	1.26	1.40
<b>E &gt; 19.6 MeV</b>				
<b>B1</b>	0.80	0.77	1.02	0.97
<b>B2</b>	0.82	0.80	1.06	1.04
<b>B3</b>	0.95	0.95	1.20	1.22
<b>B4</b>	1.10	1.09	1.45	1.52
<b>B5</b>	1.21	1.24	1.26	1.37
<b>E &gt; 100 MeV</b>				
<b>B1</b>	1.09	1.06	1.39	1.31
<b>B2</b>	1.06	1.05	1.34	1.33
<b>B3</b>	1.09	1.10	1.33	1.36
<b>B4</b>	1.25	1.26	1.59	1.67
<b>B5</b>	1.34	1.38	1.39	1.50

**Figure 8: Ratio of the energy spectra above 20 MeV including only those neutrons entering directly from the shield vs. all neutrons entering the detector regions (left panel) and ratio of current scoring vs. fluence scoring at the boundary between shielding and detector (right panel)**

Fluctuations in the data points reflect statistical uncertainties. However, corresponding error bars were omitted for clarity of the presentation.



Low-energy neutrons are attenuated by the shield such that differences in the predictions of the source spectra in this energy region are not visible behind the shield. On the other hand, the spectra behind the shield clearly reflect the differences between the source spectra at higher energies. FLUKA predicts increasingly higher fluences than MARS as the angle with the beam axis decreases (see detector positions B3-B5). This ratio of the fluences above 100 MeV reaches a maximum of about 1.6 for detector location B4. It can thus be concluded that results behind the shield, as also obtained for the CERF set-up, depend significantly on the quality and features of the particle production in the target material (here copper). Benchmark measurements of high-energy neutron spectra behind shielding can only provide a combined verification of particle production in the target material and their attenuation through the shielding. Considerable differences exist, especially at lower energies, between MARS and FLUKA predictions for the source spectra and these should be addressed by future measurements.

Finally, in order to address the importance of variations in the angular response of the NE213 detector, the cylindrical geometry was used to investigate with FLUKA the directions of incidence of the neutrons on the detector regions. For this reason all regions outside of the shield but in between the five detectors were assigned the FLUKA pseudo-material “black hole” causing any particle to be deleted as soon it enters the respective areas. Thus, only neutrons entering the detector volumes directly from the shield are scored. The ratio of the energy spectra obtained with this slightly modified setting and the original material setting provides an estimate for the contribution from particles entering the detectors laterally. Results for the five detectors are shown in the left graph of Figure 8. As expected, this ratio is close to unity for detector B2, located at approximately  $90^\circ$  to the target and decreases with angle and with increasing energy. It indicates, for example for the most forward detector B5, that high energy particles reach the detector with a direction corresponding approximately to the direct path between target and detector. Any bias introduced by a different irradiation geometry during the NE213 response measurements (see discussion above) can therefore be expected to be more significant the higher the energy of the neutron is.

Neutrons entering the detector directly from the shield exhibit also a certain angular distribution which might affect the response characteristics. The right graph in Figure 8 compares current scoring with fluence scoring at boundaries between shield and detectors. While fluence scoring weights the neutron with the inverse cosine of the angle between the neutron direction and the normal of the surface, current scoring does not consider the angle of incidence. For energies below about 50 MeV the ratio between current and fluence is comparable for all detector positions indicating similar angular distributions of neutrons at the boundary which are most likely isotropic due to neutron scattering in the shield. As the energy increases the ratio approaches unity for the detector B2 located at  $90^\circ$  angle demonstrating that high-energy neutrons enter this detector predominantly perpendicular to its front face. Any angular dependence of the detector response matrix should be of minor importance at this location. For the other detectors ratios reach asymptotic values related to the angle of the detector position with regard to the beam direction.

## Summary and conclusions

High-energy neutron spectra measured with a NE213 organic liquid scintillator in the stray radiation field outside of the shielding of the CERF facility were compared to results of detailed simulations with the FLUKA, MARS and PHITS codes. The benchmark comprised concrete shielding of 80 cm and 160 cm thicknesses as well as iron shielding of 40 cm thickness and different measurement positions along the shield.

Results obtained with the different codes in the energy range (32-380 MeV) of the experimental data show agreement within about 20% for backward and 90 degree angles. The measurements for the concrete shield confirm the calculated spectra, often within the experimental uncertainties. A systematic deviation between data and model predictions is not observed. Final conclusions can only be drawn after a detailed simulation of the measurement conditions, including the charged particle rejection in the Veto counters, and an event-by-event analysis of data. The experimental results for the iron shield carry further uncertainties due to a significant background at the measurement positions. Differences between code results and data at high energy are more pronounced for the iron than the concrete shield.

Furthermore, predictions of MARS and FLUKA for high-energy neutron spectra were studied in more detail with a simplified, cylindrical geometry. The simulations revealed differences by up to a factor of two between the neutron fluences emitted from the target, with MARS predicting a higher fluence below about 50 MeV and a lower fluence at higher energies than FLUKA. Spectra behind the shield reflect the latter and confirm the results for the CERF set-up. This study clearly shows the need for experimental verification of the particle spectra around the loss point and a more detailed simulation of the set-up of the present experiment. In addition, the simulations based on the cylindrical geometry showed that possible variations in the angular response of the NE213 detector cannot account for differences observed between measured and calculated spectra at high energy.

## Acknowledgements

The authors are grateful to Alberto Fassò, Alfredo Ferrari and Nikolai Mokhov for many stimulating discussions. This work was supported by the Department of Energy under contract DE-AC02-76SF00515.

## References

- [1] A. Mitaroff, M. Silari, "The CERN-EU High-energy Reference Field (CERF) Facility for Dosimetry at Commercial Flight Altitudes and in Space", *Radiation Protection Dosimetry*, 102, pp. 7-22 (2002).
- [2] N. Nakao, et al., "Measurement of Neutron Energy Spectra Behind Shielding of a 120 GeV/c Hadron Beam Facility, CERF", these proceedings.
- [3] A. Ferrari, P.R. Sala, A. Fassò, J. Ranft, *FLUKA, A Multi-particle Transport Code (Program Version 2005)*, CERN-2005-010 (2005).
- [4] A. Fassò, et al., "The Physics Models of FLUKA: Status and Recent Developments", *Proceedings of the International Conference on Computing in High Energy and Nuclear Physics (CHEP2003)*, La Jolla, CA, USA, 24-28 March 2003 (paper MOMT005), eConf C0303241 (2003), arXiv:hep-ph/0306267.
- [5] N.V. Mokhov, *The MARS Code System User's Guide*, Fermilab-FN-628 (1995).
- [6] N.V. Mokhov, K.K. Gudima, C.C. James, et al., *Recent Enhancements to the MARS15 Code*, Fermilab-Conf-04/053 (2004), [www-ap.fnl.gov/MARS/](http://www-ap.fnl.gov/MARS/).

- [7] H. Iwase, K. Niita, T. Nakamura, "Development of General-Purpose Particle and Heavy Ion Transport Monte Carlo Code", *Journal of Nuclear Science and Technology*, 39, pp. 1142-1151 (2002).
- [8] N. Nakao, *et al.*, "Measurement of Neutron Energy Spectra Behind Shielding of a 120 GeV/c Hadron Beam Facility, CERF", *Proceedings of the International Conference on Accelerator Applications (AccApp05)*, Venice, Italy, 28 August-1 September 2005.
- [9] H. Vincke, *et al.*, *Accurate PIC Calibration by the Use of a Coincidence of Two Scintillators*, CERN Technical Note, CERN-SC-2004-090-RP-TN (2004).



## Inter-comparison of medium-energy neutron attenuation in iron and concrete (6)

**Hideo Hirayama**

KEK, High Energy Accelerator Research Organisation, Japan

**Attenuation Length Sub-working Group of Japan**

### **Abstract**

*From results presented at SATIF7, revised problems to be calculated were prepared by the Japanese Working Group and sent to the participants of this action. Slab thickness of concrete was extended to 12 m from 6 m to obtain the attenuation length for equilibrium spectrum. The source neutrons were the same as those at SATIF7.*

*This paper presents a comparison of the neutron attenuation length of iron and concrete sent from eight groups to the organiser by the end of April, including results presented at previous SATIF meetings and future themes resulting from this inter-comparison.*

## Introduction

Neutron attenuation at a high energy above a few GeVs is not supposed to depend on the energy. Its energy dependence below this energy, especially below 1 GeV, is not been well understood. It is desired to obtain common agreements concerning the behavior of neutrons inside various materials. This is necessary in order to agree on definitions of the attenuation length, which is very important for shielding calculations involving high-energy accelerators. As one attempt, it was proposed by Japanese participants of SATIF2 to compare the attenuation of medium-energy neutrons inside iron and concrete shields between various computer codes and data, and was cited as a suitable SATIF action. From the results for neutrons below 400 MeV presented at SATIF3 [1], it has become clear that neutrons above 20 MeV are important for understanding that the attenuation length and the geometry, planar or spherical, do not affect the results very much. The attenuation length of neutrons above 20 MeV was compared with the planer geometry included for secondary neutrons produced by medium-energy protons at SATIF4 [2]. Though the attenuation lengths were different, all of the results showed the same tendency for an attenuation length to increase along with an increase in the neutron energy up to 10 GeV [2-4]. In the case of iron, the attenuation length seemed to reach an almost constant value above 10 GeV [5]. On the other hand, the attenuation length of concrete showed a tendency to increase with an increase of neutron energy up to 100 GeV. The neutron spectrum in the 300-500 cm region in concrete is supposed not to reach equilibrium for high energy neutrons above GeV [5].

Considering these results, revised problems to be calculated were prepared by the Japanese Working Group and sent to the participants of this action. The length of the concrete slab was extended to 12 m from 6 m. Source neutrons were the same as those used at SATIF-6.

The results from eight groups were sent to the organiser by the end of April. This paper presents a comparison of the neutron attenuation lengths of iron and concrete, including the results presented at previous meetings and the future themes resulting from this inter-comparison.

## Problems for an inter-comparison (6)

Considering the results presented at SATIF7 [5], the following revised problems were proposed to be calculated by various codes with their own databases.

### Attenuation calculation

#### Source neutron energy

- a) Source neutrons are uniformly distributed within the following energy regions:
 

(1) 40- 50 MeV	(2) 90-100 MeV	(3) 180-200 MeV	(4) 375-400 MeV
(5) 1 GeV	(6) 1.5 GeV	(7) 3 GeV	(8) 5 GeV
(9) 10 GeV	(10) 50 GeV	(11) 100 GeV	
- b) Secondary neutrons to 90 degrees from Fe target (5 cm diameter) (Figure 1):
 

(1) 200 MeV (5cm thick)	(2) 500 MeV (25 cm thick)
(3) 1 GeV (60cm thick)	(4) 3 GeV (60 cm thick)
(5) 5 GeV (60cm thick)	
- c) Secondary neutrons in various directions from a Hg target with a Pb moderator (120 cm diameter and 120 cm length) shown in Figure 2 with 3 GeV protons.
- d) Secondary neutrons toward 90 degrees from a Hg target shown with 24 GeV protons (Figure 2).

### Geometry

Plane 6 m thick for iron and 12 m thick for concrete with normal-incident parallel beams.

### Shielding material

Iron and concrete were selected as typical shielding materials. The densities of the two materials and the composition of concrete are also given (Table 1).

- iron (density  $7.87 \text{ g cm}^{-3}$ );
- concrete (density  $2.27 \text{ g cm}^{-3}$ ) [Type 02-a, ANL-5800, 660(1963)].

**Figure 1: Secondary neutron at  $90^\circ$  from an iron target bombarded by protons (FLUKA calculations)**

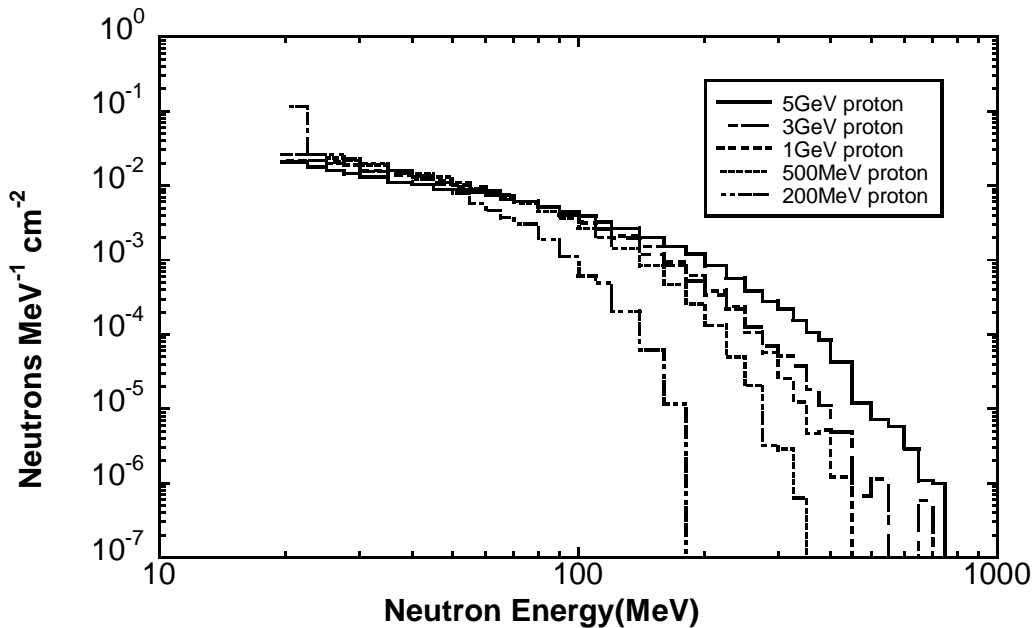
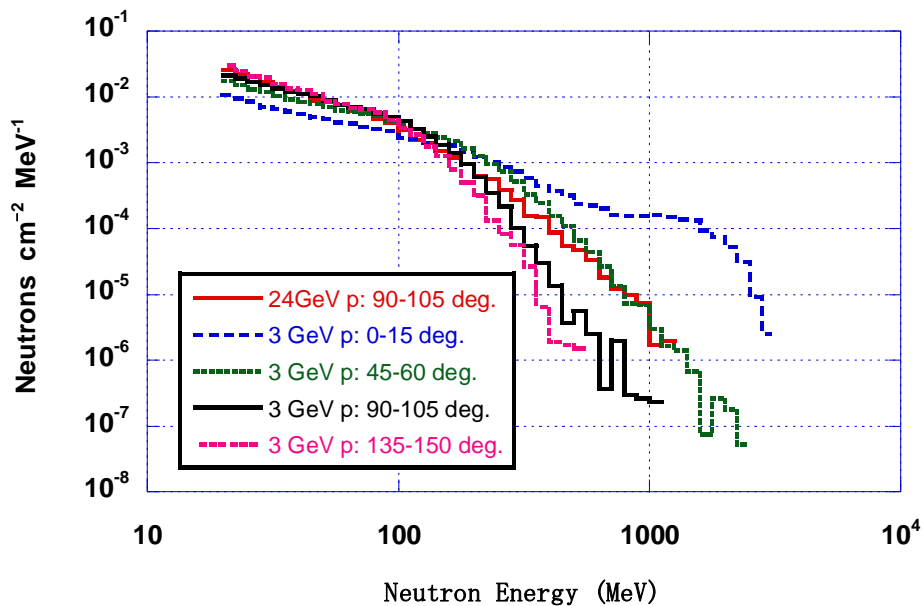


**Figure 2: Secondary neutron spectrum from a Hg target bombarded by 3 GeV protons (by MCNPX) and 24 GeV protons (by NMTC/JAM)**



*Energy group and fluence to the dose-equivalent conversion factor*

The energy group in Table 2 is presented as the standard one; it is required that the neutron spectra be presented in this energy group, if possible.

In dose calculations, it is recommended to use the neutron flux-to-dose equivalent conversion factor (Table 3), so as to avoid any ambiguity due to the conversion factor used. The values given in Table 3 are conversion factors to the neutron energy corresponding to that given in Table 2.

**Table 1: Composition of concrete**

Element	Atomic number density ( $10^{24}/\text{cm}^3$ )	Weight per cent	Element	Atomic number density ( $10^{24}/\text{cm}^3$ )	Weight per cent
H	1.3851E-2	1.02	Si	1.6621E-2	34.21
C	1.1542E-4	1.00	K	4.6205E-4	1.32
O	4.5921E-2	53.85	Ca	1.5025E-3	4.41
Mg	1.2388E-4	0.22	Fe	3.4510E-4	1.41
Al	1.7409E-3	3.44			

**Table 2: Upper energy of 66 neutron energy groups (MeV)**

1.00E+5	9.00E+4	8.00E+4	7.00E+4	6.00E+4	5.00E+4	4.00E+4	3.00E+4	2.00E+4
1.80E+4	1.60E+4	1.40E+4	1.20E+4	1.00E+4	9.00E+3	8.00E+3	7.00E+3	6.00E+3
5.00E+3	4.50E+3	4.00E+3	3.50E+3	3.00E+3	2.50E+3	2.00E+3	1.90E+3	1.80E+3
1.70E+3	1.60E+3	1.50E+3	1.40E+3	1.30E+3	1.20E+3	1.10E+3	1.00E+3	9.00E+2
8.00E+2	7.00E+2	6.00E+2	5.00E+2	4.00E+2	3.75E+2	3.50E+2	3.25E+2	3.00E+2
2.75E+2	2.50E+2	2.25E+2	2.00E+2	1.80E+2	1.60E+2	1.40E+2	1.20E+2	1.10E+2
1.00E+2	9.00E+1	8.00E+1	7.00E+1	6.50E+1	6.00E+1	5.50E+1	5.00E+1	4.50E+1
4.00E+1	3.50E+1	3.00E+1	2.75E+1	2.50E+1	2.25E+1	2.00E+1		

**Table 3: Neutron flux-to-dose conversion factor [(Sv/hr)/(n/sec/cm<sup>2</sup>)]**

ICRP51 (1987) [6], Maximum Dose Equivalent Table 23

1.98E-5	1.96E-5	1.93E-5	1.93E-5	1.90E-5	1.85E-5	1.78E-5	1.58E-5	1.40E-5
1.35E-5	1.30E-5	1.24E-5	1.17E-5	1.09E-5	1.05E-5	1.00E-5	9.55E-6	9.01E-6
8.42E-6	8.11E-6	7.77E-6	7.41E-6	7.02E-6	6.72E-6	6.32E-6	6.22E-6	6.11E-6
5.98E-6	5.84E-6	5.69E-6	5.52E-6	5.34E-6	5.14E-6	4.94E-6	4.72E-6	4.47E-6
4.18E-6	3.78E-6	3.26E-6	2.72E-6	2.25E-6	2.20E-6	2.15E-6	2.10E-6	2.05E-6
1.99E-6	1.93E-6	1.86E-6	1.82E-6	1.79E-6	1.77E-6	1.74E-6	1.72E-6	1.70E-6
1.68E-6	1.67E-6	1.65E-6	1.64E-6	1.63E-6	1.62E-6	1.61E-6	1.60E-6	1.59E-6
1.58E-6	1.57E-6	1.56E-6	1.55E-6	1.54E-6	1.53E-6	1.52E-6		

*Quantities to be calculated*

The following quantities must be calculated for inter-comparisons:

- A. Dose equivalent due to neutrons above 20MeV at 50, 100, 150, 200, 250, 300, 350, 400, 450 and 500 cm for iron and at 100, 200, 300, 400, 500, 600, 700, 800, 900, 1 000 and 1 100 cm for concrete.
- B. Neutron spectrum in  $\text{n cm}^{-2}\text{MeV}^{-1}$  per source neutron at 100, 200, 300, 400 and 500 cm for iron and at 100, 200, 300, 400, 500, 600, 700, 800, 900, 1 000 and 1 100 cm for concrete.

**Summary of contributors**

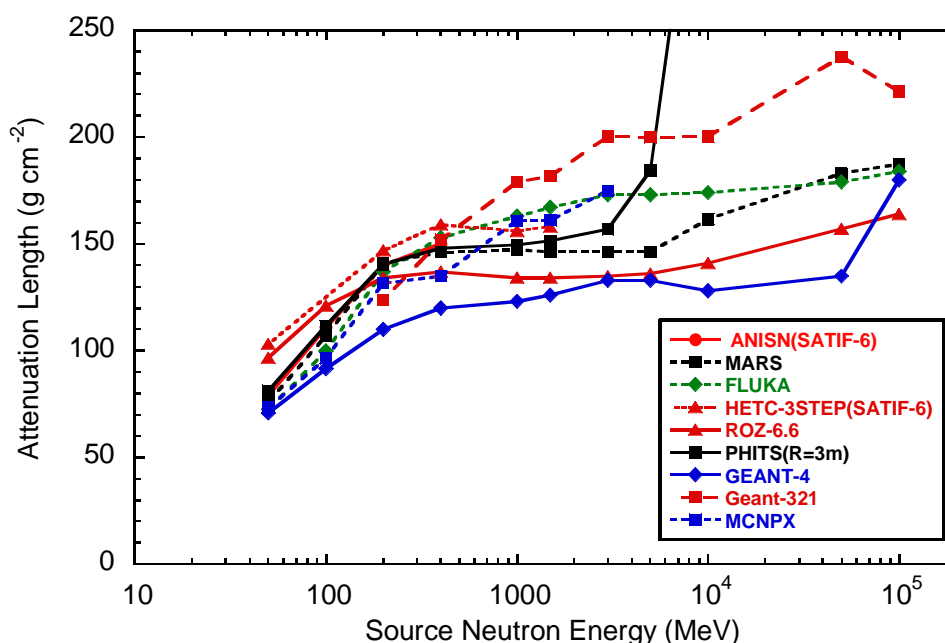
Eight groups sent their results to Hideo Hirayama at KEK before the end of April. Table 4 lists the participants, the names of the computer codes used and the names of databases used in the computer codes. Table 4 includes the most Monte Carlo hadron transport codes used for shielding calculations

and one discrete-ordinate transport codes, ROZ-6.6. This fact constitutes a very important progress for this inter-comparison to understand the attenuation tendency for the deep penetration problem and for comparisons of programs used for shielding calculations of high energy neutrons.

**Table 4: Summary of contributors**

Name of participants and organisation	Name of computer code	Name of database used in the computer code
N. Matsuda and H. Nakashima (JAEA)	PHITS [7]	Library data in PHITS
N. Nakao (KEK,SLAC)	MARS15 [8,9,10]	Library data in MARS15(04)
S. Roesler (CERN)	FLUKA [11,12]	Library data in FLUKA
Y. Uwamino (Riken)	HETC-3STEP [13]	Library data in HETC
T. Koi and D. Wright (SLAC)	Geant4 v8.0 [14,15]	Library data in Geant4 v8.0
B.Gaveau, G. Maurel, J. Maillard, J. Silva and J. Parisi (CNRS/IN2P3)	GEANT 321 [16]	Library data in GEANT 321
Y. Romanets, I.F. Gonçalves, and P. Vaz (ITN)	MCNPX [17]	Library data in MCNPX
Andrei M. Voloschenko (Keldysh Institute of Applied Mathematics)	ROZ-6.6 [18,19,20,21]	SADCO-2.4

**Figure 3: Comparison of the neutron attenuation length of iron**



## Results and discussions

### Attenuation length for mono-energy neutron

The attenuation length ( $\lambda$ ;  $\text{g cm}^{-2}$ ) for each case was obtained by a least-squares fitting at the region where the dose decreased exponentially. This region was from 3 to 6 m for iron and from 6 to 12 for concrete if results were presented in this region and if doses in this region were presented.

The neutron attenuation lengths of iron are shown in Figure 3 in which the results of ANISN and HETC-3STEP presented at SATIF-6 are also plotted. The attenuation lengths for iron are scattered within about  $50 \text{ g cm}^{-2}$  for the energy region above  $0.4 \text{ GeV}$  and have the tendency to reach an almost constant value except PHITS results above  $5 \text{ GeV}$  and GEANT-321 ones above  $1 \text{ GeV}$ . The difference of  $50 \text{ g cm}^{-2}$  for attenuation length means that there are large differences of dose deep inside iron. Dose distributions for  $1 \text{ GeV}$  neutrons in Figure 4 clearly show this fact. The difference becomes about three digits at  $4 \text{ m}$ . Figure 5 shows the neutron spectrum at  $4 \text{ m}$  to show the differences in spectrum.

The neutron attenuation lengths of concrete are shown in Figure 6 in which the results of ANISN presented at SATIF-6 are also plotted. In the case of concrete, the differences between the attenuation lengths between each code are relatively small at low-energy region and increase with the increase of neutron energy and have the tendency to reach an almost constant value for  $12 \text{ m}$  slab. The differences are about  $30 \text{ g cm}^{-2}$  at  $1 \text{ GeV}$  and about  $50 \text{ g cm}^{-2}$  at  $100 \text{ GeV}$ , respectively. Dose distributions for  $1 \text{ GeV}$  neutrons are shown in Figure 7 and the neutron spectra at  $4 \text{ m}$  are shown in Figure 8.

Figure 4: Dose distribution inside iron for 1 GeV neutrons

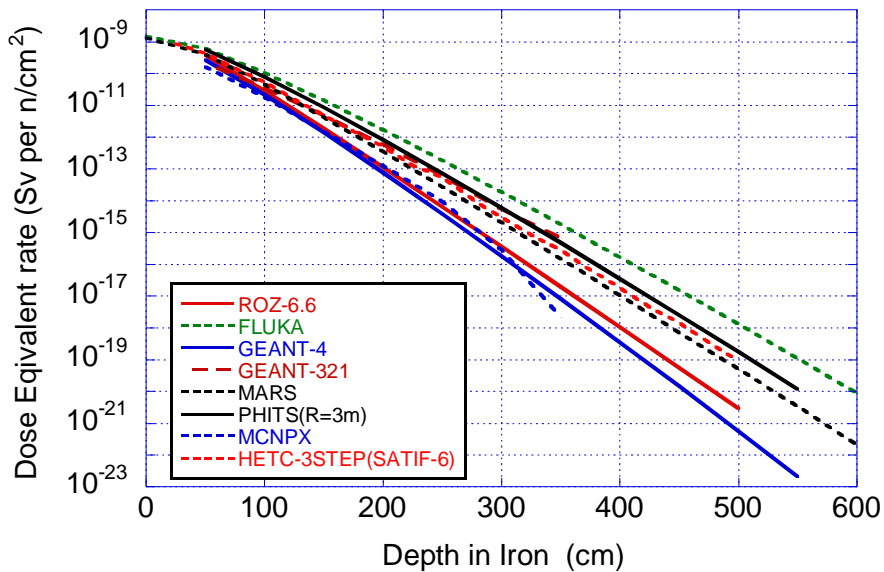


Figure 5: Neutron spectra at 4 m inside iron for 1 GeV neutrons

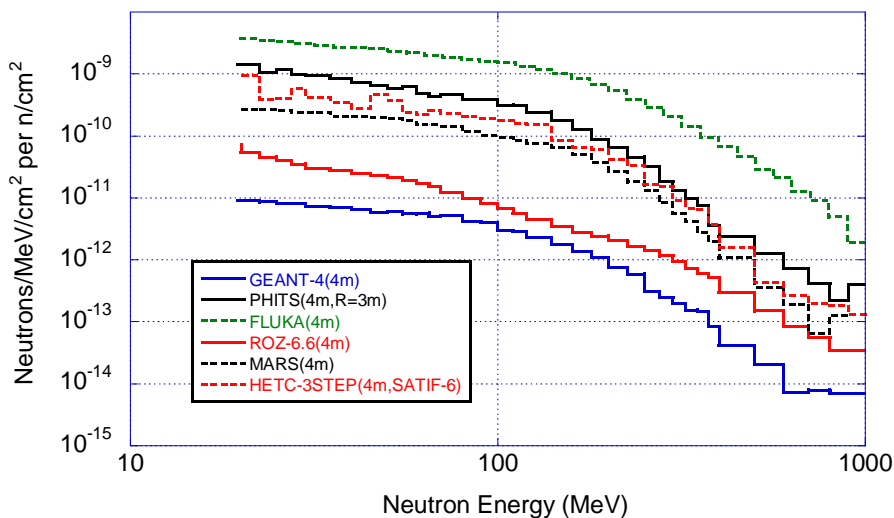


Figure 6: Comparison of the neutron attenuation length of concrete

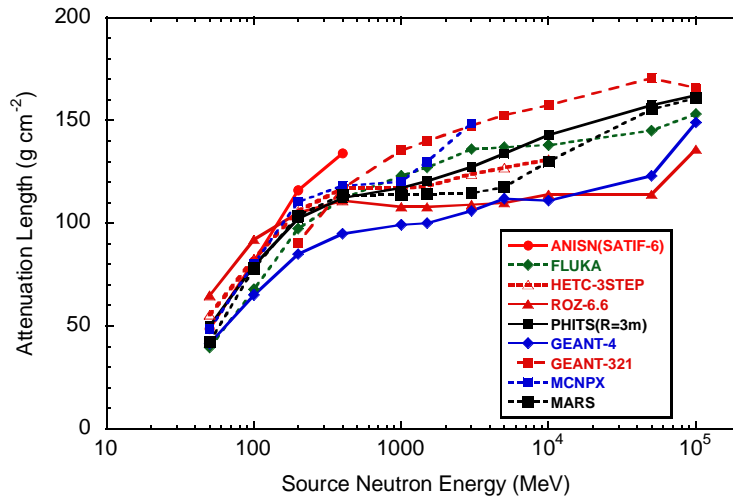


Figure7: Dose distribution inside concrete for 1 GeV neutrons

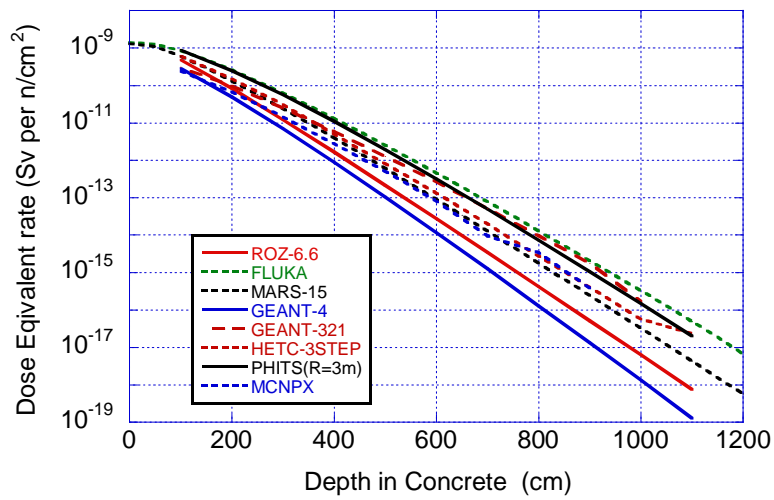
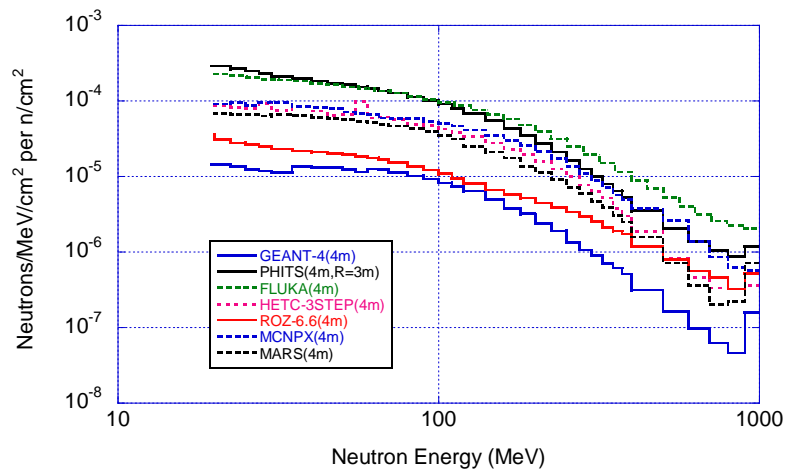


Figure 8: Neutron spectra at 4 m inside concrete for 1 GeV neutrons



**Attenuation length for secondary neutron**

The attenuation lengths of iron and concrete for secondary neutrons from a Hg target with 3 GeV protons are shown as a function of the emission angle in Figures 9 and 10, respectively, together with the experimental results at ISIS [7] and LANSCE [8] for 800 MeV protons. In the case of iron, all results show similar weak dependence on the emission angle but their values are largely scattered between each other. Dose distributions for 0-15 degrees and energy spectra at 4 m are shown in Figure 11 and Figure 12, respectively.

In the case of concrete, all results show stronger dependence on the emission angle than in the case of iron and a different dependence between the code used. Dose distributions for 0-15 degrees and energy spectra at 4 m are shown in Figure 13 and Figure 14, respectively.

**Figure 9: Comparison of the neutron attenuation length of iron for secondary neutrons from a Hg target with 3 GeV protons**

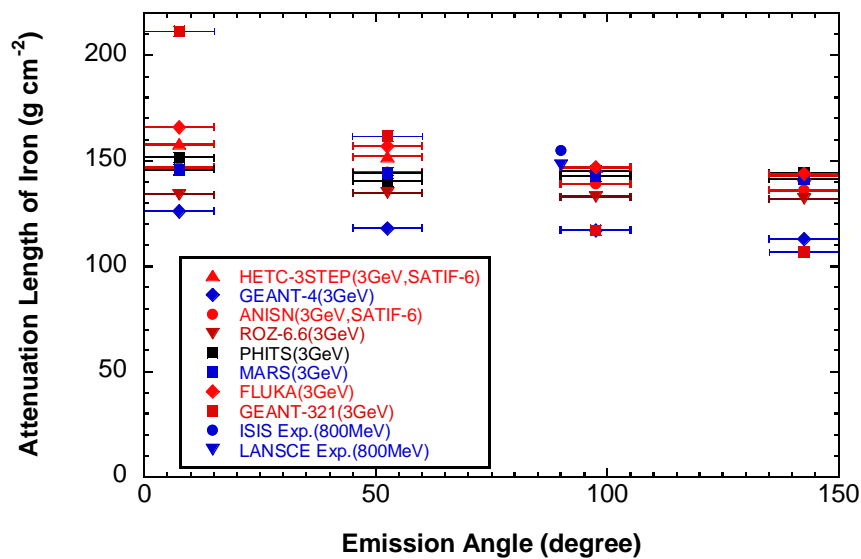


**Figure 10: Comparison of the neutron attenuation length of concrete for secondary neutrons from an Hg target with 3 GeV protons**

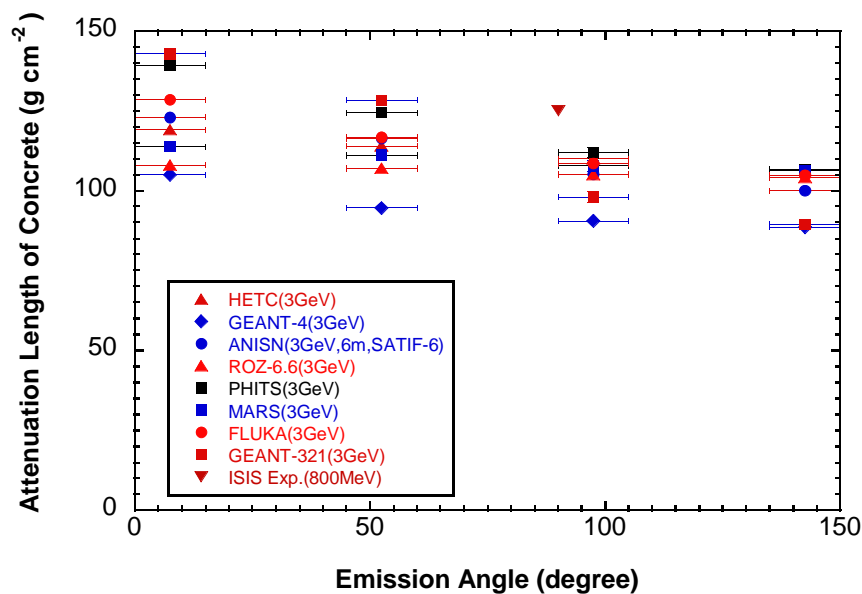


**Figure 11: Dose distribution inside iron from secondary neutrons emitted 0 to 15 degrees from a Hg target with 3 GeV protons**

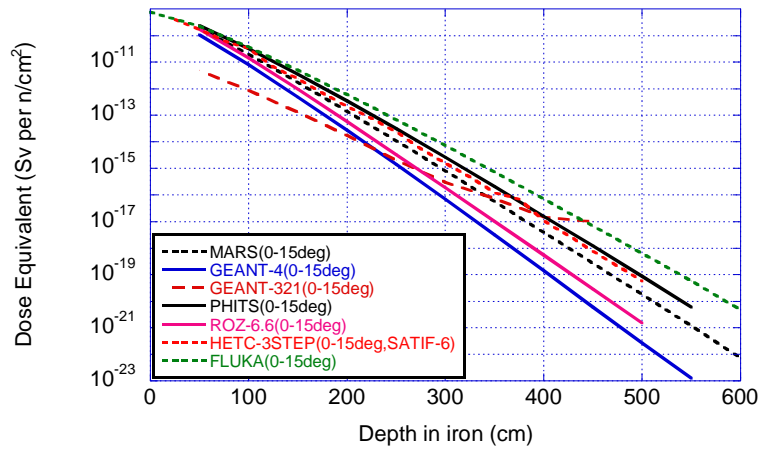


**Figure 12: Neutron spectra inside iron from secondary neutrons emitted 0 to 15 degrees from a Hg target with 3 GeV protons**

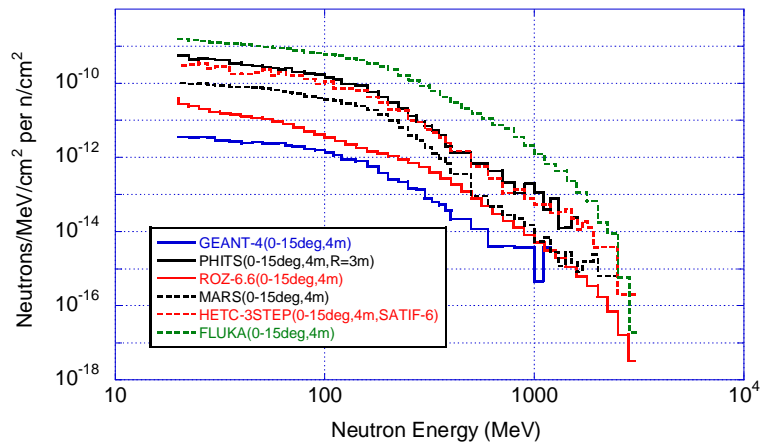


**Figure 13: Dose distribution inside concrete from secondary neutrons emitted 0 to 15 degrees from a Hg target with 3 GeV protons**

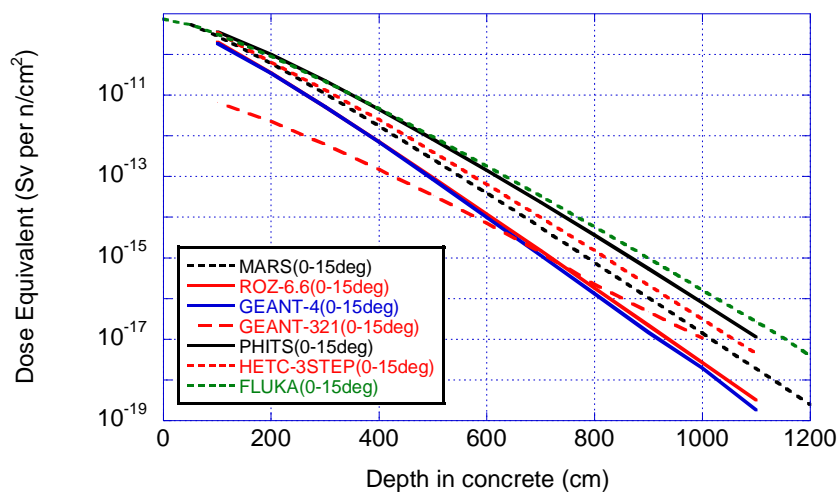
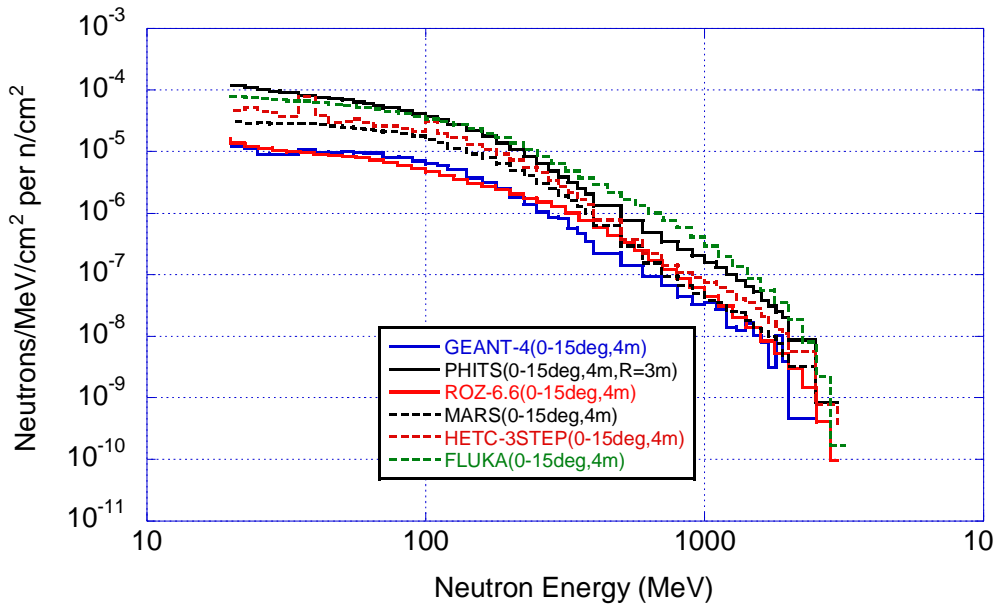


**Figure 14: Neutron spectra inside concrete from secondary neutrons emitted 0 to 15 degrees from a Hg target with 3 GeV protons**



The attenuation lengths of iron and concrete for secondary neutrons emitted 90 degrees from an iron target from high-energy protons and from a Hg target from 24 GeV protons are shown in Figures 15 and 16, respectively. In these figures, the experimental results at ISIS [22] and LANSCE [23] for 800 MeV protons are also plotted for comparison. All results show similar tendency to reach an almost constant value above 1 GeV protons. Dose distributions inside iron and concrete for secondary neutrons from 1 GeV protons are shown in Figure 15 and Figure 16, respectively. Energy spectra at 4m inside iron and concrete for secondary neutrons from 1 GeV neutrons are shown in Figure 17 and Figure 18, respectively.

**Figure 15: Comparison of the neutron attenuation length of iron for secondary neutrons emitted to 90 degrees from Fe and Hg (24 GeV) targets with protons**

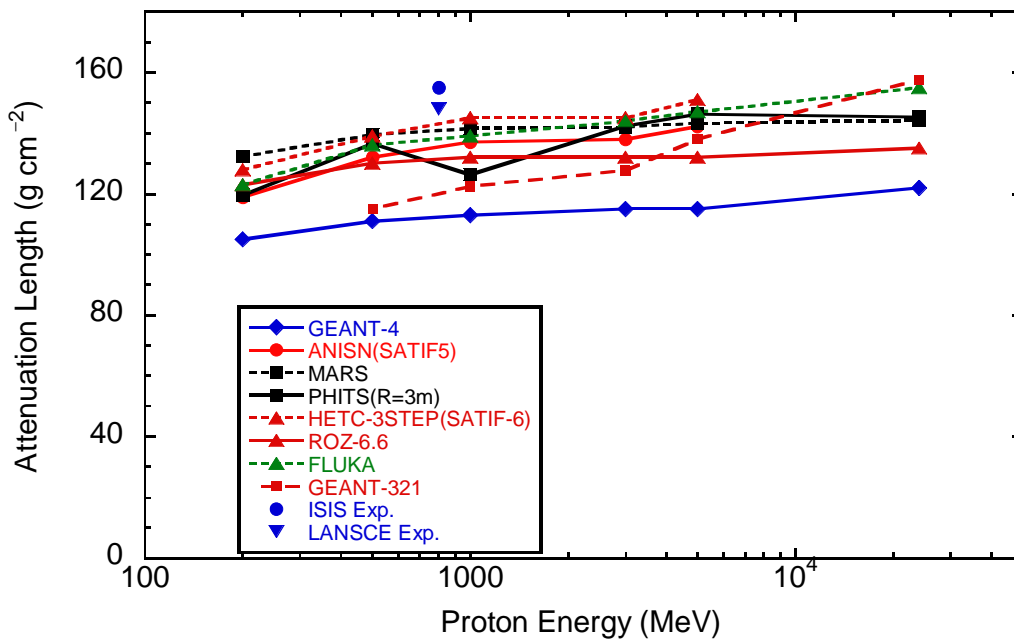


Figure 16: Comparison of the attenuation length of the concrete for secondary neutrons emitted to 90 degrees from Fe and Hg (24 GeV) targets with protons

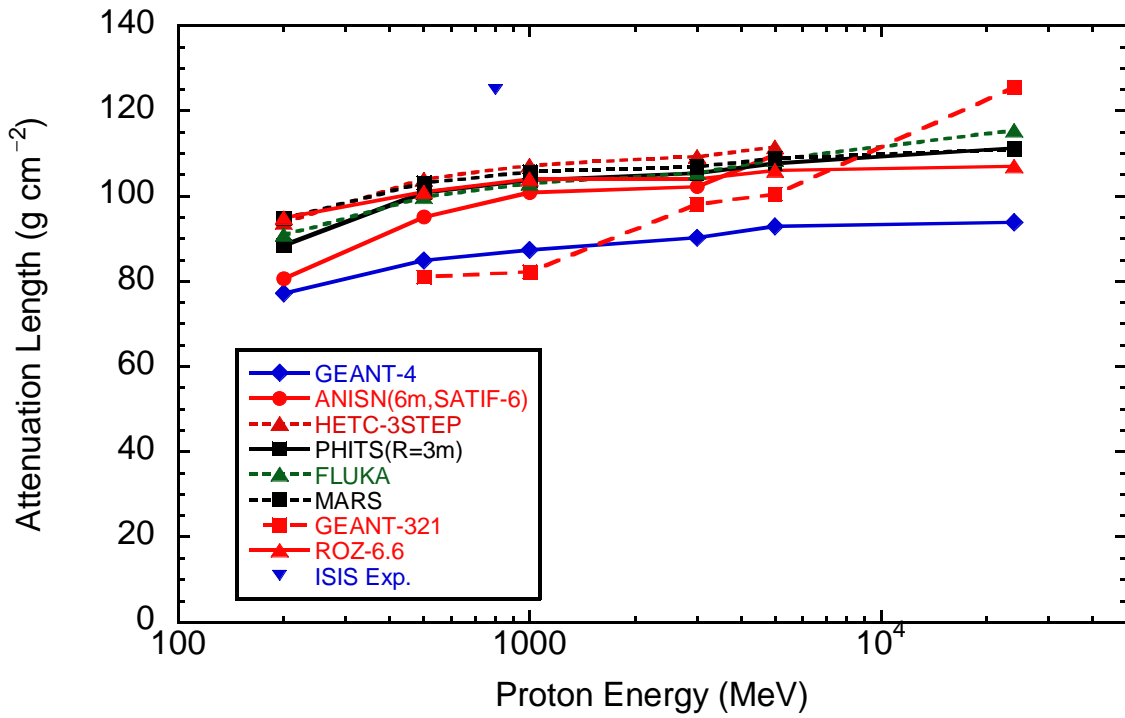
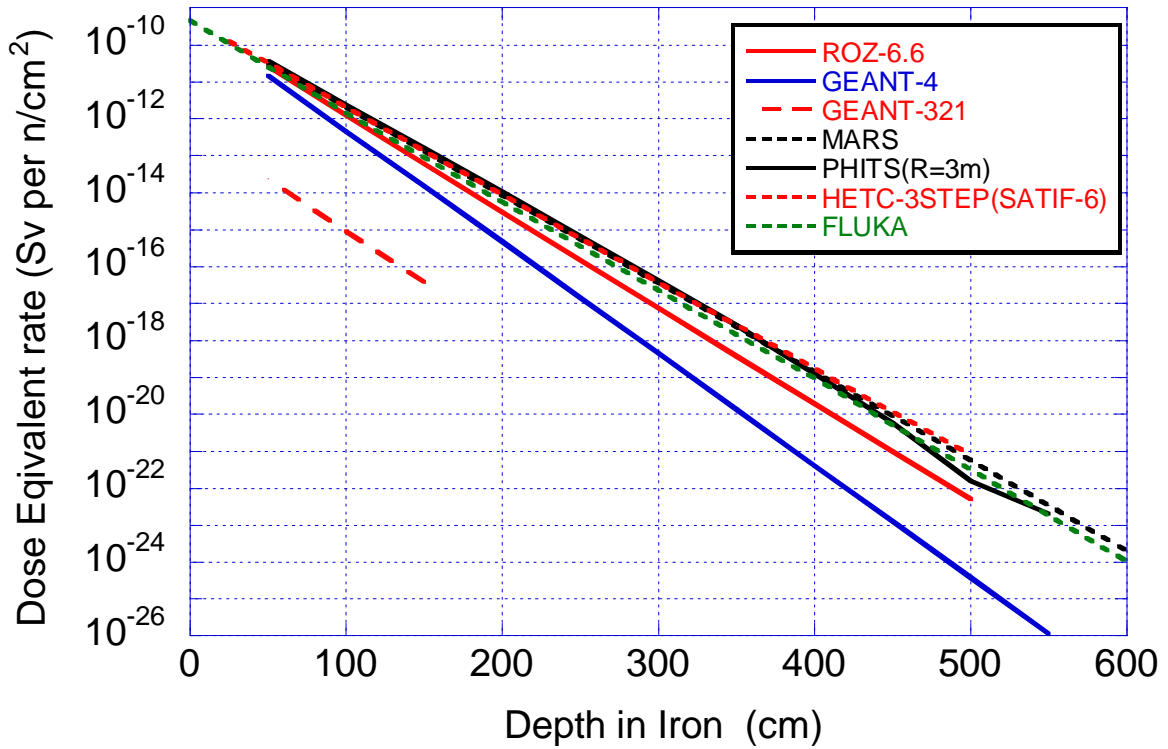
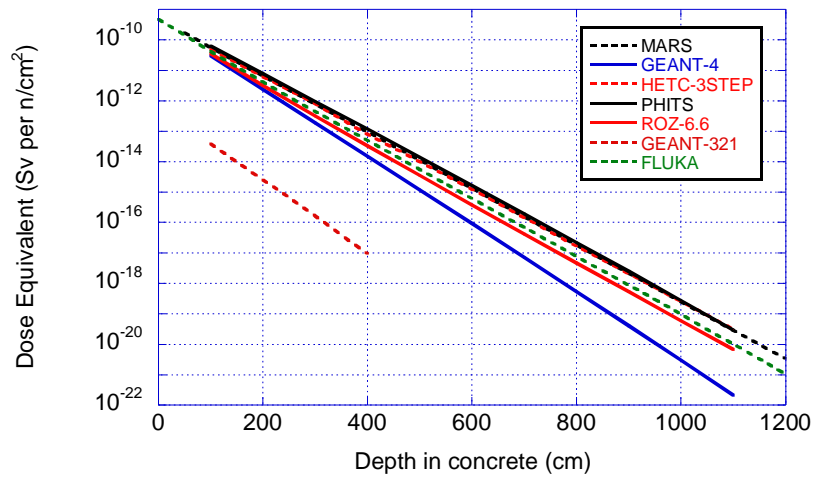


Figure 17: Dose distribution inside iron from secondary neutrons emitted to 90 degrees from an iron target with 1 GeV protons



**Figure 18: Dose distribution inside concrete from secondary neutrons emitted to 90 degrees from an iron target with 1 GeV protons**



**Figure 19: Neutron spectra inside iron for secondary neutrons emitted to 90 degrees from an iron target with 1 GeV protons**

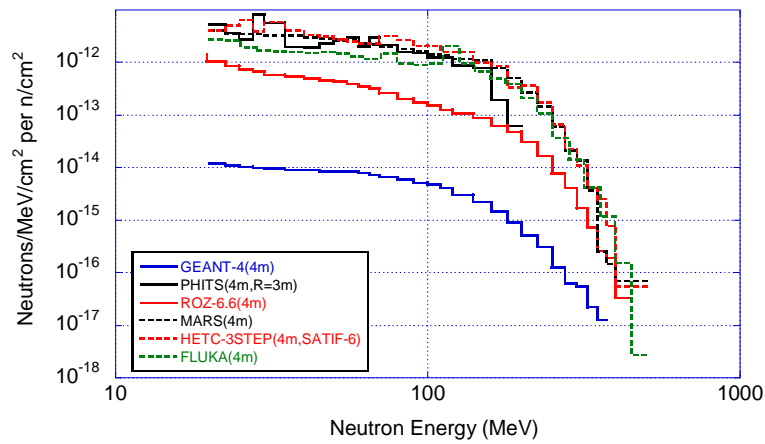
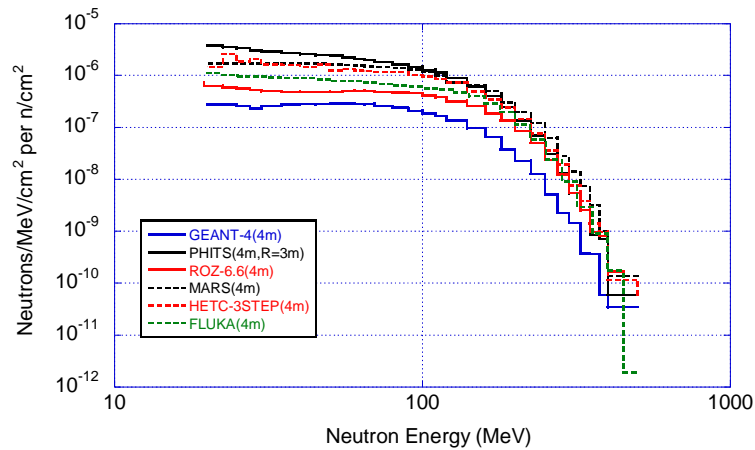


**Figure 20: Neutron spectra at 4 m inside concrete for secondary neutrons emitted to 90 degrees from an iron target with 1 GeV protons**



## Summary

From the comparisons given above, the following results are summarised:

- a) In general, the attenuation lengths calculated with various codes for mono-energy neutrons increases with the increase of neutron energy and this tendency becomes moderate above several GeV both for iron and concrete but the values of the attenuation length are largely different from each other.
- b) The difference of dose increases with an increase of depth both for iron and concrete.
- c) The attenuation lengths for secondary neutrons from a Hg target with 3 GeV protons show a slight dependence on the emission angle for the results of all codes but the values of the attenuation length are different from each other.
- d) The attenuation length for secondary neutrons emitted to 90 degrees from an iron or Hg target with high energy protons reach almost a constant value above 1 GeV.

## Future themes

It is necessary to discuss and perform the following activities as the next step:

- a) Study the reason for the large difference in the attenuation length between codes.
- b) Select suitable experiments to compare for understanding the attenuation length of secondary neutrons from high-energy protons. The results of AGS shielding experiments presented by H. Nakashima, *et al.* will be suitable for this purpose.
- c) Dose equivalents are largely different between codes for the simple problems used in this inter-comparison. Good benchmark experiments are desired to check models used in each code system.

## References

- [1] H. Hirayama, *et al.* "Inter-comparison of the Medium-energy Neutron Attenuation in Iron and Concrete", *Shielding Aspects of Accelerators, Targets and Irradiation Facilities (SATIF3)*, Tohoku University, Japan, 12-13 May 1997, OECD/NEA, Paris (1998), pp. 185-195.
- [2] H. Hirayama, *et al.* "Inter-comparison of the Medium-energy Neutron Attenuation in Iron and Concrete (2)", *Shielding Aspects of Accelerators, Targets and Irradiation Facilities (SATIF4)*, Knoxville, Tennessee, USA, 17-18 September 1998, OECD/NEA, Paris (1999), pp. 143-154.
- [3] H. Hirayama, *et al.*, "Inter-comparison of the Medium-energy Neutron Attenuation in Iron and Concrete (3)", *Shielding Aspects of Accelerators, Targets and Irradiation Facilities (SATIF5)*, Paris, France, 18-21 July 2000, OECD/NEA, Paris (2001), pp. 189-201.
- [4] H. Hirayama, *et al.*, "Inter-comparison of the Medium-energy Neutron Attenuation in Iron and Concrete (4)", *Shielding Aspects of Accelerators, Targets and Irradiation Facilities (SATIF6)*, SLAC, USA, 10-12 April 2002, OECD/NEA, Paris (2003), pp. 173-182.
- [5] H. Hirayama, *et al.*, "Inter-comparison of the Medium-energy Neutron Attenuation in Iron and Concrete (5)", *Shielding Aspects of Accelerators, Targets and Irradiation Facilities (SATIF7)*, Sacavém, Portugal, 17-18 May 2004, OECD/NEA, Paris (2005), pp. 117-126.
- [6] ICRP Publication 51, "Data for Use in Protection Against External Radiation", *Annals of the ICRP* 17 (2/3) (1987).

- [7] H. Iwase, K. Niita, T. Nakamura, "Development of General-purpose Particle and Heavy Ion Transport Monte Carlo Code", *J. Nucl. Sci. Technol.*, 39, 1142-1151 (2002).
- [8] N.V. Mokhov, *The MARS Code System User's Guide*, Fermilab-FN-628 (1995).
- [9] O.E. Krivosheev, N.V. Mokhov, "MARS Code Status", *Proc. Monte Carlo 2000*, Lisbon, Portugal, 23-26 October 2000, Fermilab-Conf-00/181, p. 943 (2000).
- [10] N.V. Mokhov, *Status of MARS Code*, Fermilab-Conf-03/053 (2003).
- [11] A. Ferrari, P.R. Sala, A. Fassò, J. Ranft, *FLUKA: A Multi-particle Transport Code (Program version 2005)*, CERN-2005-010, INFN TC\_05/11, SLAC-R-773 (2005).
- [12] A. Fassò, A. Ferrari, S. Roesler, P.R. Sala, G. Battistoni, F. Cerutti, E. Gadioli, M.V. Garzelli, F. Ballarini, A. Ottolenghi, A. Empl, J. Ranft, "The Physics Models of FLUKA: Status and Recent Developments", *Computing in High Energy and Nuclear Physics 2003 Conference (CHEP2003)*, La Jolla, CA, USA, 24-28 March 2003 (paper MOMT005), eConf C0303241 (2003).
- [13] N. Yoshizawa, et al., "Development of High Energy Transport Code HETC-3STEP Applicable to the Nuclear Reaction with Incident Energies Above 20 MeV", *J. Nucl. Sci. Technol.*, 32, 601 (1995).
- [14] J. Allison, et al., "Geant4 Developments and Applications", *IEEE Transactions in Nucl. Sci.*, 53 (2006), forthcoming.
- [15] S. Agostinelli, et al., "Geant4 – A Simulation Toolkit", *Nucl. Instr. and Meth.*, A 506, 250-303 (2003).
- [16] GEANT 3 – *Detector Description and Simulation Tool*, CERN program library long write-up W5013 (1993).
- [17] Pelowitz (Ed.), *MCNPX Version 2.5.0 User's Manual*, LA-CP-05-0369 (2005).
- [18] A.M. Voloschenko, A.A. Dubinin, ROZ-6.6: *One-dimensional Discrete Ordinates Neutron, Photon and Charged Particles Transport Code, User's Guide*, Report of Keldysh Inst. of Appl. Math., Russian Ac. of Sci., No. 7-25-2004.
- [19] M. Voloschenko, S.V. Gukov, V.P. Kryuchkov, A.A. Dubinin, O.V. Sumaneev, "The CNCSN: One, Two- and Three-dimensional Coupled Neutral and Charged Particle Discrete Ordinates Code Package", *Proc. of International Conference on Mathematics and Computation, Supercomputing, Reactor Physics and Nuclear and Biological Applications*, Avignon, France, 12-15 September 2005, CD-ROM.
- [20] V.P. Kryuchkov, J. Chang, Y.S. Cho, A.M. Voloschenko, O.V. Sumaneev, "An Experience in the Use the Method for 1D/2D/3D Spallation Target Neutronics and Shielding Calculations", *Proc. of International Conference on Mathematics and Computation, Supercomputing, Reactor Physics and Nuclear and Biological Applications*, Avignon, France, 12-15 September 2005, CD-ROM.
- [21] D.V. Gorbakov, V.P. Kryuchkov, "SADCO-2: A Modular Code System for Generating Coupled Nuclear Data Libraries to Provide High-energy Particle Transport Calculation by Multigroup Methods", *Nucl. Instr. and Meth. in Phys. Res.*, A372, 297 (1996).
- [22] T. Nunomiya, et al., "Measurement of Deep Penetration of Neutrons Produced by 800 MeV Proton Beam Through Concrete and Iron at ISIS", *Nucl. Instr. And Meth.*, B179, 89-102 (2001).
- [23] Bull, J.S., J.B. Donahue, R.L. Burman, "Measurement of Neutron Attenuation Through Thick Shields and Comparison with Calculation", *Proceedings of the 4<sup>th</sup> Workshop on Simulating Accelerator Radiation Environments (SARE4)*, Knoxville, Tennessee, 14-16 September 1998, pp. 201-208.

## Benchmarking of the modelling tools within the EURISOL DS project

**B. Rapp, J-C. David, V. Blideanu, D. Doré, D. Ridikas, N. Thiollière**  
CEA Saclay, Gif-sur-Yvette, France

### Abstract

*The European Community decided to support the design study and R&D for a next generation ISOL radioactive ion beam facility in Europe named EURISOL. The envisaged increase of beam intensities, by several orders of magnitude compared to actual facilities, means a drastic increase of the radioactive inventory and corresponding radioprotection related issues. Benchmark calculations with the MCNPX and FLUKA codes on neutron, charged particle and residual nuclei production within the pre-defined EURISOL parameters (e.g. incident particle-energy, targets, structure materials, etc.), have been done. The extensive comparison of different model predictions with data allowed us to recommend the best physics model parameters within the above particle transport codes. The importance of these benchmarks is illustrated by sensitivity simulations using realistic target geometries.*

## Introduction

The validation of the physics models implemented in the MCNPX [1] and FLUKA [2] codes, which will be the main Monte Carlo tools used for the EURISOL Design Study (DS) [3], is very important in order to ensure the reliability of the results obtained for the RIB production target optimisation, radioprotection and safety, and beam intensity calculations.

The neutron production by spallation reactions in different materials has to be well reproduced by simulation codes for both radioprotection purposes and the EURISOL primary target optimisation. It is also an important ingredient for the beam intensity calculations in the double stage production targets. Scattered primary protons and secondary proton production will contribute to the energy deposition and radiation level around the targets and accelerator structures. Equally, it is important to take into account with a good precision the production of other light charged particles as deuterons, tritons, and helium particles being the important contributors to the gas production and damage rates in the target window or other structure materials.

The results obtained from the simulation of double differential cross-sections of neutron and light charged particle production for various target materials as a function of incident proton energy are reported in this paper. Model calculations are compared with existing experimental data. The importance of these benchmarks is illustrated by sensitivity simulations using realistic target geometries.

## Benchmark calculations

The beam energy foreseen for the proton driver of EURISOL is about 1 GeV, consequently data around this energy have been selected for the benchmarks. Two major observables were examined, namely neutron and light charged particle production.

Both MCNPX [1] (Version 2.5.f) and FLUKA [2] (Version 2005.6) have been used for benchmark. The physics models used by FLUKA are fixed and cannot be changed by the user. In this case, a pre-equilibrium cascade model called PEANUT is coupled to an implementation of the RAL fission evaporation code, both with predefined input parameters [2].

The code MCNPX allows the user to choose between different intra-nuclear cascade and fission-evaporation model combinations among ISABEL, BERTINI and INCL4 for cascade and DRESNER (associated with RAL or ORNL fission models) and ABLA for de-excitation. The last possibility with MCNPX is to use the package CEM2k (cascade and de-excitation). For both ISABEL and BERTINI models, pre-equilibrium has been used. For microscopic cross-section predictions the code MCNPX has been used without the particle transport [1].

## Neutron double differential cross-sections (thin targets)

Among a large number of combinations of incident proton energy, material and angles we could study, we have chosen to make calculations for 6 materials, namely Be, C, Fe, W, Pb, and U at the energy of 800 MeV for five angles (2.5°, 30°, 60°, 120° and 150°). The data are taken from [4] using the EXFOR database [5].

Figures 1 and 2 show the neutron double differential cross-section for light target nucleus as Be and heavy target nucleus as U correspondingly. Both FLUKA and MCNPX reproduce well the shape and magnitude of the double differential cross-section spectra. Two distinct contributions are visible in the spectra: the evaporation neutrons between 1 and ~20 MeV are emitted isotropically, and cascade neutrons, being more forward peaked, with energies above ~20 MeV. We note that the results obtained are more accurate for heavy nuclei than for light nuclei, where some important discrepancies appear at low neutron energy, say, below 10 MeV. For MCNPX, five models combinations have been used: INCL4-ABLA, ISABEL-ABLA, BERTINI-RAL, ISABEL-RAL, and CEM2k as explicitly shown in Figures 1-2.

**Figure 1: Neutron double differential cross-section in the case of the reaction  $\text{Be}(p,xn)$  at  $E_p = 800$  MeV**

The experimental data are represented in black, and the results of different model predictions in red

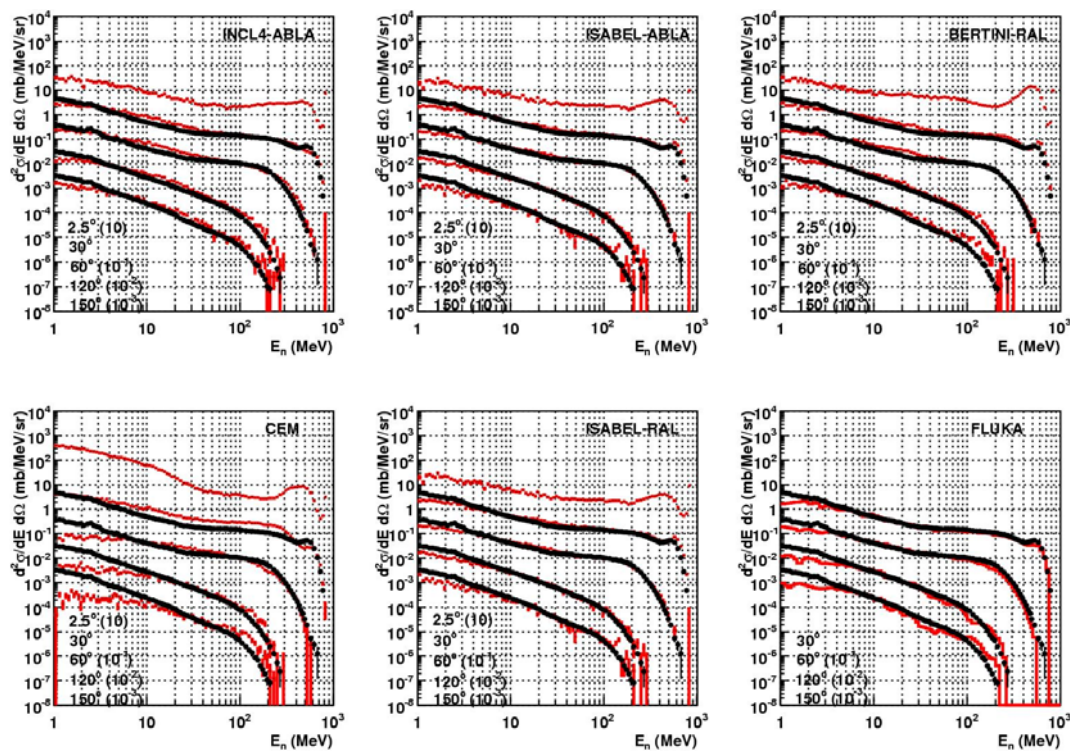


**Figure 2: Same as Figure 1 but for the reaction  $\text{U}(p,xn)$  at  $E_p = 800$  MeV**

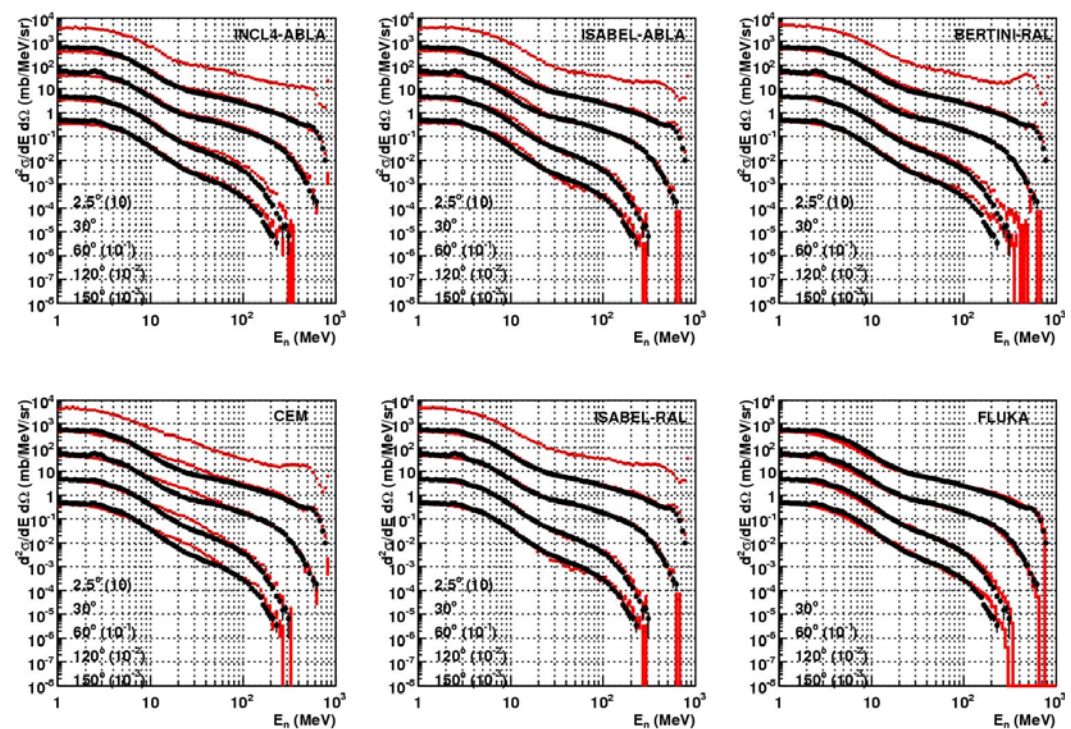
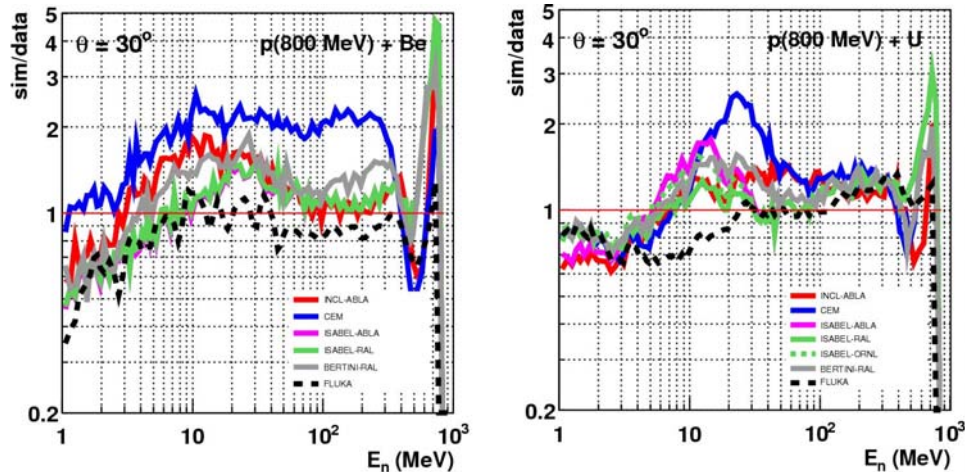


**Figure 3: Ratio between simulation and data for the Be(p,xn) reaction (left) and the U(p,xn) reaction (right) for the emission angle of 30°**

Note that the thickness of the lines is larger than the resulting error from data and simulation



For a more quantitative comparison we have also plotted the ratio between model predictions and data (an example is given in Figure 3 for the emission angle of 30°). Taking into account the combined statistical and systematic error on data and simulation, the agreement is within a factor of 2 up to 600 MeV, except for the CEM2k model used within MCNPX. Above 600 MeV, and for forward angles in particular, around the quasi-elastic and quasi-inelastic peaks, the agreement is not so good whatever the code and models are used. We expect that this disagreement is less important for realistic target simulations, where the neutron energy and angular distributions will be influenced by the multiple scattering with the increasing target thickness.

### Light charged particle production

Figure 4 shows the proton double differential production cross-section obtained for thin carbon and niobium targets. Data are taken from [6]. Results obtained by simulation are rather good for FLUKA and MCNPX used with ISABEL, INCL4 and CEM2k models. On the other hand, some important discrepancies are seen at forward angles and high secondary proton energies.

In the case of production of helium (Figure 5) also huge differences between models have been seen: except for CEM2k there is no  $^4\text{He}$  particles emitted above ~50 MeV at all, and the shape of the distribution is not reproduced correctly. It has to be stressed separately that only CEM2k is able to emit high energy alphas, while the other intranuclear cascade models (like ISABEL, INCL4, Bertini inside MCNPX and PEANUT inside FLUKA) are unable to emit energetic composites (clusters). Data are taken from [7].

Various data on tritium production cross-sections have been compiled [8-11] for the natural lead target, and are compared (see Figure 5) to the results given by MCNPX code using model combinations only which result in non zero tritium emission. The ISABEL-ABLA and INCL4-ABLA models combination are then excluded, and only CEM2k, BERTINI-RAL and ISABEL-RAL can be used for this particular observable. The first and the second model combinations seem to overestimate the data, with only ISABEL-RAL showing the saturation visible in the data occurring around 1-2 GeV incident proton energy.

### Residue production

Comparison of fission yields from thick targets between MCNPX models and ISOLDE data [12] has also been performed. ISOLDE experiment at CERN collected data of yields and release of noble-gas isotopes from UCx/graphite and ThCx/graphite targets. Proton beams of 1.0 and 1.4 GeV were used. Figure 6 presents the in-target production yield of Krypton isotopes for CEM2k, INCL4-ABLA, ISABEL-ABLA and

Figure 4: Double differential cross-section for proton production from 392 MeV incident protons interacting with carbon (left) and niobium (right) targets

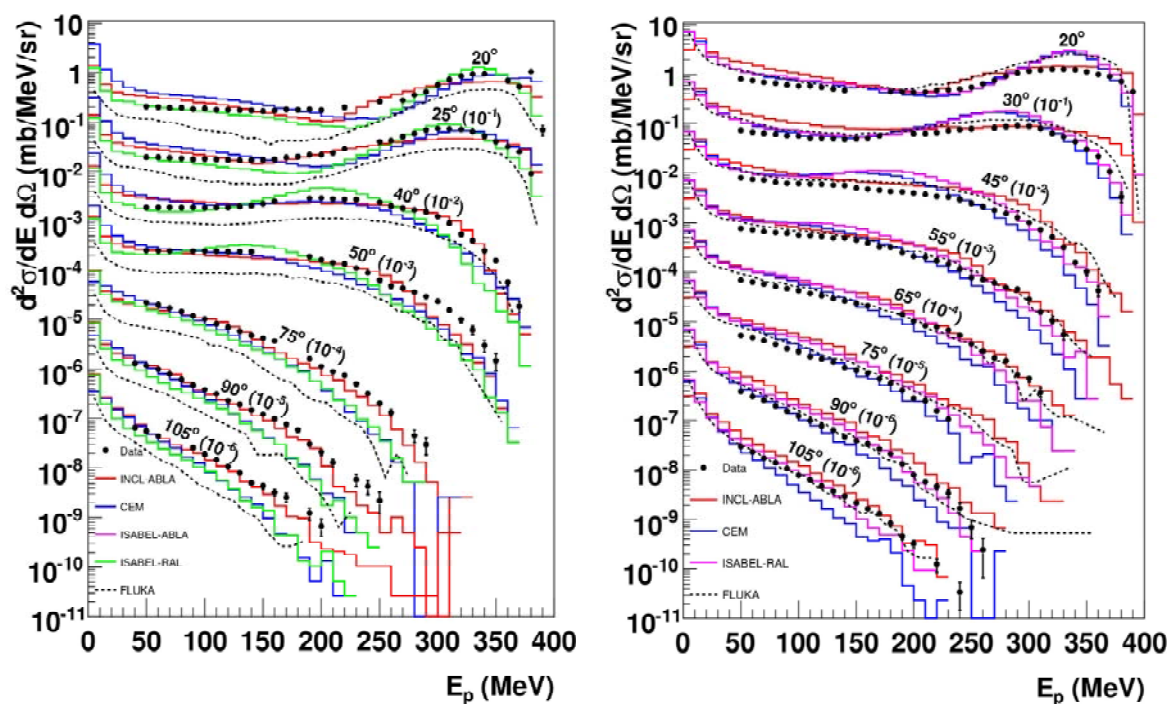
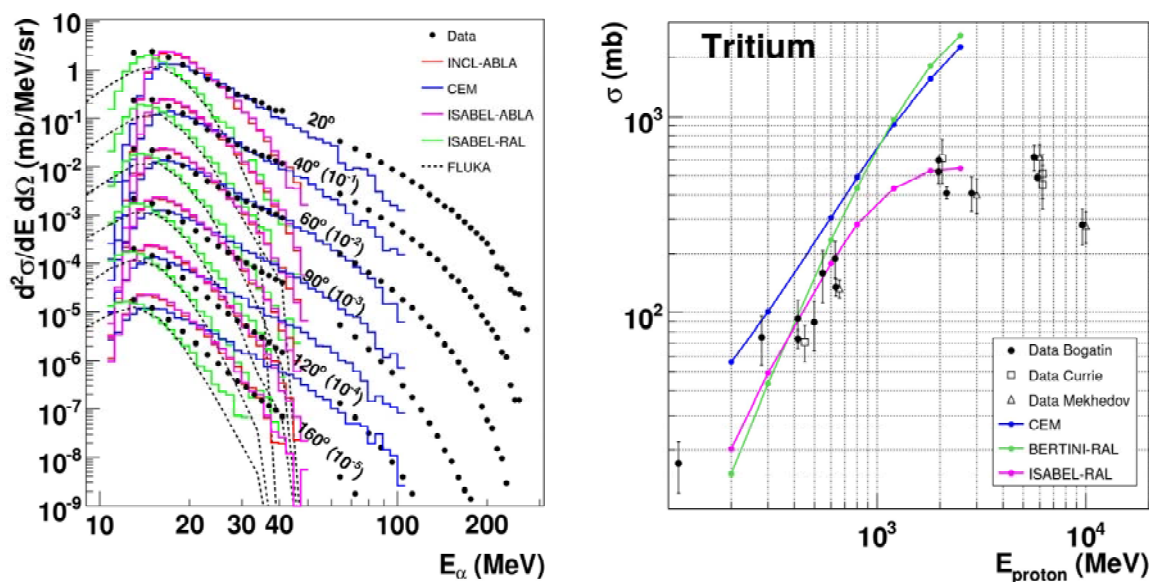
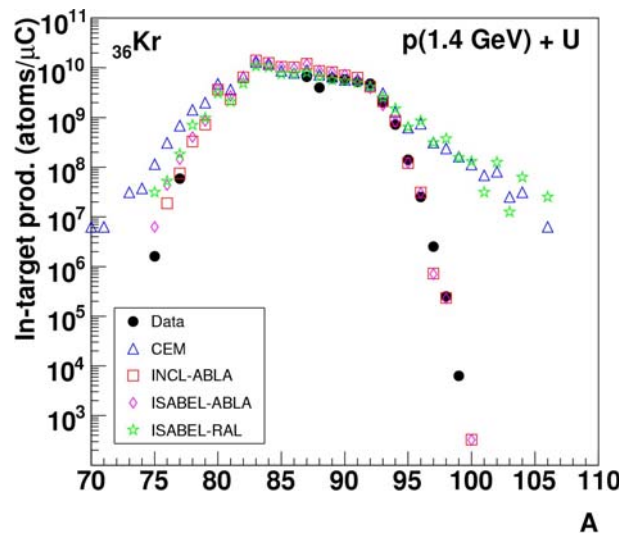


Figure 5: (Left) Helium double differential cross-section production in the case of the reaction  $\text{Ag}(p,^4\text{He})$  at  $E_p = 300$  MeV (left); (right) tritium production cross-section in a thin lead target as a function of proton incident energy.



**Figure 6: Mass distribution of krypton isotopes given by different models within MCNPX and compared to ISOLDE data**



ISABEL-RAL models with 1.4 GeV protons impinged on the uranium carbide target. Note that in these simulations all secondary reactions, including low energy neutrons, are taken into account. In brief, we can see that only the combinations using ABLA fission-evaporation model are able to reproduce the shape of the mass distribution. The CEM2k and ISABEL-RAL models predict too broad distribution and therefore overestimating the production of isotopes on the neutron rich side in particular. Similar conclusions are drawn also for the isotopic distribution of Xe (J.C. David, et al., “Megapie: Residue Yields and Radioactivity Predictions with Different Models in MCNPX”, these proceedings).

### Realistic target calculations

The first simulation of the EURISOL 4 MW power target for the radioprotection purposes has been done using the MCNPX code. A view of the geometry implemented in MCNPX is shown in Figure 7. In brief, this is a two-stage target, in which the power of the primary incident proton beam is dissipated in the liquid Hg (target-converter), whereas the resultant neutron flux is used to induce fissions in the secondary uranium carbide target (production target), which in principle should not be overheated by the primary beam. The target-converter (liquid Hg) is of 16 cm diameter and of the stopping length (~45 cm long). The mercury is surrounded by eight production targets that contain the fission material (uranium or thorium carbide tablets), which will be heating to ~2 000°C in order to increase the effusion-diffusion process (extraction efficiency) of the fission products. Extracted fission products are driven to a single or multiple ion sources by eight beam tubes. The entire target assembly is maintained by a stainless steel structure isolated electrically and surrounded by a moderator (thick graphite layers). The incident beam is 1 GeV protons (up to 4 mA beam intensity) with a Gaussian profile.

Using the target geometry presented in Figure 7 we calculated the spallation residues charge and mass distributions in the mercury target using ISABEL-ABLA, INCL4-ABLA and CEM2k model combinations. The results are shown in Figure 8, where important discrepancies are observed among different model predictions. Note that these differences will accumulate with the irradiation time of the target, and will give increased difference in production yield.

A more detailed examination of the mass distribution for a particular isotope, for example Krypton isotope mass distribution as presented in Figure 9, confirms, as already earlier in this work, that CEM2k gives too broad distributions.

The activation calculation of the mercury was done with the CINDER transmutation code [13] for a continuous irradiation time of 40 years with the proton beam intensity of 2.28 mA, representing an average load of the installation. The results are summarised in Figure 10 and Table 1. The calculation has been done with three models (INCL4-ABLA, ISABEL-ABLA and CEM2k) resulting in three different distributions of spallation residues and gas production in target.

Figure 7: Schematic view of the “realistic” EURISOL 4 MW power target geometry implemented in MCNPX

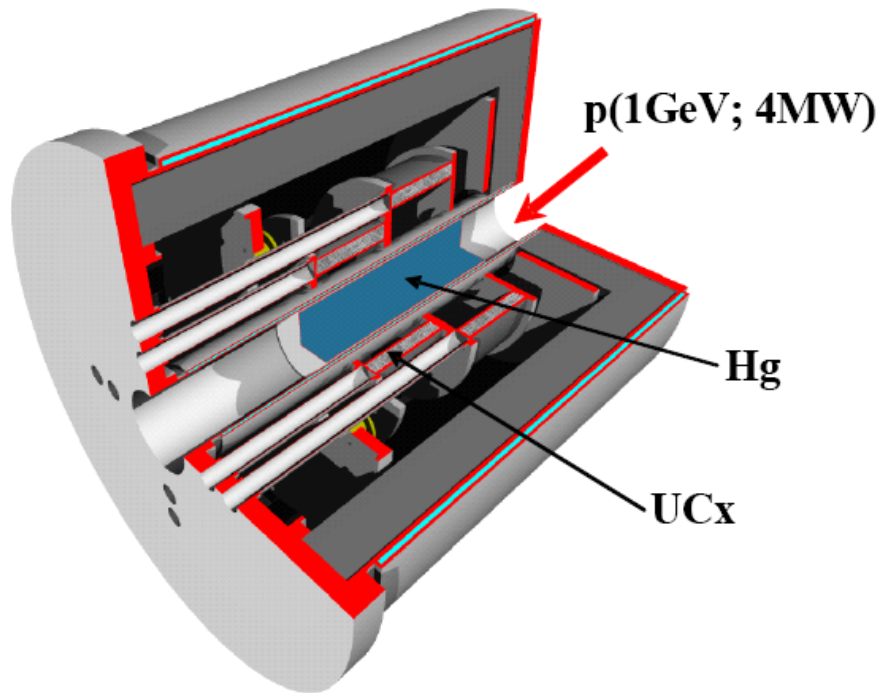


Figure 8: Mass (left) and charge (right) distributions of spallation residues in thick mercury target interacting with 1 GeV protons

The following model combinations were used: ISABEL-ABLA (magenta), INCL4-ABLA (red) and CEM2k (blue)

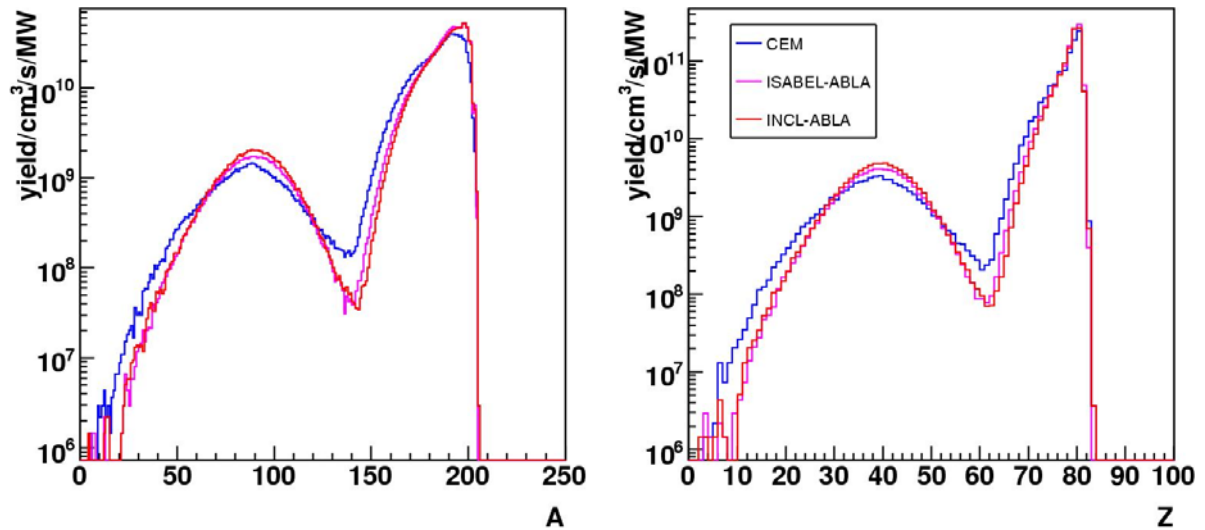


Figure 9: Same as Figure 8 but for mass distribution of krypton isotopes

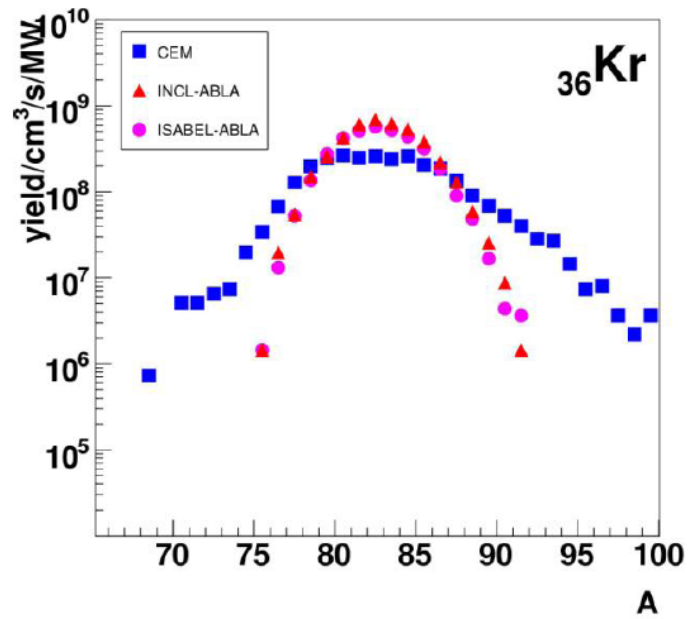
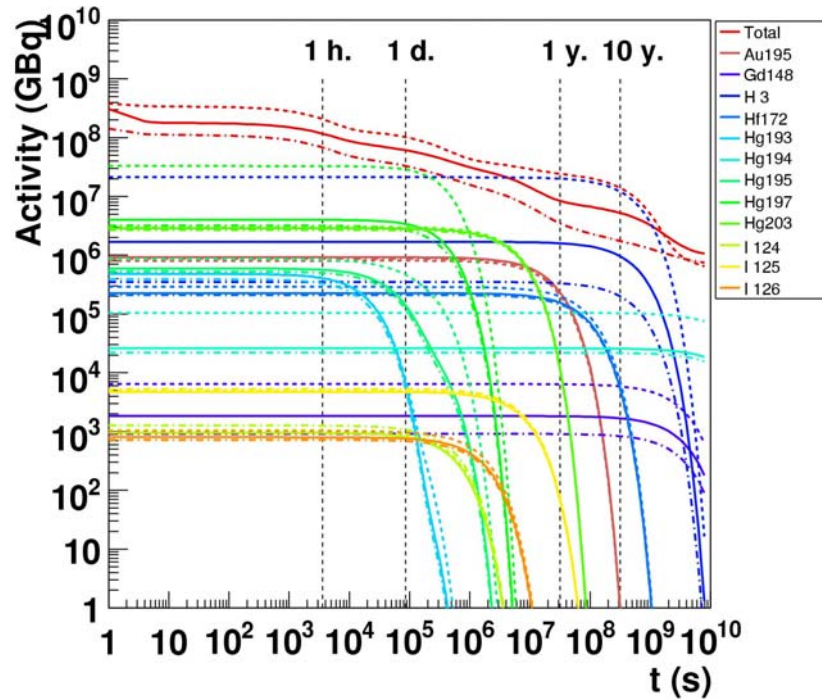


Figure 10: Radioactivity estimates as a function of cooling time using ISABEL-ABLA (solid line), CEM2k (dashed line) and INCL4-ABLA (dashed-dotted line) models



**Table 1: Activity (in GBq) contribution due to a few important isotopes for radioprotection in the irradiated mercury target as a function of ISABEL-ABLA, CEM2k and INCL4-ABLA models within MCNPX**

	1 year after irradiation			10 years after irradiation		
	ISABEL-ABLA	CEM2k	INCL4-ABLA	ISABEL-ABLA	CEM2k	INCL4-ABLA
Total activity	8.410 <sup>6</sup>	2.4 10 <sup>7</sup>	3.5 10 <sup>6</sup>	5.2 10 <sup>6</sup>	1.4 10 <sup>7</sup>	1.7 10 <sup>6</sup>
<sup>195</sup> Au	2.4 10 <sup>5</sup>	2.110 <sup>5</sup>	2.2 10 <sup>5</sup>	1.8	1.6	1.7
<sup>148</sup> Gd	1.810 <sup>3</sup>	6.4 10 <sup>3</sup>	9.0 10 <sup>2</sup>	1.710 <sup>3</sup>	5.910 <sup>3</sup>	8.3 10 <sup>2</sup>
<sup>3</sup> H	1.6 10 <sup>6</sup>	2.0 10 <sup>7</sup>	3.3 10 <sup>5</sup>	9.610 <sup>5</sup>	1.2 10 <sup>7</sup>	2.0 10 <sup>5</sup>
<sup>172</sup> Hf	1.610 <sup>5</sup>	2.010 <sup>5</sup>	1.5 10 <sup>5</sup>	5.610 <sup>3</sup>	7.110 <sup>3</sup>	5.2 10 <sup>3</sup>
<sup>194</sup> Hg	2.610 <sup>4</sup>	1.010 <sup>5</sup>	2.2 10 <sup>4</sup>	2.610 <sup>4</sup>	1.010 <sup>5</sup>	2.2 10 <sup>4</sup>

As one could expect, we can see that the different microscopic models are giving significant differences in isotope radioactivity, particularly for the important  $\alpha$  emitter as <sup>148</sup>Gd (see Table 1), and also for tritium gas emission (see Figure 10) between 1 and 10 years of the decay time.

## Conclusions

We have benchmarked the MCNPX and FLUKA codes to predict the production of neutrons, protons, tritons and alphas from incident protons on thin targets of different materials in the energy range around 1 GeV. Comparison of the model predictions with experimental data shows a good agreement of codes for neutron production. For secondary proton production FLUKA have difficulties to reproduce the energy-angle distributions for light targets. As long as production of alphas is concerned, only CEM2k within MCNPX gives reasonable results. The tritium production seems to be overestimated by CEM2k and BERTINI-RAL models above 1-2 GeV but well reproduced by ISABEL-RAL, i.e. the energy where the saturation of tritium production is observed experimentally.

Finally, the simulation done with MCNPX using realistic target geometry proves the importance of benchmark calculations and suggests a careful selection of adequate model combinations for different observables. It seems that up to know there is no a “unique” model combination able to reproduce all observables at the same time with desired precision.

## Acknowledgements

We would like to acknowledge the financial support of the EC under the FP6 “Research Infrastructure Action - Structuring the European Research Area” EURISOL DS Project; contract no. 515768 RIDS; [www.eurisol.org](http://www.eurisol.org). The EC is not liable for any use that may be made of the information contained herein.

## References

- [1] MCNPX – Monte Carlo N-particle Transport Code System for Multiparticle and High Energy Applications, <http://mcnpx.lanl.gov/> (March 2006).
- [2] A. Ferrari, P.R. Sala, A. Fassò, J. Ranft, FLUKA: A Multiparticle Transport Code, CERN 2005-10 (2005), INFN/TC-05/11, SLAC-R-773; <http://pcfluka.mi.infn.it/> (March 2006).
- [3] EURISOL Design Study web page, [www.eurisol.org](http://www.eurisol.org) (March 2006).
- [4] W.B. Amian, et al., Nucl. Sci. Eng., Vol. 112, p. 78 (1992).

- [5] EXFOR: Experimental Nuclear Reaction Data (EXFOR/CSISRS), [www.nndc.bnl.gov/exfor3/exfor00.htm](http://www.nndc.bnl.gov/exfor3/exfor00.htm).
- [6] Tadahiro Kin, et al., *Physical Review*, C 72, 014606 (2005).
- [7] R.E.L. Green, et al., *Physical Review*, C, Vol. 35, Number 4, p. 1341 (1987).
- [8] V.I. Bogatin, V.F. Litvin, O.V. Lozhkin, N.A. Perfilov, Y.P. Yakovlev *Nuclear Physics, Section A* Vol. 260, p. 446 (1976).
- [9] L.A. Currie, W.F. Libby, R.L. Wolfgang, *Physical Review*, Vol. 101, p. 1557 (1956).
- [10] L.A. Currie, *Physical Review*, Vol. 114, p. 878 (1959).
- [11] B.N. Mekhedov, V.N. Mekhedov, *Yadernaya Fizika*, Vol. 11, p. 708 (1970).
- [12] U.C. Bergmann, et al., "Production Yields of Noble-gas Isotopes from ISOLDE UCx/Graphite Targets", *NIM B*, Vol. 204, p. 220 (2003).
- [13] W.B. Wilson, T.R. England, *A Manual for CINDER'90 Version C00D and Associated Codes and Data*, LA-UR-00-Draft (April 2001).

## Benchmarking the MCSHAPE3D code with 1-D, 2-D and 3-D imaging experiments

J.E. Fernandez,<sup>1,2</sup> Viviana Scot<sup>1</sup>

<sup>1</sup>Laboratory of Montecuccolino-DIENCA, University of Bologna, Italy and CNR/INFM

<sup>2</sup>National Institute of Nuclear Physics (INFN)

### Abstract

MCSHAPE is a Monte Carlo code for the simulation of gamma and X-ray diffusion in matter which gives a general description of the evolution of the polarisation state of the photons. The model is derived from the so-called “vector” transport equation [1]. The three-dimensional (3-D) version of the code can accurately simulate the propagation of photons in heterogeneous media originating from either polarised (i.e. synchrotron) or unpolarised sources, such as X-ray tubes. Photoelectric effect, Rayleigh and Compton scattering, the three most important interaction types for photons in the considered energy range (1-1 000 keV), are included in the simulation. Recently the 3-D version of the code MCSHAPE was presented. [2] The 3-D extension of the code is based on a sample modelling using a 3-D regular grid of cubic voxels. At each voxel, the local composition is specified by giving the number of chemical elements, their weight fractions, the atomic characteristics of each element, the total mass attenuation coefficient and the total density. In this paper, the 3-D extension of MCSHAPE was validated by simulating the output for 1-D, 2-D and 3-D imaging experiments.

## Applications of MCSHAPE3D

To explore the possibility of using MCSHAPE3D as an instrument for XRF techniques, both, scanning XRF experiments and XRF tomography experiments, have been simulated (see Section 1). Finally, it is presented an application of MCSHAPE3D to a practical scattering problem (see Section 2) in order to correct the higher-orders scattering contribution to the spectrum.

### 1 Simulation of X-ray fluorescence experiments

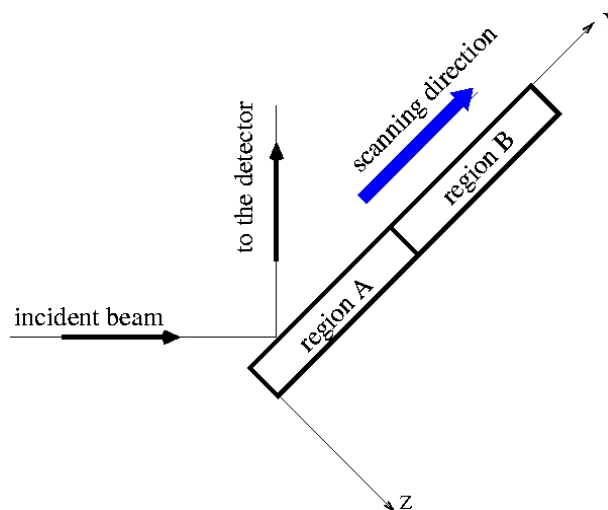
X-ray fluorescence (XRF) is a widely known and used non destructive technique for qualitative and quantitative analysis of most of the elements (atomic number  $> 11$ ) in the sample under investigation. By collecting the intensities of the fluorescent lines coming from the sample is possible to obtain a map of elements contained in the specimen under investigation. Simulation codes (based on analytical calculations, Monte Carlo method or other numerical integration) can be important tools for XRF techniques. For example, they are useful in quantification of trace elements, to study the second-order effects such as enhancement of fluorescent lines by scattered photons or higher-order enhancement, or, moreover, to optimise the experimental set-up (excitation and detection geometry, excitation type) before its realisation. The results of the simulations performed using MCSHAPE3D allow us to assume that our code is a suitable instrument for this kind of experiments.

#### 1.1 Simulation of linear scanning XRF experiments

To verify the correct behaviour of the code MCSHAPE3D, some simulations of linear scanning XRF experiments were performed. For the first test the geometry in Figure 1 was considered and Table 1 shows all the parameters of the simulation. The sample has two regions: region A is made by water with some other chemical elements in low concentration (1% of Fe, Ca, Ba and Zr), while region B is  $\text{SiO}_2$ . We performed a linear surface scan along the x direction and, for every step, the full spectrum was collected. The integrated intensities of the emitted fluorescent lines ( $\text{Fe-K}\alpha$ ,  $\text{Ba-K}\alpha$  and  $\text{Zn-K}\alpha$ ) have been used for the visualisation of the scanning result, as shown in Figure 2.

**Figure 1: Schematic representation of the simulation set-up for the first test of linear scanning**

XRF. The sample has two regions: region A is made by water with some other chemical elements added in low concentration (1% of Fe, Ca, Ba and Zr), while region B is  $\text{SiO}_2$ . The scattering angle is  $90^\circ$ .



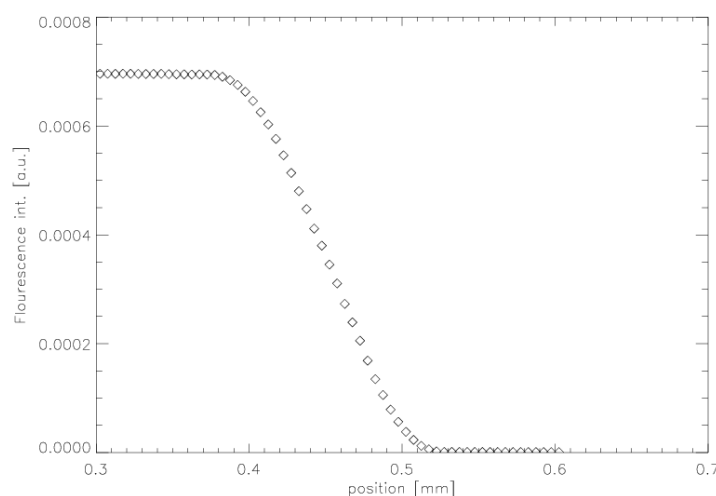
The linear scanning simulation was then repeated for a different geometry and using another sample composition (see Figure 3 for the simulation set-up). Table 2 illustrates the parameters of the simulation. As in the first test, for every step of the linear scan the full spectrum was collected. Then, the integrated intensities of the fluorescence lines are analysed to obtain an indication of the presence of the emitting elements in the sample under investigation. The results are shown in Figure 4.

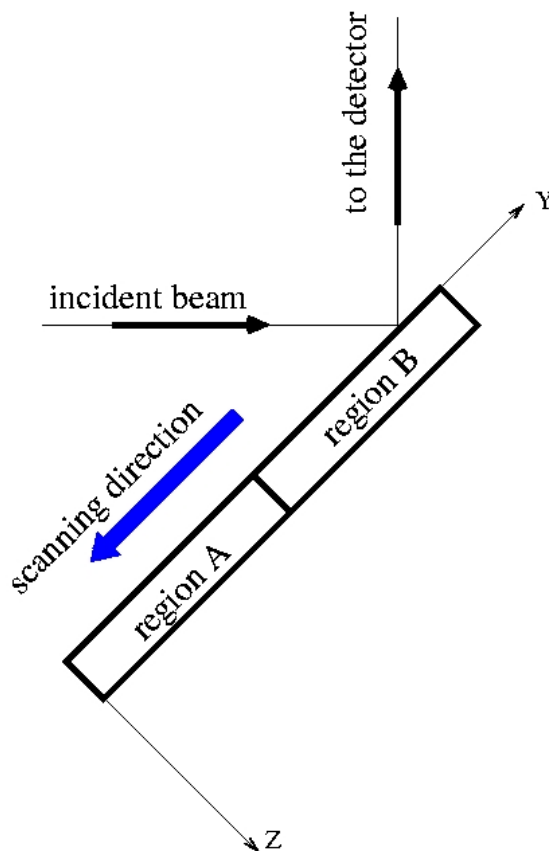
It is apparent the different profile of the plot of the XRF linear scan in this second case respect to the first example. In the first case, the plot can be divided in two regions: on the left (i.e. when the beam is scanning the region A) there is a constant x-ray emission; on the right (i.e. when the beam is in the region B), on the contrary, there is no fluorescent emission. On the border between region A and region B, the intensity of the emitted lines decreases as the non-emitting region enters in the volume irradiated by the beam. In the second case, we do not have a monotone decreasing of the emission going from the emitting region to the non-emitting one, as could be expected. On the contrary, the fluorescent emission collected by the detector is first null (the investigated area is completely in the region B, the non emitting one), then increases but not in monotonic way: there is a maximum of the emitted intensity, near the border between the two regions, and, then, the collected fluorescent emission decreases until a plateau is reached. The reasons of this “strange” behaviour are the particular geometry considered and the different density and attenuation properties of the two regions. The maximum of the emission is reached when the beam irradiates the region with emitted elements (region A), but the photons have to travel across region B (and not region A) to reach the detector. In fact, in this particular case, the photons generated by Fe- $K\alpha$  emission have to travel across a region with an attenuation coefficient lower than that in region A, i.e. they are less attenuated to the pathway towards the detector.

**Table 1: Test 1 – parameters of a simulation of XRF linear scan for the sample in Figure 1**

Sample	name	sampleA
	dimension [cm]	0.1 x 0.1 x 0.01
	composition	region A $H_2O + Fe(1\%) + Ca(1\%) + Ba(1\%) + Zr(1\%)$
		region B $SiO_2$
Simulation	type	linear scan for $z=0$ and $y=0.05$
	voxel dim. [cm]	0.0005
	number of voxels	200 x 200 x 20
	number of steps	20
	scattering angle	45°/45°
	number of photons	100000
Source	numb. of collisions	10
	energy [keV]	59.54
	type	point source
Detector	semi-amplitude	$2.8648 \times 10^{-5}$ radians
	type	disk with 1 cm of diameter no collimator

**Figure 2: XRF linear scan: integrated intensities of the emitted fluorescent lines (Fe- $K\alpha$ , Ba- $K\alpha$  and Zn- $K\alpha$ ) as a function of the position (x direction) for the simulation summarised in Table 1**



**Figure 3: Schematic representation of the simulation set-up for the first test of linear scanning XRF****Table 2: Test 2 – parameters of a simulation of XRF linear scan for the sample in Figure 3**

The region A is  $\text{SiO}_2 + \text{Fe}(1\%)$ , while region B is carbon. The scattering angle is  $90^\circ$ .

Sample	name	Sample B
	dimension [cm]	0.1 x 0.1 x 0.01
composition	region A	$\text{SiO}_2 + \text{Fe}(1\%) \rho=2.23 \text{ [g/cm}^3\text{]}$
	region B	$\text{C } \rho=1.0 \text{ [g/cm}^3\text{]}$
Simulation	type	linear scan for $z=0$ and $y=0.05$
	voxel dim. [cm]	0.0005
	number of voxels	200 x 200 x 20
	number of steps	20
	scattering angle	$45^\circ/45^\circ$
	number of photons	100000
Source	numb. of collisions	10
	energy [keV]	15.0
	type	point source
Detector	semi-amplitude	$2.8648 \times 10^{-5}$ radians
	type	disk with 1 cm of diameter no collimator

**Figure 4: XRF linear scan – integrated intensities of the emitted Fe-K $\alpha$  fluorescent lines as a function of the position (x direction) for the simulation summarised in Table 2**

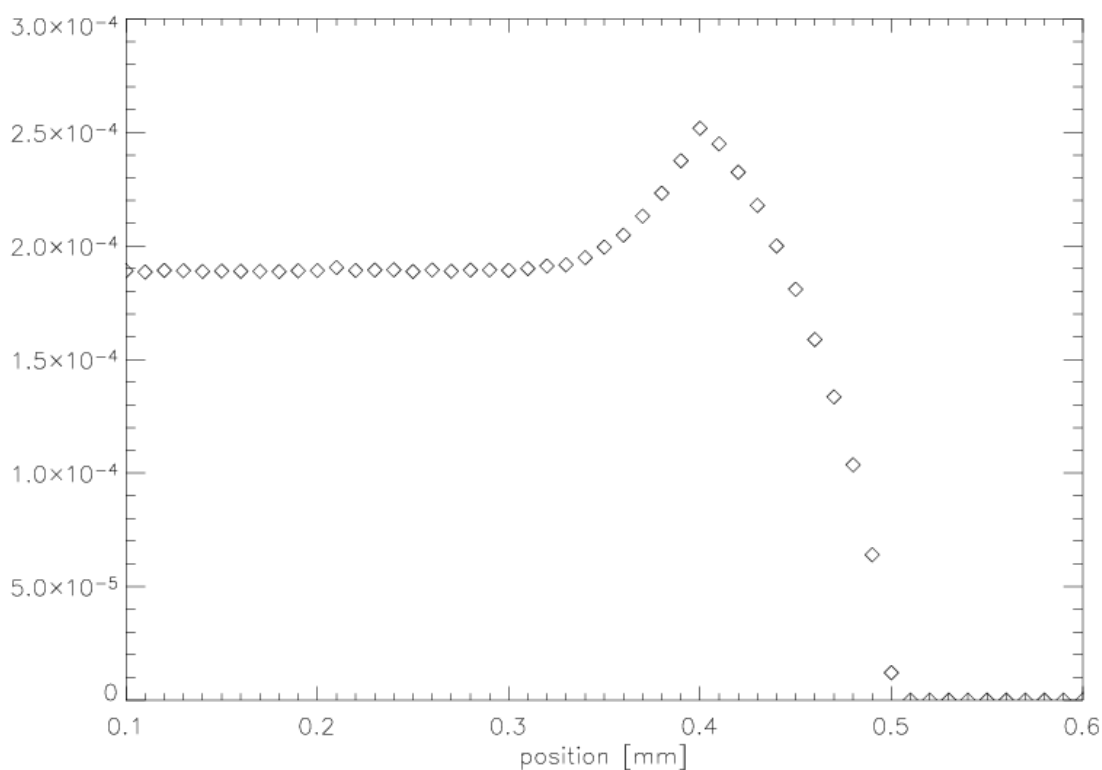


**Table 3: Parameters for the simulation of 2-D-XRF surface scan for the sample in Figure 6**

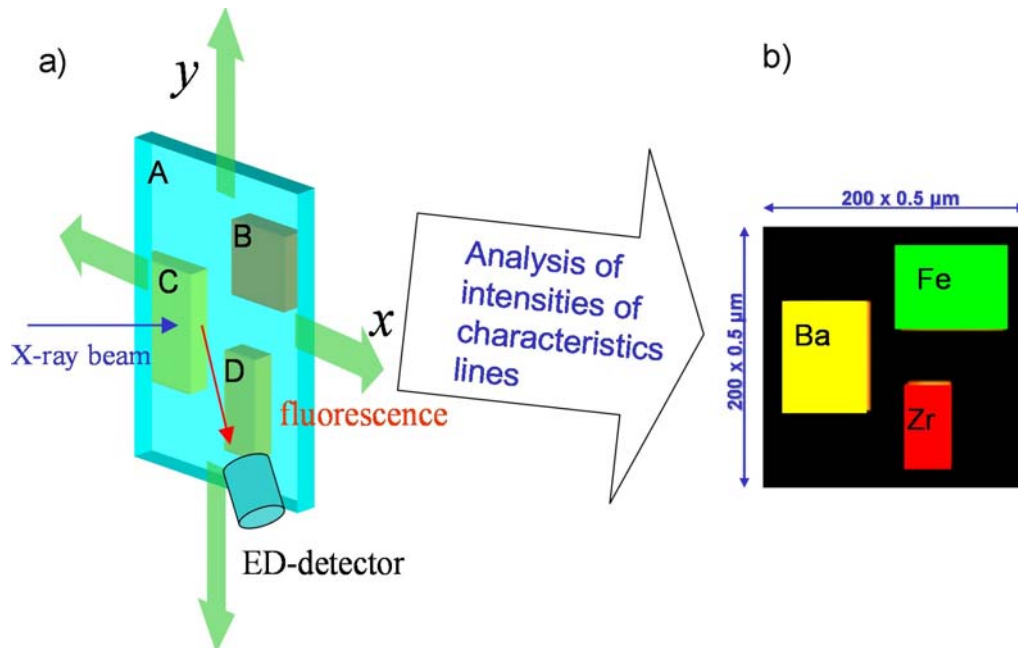
Sample	name	Sample E
	dimension [cm]	0.1 x 0.1 x 0.01
	composition	region A C $\rho=1.0$ [g/cm <sup>3</sup> ] region B SiO <sub>2</sub> + Fe(1%) $\rho=2.23$ [g/cm <sup>3</sup> ] region C SiO <sub>2</sub> + Ba(1%) $\rho=2.23$ [g/cm <sup>3</sup> ] region D SiO <sub>2</sub> + Zr(1%) $\rho=2.23$ [g/cm <sup>3</sup> ]
Simulation	type	2D surface scan for z=0
	voxel dim. [cm]	0.0005
	number of voxels	200 x 200 x 20
	number of steps	100 x 100
	scattering angle	45°/45°
	number of photons	10000
Source	numb. of collisions	10
	energy [keV]	59.54
	type	point source
Detector	semi-amplitude	2.8648 x 10 <sup>-5</sup> radians
	type	disk with 1 cm of diameter no collimator

### 1.2 Simulation of 2-D scanning XRF experiments

Figure 5(a) illustrates the set-up for the 2-D scanning XRF simulation. The sample is assumed to have a carbon matrix with three  $\text{SiO}_2$  regions, each of which doped with a given chemical element (Fe, Ba, and Zr in regions A, B and C, respectively) of 1% concentration by weight. The total dimension of the sample was  $0.1 \times 0.1 \times 0.01$  cm. For the geometrical description of the sample, a 3-D grid of  $200 \times 200 \times 20$  voxels of  $5 \times 5 \times 5 \mu\text{m}$  size was used. The X-ray source was assumed to be a point source emitting 59.54 keV photons isotropically within a given emission cone-angle, and the active detector surface was assumed to be a disk of 1 cm in diameter. The position of the target with respect to the point-source and the emission cone-angle was defined in such a way that the beam size on the sample was  $10 \mu\text{m}$  with incidence and take-off angles of  $45^\circ$ , allowing modelling the outcome of micro-XRF scanning experiments. For each step of the scanning, the full X-ray spectrum is stored. The integrated intensities of the emitted fluorescent lines (Fe- $K\alpha$ , Ba- $K\alpha$  and Zn- $K\alpha$ ) have been used for the visualisation of the 2-D scanning results, which correspond to the 2-D map of distribution of the detectable elements present in the sample [see Figure 5(b)].

**Figure 5: Simulation of a scanning XRF experiment**

a) Simulation set-up. The target can be divided into four regions: a matrix of carbon (region A);  $\text{SiO}_2 + 1\%\text{Fe}$  (region B);  $\text{SiO}_2 + 1\%\text{Ba}$  (region C);  $\text{SiO}_2 + 1\%\text{Zr}$  (region D). b) 2-D map of the surface of the sample, obtained by recording the intensities of the characteristic lines in the spectra collected during the simulation.

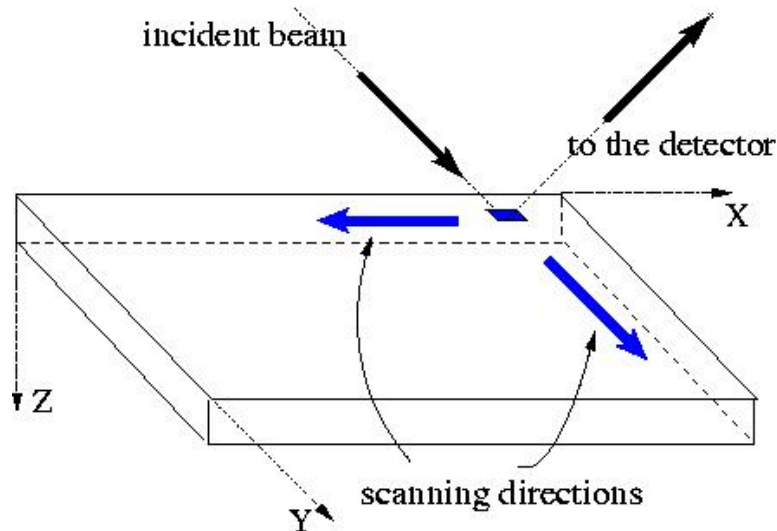


### 1.3 Simulation of XRF tomography experiments

In order to explore the possibility of simulating XRF computed tomography (XRF-CT) experiments using MCSHAPE, the simulation set-up shown in Figure 7 was employed. The target is similar to the one used for the scanning XRF simulation except that, in this case, the carbon matrix is doped with Sr (0.1%) in order to emit detectable XRF lines. The 3-D grid and the source type are the same as described in Section 1.2. The assumed detector (without collimator) has an active area of  $30 \text{ mm}^2$  located at a distance of 50 mm from the centre of the sample. The number of translation steps were 160 (translation step of  $10 \mu\text{m}$ ) and the number of angular rotations were 121, from  $0^\circ$  to  $360^\circ$  (rotation step of  $3^\circ$ ). Table 4 summarised all the parameters of the simulation. The computational time was 10 hours and a P3 cluster with six processors. Similarly to the previous example for the scanning XRF, a full set of spectra is stored.

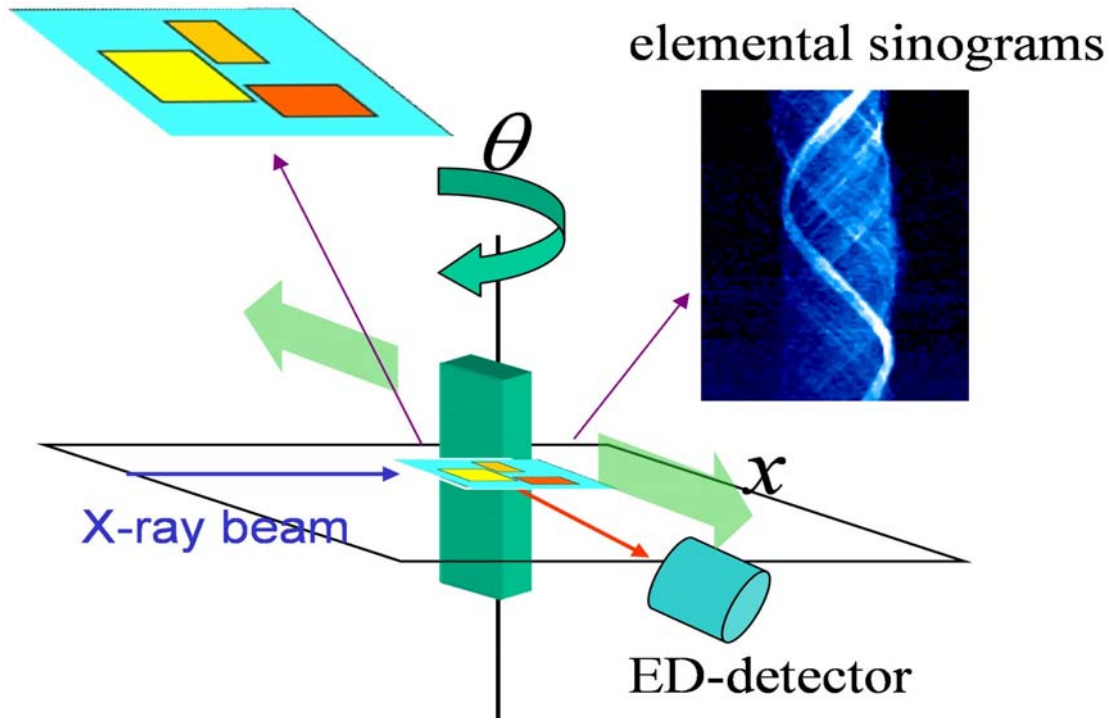
By analysing the integrated intensities of the emitted fluorescent lines, we obtain a set of elemental sinograms corresponding to the linear projections of the elemental distributions in the examined sample section as a function of the rotation angle. After the reconstruction using a filtered back-projection algorithm [3], it is possible to obtain a map of the elements in the scanned section of the target (see Figure 9), demonstrating the usability of the 3-D extension of MCSHAPE for XRF-CT.

**Figure 6: Scanning directions for the XRF experiment**



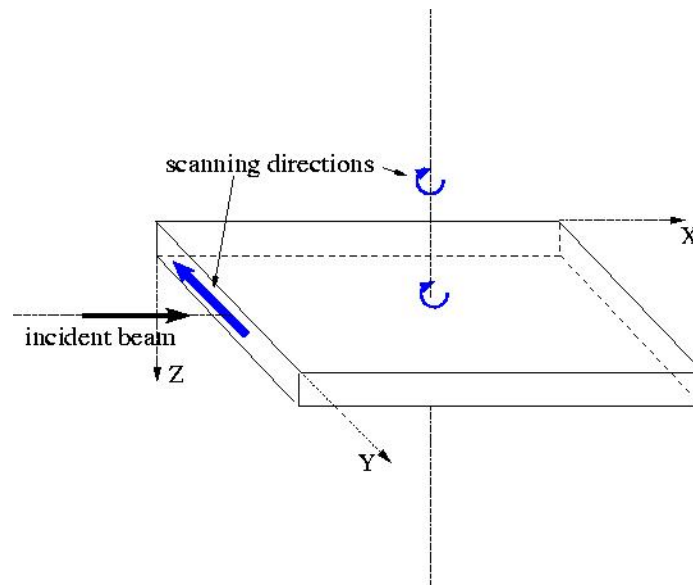
**Figure 7: Set-up of the XRF tomography simulation**

A given cross-section (slice) of the target is scanned through the X-ray beam. Recording of the fluorescent lines intensities during an XRF-CT scan yields a set of elemental sinograms, which provide the elemental distributions within the slice after tomographic reconstruction.



**Table 4: Parameters for the simulation of XRF-tomography of the sample in Figure 8**

Sample	name	Sample E	
	dimension [cm]	0.1 x 0.1 x 0.01	
	composition	region A	C + Sr(0.1%) $\rho=1.0$ [g/cm <sup>3</sup> ]
		region B	SiO <sub>2</sub> + Fe(1%) $\rho=2.23$ [g/cm <sup>3</sup> ]
		region C	SiO <sub>2</sub> + Ba(1%) $\rho=2.23$ [g/cm <sup>3</sup> ]
region D		SiO <sub>2</sub> + Zr(1%) $\rho=2.23$ [g/cm <sup>3</sup> ]	
Simulation	type	tomography for $z=0.05$ cm	
	voxel dim. [cm]	0.0005	
	number of voxels	200 x 200 x 20	
	numb. of translations	160 with step of 10 $\mu$ m	
	numb. of rotations	121 with step of 3°	
	scattering angle	90°	
	number of photons	10000	
Source	numb. of collisions	10	
	energy [keV]	59.54	
	type	point source	
	semi-amplitude	$2.8648 \times 10^{-5}$ radiants	
	distance from the centre of the sample	20 m	
Detector	type	disk with 1 cm of diameter no collimator	
	distance from the centre of the sample	20 m	

**Figure 8: Scanning directions for the tomography**

## 2 Scanning 1-D: multiple scattering correction

The code MCSHAPE3D was applied to study the multiple scattering correction in the framework of a collaboration with the private company IMAL. Multiple scattering (MS) is responsible of an increment of the single scattering (SS) contribution. On the other hand, MS is essentially a non linear process in terms of most of the physical magnitudes involved in the scattering experiment like thickness, target composition, target density, energy of the excitation, etc. This mathematical complexity makes it difficult to include MS in a mathematical model. However, the influence of MS in this particular experiment is not negligible and can be well estimated using the Monte Carlo code MCSHAPE3D.

The experimental set-up shown in Figure 10 was simulated iteratively assuming a fixed position of the source S and different positions of the detector D, which was allowed to move at fixed length steps. The source beam S was assumed to have a rectangular section of  $10 \text{ mm} \times 0.25 \text{ mm}$  and the experimental spectrum of a W X-ray tube operated at 60 kV was used. The collimator in front of the detector was assumed to have a rectangular section  $100 \text{ mm} \times 0.8 \text{ mm}$ . The detector D was assumed to move along the broken line (parallel to the source beam) at fixed steps of 0.05 mm and to behave as an ideal detector. The collimated beam source and the collimated detector projection intersect within the sample defining the primary volume where most of the scattering is produced.

To establish the extent of the multiple scattering correction, two different simulations were performed at each step of detector movement, with the characteristics shown in Table 5.

**Figure 9: After the XRF tomography simulation we obtain a set of elemental sinograms (top panel). Using a filtered backprojection technique [3], it is possible to reconstruct the distributions of detectable chemical elements within the slice investigated (bottom panel).**

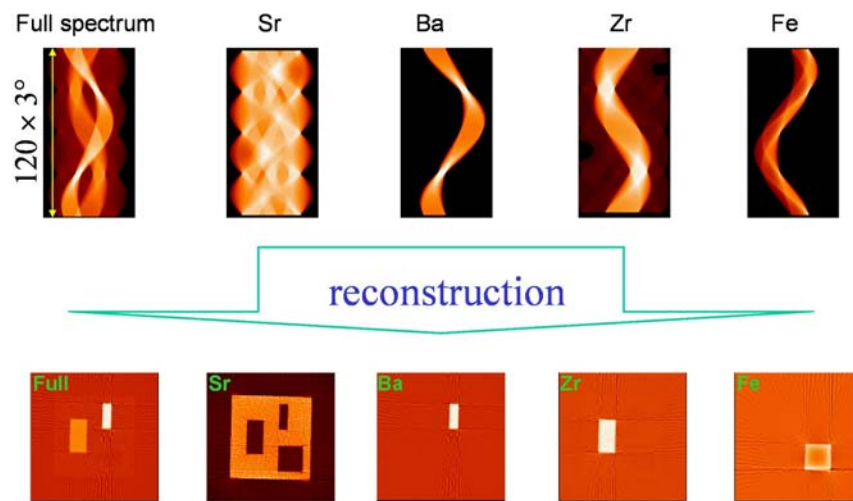


**Figure 10: Experimental set-up**

The sample is wood. The detector and the source are collimated in order to intercept a small section of the specimen. Then, the detector is moved to permit a 1-D depth scan of the sample.

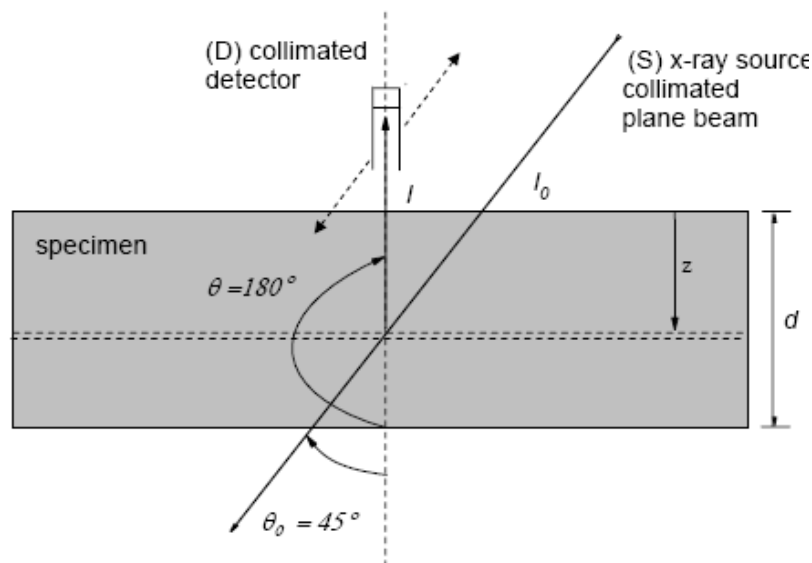


**Table 5: Parameters of the simulation**

Simulation		SS	MS
Number of collisions		1	10
Number of histories		10 <sup>5</sup>	
Source	energy distribution collimator polarization state	W 60 kV (experimental data) Rectangular section: 100 mm x 0.8 mm Unpolarized. Stokes vector (1.0,0.0)	
Target	voxel size distribution air composition wood composition	1 mm <sup>3</sup> Layer 1: 10 mm thickness air Layer 2: Wood target of the given thickness Layer 3: 10 mm thickness air N (78.04%), O (21.02%), Ar (0.94%) $\rho = 0.00129$ H (6%), C (49%), N (2%), O (43%) $\rho = 0.75$	
Detector	efficiency collimator	ideal Rectangular section: 100 mm x 0.3 mm	

**Table 6: Architecture of the parallel clusters used for the computations**

Cluster	A	B
PC	6	5
Total CPU	11	5
Used CPU	6	5
Processor type	AMD Athlon MP 2000	AMD Athlon FX-53
Architecture	32 bit	64 bit
Frequency	1.66 GHz	2.4 GHz
Cache L2	256 kB	1 MB
RAM	1 GB	2 GB

**Table 7: Number of simulated spectra for each profile and total computational time for building the profile for each target thickness**

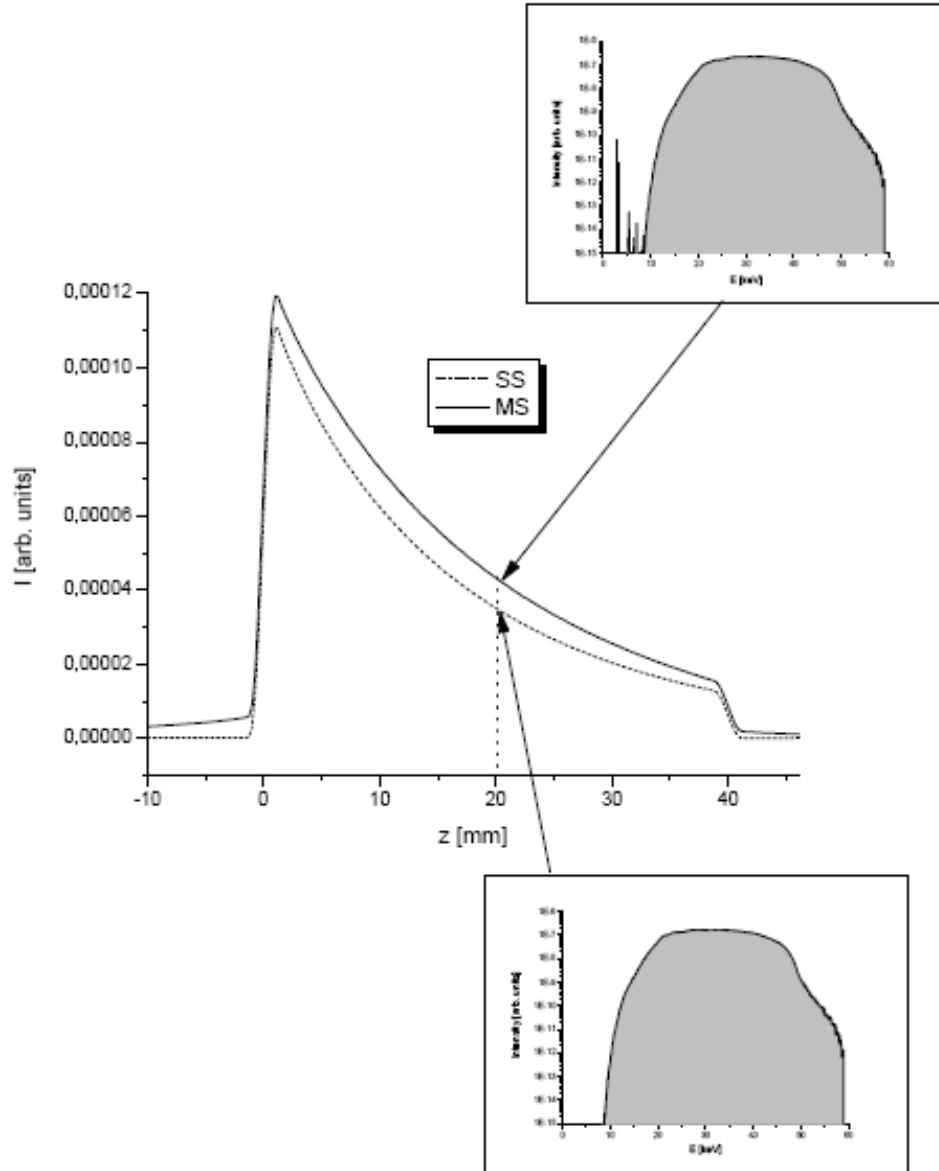
Time figures show the cluster used for the computations. It is worth noting that the spectra for 1 and 10 collisions were simulated independently. The cluster used for the computations is indicated in the thickness column.

Target thickness [mm]	Number of computed spectra (1 collision)	Number of computed spectra (10 collisions)	Profile time [min] (1 collision)	Profile time [min] (10 collisions)
03 (a)	72	72	191.30	770.87
05 (b)	100	100	125.87	575.85
10 (b)	120	120	160.34	753.26
15 (a)	140	140	418.09	1 841.23
20 (b)	160	160	253.41	1 154.29
25 (a)	180	180	591.72	2 701.32
30 (b)	198	198	356.47	1 609.44
35 (a)	220	220	804.36	3 739.60
40 (b)	240	240	484.92	2 156.44
45 (b)	260	260	564.20	2 483.65
50 (b)	280	280	616.79	2 811.57

The first one allowing only one collision was used to simulate the single scattering (SS) behaviour. The second one allowing 10 collisions was used to simulate the multiple scattering (MS) behaviour. Each simulation produced an intensity spectrum like those shown in the boxed plots in Figure 11. The spectrum was integrated (in energy) to estimate the whole counting obtained in the real experiment. Thus, the integrated spectrum represents one point in the profile curve. Figure 11 shows both profiles, SS and MS, on the same plot and exemplifies the two spectra used to compute the same position point on each profile. It is apparent from the profile plot that the different height of the left and right tails of the profile (which is measured experimentally) is due to the effect of multiple scattering.

**Figure 11: Complete profiles computed for both single (SS) and multiple (MS) scattering (central graph)**

Each point in the profiles is obtained by integration of a full spectrum like the ones shown in the upper (MS) and lower (SS) boxed plots. It is worth noting that the characteristic lines due to scattering in air are only present in the MS spectrum. The influence of MS can be also appreciated in the different heights of the left and right tails of the profile, a fact which is observed experimentally.

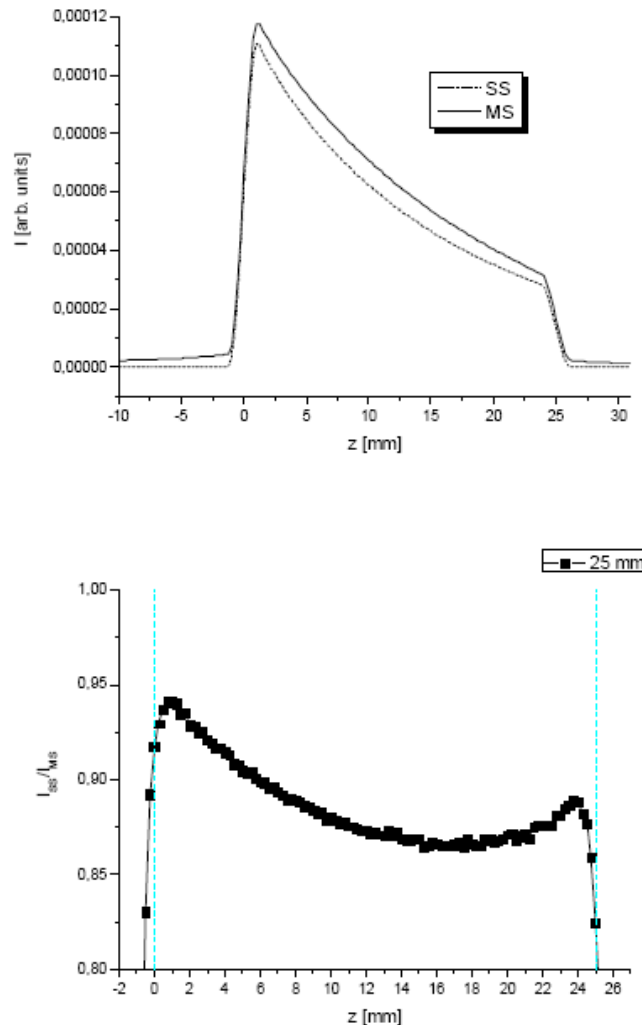


The computations were performed using two parallel clusters as described in Table 6.

The same MPI version of the code (running under LINUX OS) was used with both clusters. The detail of the computational time for the computations is shown in Table 7. The computational time increases with the thickness of the target because is greater the number of voxels (cubic voxels 0.1 mm side were used). Target was wood embedded in an external environment of air. From the table is apparent the improvement of the computational speed by a factor of 2 when using the 64 bit cluster.

**Figure 12: 25 mm thickness**

The upper plot shows the differences between both profiles, SS and MS. The growth of the height difference between the left and right profile tails for increasing thickness confirms the interpretation that is due to multiple scattering effects. The lower plot shows the multiple scattering correction as a function of the depth of the primary volume. Vertical broken lines indicate the border of the wood target. The figure is repeated for different target thicknesses.



For the sake of simplicity, only the results for a 25 mm thickness specimen (Figure 12) are shown as example. The upper plot illustrates the differences between both profiles, SS and MS. It was noted a growth of the height difference between the left and right profile tails for increasing thickness which confirms the interpretation that is due to multiple scattering effects. The lower plot instead, shows the multiple scattering correction as a function of the depth  $z$  of the primary volume. Vertical broken lines indicate the border of the wood target.

It is worth noting that in order to apply the correction is necessary to know first the positions of the target borders, since the extent of the correction is clearly related to the begin and end of the wood specimen. It was used a Savitsky-Golay filter (with  $m = 1$  or  $2$ ) to estimate the derivative from the experimental total intensity in order to determine the position of the beginning and ending borders of the sample. Then, the MS correction can be applied safely, relatively to these borders.

Of course, the few thicknesses for which the correction was calculated are not enough to apply the correction for an arbitrary thickness. A 2-D interpolation scheme feed with the above computed data is necessary in this case. The description of a suitable 2-D interpolation algorithm will be the subject of a future work.

## Conclusions

Several applications require a proper description of the geometry that cannot be described using a mono-dimensional code. To address this problem, a general-purpose 3-D version of the Monte Carlo code MCSHAPE was developed, giving the possibility of simulating the photon propagation within heterogeneous samples with arbitrary geometries. The sample was described using the so-called voxel model. In this article, MCSHAPE3D has been validated by simulating the outcome of scanning X-ray fluorescence (XRF) experiments on simple heterogeneous phantom samples, XRF tomography and a scattering problem. In all case a good agreement was obtained with experimental measurements. The results of the tests performed allow us to assume that MCSHAPE3D is a valid instrument for:

- quantitative XRF analysis;
- instrumental design for XRF;
- preliminary experimental set-up;
- radiation shielding;
- determine the nature of the sample even when it is made by light elements (*i.e.* using the ratio between Compton and Rayleigh);
- medical and industrial applications.

## References

- [1] J.E. Fernandez, V.G. Molinari, *Nuclear Instruments and Methods in Physics Research*, B73, 341 (1993).
- [2] V. Scot, J.E. Fernandez, L. Vincze, K. Janssens, "3D Extension of the Monte Carlo Code MCSHAPE for Photon-matter Interactions in Heterogeneous Media", Submitted to NIM-B (2005).
- [3] S. Park, R. Schowengerdt, *Computer Vision, Graphics and Image Processing*, 23:256 (1983).



## Measurements and benchmark simulations of photo-neutron yields from targets irradiated by 2.0 and 2.5 GeV electrons

**Hee-Seock Lee**

Pohang Accelerator Laboratory, Korea

**Syuichi Ban, Toshiya Sanami, Kazutoshi Takahashi**  
High Energy Accelerator Research Organisation, Japan

**Tatsuhiko Sato**

Japan Atomic Energy Research Institute, Japan

**Rui Qiu**

Department of Engineering Physics, Tsinghua University, China

### Abstract

*The photo-neutron yields from thin and thick targets irradiated by high energy electrons have been studied. The photo-neutron spectra at 48, 90 and 140 degrees relative to the incident electrons were measured by the pulsed beam time-of-flight technique using the Pilot-U plastic scintillator and the NE213 liquid scintillator with 2-inch in length and 2-inch in diameter. Targets, from low-Z element (carbon) to high-Z element (bismuth) and with thin (0.5 Xo) and thick (10 Xo) thickness, were used on this study. The differential photo-neutron yields between 2 MeV (Mainly 8 MeV) and 400 MeV were obtained. The benchmark simulations using well-known Monte Carlo codes have carried out. In early stage of this investigation, EGS4 and PICA were used to calculate the neutron yields from electron irradiation. Those have been benchmarked by the calculation using MCNPX 2.5, MARS-15 and FLUKA-2005. The comparison between experimental data and calculated data are discussed to give us meaningful approach for a photonuclear reaction study.*

## Introduction

The information of photo-neutron yields for high energy electron accelerator have been required constantly according to many constructions and great uses of synchrotron facility, X-FEL, and linear collider. Not only yields from thick target like beam dump or main beam loss point and but also yields from thin target like beam scraper are needed. There are only a few experimental data for high energy electron and the Monte Carlo codes have been upgraded continuously to estimate them precisely. The photo-neutron measurements have been conducted at PHERF (Pohang High Energy Radiation Facility) using electron linac of Pohang Light Source (PLS) since 1998 as co-work between PAL, KEK, and Kyoto University [1-10]. The photo-neutron spectra at 48, 90 and 140 degrees (mainly 90°) relative to the incident 2.0 or 2.5 GeV electrons were measured by the pulsed beam time-of-flight technique. The differential photo-neutron yields between 2 MeV (Mainly 8 MeV) and 400 MeV were obtained. In the process of that study, the PICA95 code was revised to PICA3 [11].

In early stage, we use the combination process with EGS4 and PICA3 to estimate the neutron yield theoretically. The MCNPX [12], MARS [13] and FLUKA [14] have been used successively for the benchmark calculation. In the paper the variation of the yields depending on target thickness and target elements are shown with the calculation results. The difference between the yields estimated by each Monte Carlo codes is discussed.

## Experiments

The spectral measurements of photo-neutrons produced from thin and thick targets by incident 2.0 and 2.5 GeV electrons were carried out at PHERF as shown in Figure 1 (a horizontal view) and Figure 2 (a vertical view). The details of experiment process are described in Refs. [1-10]. The incident electron is irradiated to target samples with the pulse length of 1 nsec and repetition rate of 10 Hz. The normal beam intensity was about 0.5 nC/pulse. In order to investigate the relationship between target condition and neutron yield, several targets in the range of  $Z = 6\sim 83$  and  $t = 0.075\sim 10 X_0$  (radiation length) were tested with  $5 \times 5 \text{ cm}^2$  cross-section. The detail information of target material which yields were measured is listed in Table 1.

The flight distances of three TOF experimental lines were 6.8 m (48°), 10.4 m (90°) and 8.1 m (140°). The BC418 (Pilot-U) plastic scintillator with very short pulse decay time were used as a neutron detector to avoid pulse pile-up of neutron signal and to separate neutron signal and huge X-ray signal. Also the NE213 liquid scintillator with the same size was used to measure lower energy neutrons with n-gamma discrimination technique. A few measurement results were verified in latest experiments using a veto counter system to eliminate the contribution of charged particles [10]. Both sizes of neutron detectors were 2 inches in length and 2 inches in diameter.

A high resolution multi-channel scaler (FAST ComTech 7886A) and a CAMAC TDC (LeCroy TDC3377) with 0.5 nsec per channel were used to measure the flight time of neutrons. The start signal of the time-of-flight electronics was given from the beam current monitor in Figures 1 and 2. The multi-stop mode was applied to measure a few neutrons and X-rays generated from electron burst. The discrimination level was set to 4.2 MeVee (electron equivalent), which corresponded to about 9 MeV. In the n- $\gamma$  discrimination using NE213 detector, we could get the neutron energy down to 2 MeV, which is 1.15 MeVee [5].

## Calculation

Those experimental results were compared with several calculation using well-known Monte Carlo codes. First, the combined calculation of EGS4 and PICA3 were applied to estimate the neutron yields. The photon track length in each targets were calculated using EGS4 and those distributions were used as input of PICA3. The self-attenuation of neutron in a target was compensated by the LAHET 2.1.5 calculation. Next MCNPX 2.5d were used for the same estimation. In this case, the simplified geometry as shown in Figure 3 was applied to get good statistics in short time. Those results reproduced well the measurements. However the MCNPX code supplies the electron library only up to 1 GeV. Our calculation to put 2 GeV as the incident energy worked well, but the extrapolation for electron energy

higher than 1 GeV may be operated in MCNPX code (commented by John Hendricks). The method to multiply two to neutron yields which is calculated using 1 GeV electron was also tested. (S. Mashnik and F Gallmeier also benchmarked earlier with the same method). Those results presented lower yields.

In the same geometry as MCNPX, MARS15(04 and 05) were applied. The data in Figure 4 was calculated by MARS15 (04) and in Figure 5 was calculated by MARS15 (05). The MARS15 was an updated version embedding the cascade-exciton model code, CEM03 for photonuclear reaction in intermediate energy. The neutron transport below 14 MeV can be calculated by the MCNP code automatically in MARS15 code. But because the transport is not important for this calculation, all calculations were carried out at inclusive mode without MCNP connection [10].

Finally the FLUKA (Version 2005) was applied. A USRYIELD subroutine and a USRBDX subroutine were tested to calculate neutron yields for real target geometry. The surface of sphere of 1 m radius was defined to apply a USRBDX subroutine. Both results were agreed with each other. The results in Figure 5 are what were produced by a USRYIELD subroutine.

## Results and discussion

As shown in Figure 4, the Monte Carlo calculation, especially MARS15, regenerated the experimental results well in the case of thicker target. In thinner case of 1 Xo, most of calculation results showed large difference with the experimental results. This phenomenon is more distinctive at high Z material [10]. A discrepancy was found in the range from 30 MeV to 110 MeV in every calculation, but they are smaller than factor of two.

Figure 5 shows the comparison of thick target calculations by each Monte Carlo code. MARS results and MCNPX results reproduce the experiment well in the view of overall spectral distribution. The FLUKA results showed that yields were lower relatively at energy below 20 MeV and higher at energy higher than 150 MeV. The discrepancy becomes larger below 10 MeV and above 400 MeV.

There are three discussion points in the distribution: discrepancy below 20 MeV, around 70~80, and above 150 MeV. One of common idea of discrepancy can be whether use CEM code or not because Monte Carlo calculations which do not use CEM showed normally lower yield than the experimental results. As codes are upgraded, it is presented that the amount of difference becomes smaller. Authors expect that the developer or theorist give some solution to eliminate such discrepancy at three energy range soon.

## References

- [1] H.S. Lee, et al., *J. Nucl. Sci. Tech.*, Suppl. 1, 207 (2000).
- [2] T. Sato, et al., *Nucl. Instr. Meth.*, A463, 299 (2001).
- [3] K. Shin, et al., "Measurement and Systematic Study of Photoneutron Yields from Thick Targets Bombarded by 2 GeV Electrons", *Proc. of RPS2000*, Washington, 17-21 September 148 (2000).
- [4] H.S. Lee, et al., "Systematics of Differential Photoneutron Yields Produced from Al, T, Cu, Sn, W, and Pb Targets by Irradiation of 2.04 GeV Electrons", *Proc. ND2001*, Tsukuba, 7-12 October 2001, *J. Nucl. Sci. Tech.*, Suppl. 2, 1228 (2002).
- [5] S. Ban, et al., "Measurements of Photo-neutrons from Thick Targets Irradiated by 2 GeV Electrons", *Proc. of AccApp03*, San Diego, California, June 2003, 955 (2003).
- [6] H.S. Lee, et al. "Status of Angular Distribution Measurements of Photo-neutron Yields from Cu, Sn, and Pb Targets Irradiated by 2 GeV Electrons", *2<sup>nd</sup> International Symposium on Radiation Safety and Detection Technology*, Sendai, July 2003, *J. Nucl. Sci. Tech.*, Suppl. 4, 10 (2004).

- [7] H.S. Lee, et al., "Differential Photo-neutron Yields from C, Al, Cu, Sn, and Pb Targets by 2.04 GeV Incident Electrons", 1<sup>st</sup> Int. Meeting on Applied Physics, Badajoz, 13-18 October 2003.
- [8] H.S. Lee, et al., "Angular Distribution Measurements of Photo-neutron Yields Produced by 2.0 GeV Electrons Incident on Thick Target", 10<sup>th</sup> International Conference of Radiation Shielding, Madeira, 9-14 May 2005, *Radia. Prot. Dosim.*, 116, 653 (2005).
- [9] H.S. Lee, et al., "Photo-neutron Yields from Thin and Thick Targets Irradiated by 2.0 GeV Electrons", *Shielding Aspects of Accelerators, Targets and Irradiation Facilities (SATIF7)*, Sacavem, Portugal, 17-18 May 2004, OECD/NEA, Paris (2005).
- [10] T. Sanami, et al., "Calculation of Secondary Neutron Spectrum from 2 GeV Electron Induced Reactions Using MARS15(04) Code", *Proc. of 3<sup>rd</sup> Int. Workshop on Radiation Safety of Synchrotron Radiation Sources*, Hyogo, 17-19 November 2004, SPRING-8 Document A 2005-002, 109 (2005).
- [11] T. Sato, et al. "PICA3, An Update Code of Photo-nuclear Cascade Evaporation Code PICA95, and its Benchmark Experiments", *Proc. of MC2000*, Lisbon (October 2001).
- [12] D. Pelowitz, (Ed.), *MCNPX Version 2.5.0 User's Manual*, LA-CP-05-0369 (2005).
- [13] N.V. Mokhov, et al., *Recent Enhancements to the MARS15 Code*, Fermilab-Conf-04/533, Version 15(04) and 15(05).
- [14] A. Ferrari, et al., *FLUKA: A Multi-particle Transport Code (Program Version 2005)*, CERN-2005-010 (2005).

**Table 1: Target materials and their thicknesses**

Materials	Z	Thickness (Xo)						
Graphite (C)*	6	0.075	0.225	0.375				
Aluminium (Al)	13	0.50	1.00	1.57				
Titanium (Ti)	22	0.50	0.98	1.99	2.98			
Iron (Fe)	26	1.02			5.00			
Copper (Cu)	29	0.98		1.96	2.94	4.90	6.85	9.79
Molybdenum (Mo)	42	1.04			5.00			
Tin (Sn)	50	0.50	1.00	2.00	3.00	5.00	7.00	10.00
Tungsten (W)	74	1.00		3.00			5.09	9.69
Lead (Pb)	82	0.54	0.89	1.79	2.68	4.46	7.14	9.82
Bismuth (Bi) **	83	1.83						

\* Density = 1.6 g/cc

\*\* Diameter = 8.1 cm

Figure 1: Experimental set-up for angular distribution measurement at PHERF using electron linac of Pohang Light Source

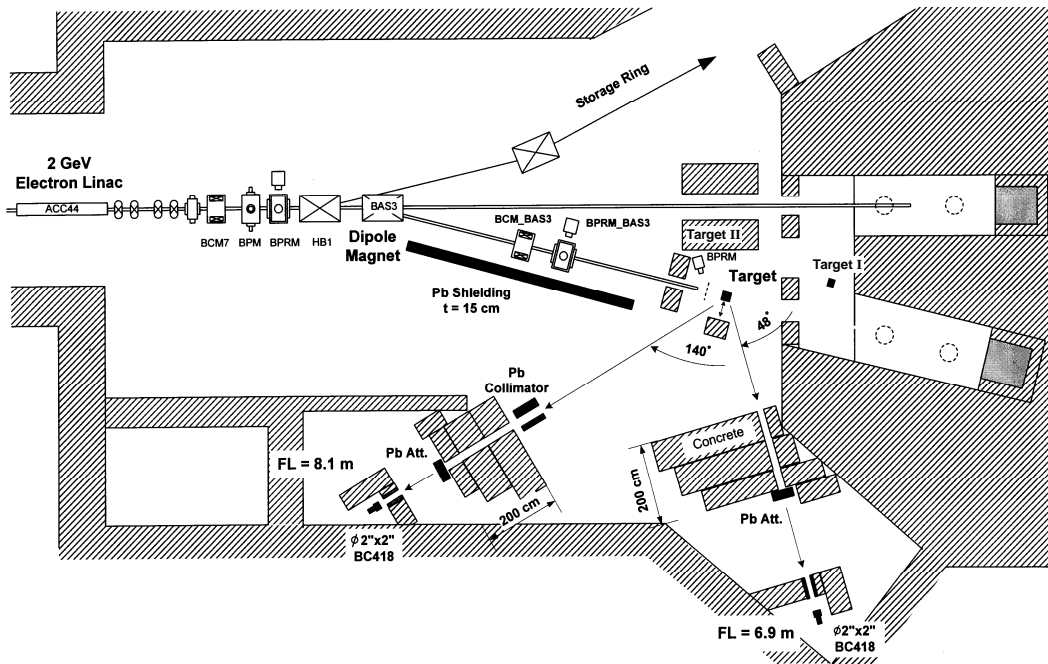


Figure 2: Vertical view of experimental set-up for photoneutron measurements at 90°

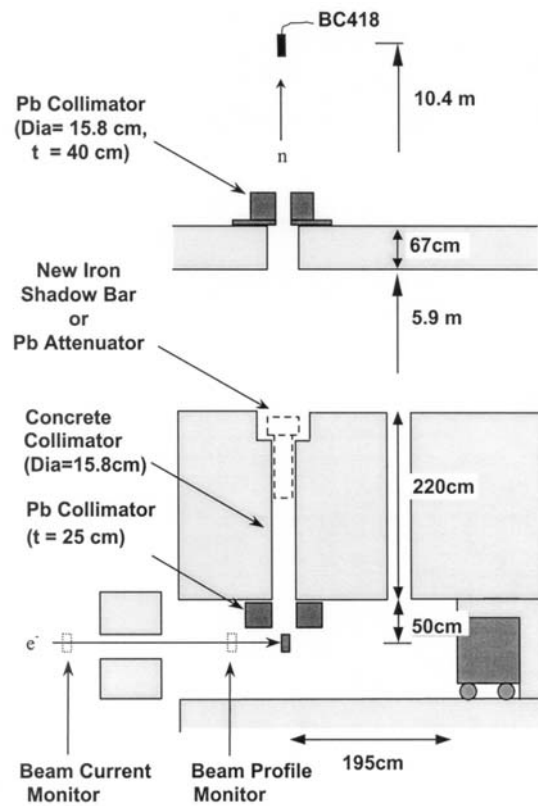


Figure 3: Simplified geometry for MC calculation

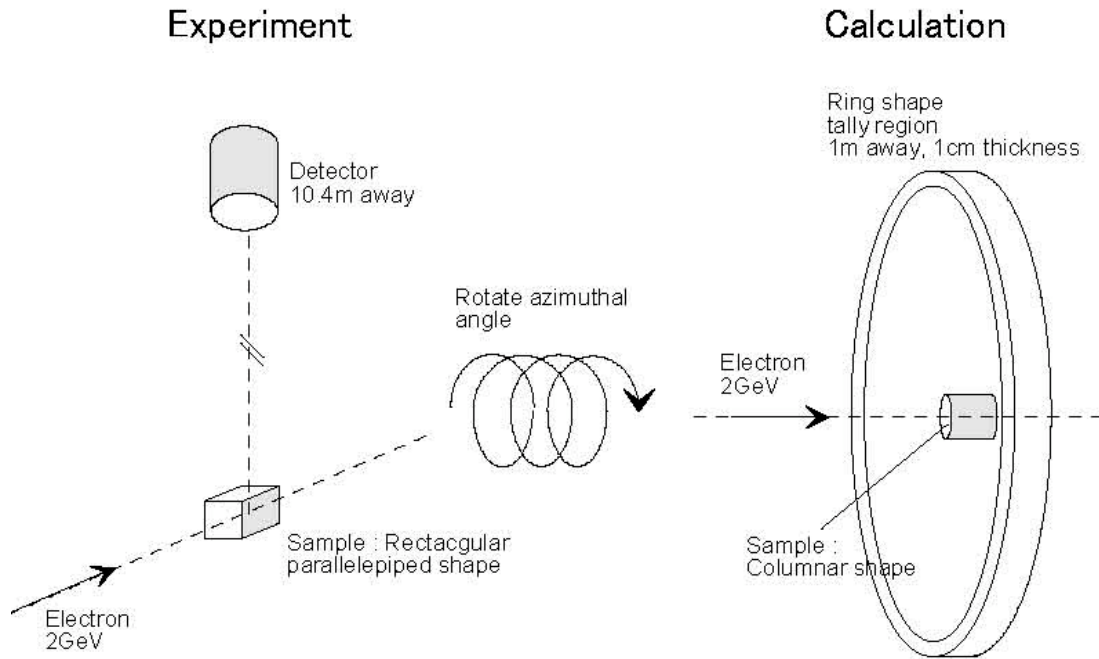


Figure 4: Comparison between experimental data and calculation results by MARS for Cu target irradiated by 2.0 GeV electron

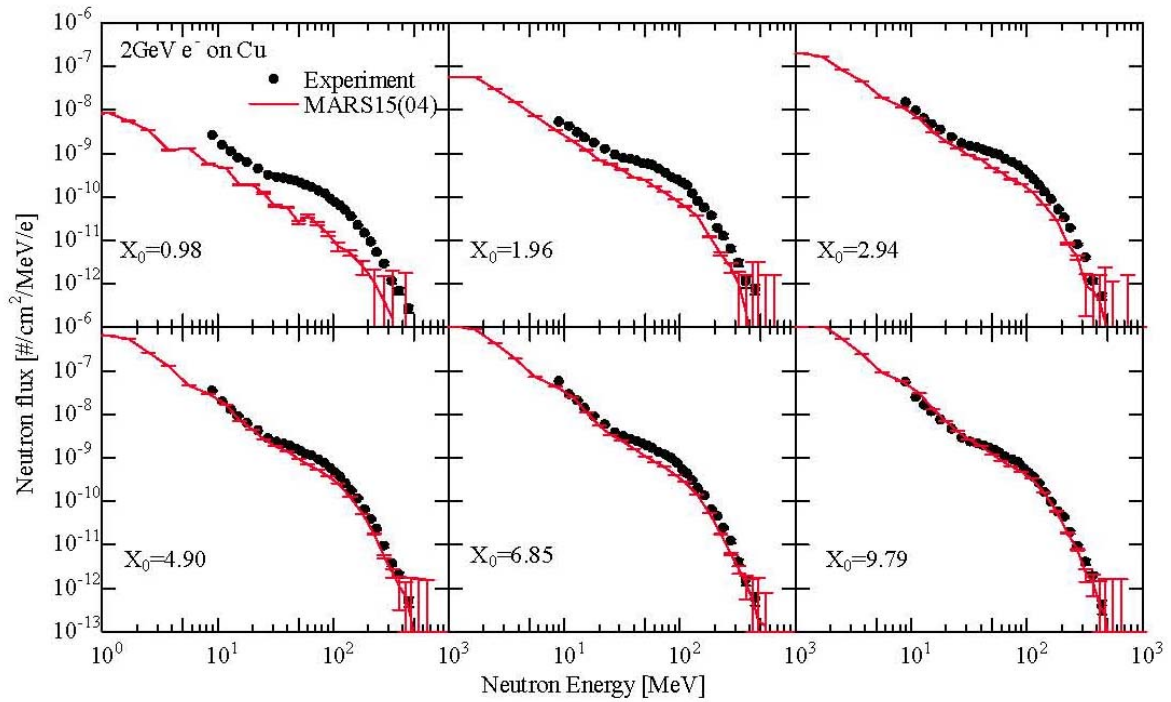
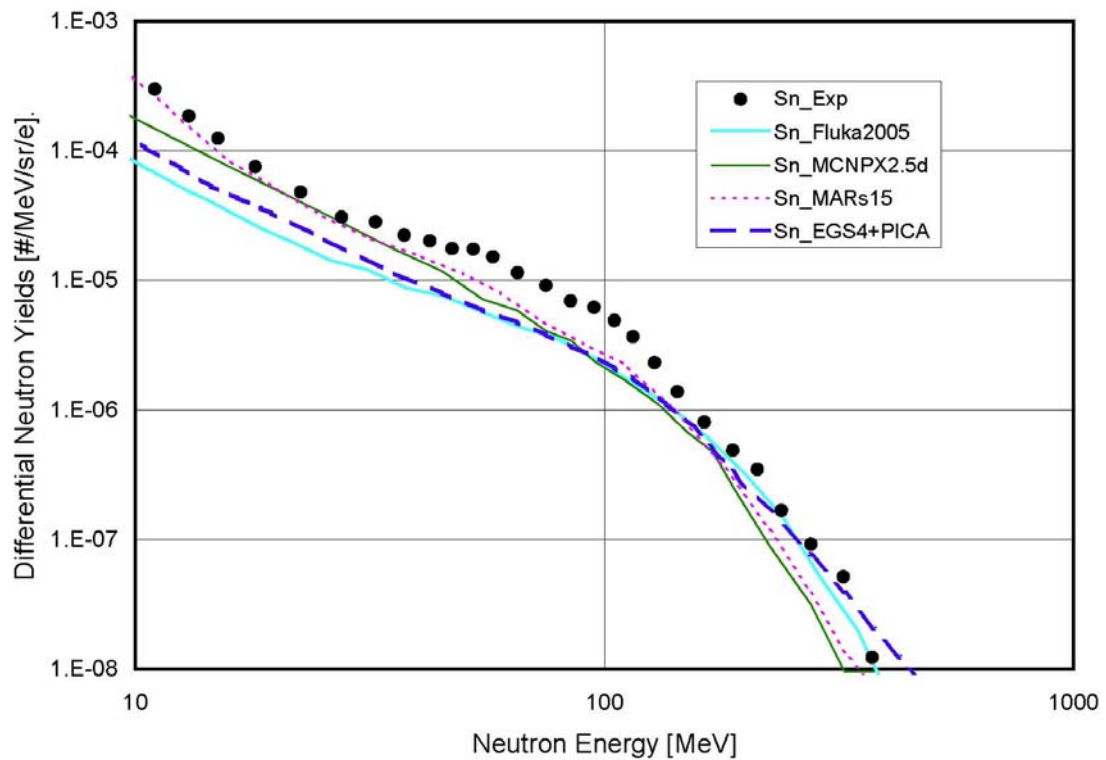
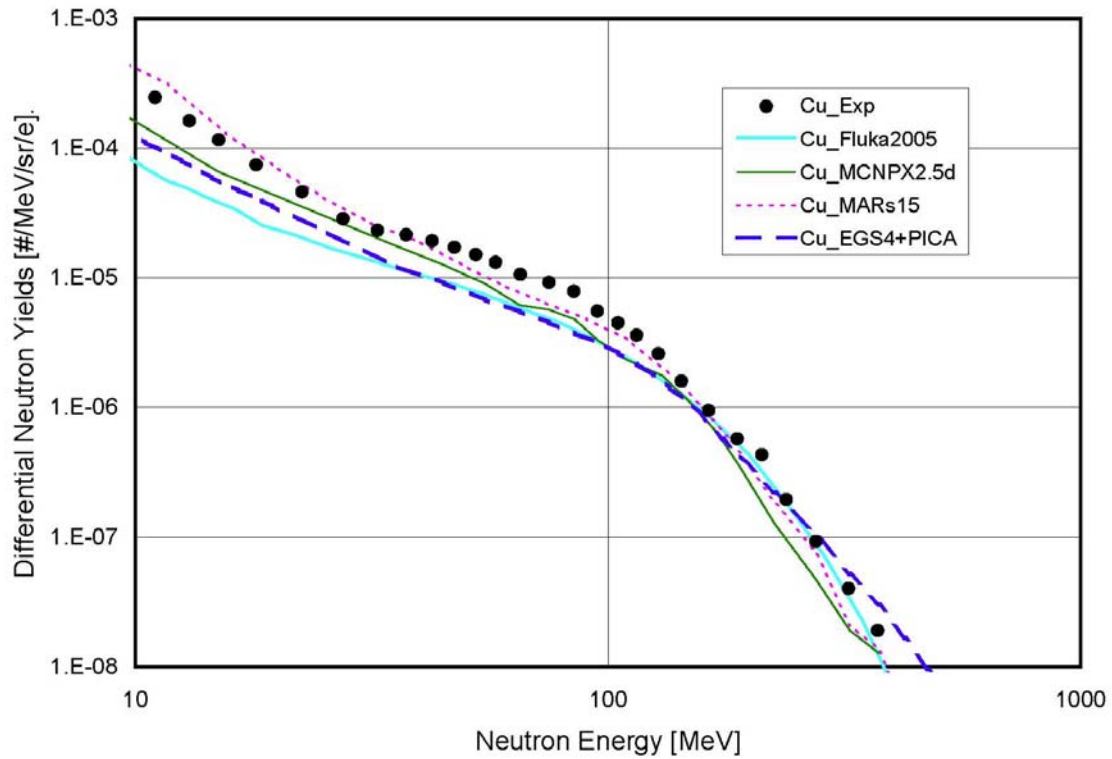
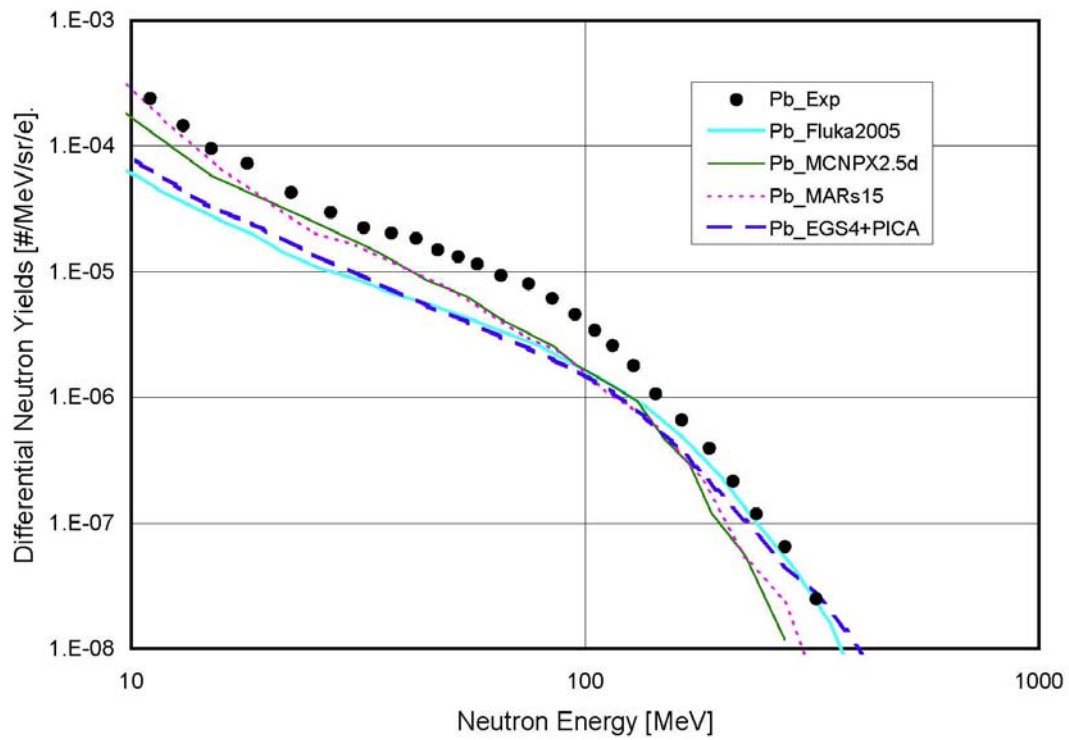
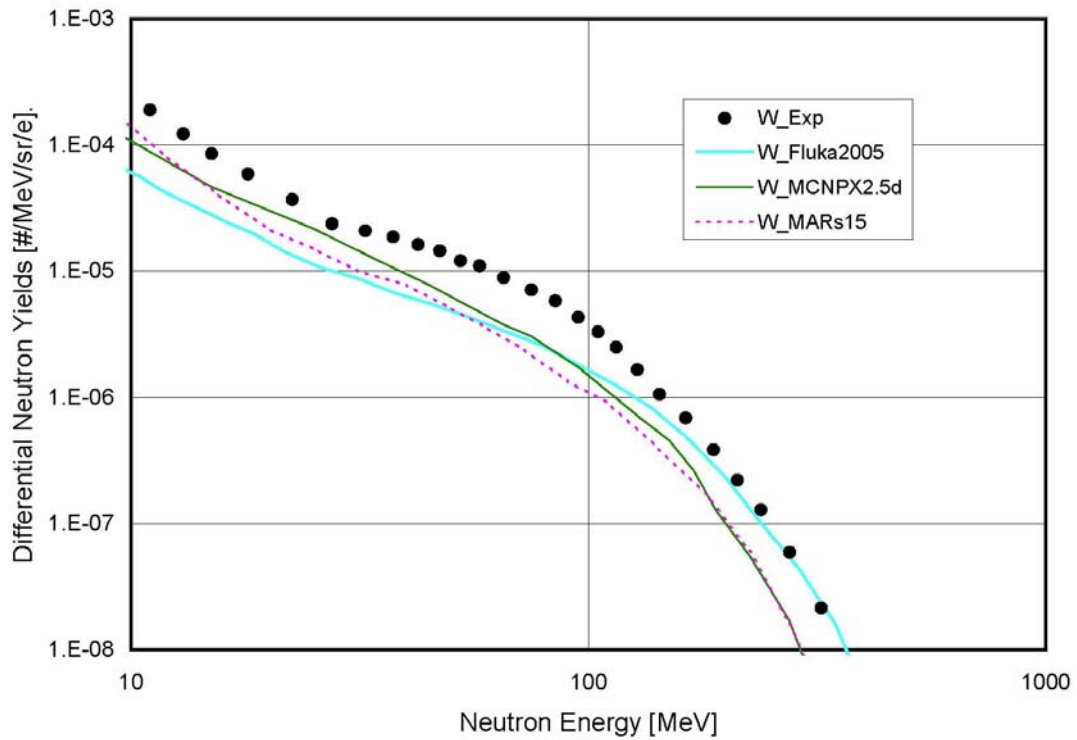


Figure 5(a): Comparison of calculated neutron spectra from 10 Xo-thick Cu and Sn targets using FLUKA (Ver2005), MARS15 (05), MCNPX 2.5d and EGS4+PICA3 with measured one



**Figure 5(b): Comparison of calculated neutron spectra from 10 Xo-thick W and Bi targets using FLUKA (Ver2005), MARS15(05), MCNPX 2.5d and EGS4+PICA3 with measured one**



## **Analysis of the residual radiation field in the proton accelerator facility of the Proton Engineering Frontier Project (PEFP) in Korea**

**Cheol Woo Lee, Young-Sik Cho, Young-Ouk Lee**

Nuclear Data Evaluation Laboratory  
Korea Atomic Energy Research Institute  
Daejeon, Korea

### **Abstract**

*In Korea, the Proton Engineering Frontier Project (PEFP) is building a proton linear accelerator facility with 100 MeV-20 mA. In this study, a radiation field in the accelerator facility of the PEFP was evaluated for the purpose of the radiation shielding using MCNPX code. A facility modelling was performed for the accelerator tunnel building and the accelerator chain, and radiation source terms were evaluated at the outer surface of the equipments in the accelerator chain. With this facility model and radiation source terms, a prompt radiation field was calculated as a dose distribution during an accelerator operation. After shutdown, the activity of radionuclides from the air in the accelerator tunnel building was calculated for estimating the residual radiation field.*

## Introduction

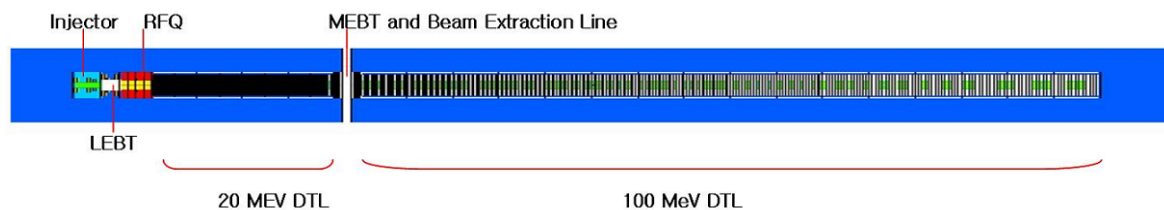
In Korea, the Proton Engineering Frontier Project (PEFP) is building a proton linear accelerator facility with 100 MeV-20 mA. Presently, a 20 MeV proton acceleration beam line has been assembled and the acceleration equipment of 100 MeV has been designed. Because of the high current of the proton beam from this facility, the analysis of the radiation shielding must be performed.

In this study, radiation fields from the accelerator of the PEFP were analysed for the purpose of the radiation shielding. The radiation fields were evaluated in the whole space of the accelerator tunnel building inside with beam losses from the accelerator equipments of the PEFP. The radiation source terms due to beam losses from the accelerator of the PEFP were evaluated in the vicinity of the each component in the beam line for the normal operation. MCNPX code was used in these calculations and the calculations were divided into three steps. In the first step, radiation source terms were calculated with the model of the accelerator equipments. In the second step, the prompt radiation field was evaluated with the radiation source term in the normal operation. In the last step, the activation products in the accelerator tunnel building were evaluated as a residual radiation field [1].

## Facility modelling

The 100 MeV beam line will be set in the accelerator tunnel building. The high-level radiation area (12.5  $\mu\text{Sv/hr}$ ) is formed in the area where is the inside of the accelerator tunnel building during operation. And this area will be limited as a radiation worker area (0.25~12.5 Sv/hr) during over-hole period. Therefore the information on the radiation field in the accelerator tunnel building is required to decide the shielding conditions satisfying the dose limits for each case. In this study, the whole space of the accelerator tunnel building inside is a target for the radiation field calculation. The accelerator tunnel building was modelled with the MCNPX 2.5e. The models in this study are shown in Figure 1.

**Figure 1: 100 MeV Beam line modelling for an accelerator chain of the PEFP**



## Evaluation of the radiation source terms from beam losses

In these beam loss mechanism, beam losses from a chopper and H<sup>-</sup> ion losses on the accelerator of the PEFP were not considered, because PEFP uses a plasma ion source without choppers. Therefore, most of the controlled losses were neglected. And experimental studies (or measurements) for the accelerator chain of the PEFP about each beam losses mechanism has not performed yet. Therefore the information on the particular beam was not applied to the calculation of the source term evaluation. In this study, the maximum beam losses are assumed in the source term evaluation considering a radiation shielding. The most demanding requirement in the design of a proton accelerator chain is to keep the accelerator complex under hands-on maintenance. This requirement implies a hard limit for residual radiation considering worker's exposure limit. The average beam losses must be kept under 1 W/m. Therefore the proton beam losses of 1 W/m are applied in this study [2,4].

Generally, by the way, the radiation fields from beam losses in the accelerator tunnel building should be calculated finally in this study. But, in the geometrical scale of the accelerator tunnel building, the beam line as a radiation source is too thin and long. Large difference in the geometrical scale has difficulties about a calculation efficiency and accuracy for using MCNPX code of the Monte Carlo method. So, the radiation source terms from each component which consisted acceleration beam line were evaluated [5,6].

In this calculation, the proton beam current of the 20 mA and duty factor of the 24% were applied based on design report. And at the outer surface of the each equipment, the energy spectra of the particles escaped from the equipment are calculated. Because the results from this calculation showed that other particles beside neutrons are negligible, the neutron spectra were only considered as a radiation source term. Finally, the information for the produced neutron is written in binary files which will be then applied to the next calculation for the radiation field in the accelerator tunnel building using the SSW/SSR option of the MCNPX code [7].

### Calculation of the dose distribution for the prompt radiation field

Because the dose or radiation spectrum are distributed differently from place to place in the accelerator tunnel building, the information on the whole space in the building is required to analyse shielding condition and evaluate the activation products from air in the building. Therefore, a radiation transport calculation should be performed for the whole space in the accelerator tunnel building. In this study, a radiation transport calculation in the accelerator tunnel building is simulated with a model describing an accelerator tunnel building and the evaluated radiation source terms using the MCNPX code. At the surface of the all components in the accelerator beam line, the evaluated radiation source file is applied using SSR option of the MCNPX code, and the space in the accelerator tunnel building is divided into  $5 \times 1 \times 1$  ( $X \times Y \times Z$ ) m meshes. Finally, the ambient dose values were calculated for each mesh. The average ambient dose for each mesh is calculated using the mesh tally cards of the MCNPX code and with the option for an ambient dose calculation based on the ICRP-74. The calculated dose distribution is shown in Figure 2.

### Evaluation of the radionuclides in the air as a residual radiation

When considering an exposure for a worker, the residual radiation field is important to determine the operating conditions. This residual radiation field is mostly due to the radiations from the activation products in the accelerator tunnel building. Therefore, the radionuclides from activation products were evaluated with the prompt radiation field and geometrical model in this study.

Radionuclides produced in the air with neutron are  $^3\text{H}$ ,  $^7\text{Be}$ ,  $^{11}\text{C}$ ,  $^{13}\text{N}$ ,  $^{15}\text{O}$ , and  $^{41}\text{Ar}$ . These nuclides are produced generally from spallation reactions except for  $^{41}\text{Ar}$ .  $^{41}\text{Ar}$  is produced from  $^{40}\text{Ar}(n,\gamma)^{41}\text{Ar}$  reaction. In this study, all of these radionuclides were considered and the operation time of 8 hours was applied. First, the activity of the produced radionuclides during an operation was calculated. Second, the change of the concentration of the radionuclides was evaluated with consideration for the decay and ventilation.

In the above reactions which produce radionuclides,  $^{41}\text{Ar}$  was only produced under the 20 MeV acceleration beam line. In the 20-100 MeV acceleration beam line,  $^{41}\text{Ar}$  and  $^3\text{H}$  were produced. In this calculation, Eq. (1) was applied.

$$RI = \sum_{i=\text{radionuclide}} \sum_{j=\text{energy}} \left( \frac{\lambda_i}{\lambda_i + \alpha} \right) N_{0i} \phi_j \sigma_{ij} [1 - e^{-(\lambda_i + \alpha)t}] \quad (1)$$

where: RI = Production of the activation products [ $\#/\text{cm}^3$ ]

$\lambda_i$  = Decay constant of the  $i$ th radionuclide [ $1/\text{hr}$ ]

$\alpha$  = Ventilation capacity [ $1/\text{hr}$ ]

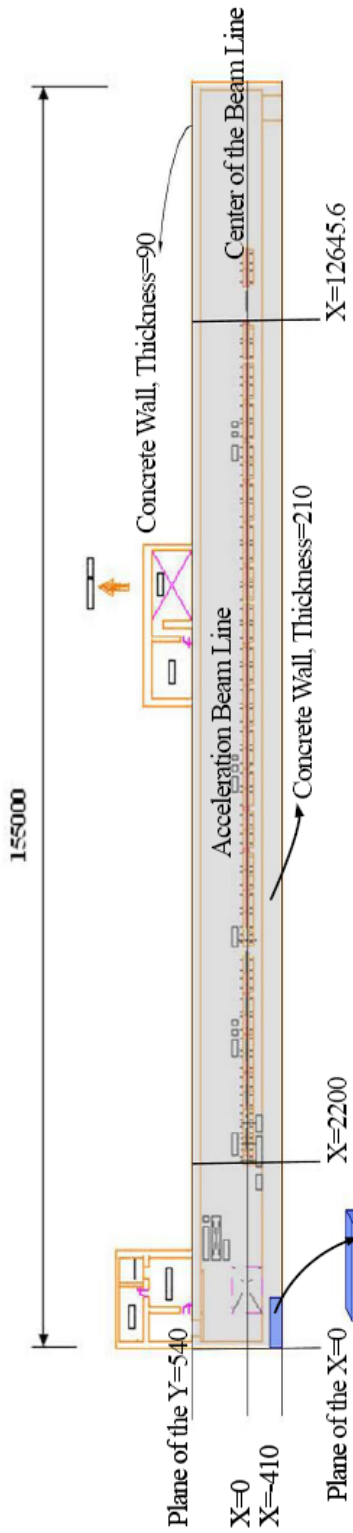
$\alpha = v/V$  ( $v$ : ventilation rate,  $V$ : inside volume of the building)

$N_{0i}$  = Number density of the atom which produces an  $i$ th nuclide [ $\#/\text{cm}^3$ ]

$\phi_j$  = Neutron flux in the  $j$ th energy group [ $\#/\text{cm}^2 \cdot \text{sec}$ ]

$\sigma_{ij}$  = Cross-section producing the  $i$ th radionuclide in the  $j$ th energy group [ $\text{cm}^2$ ]

Figure 2: Ambient dose distribution in the accelerator tunnel building in an accelerator operation

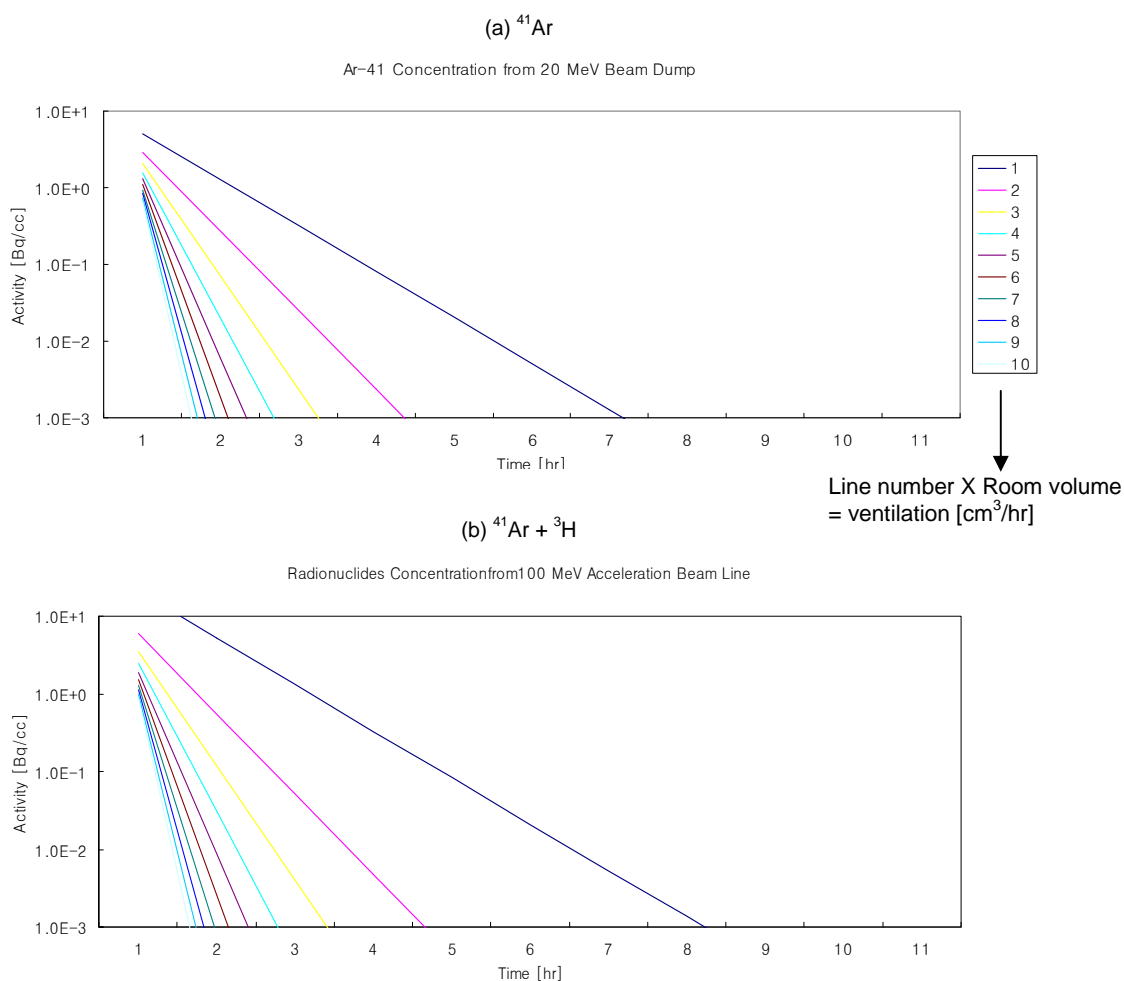


One of the Meshes for Dose Calculation

Coordinate of the Y [cm]	500	1000	1500	2000	2500	3000	3500	4000	4500	5000	5500	6000	6500	7000	7500	8000	8500	9000	9500	10000	10500	11000	11500	12000	12500	13000
550	0.00E+00	0.00E+00	0.00E+00	0.00E+00	0.00E+00	1.02E-01	2.83E-01	1.83E-01	2.69E-01	7.23E-01	3.70E+00	5.13E+00	5.07E+00	6.69E+00	8.97E+00	1.11E+01	1.37E+01	1.67E+01	1.88E+01	1.84E+01	2.22E+01	3.31E+01	3.64E+01	4.78E+01	3.72E+01	1.72E+01
450	2.80E-01	2.89E-00	2.78E-01	4.95E-01	4.88E-01	1.18E-02	1.01E-02	2.81E-02	5.02E-02	1.54E-03	5.10E-03	7.29E-03	8.40E-03	8.68E-03	9.95E-03	9.57E-03	9.69E-03	1.07E-04	1.04E-04	1.04E-04	1.18E-04	1.23E-04	1.28E-04	1.32E-04	1.15E-04	5.88E-03
350	4.48E-01	4.76E-01	4.45E-01	6.31E-01	1.03E-02	2.21E-02	3.06E-02	5.27E-02	1.32E-02	3.39E-02	1.10E-04	1.57E-04	1.75E-04	1.82E-04	1.95E-04	2.40E-04	2.03E-04	2.31E-04	2.11E-04	2.14E-04	2.31E-04	2.48E-04	2.48E-04	2.51E-04	2.15E-04	1.03E-04
250	4.59E-01	7.49E-01	5.82E-01	6.22E-01	6.22E-01	1.24E-02	2.72E-02	5.24E-02	1.05E-03	3.51E-03	1.41E-04	1.99E-04	2.07E-04	2.25E-04	2.39E-04	3.41E-04	2.48E-04	2.57E-04	2.58E-04	2.61E-04	2.88E-04	2.91E-04	3.02E-04	3.04E-04	2.70E-04	1.20E-04
150	1.34E-01	2.94E-01	7.34E-01	1.13E-02	1.69E-02	2.49E-02	3.98E-02	9.08E-02	3.14E-03	2.04E-04	2.84E-04	2.94E-04	3.10E-04	3.10E-04	3.34E-04	5.75E-04	3.47E-04	3.50E-04	3.58E-04	3.60E-04	3.91E-04	4.05E-04	4.10E-04	4.23E-04	3.92E-04	1.52E-04
50	4.03E-01	5.80E-01	8.28E-01	9.13E-01	1.06E-02	1.60E-02	3.05E-02	4.66E-02	9.59E-02	2.55E-03	3.55E-04	4.33E-04	5.01E-04	5.25E-04	5.52E-04	5.75E-04	5.88E-04	5.88E-04	5.88E-04	5.88E-04	5.88E-04	6.71E-04	6.92E-04	7.04E-04	6.74E-04	2.29E-04
-50	4.35E-01	1.23E-01	1.20E-01	1.20E-01	1.20E-01	1.07E-02	1.83E-02	4.25E-02	8.68E-02	2.55E-03	3.67E-04	4.91E-04	5.13E-04	5.02E-04	5.50E-04	3.65E-04	5.89E-04	5.93E-04	5.93E-04	6.03E-04	5.88E-04	6.90E-04	6.96E-04	7.00E-04	6.90E-04	2.31E-04
-150	8.28E-01	1.06E-01	1.06E-01	1.06E-01	1.06E-01	1.77E-02	2.12E-02	4.95E-02	8.70E-02	3.10E-03	2.18E-04	3.09E-04	3.25E-04	3.02E-04	3.47E-04	6.07E-03	3.70E-04	3.70E-04	3.83E-04	3.78E-04	4.21E-04	4.32E-04	4.38E-04	4.54E-04	4.77E-04	1.58E-04
-250	1.18E-01	2.55E-00	3.44E-01	1.48E+00	1.48E+00	5.26E-00	1.62E-01	3.72E-01	6.39E-01	2.61E-02	3.07E-03	4.37E-03	4.81E-03	5.14E-03	5.67E-03	4.70E-01	6.34E-03	6.96E-03	6.65E-03	6.14E-03	7.50E-03	8.84E-03	9.07E-03	1.00E-04	9.26E-03	3.13E-03
-350	0.00E+00	0.00E+00	0.00E+00	0.00E+00	0.00E+00	0.00E+00	1.13E-14	2.01E-15	1.63E-15	2.23E-17	2.64E+00	4.59E+00	6.39E+00	3.11E-01	3.30E-01	7.07E-03	3.50E-01	7.20E-01	5.69E-01	4.77E-01	1.28E+02	2.21E+02	2.41E+02	3.77E+02	3.48E+02	9.97E+02
-450	0.00E+00	7.07E-03	0.00E+00	0.00E+00	0.00E+00	2.88E-01	1.78E-02	5.08E-01	2.37E-01	8.63E-01	1.97E+00	2.45E-01														

In the calculation with Eq. (1), two neutron spectra were applied. First one was the neutron spectrum from 20 MeV beam dump, and second one was the neutron spectrum from 16<sup>th</sup> tank in the 20~100 MeV DTL. Because worker's exposure should keep under the dose limit, they were selected as the neutron spectra have the maximum flux and are most hard. When 20 MeV beam line is set in the PEFP, the <sup>41</sup>Ar is produced in the accelerator building because of the soft neutron spectrum from the low energy acceleration. And in this case the neutron flux is most high at the beam dump. After 100 MeV full beam line is set, <sup>3</sup>H and <sup>41</sup>Ar are produced. In this case, <sup>3</sup>H are produced with high energy neutrons above 10 MeV. Because the neutron spectrum from the 16<sup>th</sup> tank in the 20~100 MeV DTL are most hard, that was selected.

**Figure 3: Radionuclides concentration with various ventilations**



In this study, the cooling time should be evaluated finally to keep under the worker's dose limit. The concentration of the radionuclides changes with decay of the nuclide and ventilation for the air in the building. Because the decay time is the nuclide's own characteristics, a required cooling time is decided with the ventilation. Therefore, various ventilations were applied in this calculation and the changes of the activity of the radionuclide were evaluated for each case. The ventilations were applied as from 1 to 10 multiples of the building inside volume per hour. The produced radionuclides in PEFP were <sup>41</sup>Ar and <sup>3</sup>H. Because <sup>40</sup>Ar(n, $\lambda$ )<sup>41</sup>Ar has high reaction cross-sections for the thermal energy neutrons, it was produced in the whole space in the accelerator tunnel building. But <sup>3</sup>H was produced in a restricted region in during the acceleration for a high energy, above 10 MeV. Figure 3 shows the results from this calculation.

## Conclusion

In this study, modelling for the accelerator chain and accelerator tunnel building of the PEFP has performed and the radiation source terms from beam losses were evaluated. The simulations for radiation transport in the accelerator tunnel building of the PEFP were performed to evaluate the radiation distribution. With evaluated prompt radiation field, the activity of the radionuclide in the air was calculated after shutdown. As a result of this study, the concrete wall thickness of the accelerator tunnel building, based on design value, satisfies the dose limit at the outside of the accelerator tunnel building during the accelerator operation. And the activity of the radionuclides from air in the accelerator tunnel building is possible to keep under the limits after shutdown with cooling time of the five hours and the specific ventilation capacity which ventilates the amount of the air above one multiple of the room volume per hour.

## References

- [1] IAEA, *Radiological Safety Aspect of the Operation of Proton Accelerators*, Technical Reports Series No. 238, International Atomic Energy Agency (1988).
- [2] J.H. Park, C.S. Lee, I.C. Kim, "Test Facility of Proton Beam Utilization of the PEFP at the SUN-AMS Tandem Accelerator", *Journal of the Korean Physical Society*, 44, 1062 (2004).
- [3] L.S. Taylor, et al., *Radiation Protection Design Guidelines for 0.1-100 MeV Particle Accelerator Facilities*, Recommendations of the National Council on Radiation Protection and Measurements (1977).
- [4] J.H. Park, et al., "Development of a Beam Current and Positron Measurement System for the Korea Multipurpose Accelerator (KOMAC)", *Journal of the Korean Physical Society*, 44, 1067 (2004).
- [5] S. Agosteo, et al., "Shielding Calculation for a 250 MeV Hospital-based Proton Accelerator", *Nuclear Instruments and Methods in Physics Research*, A 374, 254 (1996).
- [6] C.W. Lee, Y.U. Lee, Y.S. Cho, "Calculation of Radiation Field for KOMAC with 20 MeV Acceleration Beam Line", *Proceedings on Symposium of the 2005 Korea Nuclear Society* (2005).
- [7] H. Dinter, K. Tesch, D. Dworak, "Studies on the Neutron Field Behind Shielding of Proton Accelerators Part I: Concrete Shielding", *Nuclear Instruments and Methods in Physics Research* A 368, 256 (1996).

## Measurement of neutron total cross-sections at the Pohang Neutron Facility

**Guinyun Kim, A.K.M.M.H. Meaze, Mayeen Uddin Khandaker**

Department of Physics, Kyungpook National University, Korea

**Young Do Oh, Hengsik Kang, Moo-Hyun Cho, In Soo Ko, Won Namkung**

Pohang Accelerator Laboratory, Pohang University of Science and Technology, Korea

**Tae-Ik Ro, Won-Chung Chung**

Department of Physics, Dong-A University, Korea

**Young Ae Kim, Kun Joong Yoo, Young Ouk Lee**

Nuclear Data Evaluation Laboratory, Korea Atomic Energy Research Institute, Korea

### Abstract

*We report the status of the Pohang Neutron Facility which consists of an electron linear accelerator, a water-cooled Ta target, and a 12-m time-of-flight path. We measured the neutron total cross-sections in the neutron energy range from 0.1 eV to few hundreds eV by using the neutron time-of-flight method. A  ${}^6\text{LiZnS(Ag)}$  glass scintillator was used as a neutron detector. The neutron flight path from the water-cooled Ta target to the neutron detector was 12.1 m. The background level was determined by using notch-filters of Co, In, Ta, and Cd sheets. In order to reduce the gamma rays from bremsstrahlung and those from neutron capture, we employed a neutron-gamma separation system based on their different pulse shapes. The present measurements of Ta, Hf, Ag, and Mo samples are in general agreement with the evaluated data in ENDF/B-VI. The resonance parameters were extracted from the transmission data from the SAMMY fitting and compared with the previous ones.*

## Introduction

The Pohang Neutron Facility (PNF) was proposed in 1997 and constructed at the Pohang Accelerator Laboratory on December 1998 [1]. It consists of a 100-MeV electron linac, water-cooled Ta neutron producing target, and an 11-m-long evacuated vertical flight tube leading to the detector location. The electron linac consists of a thermionic RF-gun, an alpha magnet, four quadrupole magnets, two SLAC-type accelerating sections, a quadrupole triplet, and a beam-analysing magnet. The overall length of the linac is about 15 m. The characteristics of PNF are described elsewhere [2].

We report the measured neutron total cross-sections of natural Ta, Hf, and Mo in the neutron energy range between 0.1 eV and 100 eV by using the neutron time-of-flight (TOF) method at the PNF. The results were compared with other measurements and the evaluated data in ENDF/B-VI. The resonance parameters for Ta, Hf, Ag, and Mo isotopes were determined from the fitting of transmission data by using the Multilevel R-Matrix code SAMMY [3].

## Experimental arrangement

The experimental arrangement and data acquisition system for the transmission measurements are described in elsewhere [2]. The target is located in the position where the electron beam hits its centre. The target was composed of ten Ta plates with a diameter of 4.9 cm and an effective thickness of 7.4 cm. This target was set at the centre of a cylindrical water moderator contained in an aluminum cylinder with a thickness of 0.5 cm, a diameter of 30 cm, and a height of 30 cm. The water level in the moderator was 3 cm above the target surface, which was decided based on a measurement of the thermal neutron flux. The neutron guide tubes were constructed by stainless steel with two different diameters, 15 cm and 20 cm, and were placed perpendicularly to the electron beam. The neutron collimation system was mainly composed of  $H_3BO_3$ , Pb and Fe collimators, which were symmetrically tapered from a 10-cm diameter at the beginning to a 5-cm diameter in the middle position where the sample changer was located, to an 8-cm diameter at the end of guide tube where the neutron detector was placed. There was 1.8-m-thick concrete between the target and the detector room. The sample changer consists of a disc with four holes; each hole is 8 cm in diameter, which matches the hole of the collimator in the neutron beam line. The sample changer is controlled remotely by the CAMAC module. The distance between centres of two opposite holes is 31 cm. The transmission samples were placed at the midpoint of the flight path and were cycled into the neutron beam by using the sample changer with four positions. The physical parameters of the samples used in the total cross-section measurements are given in Table 1. A set of notch filters of Co, In, and Cd plates with thickness of 0.5 mm, 0.2 mm, and 0.5 mm, respectively, was also used for the background measurement and the energy calibration.

The neutron detector was located at a distance of 10.81 m from the photo-neutron target. A  ${}^6Li$ -ZnS(Ag) scintillator BC702 from Bicron (Newbury, Ohio) with a diameter of 127 mm and a thickness of 15.9 mm mounted on an EMI-93090 photomultiplier was used as a detector for the neutron TOF spectrum measurement.

During the measurement, the electron linac was operated with a repetition rate of 10 Hz, a pulse width of 1.5  $\mu$ s and the electron energy of 60 MeV. The peak current in the beam current monitor located at the end of the second accelerator section is above 50 mA, which is the same as that in the photo-neutron target.

## Data taking and analysis

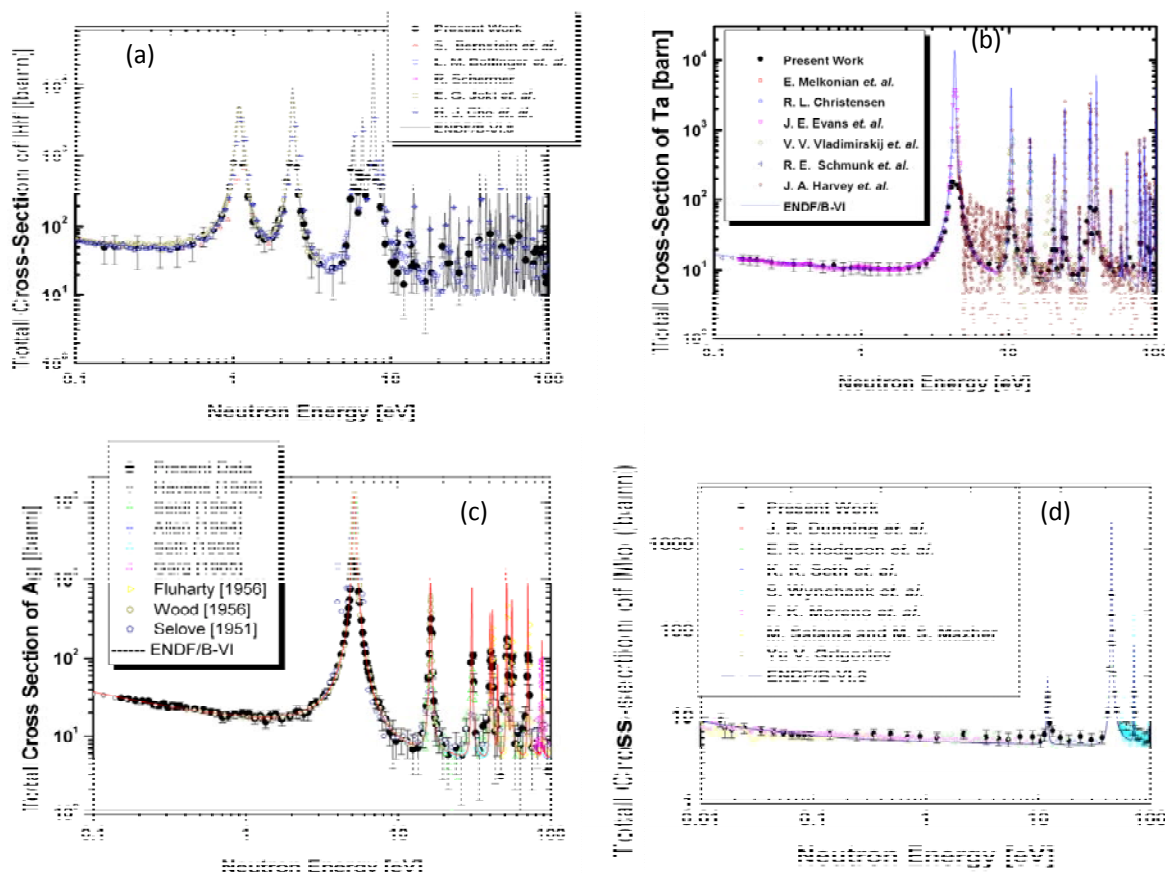
Two different data acquisition systems were used for the neutron TOF spectra measurements: one for the NIM-based system and the other for the CAMAC-based system. The main purpose of the NIM-based system was neutron-gamma separation and the parallel accumulation of the neutron TOF spectra if necessary. The CAMAC-based system consists of a main data acquisition part and a control part of the sample changer. The 10-Hz RF trigger signal for the modulator of the electron linac was used as a start signal of the time digitiser. The details of data acquisition system are described in elsewhere [2].

The measurements were performed with two samples simultaneously. The two other positions of the sample changer were empty to collect the neutron TOF spectra without a sample (open beam). The positions of the samples were chosen in the following sequence: sample 1 – empty – sample 2 – empty. The exposition times for both sample 1 and sample 2 were 15 minutes (9 000 pulses of PNF linac); for each empty position, it was 7.5 minutes. Thus, the durations for the samples were the same as those for the total open beam measurements. The interleaving sequence of free positions of the sample changer was chosen to minimise the influence of slow and/or small variation of the neutron beam intensity. If the beam intensity variations or its drift was fast and/or large, then these partial measurements were excluded from the total statistics. The total data taking times for Ta, Hf, Ag, and Mo were 21.75, 8.5, 65, and 48 hours, respectively, with the same times for the open beams.

**Table 1: Physical parameters of the samples used in the experiment**

Sample	Purity (%)	Size (cm <sup>2</sup> )	Thickness (mm)	Weight (g)
Ta	99.7	10 × 10	0.45	16.60
Hf	99.9	5 × 5	0.5	16.44
Mo	99.9	$\pi \times 3.1 \times 3.1$	3.0	94.00
Ag	99.98	10 × 10	0.5	53.04

**Figure 1: Comparison of the experimental total cross-section of (a) Hf, (b) Ta, (c) Ag and (d) Mo with the other experiments and the evaluated one from ENDF/B-VI in the neutron energy region between 0.01 and 100 eV**



We estimated the background level by using the resonance energies of the neutron TOF spectra of the notch-filters of Co, In and Cd. The magnitude of the background level was interpolated between the black resonances by using the fitting function  $F(l) = a + be^{-l/c}$ , where  $a$ ,  $b$ , and  $c$  are constants and  $l$  is the channel number of the time digitiser.

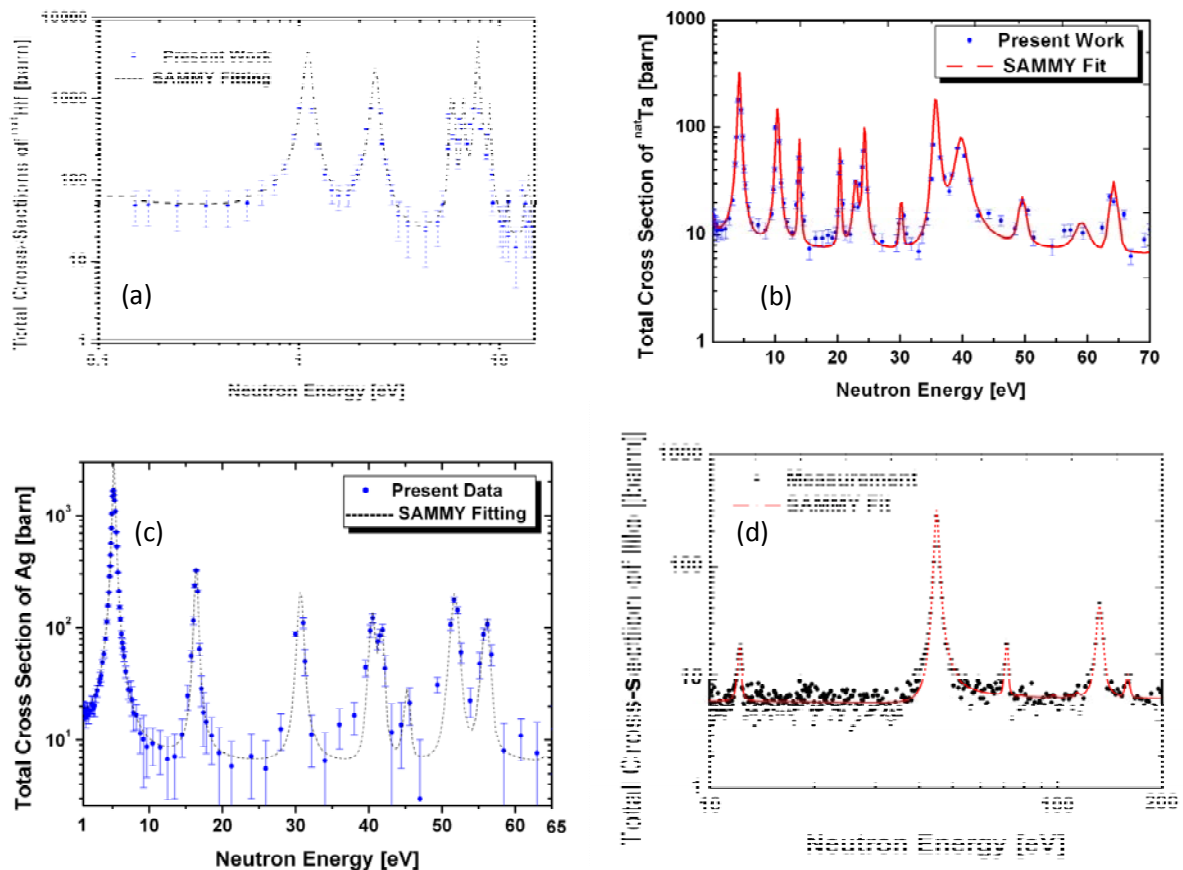
The neutron total cross-section is determined by measuring the transmission of neutrons through the sample. The transmission rate of neutrons at the  $i$ -th group energy  $E_i$  is defined as the fraction of incident neutrons passing through the sample compared to that in the open beam. Thus, the neutron total cross-section is related to the neutron transmission rate  $T(E_i)$  as follows:

$$\sigma(E_i) = -\frac{1}{N} \ln T(E_i) \quad (1)$$

where  $N$  is the atomic density per  $\text{cm}^2$  of the sample. Then, we have calculated the average total cross-sections for the same energy interval.

The total cross-sections of natural Hf and Ta were obtained in the energy range from 0.1 eV to 100 eV by using the neutron TOF method as shown in Figure 1. We only considered the statistical errors for the present measurements because the other sources of uncertainties, which include the detection efficiencies, the geometric factor for the sample, and the other systematic errors, are negligible.

**Figure 2: Comparison of the measured total cross-sections of natural (a) Hf, (b) Ta, (c) Ag, and (d) Mo with the predicted ones from the SAMMY fitting**



## Results and discussion

The present measurements for the neutron total cross-sections of Hf, Ta, Ag, and Mo are compared with the previous data measured by other groups [4-7] and the evaluated data in ENDF/B-VI [8] as shown in Figure 1. The present measurements without any corrections are generally in good agreement with other data and the evaluated ones in the energy range between 0.1 eV and 100 eV.

There are many resonance peaks in the neutron total cross-sections for Hf and Ta. In order to get the resonance parameters of each resonance peak, we fit the transmission data with the SAMMY code [3]. Resolution function  $R(E, E')$  used in this calculation is the convolution of Gaussian and exponential function and its mathematical expression is as follows:

$$R_{GE}(E, E') = \frac{1}{\Delta_E \Delta_G \sqrt{\pi}} \int_{E-\Delta E_S}^{\infty} dE^0 e^{-\frac{(E^0 - (E - \Delta E_S))}{\Delta_E}} e^{-\frac{(E' - E^0)^2}{\Delta_G^2}} \quad (2)$$

where the width of Gaussian resolution function  $\Delta_G$  is given by:

$$\Delta_G = E[aE + b]^2 \quad (3)$$

and the width of exponential resolution function  $\Delta_E$  is given by:

$$\Delta_E = cE^{3/2} \quad (4)$$

The energy shift  $\Delta E_S$  which is automatically determined in the SAMMY, is introduced to locate the maximum of the broadening function at  $E' = E$ . The constant values of  $a$ ,  $b$ , and  $c$  are  $1.3645 \times 10^{-6} \text{ eV}^1$ ,  $9.1281 \times 10^{-6}$ , and  $6.3969 \times 10^{-4} \text{ eV}^{-1/2}$ , respectively. We determined the resonance parameters for Hf, Ta, Ag, and Mo samples from the SAMMY fitting. The measured total cross-section of Hf in the neutron energy range from 0.1 eV to 15 eV was compared with the SAMMY fitting results as shown in Figure 2(a). The SAMMY prediction of total cross-section and the present data are in good agreement with each other with  $\chi^2/N = 0.33$ . In Figure 2(b), the measured total cross-section of natural Ta in the neutron energy range from 0.1 eV to 70 eV was compared with the SAMMY fitting results. The measured neutron total cross-section of natural Ag in the neutron energy range from 1 eV to 65 eV was compared with the SAMMY fitting results as shown in Figure 2(c). The neutron total cross-section of natural Mo in the neutron energy range from 10 eV to 200 eV was fitted by using the SAMMY code as shown in Figure 2(d).

## Conclusion

The Pohang Neutron Facility was constructed as a pulsed neutron facility based on an electron linac for producing nuclear data in Korea. It consists of an electron linac, a water cooled Ta target, and a 12-m long TOF path.

The neutron total cross-sections of natural Hf, Ta, Ag, and Mo samples were measured in the neutron energy region from 0.1 eV to 100 eV by using a  ${}^6\text{Li-ZnS(Ag)}$  scintillator and the neutron TOF method at the Pohang Neutron Facility. The present results are in good agreement with the evaluated data in ENDF/B-VI and the previous measurements. The resonance parameters of Hf, Ta, Ag and Mo isotopes were determined by fitting the transmission data with the SAMMY code.

## Acknowledgements

The authors would like to express their sincere thanks to the staff of the Pohang Accelerator Laboratory for the excellent operation of the electron linac and their strong support. This work is partly supported by the Long-term Nuclear R&D programme through the Korea Atomic Energy Research Institute and by the Science Research Centre (SRC) programme through the Centre for High Energy Physics, Kyungpook National University.

## References

- [1] G.N. Kim, et al., *Proceedings International Conference on Nuclear Data for Science and Technology*, G. Reffo, et al. (Ed.), Trieste, Italy, 19-24 May 1997, p. 556.
- [2] V. Skoy, et al., *J. Korean Phys. Soc.* 41, 314-321 (2002); G.N. Kim, et al., *J. Korean Phys. Soc.*, 43, 479 (2003).
- [3] N.M. Larson, *RSICC Peripheral Shielding Routine Collection SAMMY-M2a (1999): A Code System for Multilevel R-matrix Fits to Neutron Data Using Bayes' Equations (PSR-158, SAMMY-M2a)*, Oak Ridge National Laboratory.
- [4] S. Bernstein, et al., *Phys. Rev.*, 87, 487 (1952); E.G. Joki, et al., *J. Nucl. Sci. Eng.*, 11, 298 (1961); W.M. Moore, *Bull. Am. Phys. Soc.*, 6, 70 (1961); R. Schermer, *AEC Reports to the NCSAG, WASH Progress Report-1031*, 16 (1961); L.M. Bollinger, et al., *Phys. Rev.*, 92, 1527 (1953); H.J. Cho, et al., *Ann. Nucl. Energy*, 27, 1259 (2000).
- [5] E. Melkonian, et al., *Phys. Rev.*, 92, 702 (1953); R.L. Christensen, *Phys. Rev.*, 92, 1509 (1953); J.A. Harvey, et al., *Phys. Rev.*, 99, 10 (1955); J.E. Evans, et al., *Phys. Rev.*, 97, 565 (1955); V.V. Vladimirkii, et al., *Proc. 1<sup>st</sup> Conf. on Peaceful uses Atomic Energy*, Geneva, 4, p. 22 (1955); R.E. Schmunk, et al., *Nucl. Sci. Eng.*, 7, 193 (1960).
- [6] W.W. Havens Jr., *J. Rainwater*, *Phys. Rev.*, 70, 154 (1946); W. Selove, *Phys. Rev.*, 84, 869 (1951); F.G.P. Seidi, et al., *Phys. Rev.*, 95, 476 (1954); R.G. Fluharty, et al., *Phys. Rev.*, 103, 1778 (1956); R.E. Wood, *Phys. Rev.*, 104, 1425 (1956); K.K. Seth, et al., *Phys. Rev.*, 110, 692 (1958); J.B. Garg, et al., *Phys. Rev.*, 137, B547 (1965).
- [7] J.R. Dunning, et al., *Phys. Rev.*, 48, 265 (1935); S. Wynchank, et al., *Phys. Rev.*, 166, 1234 (1968); E.R. Hodgson, et al., *Proceedings of the Physical Society, London*, 65A, 992 (1952); K.K. Seth, et al., *Phys. Rev.*, 110, 692 (1952); F.K. Moreno, et al., *Atomkernenergie*, 31, 42 (1978); M. Salama, et al., *Atomkernenergie*, 45, 282 (1984); Yu.V. Grigoriev, et al., *Ser. Yadernye Konstanty*, 2002, 50 (2002).
- [8] Evaluated Nuclear Data, ENDF/B-VI, Brookhaven Nat. Lab. (2004), [www-nds.iaea.org/point2004/](http://www-nds.iaea.org/point2004/).

## **Session V**

### **Status of computer codes, cross-sections and shielding data libraries**

***Chair: N.V. Mokhov***



## **Status and future plans for the international radiation shielding and dosimetry experiments (SINBAD) database**

**I. Kodeli**

IAEA representative at OECD/NEA Data Bank, France

**E. Sartori**

OECD Nuclear Energy Agency, France

**B.L. Kirk**

RSICC, Oak Ridge National Laboratory, USA

### **Abstract**

*SINBAD is an internationally established set of radiation shielding and dosimetry data relative to experiments relevant in reactor shielding, fusion blanket neutronics and accelerator shielding. In addition to the characterisation of the radiation source, it describes shielding materials and instrumentation and the relevant detectors. The experimental results, be it dose, reaction rates or unfolded spectra are presented in tabular ASCII form that can easily be exported to different computer environments for further use. Most sets in SINBAD contain also the computer model used for the interpretation of the experiment and, where available, results from uncertainty analysis. The set of primary documents used for the benchmark compilation and evaluation are provided in computer readable form. SINBAD is available from RSICC and from the NEA Data Bank.*

## Introduction

SINBAD is an international effort between the OECD/NEA Data Bank (Organisation for Economic Co-operation and Development, Nuclear Energy Agency Data Bank, [www.nea.fr/html/databank/](http://www.nea.fr/html/databank/)) and ORNL/RSICC (Oak Ridge National Laboratory, Radiation Safety Information Computational Centre [www-rsicc.ornl.gov/](http://www-rsicc.ornl.gov/)). Co-operation from many organisations, authors, and benchmark analysts (see Table 1) have helped SINBAD become a “living database” which now incorporates 77 benchmark experiments. The database is divided into three main parts covering both low and intermediate energy particle applications:

- reactor shielding, pressure vessel dosimetry (37 experiments);
- fusion blanket neutronics (27);
- accelerator shielding (13).

The accelerator shielding part, although in number of experiments still smaller than the reactor shielding and fusion areas, was recently increased by several new experiments, and others are to be added in this and the coming years. Among experiments in preparation are also the aviation route dose and medical experiments.

**Table 1: Contributing institutions**

AEA Technology (AEAT), United Kingdom
Austrian Research Centre Seibersdorf (ARCS)
CERN SPS (Super Proton Synchrotron), Geneva, EC
Commissariat à l'Energie Atomique (CEA), France
EC Joint Research Centre (ISPRA), EC
Ente per le Nuove Tecnologie, L'Energia e l'Ambiente (ENEA),
Forschungszentrum Karlsruhe (FZK), Germany
Forschungszentrum Rossendorf e.V. (FZR), Germany
Georgia Institute of Technology (GIT), USA
High Energy Accelerator Research Organisation (KEK), Japan
Technical University of Budapest (TUB), Hungary
Institute of Physical & Chemical Research (RIKEN), Japan
Institute of Physics & Power Engineering (IPPE), Obninsk, RF
Interfaculty Reactor Institute (IRI), Delft, The Netherlands
Japan Atomic Energy Institute (JAERI), Japan
Jozef Stefan Institute (IJS), Slovenia
Lawrence Berkeley National Laboratory (LBNL), USA
Los Alamos National Laboratory (LANL), USA
Moscow Engineering-Physics Institute (MEPhI),
Michigan State University (MSU), USA
National Institute of Radiological Sciences (NIRS) of Japan
National Institute of Standards and Technology, Gaithersburg (NIST), USA
United States Nuclear Regulatory Commission (NRC),
Oak Ridge National Laboratory (ORNL), USA
Paul Scherrer Institute (PSI), Switzerland
Rutherford Appleton Laboratory (RAL), USA
Russian Federal Nuclear Centre-VNIITF (RFNC),
Research Centre Mol (SCK-CEN), Belgium
Scientific & Engineering Centre for Nuclear and Radiation Safety (SEC NRS), RF
Stanford Linear Accelerator Centre (SLAC), USA
Ente per le Nuove Tecnologie, L'Energia e l'Ambiente (ENEA),
Forschungszentrum Karlsruhe (FZK), Germany
Technische Universität Dresden (TUD), Germany
Tohoku University, Japan
University of Illinois, USA
University of Osaka, Japan
University of Pavia, Italy
University of Tokyo, Japan

**Table 2: Accelerator shielding experiments in SINBAD**

Title	Shielding material	Projectile	Measured quantity	Organisation
Transmission Through Shielding Materials of Neutrons and Photons Generated by 52 MeV Protons	C (up to 64.5 cm thick), Fe (up to 57.9 cm), H <sub>2</sub> O (up to 101 cm), concrete (up to 115 cm)	52 MeV protons on C target	Neutron and gamma spectra by NE213 scintillation	FM cyclotron of University of Tokyo
Transmission Through Shielding Materials of Neutrons and Photons Generated by 65 MeV Protons	Concrete, iron, lead and graphite (10 to 100 cm thick)	65 MeV protons on Cu target	Neutron and gamma spectra by NE213 scintillation	AVF cyclotron, Osaka University
TIARA 40 and 65 MeV Neutron Transmission Through Iron, Concrete and Polyethylene	Fe (130 cm thick), concrete (up to 200 cm), and polyethylene (up to 180 cm)	43 and 68 MeV protons on Li7 target	Neutron spectra and reaction rates by BC501Ascintillator, Bonner ball counter, fission counters, TLD and SSNTD	TIARA/JAERI
ROESTI I and III	Fe and Pb (100 cm thick)	200 GeV/c positive hadrons (2/3 protons and 1/3 positive pions)	In, S, Al, C activation detectors, radio-photoluminescent dosimeters (RPL)	CERN SPS (Super Proton Synchrotron)
ROESTI II	Fe (100 cm thick)	24 GeV/c protons	In, S, Al, C activation detectors, RPL	CERN PS (Proton Synchrotron)
RIKEN Quasi-monoenergetic Neutron Field in 70-210 MeV Energy Range		70-210 MeV protons on <sup>7</sup> Li target	TOF neutron spectra (NE213 scintillator)	RIKEN
HIMAC He, C, Ne, Ar, Fe, Xe and Si ions on C, Al, Cu and Pb targets	C, Al, Cu and Pb targets	100-800 MeV/nucleon He, C, Ne, Ar, Fe, Xe and Si ions	Angular neutron spectra by NE213 and NE102A scintillators	HIMAC/NIRS
HIMAC/NIRS High Energy Neutron (up to 800 MeV) Measurements in Iron	Fe (up to 100 cm)	400 MeV/nucleon C ions on Cu target	Neutron spectra by Self-TOF, NE213	HIMAC/NIRS
HIMAC/NIRS High Energy Neutron (up to 800 MeV) Measurements in Concrete	Concrete (up to 250 cm)	400 MeV/nucleon C ions on Cu target	Neutron spectra by Self-TOF, NE213, Bi and C activation detectors	HIMAC/NIRS
BEVALAC Experiment with Nb Ions on Nb & Al Targets	Nb (0.51 and 1 cm thick) and Al (1.27 cm thick)	272 and 435 MeV/nucleon Nb ions	Angular neutron spectra by NE-102 scintillator	LBNL
MSU experiment with He and C ions on Al target	Al (13.34 cm)	155 MeV/nucleon He and C ions	Angular neutron spectra by TOF method (BC-501 or NE213), charged particles	National Superconducting Cyclotron Laboratory (NCSL) at MSU
PSI - High Energy Neutron Spectra Generated by 590-MeV Protons on Pb Target	Pb target (60 cm)	590 MeV protons	Angular proton and neutron spectra by TOF method (NE213)	Swiss Institute for Nuclear Research, PSI
ISIS Deep Penetration of Neutrons Through Concrete and Iron	Concrete (120 cm) and Fe (60 cm)	800 MeV protons on Ta target	C, Bi, Al, In <sub>2</sub> O <sub>3</sub> activation detectors, neutron and gamma dose meters	ISIS, RAL, UK
TEPC-FLUKA Comparison for Aircraft Dose		Co60 (photons), 0.5 MeV neutron source, AmBe mixed source, CERN/CERF (120 GeV protons & pions on Cu target)	Neutron and photon absorbed dose by TEPC	ARC Seibersdorf Research GmbH

SINBAD is available at no charge from RSICC and from the NEA Data Bank. Since its beginnings in 1996 there have been many different users, including US, European, and Japanese establishments, government programmes, universities, and private companies. SINBAD was distributed to 67 research and industry establishments world wide.

**Table 3: SINBAD accelerator benchmarks – work in progress (2006 and following years)**

Title	Organisation
Transmission of Medium Energy Neutrons Through Concrete Shields	AVF Osaka University
Neutron Production from Thick Target of C, Fe, Cu, and Pb by 30- and 52-MeV Protons	INS Tokyo University
68 MeV Proton on Thick Cu target	JAERI
Neutron Yields from Stopping-length C, Al, Fe and Depleted U Targets for 256-MeV Protons	LAMPF LANL
Neutron Angular and Energy Distributions from 710-MeV Alphas Stopping in H <sub>2</sub> O, C, Steel and Pb	SREL (1980)
Photoproduction of High-energy Neutrons in Thick Lead Targets Irradiated by 150 to 270 MeV Electrons	e-Linac, University of Mainz (1973)
Secondary Neutron Fluxes Inside and Around Iron Beam Stop Irradiated by 500 MeV Protons	p-synchrotron KEK
Reaction Rate Distribution Inside Thick Concrete Shield Irradiated by 6.2 GeV Protons	Bevatron (LBL)
Radioactivity Induced by 2.83 and 24 GeV Protons and Spallation Neutrons Using AGS Accelerator	Alternative Gradient Synchrotron at BNL
Shielding Experiment Using 4 m Concrete at KENS/KEK 500 MeV Proton Accelerator Facility	KENS/KEK
Cosmic Ray Induced Neutron Spectrum at the Summit of the Zugspitze 2660m & Chacaltaya 5240m	GSF, Neuherberg
TOF Neutron Spectra at Angles 0 to 110 deg. and Radioactivity Induced in the Accelerator Material (Li, Be, Cu, C, Al, etc.) for 25-40 MeV Deuterons	Tohoku University AVF Cyclotron
Neutron Transmission Spectra from 20cm Iron Slab, D <sub>2</sub> O( <sup>3</sup> He,xn) Reaction at 40 MeV	Fast Neutron Facility of NPI Rez
Yields of Residual Product Nuclei Produced in Thin Targets Irradiated by 100-2600 MeV Protons	ITEP, Moscow
SLAC Experiment Using 28.7 GeV Electrons	SLAC
Neutron Spectra Behind Concrete and Fe of 120 GeV/c Hadron Beam	CERF/CERN
Response of Bonner Sphere Spectrometer to Charged Hadrons	CERN
Induced Radioactivity in High-energy Accelerators	CERF/CERN

## Recent developments

The objective of the SINBAD database [1,2] is to store and make available the information on high quality benchmark experiments for validation of radiation transport codes and nuclear data. A short description of accelerator shielding relevant experiments included in the present version of SINBAD is given in Table 2. New benchmark experiments are regularly added to the database, and the existing data are updated with feedback received from the users and when supplementary information becomes available. A list of experiments which are planned to be included in the near future is given in Table 3.

The ANS-6 standard on formats for benchmark problem description has been followed. SINBAD data include benchmark information on: i) the experimental facility and the source; ii) the benchmark geometry and composition; iii) the detection system, measured data, and an error analysis. A full reference section is included with the data. Relevant graphical information, such as experimental geometry or spectral data, is included. All information that is compiled for inclusion with SINBAD has been verified for accuracy and reviewed by two scientists. The set of primary documents used for the benchmark compilation and evaluation are provided in computer readable form.

## Conclusions

Information on some valuable shielding experiments has been saved along with the primary documents. Many new experiments have been added in recent years, and SINBAD incorporates at present over 70 benchmark experiments, 13 of them covering accelerator applications. Further data is being processed and much data is waiting to be processed. These experiments have been identified of being of high relevance for validation of radiation transport and shielding methods and codes. Close co-operation with other projects like the Expert Group on Shielding Aspects for Accelerators, Targets and Irradiation Facilities (SATIF) was established.

SINBAD is available from RSICC and from the NEA Data Bank.

## Acknowledgements

The NEA Data Bank would like to thank the following persons for their input and valuable work to process the experiments into SINBAD: Takashi Nakamura, Noriaki Nakao and Alberto Fassò.

## References

- [1] OECD NEA Data Bank SINBAD, [www.nea.fr/html/science/shielding/sinbad/sinbadis.htm](http://www.nea.fr/html/science/shielding/sinbad/sinbadis.htm).
- [2] Radiation Safety Inf. Computational Centre (RSICC), [www-rsicc.ornl.gov/rsiccnew/BENCHMARKS.htm](http://www-rsicc.ornl.gov/rsiccnew/BENCHMARKS.htm).



## **Update on recent computer codes and data libraries of interest to SATIF – Status: May 2006**

**H. Henriksson,<sup>1</sup> I. Kodeli,<sup>1,2</sup> E. Sartori,<sup>1</sup> B.L. Kirk<sup>3</sup>**

<sup>1</sup>OECD/NEA Data Bank, Issy les Moulineaux, France

<sup>2</sup>IAEA, Vienna, Austria

<sup>3</sup>Radiation Safety Information Computational Centre (RSICC)  
Oak Ridge National Laboratory (ORNL), Oak Ridge, USA

### **Abstract**

*The OECD Nuclear Energy Agency Data Bank (NEA DB) and the ORNL Radiation Safety Information Computational Centre (RSICC) acquire sets of computer codes, basic nuclear data and integral experiments data relevant for accelerator shielding and dosimetry applications. The following summarises those tools and data that have been released recently.*

## Introduction

The three main components required for modelling radiation shields and radiation fields around accelerator and their targets, and validating the modelling tools are:

1. basic nuclear data, derived application data libraries, group constants, continuous energy data;
2. computer codes for different accelerator shielding and dosimetry modelling aspects;
3. integral experiments database for validation of the combined use of 1 and 2.

## Scattering cross-section data at cryogenic temperatures

An inquiry concerning the need for cryogenic temperature neutron interaction cross-sections data was sent out to the SATIF members. The needs expressed are summarised in Table 1.

Efforts devoted to developing or improving thermal scattering data for cryogenic temperatures have recently been carried out in several institutes. A longstanding expertise and experience has accumulated at the Institut für Kernenergetik und Energiesysteme (IKE), University of Stuttgart [1], who have produced a number of these in addition to those required for neutron moderators at room temperature and nuclear reactor relevant temperatures. Recently a new series has been made available, listed in Table 2. These are provided in the standard ENDF-6 format and in the ACE format, used for continuous energy Monte Carlo applications. Cross-section libraries can be produced also for deterministic approaches through the use of the NJOY computer code [2]. It should be noted that for very cold temperatures special care must be taken in processing the data and occasionally patches need to be applied to the processing code.

A list of other available cryogenic temperature scattering data was collected, and some of the present work in this field identified in Table 3.

Work is progressing on measurements of scattering at cryogenic temperatures at the Paul Scherrer Institute in Switzerland (CD<sub>4</sub> solid, O solid), at Indiana University (CH<sub>4</sub> solid, O solid), some further data was produced or is being prepared at IKE Stuttgart (He liquid, Bi, Pb).

**Table 1: Request for cryogenic cross-sections**

Material	T = 1.8 K	T = 4.2 K	T = 5-10 K	T = 87 K	Requester
Argon				87	CERN, SLAC, FNAL
H (CH <sub>2</sub> bound)				87	CERN, SLAC, FNAL
Aluminium	1.8	4.2	10	87	CERN, SLAC, FNAL, PSI
Iron	1.8	4.2		87	CERN, SLAC, FNAL
Pb	1.8	4.2		87	SLAC
Ceramic*	1.8	4.2			FNAL
Copper	1.8	4.2			FNAL
Epoxy*	1.8	4.2			FNAL
G10*	1.8	4.2			FNAL
Helium	1.8	4.2			FNAL
Niobium	1.8	4.2			FNAL
Tin	1.8	4.2			FNAL
Titanium	1.8	4.2			FNAL
Deuterium-solid			5-10		PSI
Zirconium			10		PSI
Oxygen			5-10		PSI
CH <sub>4</sub> -solid			5-10		PSI
H <sub>2</sub> O (ice)					SLAC

\* Experimental data is required to estimate these cross-sections

**Table 2: Cold S( $\alpha,\beta$ ) data recently released by IKE to the OECD/NEA/Data Bank**

	Material	MAT*	Temperatures (K)	ID ACE* files
<b>Liquid hydrogen and deuterium for the two modifications: ortho and para ID ACE* files</b>	Para hydrogen	2	14, 16 and 20.38	pH.00t pH.01t pH.03t
	Ortho hydrogen	3	14, 16 and 20.38	oH.00t oH.01t oH.03t
	Para deuterium	12	19 and 23.65	pD.00t pD.01t
	Ortho deuterium	13	19 and 23.65	oD.00t oD.01t
<b>H in polyethylene (CH<sub>2</sub>)</b>	H in CH <sub>2</sub>	37	87, 293.6 and 350	poly.01t poly.03t poly.04t
<b>Liquid argon</b>	18-Ar	18	87	argon.01t
<b>Aluminium face centred cubic lattice</b>	13-Al-27	61	20, 77, 87, 100, 293.6, 400	al.00t al.01 al.05t

\* MAT numbers for the ENDF files and IDs for ACE (MCNP continuous energy data libraries)

**Table 3: Cold S( $\alpha,\beta$ ) data identified as having been produced or available**

Material	Temperature (K)	Source
ch4-s (solid methane)	22	ENDFB/VI
ch4-l (liquid methane)	100	ENDFB/VI
D-ortho (liquid ortho deuterium)	19	ENDFB/VI
D-para (liquid para deuterium)	19	ENDFB/VI
H-ortho (liquid ortho hydrogen)	20	ENDFB/VI
H-para (liquid para hydrogen)	20	ENDFB/VI
H <sub>2</sub> O (solid)	20, 77, 113.2, 165.2, 218.2, 248.8, 273	IKE
H <sub>2</sub> O (liquid)	273.2, 278.2, 293.6, 308.6	IKE
Aluminium	20, 100, 293	IKE
Beryllium	100, 300	IKE
Magnesium	20, 100, 296, 773	CEA/IKE
H-para/ortho – liquid / gas	14, 16, 20.38/ 20.4, 25	IKE
D-para/ortho –liquid / gas	19, 25	IKE
CH <sub>4</sub> solid	31, 57, 77, 89	IKE

### Updated codes and data libraries released since SATIF-7

Tools available at the NEA DB and RSICC and relevant for accelerator shielding and dosimetry analysis accelerator analytical tools released since the last SATIF7 meeting are briefly described in the following. Some of these tools are not specific to accelerator applications but could be useful in lower-energy transport analysis of particles generated from primary and secondary reactions within the accelerator target or shield. More detailed information can be found by searching the RSICC and NEA DB web pages.

#### **Codes and data released to the NEADB < <http://www.nea.fr/html/dbprog/search.htm> >**

DWBA05/DWBB05 NEA-1209/07: Elastic and inelastic nuclear scattering described by a two-body interaction which can depend on the nuclear density. DWBB05 allows to compute any observable for any non zero-spin target, combining the results obtained by DWBA05 for different spin transfers. The distorted wave Born approximation is used to describe the inelastic scattering on a zero-spin target to a state known by its particle-hole description. Besides the optical model, DWBA05 includes a fully microscopic non local optical model obtained with the description of the target by its occupation numbers and with the two-body interaction for the initial and final distorted waves.

ECIS-03 NEA-0850/16: Coupled Channel, Statistical Model, Schrödinger and Dirac Equation, Dispersion Relation. ECIS uses a sequential iteration method for solving the coupled differential equations arising in nuclear model calculations. It also performs parameter searches to fit calculated results to experimental data. It can be used for a range of models, e.g. first or second order harmonic or a harmonic vibrational model, symmetric or asymmetric rotational model, with a similar range of interaction potentials. It includes spin-orbit deformation.

TRIPOLI-4.3.3 NEA-1716/02: TRIPOLI 4.3 solves the transport equation for neutral particles in general three-dimensional geometrical configurations. Neutron, photon, coupled neutron photon transport with fixed sources both time dependent and time independent; critical problems without fixed source, research of multiplication factor due to fission and determination of neutron flux in fundamental mode; neutron sub-critical problems with fixed sources and multiplication by fission, and -electron-photon cascade showers can be modelled using the Monte Carlo method.

HEPROW NEA-1666/02: unfolds pulse height spectra for use in spectral neutron or photon fluence determination. The Bayes theorem and the maximum entropy method are used.

UMG 3.3 NEA-1665/03: UMG (Unfolding with MAXED and GRAVEL) is a package of seven programs written for the analysis of data measured with spectrometers that require the use of unfolding techniques.

SATIF/CYCLO-RADSAFE NEA-1694/03: Database contains reports on health physics and radiological safety aspects of cyclotron within the energy range 10-250 MeV

BULK-I NEA-1727/01: BULK-I is a tool for calculating neutron and photon effective dose rates after penetrating through concrete or two layers with iron and concrete in a medium energy range proton accelerator facility (energies from 50 to 500 MeV). This tool is also capable of radiation shielding calculations considering various proton energies and proton beam directions like proton beam treatment facilities.

GRTUNCL-3D/R-THETA-Z NEA-1690/01: The GRTUNCL code was converted to compute the uncollided fluence at each spatial in an R-theta-Z grid and to generate the associated distributed first-collision source moments for use as a distributed source in the TORT three-dimensional discrete ordinates computed code.

MVP/GMVP II NEA-1673/02: MVP/GMVP can solve eigenvalue and fixed-source problems. The multi-group code GMVP can solve forward and adjoint problems for neutron, photon and neutron-photon coupled transport. The continuous-energy code MVP can solve only the forward problems. Both codes can also perform time-dependent calculations.

SRNA-2K5 IAEA1382/03: SRNA-2K5 performs Monte Carlo transport simulation of proton in 3-D source and 3-D geometry of arbitrary materials. The proton transport based on condensed history model, and on model of compound nuclei decays that creates in non-elastic nuclear interaction by proton absorption.

PENELOPE2006 NEA-1525/12: PENELOPE performs Monte Carlo simulation of coupled electron-photon transport in arbitrary materials and complex quadric geometries. A mixed procedure is used for the simulation of electron and positron interactions (elastic scattering, inelastic scattering and bremsstrahlung emission), in which "hard" events (i.e. those with deflection angle and/or energy loss larger than pre-selected cut-offs) are simulated in a detailed way, while "soft" interactions are calculated from multiple scattering approaches. Photon interactions (Rayleigh scattering, Compton scattering, photoelectric effect and electron-positron pair production) and positron annihilation are simulated in a detailed way. (PENELOPE-2006 release in July 2006)

SUSD3D NEA-1628/02: SUSD3D calculates sensitivity coefficients and standard deviation in the calculated detector responses or design parameters of interest due to input cross-sections and their uncertainties. One-, two- and three-dimensional transport problems can be studied. Several types of uncertainties can be considered, i.e. those due to: i) neutron/gamma multi-group cross-sections, ii) energy-dependent response functions; iii) secondary angular distribution (SAD) or secondary energy distribution (SED) uncertainties.

### **Codes released to RSICC < <http://rsicc.ornl.gov/> >**

PSR-532/CEM03.01: Monte-Carlo code system to calculate nuclear reactions in the framework of the improved cascade-exciton model. CEM03.01 is the latest in a series of codes including CEM2k+GEM2, CEM97, and CEM95.

CCC-724/COG Version 10: Monte Carlo radiation transport code system which provides accurate answers to complex shielding, criticality, and activation problems. COG is fully 3-D, uses point-wise cross-sections and exact angular scattering, and allows a full range of biasing options to speed up

solutions for deep penetration problems. COG can compute gamma-ray doses due to neutron-activated materials, starting with just a neutron source and can solve coupled problems involving neutrons, photons, and electrons.

CCC-730 / MCNP/MCNPX: Contains the LANL MCNP5 1.40 and MCNPX 2.5.0. It also includes data libraries and a new version of VISED for use with MCNP5. MCNP5 is a general purpose Monte Carlo N-particle code that can be used for neutron, photon, electron, or coupled neutron/photon/electron transport, including the capability to calculate eigenvalues for critical systems. MCNPX is a general purpose Monte Carlo radiation transport code that tracks nearly all particles at nearly all energies. MCNPX 2.5.0 is based on MCNP4C3 merged with LAHET to extend the code to higher energies and more particle types.

CCC-707/PARTISN 4.00: Code system to solve the linear Boltzmann transport equation for neutral particles using the deterministic ( $S_N$ ) method. PARTISN (PARallel, TIme-dependent SN) solves both the static (fixed source or eigenvalue) and time-dependent forms of the transport equation in forward or adjoint mode. Vacuum, reflective, periodic, white, or inhomogeneous boundary conditions are solved. General anisotropic scattering and inhomogeneous sources are permitted. PARTISN solves the transport equation on orthogonal (single level or block-structured AMR) grids in 1-D (slab, two-angle slab, cylindrical, or spherical), 2-D (X-Y, R-Z, or R-T) and 3-D (X-Y-Z or R-Z-T) geometries.

CCC-430/EDMULT 6.4: EDMULT evaluates depth dose distributions produced by plane parallel electron beams normally incident on one to six layer slab absorbers. EDMULT is based on an analytic expression of the depth dose curve in semi-infinite medium and a simple model of electron penetration through a multilayer absorber. The effect of the different medium beyond an interface is accounted for by the difference of backscattering, which is evaluated by considering the branching of electron beam into transmitted and backscattered components.

CCC-658/VIM 4.0: Continuous energy neutron and gamma-ray transport code system that runs under Linux on personal computers. This release also includes additional libraries from JENDL 3.2 and a code that plots a 2-D slice from VIM input files. VIM solves the steady-state neutron or photon transport problem in any detailed 3-D geometry using either continuous energy-dependent ENDF nuclear data or multi-group cross-sections. Neutron transport is carried out in a criticality mode, or in a fixed source mode (optionally incorporating subcritical multiplication). Photon transport is simulated in the fixed source mode.

DLC-220/HILO2K: Coupled 83-neutron, 22-photon group cross-sections for neutron energies up to 2 GeV. HILO2k is a new high-energy neutron and photon transport cross-section library containing neutron cross-sections to 2 GeV and photon cross-sections to 20 MeV and is intended for use in multidimensional deterministic transport codes. It represents the culmination of work directed at updating and extending the DLC-119/HILO86 transport cross-section library developed at Oak Ridge National Laboratory (ORNL) in the mid 1980's.

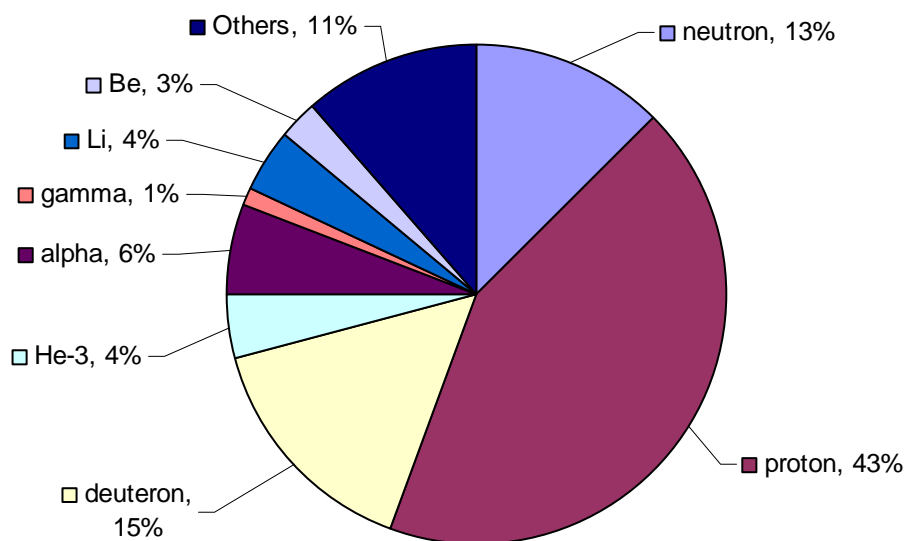
CCC-721/GRTUNCL3D: GRTUNCL3D generates uncollided flux and first collision source distributions for the three-dimensional discrete ordinates transport code TORT. GRTUNCL3D is only operational in X, Y, Z Cartesian geometries.

## EXFOR data for intermediate high energy interactions

In a collaboration between the National Nuclear Data Centre of BNL, the Nuclear Data Section of the IAEA, the Centre for Nuclear Data of the Russian Federation, and the OECD/NEA Data Bank, a large number of experimental cross-section data were compiled and entered into the EXFOR database accessible on-line. The number of datasets included for the period 2004-2005, for incident particle energies higher than 20 MeV concerned about 1 000 reactions. The most widely measured isotopes were:

*H-1, Ni-58, Zn-67, Zn-68, Cd-111, Cd-112, Cd-114, Sn-116, Te-124, Te-126, I-127, Xe-124, Pb-208, U-238 and the natural elements of Si, and Kr.*

The percentage of data by incident particles is shown in Figure 1.

**Figure 1: EXFOR data 2004-2005, E > 20 MeV**

The major contributors of data were Univ. of Bonn, Univ. of Uppsala, Technische Universität, Darmstadt, Institute of Nuclear Research ATOMKI, Debrecen, Institutul de Fizică și Inginerie Nucleară, Bucharest, University of Milan, Nuclear Physics, Czech Academy of Science, Rez, Los Alamos National Laboratory, CEN Saclay.

The EXFOR database has accumulated a set of experimental data for 42 000 reactions in the energy range 20-2 000 MeV out of a total of 120 000 reactions for the period 1964-2004 covering the full energy range (40%). More detailed information can be found by accessing: [www.nea.fr/html/dbdata/x4/](http://www.nea.fr/html/dbdata/x4/).

### Evaluated nuclear data files

The JEFF-3.1 and JENDL-3.3 evaluated nuclear data libraries were released in recent year. Soon ENDF/B-VII will be released. Some of the evaluations cover also energies of relevance for intermediate energy accelerator applications.

The beta version of ENDF/BVII contains cross-section data for the following isotopes and materials for energies up to 150-200 MeV:

H-2, C-0, N-14, Al-27, Si-28, Si-29, Si-30, P-31, Ca-40, Ca-42, Ca-43, Ca-44, Ca-46, Ca-48, Cr-50, Cr-52, Cr-53, Cr-54, Fe-54, Fe-56, Fe-57, Ni-58, Ni-60, Ni-61, Ni-62, Ni-64, Cu-63, Cu-65, Nb-93, W-182, W-183, W-184, W-186, Hg-196, Hg-198, Hg-199, Hg-200, Hg-201, Hg-202, Hg-204, Pb-204, Pb-206, Pb-207, Pb-208, Bi-209, Th-232, Pa-231, Pa-233.

JEFF-3.1 contains for incident neutron energies up to 150-200 MeV data for the following nuclides:

Neutron: H-1, H-2, C-nat, N-14, O-16, Al-27, Ca-40, Ca-42, Ca-43, Ca-44, Ca-46, Ca-48, Sc-45, Fe-54, Fe-56, Fe-57, Fe-58, Ni-61, Ni-62, Ni-64, Cu-63, Cu-65, Ge-70, Ge-72, Ge-73, Ge-74, Ge-76, Nb-93, Tc-99, Pb-204, Pb-206, Pb-207, Pb-208, Bi-209, and for proton incident particle: Ca-40, Ca-42, Ca-43, Ca-44, Ca-46, Ca-48, Sc-45, Ti-46, Ti-47, Ti-48, Ti-49, Ti-50, Fe-54, Fe-56, Fe-57, Fe-58, Ge-70, Ge-72, Ge-73, Ge-74, Ge-76, Pb-204, Pb-206, Pb-207, Pb-208, Bi-209.

### Integral experiments

The SINBAD database (International Radiation Shielding and Dosimetry Experiments) was updated in April 2006 and includes now 13 accelerator shielding and dosimetry experiments. Further data are being compiled and evaluated for inclusion and for extending the comprehensiveness. A separate paper is presented in this workshop on this topic [3].

### **Acknowledgements**

We wish to acknowledge here all those generous scientists and engineers that have made available their competence and know-how to a large research community. They are not cited individually in the references here. The results of their experiments, their analysis, their algorithms and the digest of their scientific knowledge are shared through RSICC and NEADB. We wish to thank them on behalf of the many users.

### **References**

- [1] J. Keinert, M. Mattes, W. Bernnat, *Thermal Neutron Cross Section Data for Light Water Ice, Liquid Hydrogen and Solid Methane for the Temperature Range from 14 K up to 273 K in MCNP(X) Format*, October 2002 IKE 6-198, University of Stuttgart.
- [2] R.E. MacFarlane, D.W. Muir, *The NJOY Nuclear Data Processing System, Version 91LA-12740-M* (October 1994), edition NJOY99.112.
- [3] I. Kodeli, E. Sartori, B.L. Kirk, "Status and Future Plans for the International Radiations Shielding and Dosimetry Experiments (SINBAD) Database", these proceedings.



## Recent developments and applications of the MARS15 code\*

**Nikolai V. Mokhov**

Fermi National Accelerator Laboratory, Illinois, USA

### Abstract

*Recent developments of the MARS15 code ([www-ap.fnl.gov/MARS/](http://www-ap.fnl.gov/MARS/)) are described. MARS15 is a Monte Carlo code for inclusive and exclusive simulation of three-dimensional hadronic and electromagnetic cascades, muons, heavy-ion and low-energy neutron transport in accelerators, detectors, space crafts and shielding components in the energy range from a fraction of an electron volt up to 100 TeV. Newest developments include inclusive and exclusive nuclear event generators, extended particle list in both modes, heavy-ion capability, electromagnetic interactions, enhanced geometry, tracking, histogramming and residual dose modules, and improved external interfaces. A few examples of the code benchmarking by the user community are shown. The use of the new features is demonstrated in the code applications at high-intensity proton and electron accelerators and colliders.*

### Acknowledgements

Work supported by the Universities Research Association, Inc., under contract DE-AC02-76CH03000 with the US Department of Energy.

---

\* The full paper was not available at the time of the printing of the proceedings. Interested readers can obtain a copy of the PowerPoint presentation in PDF format upon request ([cpsreq@nea.fr](mailto:cpsreq@nea.fr)).



## The present status of the PHITS code

**K. Niita**

Research Organisation for Information Science and Technology (RIST), Tokai, Japan

**H. Nakashima, T. Sato, N. Matsuda, Y. Iwamoto, Y. Sakamoto**  
JAEA, Tokai, Ibaraki, Japan

**H. Iwase**

GSI, Darmstadt, Germany

**L. Sihver, D. Mancusi**

Chalmers University of Technology, Gothenburg, Sweden

### Abstract

*The paper presents a brief description of the models incorporated in PHITS and the present status of the code, showing some benchmarking tests of the PHITS code for accelerator facilities.*

## Introduction

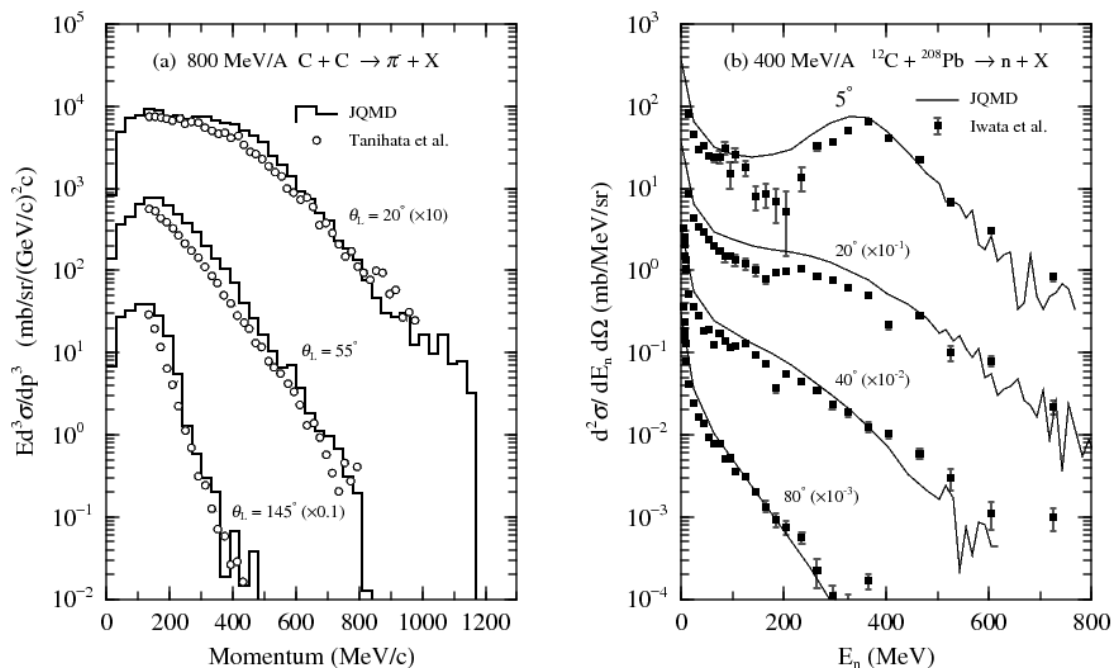
A particle and heavy ion transport code is an essential implement in the design study of accelerator facilities for various purposes such as radiotherapy, spallation neutron sources and rare isotopes production, and also in space technology. We have therefore developed a multi-purpose particle and heavy ion transport Monte Carlo code system, PHITS [1] (Particle and Heavy Ion Transport code System), based on the NMTC/JAM code [2]. PHITS has three important ingredients which enable us to simulate: i) hadron-nucleus reactions with energies up to 200 GeV; ii) nucleus-nucleus collisions from 10 MeV/nucleon up to 100 GeV/nucleon; iii) transports of heavy ions, all hadrons including low energy neutrons down to  $10^{-5}$  eV, and leptons. In this paper, we report a brief description of the models incorporated in the PHITS code and the present status of the code, showing some benchmarking tests of the PHITS code for accelerator facilities.

## Overview of PHITS

We first summarise the transport particles which we can deal with in the PHITS code and the energy range of them. We can transport neutrons from thermal energy up to 200 GeV. We have employed the same method as in the MCNP4C code [3] for neutrons below 20 MeV down to 1 meV based on the Evaluated Nuclear Data such as ENDF-B/VI [4] and JENDL-3.3 library [5] up to 20 MeV and LA150 up to 150 MeV [6], while we use the simulation model JAM [7] above 20 MeV up to 200 GeV. For protons and other hadrons, we also use the simulation model JAM above 1 MeV up to 200 GeV, but we only consider the ionisation process for charged particles below 1 MeV until they stop. PHITS can transport nucleus in the materials. Below 10 MeV/u, we only take into account the ionisation process for the nucleus transport, but above 10 MeV/u we describe nucleus-nucleus collisions up to 100 GeV/u by the simulation model JQMD [8]. We have use the same method as in the MCNP4C code for electron and photon transport. Then the energy range of these particles is restricted within 1 keV and 1 GeV at the present. The extension of the maximum energy of these particles is now in progress.

**Figure 1: (a) (left panel)  $\pi$  - energy spectra for the reaction  $^{12}\text{C}$  (800 MeV/u) +  $^{12}\text{C}$  and (b) (right panel) neutron energy spectra for the reaction  $^{12}\text{C}$  (400 MeV/u) +  $^{208}\text{Pb}$  at different laboratory angles as indicated in the figure**

The solid histograms and the solid lines are the results of the JQMD code and the open circles and solid squares denote the experimental data taken from [17,18]



For simulating the transport of charge particles and heavy ions, the knowledge of the magnetic field is sometimes necessary to estimate beam loss, heat deposition in the magnet, and beam spread. PHITS can provide dipole and quadrupole magnetic fields in any direction and any region of the setup geometry. In contrast to other beam transport codes, PHITS can simulate not only the trajectory of the charge particles in the field, but also the collisions and the ionisation process at the same time. This is a great advantage of PHITS for the design study of the high intensity proton and heavy ion accelerator facilities where one should estimate the radiation damage of the magnets and the surrounding materials and the shielding.

For the ionisation process of the charge particles and nucleus, we have used the SPAR code [9] for the average stopping power  $dE/dx$ , the first order of Moliere model for the angle straggling, and the Gaussian, Landau and Vavilov theories for the energy straggling around the average energy loss according to the charge density and velocity. In addition to SPAR code, we have recently implemented the ATIMA package [10] developed GSI group as an alternative code for the ionisation process.

It is important to use reliable data of total non-elastic and elastic cross-sections for the particle and heavy ion transport. We have used the Evaluated Nuclear Data for neutron induced reactions below 20 MeV, and the systematics above 20 MeV and for proton induced reactions of all energy range. As for the elastic cross-sections, we also use the Evaluated Nuclear Data for neutron induced reactions below 20 MeV, and the systematics [2] above 20 MeV and for proton induced reactions of all energy range concerned with the total and also the double differential cross-sections of elastic nucleon-nucleus reactions. Recently we have adopted the NASA systematics [11] for the total nucleus-nucleus reaction cross-sections, instead of the Shen formula [12].

The total reaction cross-section, or the life time of the particle for decay is an essential quantity in the determination of the mean free path of the transport particle. According to the mean free path, PHITS chooses the next collision point using the Monte Carlo method. To generate the secondary particles of the collision, we need the information of the final states of the collision. For neutron induced reactions in low energy region, PHITS employs the cross-sections from Evaluated Nuclear Data libraries. PHITS also uses Evaluated Nuclear Data for photon and electron transport below 1 GeV in the same manner as in the MCNP4C code [3] based on ITS version 3.0 code [13]. For high energy neutrons and other particles, we have incorporated two models, JAM [7] and JQMD [8] to simulate the particle induced reactions up to 200 GeV and the nucleus-nucleus collisions, respectively.

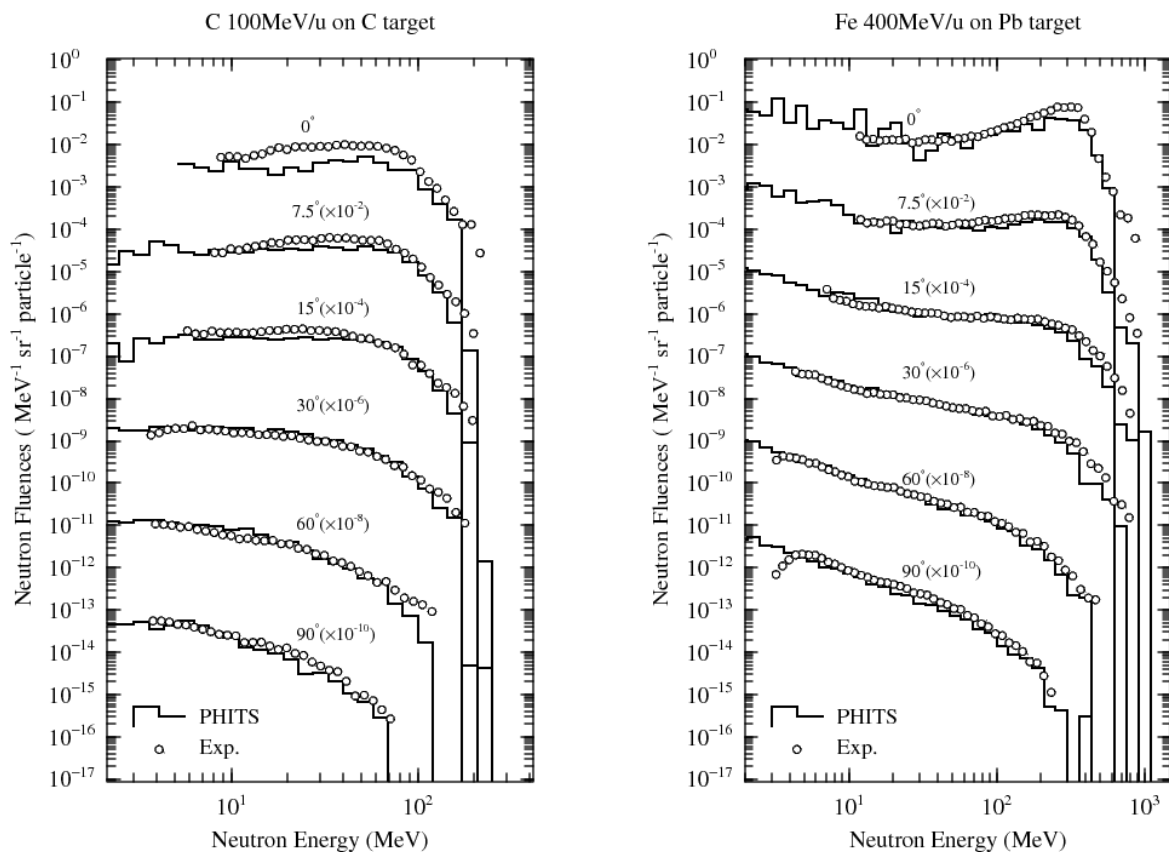
JAM (Jet AA Microscopic Transport Model) [7] is a hadronic cascade model, which explicitly treats all established hadronic states including resonances with explicit spin and isospin as well as their anti-particles. We have parameterised all hadron-hadron cross-sections based on the resonance model and string model by fitting the available experimental data. Below the energy in the centre-of-mass system (c.m.)  $\sqrt{s} < 4$  GeV, the inelastic hadron-hadron collisions are described by the resonance formations and their decays, and at higher energies, string formation and their fragmentation into hadrons are assumed.

The JQMD (JAERI Quantum Molecular Dynamics) code [8], has been widely used to analyse various aspects of heavy ion reactions as well as of nucleon-induced reactions [14]. In the QMD model, the nucleus is described as a self-binding system of nucleons, which is interacting with each other through the effective interactions in the framework of molecular dynamics. One can estimate the yields of emitted light particles, fragments and of excited residual nuclei resulting from the heavy-ion collision. The QMD simulation, the JAM simulation as well, describes the dynamical stage of the reactions. At the end of the dynamical stage, we will get the excited nuclei from these simulations. To get the final observable, these excited nuclei should be decayed in a statistical way. We have employed GEM model [15] (Generalised Evaporation Model) for light particle evaporation and fission process of the excited residual nucleus.

So far the QMD model has shed light on several exciting topics in heavy-ion physics, for example, the multi-fragmentation, the flow of the nuclear matter, and the energetic particle productions [16]. In Figure 1 we show two examples of the basic observables from heavy-ion reactions calculated by the JQMD code. In Figure 1(a) we represent the results of  $\pi^-$  energy spectra for the reaction  $^{12}\text{C} + ^{12}\text{C}$  at 800 MeV/u. The result of the JQMD code reproduces the experimental data [17]. We notice that this calculation has been done in the same formulation and also with the same parameter set as used in the nucleon-induced reactions [14]. Next example is the neutron energy spectra from the reaction  $^{12}\text{C} + ^{208}\text{Pb}$  at 400 MeV/u, which is shown in Figure 1(b). The neutron produced in heavy-ion reactions

is very important in the shielding design of the spacecraft and the other facilities because of its large attenuation length in shielding materials. Recently, secondary neutrons from heavy-ion reactions have been systematically measured using thin and thick targets by HIMAC [18,19]. Figure 1(b) shows that the JQMD code roughly reproduced the measured cross-sections for the C beams with thin target. PHITS has incorporated the JQMD code for the collision part of the nucleus-nucleus reactions to describe the secondary neutron yields from the thick target. In order to investigate the accuracy of the PHITS code in the heavy ion transport calculation, we have compared the results with the experimental data measured by Kurosawa, et al. [19]. They measured secondary neutrons produced from thick (stopping length) targets of C, Al, Cu, and Pb bombarded with various heavy ions from He to Xe. Incident energies ranged from 100 MeV/u to 800 MeV/u from HIMAC. Here we show two examples of the comparisons in Figure 2. It is confirmed from these comparisons with measurements that the PHITS code provides good results on the angular distributions of secondary neutron energy spectra produced from thick carbon, aluminium, copper, and lead targets bombarded by 100 MeV/u carbon, 400 MeV/u carbon, and 400 MeV/u iron ions.

**Figure 2: Comparison of the neutron double differential cross-section calculated with PHITS and the measured data [19] for 100 MeV/u C ion on C target (left panel) and 400 MeV/u Fe ion on Pb target (right panel)**

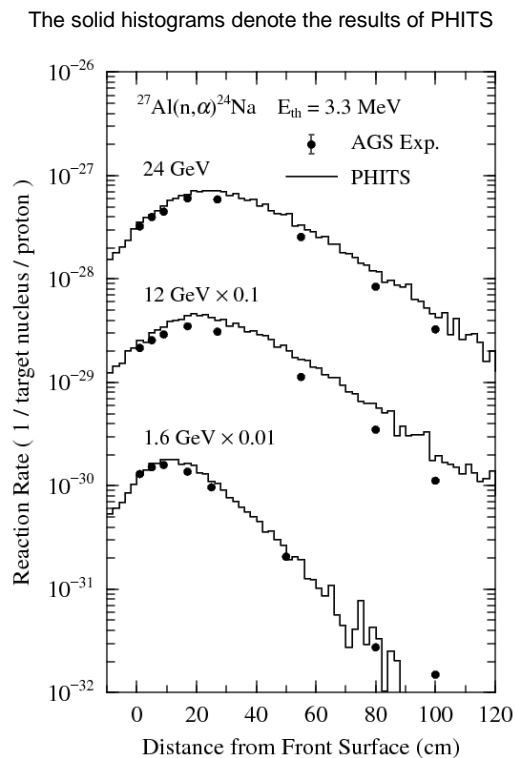


### Benchmarking of the PHITS code

PHITS has been used in a wide field of applications from semiconductor soft error up to shielding of spacecrafts. In this section, we introduce a major application field of PHITS, the spallation neutron source of J-PARC, and show some benchmarking tests of the PHITS code for the problems related to accelerator facilities.

The J-PARC [20] (Japan Proton Accelerator Research Complex) project is the main field where the NMTC/JAM code had been developed. This project has a 400 MeV normal-conducting linac, a superconducting linac from 400 to 600 MeV, a 3 GeV synchrotron ring for 1 MW proton, and a 50 GeV synchrotron ring for 0.75 MW proton beams. These are now under construction and aim to pursue frontier science in particle physics, nuclear physics, materials science, life sciences and nuclear technology, using a new proton accelerator complex at the highest beam power in the world. A reliable transport code was required for the shielding design and optimisation study of each facility in J-PARC. The conditions which should be satisfied in the transport code are very severe, since the energy range is very wide, from 50 GeV down to MeV neutrons in material science facility. Furthermore the dimension of the system is very large (about several tens of metres), but the resolution of the calculation must be of the order of millimetre. First the NMTC/JAM [2] code was developed to satisfy these severe conditions, and then the code was upgraded to PHITS, which also includes heavy ion transport.

**Figure 3: Distribution of the  $^{27}\text{Al}(n,\alpha)^{24}\text{Na}$  reaction rates along the cylindrical surface of a mercury target bombarded with 1.6, 12 and 24 GeV protons [21]**



For validation of the PHITS calculations for the neutron flux produced by the mercury spallation target, we have applied PHITS to the experiments under the ASTE (AGS Spallation Target Experiment) collaboration [21]. One of the experiments was carried out using a bare mercury target, which is a 20 cm diameter and 130 cm long cylinder, and detecting the reaction rate distributions along the cylindrical surface of the target by activation techniques at incident proton energies of 1.6, 12 and 24 GeV. Various activation detectors such as the  $^{115}\text{In}(n,n')^{115\text{m}}\text{In}$ ,  $^{93}\text{Nb}(n,2n)^{92\text{m}}\text{Nb}$  and  $^{209}\text{Bi}(n,xn)$  reactions with threshold energies ranging from 0.3 to 70.5 MeV were employed to obtain the reaction rate data for estimating spallation source neutron characteristics of the mercury target. Figure 3 shows the distribution of the  $^{27}\text{Al}(n,\alpha)^{24}\text{Na}$  reaction rates along the cylindrical surface of bare mercury target bombarded with 1.6, 12, and 24 GeV protons. The threshold of this reaction is 3.3 MeV, while the most effective neutron energy for this reaction is roughly 10 MeV. The results of PHITS, denoted by the solid histograms in these figures, reproduce the experimental distribution quite well for all positions and all energies. From these data, we have also derived the neutron flux spectra by the spectrum adjustment method. Figure 4 compares the adjusted and calculated neutron spectra at 17 cm from the front surface of the target. For all energy range, the PHITS results roughly trace the adjusted spectra.

**Figure 4: Comparison of the neutron spectra obtained by adjustment method from the experimental data [21] and by the PHITS calculation**

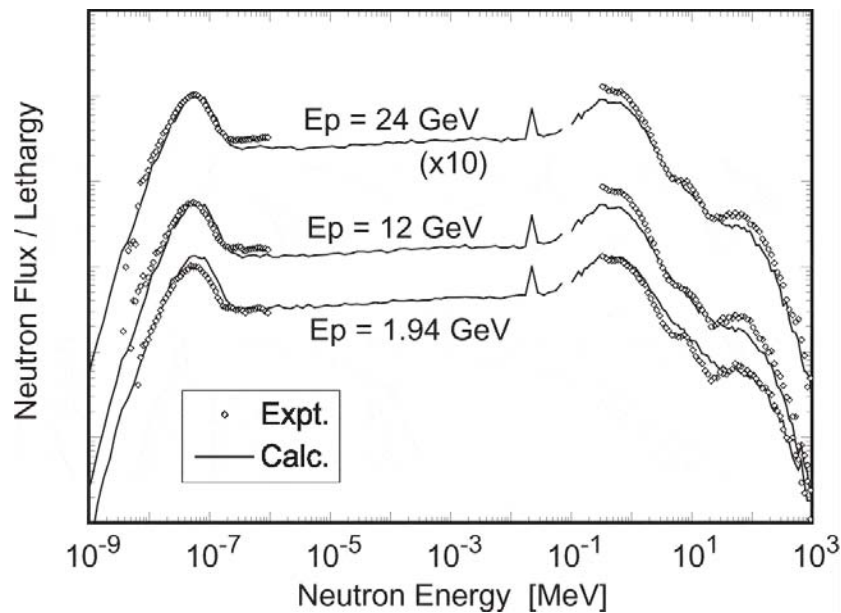
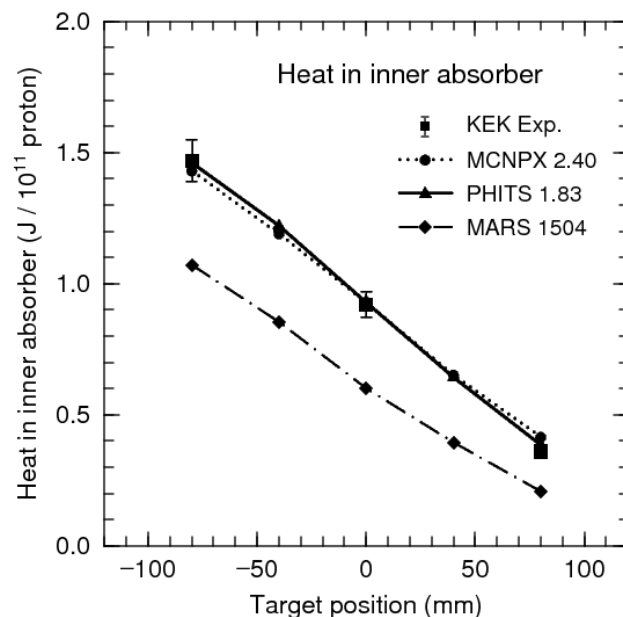


**Figure 5: Comparison of the experimental heat [23] with the simulation results by MCNPX, PHITS and MARS codes**



One of the important issues for high intense proton and heavy ion accelerator facilities is a heat deposition to magnet components, target vessels and materials of beam dump. Precise knowledge of the heat deposition is required for designing them. Monte Carlo codes such as PHITS are usually used to estimate the heat deposition. There are, however, few data to validate the codes in connection with heat measurements. Recently, Ohnishi, *et al.* [22] measured the heat deposition of secondary particles emitted from a production target interacting with a primary proton beam at the KEK 12 GeV proton synchrotron by developing a “cryogenic calorimeter”. The production target was a copper cylinder with dimensions of 30 mm in diameter and 30 mm in length, corresponding to a 0.2 interaction length.

The target was remotely controlled so as to change its position from the centre of the absorber along the beam direction. Figure 5 shows a comparison of the calculation results with the experimental data of the heat deposition. The results of PHITS and MCNPX well reproduce the experimental data, though the result of MARS underestimates the data. Ohnishi analysed the discrepancies between the results of MARS and PHITS and concluded that the details of the distribution of secondary particles produced from the copper target at 12 GeV proton beam caused the differences of the heat [23]. We also checked the differences between PHITS and MCNPX, and found that the contributions of each secondary particle to the heat in the absorber are different between them, but finally the total heats are the same due to the cancellation of the differences. We therefore concluded that the heat estimation by these Monte Carlo codes still has an uncertainty about 35% due to the difficulties with simulation models for secondary particle production around 10 GeV. Further studies are necessary to improve the accuracy.

## Summary

We have presented briefly the models incorporated in the PHITS code and the present status of the code, showing some benchmarking tests of the PHITS code for accelerator facilities. It has been shown that PHITS has a great ability of carrying out the radiation transport analysis of almost all accelerator facilities of protons and heavy ions within a wide energy range.

## References

- [1] H. Iwase, K. Niita., T. Nakamura, *J. Nucl. Sci. Technol.*, 39, 1142 (2002).
- [2] K. Niita, H. Takada, S. Meigo, Y. Ikeda, *Nucl. Instr. and Meth.*, B184, 406 (2001).
- [3] J.F. Briesmeister, et al., *MCNP General Monte Carlo N-particle Transport Code*, Los Alamos National Laboratory report LA-12625-M (1997).
- [4] V. McLane, et al., *ENDF/B-VI Summary Documentation*, BNL-NCS-17541 (1996).
- [5] K. Shibata, et al., "Japanese Evaluated Nuclear Data Library Version 3 Revision-3: JENDL-3.3", *J. Nucl. Sci. Technol.*, 39, 1125 (2002).
- [6] M.B. Chadwick, et al., *LA150 Documentation of Cross Sections, Heating, and Damage*, Los Alamos National Laboratory report LA-UR-99-1222 (1999).
- [7] Y. Nara, N. Otuka, A. Ohnishi, K. Niita, S. Chiba, *Phys. Rev.*, C61, 024901 (2000).
- [8] K. Niita, S. Chiba, T. Maruyama, H. Takada, T. Fukahori, Y. Nakahara, A. Iwamoto, *Phys. Rev.*, C52, 2620 (1995).
- [9] T.W. Armstrong, K.C. Chandler, *A FORTRAN Program for Computing Stopping Powers and Ranges for Muons, Charged Pions, Protons, and Heavy Ions*, ORNL-4869, Oak Ridge National Laboratory (1973).
- [10] [www-linux.gsi.de/~weick/atima/](http://www-linux.gsi.de/~weick/atima/).
- [11] R.K. Tripathi, F.A. Cucinotta, J.W. Wilson, *Nucl. Instr. and Meth.*, B117, 347 (1996); R.K. Tripathi, J.W. Wilson, F.A. Cucinotta, *Nucl. Instr. and Meth.*, B129, 11 (1997), R.K. Tripathi, F.A. Cucinotta, J.W. Wilson, *Nucl. Instr. and Meth.*, B155, 349 (1999).
- [12] S. Wen-quinf, W. Bing, F. Jun, Z. Wen-logn, Z. Yong-tai, F. En-pu, *Nucl. Phys.*, A491, 130 (1989).
- [13] J.A. Halbleib, et al., *ITS Version 3.0: The Integrated TIGER Series of Coupled Electron/Photon Monte Carlo Transport Codes*, SAND91-1634 (1992).

- [14] S. Chiba, O. Iwamoto, T. Fukahori, K. Niita, Toshiki Maruyama, Tomoyuki Maruyama, A. Iwamoto, *Phys. Rev.*, C54, 285 (1996); S. Chiba, M.B. Chadwick, K. Niita, Toshiki Maruyama, Tomoyuki Maruyama, A. Iwamoto, *Phys. Rev.*, C53, 1824 (1996).
- [15] S. Furihata, *Nucl. Instr. and Meth.*, B171, 251 (2000).
- [16] J. Aichelin, *Phys. Rep.*, 202, 233 (1991).
- [17] I. Tanihata, *et al.*, *Phys. Lett.*, B87, 349 (1979).
- [18] Y. Iwata, *et al.*, *Phys. Rev.*, C64, 054609 (2001).
- [19] T. Kurosawa, *et al.*, *Nucl. Sci. and Eng.*, 132, 30 (1999); *Journal of Nucl. Sci. and Technol.*, 36-1, 42 (1999); *Nucl. Instr. and Meth.*, A430, 400 (1999); *Phys. Rev.*, C62, 044615 (2000).
- [20] The Joint Project Team of JAERI and KEK, *The Joint Project for High Intensity Proton Accelerators*, JAERI-Tech, 2000-003, JAERI (2000).
- [21] H. Nakashima, *et al.*, "Research Activities on Neutronics under ASTE Collaboration at AGS/BNL", *Proc. of Int. Conference on Nuclear Data for Science and Technology*, Tsukuba, Japan, 2001; "Current Status of the AGS Spallation Target Experiment", *Proc. of the 6<sup>th</sup> meeting of the Task Force on SATIF*, SLAC (2002).
- [22] H. Ohnishi, *et al.*, *Nucl. Instr. and Meth.*, A545, 88 (2005).
- [23] H. Ohnishi, *private communication* (2005).

## FLUKA: New features and a general overview

**V. Vlachoudis,<sup>1</sup> F. Ballarini,<sup>5</sup> G. Battistoni,<sup>4</sup> M. Campanella,<sup>4</sup> M. Carboni,<sup>6</sup> F. Cerutti,<sup>4</sup> A. Empl,<sup>7</sup> A. Fassò,<sup>2</sup> A. Ferrari,<sup>1</sup> E. Gadioli,<sup>4</sup> M.V. Garzelli,<sup>4</sup> A. Mairani,<sup>5</sup> A. Mostacci,<sup>6</sup> S. Muraro,<sup>4</sup> A. Ottolenghi,<sup>5</sup> M. Pelliccioni,<sup>6</sup> L. Pinsky,<sup>7</sup> J. Ranft,<sup>3</sup> S. Roesler,<sup>1</sup> P.R. Sala,<sup>4</sup> D. Scannicchio,<sup>5</sup> R. Villari<sup>6</sup>**  
<sup>1</sup>CERN, European Organisation for Nuclear Research, Switzerland, <sup>2</sup>SLAC, <sup>3</sup>Univ. of Siegen, <sup>4</sup>INFN and Univ. Milano, <sup>5</sup>INFN and Univ. Pavia, <sup>6</sup>INFN Frascati, <sup>7</sup>Univ. of Houston

### Abstract

FLUKA is a general purpose Monte Carlo code, capable of handling all radiation components from thermal energies (for neutrons), or 1 keV (for all other particles) till cosmic ray energies. The code is a joint CERN-INFN project, and is continuously undergoing development and benchmarking. It is the standard tool used at CERN for the radioprotection and beam-machine interaction calculations.

Several improvements and additions to the code capabilities will be presented, in particular:

- new radioactive inventory evolution algorithm, which allows to compute inventories and residual dose rates for arbitrary irradiation profiles and cooling times;
- improved evaporation/fragmentation model, which allows to produce up to 600 different fragments;
- new fission model;
- the nucleus-nucleus models (interfaces to DPMJET-III, rQMD-2.4, and the newly developed BME and QMD models);
- improvements and additions to the geometry and user interface.

## Introduction

FLUKA [1-4] is a multipurpose transport Monte Carlo code, for calculations of particle transport and interactions with matter, covering an extended range of applications spanning from proton and electron accelerator shielding to target design, calorimetry, activation, dosimetry, detector design, accelerator-driven systems, cosmic rays, neutrino physics, radiotherapy etc. Presently is maintained and supported as a joint CERN-INFN project, which is continuously undergoing development and benchmarking. FLUKA is able to transport 60 different elementary particles and whichever heavy ions and can perform hadron-hadron, hadron-nucleus, neutrino, electromagnetic, and  $\mu$  interactions from 1 keV up to 10 000 TeV/n. It is able to perform charged particle transport both in magnetic and electric field (currently under development) including all relevant processes [1]. About nucleus-nucleus collisions, since ion-ion nuclear interactions were not yet treated in FLUKA, past results have been obtained in the superposition model approximation, where primary nuclei (0-10 000 TeV/A) were split into nucleons before interacting. With the integration of ion interactions codes (DPMJET, rQMD, BME) and the suitable cross-sections package, this approximation is now obsolete. FLUKA features a combinatorial geometry which was recently enhanced with the use of parenthesis expansions and geometrical optimisations, while for the tracking it has a double capability to run either fully analogue and/or biased calculations.

## Code design

FLUKA is based, as far as possible, on original and well tested microscopic models. Due to this “microscopic” approach to hadronic interaction modelling (Figures 1, 2), each step is self-consistent and has solid physical bases. Performances are optimised comparing with particle production data at single interaction level: “*theory driven, benchmarked with data*”. No tuning whatsoever is performed on “*integral*” data, such as calorimeter resolutions, thick target yields, etc. Therefore, final predictions are obtained with a minimal set of free parameters, fixed for all energies and for all target/projectile combinations. Results in complex cases as well as scaling laws and properties come forth naturally from the underlying physical models and the basic conservation laws which are fulfilled *a priori*, therefore the code provides predictive capabilities where no experimental data are directly available.

The philosophy of the FLUKA authors was not to provide a toolkit for particle physics simulations, but rather a code that provides the best physics available. For this reason all physical models in FLUKA are fully integrated in the code and the user has limited means of tweaking them. All correlations are fully preserved within interactions and among shower components. The authors continues to make a huge effort to ensure self-consistency with full cross-talk between all components (hadronic, electromagnetic, neutrons, muons, heavy ions), and to achieve the same level of accuracy for each component and for all energies. For example, the transport and interactions of electromagnetic particles are fully coupled to the hadronic sector, allowing to follow in the same event secondary hadrons from photon nuclear interactions and  $\gamma$  rays from nuclear de-excitation.

## Interface improvement

Since the official release of 2005.6 the FLUKA code went a major reworking, in view of the public release of the source code. The code now is even more robust, it is continually enhanced with modern and sound physics, and more users friendly. The major features of the latest release 2006.3 are the following:

- PEMF preprocessor eliminated. Now, electron and photon cross-sections are generated during initialisation time. Photon cross-sections have been rebased on EPDL-97. There is a small penalty in time for the initialisation, but it removes completely the hassle of creating the cross-sections with an external program, as well all the problems that could appear from miss-synchronisation of the pemf files and what is described in the input file.
- Input file now is fully name based, including all materials, geometry bodies and regions, particles and scoring cards. This allows a more flexible way of writing input files as well sharing resources among various input files.

**Figure 1: Thin target example of angle-integrated  $^{90}\text{Zr}(p,xn)$  at 80.5 MeV**

The various lines show the total in blue, intranuclear cascade in green, pre-equilibrium in cyan and evaporation magenta contributions. The experimental data are the red points and extracted from Ref. [5].

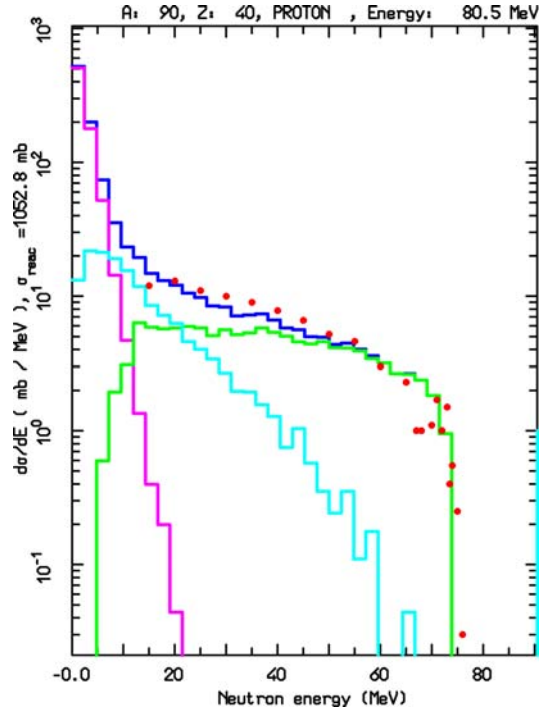
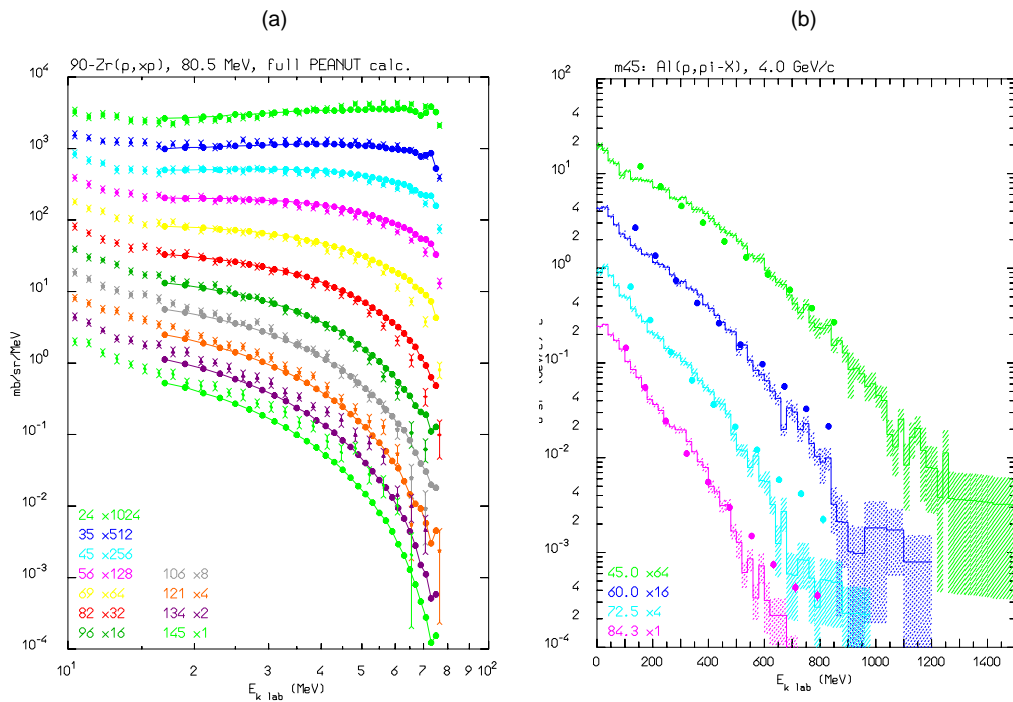
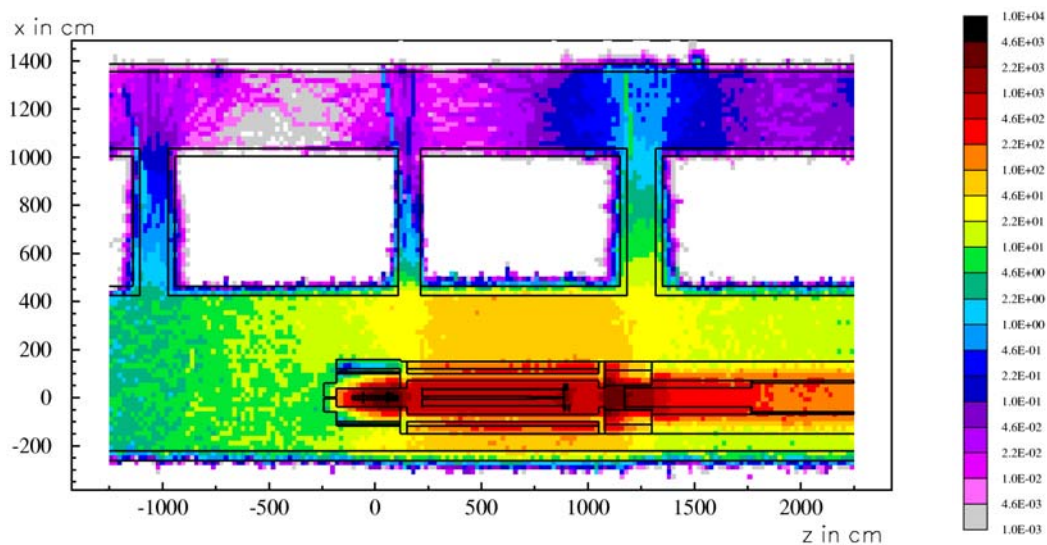


**Figure 2: Double differential of a thin target example  
(a)  $p + ^{90}\text{Zr} \rightarrow p + X$  (80 MeV) [5] and (b)  $p + \text{Al} \rightarrow \pi + X$  (4 GeV/c)**



- The input file is initially treated by the FLUKA preprocessor. A C/C++ like preprocessor that accepts definition of variables and conditional inclusion of input code. This a powerful mechanism if treated correctly by the user, that allows a more structured input file. The user can treat the input file in different ways by simply enabling or disabling some preprocessor defines.
- There are several enhancements in the voxel geometry which are quite important for comparing using of FLUKA in a way similar to the treatment planning systems usually found in radiotherapy centres. Namely: i) Voxel-by-voxel density correction factors, ii) water equivalence factors for atomic processes ( $dE/dx$ ,  $\delta$  ray) while at the same time keeping the real material for the nuclear processes.
- The geometry can now handle more complicated combinatorial geometry objects including parenthesis expansion and both algebraic and geometrical optimisations, for the minimisation of the number of produced zones in a region.
- The code is now able to follow on-line the decay radiation from unstable residual nuclei together with an exact analytical calculation of activity evolution during irradiation and cooling down. Decay,  $\beta$ ,  $\gamma$  are produced and transported “on line”, with time evolution of induced radioactivity calculated analytically using the Bateman equations. As a consequence, results for production of residuals and their effects as a function of time can now be obtained in the same run.
- The user is now able to score results for activity, energy deposition, particle fluence etc, calculated for custom irradiation/cooling down profile, as well the new scoring type activity maps ( $Bq/cm^3$ ) (Figure 3).

**Figure 3: Residual Dose Equivalent Rate (mSv/h) at the CNGS (CERN) target after 200 days irradiation with  $8 \cdot 10^{12}$  p+/s and 1 day of cooling**



### Equilibrium particle emission

The latest updates in the evaporation, fission, fragmentation and Fermi break-up made an impressive improvement in the residual nuclei prediction especially in the low mass region. This is a crucial point for many safety calculations. As an example in Figures 4 and 5 are shown the predicted mass distribution for the residual nuclei produced by Pb ions on proton target at 1 GeV/n using inverse kinematics, and Ag on proton target at 300 GeV and 800 GeV, where is evident the improved FLUKA predictions with the new fragmentation model, especially in the low mass region. A discussion of the recent improvements in these models is discussed in the following paragraphs.

### Evaporation, fragmentation and Fermi break-up

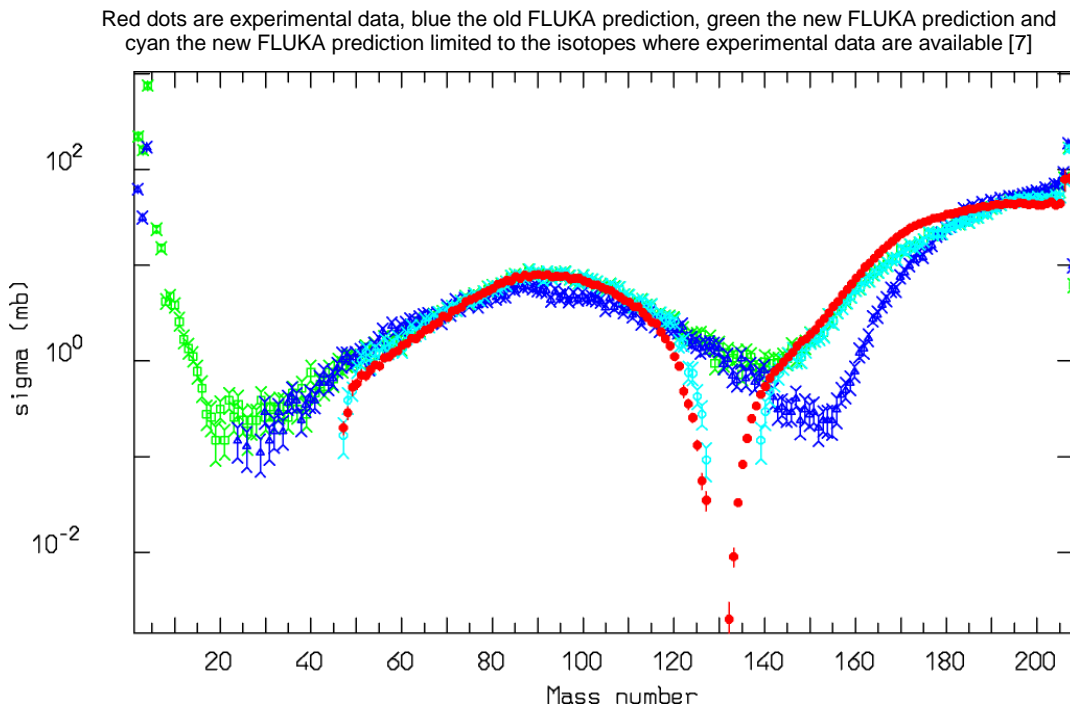
Evaporation, the latest stage of the nuclear reaction chain, is essential for the prediction of residual nuclei distribution. Therefore, it is a crucial ingredient in activation and residual dose rate simulations, but also in the exact determination of the fragment spectra following nucleus-nucleus interaction.

The FLUKA evaporation model, which is based on the Weisskopf-Ewing approach, has been continuously updated along the years, with the inclusion, for instance, of sub-barrier emission, full level density formula, and analytic solution of the emission widths. The latest upgrade is the extension to the evaporation of nuclear fragments up to  $A \leq 24$ , with impressive improvements in the low mass region of residual nuclei distributions. This, coupled to the exact energy and momentum balance in all reaction steps, allows to predict the mass and energy distribution of fragments, including very low energy, almost non-ionising ones, whose biological effects are not precisely known.

The new evaporation model how is able to handle about 600 possible emitted particle/states with an extended evaporation/fragmentation formalism. It is using the full level density formula with level density parameters and excitation dependent. The inverse cross-section is calculated with proper sub-barrier, while there is analytic solution for the emission widths, neglecting the level density parameter dependence on excitation energy which is taken into account by rejection. For the Fermi break-up for  $A < 18$  nuclei, the code is taking into account up to 6 ejectiles resulting ~50 000 possible combinations.

FLUKA is now using new energy dependent and self-consistent, evaporation level densities as well as new pairing energies, according to the IEAE working group recommendations RIPL-2 [6]. The isotopes mass table has been updated with both experimental and calculated values till  $A = 330$ . The use of masses calculated offline done with high reliability complex models, it allows: i) to extend to larger isotope masses  $A$  than those experimentally accessible; ii) to minimise resorting to empirical mass formulae which often generates artifacts. The shell corrections have been reworked also to be coherent with the new masses.

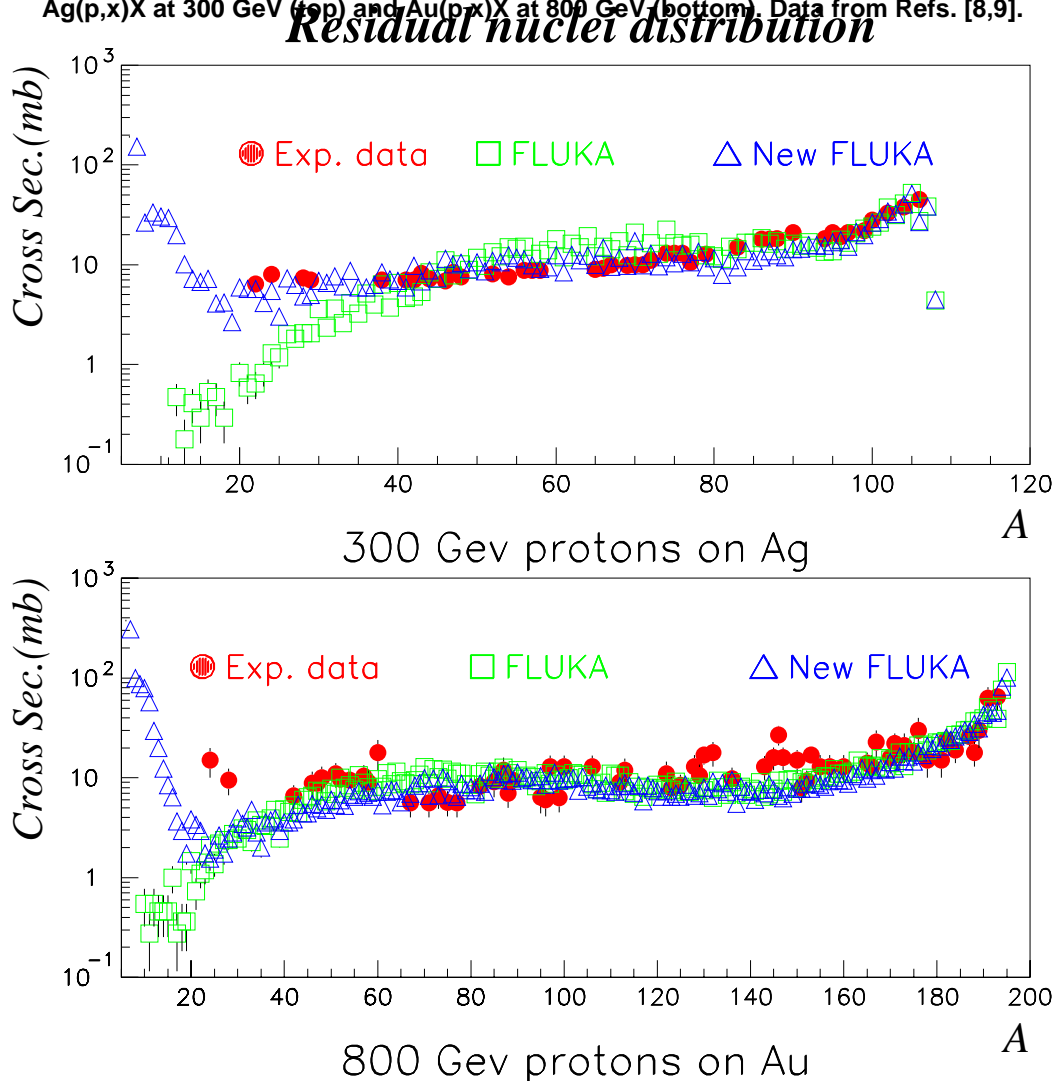
**Figure 4: Cross-section for the production of residual nuclei from the 1 GeV/n  $^{208}\text{Pb} + \text{p}$  reactions**



### New fission model

The new fission model is no longer an enhanced version of the Atchison algorithm. Fission is now done on first principles and is also in full competition with evaporation. Actinide fission is done on first principles and no longer using parameterised  $\Gamma_{\text{fis}}/\Gamma_{\text{neu}}$ . The fission barrier calculations follow the most recent suggestions by Myers and Swiatecki. An enhanced fission level density is used at saddle point, which is no longer independent from the excitation energy but now is washing out with excitation in agreement with the most recent studies. Fission product widths and asymmetric versus symmetric probabilities are better parameterised according to the most recent data/approaches.

Figure 5: Experimental and computed residual nuclei mass distribution for Ag(p,x)X at 300 GeV (top) and Au(p,x)X at 800 GeV (bottom). Data from Refs. [8,9].



### Heavy ion interaction models

Ion-ion interactions are of great interest both for therapeutic beams, and for space radiation assessment. FLUKA has the necessary interfaces to couple with the DPMJET-III, rQMD and BME models.

FLUKA implements DPMJET-III [10,11] as event generator to simulate nucleus-nucleus interactions for energies in excess of 5 GeV/n up to the highest cosmic ray energies ( $10^{18}$ - $10^{20}$  eV). DPMJET is based on the two components Dual Parton Model in connection with the Glauber formalism.

FLUKA also has an interface to rQMD-2.4 [12,13], a relativistic QMD model which has been applied successfully to relativistic A-A particle production over a wide energy range from 0.1 GeV/n up to several hundred of GeV/n. Several important modifications have been implemented in the rQMD code, in order to ensure energy-momentum conservation taking into account experimental binding energies, and to provide meaningful excitation energies for the residual fragments. A thorough discussion of the FLUKA implementation, as well as some results of this modified model can be found in [9].

FLUKA has a preliminary implementation of the BME (Boltzmann Master Equation) model [14] for lower energies ions  $E < 100$  MeV/n, which is presently under testing for  $A < 17$ .

For all generators, de-excitation and evaporation of the excited residual nuclei is performed by calling the standard FLUKA evaporation/fission/fragmentation module described above.

## References

- [1] A. Fassò, A. Ferrari, S. Roesler, P.R. Sala, G. Battistoni, F. Cerutti, E. Gadioli, M.V. Garzelli, F. Ballarini, A. Ottolenghi, A. Empl, J. Ranft, "The Physics Models of FLUKA: Status and Recent Developments", *Computing in High Energy and Nuclear Physics 2003 Conference (CHEP2003)*, La Jolla, CA, USA, 24-28 March 2003 (paper MOMT005), eConf C0303241 (2003), arXiv:hep-ph/0306267.
- [2] A. Fassò, A. Ferrari, J. Ranft, P.R. Sala, *FLUKA: a Multi-particle Transport Code*, CERN-2005-10 (2005), INFN/TC\_05/11, SLAC-R-773.
- [3] A. Ferrari, P.R. Sala, "The Physics of High Energy Reactions", *Proceedings of Workshop on Nuclear Reaction Data and Nuclear Reactors Physics, Design and Safety*, A. Gandini, G. Reffo (Eds.), Trieste, Italy, April 1996, 2, 424 (1998).
- [4] A. Ferrari, P.R. Sala, "Nuclear Reactions in Monte Carlo Codes", in *Radiation Protection Dosimetry*.
- [5] M. Trabandt, et al., *Phys. Rev.*, C39, 452 (1989).
- [6] IAEA working group, *Reference Input Parameter Library 2*, [www-nds.iaea.org/RIPL-2](http://www-nds.iaea.org/RIPL-2).
- [7] *Nucl. Phys.*, A686 (2001) 481-524.
- [8] *Phys. Rev.*, C19 2388 (1979).
- [9] *Nucl. Phys.*, A543, 703 (1992).
- [10] J. Ranft, "Dual Parton Model at Cosmic Ray Energies", *Phys. Rev.*, D51 64-84 (1995).
- [11] S. Roesler, R. Engerl, "The Monte Carlo Event Generator DPMJET-III", *Proceedings of Monte Carlo 2000*, A. Kling, F. Barão, M. Nakagawa, L. Távora, P. Vaz (Eds.), Springer-Verlag Berlin, 955 (2001).
- [12] H. Sorge, H. Stocker, W. Greiner, "Relativistic Quantum Molecular Dynamics Approach to Nuclear Collisions at Ultrarelativistic Energies", *Nucl. Phys.*, A498, 567-576 (1989).
- [13] V. Andersen, et al., "The FLUKA Code for Space Applications: Recent Developments", *Adv Space Res.*, 34, 1302 (2004).
- [14] M.V. Garzelli, et al., "Heavy-ion Collisions: Preliminary Results of a new QMD Model Coupled with FLUKA and Recent Developments of the rQMD-FLUKA Interface", *Proceedings of NPDC19 Pavia* (2005).
- [15] R. Cherubini, D.T. Goodhead, H.G. Menzel, A. Ottolenghi (Eds.), *Nuclear Technology Publishing*, Vol. 99, No.1-4, 29 (2002).



## Recent developments in Geant4

**Tatsumi Koi, Dennis H. Wright**

*On behalf of the Geant4 collaboration*

Stanford Linear Accelerator Centre, Menlo Park, California, USA

### Abstract

*Geant4 is a toolkit for simulating the passage of particles through matter and it is used by a large number of experiments and projects in a variety of application domains, including high energy physics, astrophysics and space science, medical physics and radiation protection. An overview of the physics processes in the toolkit is presented focusing on hadron interactions. The toolkit also has many other useful functionalities for shielding calculations. These include event biasing options and primitive scoring which provide an easy interface to simulation results.*

## Introduction

Recent high energy physics experiments require large-scale, accurate and comprehensive simulations of their detectors. Similar requirements also arise in other fields, such as astrophysics, space science and engineering, radiological sciences, radiation therapies and radiation protection research. Geant4 has been developed in order to satisfy such demands [1,2]. It is an object-oriented simulation toolkit which provides a variety of software components for users who want to simulate the response of their detectors. It can be used to simulate single purpose, basic and relatively simple detectors as well as the large, general purpose detectors used in modern, high energy physics experiments such as those at the Large Hadron Collider (LHC). Geant4 provides all aspects of the simulation process, such as:

1. geometry description;
2. material specification;
3. particle definitions;
4. tracking and navigation;
5. physics processes to handle the interactions of particles with materials;
6. management of events;
7. run configuration;
8. stacking for track prioritisation;
9. tools for handling the detector response;
10. interfaces to external frameworks, graphics and user interface systems.

Geant4 has abundant physics processes and models covering a wide energy range from optical photons and thermal neutrons to the high energy reactions at the LHC and in cosmic ray experiments. In addition to these processes and models, Geant4 also provides abstract interfaces to physics processes. Users are easily able to add their own physics models with these interfaces. The above features reflect the choice by Geant4 to adopt object-oriented technology and to follow an iterative-incremental software process [3]. This technology makes possible many extensions and improvements of the toolkit with no modification of the existing code. Because Geant4 is a toolkit, many users can incorporate Geant4 into their own simulation framework. However it can also be used to build a stand-alone application, in which a user defines his/her problems, executes simulations, gets results and creates graphics for presentations. Geant4 has been widely used in high-energy physics domains since its first release in 1999, and its use in many other fields of science has also increased. Radiation protection research is one such field.

In this paper, we provide an overview of the toolkit capabilities, focusing on topics related to shielding calculations. In the next section we give a brief review of Geant4 physics processes, excluding hadronic processes which will be covered in detail in another section. Selected functionalities useful for shielding calculations will be introduced in the following section. Finally we give a short summary.

## Geant4 physics processes

Geant4 has abundant physics processes for handling interactions of gammas (including X-rays and optical photons), electrons and positrons, muons, hadrons and ions. Before explaining these processes we briefly describe the particles and materials categories of Geant4 because the physics processes depend on their properties for the simulation of particle-matter interactions.

### Particles

Geant4 provides most of the particles listed by the Particle Data Group [4]. Ions can also be defined with excitation energy and charge state. These Geant4 particles are created according to the following procedure:

1. A particle definition base class is provided which describes the basic properties of a particle, such as mass, charge and so on.
2. Virtual intermediate classes for leptons, bosons, mesons, baryons, etc. are provided in order to abstract particle properties common to these types.
3. A concrete particle class is derived which has properties specific to the particle.

Users who wish to create particles not already provided by Geant4 may do so by following the above procedure. The particle class has the list of physics processes to which the particle is sensitive.

### **Materials**

In Geant4 materials are made of a single element or a mixture of elements, and elements are made of a single isotope or a mixture of isotopes. When a user needs water in his/her geometry, then he/she must first create the elements of hydrogen and oxygen. If heavy water is required in the simulation, the isotope deuterium must be created before defining the element hydrogen. Characteristics like radiation and interaction length, excitation energy loss, coefficients in the Bethe-Bloch formula, shell correction factors, etc., are computed from the element, and if necessary, the isotope composition. Users can change these properties. Geant4 also provides pre-defined materials whose properties follow the data library of the National Institute of Standards and Technology [5].

### **Processes**

All physics processes must describe the interaction of particles with matter in a unified manner which is well-defined by object-oriented programming technology. Therefore all physics processes can be treated in the same manner as the other components of the simulation such as tracking. This means that the tracking code is completely general and common to all processes of all particle types. This provides flexibility in the design of a physics process, and together with the modular architectural framework, makes possible the development of new models without affecting existing code.

It is useful to divide the functionality of a process into two parts. One part manages when and/or where the interaction occurs and the other decides what occurs in the interaction. The former usually relates to the cross-section or mean-lifetime and the latter generates the final state. In many Geant4 physics processes, the two parts are implemented separately. In such processes it is possible to have multiple final state generators as well as multiple cross-section data sets.

Geant4 physics processes are divided for convenience into seven categories: electromagnetic, hadronic, transportation, decay, optical, photo-lepton\_hadron, parameterisation. The electromagnetic and hadronic categories are further sub-divided. In this section we give a brief description of all of these except for hadronic. As the hadronic processes are of greatest relevance to shielding calculations, they will be treated separately in later sections.

#### *Electromagnetic*

Physics processes in this category handle the electromagnetic interactions of leptons, photons, hadrons and ions. Geant4 provides physics processes of ionisation, bremsstrahlung, multiple scattering, Compton and Rayleigh scattering, photo-electric effect, pair conversion, annihilation, synchrotron and transition radiation, scintillation, refraction, reflection, absorption and Cherenkov effect. For some of these processes there are multiple physics models which may be used to implement the interactions. This category is divided into *standard* and *low energy* electromagnetic processes.

Standard electromagnetic processes assume the following things: the projectile energy is more than 1 keV, the atomic electrons are quasi-free, that is, their binding energy is neglected except for some corrections at low energy, and the atomic nucleus is fixed, that is, the recoil momentum is neglected. Standard processes include Compton scattering, gamma-conversion into electron and muon pairs [6] and the photo-electric effect for photons.

Electron/positron bremsstrahlung, ionisation and delta-ray production, positron annihilation and synchrotron radiation are also included. Muon processes handle bremsstrahlung, ionisation and delta-ray production and electron-positron pair production. There are also ionisation processes with the production of delta-rays for charged hadrons and ions. The energy losses of charged particles are

computed taking fluctuations into account. The default fluctuation model is Landau-like with additional Poisson-like fluctuations for soft energy transfers. An alternative model based on Photo-Absorption Interaction (PAI) [7] is also available. The multiple scattering process of Geant4 [8] can handle all charged particles. It does not use the Moliere formalism but is based on the more complete Lewis theory [9]. It simulates the scattering of the particle after a given step, computes the path length correction and the mean lateral displacement. The correlation between direction change and lateral displacement is included.

Low energy electromagnetic processes [10] are implemented in Geant4 in order to extend the validity range of electromagnetic interactions below 1 keV and the current implementation of its electron and photon processes can be used down to 250 eV. The low energy package includes the photoelectric effect, Compton scattering, Rayleigh scattering and polarised Rayleigh scattering, bremsstrahlung, and ionisation. The gamma conversion process has also been implemented. Fluorescence emission from excited atoms can be generated as well as Auger electrons. The implementation of electron and gamma processes is based on evaluated data libraries (EPDL97 [11], EEDL [12] and EADL [13]) that provide data for the determination of cross-sections and the sampling of the final state. Proton induced X-ray emission (PIXE) [14] is also available. Moreover there is an additional set of processes for photons, electrons and positrons in the low energy package. These processes are based on the physics models developed for the PENELOPE code (PENetration and Energy LOSS of Positrons and Electrons) [15]. These implementations also provide reliable results for energies down to a few hundred eV.

The low energy electromagnetic processes are well-designed for being able to handle multiple models in a process. For example, the hadron and ion ionisation process of the low energy package adopts different models depending on the energy range. In the high energy (>2 MeV) domain the Bethe-Bloch formula [16] is used and in the low energy domain (<1 keV for protons) the free electron gas model [17] is used. In the intermediate energy range parameterised models based on experimental data from the Ziegler [18] and ICRU [19] models are implemented. The molecular structure of materials [20] and the nuclear stopping power [21] are taken into account.

### *Decay*

At rest and in flight decays of particles are supported. Default decay tables for most unstable particles such as mesons, hyperons and resonant baryons based on data from the Particle Data Group [4], are provided. Decay modes are sampled according to the branching ratios in the particle's decay table. It is also possible for users to set the proper decay time and decay mode of the primary particle. There are many models for determining the distribution of daughter particles, for example V-A theory for muon decay, Dalitz theory for  $\rho^0$  decay, or simple phase space decay. Decay of radioactive nuclei is also supported and data tables derived from the Evaluated Nuclear Structure Data Files [6] are prepared for over two thousand nuclei. However radioactive decay is currently classified as a hadronic process in Geant4.

### *Transportation*

In Geant4, transportation is also treated as a kind of physics process. The transportation process propagates a particle through a detector geometry in the presence of magnetic or other fields and guarantees that steps within particle trajectories end at geometrical boundaries. Users may also set the maximum length of a single step.

### *Optical*

Geant4 can simulate the production and propagation of optical photons. There are many detectors which use scintillation and/or Cherenkov photons for their measurements and Geant4 is able to simulate such detectors. Optical photons can be initiated by a charged particle and terminated when entering photo-sensitive areas of the detector. Geant4 provides separate particle definitions for optical photons and gammas, reflecting their very different treatment within a simulation. Refraction and reflection at medium boundaries, bulk absorption, Rayleigh scattering and wavelength shifting processes are provided for optical photons. The optical properties in the medium and at the boundaries are important parameters of these processes. They can be expressed as a function of the photon's wavelength. However in many cases the user has to supply these parameters by himself. Geant4 provides a framework which assists the user in this.

### *Photo-lepton\_hadron*

Geant4 includes photo-nuclear and electro-nuclear reactions in which the energy flow of electrons, positrons and photons is converted into the energy flow of mesons, baryons and nuclear fragments [22]. The cross-section of the photo-nuclear process is comparable with the other electromagnetic processes in the nuclear giant resonance region. The equivalent photon method is applied to the electro-nuclear reactions. Geant4 also provides the nuclear interaction of muons with production of hadrons. This interaction becomes important for the simulation of detector response to high energy muons.

### *Parameterisation*

The processes in this category are used mainly for fast simulations which enable users to take over the tracking of a particle and implement a fast algorithm of detector response. A typical use case is shower parameterisation in a calorimeter. Instead of the detailed simulation of the incident particle which may produce a huge number of secondary particles in the detector, only a few tens of energy deposits will need to be posted in the detector [23,24]. However parameterisations are usually experiment-dependent and/or detector-dependent, so that Geant4 provides only an abstract interface for users.

## **Hadronic processes of Geant4**

The “Russian dolls” (Матрёшка) approach was selected for the hadronic interaction framework in Geant4. It consists of a multi-layer hierarchy, the top level of which provides the basic interface to the other Geant4 categories, such as tracking. As the hierarchy is descended, lower framework levels refine the interfaces for increasingly more specific use cases. Each level except the top has a concrete implementation of the abstract interface from the framework level directory above it, encapsulating the common logic for a particular use-case. The granularity of abstraction and delegation is refined at each framework level in this manner. Through these multi-layered frameworks, code can be developed independently by many users. It also provides significant flexibility to the user. The complete description of all levels of the framework is beyond the aim of this paper and it is given in Ref. [25]. In this paper only the second-level framework is discussed in order to make further explanations intelligible. The components of this level are cross-sections, final state production and isotope production. This level satisfies the requirements that user-defined cross-sections may be added, final state generation and isotope production models may be assigned to processes, and that these components may be used for different parts of the simulation depending on the conditions of the interaction. Thus the hadronic processes of Geant4 can handle multiple cross-section data sets and allow multiple models for final state generation. As a result, the hadronic processes include a large variety of complementary, overlapping and alternative cross-section data sets and physics models.

Physics requirements for the Geant4 hadronic interactions include an energy range which extends from thermal neutrons up to order TeV for LHC experiments and even higher for cosmic ray physics. It extends more than 15 orders of magnitude. In addition to energy range, there is a large variety of particle species and a diversity of interaction types. Geant4 is therefore also required to include the cross-sections of any incident meson or baryon for any materials including long-lived nuclear isotopes. Models of these interactions are also required. The cross-sections and models provided by Geant4 are discussed below.

Geant4 provides the total cross-sections for inelastic scattering, capture of neutral particles, induced fission and elastic scattering for all well known mesons and baryons including ions. The default data-sets for these interactions have been carried over from GEANT3. The term “data-set” represents an object which encapsulates methods and data for computing the occurrence of a given process. It was already mentioned that the software design of Geant4 allows users to overload the default data-sets with their specialised data-sets. The data-sets are stored and retrieved through a data store that works as a First-In-Last-Out stack. In addition to the default data-sets, Geant4 also provides specific data sets for proton- and neutron-induced reactions [26]. For neutron interactions at energies below 20 MeV precise data-sets derived from evaluated neutron data libraries are also available. Later we will discuss these data sets together with the final state generators for these interactions. For ion interactions, in order to cover all combinations of colliding nuclei over a wide energy range with good precision, the cross-section formulae of Tripathi [27,28], Kox [29], Shen [30],

and Sihver [31] were implemented in Geant4. These formulae calculate the total reaction cross-section which is the total cross-section minus elastic and electromagnetic dissociation cross-sections. Geant4 also provides data sets for electromagnetic dissociation cross-sections.

The final state modelling methods in the hadronic framework of Geant4 can be classified into three categories: *data-driven*, *parameterised* and *theory-based models*. *Data-driven models* are mainly based on evaluated or measured data. *Parameterised models* are largely based on parameterisations and the extrapolation of experimental data under some theoretical assumptions. *Theory-based models* are predominantly based on theory. In the following, we describe the usage of these modeling approaches in Geant4.

### **Data-driven models**

When experimental or evaluated data are available with sufficient coverage, the data driven approach is considered to be the optimal way of modeling. Neutron High Precision models are typical examples of this category. They are based on the ENDF/B-VI data format and procedures [32] and deal with the detailed transport of neutrons from thermal energies up to 20 MeV. They use the G4NDL neutron data library which is publicly available from the Geant4 web page. This library was derived from the evaluated neutron data libraries Brond-2.1 [33], CENDL2.2 [34], EFF-3 [35], ENDF/B-VI.0 [36], ENDF/B-VI.1, ENDF/BVI.5, FENDL/E2.0 [37], JEF2.2 [38], JENDL-FF [39], JENDL-3.1, JENDL-3.2, and MENDL-2 [40]. Our selection was guided in large part by the FENDL2.0 selection. Enhancement of the libraries is continuing in response to user requests. In these models all inclusive cross-sections are treated as point-wise cross-sections for reasons of performance. For this purpose, the data from the evaluated data library have been processed to explicitly include all neutron nuclear resonances in the form of point-like cross-sections rather than in the form of parameterisations.

The interactions of neutrons at low energies are classified into four parts as are the other hadronic processes in GEANT4. We consider radiative capture, elastic scattering, fission, and inelastic scattering as separate models. The data libraries for high precision neutron models are not complete because there are no data for several key elements in the above cited evaluated neutron data libraries. In order to use the high precision models, users were therefore required to develop their detectors using only elements found in the library. In order to avoid this difficulty, alternative models were developed which use the high precision models when data are found in the library, but use low energy parameterised models (described later) when data are missing. The alternative models cover the same types of interaction as the originals, that is, elastic and inelastic scattering, capture and fission. Because the low energy parameterised part of the models is independent of G4NDL, results will not be as precise as they would be if the relevant data existed. The data driven approach is also used to simulate photon evaporation and radioactive decay. Both codes are based on the ENSDF [41] data of nuclear levels, and transition, conversion, and emission probabilities. The absorption of particles coming to rest and the low energy part of elastic scattering final states in scattering off hydrogen are modelled with this approach.

### **Parameterised models**

Parameterisations and extrapolations of cross-sections and interactions are widely used in the full range of energies and for all kinds of reactions. Low- and high-energy parameterisation models are available in Geant4. They are re-engineered models from GEANT3, predominantly GHEISHA [42]. They include induced fission, capture, elastic and inelastic interactions.

### **Theory-based models**

The models in this category can be divided into three different energy regions such as high energy (above 5 GeV), low energy (below 100 MeV) and intermediate. For high energies, parton string models are used to generate the final state inelastic interactions of hadrons with nuclei in Geant4. Such models can be divided into two phases: string excitation and string fragmentation. Two models which have different approaches to the string excitation phase are implemented. One is based on diffractive excitation and the other so-called Quark Gluon String model, is based on soft scattering with diffractive admixture according to cross-sections. In the string fragmentation phase, two models have basically common treatments, but use different fragmentation functions. For intermediate energies intra-nuclear transport models are used. Geant4 provides the Binary Cascade [43] model which is based on

a detailed three-dimensional model of the nucleus, and exclusively based on binary scattering between reaction participants and nucleons within the nuclear model, and an implementation of the Bertini Cascade [44]. At energies below 100 MeV exciton-based pre-compound models [45] are provided. They are able to describe the energy and angular distributions of the fast secondaries and soften the behavior of the quasi-elastic peaks to reproduce experimental data.

The last and lowest energy phase of a nuclear interaction is nuclear evaporation. Variants of the classical Weisskopf-Ewing model [46] are used for the interaction. Specialised improvements such as Fermi's break-up model [47] for light nuclei, and multi-fragmentation [48] for very high excitation energies are employed. Fission [49] and photon evaporation including internal conversion can be treated as competitive channels in the evaporation model. A model based on the Generalised Evaporation Model (GEM) [50] is also implemented. For ion interactions the Binary Cascade can handle light ion reactions [51] and Wilson's abrasion model [52] together with its ablation part is also implemented. Electromagnetic dissociation for ion-ion collisions is also treated in Geant4. As an alternative for all nuclear fragmentation models, including evaporation models, the chiral invariant phase space (CHIPS) model [53,54] is available. It is a quark-level 3-dimensional, SU(3) X SU(3) symmetric event generator for fragmentation of excited hadronic and nuclear systems into hadrons. A theoretical model for coherent elastic scattering [55] also exists. This is a hybrid of data-driven and theory-based models, since it utilises a large pre-processed data tabulation.

## Other functionalities for shielding calculations

### *Variance reductions*

Variance reduction techniques are an important aspect of most Monte Carlo calculations and allow the user to tune the simulation to the part of the problem space (particle species, energy, position, etc.) most relevant to his/her application [56]. To facilitate the usage of variance reduction techniques, general-purpose biasing methods have been introduced into the toolkit. Many applications, including radiation shielding studies, can profit from this functionality to achieve large gains in time efficiency. A new Geant4 module provides importance biasing, with splitting and Russian roulette [57]; an importance value is associated with each volume. Either the conventional mass geometry (the one used for physics and tracking) or a dedicated artificial parallel geometry can be used for biasing. Other biasing capabilities added in recent releases include an implementation of the weight-window method and of the related, but simpler, weight-cutoff method [58]. Leading particle and cross-section biasing are provided for hadronic processes in the corresponding physics package.

### *Scoring*

Geant4 provides two abstract base classes and one template class for defining detector sensitivity. These classes are flexible and extensible for customisation so that all user requirements may be met. However, users must implement these classes by themselves. Geant4 also offers concrete scoring classes (known as "Primitive Scorer") for common detector sensitivities so that users are not forced to implement their own sensitivities. In this way physical quantities can be obtained more directly and easily.

## Conclusion

The Geant4 toolkit provides a full set of software packages for the simulation of particles passing through matter. It adopts an object-oriented design and this implementation allows easy extensions and modifications of the toolkit. Abundant physics processes ranging from thermal neutron interactions in reactor engineering to very high energy interactions in particle physics and cosmic ray physics are provided in the toolkit. It also has variance reduction mechanisms such as importance biasing with weight windows and hands-on user-friendly tallies for simulation results. Therefore, Geant4 already encompasses all aspects of shielding calculations.

All source code and data files of Geant4 is publicly available with documentation from the web. The continuing development of Geant4 is done by the world-wide Geant4 Collaboration.

The scope of Geant4 applications continues to expand.

## References

- [1] S. Agostinelli, et al., "Geant4: A Simulation Toolkit", *Nucl. Instrum. Meth.*, A 506 (2003) 250, Geant4 web page, <http://geant4.web.cern.ch/geant4/>.
- [2] J. Allison, et al., "Geant4 Developments and Applications", *IEEE Transactions on Nuclear Science* 53 No. 1 (2006) 270.
- [3] G. Cosmo, "Software Process in Geant4", in *Proc. Computing in High Energy and Nuclear Physics*, Beijing, China (2001) 469.
- [4] Review of Particle Physics, *Eur. Phys. J.*, C 15 (2000).
- [5] M.A. Zucker, A.R. Kishore, R. Sukumar, R.A. Dragoset, Elemental Data Index (version 2.1) [Online], <http://physics.nist.gov/EDI>, 21 April 2006, National Institute of Standards and Technology, Gaithersburg, MD, (2005).
- [6] H. Burkhardt, S.R. Kelner, R.P. Kokoulin, "Monte Carlo Generator for Muon Pair Production", CERN-SL-2002-016 (AP) and CLIC Note 511, May (2002).
- [7] J. Apostolakis, et al., "An Implementation of Ionisation Energy Loss in Very Thin Absorbers for the GEANT4 Simulation Package", *Nucl. Instr. And Meth.*, A 453 (2000) 597.
- [8] See Physics Reference Manual at the Geant4 Web page under Documentation.
- [9] H.W. Lewis, "Multiple Scattering in an Infinite Medium", *Phys. Rev.*, 78 (1950) 526.
- [10] S. Chauvie, et al., "Geant4 Low Energy Electromagnetic Physics", *Proc. Computing in High Energy and Nuclear Physics*, Beijing, China, (2001) 337.
- [11] D. Cullen, et al., *EPDL97: The Evaluated Photon Data Library, 97 version*, UCRL-50400, Vol. 6, Rev. 5 (1997).
- [12] S.T. Perkins, et al., *Tables and Graphs of Electron-interaction Cross Sections from 10 eV to 100 GeV Derived from the LLNL Evaluated Electron Data Library (EEDL)*, UCRL-50400, Vol. 31 (1997).
- [13] S.T. Perkins, et al., *Tables and Graphs of Atomic Subshell and Relaxation Data Derived from the LLNL Evaluated Atomic Data Library (EADL), Z = 1~100*, UCRL-50400, Vol. 30 (1997).
- [14] S. Guatelli, et al., "Geant4 Atomic Relaxation", *Conf. Rec. 2004 IEEE Nucl. Sci. Symposium*, N44-4. (2004).
- [15] J. Baró, et al., "PENELOPE: An Algorithm for Monte Carlo Simulation of the Penetration and Energy Loss of Electrons and Positrons in Matter", *Nucl. Instr. Meth.*, B 100 (1995) 31.
- [16] H. Bethe, "Theory of the Passage of Rapid Corpuscular Rays Through Matter", *Ann. Phys.*, 5 (1930) 325.
- [17] J. Linhard, A. Winther, *Mat. Fys. Medd. Dan. Vid. Selsk.*, 34, No 10 (1963).
- [18] H.H. Andersen, J.F. Ziegler, "The Stopping and Ranges of Ions in Matter", Vol. 3, Pergamon Press, Oxford (1977).
- [19] A. Allisy, et al., *ICRU Report 49*, (1993).
- [20] J.F. Ziegler, J.M. Manoyan, "The Stopping of Ions in Compounds", *Nucl. Instr. and Meth.*, B 35 (1988) 215.
- [21] M.R. Bhat, *Evaluated Nuclear Data File (ENSDF)*, Nuclear Data for Science and Technology, Springer, Berlin, Germany, (1992) 817.
- [22] M.V. Kossov, "Approximation of Photonuclear Interaction Cross-sections", *Eur. Phys. J. A* 14 (2002) 377.

- [23] G. Grindhammer, M. Rudowicz, S. Peters, "The Fast Simulation of Electromagnetic and Hadronic Showers", *Nucl. Instr. and Meth.*, A 290 (1990) 469.
- [24] J. del Peso, E. Ros, "Fast Simulation of Electromagnetic Showers in the ZEUS Calorimeter", *Nucl. Instr. and Meth.*, A 306 (1991) 485.
- [25] J.P. Wellisch, "Hadronic Shower Models in Geant4 – the Frameworks", *Comp. Phys. Commun.*, 140 (2001) 65.
- [26] J.P. Wellisch, D. Axen, "Total Reaction Cross Section Calculations in Proton-nucleus Scattering", *Phys. Rev.*, C 54 (1996) 1329.
- [27] R.K. Tripathi, F.A. Cucinotta, J.W. Wilson, *Universal Parameterization of Absorption Cross Sections*, NASA Technical Paper TP-3621 (1997).
- [28] R.K. Tripathi, F.A. Cucinotta, J.W. Wilson, *Universal Parameterization of Absorption Cross Sections – Light Systems*, NASA Technical Paper TP-209726 (1999).
- [29] S. Kox, et al., "Trends of Total Reaction Cross Sections for Heavy Ion Collisions in the Intermediate Energy Range," *Phys. Rev.*, C35 (1987) 1678.
- [30] Wen-qing Shen, et al., "Total Reaction Cross Section for Heavy-ion Collisions and its Relation to the Neutron Excess Degree of Freedom", *Nucl. Phys.*, A 491 (1989) 130.
- [31] L. Sihver, et al., "Total Reaction and Partial Cross Section Calculations in Proton-nucleus ( $Z_t \leq 26$ ) and Nucleus-nucleus Reactions ( $Z_p$  and  $Z_t \leq 26$ )", *Phys. Rev.*, C47 (1993) 1225.
- [32] *Data Formats and Procedures for the Evaluated Nuclear Data File*, National Nuclear Data Centre, Brookhaven National Laboratory, Upton, NY, USA.
- [33] A.I. Blokhin, et al., *BROND-2.2: Current Status of Russian Nuclear Data Libraries*, *Nuclear Data for Science and Technology*, Vol. 2, American Nuclear Society, La-Grange, IL, (1994) 695.
- [34] CENDL-2: Chinese Nuclear Data Centre, CENDL-2, *The Chinese Evaluated Nuclear Data Library for Neutron Reaction Data*, IAEA-NDS-61, Rev. 3, International Atomic Energy Agency, Vienna, Austria (1996).
- [35] H.D. Lemmel, *EFF-2.4: The European Fusion File 1994, Including Revisions up to May 1995*, Summary Documentation, IAEA-NDS-170, June (1995).
- [36] ENDF/B-VI, *Cross Section Evaluation Working Group, ENDF/B-VI Summary Document*, BNL-NCS-17541 (ENDF-201) National Nuclear Data Centre, Brookhaven National Laboratory, Upton, NY, USA, (1991).
- [37] FENDL/E2.0, *The Processed Cross-section Libraries for Neutron-photon Transport Calculations, Version 1 of February 1998*, Summary documentation, H. Wienke, M. Herman, Report IAEA-NDS-176 Rev. 0, International Atomic Energy Agency, April 1998.
- [38] T. Nakagawa, et al., "JENDL-3 Japanese Evaluated Nuclear Data Library, Version 3, Revision 2", *J. Nucl. Sci. Technol.*, 32 (1995) 1259.
- [39] C. Nordborg, M. Salvatores, "JEF-2: Status of the JEF Evaluated Data Library", *Nuclear Data for Science and Technology*, American Nuclear Society, LaGrange, IL (1994).
- [40] Yu.N. Shubin, V.P. Lunev, A.Yu. Konobeyev, A.I. Ditjuk, *Cross Section Data Library MENDL-2 to Study Activation as Transmutation of Materials Irradiated by Nucleons of Intermediate Energies*, INDC(CCP)-385, International Atomic Energy Agency (May 1995).
- [41] M.R. Bhat, "Evaluated Nuclear Data File (ENSDF)", *Nuclear Data for Science and Technology*, Springer, Berlin, Germany, (1992) 817.
- [42] H.C. Fesefeldt, *Simulation of Hadronic Showers, Physics and Application*, Technical Report PITHA 85-02 (1985).
- [43] G. Folger, V.N. Ivanchenko, J.P. Wellisch, "The Binary Cascade", *Eur. Phys. J.*, A., Vol. 21, (2004) 407.
- [44] A. Heikkinen, N. Stepanov, J.P. Wellisch, "Bertini Intranuclear Cascade Implementation in Geant4", *Proc. Computing in High Energy and Nuclear Physics*, La Jolla, California, MOMT008 (2003).

- [45] V. Lara, J.P. Wellisch, "Pre-equilibrium and Equilibrium Decays in Geant4", *Proceedings of the CHEP 2000 Conference*, Padova, Italy (February 2000).
- [46] V.E. Weisskopf, D.H. Ewing, "On the Yield of Nuclear Reactions with Heavy Elements", *Phys. Rev.*, 57 (1940) 472.
- [47] E. Fermi, "High Energy Nuclear Events", *Prog. Theor. Phys.*, 5 (1950) 1570.
- [48] J.P. Bondorf, A.S. Botvina, A.S. Iljinov, I.N. Mishustin, K. Sneppen, *Phys. Rep.*, 257 (1995) 133.
- [49] N. Bohr, J.W. Wheeler, "The Mechanism of Nuclear Fission", *Phys. Rev.*, 56 (1939) 426.
- [50] S. Furihata, "Statistical Analysis of Light Fragment Production from Medium Energy Proton-induced Reactions", *Nucl. Inst. Meth.*, B 171 (2000) 251.
- [51] T. Koi, et al., "Ion Transport Simulation Using Geant4 Hadronic Physics", *The Monte Carlo Method: Versatility Unbounded in a Dynamic Computing World Chattanooga*, Tennessee, 17-21 April 2005, on CD-ROM, American Nuclear Society, LaGrange Park, IL (2005).
- [52] J.W. Wilson, R.K. Tripathy, F.A. Cucinotta, J.L. Shinn, et al., *NUCFRG2: An Evaluation of the Semiempirical Nuclear Fragmentation Database*, NASA Tech. Paper 3533 (1995).
- [53] P.V. Degtyarenko, M.V. Kossov, H.P. Wellisch, "Chiral Invariant Phase Space Event Generator. II: Nuclear Pion Capture at Rest and Photo-nuclear Reactions Below the Delta(3,3) Resonance", *Eur. Phys. J.*, A 9 (2000) 411.
- [54] P.V. Degtyarenko, M.V. Kossov, H.P. Wellisch, "Chiral Invariant Phase Space Event Generator. III: Modeling of Real and Virtual Photon Interactions with Nuclei Below Pion Production Threshold", *Eur. Phys. J.*, A 9 (2000) 421.
- [55] V.L. Korotkikh, N.I. Starkov, "Photoproduction of Heavy Vector Mesons on Nuclei with Excitation of a Discrete Level", *Sov. Journ. of Nucl. Phys.*, Vol. 37, (1983) 610.
- [56] L.L. Carter, E.D. Cashwell, *Particle Transport Simulation with the Monte Carlo Method*, TID-26607, US National Technical Information Centre, Energy Research and Development Administration (1975).
- [57] M. Dressel, *Geometrical Importance Sampling in Geant4: From Design to Verification*, CERN-OPEN-2003-048 (2003).
- [58] T. Booth, *A Sample Problem for Variance Reduction in MCNP*, Los Alamos National Laboratory Report LA-10363-MS (October 1985).

## **Session VI**

### **Shielding in medical and industrial accelerator applications**

***Chairs: N.E. Ipe, B.L. Kirk***



## Computational Medical Physics Working Group

**Bernadette L. Kirk,<sup>1</sup> Alireza Haghghat<sup>2</sup>**

<sup>1</sup>Oak Ridge National Laboratory\*, Oak Ridge, USA

<sup>2</sup>University of Florida, Gainesville, USA

### Abstract

*The newly-formed Computational Medical Physics Working Group (CMPWG) can contribute to the Shielding Aspects of Accelerators and Target Irradiation Facilities (SATIF) series of workshops through its interest in shielding benchmarks of medical facilities that employ particle accelerators and general shielding due to the use of radioisotopes in the clinical setting. The use of software tools in the analysis of radiation dose and its health effects has been increasing. CMPWG promotes the advancement of computational tools, experimental data, and enabling technologies which are applicable to clinical problems in medical and health physics.*

---

\* Managed by UT-Battelle, LLC, under contract DE-AC05-00OR22725 with the US Department of Energy.

## Introduction

The use of software tools in the analysis of radiation dose and its health effects has been increasing. Such tools include MCNP/MCNPX [1–3], ITS [4], TORT [5], ANISN [6], EGS4 [7–8], PENTRAN [9], GEANT4 [10], ATTLA [11], PARTISN [12], A<sup>3</sup>MCNP to name a few. The development of many of these software tools in the twentieth century was prompted by nuclear reactor analysis, nuclear weapons studies, accelerators, fusion reactors and health physics concerns. As the field of medical physics continues to grow, the implementation of these software codes in cancer research studies becomes more prevalent.

It is imperative that a union of research encompassing nuclear engineering on one hand and medical and health physics on the other hand be formed. CMPWG was established in 2005 within the American Nuclear Society (ANS) to address the issue. CMPWG is hosted by three divisions of the ANS – Mathematics and Computations Division (MCD), Biology and Medicine Division (BMD), Radiation Protection and Shielding (RPSD). The website is <http://cmpwg.ans.org>.

## Goals and activities

CMPWG promotes the advancement of computational tools, experimental data, and enabling technologies which are applicable to clinical problems in medical and health physics. The group concentrates on a multidisciplinary approach (nuclear engineering, medical physics and health physics) for use by the medical practitioners in the studies of radiation imaging, treatment and effects on human and animal life. The applications include computational benchmarks on phantoms and detectors, large scale optimisation, deterministic and stochastic approaches to radiation therapy and diagnostic problems.

The Nuclear Science and Technology Division (NSTD) of Oak Ridge National Laboratory (ORNL) sponsored the first workshop of CMPWG on 26 October 2005. The workshop was held to address several key areas:

- identify the medical physics problems and experiments for computational benchmarks;
- identify the software tools, their applications, strengths and weaknesses;
- identify applications suitable for parallel computing;
- identify the roadmap for benchmarking activities.

Discussions centred on the need for experimental data, the importance of both Monte Carlo and deterministic methods, and the need to evaluate current nuclear data for medical physics. These activities are aimed at improving dose predictions for radiation therapy and other medical activities that utilise ionising radiation. Proceedings of the workshop are published in the ORNL report ORNL/TM-2006/7. Copies of the proceedings can be obtained from [riceaf@ornl.gov](mailto:riceaf@ornl.gov).

The next CMPWG workshop will be held in fall 2007. Participation is voluntary.

## References

- [1] Los Alamos National Laboratory, X-5 Monte Carlo Team, *MCNP–A General Monte Carlo N-particle Transport Code, Version 5, Vol. I: Overview and Theory*, LA-UR-03-1987 (April 2003, Revised October 2005).
- [2] D.B. Pelowitz (Ed.), *MCNPX User’s Manual, Version 2.5.0*, Los Alamos National Laboratory report, Los Alamos, New Mexico, LA-CP-05-0369 (April 2005).

- 
- [3] J.S. Hendricks, *et al.*, MCNPX Extensions, Version 2.5.0, Los Alamos National Laboratory report, Los Alamos, New Mexico, LA-UR-05-2675 (April 2005).
- [4] J.A. Halbleib, R.P. Kensek, T.A. Mehlhorn, G.D. Valdez, S.M. Seltzer, M.J. Berger, *ITS Version 3.0: The Integrated TIGER Series of Coupled Electron/Photon Monte Carlo Transport Codes*, Sandia National Laboratory report, Albuquerque, New Mexico, SAND91-1634 (March 1992).
- [5] W.A. Rhoades, D.B. Simpson, *The TORT Three-dimensional Discrete Ordinates Neutron/Photon Transport Code*, Oak Ridge National Laboratory report, Oak Ridge, Tennessee, ORNL/TM-13221 (October 1997).
- [6] W.W. Engle Jr., ANISN, *A One-dimensional Discrete Ordinates Transport Code with Anisotropic Scattering*, Oak Ridge Gaseous Diffusion Plant, Oak Ridge, Tennessee, Report K-1693 (March 1967).
- [7] W.R. Nelson, H. Hirayama, D.W. Rogers, *The EGS4 Code System*, Stanford Linear Accelerator Centre report, Stanford University, Stanford, California, SLAC-265 (December 1985).
- [8] A.F. Bielajew, H. Hirayama, W.R. Nelson, D.W.O. Rogers, *History, Overview and Recent Improvements of EGS4*, Stanford Linear Accelerator Centre report, Stanford University, Stanford, California, SLAC-PUB-6499, NRC-PIRS-0436, KEK Internal 94-4, (Revised June 1, 1994).
- [9] G.E. Sjoden, A. Haghghat, "PENTRAN – A 3-D Cartesian Parallel Sn Code with Angular, Energy, and Spatial Decomposition", *Proceedings of the Joint International Conference on Mathematical Methods and Supercomputing in Nuclear Applications*, Vol. II, 1267-1276, Saratoga Springs, NY, 6-10 October 1997, <http://uflight.nre.ufl.edu/~haghgha/pentran.html>.
- [10] Geant4 Collaboration, *Geant4: An Object-oriented Toolkit for Simulation in HEP*, CERN/LHCC 98-44, <http://wwwinfo.cern.ch/asd/geant4/geant4.html>.
- [11] Transpire, Inc., ATTILA, [www.transpireinc.com/software.htm](http://www.transpireinc.com/software.htm).
- [12] R.E. Alcouffe, R.S. Baker, J.A. Dahl, S.A. Turner, R. Ward, *PARTISN: A Time-dependent, Parallel Neutral Particle Transport Code System*, Los Alamos National Laboratory report, Los Alamos, New Mexico, LA-UR-05-3925 (May 2005).
- [13] J.C. Wagner, A. Haghghat, "Automated Variance Reduction of Monte Carlo Shielding Calculations Using the Discrete Ordinates Adjoint Function", *Nuclear Science and Engineering*, 128, 186-208, 1998, <http://uflight.nre.ufl.edu/~haghgha/a3mcpn.html>.



## **Radiation measurements at the RPTC in Munich for verification of shielding measures around the cyclotron area**

**Wolfgang Dittrich**

AREVA NP GmbH – NEPR-G, Erlangen, Germany

**Thomas Hansmann**

M+W Zander Facility Engineering GmbH, Stuttgart, Germany

### **Abstract**

*The Rinecker Proton Therapy Centre (RPTC) in Munich is equipped with a cyclotron with a planned extracted current of up to 500 nA protons. By means of a degrader and energy selection system the proton energy is varied between 70 and 250 MeV. After a brief description of the method for determination of shielding thicknesses, based on AREVA NP's presentation at SATIF-7 May 2004, results of a radiation survey around the cyclotron / degrader area are presented. A comparison for the predicted and resulting annual individual doses at the survey locations is given.*



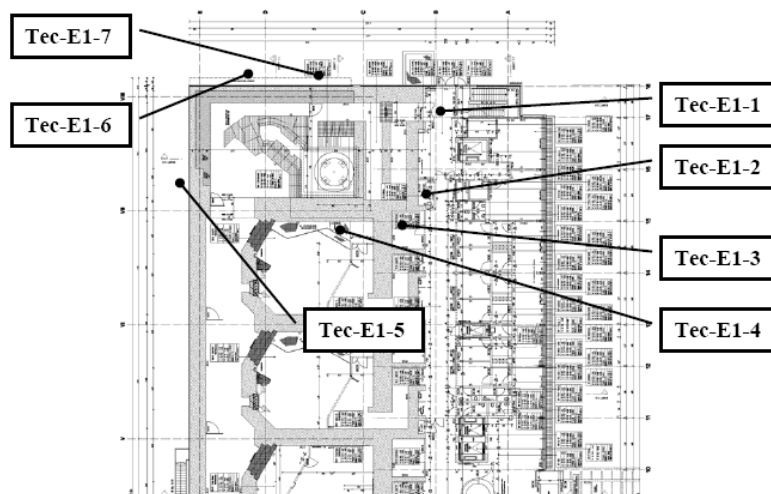
the final mobile shields around the degrader, as shown already in the corresponding presentation during SATIF-7 [1]. This representation plot is very useful to evaluate the influence of additional shielding measures or the use of specific shielding materials if one defines different colours for the various concrete mixtures (in the following Figure 1 suppressed for better representation in print).

As the shielding target not only was to keep below a certain dose rate value but also to keep below an annual dose for a single person, a reference treatment model was considered which provided proton losses in the plant with the distribution of the corresponding proton current by energy and hours per year. Based on these data conversion factors from dose rate to annual dose were derived. The determination of minimum shielding thicknesses needed was therefore based on those iso-dose-rate plots plus these conversion factors. The shielding targets for the public area were 1 mSv/yr and approx. 10  $\mu$ Sv/hr to an individual. The public area was defined to begin just in the main floor in front of the treatment rooms, as a consequence the entire plant area until the fence was considered as a public area. Safety factors to cover uncertainties in calculation were not applied.

### Survey results for the cyclotron/degrader area

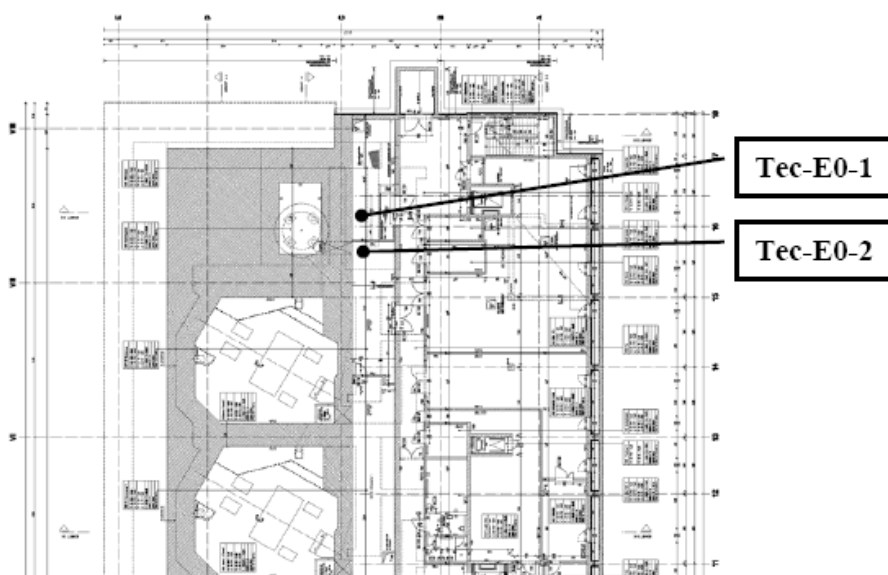
The measured dose rate values presented in the following resulted from surveys executed during autumn 2005. The survey results are the sum of neutron and gamma dose rate whereas all predictions are neutron dose rate (as only small gamma contributions had been calculated). Various detector types both for neutrons and photons have been used, especially in order to cover higher neutron energies a probe of type FHT 762 Wendi-2 (Thermo-Eberline ESM, Erlangen) was used. For the sum value at one reference point the survey result for the detector/probe showing the highest neutron dose rate was chosen. During the measurement a proton current of about 500 nA at 250 MeV was impinging on the degrader at its position set for the production of a 70 MeV beam. The comparison has been performed considering the actual, exact current and the reference treatment model mentioned above.

Figure 2: Survey results on the ground level compared with the prediction



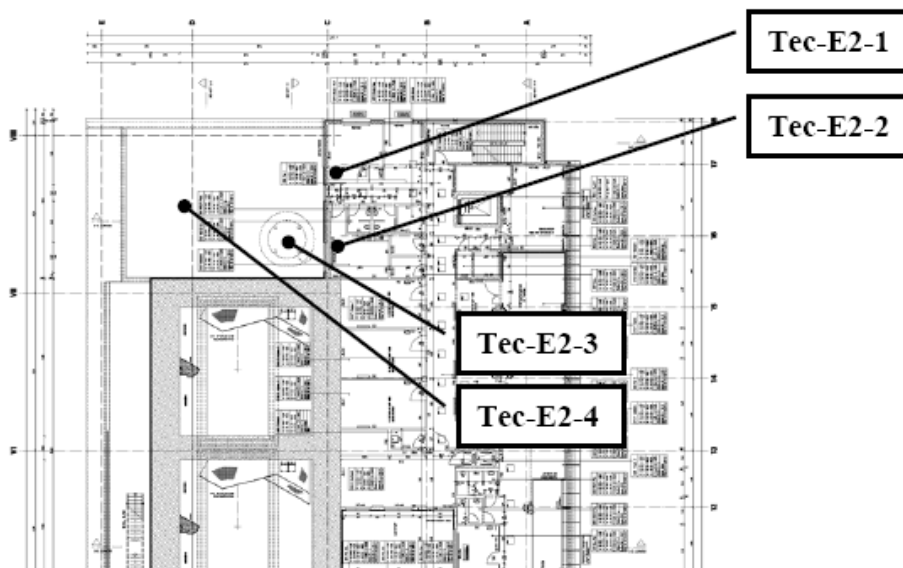
Location	No.	$\mu$ Sv/hr measured	mSv/yr (reference treatment model) MCNPX	mSv/yr (reference treatment model) measured	Factor measured/predicted with MCNPX in %
Access cyclotron maze	E1-1	0.146	0.030	0.023	77.9
Room for cleaning equipment	E1-2	0.280	0.160	0.045	28.0
Control room gantry 1	E1-3	0.066	0.020	0.011	52.8
Machine area gantry 1	E1-4	0.273	0.160	0.044	27.3
Wall, north	E1-5	0.039	0.150	0.014	9.4
Wall, near north-east corner	E1-6	0.153	0.800	0.058	7.3
Wall, near maze to cyclotron	E1-7	0.153	2.920	0.055	1.9

Figure 3: Survey results on the levels below the cyclotron compared with the prediction



Location	No.	$\mu\text{Sv/hr}$ measured	mSv/yr (reference treatment model) MCNPX	mSv/yr (reference treatment model) measured	Factor measured/predicted with MCNPX in %
Cooling water room, basement	E0-1	0.909	0.160	0.145	90.9
HF generation room, basement	E0-2	0.065	1.600	0.010	0.7

Figure 4: Survey results above the cyclotron compared with the prediction



Location	No.	$\mu\text{Sv/hr}$ measured	mSv/yr (reference treatment model) MCNPX	mSv/yr (reference treatment model) measured	Factor measured/predicted with MCNPX in %
Physician room, upper level	E2-1	0.216	0.800	0.035	4.3
Kitchen, upper level	E2-2	0.1780	0.890	0.028	3.2
Roof above cyclotron	E2-3	0.094	0.320	0.015	4.7
Roof above degrader	E2-4	0.098	0.100	0.015	14.7

## Discussion and conclusions

Looking at these three tables one can find that two major groups of survey points are apparent:

- Group 1 with survey results near prediction (10-100%).
- Group 2 with survey results less than 10% of prediction.

Evaluating this in detail a dependence on concrete compositions seems to be a likely result:

- Group 1 was measured at locations with normal concrete between source and survey point.
- Group 2 was measured at locations with heavy concrete mixtures between source and survey point.

In the case of almost only normal concrete as shielding between radiation source and reference point the agreement between prediction and result is fairly good (no safety factor was used for prediction). In the case of significant shielding constructed of heavy concrete, an evaluation of concrete samples showed a larger density than that specified which results in a significantly higher shielding factor due to relatively thick walls.

Based on the reference treatment model the shielding targets are met. The calculations provided results on the safe side.

## References

- [1] W. Dittrich, W. Hofmann, "Use of Iso-dose-rate Pictures for Shielding Design of a Proton Therapy Centre", SATIF-7, 17-18 May 2004, ITN, Sacavem, Portugal.



## **Preliminary computational models for shielding design of particle therapy facilities**

**Nisy E. Ipe**

Consultant, Shielding Design, Dosimetry and Radiation Protection, San Carlos, California, USA

**Alberto Fassò**

Radiation Protection, SLAC, Stanford, California, USA

### **Abstract**

*A typical particle therapy facility may consist of an injector, a cyclotron or a synchrotron, a high energy transport beam line, several treatment rooms including fixed beam and gantry rooms, and sometimes even a research area. Each of these areas requires shielding. At these facilities maximum proton energies typically range from about 230 to 250 MeV, while carbon ions may have energies that extend to a maximum of 320 MeV/u to 430 MeV/u. Shielding calculations can be facilitated if there are computational models comprised of source terms and attenuation lengths that are independent of geometry. Agosteo, et al. have derived such models for concrete shielding for 400 MeV/u carbon ions and 100-400 MeV protons. However, no data has been published for 430 MeV carbon ions, or for composite barriers. In this paper preliminary computational models for shielding design with concrete and composite barriers are presented. The models are based on FLUKA simulations for 430MeV/u carbon ions incident on a tissue target. Some data is also provided for carbon ions incident on an iron target. The neutron spectra at forward and large angles, as well as the relative contributions of neutrons, protons and pions and photons to total dose are also shown.*

## Introduction

There are currently about twenty five operational particle therapy facilities world wide with three facilities actually treating patients with carbon ions. Another 13 facilities or so are in the design or construction stage. Some of these facilities will also have carbon ions. A typical particle therapy facility may consist of an injector, a cyclotron or a synchrotron, a high energy transport beam line, several treatment rooms including fixed beam and gantry rooms, and sometimes even a research area. Each of these areas requires shielding. At these facilities maximum proton energies typically range from about 230 to 250 MeV, while maximum carbon ion energies may range from 320 MeV/u to 430 MeV/u. For treatment rooms, the target for carbon ions is the patient (tissue). For the machines and beam lines, the target is a beam line component such as the vacuum chamber or magnet, etc. The magnets are usually made of iron.

Performing complete Monte Carlo calculations for a specific room design is time consuming and should be avoided during the preliminary design phase, since the room configuration and shielding thicknesses are susceptible to change and various iterations, as the layout is being finalised. Thus, shielding calculations can be facilitated if there are computational models comprised of source terms and attenuation lengths that are independent of geometry [1]. Also since space is a premium, large thicknesses of concrete shielding can often be replaced by smaller thicknesses of composite shields, i.e. shielding consisting of a combination of metal (such as steel) and concrete.

Agosteo, *et al.* have derived such models for concrete shielding for 400 MeV/u carbon ions and 100-400 MeV protons [1-3]. However, no data has been published for 430 MeV carbon ions, or for composite shields. In this paper preliminary computational models for shielding design with concrete and composite shields are presented. The models are based on FLUKA simulations with 430MeV/u carbon ions incident on a tissue target [4]. Some data is also provided for carbon ions incident on an iron target.

## Simulations

Computational models that are independent of geometry can be described by the following Eq. (1):

$$H(E_p, \theta, d/\lambda_\theta) = \frac{H_0(E_p, \theta)}{r^2} \exp\left[-\frac{d}{\lambda_\theta g(\theta)}\right] \quad (1)$$

where:  $H$  is the dose equivalent at the outside the shield;

$H_0$  is source term at an angle  $\theta$  with respect to the incident beam, and is assumed to be geometry independent;

$r$  is the distance between the target and the point at which the dose equivalent is scored;

$d$  is the thickness of the shield;

$d/g(\theta)$  is the slant thickness of the shield at an angle  $\theta$ ;

$\lambda(\theta)$  is the attenuation length at an angle  $\theta$ ;

$g(\theta) = \cos\theta$  for forward shielding;

$g(\theta) = \sin\theta$  for lateral shielding;

$g(\theta) = 1$  for spherical geometry.

Agosteo, *et al.* have derived such models for 400 MeV/u Carbon ions and 100-400 MeV protons [1-3]. These studies were performed with FLUKA using experimental data as a neutron source, since heavy ion reactions in Monte Carlo codes were not available until recently. Further, experimental data were available for only a limited number of ions, targets and energies. The heavy ion interaction model is implemented in the most recent versions of FLUKA (since 2004) and has been successfully benchmarked with existing experimental data [4]. Full ion transport and interactions for beams and targets of interest can now be simulated.

Since there is no data available in the literature for 430 MeV/u carbon ions, Monte Carlo calculations were performed using FLUKA. The simulations were performed so that source terms and attenuation lengths in concrete and composite barriers could be determined for 430 MeV/u carbon ions. A monoenergetic pencil beam of carbon ions was allowed to strike the target, placed at the centre of a spherical concrete shell with an inner radius of 4 m and an outer radius of 9.1 m. The inner radius of 4 m was chosen because it was representative of typical treatment room dimensions, and further it was also felt that effects due to curvature would be insignificant. The regions between 4 m and 9.1 m were divided into 17 shells each of thickness 30 cm. The shells were further divided into polar sectors to facilitate determination of the angular distribution of the calculated fluence. Four polar sectors were used: 0-10 degrees, 10-30 degrees, 40-60 degrees and 80-100 degrees. Volume averaged fluences were scored for all particles in each sector. The most current fluence to ambient dose equivalent conversion coefficients available in the FLUKA package were used to convert the fluences to ambient dose equivalent ( $H^*10$ ) [6].

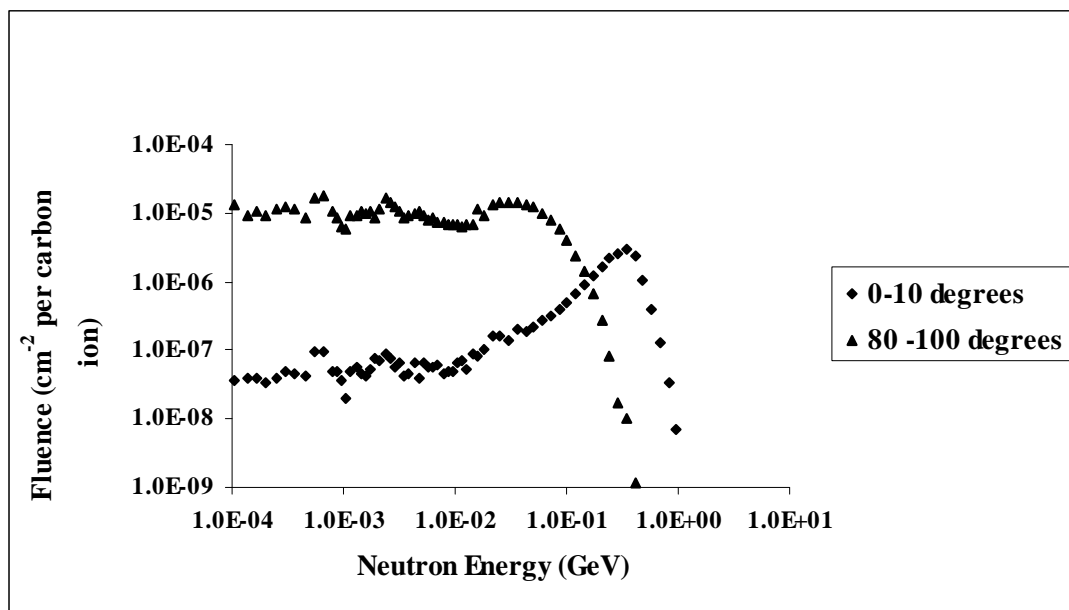
Two types of targets were used, the ICRU tissue sphere (15 cm radius, 76.2% O, 10.1% H, 11.1% C and 2.6% N), and an iron stopping target of radius 5.8 cm, and length 6 cm [7]. Since the concrete shell was fairly thick (5.1 m) variance reduction techniques (importance biasing with Russian Roulette and splitting) were used. Simulations were also performed with some of the inner layers of concrete changed to iron, and all the concrete changed to vacuum. The electron production and transport cut-off was 500 MeV. The photon production and transport cut-off was 100 keV. Errors were typically within few % at small angles and within 20% at large angles.

## Results and discussion

Nuclear interactions of heavy ions such as carbon with matter arise either from grazing collisions or head-on collisions [8]. In grazing collisions, fragmentation of either the carbon ion or the in-target nucleus occurs. Fragmentation is the predominant mechanism. Head-on collisions are less frequent but result in the transfer of much larger amounts of energy and momentum compared to grazing collisions.

The fragmentation of heavy ions is independent of the target material. It has been proposed that fragmentation of the heavy ion into nuclear products of smaller mass proceeds with little or no change in the mean velocity.

**Figure 1: Neutron energy spectra incident at concrete surface for 430 MeV/u carbon ions incident on ICRU tissue sphere**

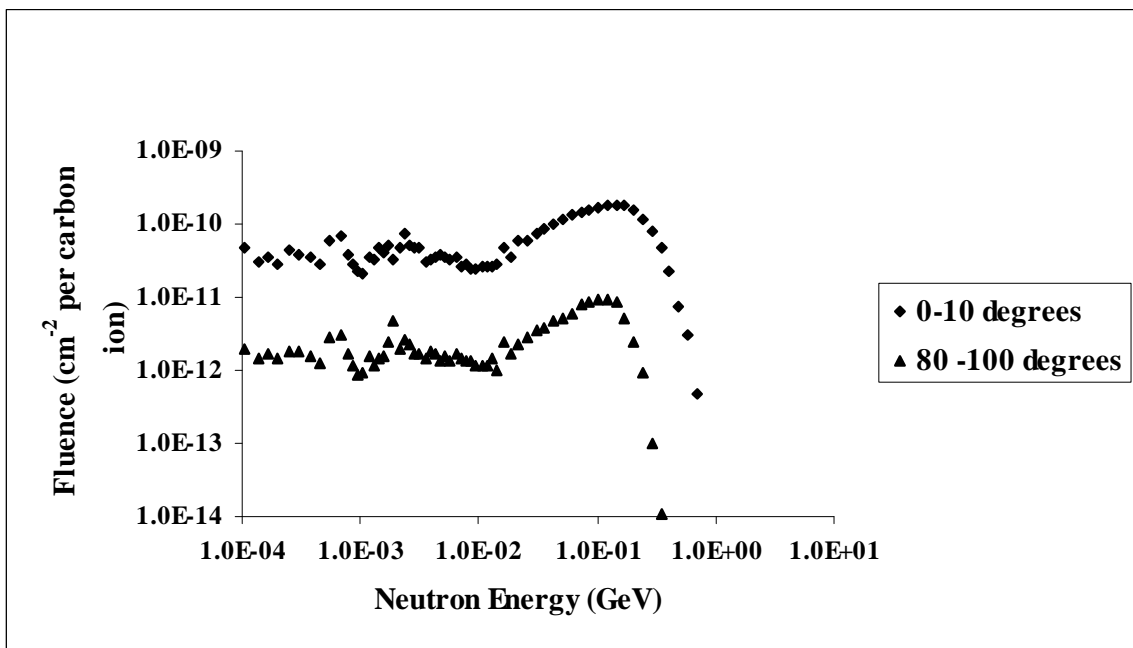


Nuclear fragmentation is described by the “abrasion ablation model” [9]. The first step is known as abrasion. In grazing collisions a small fraction of the nuclear material overlaps and this overlapping zone is known as the fireball. The abraded projectile pre-fragment keeps most of its initial energy while the abraded pre-fragment target remains at rest. The fireball recoils with an intermediate velocity. During ablation, the second step of fragmentation, the pre-fragments and the highly excited fireball evaporate nucleons and light clusters. The high-energy neutron components produced in the forward direction by a break up process and the momentum transfer from projectile to target nuclei are both higher for lighter nucleus and higher projectile energy than for heavier nucleus and lower projectile energy [9]. Thus more forward-directed neutrons will be produced in a stopping tissue target than in a stopping iron target, in the forward direction.

Figures 1 and 2 show the neutron spectra from 430 MeV/u carbon ions incident on tissue at the concrete surface and at a depth of 4.8 m in the concrete, for 0-10 degrees and for 80-90 degrees. The fluence is in lethargy units ( $E \times d\phi/dE$ , where  $E$  is the neutron energy and  $d\phi/dE$  is the differential fluence). The errors are not shown but are typically within 20%.

In Figure 1, the neutron fluence at the large angles (80-100°) is much higher than the neutron fluence in the forward direction (0-10°) at the concrete surface. The neutron spectrum in the forward direction extends up to about 1 GeV in energy, while the spectrum at the large angle extends to about 0.4 GeV. In both spectra the oxygen resonance peaks at 500 keV, and the evaporation neutron peaks at about 2.3 MeV are observed. A high-energy neutron peak is observed at about 340 MeV in the forward direction, while a broad peak is observed between about 20 and 50 MeV at the large angles.

**Figure 2: Neutron energy spectra at incident at 4.8 m depth in concrete for 430 MeV/u carbon ions incident on ICRU tissue sphere**



In Figure 2, at a depth of 4.8 m in the concrete, the neutron fluence in the forward direction is higher than the neutron fluence at the large angles. This is because the forward directed radiation generates more neutrons as it traverses through the concrete. The neutron spectrum in the forward direction extends up to about 0.7 GeV in energy, while the spectrum at the large angle extends to about 0.35 GeV. In both spectra the oxygen resonance peaks at 500 keV, and the evaporation neutron peaks at about 2.3 MeV are observed. A high-energy neutron peak is observed at about 150 MeV in the forward direction, and at 125 MeV at the large angles. Thus the large angle neutron spectrum hardens as it traverses the concrete. The discontinuity seen at about 20 MeV in both figures for both spectra is the junction between the two models used in FLUKA for neutron transport. Neutron transport is based on cross-section library below 19.6 MeV and the intranuclear cascade model above 19.6 MeV.

Figures 3 and 4 show the dose per carbon ion in picoSieverts per particle normalised to 1 m ( $\text{pSv}\cdot\text{m}^2/\text{p}$ ) as a function of concrete thickness for both iron (Fe) and tissue targets in the  $0\text{-}10^\circ$  and  $80\text{-}100^\circ$  directions. In the forward direction the doses in vacuum and concrete are higher for the tissue target when compared to the iron target whereas at the large angles the doses are lower for the tissue target when compared to the iron target. This is because more forward-directed neutrons will be produced in a stopping tissue target than in a stopping iron target as previously stated. For both targets there is a build up in dose in the first few layers of the concrete shield. The attenuation lengths reach equilibrium only after about a metre or more of concrete in the forward direction.

**Figure 3: Dose per carbon ion ( $0\text{-}10^\circ$ ) as a function of concrete thickness for 430 MeV/u carbon ions incident on ICRU tissue and iron targets**

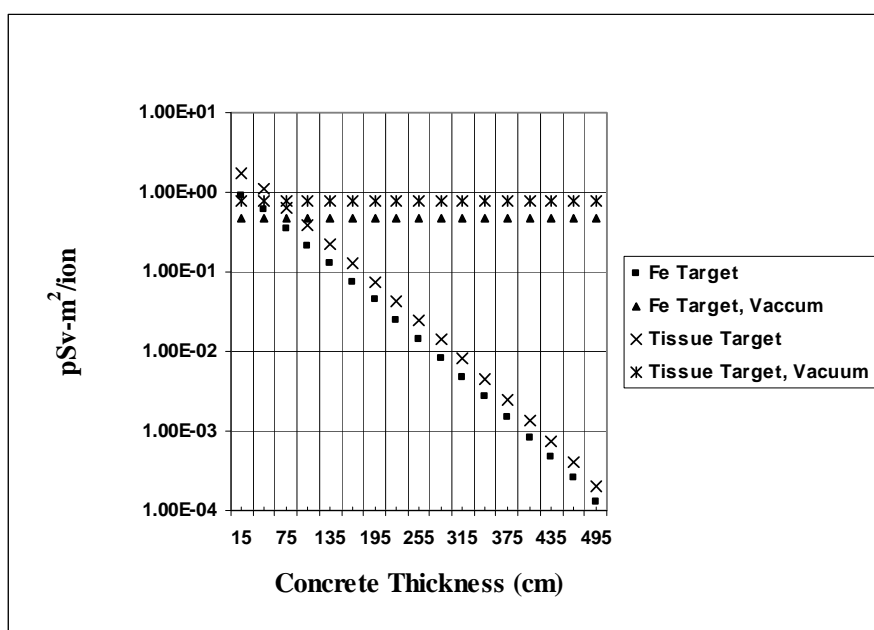
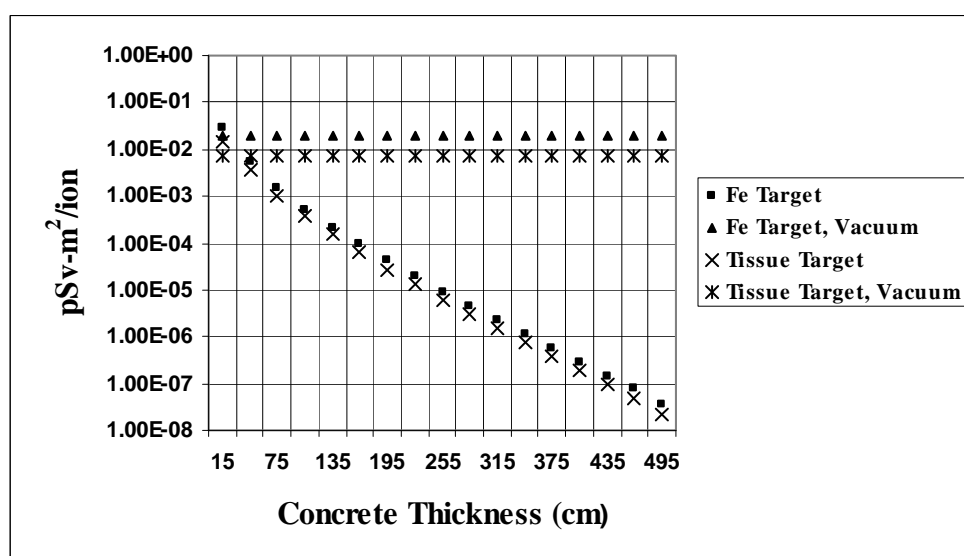


**Figure 4: Dose per carbon ion ( $80\text{-}100^\circ$ ) as a function of concrete thickness for 430 MeV/u carbon ions incident on ICRU tissue and iron targets**



Figures 5 and 6 show the relative dose contributions from various particles per carbon ion at 1 m from the tissue target as a function of concrete thickness. The errors are not shown but are typically within 20%. In the forward direction and at large angles neutrons are the largest contributor to the total dose. In the forward direction at a depth of 15 cm in concrete, about 66% of the dose is from neutrons, about 32% from protons, less than 2% from photons and less than 0.2% from charged pions. At greater depths the neutron contribution increases to about 95%. At large angles, the neutron contribution remains fairly constant (96%) at all depths, while the proton contribution increases from less than 1% to about 2% with increasing depths. Thus neutrons dominate the dose outside the shielding. The pion contribution is not shown in Figure 6 because of its poor statistics.

Figure 5: Relative dose contributions at 0-10° per carbon ion at 1 m from ICRU tissue sphere

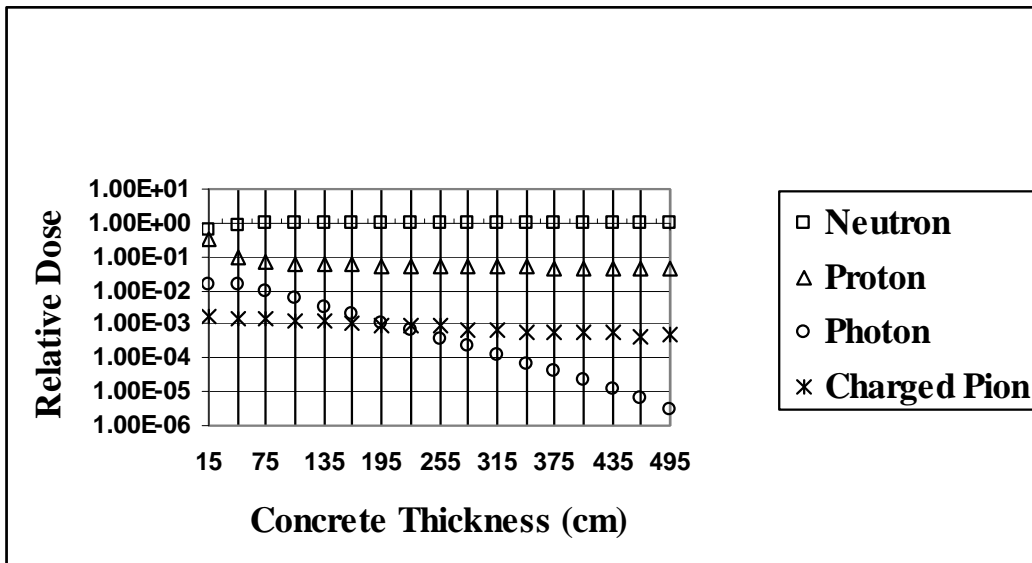


Figure 6: Relative dose contributions at 80-100° per carbon ion at 1 m from ICRU tissue sphere

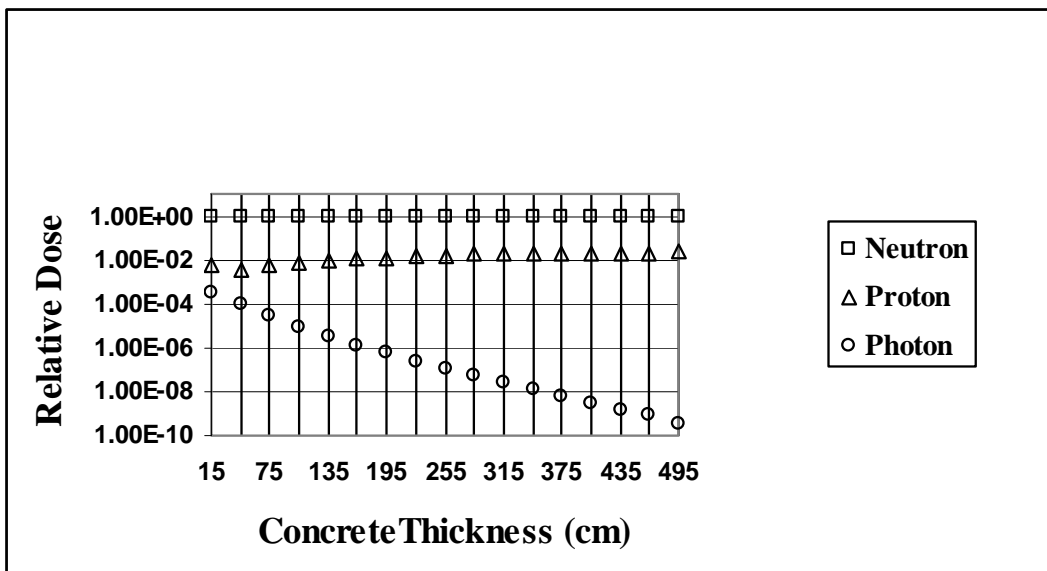
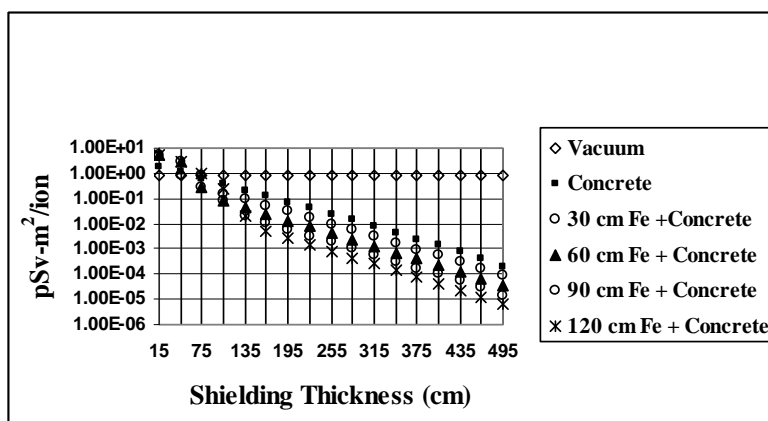


Figure 7 shows the dose per carbon ion for a tissue target in the forward direction as a function of shielding thickness for a composite shield.

**Figure 7: Dose per carbon ion (0-10°) as a function of shielding thickness for 430 MeV/u carbon ions incident on ICRU tissue sphere for composite shield**



The data in Figure 7 were fitted with the classical two parameter formula as shown in Equation 1. The equilibrium attenuation length is given by the reciprocal of the exponent. The results are shown in Table 1 for three polar sectors and are valid for concrete thicknesses greater than 1.35 m.

**Table 1: Preliminary computational models for concrete and composite shield (concrete + iron) for 430 MeV/u carbon ions incident on ICRU tissue sphere**

Iron thickness (cm)	0-10°		10-30°		40-60°	
	$H_0$ (Sv·m <sup>2</sup> /ion)	$\lambda$ (g/cm <sup>2</sup> )	$H_0$ (Sv·m <sup>2</sup> /ion)	$\lambda$ (g/cm <sup>2</sup> )	$H_0$ (Sv·m <sup>2</sup> /ion)	$\lambda$ (g/cm <sup>2</sup> )
0	$(3.02 \pm 0.04) \times 10^{-12}$	123.81 ± 0.48	$(4.81 \pm 0.06) \times 10^{-13}$	133.09 ± 0.74	$(4.71 \pm 0.21) \times 10^{-14}$	117.64 ± 1.32
30	$(1.25 \pm 0.02) \times 10^{-12}$	123.12 ± 0.38	$(2.44 \pm 0.03) \times 10^{-13}$	129.64 ± 0.36	$(1.91 \pm 0.08) \times 10^{-14}$	119.38 ± 0.48
60	$(6.05 \pm 0.03) \times 10^{-13}$	120.32 ± 0.46	$(1.11 \pm 0.04) \times 10^{-13}$	128.66 ± 0.70	$(8.29 \pm 0.66) \times 10^{-15}$	118.5 ± 0.80
90	$(2.77 \pm 0.09) \times 10^{-13}$	119.58 ± 1.25	$(5.27 \pm 0.29) \times 10^{-14}$	126.09 ± 0.80	$(3.29 \pm 0.69) \times 10^{-15}$	119.14 ± 1.34
120	$(1.33 \pm 0.05) \times 10^{-13}$	117.68 ± 0.91	$(2.48 \pm 0.24) \times 10^{-14}$	124.29 ± 0.94	$(1.34 \pm 0.68) \times 10^{-15}$	118.83 ± 2.89

The results indicate that for concrete thicknesses greater than 1.35 m, when there is no iron, the half value layers for concrete are about 36.5 cm, 39 cm and 34.6 in the 0-10, 10-30 and 40-60 degrees directions, respectively. In general the addition of 30 cm of iron provides a reduction in total dose by a factor of about 2. In the 0-10° direction, there is a slight softening of the spectrum with 60 cm of iron, compared to no iron, as can be observed by the change in attenuation length. In the 10-30° direction 30 cm of iron produces a significant softening of the spectrum, with slight softening for additional thicknesses of iron. In the 40-60° direction, the iron does not appear to provide any significant softening of the spectrum. It is important to note that the source terms and attenuation lengths will depend upon the particle energy, the material and dimensions of the target, the angle of production, the fluence to dose equivalent conversion factors that are used, etc. Additionally the source terms and attenuation lengths will also depend on how good the fit is.

Table 2 shows a comparison of doses from carbon ions incident on carbon and tissue targets. The various parameters under which the calculations have been made are summarised in the table. For carbon the calculated source strengths (Ipe 2006) are about 1.6 times higher than the published values (Agosteo 2001). As expected, the attenuation length for 430 MeV/u carbon ions is slightly higher than for 400 MeV/u carbon ions. Considering the many differences in the methodologies (target material, energy, use of measured neutron spectra as source, differences in conversion coefficients, differences in concrete), the factor of 1.6 difference between the two data sets is not surprising. The energy of the carbon ions in the present work (430 MeV/u) is higher, resulting in higher source strength. The target materials are different, i.e. carbon and tissue. The target thicknesses (20 cm vs. 30 cm) and dimensions

(5 cm vs. 15 cm) are also different. In the present work, the carbon ions were incident on a 15 cm radius ICRU tissue. In the published work, measured neutron spectra were used as the input for the source, which can lead to some error since the other secondary particles generated by the interaction of the carbon with the target are not included.

**Table 2: Comparison of computational models for carbon ions on carbon/tissue targets (0-10°)**

Parameter	Agosteo 2001	Ipe 2006
Particle	Carbon	Carbon
Energy	400 MeV	430 MeV
Target	Carbon	ICRU Sphere: Tissue
Radius/lateral dimensions	10 cm × 10 cm	15 cm
Length	20 cm	30 cm
Angle (degrees)	0-10	0 to 10
Source term (Sv·m <sup>2</sup> /particle)	$(1.93 \pm 0.04) \times 10^{-12}$	$(3.02 \pm 0.04) \times 10^{-12}$
Attenuation length (g/cm <sup>2</sup> )	120.98 ± 0.21	123.81 ± 0.48
Monte Carlo code	FLUKA	FLUKA 2005
Geometry	Spherical concrete shells 20 cm thick, inner radius 90 m	Spherical concrete shells 30 cm thick
Concrete/density (g/cm <sup>3</sup> )	TSF-5/2.31	Portland Cement/2.35
Source	Neutron source at centre with double differential spectra based on measurements by Kurasawa, <i>et al.</i> [9]	Carbon ions incident on target at centre

## Conclusions

Preliminary computational models have been derived for 430 MeV/u carbon ions incident on ICRU tissue for concrete and composite shields, for 0-10°, 10-30° and 40-60°. Some data has also been provided for carbon ions incident on an iron target. Neutrons are the dominant contributor to dose outside the shielding, and neutron spectra in the forward direction extend to energies of about 1 GeV for carbon ions incident on ICRU tissue target.

## Acknowledgements

This work was partially funded by Siemens Medical Solutions, USA.

## References

- [1] S. Agosteo, A. Fassò, A. Ferrari, P.R. Sala, M. Silari, P. Tabarelli de Fatis, "Double Differential Distributions and Attenuation in Concrete for Neutrons Produced by 100-400 MeV Protons on Iron and Tissue Targets", *NIM Phys. Res.*, B114, 70-80 (1996).
- [2] S. Agosteo, "Radiation Production at Medical Accelerators", *Rad. Prot. Dosim.*, Vol. 96, No. 4, 393-406 (2001).
- [3] S. Agosteo, A. Porta, M. Silari, L. Ulricci, "Monte Carlo Simulations for the Design of a Hadron Therapy Centre", *Proceedings of Bologna-Italy International Workshop, Inter Comparison on the Usage of Computational Codes in Radiation Dosimetry*, G. Gualdrini, P. Ferrari (Eds.), 14-16 July (2003).

- [4] A. Fassò, *et al*, "FLUKA: Status and Prospective for Hadronic Applications", *Proceedings of the Monte Carlo 2000 Conference*, Lisbon, 23-26 October 2000, A. Kling, F. Barao, M. Nakagawa, L. Tavora, P. Vaz (Eds.), Springer-Verlag, Berlin, 955-960 (2001).
- [5] V. Andersen, F. Ballarini, G. Battistoni, M. Campanella, M. Carboni, F. Cerutti, A. Empl, A. Fassò, A. Ferrari, E. Gadioli, M.V. Garzelli, K. Lee, A. Ottolenghi, M. Pelliccioni, L.S. Pinsky, J. Ranft, S. Roessler, P.R. Sala, T.L. Wilson, "The FLUKA Code for Space Applications: Recent Developments", *Adv. Space Res.*, 34, 1338 (2004).
- [6] International Commission on Radiological Protection (ICRP), *Conversion Coefficients for Use in Radiological Protection Against External Radiation*, ICRP Publication 74, *Annals of ICRP* 26, Elsevier Science, New York (1996).
- [7] International Commission on Radiation Units and Measurements (ICRU), *Radiation Quantities and Units*, ICRU Report 33, International Commission on Radiation Units and Measurements, Bethesda, Maryland (1980).
- [8] M.R. Raju, *Heavy Particle Radiotherapy*, Academic Press, New York (1980).
- [9] K. Gunzert-Marx, D. Schardt, R.S. Simon, "Fast Neutrons Produced by Nuclear Fragmentation in Treatment Rooms with  $^{12}\text{C}$  Beam", *Rad. Prot. Dosim.*, Vol. 110, Nos. 1-4, pp. 595-600 (2004).
- [10] T. Kurosawa, N. Nakao, T. Nakamura, Y. Uwamino, T. Shibata, N. Nakashima, A. Fukumara, K. Murakami, "Measurements of Secondary Neutrons Produced from Thick Targets Bombarded by High-energy Helium and Carbon Ions", *Nuclear Science and Engineering*, 132, 30-57 (1999).



## **Simulations and measurements of neutron equivalent doses for the proton therapy facility at the National Cancer Centre**

**Hyung-Jun Ryu, Jai-Ki Lee**

Department of Nuclear Engineering, Hanyang University, Korea

**Jong-Won Kim**

National Cancer Centre, Korea

**Hong-Seok Kim, Jeong-Wan Kwon**

Korea Institute of Nuclear Safety

**John Blaze**

Ion Beam Applications SA, Belgium

### **Abstract**

*A proton therapy facility, which uses the proton beam of 70-230 MeV, has been constructed at the National Cancer Centre in Korea. The facility is now in the final phase of therapeutic beam validations to start the patient treatments this year. Along with the first use of the beams on November 2005 the radiation levels around the facility have been measured. The neutron equivalent doses near the doors of the treatment rooms and the cyclotron area, where the radiation leakages are mainly determined by the maze, are measured to be around 1-4  $\mu\text{Sv/hr}$  at the nominal proton dose rate. Some results of the measurements and Monte Carlo simulations are presented.*

## Introduction

A proton therapy facility, which has been constructed at the National Cancer Centre in Korea from 2002 [1], is nearly complete for the patient treatments to begin in 2006. The proton beam is produced from a 230-MeV fixed-energy cyclotron, and delivered to one fixed beam treatment room, two gantry rooms, and an experimental area. The beam energy for therapy is varied to control the depth of dose with the use of a graphite degrader, and the precise energy is selected by the energy selection system composed of sets of the vertical and horizontal slits. This mechanism of energy variation generates rather high dose of radiation, so that the radiation shielding has been carefully evaluated prior to the construction of the facility [2].

The area monitoring systems of neutrons and gammas are installed around the facility as a measure for the radiation safety. The neutron equivalent doses are monitored in the main control room in real time, which is a convenient feature to identify the beam loss locations. On the other hand the gamma monitors are placed in the regions of major beam losses.

The proton therapy equipment has an extensively redundant safety system. All the doors to the beam region are interlocked for instance, and the beam delivery is interrupted in a safe way whenever any unexpected incident occurs. The proton beam was first accelerated in November 2005, and the beam tests have been under way to check and validate the equipment.

Major radiation safety concerns such as neutron equivalent dose rates in the public area and air ventilation in the treatment rooms have been checked by the Korea Institute of Nuclear Safety (KINS), and are found to conform to the regulation set by the Korean law. The facility has been operated with a careful monitoring of the radiation dose rates.

## Design of the radiation shielding

The shielding design was initially based on that of the Northeast Proton Therapy Centre (NPTC) in Boston, MA because the main therapy equipments of the two facilities are similar, the same kinds of a 230-MeV proton cyclotron and gantries being used [3]. First, some analytic evaluations [4] were made in the shielding design before we finalise the facility design. The calculation of the neutron doses using the Monte Carlo code MCNPX [5] is more realistic, but it took a longer time. Thus we used the MCNPX results primarily for the final confirmation of the shielding design. We also considered the different clinical beam time from the NPCT case, and the presence of a rather large experimental area was another factor included in the shielding calculation. The time and current of the beam allowed for proton-beam experiments are partly determined by the shielding wall thickness. The thickness of shielding wall is mostly over 1.5 m, so that evaporation neutrons are negligible, and the low energy neutrons passing the walls are in thermal equilibrium, which is a good approximation to use the analytic expressions of Tesch [4].

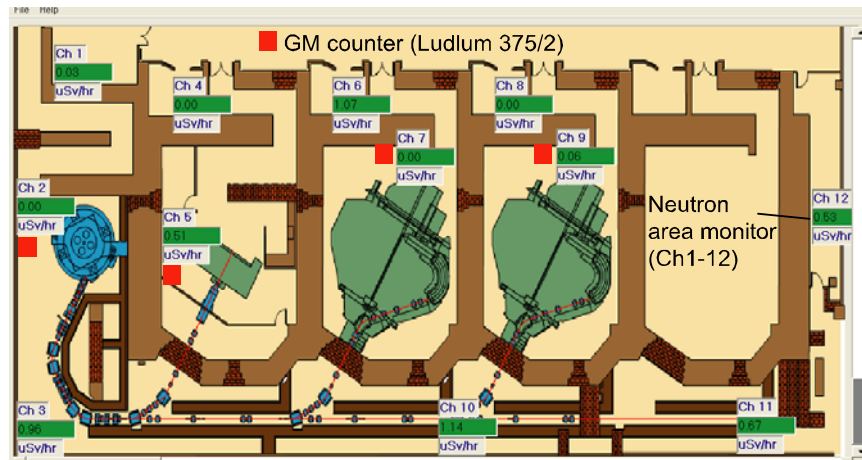
The building structure contains a large number of cable ducts penetrating the shielding walls. The proton therapy equipment is designed to place most of the electrical components in one room called power supply room. The cable ducts pass thru the shielding walls, and they are arranged to bear at least two bends to prevent any significant neutron leakage.

## Monitoring of the neutron and gamma doses

The neutron area monitors (Ludlum Model 375) are placed around the facility to monitor the doses in the real time as shown in Figure 1. The monitors in the beam area clearly show the status of the beam delivery, which is a convenient feature in the operation of therapy beams. In fact the upper limit of neutron energy detected with a 25 cm polyethylene moderator and a  $\text{BF}_3$  detector is less than 12 MeV, so that the dose reading near the beam area is not correct, where the neutron energy can be above 200 MeV. Neutron energy outside of the beam region is sufficiently moderated by the thick shielding wall or maze structures [6].

Figure 1 also shows the locations of the gamma monitors of a GM type. They are located in the major beam loss areas such as the cyclotron vault and the treatment rooms.

**Figure 1: Neutron area monitor system around the facility and gamma detectors of the GM type in the cyclotron vault and the treatment rooms**



### Further measurements and Monte Carlo calculations

The neutron equivalent doses have been calculated around the facility using MCNPX and associated programs. These results together with the results of analytical evaluations have been used to validate the shielding design [2] and to apply for the permission to use the facility from the KINS. The main features of the building structure for the proton therapy equipment, which employs a cyclotron, have been better established these days with accumulated experiences from the existing facility and several new facilities being designed, and thus were kept for the NCC facility.

The neutron dose rates depending on the proton energy were measured outside of the cyclotron vault and the treatment rooms at the nominal dose rates of around 2 Gy/min as part of validations for the KINS. Table 1 tabulates the measured doses at the gantry door for two different beam-stop materials when the beam current in the treatment room is 5 nA. The dose rate drops rapidly when it is measured away from the door.

**Table 1: Neutron dose rates at the gantry door at the nominal beam current of 5 nA**

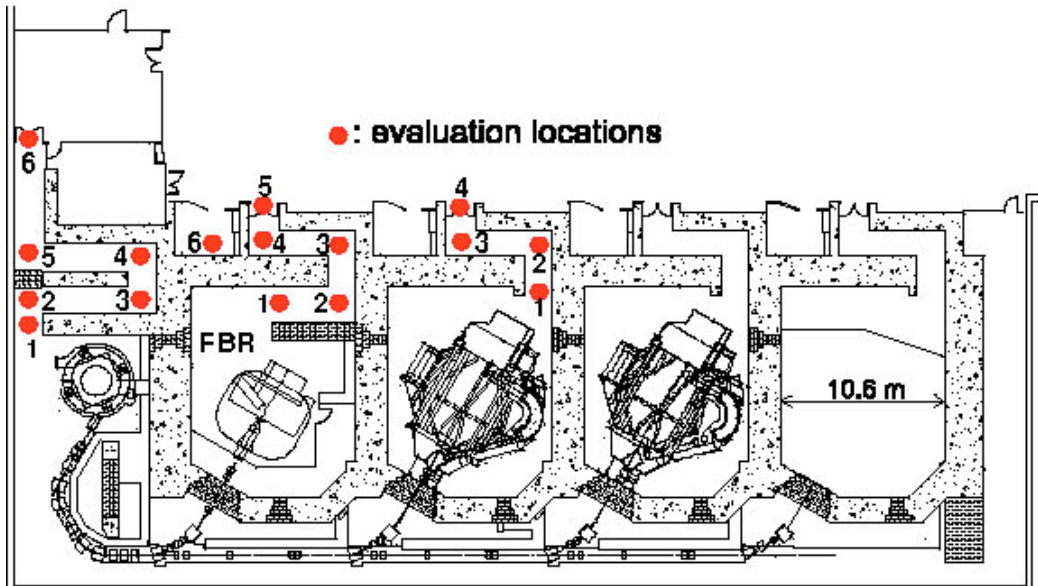
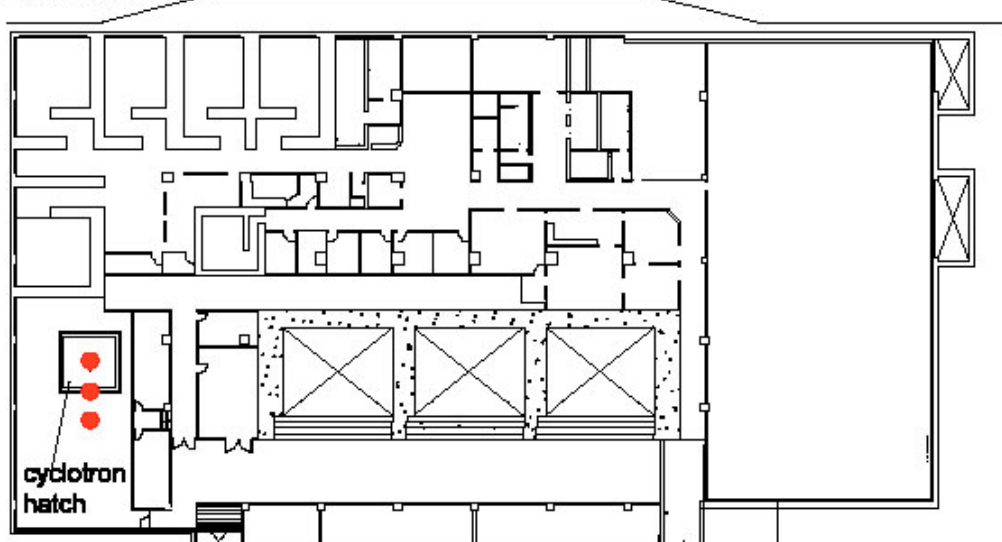
Beam stop	226 MeV	150 MeV
Water	3.8 $\mu\text{Sv/h}$	0.8 $\mu\text{Sv/h}$
Brass	4.8 $\mu\text{Sv/h}$	0.5 $\mu\text{Sv/h}$

The neutron equivalent doses were measured as shown in Figures 2 and 3 along the mazes of the cyclotron, fixed-beam and gantry rooms. One of our aims was to validate the MCNPX calculations in the light of the maze design, but it seemed to take more iteration for the final results to be acceptable (the results will be published elsewhere). The neutron dosimeter used was an EG&G Berthold with a 25 cm diameter polyethylene moderator and a  $\text{BF}_3$  detector, for which the highest neutron energy detected is around 20 MeV. The dose reading was recently calibrated at the Korea Research Institute of Standards and Science.

Beam losses occurring in the operation of the proton therapy equipment can be divided into two different modes. One is during the beam tuning of the cyclotron and the beam line. The beam usually stops at the beam stop position of the degrader during the tunings of the cyclotron and its beam extraction elements, while the extracted beam stops at other beam stops in the beam line tuning. The beam-stops are made of nickel, and the beam losses are well confined in this mode. The other loss mode occurs during patient treatments. Beam losses are then largely concentrated in the nozzle (therapeutic beam formation device) and in the inside of the patient or phantom. When the beam energy is lowered from 230 MeV in the energy selection system, a large loss of course occurs in the graphite degrader.

**Figure 2: Locations of the dose rate evaluations in the treatment floors**

The evaluations are mainly made in the mazes of the gantry and fixed-beam treatment rooms, cyclotron vault

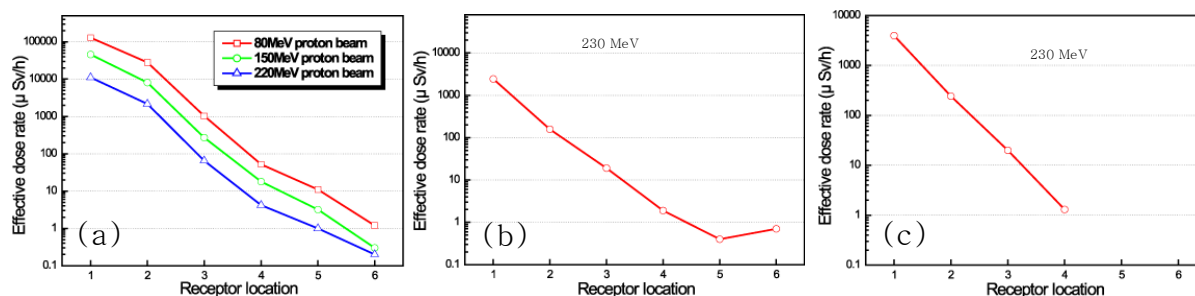
**B2 Floor****B1 Floor**

The analytical estimations were made for reduction of the neutron doses along the maze of the gantry using the expressions given by Cossairt [7,8] as shown in Table 2, where the positions are labelled in Figure 2. A difficulty of using the analytical expressions is that the direction of neutron is different in each room as the direction of the proton beam differs, which is thought to cause considerable errors in the analytic evaluations.

**Table 2: Measurement and analytic values of the dose reduction along the gantry maze**

Position in the maze	Measurement	Analytical result
1-2	0.061	–
2-3	0.082	0.017
3-4	0.065	0.073

**Figure 3: (a) Measurement results of the neutron dose rates along the cyclotron maze. Receptor locations are indicated in Figure 2, (b) along the fixed-beam room maze, (c) along the gantry maze.**



## Conclusions

The radiation shielding of the proton therapy facility at the NCC has been checked with a series of measurements of the neutron equivalent doses around the facility. The central monitoring of the neutron doses in the main control room appears to be very useful in the beam operation. In addition, the neutron dose rates were measured along the mazes of the cyclotron vault and treatment rooms, being compared with the MCNPX calculations as an effort to verify the MCNPX calculations. These calculations will take more time to be finalised.

## References

- [1] J. Kim, "Proton Therapy Facility Project in National Cancer Center, Korea", *J. Korean Phys. Soc.*, 43, S50 (2003).
- [2] J. Kim, J. Kwon, J. Lee, "Design of Radiation Shielding for the Proton Therapy Facility at the National Cancer Center in Korea", *Radiat. Prot. Dosimetry*, 115, 271 (2005).
- [3] W. Newhauser, U. Titt, D. Dexheimer, X. Yan, S. Nill, "Neutron Shielding Verification Measurements and Simulations for a 235-MeV Proton Therapy Center", *Nucl. Instrum. Methods Phys. Res., A* 476, 80 (2002).
- [4] K. Tesch, *Radiat. Prot. Dosim.*, 11 (3), 165 (1985).
- [5] MCNPX User's Manual Version 2.4.0, Report LA-CP-02-408, Los Alamos National Laboratory, Los Alamos, NM (2002).
- [6] R. Thomas, G. Stevenson, *Radiological Safety Aspects of the Operation of Proton Accelerators*, Technical Report No. 283, International Atomic Energy Agency, Vienna (1988).
- [7] J. Cossairt, "Approximate Technique for Estimating Labyrinth Attenuation of Accelerator-produced Neutrons", *Fermilab Radiation Physics Note*, No. 118, October (1995).
- [8] K. Tesch, "The Attenuation of the Neutron Dose Equivalent in a Labyrinth Through an Accelerator Shield", *Particle Accelerators*, 12 (1982) 169.



## **An overview of NCRP Report 151: Structural shielding design and evaluation report for megavoltage X- and gamma-ray radiotherapy facilities**

**Nisy E. Ipe**

Consultant

Shielding Design, Dosimetry and Radiation Protection  
San Carlos, CA, USA

### **Abstract**

*The new NCRP Report No. 151 presents recommendations and technical information pertaining to the structural shielding design and its implementation for megavoltage X- and gamma-ray medical facilities. The recommendations in this report supersede those of NCRP Report No. 49, and also address photon energies higher than 10 MV, and the resulting photo-neutron production. This paper provides an overview of the report.*

## Introduction

The new NCRP Report No. 151 addresses the structural shielding design and evaluation for medical use of megavoltage X- and gamma rays for radiotherapy [1]. This report supersedes NCRP Report No. 49, but does not include brachytherapy and X-ray installations operating at voltages less than 500 kV [2]. Thickness “look up” tables have been replaced by example calculations. Diagnostic facilities are addressed in NCRP Report No. 147 [3]. The report was the result of a joint effort of NCRP Scientific Committee 46-13 on Design of Facilities for Medical Radiation Therapy and the American Association of Physicists in Medicine. The committee members were James A. Deye (Chairman), James E. Rodgers (Vice Chairman), Raymond K. Wu, Peter J. Biggs, Patton H. McGinley and Richard C. McCall. The liaisons were Kenneth R. Kase and Marc Edwards. The consultants were Robert O. Gorson, Jeffrey H. Kleck and Nisy E. Ipe.

## New issues since NCRP Report No. 49

NCRP Report No. 49 only addressed single energy therapy facilities with energies  $\leq 10$  MV [2]. NCRP Report No. 151 includes dual energy machines and energies above 10 MV [1]. Several new treatment techniques and modalities such as total body irradiation, intensity modulated radiation therapy (IMRT), and stereotactic radio surgery (SRS) i.e. CyberKnife® and tomotherapy are addressed. The design of rooms without mazes and the use of laminated or composite barriers are also covered. More published data on empirical methods and on neutron production, capture gamma rays, IMRT factors, have been included. The report is comprised of seven chapters and three appendices.

## Chapter 1: Introduction

The first chapter covers the purpose and scope of the report. It includes quantities and units, definitions of controlled and uncontrolled areas, workload, use factor, occupancy factor, primary and secondary barriers; basic principles of shielding; types of radiotherapy facilities; and general concepts. It also includes the need for qualified experts to perform the shielding design and participate in the various stages of the project such as schematic design, design development, construction document preparation, and construction inspection.

The quantity used for shielding design is the dose equivalent, and the unit is Sv. Controlled areas and uncontrolled areas are defined. Examination rooms are classified as an uncontrolled area.

Different shielding design goals are used for controlled and uncontrolled areas, and are stated in terms of dose equivalent and not effective dose. When the shielding design goals are used in conjunction with the conservatively safe assumptions in the report, the shielding design goals will ensure that the respective annual effective doses recommended in NCRP Report No. 147 are not exceeded [3]. NCRP Report No. 151 recommends shielding design goals of 5 mSv/y and 1 mSv/y for controlled and uncontrolled areas, respectively [1]. Conservative assumptions in the report include the neglect of primary beam attenuation by the patient (~30%), perpendicular incidence of radiation in shielding calculations, maximum value for leakage radiation as recommended by IEC, high occupancy factors, minimum distance of 0.3 m to occupied area, use of safety factors, and the “two source rule” (i.e. procedure when more than one source is used).

The workload is defined as the time integral of the absorbed dose rate determined at the depth of the maximum absorbed dose at 1 m from the source. It is usually specified over one week. It is estimated from the number of patients (or fields) treated in a week and the absorbed dose per patient (or field). For dual energy machines, the workload at the higher energy will determine the shielding requirement. New techniques such as intensity modulated radiation therapy (IMRT) can result in leakage workloads that are significantly higher than for conventional therapy.

Use Factor is the fraction of the primary-beam workload that is directed toward a given primary barrier, and will depend on the installation. A traditional facility will usually have a symmetric distribution of gantry treatment angles. However for a facility using Total Body Irradiation (TBI) the use factor will be much larger in the direction of the TBI treatments.

The Occupancy Factor (T) for an area is the average fraction of time that the maximally exposed individual is present while the beam is on. The occupancy factor is not the fraction of time that an area is occupied, but rather the fraction of time it is occupied by a single person who spends time there.

A qualified expert is defined as a medical physicist or health physicist who is competent to design radiation shielding in radiotherapy facilities, and who is certified by the American Board of Radiology, American Board of Medical Physics, American Board of Health Physics, or Canadian College of Physicist in Medicine. Radiation shielding shall be designed by a qualified expert. The latter shall also review final drawings and specifications before construction, perform construction inspection.

New techniques such as TBI, IMRT, and SRS and SRT (Stereotactic Radiation Therapy) result in significant changes in the workload and use factors when compared to conventional therapy.

Shielding design reports, construction or as-built drawings, radiation survey reports and mitigating measures are required to be maintained by the facility

## Chapter 2: Calculational methods

The second chapter is devoted entirely to calculational methods. Standard approaches for determination of the thicknesses of primary and secondary barriers, and the widths of primary barriers are discussed. Also included are patient scatter and wall scatter. An empirical method for determination of neutron dose from primary laminated barriers is also included. Treatments of doors and mazes for both low energy ( $\leq 10$  MV) and high energy accelerators ( $> 10$  MV) are provided, including calculation of neutron and photon dose equivalents at the maze entrance. Design issues with direct shielded doors which are used when space is a premium, are also discussed.

Equations for the transmission of primary and secondary barriers are similar to those provided in NCRP Report No. 49 [2]. For secondary barriers, if the thickness required for leakage and scattered radiation is about the same, one Half Value Layer (HVL) is added to the larger of the two barrier thicknesses. If the two components differ by a Tenth Value Layer (TVL) or more, the larger barrier thickness is used.

Laminated barriers consisting of steel or lead, and concrete are used when space is a premium. For accelerating voltages above 10 MV, neutron production occurs in the lead or steel and should be taken into consideration in the shielding calculations.

The various components to dose at the maze entrance include primary radiation scattered from the walls, leakage radiation scattered from the walls, primary radiation scattered from the patient and leakage radiation transmitted through the inner maze wall. For high energy machines the neutron dose equivalent at the door from neutrons scattering along the maze, and the capture gamma rays must also be considered. A second turn in the maze can reduce the neutron dose by about a factor of two or three.

Neutron dose at the maze entrance can be reduced by reducing the opening at the inside maze entrance and/or adding a borated polyethylene door or a light weight door containing boron, at the inner maze entrance.

Direct shielded doors are used when space is a premium. These doors are very heavy and consist of a combination of high-z material such as lead or steel and polyethylene/borated polyethylene. These doors require either a sufficient overlap with the wall or a shielded door stop.

## Chapter 3: Workload, use factor, and absorbed-dose rate considerations

The third chapter describes the various treatment modalities such as conventional procedures, total body irradiation, intensity modulated radiation therapy and dedicated purpose machines, and their associated workloads. The use of a measured instantaneous dose-equivalent rate (IDR), with the accelerator operating at maximum output does not represent true operating conditions. Thus the concepts of weekly averaged time dose-equivalent rate (TADR), and the in-any-one-hour time averaged dose-equivalent rate are introduced. The TADR is the barrier attenuated dose-equivalent rate averaged over a specified time or period of operation and is proportional to IDR and depends on values of W and U.

## Chapter 4: Structural details

Structural details are covered in the fourth chapter. The need for interlocks, warning lights and requirements for control console are stressed. The properties of various commonly used shielding materials such as ordinary concrete, heavy concrete, lead, steel, polyethylene, paraffin, earth and wood are summarised. The impacts of rebar and form ties used for construction on the shielding of photons and neutrons are discussed. Requirements for the handling of joints and junctions are provided. Shielding of ducts and penetrations are also covered. Special topics such as lead-only rooms and beamstoppers are also covered.

## Chapter 5: Special considerations

The fifth chapter includes skyshine, groundshine, side scatter, activation and ozone production. The skyshine equations are similar to those found in NCRP49. Groundshine may be a problem for a high-energy treatment room constructed with thin laminated barriers. Side-scatter may pose a concern for adjacent structures when the roof is thin.

For high-energy accelerators, thermal neutron activation in aluminium (couch frame), antimony (lead shielding in accelerator head), and concrete have been observed. For electron beams, ozone production represents a safety hazard, and therefore normal clinical use of electron beams requires a room ventilation rate of about three room changes per hour.

Special considerations for various treatment methods and machines such as tomotherapy, robotic arm (CyberKnife®) and dedicated intraoperative radiotherapy units are discussed in this chapter. For tomotherapy even though the primary beam is reduced in width, the number of monitor units delivered to the isocentre is very large compared to the dose in centigray, because the beam rotates around the patient several times. For the CyberKnife®, the average ratio of monitor units to the dose in centigray is also quite high (~15), but the use factor for the primary beam is much lower (0.05).

## Chapter 6: Shielding evaluation (surveys)

Shielding evaluation is covered in Chapter 6. New facilities and modified old facilities require shielding evaluation and radiation surveys. An inspection of the facility during construction is recommended. Testing requirements for interlocks and restrictive devices are mandatory. Appropriate warning signs and lights are required.

Radiation surveys are required in order to ensure that personnel exposures are within design goals and time-averaged dose equivalent rates. Portable ionisation chambers with both rate and integrate modes and a range extending to 50 mGy/h are recommended for photon measurements outside the barriers. For accelerators operating above 10 MV, neutron surveys should also be performed. Primary barriers should be surveyed with a maximum field size and without a phantom in the beam. Gantry angles of 0, 90, 180 and 270 degrees, as well as oblique angles that intercept wall-floor intersections should be used. Where groundshine may be of concern, wall-floor intersections should also be surveyed. Secondary barriers should be surveyed with a phantom in the primary beam and the collimators fully open. Measurements should also be made outside the facility and in adjacent buildings when skyshine or side-scatter is of concern. Items that need to be included in the shielding evaluation report are also discussed in detail.

## Chapter 7: Examples

Detailed examples of calculations are provided for a conventional dual energy treatment unit with maze, with IMRT, and for a robotic stereotactic radiosurgery room in Chapter 7.

## Appendix A: Supporting data (figures)

Supporting data consisting of figures with average HVLs and TVLs (equilibrium) for broad beams of various shielding materials as a function of energy are provided. The materials include water, hollow

brick, concrete, heavy concrete, iron, lead, tungsten and uranium. Primary TVLs for concrete, heavy concrete, iron and lead are also provided as a function of energy up to 50 MeV. Calculated dose equivalent (including neutron capture gamma rays) transmitted per unit fluence of neutrons are shown as a function of concrete slab thickness for various average neutron energies ranging from thermal to 2.7 MeV.

## **Appendix B: Supporting data (tables)**

Suggested Occupancy Factors differ from those found in NCRP 49. Occupancy Factors vary from 1 for fully occupied areas to as low as 1/40 for very low occupancy areas such as outdoor areas with only transient pedestrian or vehicular traffic, etc.

Primary barrier TVLs for concrete, steel and lead are included for Co-60 and photon energies ranging from 4 to 30 MV. Properties of various shielding materials such as ordinary concrete, heavy concrete, lead, iron and polyethylene are included. TVL for leakage radiation in ordinary concrete are also included.

Patient scatter factors for various angles and various energies including Co-60 are provided. TVL for various scatter angles for concrete and lead are also included, as well as mean energies of patient scattered radiation as a function of scatter angle and endpoint energy. Differential dose albedos for concrete, lead and iron for various energies including Co-60 are provided.

Neutron yields for various energies and manufacturer types are provided. A graph of neutron source strength as a function of nominal end point energy is also included.

## **Appendix C: Neutron monitoring for radiotherapy facilities**

Neutron measurements inside the treatment room are fraught with difficulties because of photon interference from the primary photon beam, its pulsed nature, and high intensity. Further the requirement of measuring neutrons with energies ranging over several decades from thermal to several MeV precludes the use of a single detector for accurate measurement. Additionally neutron detectors can have photon-induced reactions. Thus active detectors can only be used outside the treatment room and at the outer maze area, while some passive detectors can be used inside the treatment room and inside the primary photon beam.

Active monitoring usually relies on moderating fast neutrons until they reach thermal energies, and include the use of rem and fluence metres. Passive methods include the use of activation detectors such as moderated gold and indium foils and phosphorous powder, thermoluminescent dosimeters (TLD), solid state nuclear track detectors, and bubble detectors. The various types of detectors and their advantages and disadvantages are discussed. Examples of some commercially available detectors are also provided.

## **Conclusions**

An overview of the new NCRP Report 151 comprised of seven chapters, and three appendices has been provided. This report though mainly intended for individuals specialising in radiation protection and shielding design, will also be of use to architects and other professionals involved with the planning of new radiation therapy facilities.

## References

- [1] National Council on Radiation Protection and Measurements (NCRP), *Structural Shielding Design and Evaluation for Megavoltage X- and Gamma-Ray Radiotherapy Facilities*, Report No. 151, National Council on Radiation Protection and Measurements, Bethesda, Maryland (2006).
- [2] NCRP, *Structural Shielding Design and Evaluation for Medical Use of X-rays and Gamma Rays of Energies Up to 10 MeV*, Report No. 49, National Council on Radiation Protection and Measurements, Bethesda, Maryland (1976).
- [3] NCRP, *Structural Shielding Design for Medical X-ray Imaging Facilities*, Report No. 147, National Council on Radiation Protection and Measurements, Bethesda, Maryland (2004).

## Estimation of radiation shielding for a cyclotron vault

**Hyun-Duk Kim, Gyu-Seong Cho, Bo-Kyung Cha**

Korea Advanced Institute of Science and Technology, Daejeon, Korea

**Jung-Keun Ahn**

Pusan National University, Pusan, Korea

### Abstract

*A 13 MeV cyclotron facility for radiopharmaceutical production and nuclear experiment will be constructed at Pusan National University (PNU) in Korea. Due to the proton-induced reactions between thresholds and the maximum energy of 13 MeV, the working area in the vault will be restricted during operation and after shutdown. Identification of neutron production radionuclides and a evaluation of the dose rate in the vault are required as guiding principles of radiation protection. Decay gamma-ray dose rates by secondary gamma radiation from the 1.5 m thick concrete will be calculated using MCNP code and the inventory code, FISPACT in this study.*

## Introduction

The cyclotron laboratory at Pusan National University (PNU) will have a 13 MeV proton source that will be used for producing radiation isotopes for PET and performing nuclear physics experiments. Various radiations are emitted when an accelerated proton beam bombards components of laboratory, such as water target, beam dump and concrete. As a result, there is a probability that high energy gamma and neutron could penetrate shielding material. Neutrons can undergo inelastic and elastic scattering in the shielding material and be slowed down enough for capture reactions to occur. There are many elements in an accelerator facility that become activated by neutron. Gamma rays are emitted from activated material.

On demand for effective radiopharmaceutical supply for increasing PET centres in Korea a total of seven regional cyclotron facilities have been being built at universities and university hospitals with government support. The regional cyclotron centres also perform research in nuclear science and develop peripheral equipments for extensive operation of a 13 MeV proton cyclotron. The cyclotron is operated at a typical beam current of 30  $\mu\text{A}$ , which generates high-flux neutrons at the cyclotron vault. Such neutrons highly activate surrounding materials to produce gamma rays for a long time. Therefore, design of radiation shielding is the most critical issue to keep radiation dose to operators under the allowed limit.

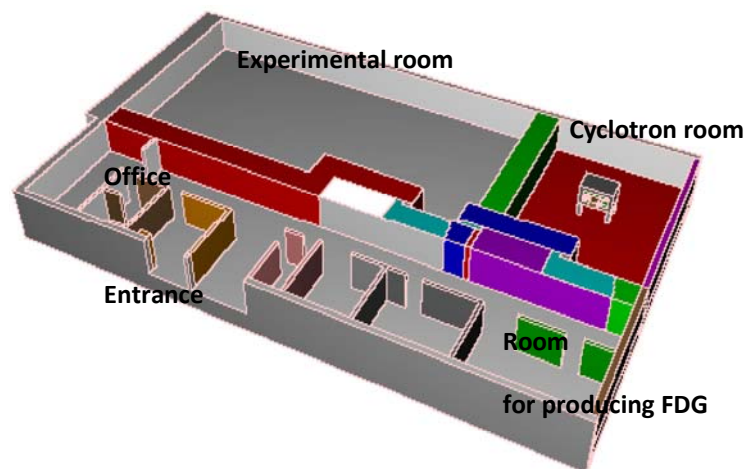
In this paper, radiation shielding design for the cyclotron vault was carried out by MCNPX. In modelling the shielding wall geometry two configurations are taken into account. One is a bulk configuration of shielding wall and the other is a three-layer configuration for more detailed study. Neutron flux at each segment, so-called cell, of the vault structure was calculated by using MCNPX. From this result, the identification of radionuclides which emit decay gamma-rays in the shielding concrete after shutdown and the induced activity is determined. Gamma ray production from radioactive nuclides through neutron activation was evaluated by the transport code, FISFACT. Finally, the absorbed dose was calculated with the flux-to-dose conversion factors, ANSI/ANS-6.1.1-1977 [1].

## Calculation

The calculations were carried out using a proton source from a cyclotron, KIRAMS-13 [2], the water target was  $\text{H}_2^{18}\text{O}$ , developed so as to produce radiation isotopes for Positron Emission Tomography (PET) by the Korea Institute of Radiological and Medical Sciences. It has the ability to accelerate proton and deuteron with 60  $\mu\text{A}$ . The maximum proton energy was 13 MeV, and the radio frequency was 77.3 MHz. This facility is composed of cyclotron room where the cyclotron will be installed, experimental room for performing the nuclear experiments, room for staff, room where the equipment will be installed for producing [ $^{18}\text{F}$ ] FDG and passage as shown in Figure 1.

**Figure 1: View of the cyclotron facility at PNU**

The cyclotron will be installed in the cyclotron room

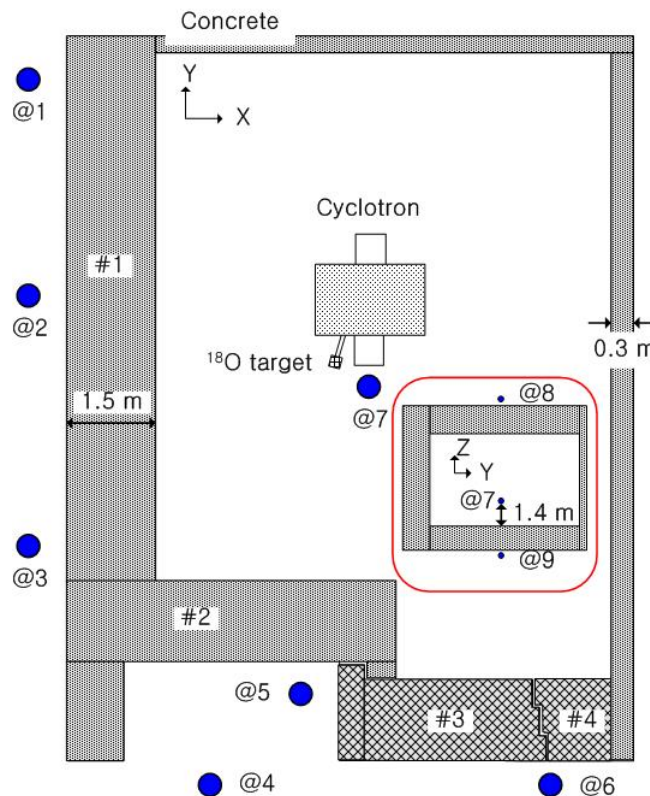


When a proton beam is accelerated to 13 MeV, a neutron is promptly induced by a nuclear reaction with the water target. The neutron that could be generated by a lost proton in the cyclotron body is not considered. There is no detailed information about the target system for producing  $^{18}\text{F}$ . The thickness of the water target used for producing FDG ( $^{18}\text{F}$ )  $\text{H}_2\ ^{18}\text{O}$  is 3 cm and the beam dump is 5 cm. The distance from the centre of the beam line of the cyclotron and water target to floor is 1.4 m.

The room where the cyclotron is installed will be cut from the overall structure for calculating gamma-ray dose rate as shown in Figure 2. The calculation of neutron flux and dose rates was performed with two cases. The first case is shown in Figure 2 with shielding concrete as one block on each side (model 1). The thickness of the shielding concrete is 1.5 m. Another concrete for isolating the cyclotron from the outside is 0.3 m. The concrete thickness of the ceiling and floor is 1.5 m and 1.26 m, respectively. In the second case, the cell structure of the shielding concrete on the passage and experimental room was divided into 3 parts (model 2) from Figure 2. The chemical composition of the shielding concrete is given by Carroll, *et al.* [3].

**Figure 2: View of the cyclotron facility used for calculating decay gamma-ray dose rates, showing 1.5 m thickness shielding concreted door (model 1)**

Also the shielding concretes (#1, #2) and door(#3) were divided into three parts, where the thickness of each concrete cell is 50 cm (model 2) as like #1-1 (inside), #1-2 (middle) and #1-3 (outside). Location of spherical phantoms of 30 cm diameter, filled with O, C, H and N, that are used for calculating the decay gamma-ray dose rates, eight phantoms are located at the outside of the shielding concrete and one phantom was installed in the inner shielding concrete. A lateral view of the facility is shown in the red box.



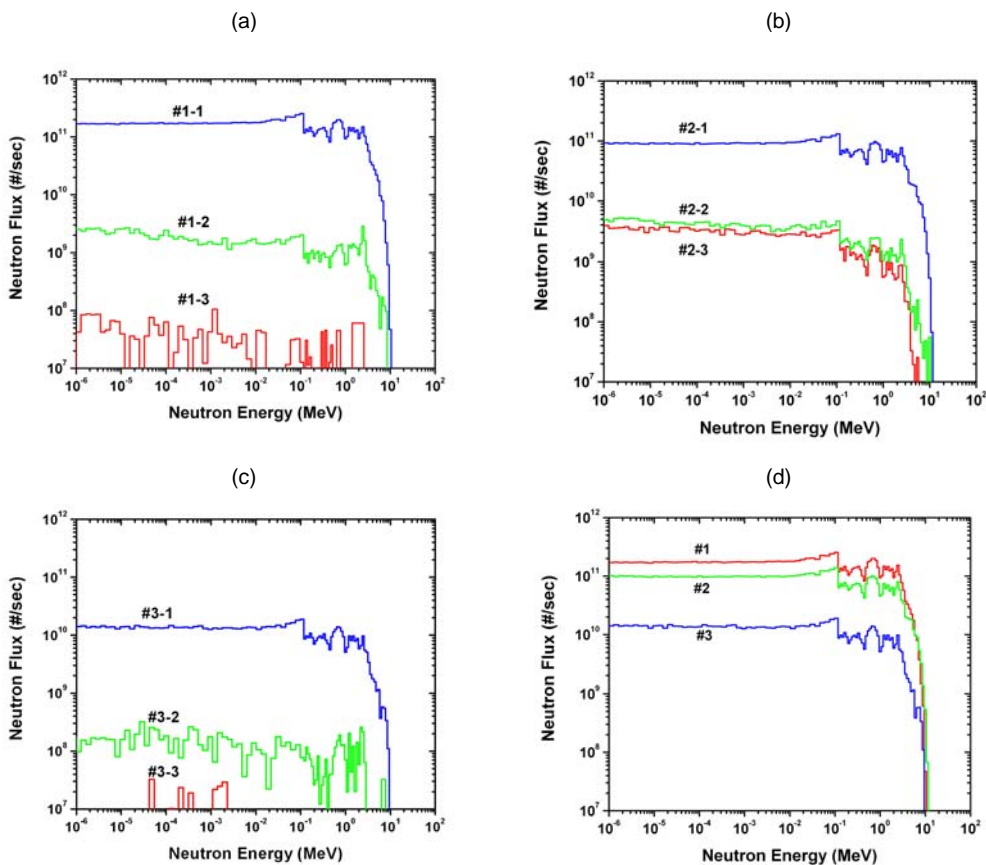
A spherical phantom [4] was used for calculating gamma-ray dose rates as shown in Figure 2. The distance from the shielding concrete to phantom is 0.2 m and from floor to centre of the phantom is 1.4 m. The phantom sphere was made of tissue equivalent material with a density of  $1\text{ g/cm}^3$ , a 0.3 m diameter and a mass composition of 76.2% O, 11.1% C, 10.1% H and 2.6% N. Phantom 4 was located toward the beam direction so as to evaluate beam direction dose rates. Phantom 6 was located at the gap between the door and the pillar, Phantom 7 was installed in the inner cyclotron room and the two spherical phantoms were laid on the ceiling and below the floor.

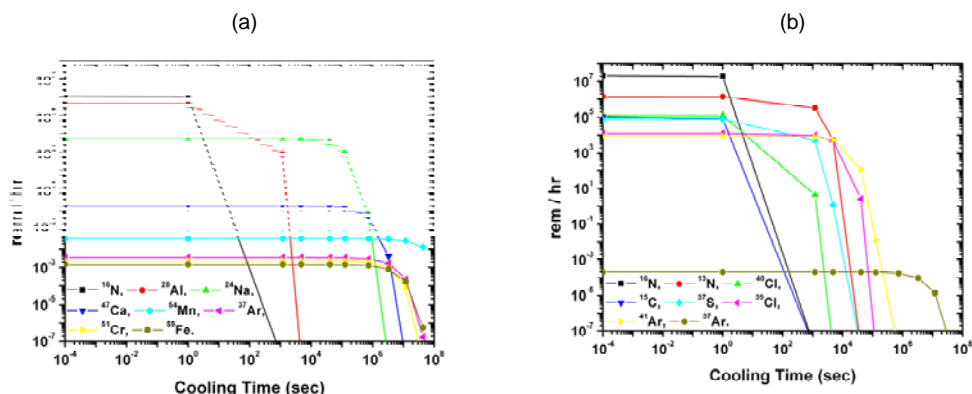
The process for estimating the gamma-ray dose rates follows that of previous studies [5,6]. The method for evaluating the effective dose is divided into three parts. The first part is a neutron spectrum calibration; the second is a photon spectrum calibration and identification of the radionuclides; and the third part is a decay gamma-ray dose calculation. Necessary information, such as the neutron spectrum for the activation analysis, was derived using the MCNP code. The output includes the gamma-ray spectrum due to the activated concrete structure, which is used in the MCNP photon transport calculation to obtain the absorbed dose using the FISPACT code. This study adopted the methodology of ANSI/ANS-6.1.1-1977 [1] as the flux-to-dose conversion factors.

## Results

The spectra of the neutron flux that penetrated the concrete were obtained by MCNPX so as to be used as the input file of FISPACT code (Figure 3). A comparison between the neutron flux that was calculated for the one block concrete (model 1) where the thickness is 1.5 m (Figure 2) and those for the each cell of the shielding concrete divided into three parts (model 2) where the thickness is 0.5 m is performed using MCNPX output. The ratio for the two results shows the dependency of absorption or penetration on thickness, previously reported energy distributions and whether these results could be distinguished from previous results [3,7-12]. A high proportion of hydrogen in concrete is the most effective means of scattering because the hydrogen cross-section increases with decreasing fast-neutron energies. Thus, the first scatter with hydrogen effectively removes the neutron from the fast energy region. In this study and in Carroll, *et al.* [3], the proportion of hydrogen was 10.47%.

**Figure 3: (a), (b) and (c) Neutron flux obtained from shielding concrete divided into 3 parts from Figure 2 and (d) from one block model**



**Figure 4: The produced radionuclides (a) in concrete (b) in air**

Radionuclides in the concrete, #2, and air from model 1 generated by neutron reactions in the concrete and air, that result in decay gamma-ray source, are shown in Figure 4. The total radiated dose rates is  $1.84 \times 10^6$  rem/h in concrete #2 that is exposed for 1 hour.  $^{16}\text{N}$ ,  $^{28}\text{Al}$  and  $^{24}\text{Na}$  were the dominant radionuclides for 20 minutes after operation shutdown. Especially, the half-life of  $^{16}\text{N}$  is the very short however the intensity is very large as  $1.28 \times 10^6$  rem/h ( $t_{1/2} = 7.13$  s). Therefore it contributes to the decay gamma-ray dose rates for an instant after shutdown. The half life for  $^{28}\text{Al}$ , is 2.24 min, so  $^{28}\text{Al}$  is absent after 1 hour. In the case of  $^{24}\text{Na}$ , it largely contribute to the gamma-ray dose rates after 20 minutes, since the half lives  $^{24}\text{Na}$  is 14.959 h. The radiation of concrete is rapidly decreased toward about  $4 \times 10^{-2}$  rem/h because  $^{54}\text{Mn}$  is a long-lived radionuclide ( $t_{1/2} = 312$  d). The air is composed of C, N, O and Ar, and contained radionuclides that contribute to the radiated dose rates after irradiation.  $^{15}\text{C}$  ( $t_{1/2} = 2.449$  s),  $^{13}\text{N}$  ( $t_{1/2} = 9.965$  m) and  $^{16}\text{N}$  ( $t_{1/2} = 7.13$  s) were the dominant radionuclides after shutdown. The total radiated dose rate in the air was  $2.29 \times 10^7$  rem/h due to neutrons [Figure 4(b)]. However the half-life of most radionuclides generated by neutron reactions are very short except  $^{37}\text{Ar}$  ( $t_{1/2} = 35.04$  d). They contribute little to the exposure dose after 1 day.

A sphere of water with 15 cm in radius was used to estimate gamma-ray dose rates through concrete and air. One was placed in the cyclotron room, which provided dose information. The results calculated in the case of Figure 2 are shown in Figure 5. In the case of model 1, the decay gamma-ray dose rates of the phantom that was located at the inner cyclotron room is 0.527 mrem/h after shutdown.

The results from the other phantoms are  $0.9 \sim 0.46 \times 10^{-3}$  mrem/h. Furthermore in the case of model 2, the dose rate of the inner cyclotron room is 0.531 mrem/h. The other phantoms are  $0.928 \sim 0.1.70 \times 10^{-3}$  mrem/h after shutdown.

**Figure 5: (a) The decay gamma-ray dose rates from one block concrete model and (b) from the shielding concrete model divided into 3 parts**

The yellow line was estimated at the inner cyclotron room after shutdown.  
The other lines were calculated at the outside of the shielding concrete.

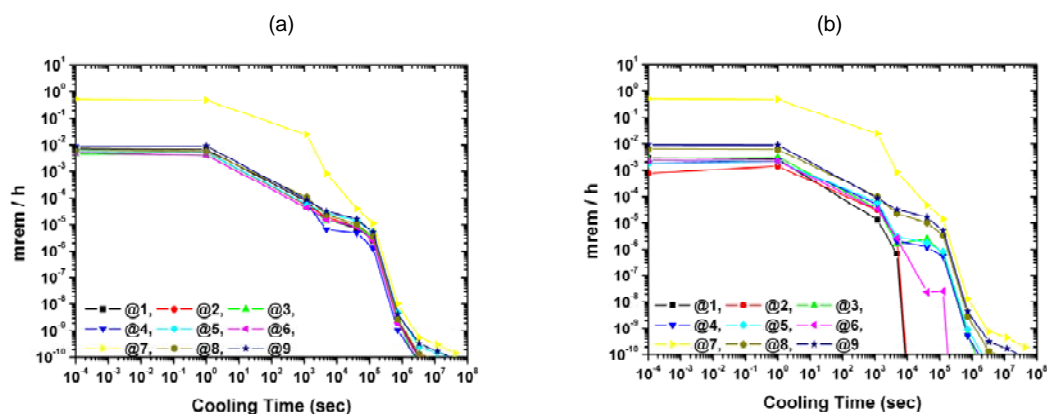
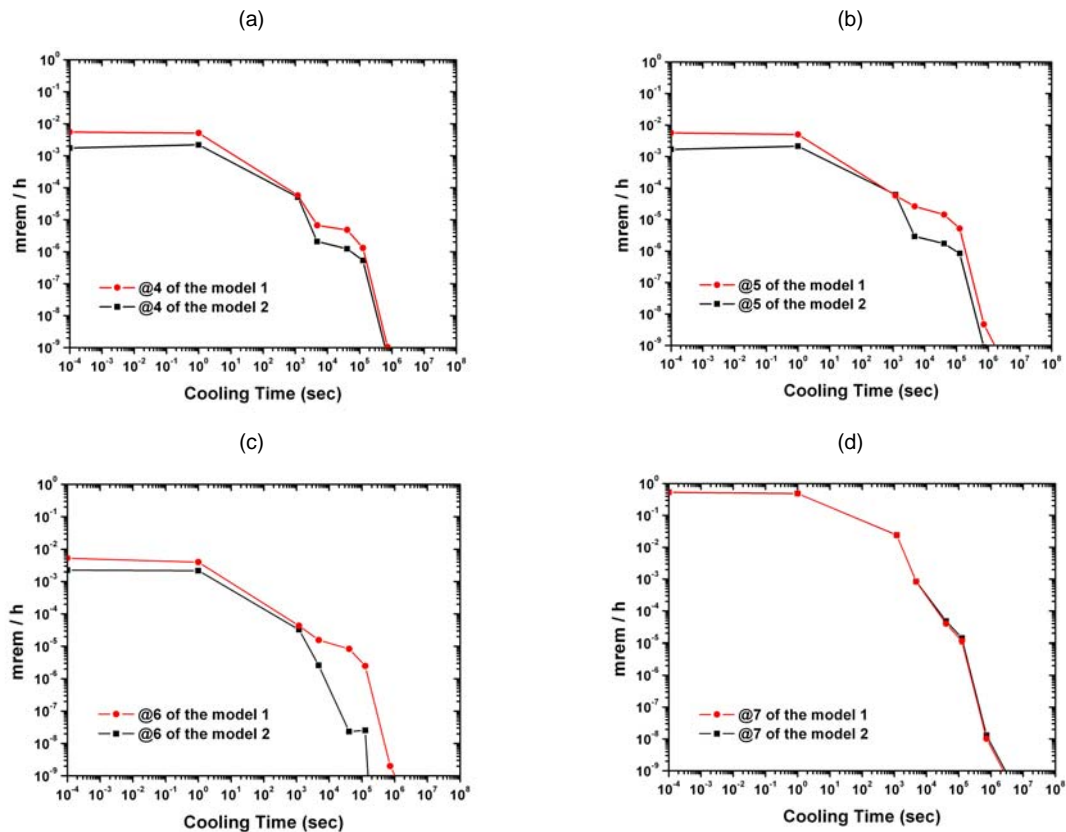


**Figure 6: Comparison of the two models**

The solid red line, model 1, is the decay gamma-ray dose rates of the one block shielding concrete model (model 1) and the black line, model 2, is that of the shielding concrete model divided into three parts(model 2)



The comparison of the two models from Figure 2 was performed in order to obtain the gamma-ray dose rates with good accuracy. In the case of phantom @4, @5 and @6 located at the outside of the 1.5 m one block shielding concrete wall, gamma-ray dose rates are  $5.52 \times 10^{-3}$ ,  $5.70 \times 10^{-3}$  and  $5.28 \times 10^{-3}$  mrem/h. On the other hand, gamma-ray dose rates for model 2 are  $1.752 \times 10^{-3}$ ,  $1.70 \times 10^{-3}$  and  $2.26 \times 10^{-3}$  mrem/h. The gamma-ray dose rate is affected by the concrete geometry because absorption of neutrons is related to the thickness of shielding material. The dose rate shown in Figure 5 (d) is also influenced by the thickness of shielding material so that gamma-ray dose rates,  $0.53 \times 10^{-1}$  mrem/h, of model 1 is similar to that,  $0.53 \times 10^{-1}$  mrem/h, of model 2 because neutrons were absorbed in the first divided concrete, #1, #2 and #3, as shown in Figure 3.

These accuracy results indicated that we can adjust the operational parameters from radiation to protect workers and equipment if the thickness of shielding concrete is properly selected. We expect that these preliminary calculations of the gamma-ray dose rates for a various concrete geometry will contribute to the proper design and construction of radiation shielding. Those calculations offer guiding principles for safety when maintenance or repair is carried out near a cyclotron.

## Conclusions

A 13 MeV cyclotron facility for radiopharmaceutical production will be constructed as Pusan National University (PNU) in Korea. Radiation safety is an important issue for high intensity proton accelerators due to radiation hazard from neutrons and gamma-rays. Induced radionuclides in the 1.5 m thick concrete walls dominate the contributions to decay gamma-ray dose rate with  $1.84 \times 10^6$  rem/h after irradiation for 1 hour. A few differences for gamma-ray dose rates outside the shielding concrete is shown from the comparison between the one block shielding concrete model and shielding concrete

model divided into three parts. From this result, we can obtain improved accuracy for shielding concrete divided into many parts. However the work requires a very large calculation time to obtain the detailed neutron flux distribution in the overall region required to determine radiation dose rates.

## References

- [1] ANS-6.1.1 Working Group, M.E. Battat (Chairman), *American National Standard Neutron and Gamma-ray Flux-to-dose Rate Factors*, ANSI/ANS-6.1.1-1977(N666), American Nuclear Society, LaGrange Park, Illinois, 1977.
- [2] Y.S. Kim, D.H. An, J.S. Chai, H.S. Chang, B.H. Hong, S.S. Hong, I.S. Jung, J.S. Kang, M.Y. Lee, C.S. Park, J.Y. Suk, T.K. Yang, "KIRAMS-13 Cyclotron for Regional Cyclotron Center", 3<sup>rd</sup> APAC (unpublished), 2004.
- [3] L.R. Carroll, "Predicting Long-lived, Neutron-induced Activation of Concrete in a Cyclotron Vault", *AIP Conference Proceedings*, 576 (1), p. 301, 2001.
- [4] International Commission on Radiation Units and Measurements, *Radiation Quantities and Units*, ICRU Report 33, ICRU, Bethesda, 1980.
- [5] J.H. Park, N.Z. Cho, J. Kim, "Neutron Analysis of the KSTAR Tokamak Using Beowulf Cluster", *J. Nucl. Sci. Technol.*, Sup. 1, p. 276, 2000.
- [6] H.D. Kim, H.S. Lee, S.M. Hong, M.H. Kim, C.W. Chung, C.S. Kim, "Radioactivity Evaluation for the KSTAR Tokmak", 10<sup>th</sup> Int. Conf. Radiation Shielding(ICRS-10) and 13<sup>th</sup> Topical Meeting on Radiation Protection and Shielding (RPS-2004), 2004.
- [7] T. Zaga, M. Ravnik, "Neutron Activation Measurements in Research Reactor Concrete Shield", *Int. Conf. Nuclear Energy in Central Europe*, 2001.
- [8] T. Ichikawa, H. Koizumi, "Possibility of Radiation-induced Degradation of Concrete by Alkali-silica Reaction of Aggregates", *J. Nucl. Sci. Technol.*, 39 (8), p. 880, 2002.
- [9] M. Kinno, K.I. Kimura, T. Nakamura, "Raw Materials for Low-activation Concrete Neutron Shields", *J. Nucl. Sci. Technol.*, 39 (12), p. 1275, 2002.
- [10] H. Dinter, et al., "Studies on the Neutron Field Behind Shielding of Proton Accelerators, Part I: Concrete Shielding", *Nucl. Instrum. Methods*, A368, 265, 1996.
- [11] G.C. Moeller, R.J. Donahue, *Induced Radioactivity in Bevatron Concrete Radiation Shielding Blocks*, LBL-36072, 1994.
- [12] K. Nunighoff, et al., *Estimations of the Shielding Requirements for the Neutron Beam Line of the NSE Instrument at SNS and a First Engineering Design* (unpublished), 2004.



## Comparison between measured and calculated results of dose rate in 18 MeV X-ray radiotherapy room

**Koji Oishi,<sup>1</sup> Kosako Kazuaki,<sup>1</sup> Yuki Kobayashi,<sup>2</sup> Kiyoshi Kagawa,<sup>2</sup> Takashi Nakamura<sup>1</sup>**

<sup>1</sup>Institute of Technology, Shimizu Corporation, Koto-ku, Tokyo, Japan

<sup>2</sup>Giken Kogyo Co., LTD, Shibuya-ku, Tokyo, Japan

### Abstract

Measurements of dose rate for photons and neutrons have been performed in 18 MeV X-ray radiotherapy rooms by using glass dosimeter and CR-39. Dose rates in the maze and outside of the shielding door were also measured by using ionisation chamber and rem-counter.

The measured values were compared with calculated ones by using MCNP5 and empirical formula. For MCNP5 calculation, good agreements of photon dose rates were observed except few measured points, but overestimations for calculated neutron dose rates of about factor 2-4 were observed in the treatment room, except outside of the shielding wall. Investigations for the thickness of the target shield and the difference of the used nuclear data libraries were performed, but we could not solve these discrepancies. Good agreements in the maze were also observed between measured value and calculated results by empirical formula, though there existed large discrepancy of the calculated results outside of the shielding door greater than 1 order of magnitude.

To improve the accuracy of MCNP5 calculation, further investigation of layout and composition of structural and shielding materials around the target would be very necessary.

## 1 Introduction

We have indicated the validity of Monte Carlo calculation method for the estimation of penetrating dose rate behind the laminated shielding wall composed by concrete and iron at the last SATIF 7<sup>th</sup> meeting which was held in 2004 at Lisbon, Portugal [1]. It was found that the precise estimation of neutron dose rate produced by ( $\gamma,n$ ) reaction in the iron and secondary photon dose rate produced by ( $n,\gamma$ ) reaction in the rear concrete was very important for obtaining the dose rate behind the shielding wall.

The investigation of dose rate distribution of neutrons in the treatment room, which were produced by ( $\gamma,n$ ) reaction around the target and its shielding materials isotropically, is also very important for the estimation of exposure to patients from the safety stand point of view.

In this study, the measurements of neutron dose rate around the target of 18 MeV electron linac for medical use have been performed and compared with the calculated results by the Monte Carlo calculation code MCNP5 with its related nuclear data libraries.

We have also measured neutron and photon dose rate along the maze to verify the Monte Carlo calculation code system and the empirical calculation method.

## 2 Measurement

### 2.1 Irradiation condition

The plain view of 18 MeV electron linac treatment room is shown in Figure 2.1.

The linac was Varian CLINAC23EX which accelerating energy was 18 MeV and the dose rate at the isocentre was 6 Gy/min. Figure 2.2 shows the characteristics of beam condition of linac. The peak current and pulse width is 30 mA and 4  $\mu$ s, respectively. The repetition period was 188 pulses per second and the average current of the linac was 22.6  $\mu$ A.

Figure 2.1: Plain view of 18-MeV electron linac facility

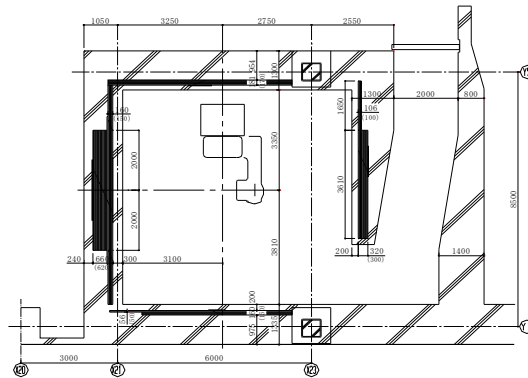
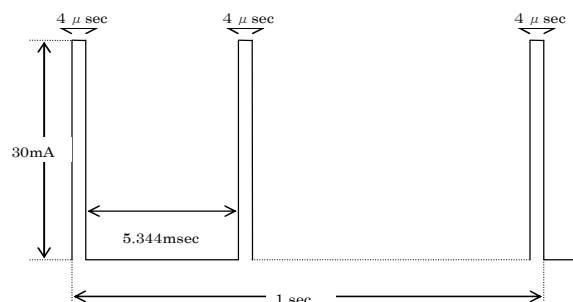


Figure 2.2: Beam condition of 18 MeV linac



## 2.2 Detectors

Since the nature of accelerator beam is pulsed one and the photon field is highly intense, the active detectors could not be adopted around the target. Passive detectors, CR-39 and glass dosimeters, were adopted for the measurement of dose rate of neutrons and photons, respectively. The measured position was along the beam line in the direction of 0 degree for neutrons and those of 45, 90, 135, 180, 225 and 315 degrees for neutrons and photons. We have also measured the distribution of dose rate of neutrons and photons in the vertical plain of the isocentre. The irradiation periods were varied from 1 minute to few minutes.

In the outer maze area where the influence of the primary beam would not be so high, we have adopted the rem-counter (Aloka TPS-451C) and ionisation detector (Victoreen 450-DE-SI) for the measurement of neutron dose and photon one, respectively. The measured positions were along the maze and outside of the shielding door.

## 3 Calculation

### 3.1 Around the target

Neutron and photon dose rate calculation by MCNP5 [2] was performed. The block diagram of calculation code system is shown in Figure 3.1.

The calculational condition is listed in Table 3.1. Since the detailed information of the structure and material around the target would not be well informed, we have simply modelled the structure around the target shown in Figure 3.2. We have mainly adopted LA150 as the nuclear data library, but to investigate the difference to the other nuclear libraries, we have also calculated by using other libraries which were processed from KAERI and JENDL evaluated nuclear data files. The process code was NJOY code system.

Figure 3.1: Block diagram of calculation code system

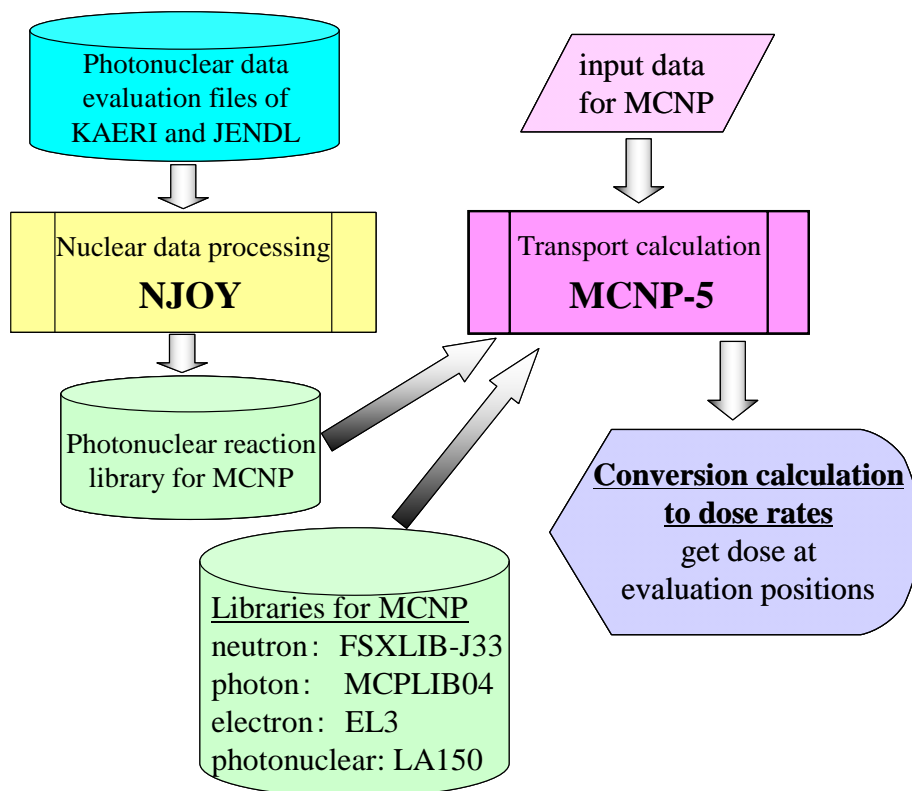


**Table 3.1: Calculational condition of dose rate around the target**

<b>Transport code</b>	MCNP5
<b>Cross-section library</b>	Neutron FSXLIB-J33 (JENDL-3.3) Photon & electron MCNPDATA Photonuclear LA150 (MCNPXDATA)
<b>Particle</b>	Neutron, photon, electron
<b>Target model</b>	Copper target ( $2 \times 2 \times 2$ [cm <sup>3</sup> ] of cubic) 18 MeV electron (pencil beam incident vertically to rear surface of target) Tungsten collimator (cylinder: inner is 3 cm-radius, outer 4 cm-radius, 5 cm-length; distance from target is 1 cm)
<b>Wall component</b>	Concrete (Type 02-a, density 2.3 [g/cm <sup>3</sup> ])
<b>Variance reduction</b>	None
<b>Cut-off energy</b>	0.3 MeV for electron
<b>Tally</b>	Point detector and cell tally
<b>Number of sources</b>	400-600 millions for electron
<b>Calculation time</b>	About 200 hours by 400 millions electrons (CPU: Intel Pentium-4, 3 GHz)

### 3.2 Maze

For the dose rate calculation along the maze, the empirical calculation method [3] was also performed in addition to the Monte Carlo calculation. The empirical equation adopted was as follows:

$$E_{sl} = S \times \dot{E}_1 \times \alpha \times T / a^2 b^2$$

where  $S$ : area of the wall that can be seen from the estimated position along the maze  
 $\dot{E}_1$ : neutron dose rate (mSv/min) 1 m from the target  
 $T$ : operation time  
 $a$ : distance from the target to the maze centreline at the wall  
 $b$ : centreline distance along the maze  
 $\alpha$ : scattering ratio for concrete,  $\alpha = 0.11(\cos\theta_0)^{2/3}\cos\theta$

Around the maze it is estimated that the ratio of thermal neutrons to the total was 0.3.

$$E_{th} = 0.3(E_{sl} + E_{th})$$

Total neutron dose will be:

$$E_{total} = E_{sl} + E_{th} = 1.43E_{sl}$$

Dose rate outside of the shielding door was estimated by using ANISN transport code and neutron dose rate was described by the combination of fast and slow neutron components.

$$E_n = E_{0n} [ae^{-\mu_1 x_1} + (1-a)e^{-\mu_2 x_1}]$$

where  $E_{0n}$ : neutron dose rate without shielding door  
 $x_1$ : thickness of polyethylene  
 $a, \mu_1, \mu_2$ : listed in Ref. [3]

The attenuation of secondary gamma-ray by the polyethylene with boron was:

$$E_\gamma = E_{1\gamma} [fe^{-\nu_1 x_2} + (1-f)e^{-\nu_2 x_2}]$$

The total dose rate of neutron and gamma-ray behind the shielding wall was:

$$E = E_{0n} \{ [ae^{-\mu_1 x_1} + (1-a)e^{-\mu_2 x_1}] + 0.1e^{-bx_1} [fe^{-\nu_1 x_2} + (1-f)e^{-\nu_2 x_2}] \}$$

Figure 3.2: Model of target assembly adopted by Monte Carlo calculation

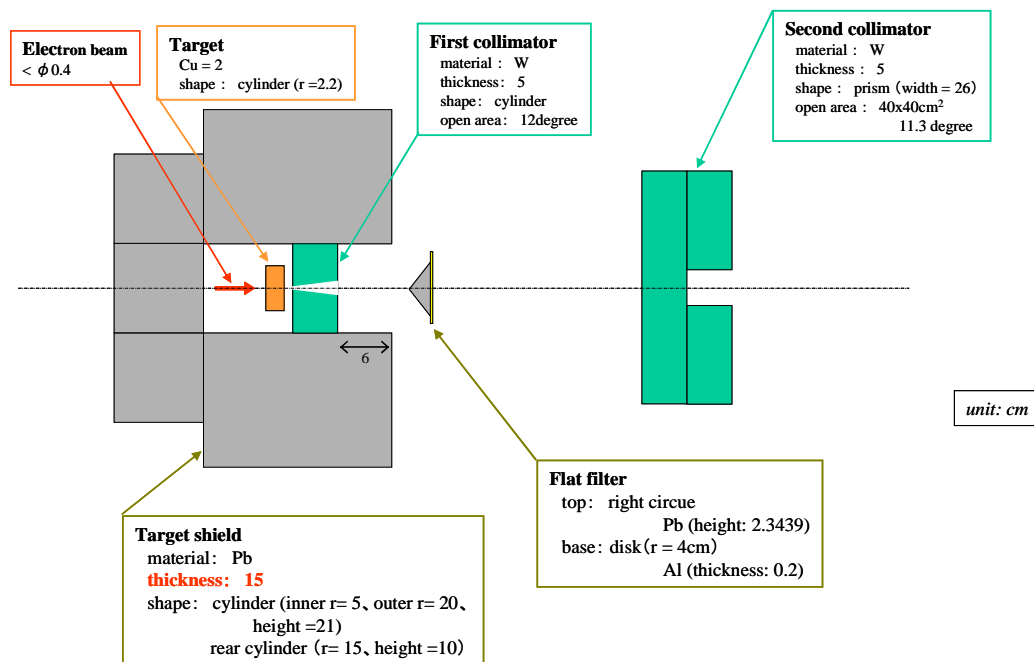
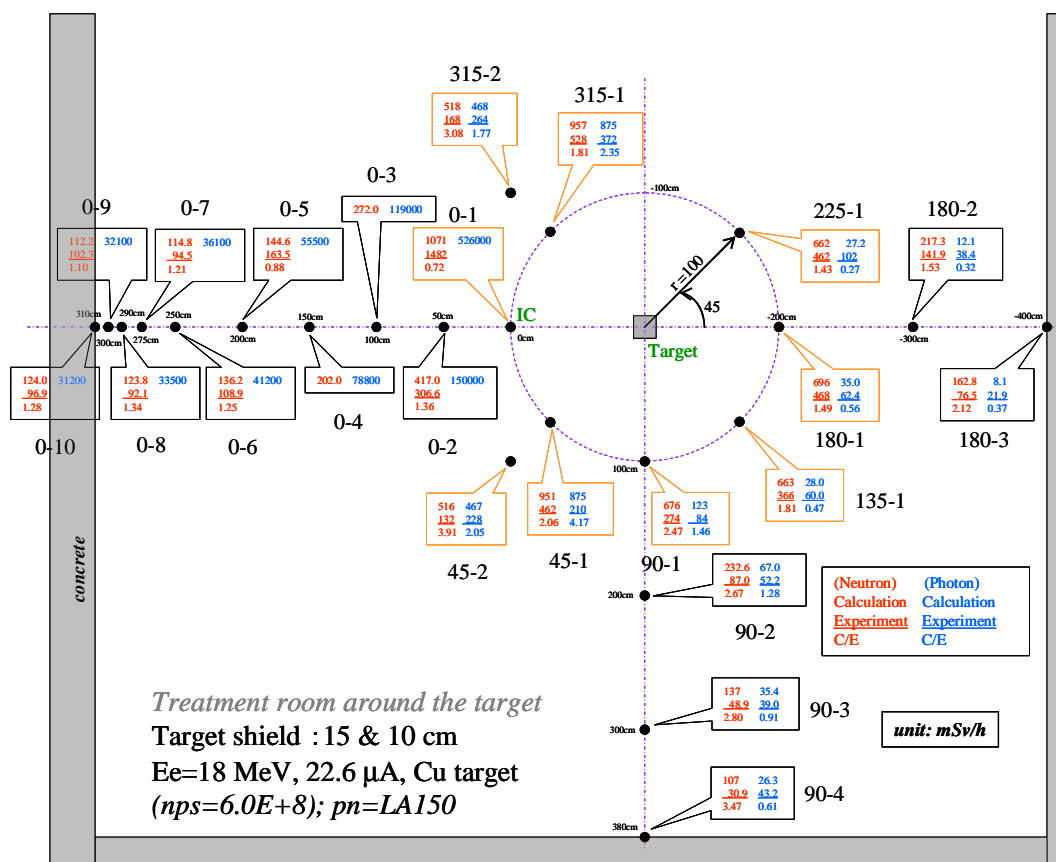
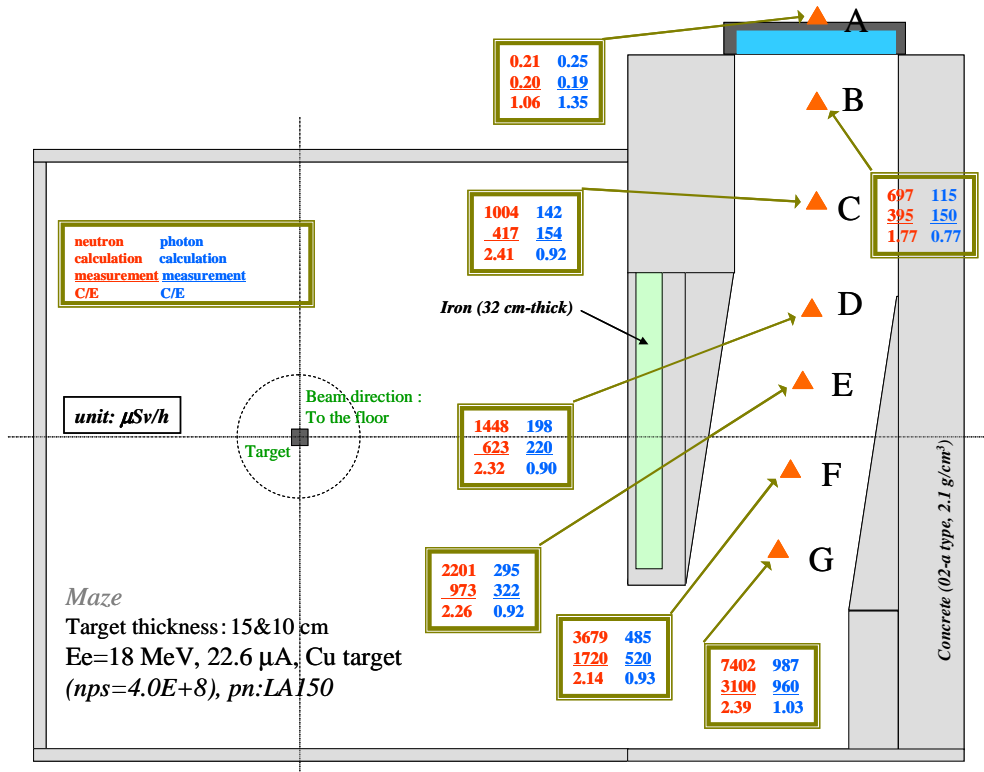


Figure 4.1: Comparison between measured and calculated results in the treatment room around the target



**Figure 4.2: Measured and calculated results by MCNP5 for dose rate of neutrons and photons along the maze**



## 4 Comparison between measurements and calculations

### 4.1 Treatment room around the target

The measured and calculated results by MCNP5 are shown in Figure 4.1. The C/E values of neutron dose rate in the direction of 0 degree to the beam line varied from 0.72 to 1.34. Very good agreement within 30% was obtained in the beam axis. However, in the other directions, 45, 90 and 180 degrees, all the calculated results of neutron dose rate overestimated measured ones of about factor 1.5~4.0. On the other hand, almost all of the calculated results for the photon dose rate in the direction of 90 and 180 degree to the beam line underestimated the measured ones.

This would be caused by the improper estimation of shield thickness around the target which is not being well informed. If the shield thickness were thinner than this model, the production of neutrons by the ( $\gamma,n$ ) reaction and the attenuation of photon would decrease.

The information of the fine structure of the shield and the collimator around the target is very necessary for the precise estimation of neutron and photon dose rate around the target except the beam line.

### 4.2 Maze

#### 4.2.1 MCNP5 calculation

Figure 4.2 shows the measured and calculated results by MCNP5 for dose rate of neutrons and photons along the maze. The estimated position is from A to G. The distance between the measured position was 1 m, except A and B. The distance between A and B was 0.75 m. The position of A is outside of the shielding door made of iron, polyethylene, lead and iron, which thickness were 12 mm, 160 mm, 80 mm and 12 mm. Note that the beam direction was to the floor.

Very good agreements between measured and calculated results of dose rate distributions for photons were obtained, C/E value from 0.77 to 1.35, though some discrepancies were observed those in the treatment room. It is assumed that the photon dose distribution in the treatment room would be averaged and canceled the inconsistencies at each estimated position.

For neutron dose rate distribution, calculated results overestimated the measured ones except at the position A, outside of the shielding door. The C/E values were very similar to those of treatment room, except beam line. The overestimation of neutron dose rates along the maze would also be due to the lack of detail information of the shielding structure around the target.

#### 4.2.2 Empirical calculation method

C/E value at each position of empirical calculation method is listed in Table 4.1 with those of MCNP5. Good agreements between empirical calculation method and measured one were obtained except position A and G for total dose rate. The empirical calculation method also underestimate photon dose and overestimate neutron dose as in case of MCNP5. However, very large overestimation of the neutron dose rate outside of the shielding door was observed, though the calculated result of MCNP5 agreed well with measured one.

## 5 Discussion

From the comparison between measured and calculated results by using MCNP5, it is concluded that the calculated dose rates of neutrons overestimated the measured ones both treatment room and maze. Since good agreements were obtained in the direction of 0 degree to the beam line, it may result from the ambiguities of calculation model of the shield structure around the target and/or applied nuclear data libraries. We have studied the influence on the calculated results by changing the model and nuclear data libraries.

### 5.1 Calculation model

We have applied the model of shielding structure around the target shown in Figure 3.2, the thickness of the cylinder was 15 cm and the height of the rear shield was 10 cm. We have recalculated two other cases, whole thickness was 10 cm and 15 cm, which kept consistencies for photon dose rate.

Figure 5.1 shows the calculated results of three cases of shielding structure. Horizontal axis is the estimated position and vertical one is the C/Es. Along the beam axis, position 0-1 to 0-10, very good agreement between measured and calculated results were obtained, where the influence of shielding structure is small. Though the overestimations of the calculated results were observed in the direction of 45, 90 and 315 degrees to the beam line, there was no significant difference among three shielding structure models.

The reason of the discrepancies would be due to the calculation model of the shielding structure around the target.

### 5.2 Nuclear data libraries

To examine the calculated results on the effect of difference of nuclear data libraries used for the calculations, two libraries are newly produced from photonuclear data library of KAERI and JENDL by using process code NJOY.

Figure 5.2 shows the results calculated by three different libraries. Some differences were observed in the direction of 90 degree to the beam axis, but other directions there were no significant difference among the results of calculations.

It is concluded that the ambiguities between measured and calculated results were not ascribable to the difference of nuclear data libraries.

Figure 5.1: C/Es of three cases of shielding structure

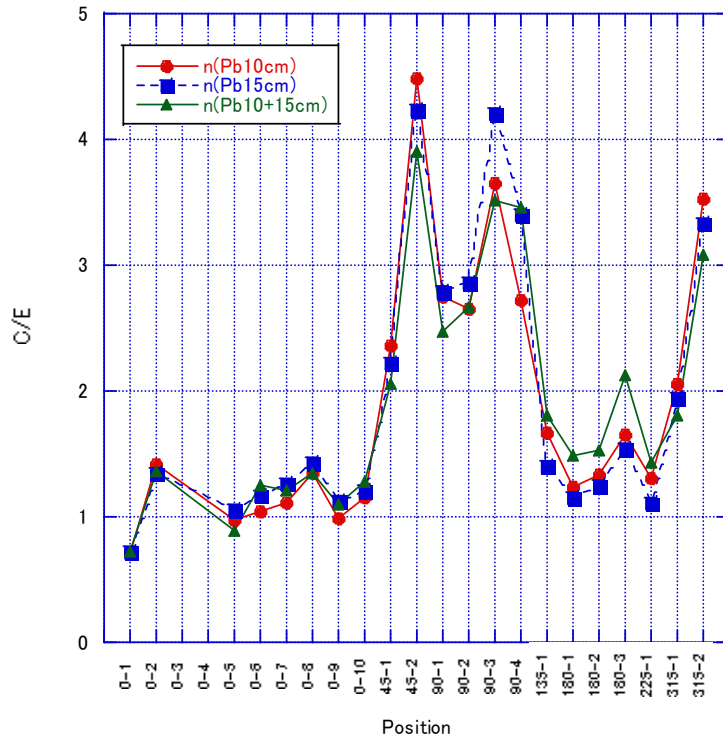
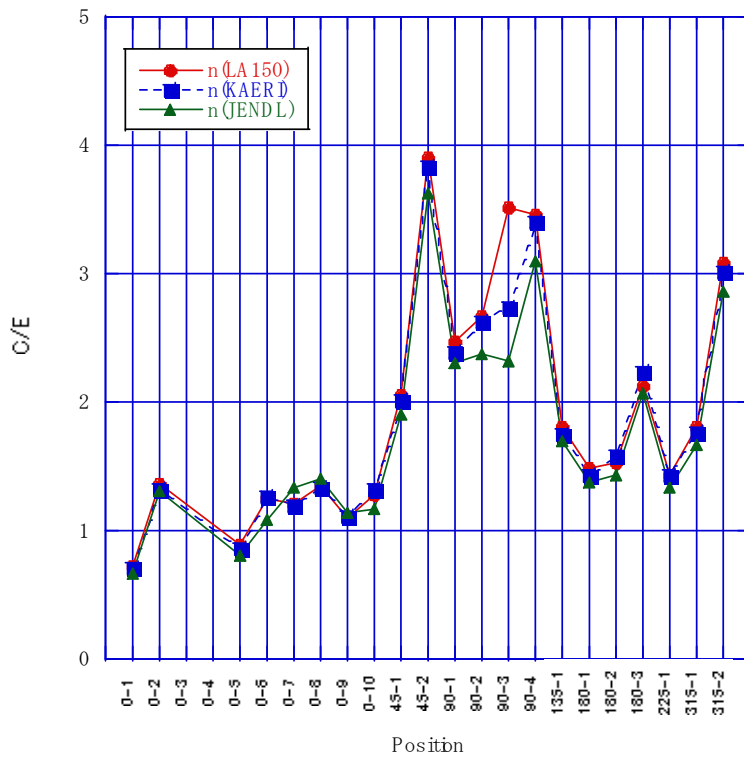


Figure 5.2: C/Es of different nuclear libraries



## 6 Conclusion

Measurements of neutron and photon dose rate in the treatment room of 18 MeV linac facility were performed and compared with calculated results by MCNP5 Monte Carlo calculation code with its related nuclear data libraries. Good agreements were obtained in the direction of 0-degree to the beam line for neutron dose rates, however overestimation up to factor 4 of the calculated results were observed. For the dose rates along the maze, there existed same tendencies as in the case with those of treatment room, though good agreements for photon dose rates were obtained.

Investigation for the thickness of the target shield and the difference of the used nuclear data libraries were performed, but we could not solve these discrepancies. Further investigation should be very necessary for the precise estimation of dose rate distribution around the gantry head of electron linac by the Monte Carlo calculation code system.

## References

- [1] K. Oishi, *et al.*, "Measurement and Analysis on Radiation Shielding of 18 MeV Electron Linac for Medical Use", pp. 159-170, SATIF-7, 17-18 May 2004.
- [2] X-5 Monte Carlo Team, *MCNP – A General-purpose Monte Carlo N-particle Transport Code, Version 5*, LA-UR-03-1987 (2003).
- [3] *Radiation Shielding Manual 2004* (in Japanese).



## Annex 1: List of participants

### France

DAVID, Jean-Christophe  
CEA-Saclay  
DAPNIA/SPHN  
F-91191 Gif-sur-Yvette

Tel: +33 169087277  
Fax: +33 169087584  
Eml: jean-christophe.david@cea.fr

RAPP, Benjamin  
CEA Saclay  
DSM/DAPNIA  
F-91191 Gif-sur-Yvette

Tel: +33 1 69087658  
Fax:  
Eml: benjamin.rapp@cea.fr

### Germany

DITTRICH, Wolfgang  
AREVA NP GmbH  
NEPR-G Strahlenschutz (Radiation Protection)  
Postfach 3220  
D-91050 Erlangen

Tel: +49 9131 18 96535  
Fax: +49 9131 18 97507  
Eml: Wolfgang.Dittrich@areva.com

KNAPP, Alexandra  
Safety and Radiation Protection  
GSI – Gesellschaft für Schwerionenforsch  
Planckstrasse 1  
D-64291 Darmstadt

Tel: +49 6159 71 1381  
Fax:  
Eml: a.knapp@gsi.de

LEUSCHNER, Albrecht  
Deutsches Elektronen-Synchrotron (DESY)  
Notkestrasse 85  
D-22607 Hamburg

Tel: +49 40 8998 2043  
Fax: +49 40 8994 2043  
Eml: Albrecht.Leuschner@desy.de

### Italy

FERNANDEZ, Jorge E.  
Laboratory of Montecuccolino-DIENCA  
University of Bologna  
via dei Colli, 16  
I-40136 Bologna

Tel: +39 051 644 1718  
Fax: +39 051 644 1747  
Eml: jorge.fernandez@unibo.it

### Japan

HIRAYAMA, Hideo  
Director, Applied Research Laboratory  
High Energy Accelerator  
Research Organisation (KEK)  
1-1 Oho  
Tsukuba-shi, Ibaraki-ken 305-0801

Tel: +81 298 64 5451  
Fax: +81 298 64 4051  
Eml: hideo.hirayama@kek.jp

IWAMOTO, Yousuke  
Japan Atomic Energy Agency  
Applied Radiation Physics Research  
2-4, Shirakata-shirane  
Tokai-mura, Naka-gun, Ibaraki 319-1195

Tel: +81 29 282 6704  
Fax: +81 29 284 3741  
Eml: iwamoto.yosuke@jaea.go.jp

MATSUMURA, Hiroshi  
KEK  
Radiation Science Center  
1-1 Oho, Tsukuba, Ibaraki 305-0801

Tel: +81 29 879 6003  
Fax: +81 29 864 4051  
Eml: hiroshi.matsumura@kek.jp

NAKAMURA, Takashi  
Prof. Emeritus  
Adviser of Shimizu Corp.  
Naka-cho  
2-19-5-104, Musashino, Tokyo 180-0006

Tel:  
Fax: +81 422-54-7899.  
Eml: nakamura.takashi@shimz.co.jp  
Eml: nakamura@cyric.tohoku.ac.jp

NAKASHIMA, Hiroshi  
Leader of Facility Safety Group  
Quantum Beam Science Directorate  
Japan Atomic Energy Agency  
Tokai, Naka, Ibaraki, 319-1195

Tel: +81-29-282-6144  
Fax: +81-29-284-3741  
Eml: nakashima.hiroshi@jaea.go.jp

NIITA, Koji  
Research Organisation for  
Information Science & Technology  
2-4 Shirane, Shirakata, Tokai, Naka  
Ibaraki, 319-1106

Tel: +81 29 284 3825  
Fax: +81 29 284 3741  
Eml: niita@tokai.rist.or.jp

OISHI, Koji  
Technology-Knowledge Management Centre  
Institute of Technology  
Shimizu Corporation  
3-4-17 Etsujima, Koto-ku, Tokyo 135-8530

Tel: +81 3-3820-6416  
Fax: +81 3-3643-7260  
Eml: koji\_oishi@shimz.co.jp

SAKAMOTO, Yukio  
Research Group for Applied Radiation Physics  
Nuclear Science and Engineering Directorate  
Japan Atomic Energy Agency  
Tokai-mura, Naka-gun  
Ibaraki-ken 319-1195

Tel: +81 29 282 5827  
Fax: +81 29 284 3741  
Eml: sakamoto.yukio@jaea.go.jp

SANAMI, Toshiya  
Radiation Science Center  
High Energy Accelerator  
Research Organisation (KEK)  
Oho 1-1, Tsukuba, Ibaraki 305-0801

Tel: +81 29 864 5490  
Fax: +81 29 864 1993  
Eml: toshiya.sanami@kek.jp

UWAMINO, Yoshitomo  
Safety Center, RIKEN  
2-1, Hirosawa, Wako, Saitama 351-0198

Tel: +81 48 462 6499  
Fax: +81 48 461 5301  
Eml: uwamino@riken.jp

## Republic of Korea

CHA, Bo Kyung  
Dept. Nuclear & Quantum Engineering  
Korea Advanced Institute of  
Science and Technology (KAIST)  
Daejeon 305-701

Tel: +82 42 869 3880  
Fax: +82 42 869 3810  
Eml: goldrain99@kaist.ac.kr

CHUNG, Chinwha  
 Head of Engineering Division  
 Pohang Accelerator Laboratory  
 Pohang Univ. of Science and Technology  
 31, Nam-gu, Pohang  
 Gyeongbuk 790-784

Tel: +82 54 279 1008  
 Fax: +82 54 279 1799  
 Eml: cwchung@postech.ac.kr

GIL, Choong Sup  
 Nuclear Data Evaluation Lab.  
 Koea Atomic Energy Research Institute  
 P.O. Box 105, Yuseong  
 Daejeon 305-600

Tel: +82 42 868  
 Fax: +82 42 868 2656  
 Eml: csgil@kaeri.re.kr

HONG, Sukmo  
 Radiation Safety Group  
 Pohang Accelerator Laboratory  
 Pohang Univ. of Science and Technology  
 31, Nam-gu, Pohang  
 Gyeongbuk 790-784

Tel: +82 54 279 1858  
 Fax: +82 54 279 1799  
 Eml: mo@postech.ac.kr

KHANDAKER, Mayeen Uddin  
 Kyungpook National University  
 Ph.D. Student  
 Department of Physics  
 Kyungpook National University  
 702-701, Daegu

Tel: +82 53 950 6383  
 Fax: +82 53 955 5356  
 Eml: mu\_khandaker@yahoo.com

KIM, Bong-Hwan  
 Health Physics Department  
 Korea Atomic Energy Research Institute  
 P.O. Box 105, Yuseong, Daejeon 305-600

Tel: +82 42 868 8386  
 Fax: +82 42 868 8609  
 Eml: bhkim2@kaeri.re.kr

KIM, Guinyun  
 Department of Physics  
 Kyungpook National University  
 1370 Sankyuk-Dong  
 Buk-Gu, Daegu 702-701

Tel: +82 53 950 5320  
 Fax: +82 53 955 5356  
 Eml: gnkim@knu.ac.kr

KIM, Hyunduk  
 Korea Advanced Institute of  
 Science and Technology (KAIST)  
 Dept. Nuclear & Quantum Engineering  
 Daejeon 305-701

Tel: +82 42 869 3880  
 Fax: +82 869 3810  
 Eml: kimhd@kaist.ac.kr

KIM, Jong-Won  
 National Cancer Centre  
 Dept. Biochemical Engineering  
 809 Madu-dong, Ilsan-gu  
 Koyang, Kyonggi, 410-769

Tel: +82 31 920 1727  
 Fax:  
 Eml: jwkim@ncc.re.kr

KO, Insoo  
 Director  
 Pohang Accelerator Laboratory  
 Pohang Univ. of Science and Technology  
 31, Nam-gu, Pohang  
 Gyongbuk Province, 790-784

Tel: +82 54 279 1001  
 Fax: +82 54 279 0999  
 Eml: isko@postech.ac.kr

LEE, Cheol Woo Nuclear Data Evaluation Lab. Korea Atomic Energy Research Institute P.O. Box 105, Yuseong Daejeon 305-600	Tel: +82 42 868 2297 Fax: +82 42 868 2656 Eml: cwl@kaeri.re.kr
LEE, Hee-Seock(Chairman) Manager of Radiation Safety Group Pohang Accelerator Laboratory Pohang Univ. of Science and Technology 31, Nam-gu, Pohang Gyeongbuk Province, 790-784	Tel: +82 54 279 1854 Fax: +82 54 279 1799 Eml: lee@postech.ac.kr
LEE, Jae-Seong Regulatory Research Division Korea Institute of Nuclear Safety 19 Kusong-dong, Yusung-gu Daejeon 305-338	Tel: +82 42 868 0332 Fax: +82 42 861 9945 Eml: jslee@kins.re.kr
LEE, Young-Ouk Korea Atomic Energy Research Institute P.O. Box 105 Yuseong, 305-600 Daejeon	Tel: +82 42 868 2764 Fax: +82 42 868 2636 Eml: yolee@kaeri.re.kr
MIN, Chul Hee Hanyang University Department of Nuclear Engineering Seoul 133-791	Tel: +82 2 2299 3057 Fax: +82 2 2299 3057 Eml: mch0909@hotmail.com
NA, Seong Ho Regulatory Research Division Korea Institute of Nuclear Safety 19 Kusong-dong, Yusung-gu Daejeon 305-338	Tel: +82 42 868 0302 Fax: +82 42 861 9945 Eml: shna@kins.re.kr
QIU, Rui Radiation Safety Group Pohang Accelerator Laboratory Pohang Univ. of Science and Technology 31, Nam-gu, Pohang Gyeongbuk 790-784 PhD Student of Tsinghua University	Tel: +82 54 279 1860 Fax: +82 54 279 1799 Eml: qiur@postech.ac.kr
RYU, Hyung-Jun Student Dept. of Nuclear Engineering Hanyang University 17 Haengdang-dong Seongdong-gu, Seoul	Tel: +82 2 2220 0571 Fax: +82 2 2296 3690 Eml: hjryu@rrl.hanyang.ac.kr

## Portugal

VAZ, Pedro Instituto Tecnológico e Nuclear/DPRSN Estrada Nacional 10 P-2686-953 Sacavem	Tel: +351 21 994 62 30 Fax: +351 21 994 19 95 Eml: pedrovaz@itn.pt
--	--

**Switzerland**

TEICHMANN, Sabine  
Paul Scherrer Institut  
AEA Division WMHA/C44  
CH-5232 Villigen PSI

Tel: +41 (0) 56 310 4375  
Fax: +41 (0) 56 310 3717  
Eml: sabine.teichmann@psi.ch

**United States of America**

IPE, Nisy Elizabeth  
Consultant,  
Shielding Design  
Dosimetry & Radiation Protection  
3117 La Mesa Drive  
San Carlos, CA 94070

Tel: +1 650 631 1916  
Fax: +1 650 631 1916  
Eml: nisy@comcast.net

KIRK, Bernadette L.  
Director  
RSICC/ORNL  
PO Box 2008  
Bldg. 5700, MS 6171  
Oak Ridge, TN 37831-6171

Tel: +1 865 574 6176  
Fax: +1 8652414046  
Eml: kirkbl@ornl.gov

KOI, Tatsumi  
SCCS  
Stanford Linear Accelerator Center  
MS 97  
P.O. Box 20450  
Stanford, CA 94205

Tel: +1 650 926 4816  
Fax: +1 650 926 3329  
Eml: tkoi@slac.stanford.edu

MAO, X. Stan  
Stanford Linear Accelerator Center  
2575 Sand Hill Road  
Menlo Park, CA 94025

Tel: +1 650 926 4317  
Fax: +1 650 926 3569  
Eml: mao@slac.stanford.edu

MOKHOV, Nikolai V.  
FERMILAB  
MS 220  
P.O. Box 500  
Batavia, IL 60510

Tel: +1 (630) 840 4409  
Fax: +1 (630) 840 6039  
Eml: mokhov@fnal.gov

ROKNI, Sayed H.  
Radiation Physicist  
Stanford Linear Accelerator Center  
MS 48, P.O. Box 20450  
Stanford, CA 94309

Tel: +1 650 926 3544  
Fax: +1 650 926 3169  
Eml: rokni@slac.stanford.edu

**International organisations**

BRUGGER, Markus  
CERN/AB  
865-RC-009  
CH-1211 Geneva 23

Tel: +41 22 767 6556  
Fax: +41 22 767 5700  
Eml: markus.brugger@cern.ch

FELCINI, Marta  
CERN  
AB Department  
CH-1211 Geneva

Tel: +41 22 7671749  
Fax:  
Eml: marta.felcini@cern.ch

ROESLER, Stefan  
CERN  
SC/RP  
CH-1211 Geneva 23

Tel: +41 22 7679891  
Fax: +41 22 7669639  
Eml: Stefan.Roesler@cern.ch

SILARI, Marco  
CERN  
SC/RP  
CH-1211 Geneva 23

Tel: +41 22 767 3937  
Fax: +41 22 767 9360  
Eml: marco.silari@cern.ch

VLACHOUDIS, Vasilis  
CERN  
Dep. AB  
CERN-1211  
CH-1211 Geneva 23

Tel: +41 22 76 79 851  
Fax: +41 22 76 69644  
Eml: Vasilis.Vlachoudis@cern.ch

SARTORI, Enrico (Secretary)  
OECD/NEA Data Bank  
Le Seine-Saint Germain  
12 boulevard des Iles  
F-92130 Issy-les-Moulineaux

Tel: +33 1 45 24 10 72 / 78  
Fax: +33 1 45 24 11 10 / 28  
Eml: sartori@nea.fr

## Annex 2: Technical programme

**Monday, 22 May 2006**

Registration

Welcome

### Introduction

**Chair: H.S. Lee**

*T. Nakamura, L. Heilbronn*

Introduction to “Handbook on Secondary Particle Production and Transport by High-energy Heavy Ions”

*Y. Sakamoto, O. Sato, H. Hirayama*

Standard data of dose conversion coefficients in Japan

*A. Leuschner, A. Klett*

A new method for pulsed neutron monitoring with the rem-counter lb 6411 and time-resolved readout

### Session I **Source term and related topics**

**Chair: S. Teichmann**

*S. Teichmann*

Shielding parameters of concrete and polyethylene for the PSI proton accelerator facilities

*B-H. Kim, H-K. Kim, S-W. Kwak, H-S. Lee*

Calculation of the neutron spectra at the electron test linac of PAL and the MC50 proton accelerator of KIRAMS

*X.S. Mao, W.R. Nelson, A.A. Prinz*

Comparison between the source terms used in SHIELD11 and the source terms calculated by FLUKA

*T. Sanami, M. Hagiwara, T. Oishi, S. Kamada, T. Okuji, M. Baba, M. Takada, N. Miyahara, H. Nakashima, Y. Iwamoto, S. Tanaka, T. Kaneko*

Double differential cross-section of fragment production by tens of MeV protons and neutrons

### Session II **Shielding at high energy accelerators**

**Chair: T. Nakamura**

*H. Nakashima, T. Shibata, Y. Nakane, F. Masukawa, N. Matsuda, Y. Iwamoto, M. Harada, S. Meigo, Y. Kasugai, F. Maekawa, H. Takada, C. Konno, M. Teshigawara, M. Ohi, T. Kai, H. Hirayama, T. Suzuki, T. Miura, M. Numajiri, N. Nakao*

Radiation shielding design for the J-PARC project

*Y. Uwamino, N. Fukunishi, H. Sakamoto, S. Fujita*

Safety design of the Radioactive Isotope Beam Factory (RIBF) at RIKEN

*A. Knapp, T. Radon, G. Moustafina, F. Gutermuth, G. Fehrenbacher*

Monte Carlo simulations for the shielding of FLAIR

*M. Felcini, A. Herrera-Martínez, Y. Kadi, T. Otto, L. Tecchio*  
Design of the EURISOL Multi-MW target assembly: Radiation and safety issues

*V. Vlachoudis, A. Ferrari, M. Magistris, M. Santana-Leitner*  
Overview of the protection and shielding studies for the Betatron cleaning insertion at LHC

### **Session III Induced radioactivity and activation data**

#### **Chair: M. Silari**

*M. Brugger, A. Ferrari, M. Magistris, S. Roesler, J. Voltaire*  
Calculation of radioactive isotope production cross-sections with FLUKA and their application to radiological studies

*M.U. Khandaker, K. Kim, G. Kim, Y.S. Lee*  
Experimental studies of proton induced reaction cross-sections on natural molybdenum

*R. Qiu, H-S. Lee, S. Hong, J. Li*  
Simulation and measurement of induced radioactivity in permanent magnet

*H. Matsumura, N. Nakao, K. Masumoto, K. Oishi, M. Kawai, T. Aze, A. Toyoda, M. Numajiri, K. Takahashi, M. Fujimura, Q. Wang, K. Bessho, T. Sanami*  
Production yields of the radionuclides induced in various targets fixed in concrete shield at the 500-MeV neutron irradiation facility of KENS

*J-C. David, A. Boudard, S. Lemaire, S. Leray, S. Panebianco*  
Megapie: Residue yields and radioactivity predictions with different models in MCNPX

*V. Hedberg, M. Magistris, M.N. Morev, M. Silari, Z. Zajacova*  
Radioactive waste study of the ATLAS detector

## **Tuesday, 23 May 2006**

### **Session IV Benchmarking – calculations and results**

#### **Chairs: H. Hirayama, A. Leuschner**

*Y. Iwamoto, S. Taniguchi, N. Nakao, T. Itoga, T. Nakamura, Y. Nakane, H. Nakashima, D. Satoh, H. Yashima, H. Yamakawa, K. Oishi, A. Tamii, K. Hatanaka*  
Thick target neutron yield at 0 degree by 250 and 350 MeV protons

*M. Felcini, P. Vaz*  
Proposal for multi-megawatt power target benchmarks

*N. Nakao, S. Taniguchi, S.H. Rokni, S. Roesler, M. Brugger, M. Hagiwara, H. Vincke, H. Khater, A.A. Prinz*  
Measurement of neutron energy spectra behind shielding at 120 GeV/c hadron beam facility, CERF

*N. Nakao, S.H. Rokni, M. Brugger, S. Roesler, H. Vincke, K. Kosako*  
Calculation of high-energy neutron spectra with different Monte Carlo transport codes and comparison to experimental data obtained at the CERF facility

*H. Hirayama, Attenuation Length Sub-working Group of Japan*  
Inter-comparison of medium-energy neutron attenuation in iron and concrete (6)

*B. Rapp, J.C. David, V. Blideanu, D. Doré, D. Ridikas, N. Thiollière*  
Benchmarking of the modelling tools within the EURISOL DS project

*J.E. Fernandez, V. Scot*  
Benchmarking the MCSHAPE3D code with 1-D, 2-D and 3-D imaging experiments

*H-S. Lee, S. Ban, T. Sanami, K. Takahashi, T. Sato, R. Qiu*  
Measurements and benchmark simulations of photo-neutron yields from targets irradiated by 2.0 and 2.5 GeV electrons

C.W. Lee, Y-S. Cho, Y-O. Lee

Analysis of the residual radiation field in the proton accelerator facility of the Proton Engineering Frontier Project (PEFP) in Korea

G. Kim, A.K.M.M.H. Meaze, M.U. Khandaker, Y.D. Oh, H. Kang, M-H. Cho, I.S. Ko, W. Namkung, T-I. Ro, W-C. Chung, Y.A. Kim, K.J. Yoo, Y.O. Lee

Measurement of neutron total cross-sections at the Pohang neutron facility

## **Session V Status of computer codes, cross sections and shielding data libraries**

**Chair: N.V. Mokhov**

I. Kodeli, E. Sartori, B.L. Kirk

Status and future plans for the international radiations shielding and dosimetry experiments (SINBAD) database

H. Henriksson, I. Kodeli, E. Sartori, B.L. Kirk

Update on recent computer codes and data libraries of interest to SATIF – Status: May 2006

N.V. Mokhov

Recent developments and applications of the MARS15 code

K. Niita, H. Nakashima, T. Sato, N. Matsuda, Y. Iwamoto, Y. Sakamoto, H. Iwase, L. Sihver, D. Mancusi

The present status of the PHITS code

V. Vlachoudis, F. Ballarini, G. Battistoni, M. Campanella, M. Carboni, F. Cerutti, A. Empl, A. Fassò, A. Ferrari, E. Gadioli, M.V. Garzelli, A. Mairani, A. Mostacci, S. Muraro, A. Ottolenghi, M. Pelliccioni, L. Pinsky, J. Ranft, S. Roesler, P.R. Sala, D. Scannicchio, R. Villari

FLUKA: New features and a general overview

T. Koi, D.H. Wright

Recent developments in Geant4

## **Wednesday, 24 May 2006**

### **Session VI Shielding in medical and industrial accelerator applications**

**Chairs: N.E. Ipe, B.L. Kirk**

B.L. Kirk, A. Haghighat

Computational medical physics working group

W. Dittrich, T. Hansmann

Radiation measurements at the RPTC in Munich for verification of shielding measures around the cyclotron area

N.E. Ipe, A. Fassò

Preliminary computational models for shielding design of particle therapy facilities

H-J. Ryu, J-K. Lee, J-W. Kim, H-S. Kim, J-W. Kwon, J. Blaze

Simulations and measurements of the neutron equivalent doses for the proton therapy facility at the National Cancer Centre

N.E. Ipe

An overview of NCRP report 151: Structural shielding design and evaluation report for megavoltage X- and gamma-ray radiotherapy facilities

H-D. Kim, G-S. Cho, B-K. Cha, J-K. Ahn

Estimation of radiation shielding for a cyclotron vault

K. Oishi, K. Kazuaki, Y. Kobayashi, K. Kagawa, T. Nakamura

Comparison between measured and calculated results of dose rate in 18 MeV X-ray radiotherapy room

**Session VII Follow-up of past SATIF agreements and actions**

**Chair: P. Vaz**

*P. Vaz*

Status of accelerator shielding handbook

**Session VIII Discussion/summary and future actions**

**Chairs: H.S. Lee, P. Vaz**